ICET 2015

ICET 2015

The 7th PSU-UNS International Conference on Engineering and Technology

June 19-20, 2015

DUANGJITT RESORT & SPA Patong Beach, Phuket Thailand

The 7th PSU-UNS International Conference on Engineering and Technology

June 19-20, 2015

DUANGJITT RESORT & SPA Patong Beach, Phuket Thailand

Main Sponsor

Sponsors

Message from Our Advisory Committee

Associate Professor Dr.Chusak Limsakul
THE PRESIDENT OF PRINCE OF SONGKLA UNIVERSITY

For nearly a decade, our relationship with the University of Novi Sad has grown more and more bountiful. Beginning with a visiting Professor called Mio Thai to a group of energetic and spirited students from Novi Sad, our friendship had blossomed. The fruits from our agreements have been the establishment of the PSU-UNS International Conferences. This year, the Faculty of Engineering has the great pleasure of hosting the 7th PSU-UNS International Conferences on Engineering and Technology (ICET-2015). With so many researchers and participants from varying fields of engineering and sciences present, these conferences should provide a wonderful environment for the gathering of ideas and experiences which could essentially lead to future research collaborations and the development of new technology and innovations. Not only will these academic exchanges support the critical national and global agenda on energy and the environment, they will also help to promote the development of applicable technology that can serve from regional communities to small and large industries alike. At this time, I would like to once again congratulate Faculty of Engineering here at Price of Songkla University and the Faculty of Technical Sciences from the University of Novi Sad for working together in putting forth the ICET-2015, as well as all of the other valuable organizers who have made the ICET-2015 possible. Finally, I would also like to wish the conference lead to a series of enlightening discussions that will benefit all of your future research works. I would like to wish the conference great success and achieve all of the goals that it has set for.

Associate Professor Dr. Chusak Limsakul
(President, Prince of Songkla University)

Message from the Conference Chair

Associate Professor Dr.Udomphon Puetpaiboon
Dean of the Faculty of Engineering, Prince of Songkla University

It is a great honor and privilege for us, in conjunction with the Faculty of Technical Sciences at the University of Novi Sad (UNS), to have the opportunity to host the 7th PSU-UNS International Conference on Engineering and Technology (ICET-2015). In order to make note of this wonderful occasion, the faculty decided to hold the ICET-2015 with the 11th Annual PSU Engineering Conference (PEC-11). Moreover, we select the beautiful Duangjitt Resort and Spa to truly provide all participants with an enjoyable and relaxing atmosphere for the grand event. As our main objective, we hope to offer these conferences as a forum for researchers from the field of engineering, sciences, and technology from around the world to come together, to share their valuable findings and to take part in stimulating discussions. Over 100 participants are expected at these 2 conferences.

In addition, the conference will have the honor of presenting Professor Dr. Branislav Borovac from University of Novi Sad, Associate Professor Dr.Suchart Limkatanyu from Prince of Songkla University, Professor Dr.Dragan Seslija from University of Novi Sad and Professor Ir. Dr. Mohd Zainal Abidin Abdul Kadir from University Putra Malaysia as our keynote speakers. Last, but not least, in the name of the conference organizing committee, I would like to thank PSU and Thailand's Commission on Higher Education for their valuable support. Special thanks must also go out to members of the Advisory Committee, the Organizing Committee, everyone from the Faculty of Engineering at PSU and our correspondence from the Faculty of Technical Sciences at UNS who have contributed their valuable time and efforts in putting these conferences together.

U. Puetpaiboon.

Associate Professor Dr.Udomphon Puetpaiboon
(Dean, Faculty of Engineering, PSU)

Conference Committee

Advisory Committee
Prof. Dr. Miroslav Veskovic
University of Novi Sad

Advisory Committee
Assoc. Prof. Dr. Chusak Limsakul
Prince of Songkla University

Conference Chair
Assoc. Prof. Dr.Udomphon Puetpaiboon
Prince of Songkla University

Conference Co-Chair
Prof. Dr. Rade Doroslovacki
University of Novi Sad

Conference Committee

Prof. Dr. Rade Doroslovački (UNS)
Assoc. Prof. Panyarak Ngamsritragul (PSU)
Assoc. Prof. Kanadit Chetpattananondh (PSU)
Assoc. Prof. Dr. Sukritthira Ratanawilai (PSU)
Asst. Prof. Dr. Theerayut Leevijit (PSU)
Assoc. Prof. Dr. Pornchai Phukpattaranont (PSU)
Asst. Prof. Dr. Jareerat Sakulrat (PSU)
Dr. Wissanoo Rachpech (PSU)
Asst. Prof. Dr. Nikom Suvonvorn (PSU)
Assoc. Prof. Dr. Chayanoot Sangwichien (PSU)
Assoc. Prof. Dr. Thaniya Kaosol (PSU)
Asst. Prof. Dr. Wannarat Suntiamorntut (PSU)
Dr. Kiattisak Wongsopanakul (PSU)
Asst. Prof. Charoen Jaitwijitra (PSU)
Assoc. Prof. Dr. Wiriya Thongruang (PSU)
Asst. Prof. Dr. Manoon Masniyom (PSU)
Asst. Prof. Dr. Sangsuree Vasupongayya (PSU)
Prof. Dr. Vladimir Katić (UNS)
Prof. Dr. Dragan Šešlija (UNS)
Prof. Dr. Branislav Borovac (UNS)
Prof. Dr. Dušan Gvozdenac (UNS)
Prof. Dr. Miodrag Zlokolica (UNS)
Assoc. Prof. Dr. Goran Vujić (UNS)
Vladimir Todorović (UNS)

Programming committee

Asst. Prof. Dr. Napisphon Meemongkol, Thailand
Assoc. Prof. Somchai Chuchom, Thailand
Assoc. Prof. Dr. Seksan Suthummanon, Thailand
Asst. Prof. Dr. Tanan Chub-uppakarn, Thailand
Assoc. Prof. Dr. Thaniya Kaosol, Thailand
Assoc. Prof. Dr. Supawan Tirawanichakul, Thailand
Asst. Prof. Dr. Manoon Masniyom, Thailand
Dr. Somjai janudom, Thailand
Asst. Prof. Dr. Pichaya Tandayya, Thailand
Asst. Prof. Dr. Chayut Nuntadusit, Thailand
Ms. Chalita Hiransoog, Thailand
Asst. Prof. Dr. Kusumal Chalermyanont, Thailand
Assoc. Prof. Booncharoen Wongkittisuksa, Thailand
Asst. Prof. Dr. Watcharawalee Tangkuptanon, Thailand
Asst. Prof. Dr. Sangsuree Vasupongayya, Thailand
Prof. Dr. Dragan Spasić , Serbia
Prof. Dr. Nikola Jorgovanović, Serbia
Prof. Dr. Neda Mimica-Dukić, Serbia
Prof. Dr. Marijana Ačanski, Serbia
Prof. Dr. Radomir Folić, Prof. Emeritus, Serbia
Prof. Dr. Srdjan Kolaković, Serbia
Prof. Dr. Vlastimir Radonjanin, Serbia
Prof. Dr. Nikola Teslić, Serbia
Prof. Dr. Miodrag Temerinac, Serbia
Prof. Dr. Dragan Kukolj, Serbia
Prof. Dr. Dušan Gvozdenac, Serbia
Prof. Dr. Vladimir Katić, Serbia
Prof. Dr. Mila Stojaković, Serbia
Prof. Dr. Dragiša Vilotić, Serbia
Assoc. Prof. Dr. Goran Vujić, Serbia
Prof. Dr. Milan Martinov, Serbia
Prof. Dr. Dragan Šešlija, Serbia
Prof. Dr. Ilija Ćosić, Serbia
Asst. Prof. Dr. Bojan Lalić, Serbia
Prof. Dr. Ivan Beker, Serbia
Prof. Dr. Branislav Borovac, Serbia
Prof. Dr. Livija Cvetićanin, Serbia
Prof. Dr. Miodrag Zlokolica, Prof. Emeritus, Serbia
Prof. Dr. Leposava Šiđanin, Prof. Emeritus, Serbia
Assoc. Prof. Dr. Sebastijan Baloš, Serbia
Prof. Dr. Katarina Gerić, Serbia
Prof. Dr. Milan Pavlovic, Serbia
Prof. Dr. Vladimir Strezoski, Serbia
Prof. Dr. Zora Konjović, Serbia
Prof. Dr. Miroslav Hajduković, Serbia
Asst. Prof. Dr. Vladimir Zlokolica, Serbia
Prof. Dr. Vojin Grković, Serbia
Prof. Dr. Dušan Uzelac, Serbia
Assoc. Prof. Dr. Maša Bukurov, Serbia
Prof. Dr. Milan Zeljković, Serbia
Prof. Dr. Pavel Kovač, Serbia
Prof. Dr. Branko Škorić, Serbia
Assoc. Prof. Dr. Miodrag Hadžistević, Serbia
Prof. Dr. Marin Gostimirović, Serbia
Assoc. Prof. Dr. Slobodan Tabaković, Serbia
Prof. Dr. Mirjana Vojinović Miloradov, Prof. Emeritus, Serbia
Assoc. Prof. Dr. Branka Nakomčić-Smaragdakis, Serbia
Prof. Dr. Stevan Stankovski, Serbia
Prof. Dr. Jovan Vladić, Serbia
Prof. Dr. Milosav Georgijević, Serbia
Prof. Dr. Chunhong Liu, China
Prof. Dr. Xu Ming, China
Prof. Dr. Xu Qi, China
Prof. Dr. Zhao Xiaokang, China
Prof. Dr. David Cui, China
Prof. Dr. Ni Lan, China
Prof. Dr. Wang Wen, China
Prof. Dr. Alexander Makedonski, Bulgaria
Prof. Dr. Georgi Popov, Bulgaria
Prof. Dr. Branko Katalinić, Austria
Prof. Dr. Sabahudin Ekinović, BiH
Prof. Dr. Darko Petković, BiH
Prof. Dr. Csaba Gyenge, Romania
Prof. Dr. Nenad Pavlović, Serbia
Prof. Dr. Miodrag Stoimenov, Serbia
Prof. Dr. Ivan Prebil, Slovenia
Prof. Dr. Gyula Varga, Hungary
Prof. Dr. Vincent Hugel, France
Prof. Dr. Wilfred Kubinger, Austria
Prof. Dr Achim Gottscheber, Germany

Reviewer List

1.	Marijana	Ačanski	UNS
2.	Touchai	Angchuan	PSU
3.	Jutamanee	Auysakul	PSU
4.	Sebastijan	Baloš	UNS
5.	Ivan	Beker	UNS
6.	Branislav	Borovac	UNS
7.	Maša	Bukurov	UNS
8.	Pitsanu	Bunnaul	PSU
9.	Charun	Bunyakan	PSU
10.	Dujdow	Buranapanichkit	PSU
11.	Panyayot	Chaikan	PSU
12.	Sumate	Chaiprapat	PSU
13.	Supapan	Chaiprapat	PSU
14.	Passagorn	Chaiviriyawong	PSU
15.	Tanit	Chalermyanont	PSU
16.	Kusumal	Chalermyanont	PSU
17.	Wisarut	Chantara	PSU
18.	Kullawat	Chaowanawatee	PSU
19.	Sakuna	Charoenpanyasak	PSU
20.	Pakamas	Chetpattananondh	PSU
21.	Kanadit	Chetpattananondh	PSU
22.	Anant	Choksuriwong	PSU
23.	Mitchai	Chongcheawchamnan	PSU
24.	Sininart	Chongkhong	PSU
25.	Tanan	Chub-uppakarn	PSU
26.	Somchai	Chuchom	PSU
27.	Worraprot	Chukumnird	PSU
28.	Juntima	Chungsiriporn	PSU
29.	Ilija	Ćosić	UNS
30.	Livija	Cvetićanin	UNS
31.	Wikhanet	Damkhong	PSU
32.	Andrew	Davison	PSU
33.	Charoenyut	Dechwayukul	PSU
34.	Amarin	Deemagarn	PSU
35.	Rakkrit	Duangsoithong	PSU
36.	Chanint	Dumraskarn	PSU
37.	Radomir	Folić	UNS
38.	Katarina	Gerić	UNS
39.	Sarawut	Gonsrang	PSU
40.	Marin	Gostimirović	UNS
41.	Vojin	Grković	UNS
42.	Dušan	Gvozdenac	UNS
43.	Miodrag	Hadžistević	UNS
44.	Miroslav	Hajduković	UNS
45.	Chalita	Hiransoog	PSU
46.	Prakit	Honghirunruang	PSU
47.	Pakpoom	Hoyingcharoen	PSU
48.	Charoen	Jaitwijitra	PSU
49.	Chatchai	Jantaraprim	PSU
50.	Somjai	janudom	PSU
51.	Saravut	Jaritngam	PSU
52.	Nattha	Jindapetch	PSU
53.	Suriya	Jirasatitsin	PSU
54.	Nikola	Jorgovanović	UNS
55.	Pongsiri	Julapong	PSU
56.	Winit	Jungcharoentham	PSU
57.	Watcharin	Kaewapichai	PSU
58.	Wichairat	Kaewjuea	PSU
59.	Yossawee	Kaewmanee	PSU
60.	Pornsiri	Kaewpradit	PSU
61.	Damrong	Kalawdee	PSU
62.	Thossaporn	Kamolphiwong	PSU
63.	Sinchai	Kamolphiwong	PSU
64.	Komsan	Kanjanasit	PSU
65.	Thaniya	Kaosol	PSU
66.	Montri	Karnjanadecha	PSU
67.	Vladimir	Katić	UNS
68.	Thanate	Khaorapapong	PSU
69.	Watsa	Khongnakorn	PSU
70.	Phanumas	Khumsat	PSU
71.	Montep	Kiatweerasakul	PSU
72.	Pairoj	Kirirat	PSU
73.	Nattawan	Kladkaew	PSU
74.	Paijit	Kochakornjarupong	PSU
75.	Srdjan	Kolaković	UNS
76.	Wanatchapong	Kongkaew	PSU

Reviewer List

77. Zora Konjović UNS
78. Kalayanee Kooptarnond PSU
79. Pavel Kovač UNS
80. Suratsawadee Kungsanant PSU
81. Bojan Lalić UNS
82. Theerayut Leevijit PSU
83. Noppon Lertchuwongsa PSU
84. Suchart Limkatanyu PSU
85. Chusak Limsakul PSU
86. Somchai Limsiroratana PSU
87. Paramet Luathep PSU
88. Kittinan Maliwan PSU
89. Boonrueing Manasurakan PSU
90. Milan Martinov UNS
91. Manoon Masniyom PSU
92. Napisphon Meemongkol PSU
93. Mirjana Vojinović Miloradov UNS
94. Neda Mimica-Dukić UNS
95. Prapas Muangjunburee PSU
96. Charongpun Musikavong PSU
97. Somkiat Nakgul PSU
98. Branka Nakomčić-Smaragdakis UNS
99. Nunthaphan Naphattharanun PSU
100. Paramin Neranon PSU
101. Panyarak Ngamsritragul PSU
102. Chayut Nuntadusit PSU
103. Pattamad Panedpojaman PSU
104. Wasimon Panichpattanakul PSU
105. Paripon Pattanasattayavong PSU
106. Pornchai Phukpattaranont PSU
107. Sitthichai Piriyakoontorn PSU
108. Pijit Pissuwan PSU
109. Kamron Pitak PSU
110. Soontorn Piyaratanawong PSU
111. Klangduen Pochana PSU
112. Somboon Pornpinatepong PSU
113. Woraphot Prachasaree PSU
114. Suteera Prasertsan PSU
115. Kulchanat Prasertsit PSU
116. Anuwat Prasertsit PSU
117. Gumpon Prateepchaikul PSU
118. Sakchai Prechaverakul PSU
119. Udomphon Puetpaiboon PSU
120. Vishnu RachPhet PSU
121. Vlastimir Radonjanin UNS
122. Thanate Ratanawilai PSU
123. Sukritthira Ratanawilai PSU
124. Wanida Rattanamanee PSU
125. Payom Rattanamanee PSU
126. Taweesak Reungpeerakul PSU
127. Sompat Roongtawanreongsri PSU
128. Mongkol Saechia PSU
129. Somchai Saeung PSU
130. Suthon Sae-wong PSU
131. Agarat Samakrattakit PSU
132. Thammaratt Samitalampa PSU
133. Chayanoot Sangwichien PSU
134. Leposava Šiđanin UNS
135. Lek Sikong PSU
136. Runchana Sinthavalai PSU
137. Nikorn Sirivongpaisal PSU
138. Branko Škorić UNS
139. Pruittikorn Smithmaitrie PSU
140. Krit Somnuk PSU
141. Phongpat Sontamino PSU
142. Jeerapa Sookgaew PSU
143. Dragan Spasić UNS
144. Chatchawin Srisuwan PSU
145. Mila Stojaković UNS
146. Jakapan Suaboot PSU
147. Jareerat Sukkulrat PSU
148. Sutham Sukmanee PSU
149. Chaisri Suksaroj PSU
150. Angoon Sungkapong PSU
151. Wannarat Suntiamorntut PSU
152. Petcharat Suriyachai PSU

Reviewer List

153. Seksan Suthummanon PSU
154. Nikom Suvonvorn PSU
155. Seksun Suwanmanee PSU
156. Slobodan Tabaković UNS
157. Pichaya Tandayya PSU
158. Pichai Taneerananon PSU
159. Kuljaree Tantayakul PSU
160. Sawit Tanthanuch PSU
161. Sanguan Taungbodhitham PSU
162. Jantakan Taweekun PSU
163. Wiklom Teerapabkajorndet PSU
164. Aree Teeraparbseree PSU
165. Perapong Tekasakul PSU
166. Miodrag Temerinac UNS
167. Nikola Teslić UNS
168. Chakadkit Thaenchaikun PSU
169. Thawatchai Thangrattanasuwan PSU
170. Thanansak Theppaya PSU
171. Surapol Thienmontri PSU
172. Kunlapat Thongkaew PSU
173. Suriyah Thongmunee PSU
174. Krerkchai Thongnoo PSU
175. Kittikhun Thongpull PSU
176. Wiriya Thongruang PSU
177. Supawan Tirawanichakul PSU
178. Chakrit Tongurai PSU
179. Danupon Tonnayopas PSU
180. Pichet Trakanchaisiri PSU
181. Laksiri Treeranurat PSU
182. Mallika Unhawiwat PSU
183. Dušan Uzelac UNS
184. Apichat vapichart PSU
185. Sangsuree Vasupongayya PSU
186. Hathaichanok Vattanasak PSU
187. Passakorn Vessakosol PSU
188. Dragiša Vilotić UNS
189. Nitipan Vittayaphadung PSU
190. Goran Vujic UNS
191. Jessada Wanansin PSU
192. Ornkamon Wang-a-pisit PSU
193. Warodom Werapun PSU
194. Warit Wichkul PSU
195. Worawut Wisutmethangoon PSU
196. Suntorn Witosurapot PSU
197. Sivasit Wittayasilp PSU
198. Booncharoen Wongkittisuksa PSU
199. Kiattisak Wongsopanakul PSU
200. Phairote Woonchum PSU
201. Ram Yamsaengsung PSU
202. Jindaporn Yaothak PSU
203. Vladimir Zlokolica UNS

Conference Schedule

"The 11th PSU Engineering Conference (PEC-11) and The 7th International Conference on Engineering and Technology (ICET 2015)"

FRIDAY, June 19, 2015

8:00 am – 9:00 am	Registration			
9:00 am – 9:30 am	Opening Ceremonies (Duangchanok Room)			
9:30 am – 10:00 am	**Keynote Address :** Prof. Dr. Branislav Borovac ; University of Novi Sad **Title "Biped locomotion: history and perspectives"** **(Duangchanok Room)**			
10:00 am - 10:15 am	Tea Break (Duangdao Square)			
10:15 am – 12:15 pm	**ICET I** Assoc.Dr.Pornchai Phukpattaranont **Duangthip Room**	**ICET II** Assoc.Prof.Dr. Suchart Limkatanyu **Duangkamol Room**	**PEC I** Asst.Prof.Sanguan Taungbodhitham **Duangkaew Room**	**PEC II** Mr.Pakpoom Hoyingcharoen **Duangmanee Room**
12:15 pm – 1:00 pm	Lunch Break (Duangchanok Room)			
1:00 pm – 3:00 pm	**ICET III** Assoc.Prof.Dr. Nattha Jindapetch **Duangthip Room**	**ICET IV** Assoc.Prof.Panyarak Ngamsritragul **Duangkamol Room**	**PEC III** Asst.Prof.Dr.Nikom Suvonvorn **Duangkaew Room**	**PEC IV** Asst.Prof.Dr.Jareerat Sukkulrat **Duangmanee Room**
3:00 pm – 3:15 pm	Tea Break (Duangdao Square)			
3:15 pm – 4:45 pm	**ICET V** Asst.Prof.Dr.Ram Yamsaengsung **Duangthip Room**	**ICET VI** Asst.Prof.Dr.Manoon Masniyom **Duangkamol Room**	**PEC V** Asst.Prof.Dr. Theerayut Leevijit **Duangkaew Room**	**PEC VI** PSU.UPM.SEMINAR **Duangmanee Room**
6:30 pm – 9:00 pm	Welcome Dinner **"Andaman Theme"** (Duangchanok Room)			

Conference Schedule

"The 11th PSU Engineering Conference (PEC-11) and The 7th International Conference on Engineering and Technology (ICET 2015)"

SATURDAY, June 20, 2015

9:00 am - 9:25 am 9:25 am – 9:50 am 9.50 am – 10.15 am		**Keynote Address 1 :** Assoc. Prof. Suchart Limkatanyu ; Prince of Songkla University **Title "Finite frame elements with lateral interfaces : from geotechnical-engineering to nano-engineering applications"** **Keynote Address 2 :** Prof. Dr. Dragan Seslija ; University of Novi Sad **Title "An Overview of Energy Efficient Pneumatic Control"** **Keynote Address 3 :** Prof. Ir. Dr Mohd Zainal Abidin Abdul Kadir (Top Young Scientist Malaysia) ; University Putra Malaysia **Title "Lightning Parameters for Engineering Application in Tropical Countries"** **(Duangthip Room)**			
10:15 am - 10:30 am		Tea Break (Duangdao Square)			
10:30 am - 12:30 am		**ICET VII** Dr.Warit Wichakool **Duangthip Room**	**ICET VIII** Asst.Prof.Dr.Kusumal Chalermyanont **Duangkamol Room**	**PEC VII** Dr.Phairote wounchoum **Duangkaew Room**	**PEC VIII** **Duangmanee Room**
12:30 pm – 1:30 pm		Lunch Break (Duangchanok Room)			

ICET 2015 Schedule

FRIDAY, JUNE 19, 2015			
ICET I : Duangthip Room		Session Chair : Assoc.Prof.Dr.Pornchai Phukpattaranont	
Time	Paper ID	Title	Authors
10.15-10.30	20	A low cost, rapid prototyping of microfluidic device: an approach to separate blood plasma	Cheewarak Rodniam, Somyot Chirasatitsin
10.30-10.45	23	Passive Micromixer of a Microfluidic Chip Fabricated by the Xurographic Technique	Mahdee Samae, Somyot Chirasatitsin
10.45-11.00	33	Traffic Conditions Influence on Critical Headway at Unsignalized Intersections	Vuk Bogdanović, Zoran Papić, Valentina Basarić, Nenad Ruškić
11.00-11.15	96	Modification of baroreflex sensitivity in Control breathing	Isoon Kanjanasurat, Suradej Tretriluxana
11.15-11.30	31	Formal Verification of Gearman Framework based on PHP	Warush Leekasem, Denduang Pradubsuwun
11.30-11.45	87	A Conceptual Framework transforms The Player into Buyers on Mobile Applications: A Case Study of Mobile Social Network Games	Metawat Kavilkrue, Witchakon Khuankaew

ICET 2015 Schedule

FRIDAY, JUNE 19, 2015			
ICET II : Duangkamol Room		Session Chair : Assoc.Prof.Dr.Suchart Limkatanyu	
Time	Paper ID	Title	Authors
10.15-10.30	66	Air Quality modeling: Case study Novi Sad	Bogdana Vujic, Milan Pavlovic, Aleksandar Tomovic
10.30-10.45	91	Risk Assessment of Landfills in Serbia Based on Flooding Potential	Dejan Ubavin, Nikola Maodus, Srdjan Kovacevic, Bojan Batinic, Maja Djogo
10.45-11.00	113	Low Population Density Influence on Waste Management System in Serbia	Dusan Milovanovic, Nemanja Stanisavljevic, Miodrag Zivancev, Bojan Batinic, Dejan Ubavin, Maja Djogo, Marjan Ranogajec
11.00-11.15	27	Determination of Mean Values of Common Distributions in Civil Engineering from the Specifications for Mass Production	Kong Kamollertvara, Winai Ouypornprasert
11.15-11.30	75	Model selection for minimal daily pavement temperatures at Awbari in Libya	Hassan Awadat Salem, Zagorka Lozanov-Crvenković, Emilija Nikolić-Đorić, Bojan Matić
11.30-11.45	86	Seasonal Asphalt Concrete Surface Pavement Temperature Models Using Neural Networks	Bojan Matić, Vlastimir Radonjanin, Mirjana Malešev, Nebojša Radović, Siniša Sremac
11.45-12.00	126	Basic Properties of Structural LWAC Based on Waste Materials	Vlastimir Radonjanin, Mirjana Malešev, Miroslava Radeka, Ivan Lukić, Vesna Bulatović
12.00-12.15	127	LWAC Based on Waste Materials and Application in Thermally Improved Masonry	Mirjana Malešev, Vlastimir Radonjanin, Vesna Bulatovic, Ivan Lukic, Gordana Broceta

ICET 2015 Schedule

FRIDAY, JUNE 19, 2015			
ICET III : Duangthip Room		Session Chair : Assoc.Prof.Dr.Nattha Jindapetch	
Time	Paper ID	Title	Authors
13:00-13:15	6	Animated 3D Virtual Worlds Using Java and SketchUp	Chonmaphat Roonnapak, Andrew Davison
13:15-13:30	77	Small project examination timetabling assignment with multi-level penalty values	Trirat Soemsap
13:30-13:45	101	Evaluation of a Map Matching Algorithm for Indoor Localization with OpenStreetMap	Levent Bayindir
13:45-14:00	46	Automatic Onset Time Detection for a SEMG Measurement System	Chaiwat Lersviriyanantakul, Apidet Booranawong, Pornchai Phukpattaranont, Nattha Jindapetch
14:00-14:15	68	The Choice of Muscles Impacts the Linear Relationship between the Probability Density Function of Surface EMG Signal and the Level of Contraction Force	Sirinee Thongpanja, Angkoon Phinyomark, Franck Quaine, Chusak Limsakul, Pornchai Phukpattaranont
14:15-14:30	128	Dielectric Properties of Palm Oil and Coconut Oil under Thermal Ageing	N. A. Mohamad, N. Azis, J. Jasni, M.Z.A. Ab Kadir, R. Yunus, M. T. Ishak, Z. Yaakub
14:30-14:45	129	Hydrogen Gas Sensor Using Double SAW Resonator System	Zainab Yunusa, Mohd Nizar Hamidon, Alyani Ismail, Maryam Mohd Isa, Mohd Hanif Yaacob, Saeed Rahmanian, Siti Azlida Ibrahim, Arafat A.A Shabaneh
14:45-15:00	130	Investigation on Touch Area of Under Foot Pressure Based-on Weight Measurements	O. Hussein, W.Z. Wan Hasan, A. Che Soh. H. Jafaar

ICET 2015 Schedule

FRIDAY, JUNE 19, 2015			
ICET IV : Duangkamol Room		Session Chair : Assoc.Prof.Panyarak Ngamsritragul	
Time	Paper ID	Title	Authors
13:00-13:15	120	Energy and Economic Effects of Electricity and Heat Cogeneration with Combined Technologies of Corn Cobs Gasification and Gas Turbines	Milana Guteša, Branka Gvozdenac Urošević, Vojin Grković
13:15-13:30	121	Advanced Wind Energy System with Sensorless Controlled Six-phase Generator	Boris Dumnic, Dragan Milicevic, Bane Popadic, Vladimir Katic, Zoltan Corba
13:30-13:45	124	Solar PV System Grid Integration Issues - Harmonics	Vladimir A. Katic, Zoltan Corba, Boris Dumnic, Dragan Milicevic, Stevan Grabic, Nenad Katic
13:45-14:00	7	The Role of Energy Efficiency in Decarbonizing Thailand's Energy System	Aumnad Phdungsilp
14:00-14:15	70	Energy Indicators Of Public Buildings In Ap Vojvodina With Focus On Hospitals, Schools and Administrative Buildings	Jovan Petrovic, Milovan Medojevic, Milana Peric, Igor Mujan
14:15-14:30	94	Modelling of Energy Efficiency Cart of Solar Energy Collectors	Pavel Kovač, Vladan Petrovic, Vladimir Pucovski, Bojan Bircanin, Borislav Savkovic, Marin Gostimirovic, Krzysztof Rokosz
14:30-14:45	10	Analytical Solution of Temperature Fields and Effectiveness of Multi-Pass Cross-Flow Heat Exchanger	Dušan Gvozdenac
14:45-15:00	114	Investigation of air pressure drop through porous wheat straw bed	Đorđije Doder, Borivoj Stepanov

ICET 2015 Schedule

FRIDAY, JUNE 19, 2015			
ICET V : Duangthip Room		Session Chair : Asst.Prof.Dr.Ram Yamsaengsung	
Time	Paper ID	Title	Authors
15:15-15:30	26	Set-point Optimization Using Kalman Filter for Vertical Filling Weighing System	Sakkarin Sinchai, Jeerasuda Koseeyaporn, Paramote Wardkein
15:30-15:45	76	Experimental Research on the Surface Roughness of Creep-Feed Grinding Process	Marin Gostimirovic, Pavel Kovač, Ildiko Mankova, Borislav Savkovic, Milenko Sekulić
15:45-16:00	88	The Effects of High Temperature to Read-Head Instability	Tossapon Kijpitak, Wanchai Pijitrojana, Kasin Vichienchom
16:00-16:15	89	Characteristics of Head Gimbal Assembly (HGA) component relate to solder joint reliability.	Kanokpong Thongkorn, Monsak Pimsarn
16:15-16:30	52	Perceptions of Distributive Justice Among Employees in Country in Transition: The case of the Republic of Serbia	Srecko Stamenkovic, Biljana Ratkovic Njegovan
16:30-16:45	24	Analysis of Active Filter Circuit Basic using MATLAB-GUI for Electrical Engineering Education	Sommart Khamkleang
16:45-17:00	131	Software for Market Validation of the Recycling Equipment	Pavlović Milan, Arsovski Slavko, Tadić Danijela, Pavlović Aleksandar, Tomović Aleksandar

ICET 2015 Schedule

FRIDAY, JUNE 19, 2015			
ICET VI : Duangkamol Room		Session Chair : Asst.Prof.Dr.Manoon Masniyom	
Time	Paper ID	Title	Authors
15:15-15:30	95	Removal of H2S from Biogas by KMnO4 Impregnated Activated Carbon	Kawalin Prathomravee, Wisitsree Wiyaratn, Juntima Chungsiriporn
15:30-15:45	40	Effect of Gas Metal Arc Welding Speed on Tensile Properties of SUS304 Stainless Steel and SS400 Carbon Steel Butt Joint	Pramote Poonnayom, Paiboon Yaemphuarn, Kittipong Kimapong
15:45-16:00	41	Fracture Strength and Failure Location of GMAW Lap Joint between SS400 Carbon Steel and SUS304 Stainless Steel	Sakchai Chantasri, Kittipong Kimapong
16:00-16:15	4	Movement of feldspar mining cost at Noppitam District	Parinya Pattanadech, Manoon Masniyom
16:15-16:30	8	Effects of Sugar Cane Bagasse Ash with High LOI Value on Basalt Aggregate Concrete Properties	Rapipat Yongmanee, Danupon Tonnayopas
16:30-16:45	12	Simulation model of haulage system(Shovel and trucks) at Mae Moh Lignite mine Lampang	Siwarin Kanthik, Manoon Masniyom
16:45-17:00	35	Effects of US-EDM-Complex Vibration on Machining of WC-Co	Chaiya Praneetpongrung, Sakchai Chantasri, Paitoon Poolsukho

ICET 2015 Schedule

SATURDAY, JUNE 20, 2015			
ICET VII : Duangthip Room		Session Chair : Dr.Warit Wichakool	
Time	Paper ID	Title	Authors
10:30-10:45	29	The Dynamic Behavior of the Speed Variator with Unpredictably Changing Mode of Operation	Miodrag Zlokolica, Maja Čavić, Milan Kostić
10:45-11:00	62	Dual Mode Impedance Controller for Safe Human-Robot Interaction	Srđan Savić, Branislav Borovac, Mirko Raković, Milutin Nikolić
11:00-11:15	67	Implementing Augmented Reality in Disassembly Process	Srdjan Tegeltija, Milovan Lazarevic, Stevan Stankovski, Gordana Ostojic
11:15-11:30	98	Design of Real-Time External Force/Position Controller for Human-Robot Interaction	Paramin Neranon, Robert Bicker
11:30-11:45	99	System for assistance during evacuation process	Srdjan Tegeltija, Nikola Djukic, Branislav Tejic, Gordana Ostojic, Stevan Stankovski
11:45-12:00	100	Comparison of PI and Fuzzy Logic Controllers in Human-Robot Handover Task	Paramin Neranon, Robert Bicker
12:00-12:15	111	FEM Modeling of the Multi-Segment Lumbar Spine for Humanoid Robots	Marko Penčić, Branislav Borovac, Dušan Kovačević
12:15-12:30	32	Peak Vehicle Lateral Acceleration at Obstacle Evasive Manoeuvre	Zoran Papić, Vuk Bogdanovic, Milan Simeunovic, Nenad Saulic

ICET 2015 Schedule

SATURDAY, JUNE 20, 2015			
ICET VIII : Duangkamol Room		Session Chair : Asst.Prof.Dr.Kusumal Chalermyanont	
Time	Paper ID	Title	Authors
10:30-10:45	83	Procedure for Development and Testing of Power Electronics Control Systems Based on HIL Technology	Marko Vekic, Stevan Grabic, Zoran Ivanovic, Vlado Porobic, Vladimir Katic
10:45-11:00	84	Wind Turbine integration into the smart grid in case of unbalanced voltage conditions	Zoran Ivanovic, Marko Vekic, Evgenije Adzic, Vlado Porobic, Vladimir Katic
11:00-11:15	85	Sensorless vector control of induction motor with current reconstruction method	Evgenije Adzic, Vlado Porobic, Zoran Ivanovic, Marko Vekic, Stevan Grabic
11:15-11:30	118	Controller Embedded Oscilloscope Functionality for Power Converter Applications	Vlado Porobic, Milan Rapaic, Stevan Grabic, Evgenije Adzic, Marko Vekic
11:30-11:45	79	Factors Influencing the Implementation of NFC Smart Posters	Wasinee Noonpakdee, Patchareerat Mitchorb
11:45-12:00	115	Speech Emotion Classifier using Support Vector Machine with FFT and MFCC	Chaidiaw Thiangtham, Jakkree Srinonchat
12:00-12:15	80	DECCE - Development of Engineer's Competencies by Changes in Education	Dušan Kovačević, Leposava Grubic-Nesic, Aco Antic, Slavica Mitrovic, Jelena Nikolic

Keynote Speaker

Professor Dr. Branislav Borovac

University of Novi Sad

Title: **Biped locomotion: history and perspectives**

The synthesis of artificial gait of humanoid robots has been for a long time based on an approach that is currently still in use, and which assumes the calculation of the reference trajectories of all joints which are afterwards realized as accurately as possible. The first method for synthesis of dynamically balanced gait was the semi-inverse method introduced by Vukobratovic. In this approach, for one part of the system (legs), the motion is prescribed. The motion of the rest of the system is such determined to ensure a dynamic balance while walking, i.e. zero-moment point (ZMP) should be at reference position inside support area. Numerous methods that have appeared afterwards represent only modifications and upgrading of this basic method.

Motion of the robots acting in living and working environment of humans cannot be programmed in advance because environment is unstructured and dynamic. This means that it is not possible to know in advance the exact arrangement and positions of the objects in the robot's immediate environment, and it is necessary to ensure that the decision about the motion characteristics (direction, speed, etc.), generation of the trajectory and its realization are performed on-line. Additional specificity of such environment is that ground floor may not always be perfectly flat and uniform (stairs, different ground levels, sills,...) and wheels are not able to ensure required mobility. Locomotion on two legs seems to be only way to be appropriate. However, biped locomotion is not an easy and simple engineering task. At least two requirements have to be fulfilled simultaneously:

1. legs have to be driven in such a way to ensure system to be "transferred" to desired location along selected path, while

2. whole body motion have to be coordinated in such a synergetic manner to permanently ensure dynamic balance.

However, looking at humans, walk itself appear to be simple and easy for realization. Neurological studies of human walk have shown that certain modes of legs motion become the patterns that are constantly repeated. However, there is no need that all steps are identical. Shape of the movements that constitute the pattern are often changed and modified to adapt to the instantaneous situation. If the robot has an humanoid structure whose characteristics are similar to those of man, then it is possible for gait realization to apply the same concept.

In this presentation it will be presented new approach to the synthesis and realization of the modifiable walk of biped humanoid robots, which is based on the generation of complex motion by composing it from a set of predefined simple basic movements, called motion primitives. Based on the information about the current state of the environment, proposed approach enables on-line modification of the walking speed, step length, height of the leg during the swing phase and motion direction. To achieve this, system changes appropriately the parameters of the primitives during the motion, while constantly ensuring the dynamic balance.

Keynote Speaker

Associate Professor Dr. Suchart Limkatanyu

Prince of Songkla University

Title: **Finite frame elements with lateral interfaces: from geotechnical-engineering to nano-engineering applications**

This paper gathers the research work on the frame element with lateral interfaces. Several frame elements with lateral interfaces have been formulated by the author for the last ten years and have found a wide spectrum of engineering applications ranging from the problems of soil-geosynthetic interaction to nanobeams resting on elastic substrate medium. The general formulation of the frame element (bar and beam) with lateral interfaces is first discussed. Two conventional applications on geotechnical-engineering problems, namely: soil-geosynthetic and soil-pile systems are then presented. Finally, two novel applications on nano- and micro-engineering problems, namely: nanowire-elastic substrate and microbeam-elastic substrate systems are discussed.

Keynote Speaker

Professor Dr. Dragan Seslija

University of Novi Sad

Title: **An Overview of Energy Efficient Pneumatic Control**

Compressed-air systems account for approximately 10% of total energy use in industry as can be found in literature. In this paper is given an overview of compressed air energy savings with the emphasis on possibilities of savings at the compressed air end uses, particularly in pneumatic control systems. In a first part, an emphasis is given to systematic approach to energy savings. After that, various energy-saving measures, such as leak prevention (identification and quantification of leakages), reducing pressure drop on filters, optimization of pneumatic control (by-pass control, PWM control and usage of exhaust air) have been reviewed. Finally, attention is paid to the energy efficiency optimization of complex automated cells.

Keynote Speaker

Professor Ir. Dr. Mohd Zainal Abidin Abdul Kadir

University Putra Malaysia

Title: **Lightning Parameters for Engineering Application in Tropical Countries**

To the electric utility engineer, the parameters of the flash that are of primary interest are the crest current for the first and subsequent strokes, the waveshape of these currents, correlation between the parameters, the number of strokes per flash and flash incidence rates where the ground flash density, denoted as flashes per square km-year and symbolized by Ng. Also of some interest may be the charge lowered by the flash and perhaps the integral of the current squared, frequently called the "action integral. The first three parameters, as we know them today, are to a very large extent based on the measurements of Berger. Berger's masts, 70 and 80 meters high, were mounted atop Mt. San Salvatore (Switzerland), which is 650 meters above Lake Lugano. As stated previously, although 75% of the 1196 flashes measured were negative upward, about 11% or 125 flashes were negative downward. When it is realized that Berger made oscillographic recordings of the currents in both the first and the subsequent strokes of the flash, making all waveshape parameters and their correlation available, it can be readily noted that these 125 records represent one of the best and most extensive set of data available to the industry to date. However, several studies done to take photo from lightning, where the natural lightning channel usually has a ‘zigzag’ shape with some branches. In addition, the triggered lightning channel has usually a straight shape (or at least at some hundred meters to the ground surface) without any branches. While the triggered lightning remains as an important method for validation of the calculated electric and magnetic fields, this issue of vertical and inclined channel for instance remained as one of the parameters that need to be considered which can result in inaccuracy of the calculation.

Table of Contents

ID	Title	Page
4	Movement of feldspar mining cost at Noppitam District, Nakhon Si Thammarat Province	1
6	Animated 3D Virtual Worlds using JAVA and Sketchup	5
7	The Role of Energy Efficiency in Decarbonizing Thailand's Energy System	9
8	Effects of Sugar Cane Bagasse Ash with High LOI Value on Basalt Aggregate Concrete Properties	13
10	Analytical Solution of Temperature Fields and Effectiveness of Multi-Pass Cross-Flow Heat Exchanger	17
12	Simulation model of haulage system (Shovel and trucks) at Mae Moh Lignite mine Lampang, Thailand	21
20	A low cost, Rapid prototyping of Microfluidicdevice: an approach to separateblood plasma	24
23	Passive Micromixer of a Microfluidic Chip Fabricated by the Xurographic Technique	28
24	Analysis of Active Filter Circuit Basic using MATLAB-GUI for Electrical Engineering Education	32
26	Set-point Optimization Using Kálmán Filter for Vertical Filling Weighing System	36
27	Determination of Mean Values of Common Distributions in Civil Engineering from the Specifications for Mass Production	40
29	The Dynamic Behavior of the Speed Variator with Unpredictably Changing Mode of Operation	44
31	Formal Verification of Gearman Framework based on PHP	48
32	Peak Vehicle Lateral Acceleration at Obstacle Evasive Manoeuvre	52
33	Traffic Conditions Influence on Critical Headway at Unsignalized Intersections	56
35	Effects of US-EDM-Complex Vibration on Machining of WC-Co	60
40	Effect of Gas Metal Arc Welding Speed on Tensile Properties of SUS304 Stainless Steel and SS400 Carbon Steel Butt Joint	64
41	Fracture Strength and Failure Location of GMAW Lap Joint between SS400 Carbon Steel and SUS304 Stainless Steel	68
46	Automatic Onset Time Detection for a SEMG Measurement System	72
52	Perceptions of Distributive Justice Among Employees in Country in Transition: The case of the Republic of Serbia	76
62	Dual Mode Impedance Controller for Safe Human-Robot Interaction	80
66	Air Quality modeling: Case study Novi Sad	84
67	Implementing Augmented Reality in Disassembly Process	88
68	The Choice of Muscles Impacts the Linear Relationship between the Probability Density Function of surface EMG Signal and the Level of Contraction Force	92

Table of Contents

ID	Title	Page
70	Energy Indicators of Public buildings in AP Vojvodina with focus on Hospitals, Schools and Administrative buildings	96
75	Model selection for minimal daily pavement temperatures at Awbari in Libya	100
76	Experimental Research on the Surface Roughness of Creep-Feed Grinding Process	104
77	Small Project Examination Timetabling Assignment with Multi-level Penalty Values	108
79	Factors Influencing the Implementation of NFC Smart Posters	112
80	DECCE - Development of Engineer's Competencies by Changes in Education	115
83	Procedure for Development and Testing of Power Electronics Control Systems Based on HIL Technology	119
84	Wind Turbine integration into the smart grid in case of unbalanced voltage conditions	123
85	Sensorless vector control of induction motor with current reconstruction method	127
86	Seasonal Asphalt Concrete Surface Pavement Temperature Models Using Neural Networks	131
87	A Conceptual Framework transforms The Player into Buyers on Mobile Applications: A Case Study of Mobile Social Network Games	135
88	The Effects of High Temperature to Read-Head Instability	139
89	Characteristics of Head Gimbal Assembly (HGA) component relate to solder joint reliability	143
91	Risk assessment of landfill in Serbia based on flooding potential	147
94	Modeling of Energy Efficiency Cart of Solar Energy Collectors	151
95	Removal of H2S from Biogas by KMnO4 Impregnated Activated Carbon	155
96	Modification of baroreflex sensitivity in Control breathing	159
98	Design of Real-Time External Force/Position Controller for Human-Robot Interaction	163
99	System for assistance during evacuation process	167
100	Comparison of PI and Fuzzy Logic Controllers in Human-Robot Handover Task	171
101	Evaluation of a Map Matching Algorithm for Indoor Localization with OpenStreetMap	175
111	FEM Modeling of the Multi-Segment Lumbar Spine for Humanoid Robots	179
113	Low Population Density Influence on Waste Management System in Serbia	183
114	Investigation of air pressure drop through porous wheat straw bed	187
115	Speech Emotion Classifier using Support Vector Machine with FFT and MFCC	190
118	Controller Embedded Oscilloscope Functionality for Power Converter Applications	194
120	Energy and Economic Effects of Electricity and Heat Cogeneration with Combined Technologies of Corn Cobs Gasification and Gas Turbines	198
121	Advanced Wind Energy System with Sensorless Controlled Six-phase Generator	202

Table of Contents

ID	Title	Page
124	Solar PV System Grid Integration Issues - Harmonics	206
126	Basic Properties of Structural LWAC Based on Waste Materials	210
127	LWAC Based on Waste Materials and Application in Thermally Improved Masonry	214
128	Dielectric Properties of Palm Oil and Coconut Oil under Thermal Ageing	218
129	Hydrogen Gas Sensor Using Double SAW Resonator System	221
130	Investigation on Touch Area of Under Foot Pressure Based-on Weight Measurements	224
131	Software for Market Validation of the Recycling Equipment	227

The 7th International Conference on Engineering and Technology
ICET-2015, Phuket, June 19-20, 2015
Prince of Songkla University, Faculty of Engineering
Hat Yai, Songkhla, Thailand 90112

Movement of feldspar mining cost at Noppitam District, Nakhon Si Thammarat Province.

Parinya Pattanadech[1]*, Manoon Masniyom[2]
[1]Mining Engineer, Sinluang Company, Noppitam District, Nakhon Si Thammarat Province, Thailand
[2]Prince of Songkla University, Faculty of Engineering, Thailand
*E-mail: minetechno@yahoo.com

Abstract: *Feldspar deposits in Noppitam district, Nakhon si thammarat province, Thailand, produced from alaskite, are the important area which is able to produce to be the fourth of the world for 2012-2013. This mining lease area is about 4.5 sq.km. The mining has been started in 1978 and produced feldspar about 15 million tons to present and it still have the reserved more than 10 million tons. Open pit mining has been operated more than 100 meters from surface with stripping ratio ≤ 1:1. More than 95% of production has been exported to Malaysia, Indonesia, Vietnam, Bangladesh, India, United Arab Emirates and Taiwan. From 10 years ago, the production cost has been increasing continuously, especially, Diesel fuel and wage which increased 122% with high stripping ratio. Production cost increased ~117%, but on the other hand the ore price has just increased only 25%. It lead to increase more production capacity than 99% to absorb the cost. Therefore, process development, mining technique need to improve as soon as possible to encounter the issues.*

Key Words: ***Feldspar / Alaskite / Mining Cost/ Noppitam / Nakhon Si Thammarrat***

1. INTRODUCTION

Since 1978 feldspar has been mined in area of Amphoe (district) Noppitam, Changwat (province) Nakhon Si Thammarat (Fig.1-2), produced approximately 15 million metric tons, Majority of feldspar is mined from alaskite and a few is produced from pegmatite. The area of mining lease is about 4.5 sq.km., 3.0 km in length and 1.5 km. in width. Production of feldspar has been operated under five mining companies.

The area is accessible by Highway No. 4140 from Tha Sala district to Noppitam district about 29 km. and joined by temporary lateritic road for another 5 km.

The mining cost is really high because alaskite and granite (country rock) consist of high silica, It very high abrasive wear and not only price of production factor also stripping ratio increasing continuously.

Fig.1 Noppitam feldspar deposits.

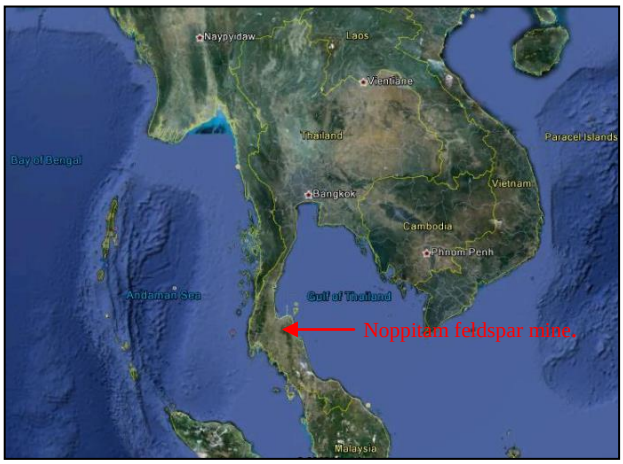

Fig.2 Location of Noppitam feldspar mine.

2. ORE PROPERTIES

The Noppitam alaskite generally consists of plagioclase, orthoclase, microcline, perthite and quartz with occasional muscovite, biotite, chlorite and garnet.

Chemical analysis of alaskite is SiO_2 60-70 %, Fe_2O_3 0.1-0.8 %, Na_2O 5-10 %, K_2O 0.1-4 %,

Physical analysis of alaskite is L* 60-90, %Refractoriness 30-80%, Hardness 6-7, Abrasiveness 1,400-1,500 g/t. (L* is Lightness)

3. MINING METHOD

At the present, the mining method is open pit mining follow ore veins with stripping ratio ≤ 1:1(Fig.3). Covering of 6 concessions in Noppitam area; 3 concessions are for Asia Mineral Processing Co.,Ltd. 2 concessions are for Synraejaroenphol Ltd., Part. and the others is for Siri Feldspar Ltd., Part. For blasting use hydraulic drilling crawler (top hammer, 3 inch. diameter of bit.) Do drilling-blasting as bench, ground (no free face) or horizontal along the vein with pattern (burden x spacing x hole depth), 1-2.5m x 1-2.8m x 2.8-15m and initiated by cap to high explosives (Emulsion) to be a primer and use ANFO to be the blasting agent by power factor 0.3-1.1 kg./cu.m., bench high is 5-15 m. and some areas are not doing bench just leave to be high wall 40-120 m. of big sump. Blasted ore are loaded by backhoe (size 20-30 tons) to truck and hauling to ore dressing plant which located around 12-40 km. from mining site. The mining have done around 40-120 m. depth from the surface and recover the ore around 15 million tons.

Fig.3 Mining area

4. Mine Production

Mine production capacities of feldspar in Noppitam deposits has been increasing continuously from 374,000 tons (2004) to 745,000 tons (2013) and in 2012 – 2013 this area produced to be the fourth of the world (Table 1), So the deposits are very importance for the world.

Table 1. Mine production from Noppitam district.

year	Noppitam mine production	% of world production	World ranking
2004	374	3.37	9
2005	349	2.71	12
2006	725	4.71	6
2007	557	3.08	8
2008	580	2.65	8
2009	386	1.93	14
2010	522	2.53	9
2011	648	3.06	7
2012	714	3.15	4
2013	745	3.24	4

Remark : Data in thousand tons

5. MINING COST MOVEMENT

Major mining cost consists of wage, depreciation, maintenance cost and fuel cost. For 10 years, this make the production cost are also increasing, especially, diesel fuel and wage. The diesel fuel cost has increased from 14 baht/liter to 31 baht/liter (Fig.4) and the wage cost has been expended from 135 baht/day to 300 baht/day (Fig.5). Both of them have increased 122%. For other cost, machine has increase 13-47% (Fig.6), truck tires 63% increasing (Fig.7), drilling part 32-132% increasing (Fig.8), Emulsion 24% increasing and Electric cap 8% increasing, but this time ammonium nitrate (Fig.9) and mild steel not increasing from 2004 (Fig10).

Another factor that causes to increase the cost is the mining has been being operated by increasing its depth continuously, so stripping ratio increasing from 0.5:1 in 2004 to 1:1 recently.

Therefore, the production cost increase from ~60 bath/tons in 2004 to ~130 bath/tons in 2013 (Fig.11)

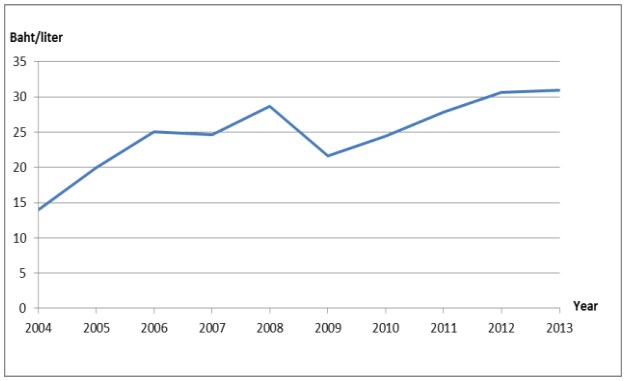

Fig.4 Diesel fuel price movement. [2]

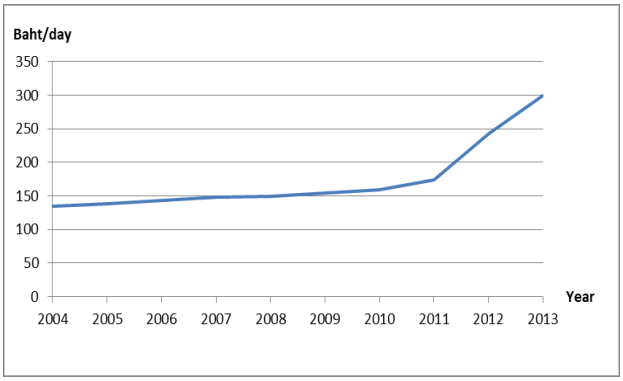

Fig.5 Minimum wage movement at Nakhon Si Thammarat province. [2]

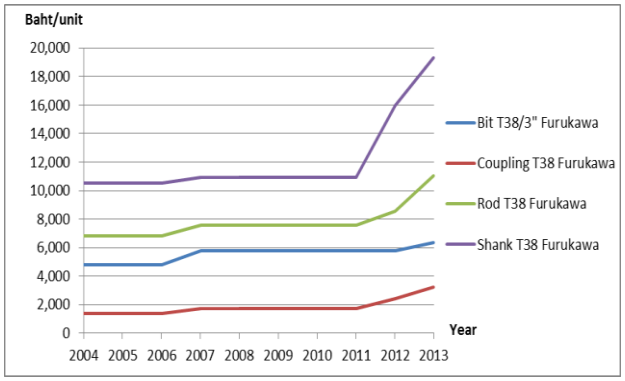

Fig.8 Drilling part price movement. [2]

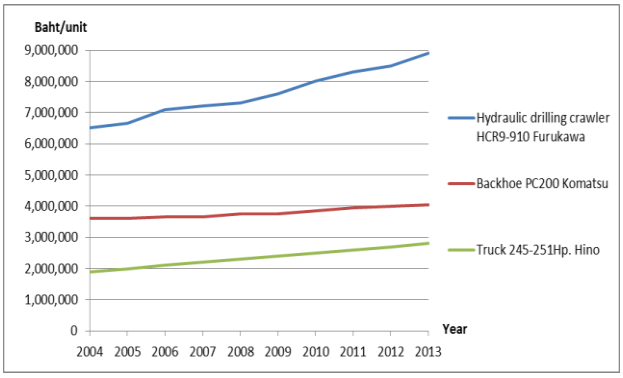

Fig.6 Mining machine price movement. [2]

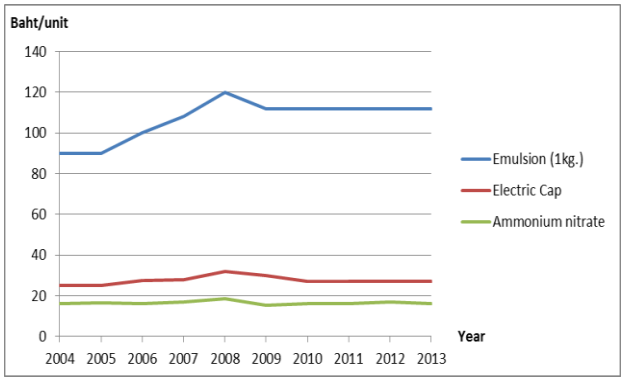

Fig.9 Explosive price movement. [2]

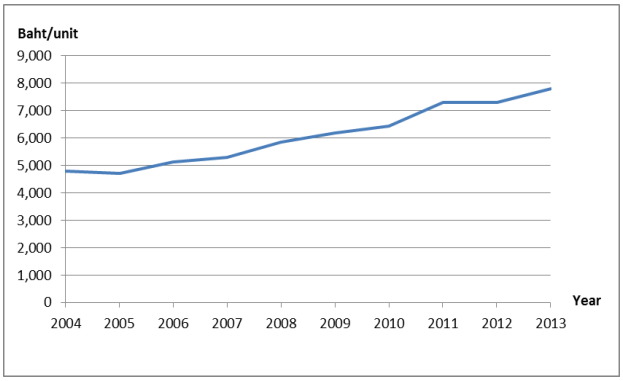

Fig.7 Truck tires price movement.
(BRIDGESTONE 10.00-20 16PLY RATING H.T.NYLON). [2]

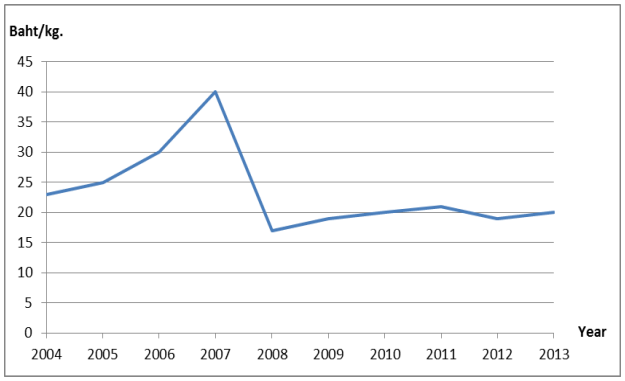

Fig.10 Mild steel price movement. [2]

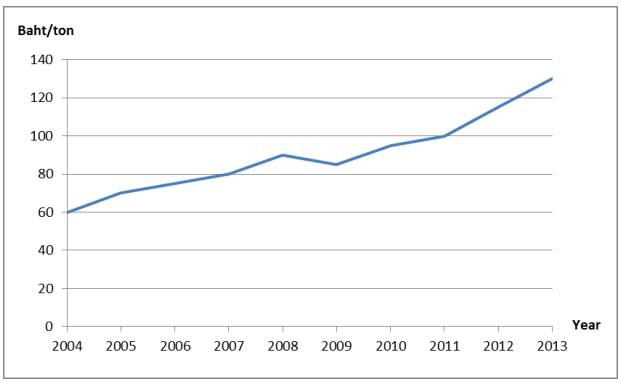

Fig.11 Mining cost movement. [2]

6. MOVEMENT OF FELDSPAR EXPORT PRICE

The ores is exported more than 95%, to Malaysia, Indonesia, Vietnam, Bangladesh, India, United Arab Emirates and Taiwan. For 10 years ago, feldspar (size -5mm) price (FOB price Nakhon Si Thammarat customs post) is not much change, 650 baht/ ton in 2004 and 813 baht/ ton in 2013, which has increased about 25% (Fig.12).

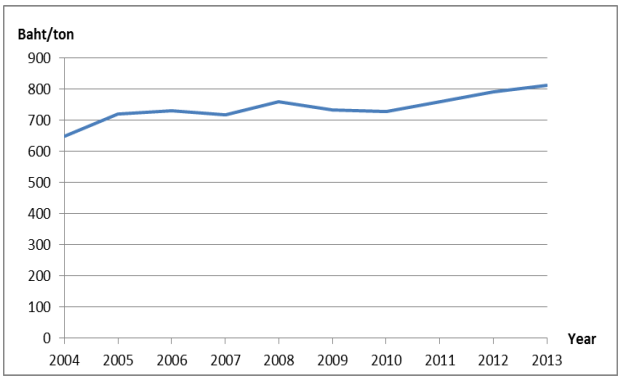

Fig.12 FOB price movement at Nakhon Si Thammarat customs post. [2]

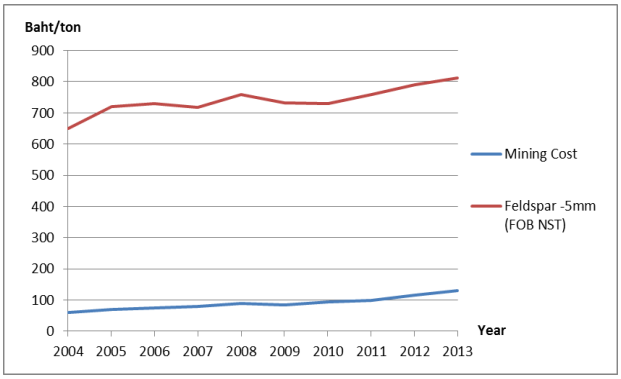

Fig.13 Comparison between mining cost and feldspar export price. [2]

7. CONCLUSIONS

For feldspar mining in Noppitam district, Nakhon si thammarat province, 2004-2013, There are operated which deep >100 meters from surface and there is the production cost increasing. From 10 years ago to present, the production cost has increased ~117% dramatically, however, the ore price has just increased only 25%. Thus, the entrepreneurs have to expend the production capability to 99% for 10 years to survive their business. Therefore, the most important factor that has to develop to solve or absorb this kind of problem is process development, mining technique to support mining business.

REFERENCE

[1] Pungrassami T., Pattanadech P., and Watcharasutha korn U., "Feldspar mining form alaskite Amphoe Noppitam, Changwat Nakhon Si Thammarat" The 10th International Conference on Mining, Materials and Petroleum Engineering. The 6th International Conference on Earth Resources Technology. "Sciences and Technologies Towards 2012" : PSU-IC 2012, Songkhla, Thailand, May 9-11, 2012.

[2] Pattanadech P. "Decade mining cost of feldspar Noppitam deposits report (2004-2013)" Sinluang company limited. Nakhon Si Thammarat, Thailand, Jan 20, 2014.

The 7th International Conference on Engineering and Technology
ICET-2015, Phuket, June 19-20, 2015
Prince of Songkla University, Faculty of Engineering
Hat Yai, Songkhla, Thailand 90112

ANIMATED 3D VIRTUAL WORLDS USING JAVA AND SKETCHUP

Chonmaphat Roonnapak, Andrew Davison
Dept. of Computer Eng. Faculty of Eng., Prince of Songkla University, Hat Yai, Thailand
Email: 5610120049@email.psu.ac.th, ad@fivedots.coe.psu.ac.th

Abstract: *This paper introduces a Java API for creating animated 3D virtual worlds in SketchUp, offering a feature set aimed at novice graphics programmers. The API provides methods for generating a landscape, loading (and creating) scenery, camera mobility, and discrete-event based animation of models. The API supports a listener interface, which supplies information about changing events in the world, such as collisions between models.*

Key Words: ***3D virtual worlds/animation/ SketchUp/ discrete time events***

1. INTRODUCTION

There are many excellent tools for constructing 3D scenes, including 3D Max, Unity 3D, AutoCAD, IMAGIS and SketchUp (http://www.sketchup.com/). SketchUp has several advantages for users new to 3D graphics: simple modeling, free online materials, and a Ruby console interface [1]. Java programmers can choose from several 3D APIs e.g. Java 3D, JOGL, and JMonkey Engine. However, they are designed for general 3D programming, such as games development, and most are OpenGL-based, making them difficult for novices to understand and apply.

Our Java API focuses on virtual world creation for programmers new to 3D graphics by utilizing SketchUp. It supports landscape generation, dynamic and static models, camera mobility, animation, and high-level event handling. A typical scene is shown in Figure 1.

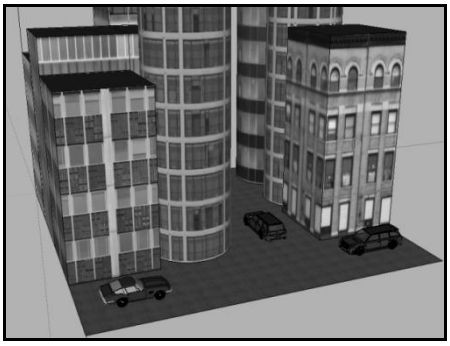

Fig. 1. Example 3D virtual world

2. SYSTEM OVERVIEW

The system consists of two parts, shown in Figure 2. A programmer utilizes the Java API for defining a 3D scene, which is rendered and animated by SketchUp.

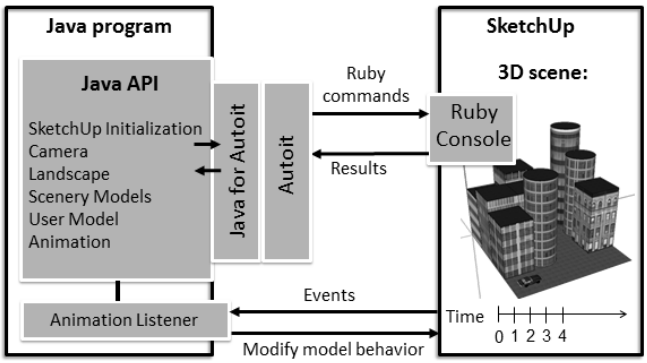

Fig. 2. 3D World Generating System

SketchUp's Ruby interface is based around the user typing commands into an on-screen console [2], rather than through an exported API. This makes it rather difficult to interface an external program with SketchUp.

Our solution is to utilize AutoIt (https://www.autoitscript.com/site/autoit/), a popular freeware scripting language for automating on-screen actions involving the keyboard and mouse (e.g. clicking on a close box to terminate an application). We call AutoIt through a Java interface to send commands to the SketchUp-Ruby console (http://fivedots.coe.psu.ac.th/~ad/jau/).

Another problem is that SketchUp does not issue events when things change inside its 3D scene. We implement this functionality by having SketchUp modify and create various data files; any modifications to these files are detected by a Java thread running inside our API. This low-level file manipulation and monitoring is hidden from the API programmer, who is notified of events via a listener interface. For example, when two models collide in the 3D scene, SketchUp creates a new file. The Java thread detects the file creation, reads information about the event from the file, and calls a suitable event handling method in the programmer's code.

3. VIRTUAL WORLD GENERATION

A typical virtual world is composed of a landscape, various static scenery models, dynamically moving models, a model representing the user, and a camera. This section briefly describes how the programmer can generate these elements

A landscape is created by employing the Diamond-Square algorithm [3], which is controlled through a simple interface suitable for graphics programming beginners, while still being capable of achieving interesting results.

Terrain texturing is based on landscape height ranges, with the API automatically generating blended texture transitions between those ranges.

One of the advantages of using SketchUp is the availability of free or low-priced models (e.g. from the 3D Warehouse, https://3dwarehouse.sketchup.com/). The programmer must specify a model's (x, y) position, z-axis orientation, scale, and whether the model will be static or dynamic. The API calculates the model's z position by assuming that all models rest on top of the terrain.

We include support for textured block and cylinder shape creation, which is useful when creating city-like scenes (several examples can be seen in Figure 1),

The API includes a 'user' model, a dynamic model representing the user, which can be automatically followed by the camera as the model moves.

4. ANIMATION

Each dynamic model is assigned a "steps" array which determines its motion during a specified period. Each animation begins and ends relative to SketchUp's global time, as illustrated in Figure 3. Car1 starts moving at time 1 while Car2 starts at time 5.

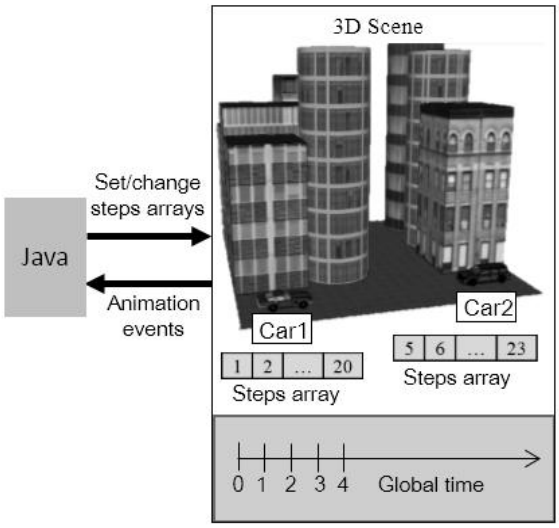

Fig. 3. The Animation Behavior

If an animation-related event occurs, such as a collision between models, the Java programmer will be notified via a collision event, and can then choose to modify the steps arrays of the models involved in the collision.

This section examines five aspects of our animation support in more detail: movement generation (i.e. how a steps array is created), how steps arrays can be changed at run time, collision detection, listening for events on the Java side, and collision recovery.

4.1 Movement Generation

On the SketchUp side, each model is animated via the execution of its steps array. An example appears in Figure 4.

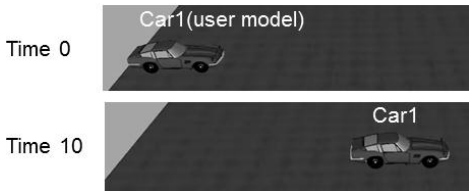

Fig. 4. Animating Car1

The programmer supplies information about a model's position and orientation at the start of the animation, and its final position and orientation. For instance, the car in Figure 4 starts moving at time 1, and finishes at time 20. During that period, it will move 170 units along the x-axis with no change in its orientation (i.e. it remains pointing to the right). A suitable steps array is created by calling Movement.genMovement():

```
Step[] steps1 = mover.genMovements(
  landscape,
  new Point2f(10, 100),  // start pos
  new Point2f(180, 100), // stop pos
  0, 0,      // start/end rotations
  1, 20);    // start/stop times
```

The programmer only has to supply (x, y) positions for the model. The API assumes that it will move over the surface of the specified landscape, and calculates its z-positions accordingly, using a variation of the standard Barycentric approach [4]. When the vertices of the current landscape triangle are known, the z-position of any (x, y) position in the triangle can be computed

However, a problem occurs if the steps array contains two points (e.g. S0 and S1) which cross a boundary between two terrain triangles. If the terrain is rough, the orientation of the triangles may not be in the same plane, as in Figure 5. If the model moves directly between the two points, then it will disappear beneath the landscape (the dotted line in Figure 5). An extra coordinate at the intersecting edge of the triangles must be added to the steps array (i.e. S01 in Figure 5).

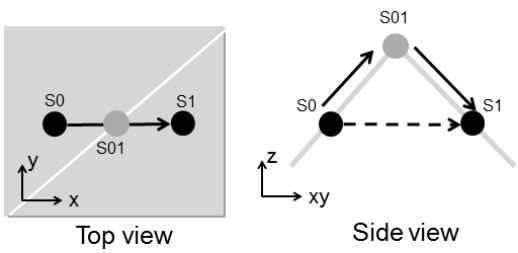

Fig. 5. Extra Coordinate on the Intersected Edge

4.2 Animating a Model with a Steps Array

The API allows a model to be assigned multiple animation sequences. Therefore, it's quite likely that the resulting steps array will not be contiguous, as in Figure 6.

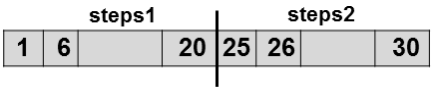

Fig. 6. Steps Array with a Waiting Period

The first part of the array defines an animation between times 1 and 20, while the second commences at time 25 and ends at time 30. These are processed by having the model waits for 4 seconds during the times 21-24.

Another issue is when the times of two animations for a model overlap in time. The API handles this by ignoring the overlapping period of the latest animation, while issuing a warning to the programmer. The following pseudo code demonstrates the behavior of the animation processing loop on the SketchUp side:

```
max = max stop time of all models
 0...max {|i|   // global time of the scene
  for each model, m
    if i ≥ start time of m
     animate using m's steps array at time i
     or do nothing if no value at time i
}
```

The main problem with this pseudo code is that it does not deal with collisions, which are covered in the next sections.

4.3 Collision Detection

There are two types of collision detection: *dynamic* (between two moving models) and *static* (when a moving model hits a piece of scenery, such as a building).

Assume that Car1 is about to move from position (x1, y1) to (x2, x2) at time 5. The mechanism for dynamic collision detection between Car1 and another model, Car2, can be explained by reference to Figure 7.

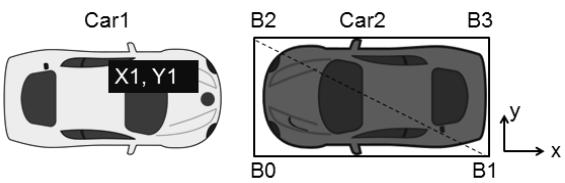

Fig. 7. Dynamic Collision Detection

The boundary of Car2 is split into two triangles. If (x2, y2) falls inside one of these, then a collision will occur. The model's movement is temporarily stopped, and a new file of collision information is created. The animation loop's pseudo code can be modified to include this behavior:

```
max = max stop time of all models
0...max {|i|   // global time of the scene
  for each model, m
    if i ≥ start time of m
      if isCollision(m, nextPosition)
          stop m moving;
          create a collision file for m
      else
          animate by m's step array at time i
          or do nothing if no value at time i
}
```

Static collision detection (between moving and stationary models) uses a similar algorithm, but is performed outside the time-critical SketchUp animation loop, during the generation of a steps array. As each coordinate is calculated, the collision detection test is carried out to determine if the point falls inside any of the static models. The API raises an exception to inform the programmer to change their animation sequence.

4.4 Animation Listener

The Java-side animation listener allows a programmer to handle a range of collision-related and animation events. Its underlying file-based mechanism, which is hidden from the programmer, is shown in Figure 8.

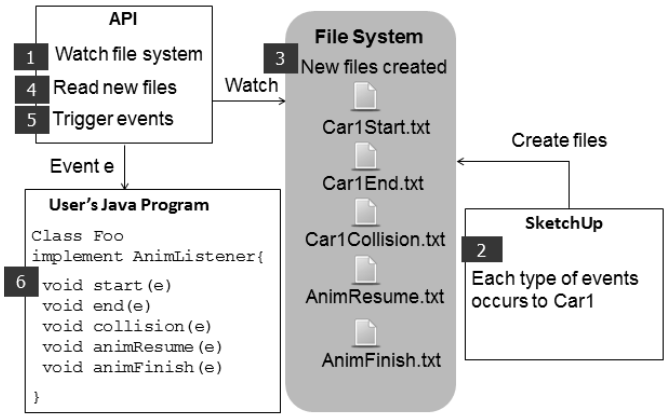

Fig. 8: Animation Listener Mechanism

Our API employs this approach due to the communication limitations of SketchUp's Ruby API.

In stage 1 of Figure 8, a Java thread is created to act as a file system monitor. When an important event, such as a collision, occurs inside SketchUp (stage 2), a new file is created (or an existing one modified) in stage 3. This change is detected on the Java side (stage 4), and the thread uses the file's information to create a Java event (stage 5), which is passed to the programmer's AnimListener interface (stage 6) where a relevant method is called.

Currently our API supports five event types: StartEvent, EndEvent, ResumeEvent, FinishEvent, and CollisionEvent. Each event is handled by a different method in the AnimListener interface. For example, CollisionEvent objects are passed to the collision() method.

4.5 Collision Recovery

The API's design allows the programmer to define their own collision recovery behavior inside the AnimListener collision() method. Since such behaviors are rather complicated, the API offers a good default behavior, implemented as the basicRecovery() method. This allows collision recovery to be defined as:

```
public void collision(CollisionEvent e)
{ CollisionRecovery.basicRecovery(
                        landscape, e); }
```

The CollisionEvent object contains a variety of information, including the collision model's name, dimensions, the other model's name, the collision position, and time.

basicRecovery() utilizes the landscape and the collision event object. The recovery approach is presented in Figure 9.

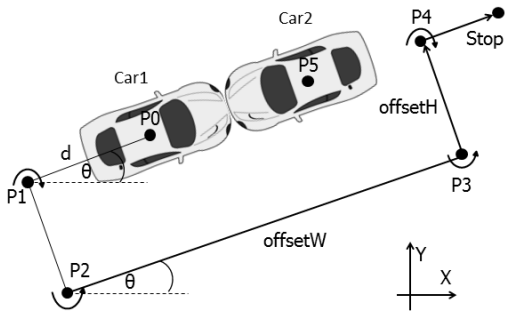

Fig. 9: Collision Recovery

Assume that Car1 is currently being animating and a potential collision with Car2 is detected. basicRecovery() calculates four positions (P1, P2, P3 and P4 in Figure 9) and updates Car1's steps array with an animation sequence that passes through those points. The calculation of the coordinates is described by the following equations:

```
d = Car1.width
offsetH = Car1.height + Car2.height
offsetW = Car1.width + Car2.width + d
P1 = (P0.x - d*cos(θ), P0.y - d*sin(θ))
P2 = (P1.x + offsetH*cos(90-θ),
      P1.y - offsetH*sin(90-θ))
P3 = (P2.x + offsetW*cos(θ),
      P2.y + offsetW*sin(θ))
P4 = (P1.x + offsetW*cos(θ),
      P2.1 + offsetW*sin(θ))
```

Car2's animation behavior is also modified: it remains stationary for a short time, and then resumes its steps array sequence.

For example, assume that the collision happens at time 10. The steps array for Car1 is updated so that the model moves around Car2. Assuming that the animation through points P0-P4 takes five seconds, then a new array is generated as shown in Figure 10.

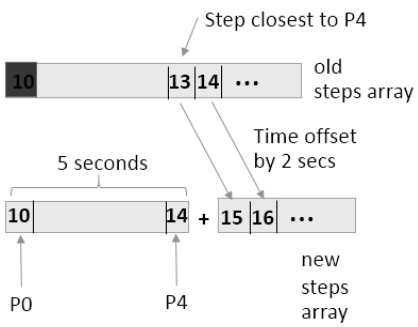

Fig. 10. New Steps Array for Car1

The steps array is modified in two ways. A new sequence is added extending from times 10 to 14 which moves the model from point P0 to P4. The old step array is discarded up to time 13 which is determined to be the position in the old animation sequence closest to P4. The sequence starting at time 13 is then time-displaced by 2 units so that it continues after the car has reached P4.

The generation of the P0-to-P4 animation sequence may be more complicated than this since the collision recovery path may itself collide with a static model, in which case it will need to be modified. In the worst case, basicRecovery() may be unable to modify the model's steps array and so an exception is raised.

The model involved in the collision (Car2 in this example) waits for three seconds before continuing on its previous route. The new steps array for Car2 is shown in Figure 11.

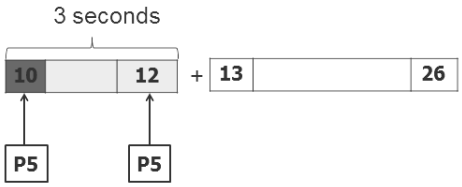

Fig. 11. New Steps Array for Car2

The collision position of the car (P5) remain unchanged from time 10 to 12, and then the old steps array sequence that started at time 11 is resumed at time 13, after being time-displaced by 2 units. After the steps arrays of Car1 and Car2 are updated and reloaded, SketchUp will resume the animation starting from the collision time (time 10 in this example).

5. CONCLUSIONS

Existing 3D libraries for Java are designed for general needs too complicated for novice graphics programmers. Our simpler API can generate complex, visually pleasing, virtual worlds in SketchUp and supports robust discrete-time event-based animation, with collision detection and recovery.

Future work will focus on extending the event model, adding skeletal animation to the user model, improving the dynamic camera behavior, and supporting lighting variations.

REFERENCES

[1] Tal, D. 2009. "Google SketchUp for Site Design: A Guide to Modeling Site Plans, Terrain and Architecture", Wiley.

[2] Scarpino, M. 2010. "Automatic SketchUp: Creating 3-D Models in Ruby", Eclipse Engineering LLC, Hanover.

[3] Kui-Ru, L. and Xiao-Feng, L. 2010. "An Accumulated Method Based on Fractal for Automatic Terrain Generation", In *E- Health Networking, Digital Ecosystems and Technologies (EDT), 2010 International Conference* (Shenzhen Apr 17- 18), IEEE, Piscataway, N.J., 426-430.

[4] Dunn, F. and Parberry, I. 2002. "3D Math Primer for Graphics and Game Development", Wordware, 260-267.

The 7th International Conference on Engineering and Technology
ICET-2015, Phuket, June 19-20, 2015
Prince of Songkla University, Faculty of Engineering
Hat Yai, Songkhla, Thailand 90112

The Role of Energy Efficiency in Decarbonizing Thailand's Energy System

Aumnad Phdungsilp[1]*
[1]Dhurakij Pundit University, Faculty of Engineering, Thailand
*Email of corresponding author: aumnad@dpu.ac.th

Abstract: *The improvement of energy efficiency is considered a major priority in energy policy and planning. The aim of this study is to explore the role of energy efficiency improvements in Thailand's energy system. The scenario-based energy modeling was used to examine the potentials of energy savings and energy-related CO_2 emissions in four demand sectors and a power sector. The obtained results show that under the BAU (Business-as-Usual) case, the projections of energy demand and energy-related CO_2 emissions are expected to be 170,964 ktoe and 521 $MtCO_2$ in 2030. The energy efficiency case results in total energy savings of 25 Mtoe and CO_2 emission reductions of 95 $MtCO_2$ compared to the BAU case. This study can provide insight for design and update the energy efficiency program.*

Key Words: ***Energy Efficiency / Energy System / Decarbonization / Thailand***

1. INTRODUCTION

A growing awareness of energy security, climate change and sustainable development has been observed at all levels of the society. Energy and climate change are urgent agendas for policy-making around the world. A low-carbon society is the most attention in both develped and developing nations. Planning for low-carbon society requires significant changes in existing energy systems. Thailand's energy sector emits large amount of CO_2 emisions, ranking the 20th in the world [1]. With the rising energy demand and energy-related CO_2 emissions, it is imperative that Thailand starts to avoid embarking on a high-carbon growth path and instead takes a low-carbon pathway. Delay action would lock the country into high-carbon infrastructures and would require more costly retrofitting of energy capital stocks such as power plants, buildings and transport networks in the future.

Improving energy efficiency has been recognized as one of the most important meaures to reduce energy demand, CO_2 emissions and the dependency of countries on energy imports. A number of studies on national and international energy policy measures confirms the important role of energy efficiency improvements in the development of energy systems, for example [2,3]. However, there has been little publicly available modeling based analysis of the role of energy efficiency improvements in decarbonization of energy systems in developing countries. To address the lack of analysis, this study modeled Thailand's energy system for baseline and energy efficiency cases with four demand sectors and a power sector. The demand sectors include residential, commercial, industry, and transport sectors. This study would provide guidance and perspective to the design and update on national energy efficiency programs. It will also constribute to policy-making in developing low-carbon energy systems.

2. METHOD

The Long-range Energy Alternatives Planning (LEAP) system was used to model Thailand's energy system and assessed the energy efficiency improvements. LEAP has been developed by Stockholm Environment Institute. It is an accounting and scenario-based energy modeling platform [4]. It is not a model of a particular energy system, but rather a tool that can be used to create models of different energy systems. Scenarios are based on a comprehensive accounting of how energy is utilized, converted and transformed in a given economy under a range of alternative assumptions for future changes of parameters.

LEAP was developed to model the energy demand and supply and associated CO_2 emissions in Thailand from 2010–2030, with taken 2010 as the base year. The model structure is disaggregated in a hierarchial format based on four levels: sector, sub-sector, end-use, and device levels for four demand sectors and a power sector. Energy demand for each sector is calculated using a set of equations built around technology energy intensities, saturation levels and activity drivers within each sector (demand or supply). Table 1 summarizes the general equations for calculating energy demand and supply.

Energy demand is calculated for each sector (four demand sectors) and thereby the total final energy demand. The power sector is based on Thailand Power Development Plan (PDP 2010: Revision 3)[5]. The emission factors in the Technology and Environmental Database module in LEAP is linked to the device level (fuels) in demand module to appraise the CO_2 emissions. In this study, only energy-related CO_2 emissions are considered.

Table 1. *General equations for estimating energy demand and power generation*

Commercial	(floor space in m^2) * (building type % share of floor space) * (end-use % saturation) * (energy use/m^2.yr)
Industrial	(industrial value added) * (sub-sector % share of value added) * (fuel share) * (energy intensity)
Residential	(no. of household by income class) * (end-use % saturation) * (technology % saturation) * (energy intensity)
Transport	(number of vehicle by types) * (average vehicle-kilometer traveled or VKT by types) * (% VKT share) * (technology % vehicle share) * (fuel economy)
Power generation	Technology capacity, maximum capacity factor, efficiency, fuel share, and transmission and distribution losses

2.1. Model descriptions

The base year (2010) was developed from existing data. It computes energy consumption and CO_2 emissions. It also provides a common starting point and determines how the composition of energy demand and supply structure will change over the planning horizon.

The BAU (Business-as-Usual) case assumes that past trends continue in the future and no new policy interventions will be implemented. Projections of driving factor, such as number of households, floor spaces, industrial value added, and VKT, are exogenously determined up to 2030. Technical variables, for example energy efficiencies of particular technologies and shares in total activity levels, are estimated from government planning documents and literature surveys.

2.2. Assumptions of energy efficiency issue

The aim of this study is to exmine the possible energy efficiency measures for reducing energy demand and energy-related CO_2 emission reductions. Thus, the policy intervention case is built on the BAU case and taken into account only energy efficiency in demand side and power sector to examine the implications. Table 2 presents the assumptions of the energy efficiency policy interventions. It should be noted that this study takes a conservative approach by including options that are already commercially available and expecting to be commercialized by 2030. The study does not include the cost of implementation.

2.3. Data collection

The work on energy modeling depends on the available of data. However, there is no single source for dataset to construct the model. In this study, the dataset draws on information from a large number of national and international agencies and research reports.

Data were collected from several sources. These data are economic parameters [6], population [7], service demand [8,9], technology characteristics [9,10,11], proportion of energy utilization [9,12], number of vehicles, and vehicle types [13,14].

3. FINDINGS AND ANALYSIS

Thailand's eneregy system is highly dependent on fossil fuels. This has led the country to impliment new strategies to decarbonizing energy system while maintaining the economic competitiveness and energy security issue. During 1980–2010, Thailand's energy-related CO_2 emissions increased by 24.3% from 33.56 $MtCO_2$ to 278.49 $MtCO_2$. Comparing with other ASEAN mdember states during the same period, Thailand was the second after Indonesia. In terms of CO_2 emissions per capita, Singapore ranked the first and Thailand was the fourth in ASEAN [1]. The key challenge is to avoid a high-carbon growth path.

Table 2. *Assumptions of energy efficiency policy interventions*

Policy Interventions	Assumptions
Residential: Promoting high energy-efficient appliances in (R-HEF)	Conventional refrigerators, A/Cs and fans are replaced by high efficiency ones by 2020.
Residential: Promoting high-efficiency LPG cooking stoves (R-LPG)	High-efficiency stoves are expected to replace normal LGP stoves during 2011-2030 with the replacement rate of 20% every five years.
Commercial: Efficient HVAC systems (C-HVAC)	HVAC systems are improved the efficiency by 10% in 2015, 20% in 2020 and 30% in 2030. This measure will be applied in all building type.
Industry: Improvments of energy efficiency in selected equipment (I-EE)	Target of 10% and 20% increasing energy efficiency by 2015 and 2030. This measure will be applied to compressed air, boiler and steam systems, and lighting systems.
Industry: Efficient electricity end-use devices (I-ELE)	It is assumed the increased 20% of efficiency by 2015 in pumps, compressors and motors for industrial processes.
Transport: Promoting eco-cars (T-ECO)	Promoting eco-cars that have fuel economy improvements corresonding to Euro 4 standard. It will be applied in passenger car with the penetration rate of 15% in 2020 and 30% by 2030.
Power: Increasing efficiency of power plants (P-EFPP)	Improving energy efficiency to 65% for natural gas based power plant and 50% for coal-fired

At the sectoral level, industrial sector contributes the largest share of total final energy demand and follows closely by transport sector. High energy intensive industries, such as food and beverage, non-metallic and chemical, make up over 70% of total industrial energy demand. The transport sector is expected to grow faster due to rapid urbanization and the rise of consumer income. Road transport dominates the transport modes and contributes the largest share of transport energy demand. The residential and commercial sectors consume mainly electricity to provide energy services to the end-users. They are expected to grow significantly due to increasing floor spaces in commercial buildings.

3.1. BAU case

The BAU case represents a base case without policy interventions. It presents a path of energy development. Under the BAU case, the projections of total energy demand in 2030 are expected to be 171 Mtoe. The industrial and transport sectors dominate Thailand's energy demand while other sectors contribute smaller shares. Results for the BAU case are presented in Fig. 1. The final energy demand in four sectors from 2010 to 2030 is expected to grow at 4.42%. It was found that by 2030 Thailand's per capita energy demand will reach 2.4 TOE per capita. This finding is consistent with the projections from Asian Development Bank (ADB) and International Energy Agency (IEA) [15].

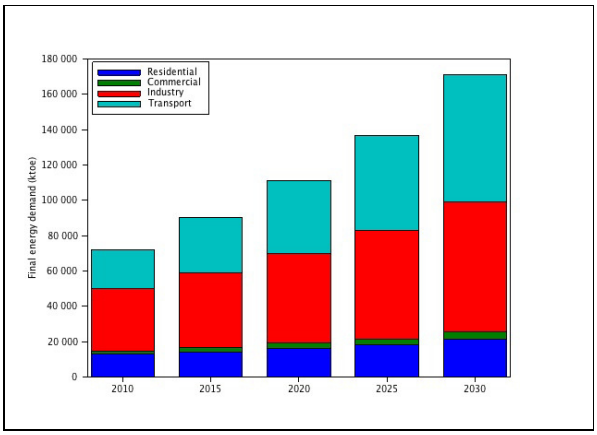

Fig. 1. Final energy demand by sectors under BAU case (ktoe)

Nine manufacturing industries have been considered. Industrial energy demand is increased from 35,409 ktoe in 2010 to 73,230 ktoe in 2030. The energy use is disaggreated into three end-uses, including thermal use, mechanical use and electrical use. Thermal energy use is mainly in boilers and furnaces. The fuels are coal, fuel oil and natural gas. Mechanical use is basically diesel. The electricity use consists of all electric equipment.

Only road transport is considered in this study due to its high influence on energy demand in the transport sector. Transport energy demand is expected to reach 41,037 ktoe in 2020 and 71,987 ktoe in 2030. The high energy demand in this sector is a result of population growth and less development of transportation modes.

The residential sector is divided into three income classes. Each income class is further divided into end-uses: cooling, cooking, lighting, and electric device. The projected energy demand is to be 16,201 ktoe in 2020 and 21,597 ktoe in 2030. The main end-uses are cooling and cooking.

The energy use in commercial sector is mainly for air-conditioning. Six building types are considered (i.e., office, hotel, hospital, department store, academic institution, and etc) and each building type is divided into three end-uses: air-conditioning, lighting and others. The projections of energy demand are 2,860 ktoe in 2020 and 4,150 ktoe in 2030.

For the power sector, the BAU case is followed the PDP 2010: Revision 3 [5]. This plan is the most reliable source for technical parameters. The conventional fossil fuel technologies continue to dominate Thai power sector, while renewable electricity is expected to grow significantly. Natural gas, coal and lignite are the main sources for power sector. The electricity generation is expected to increase from 151,940 GWh in 2010 to 304,504 GWh in 2030.

Results show that Thailand's energy system would increase the use of fossil fuels. The CO_2 emissions are projected to be 339 $MtCO_2$ in 2020 and 521 $MtCO_2$ in 2030. These CO_2 emissions are from four demand sectors and a power sector in which the demand sector accounts for about 70%. The CO_2 emissions from only energy consumption are projected to increase from 138 $MtCO_2$ in 2010 to 361 $MtCO_2$ in 2030.

3.2. Energy efficiency case

A large share of energy demand in residential sector comes from cooling and cooking purposes. Therefore, energy efficiency improvements in this sector are considered for promoting high energy-efficient appliances (R-HEF) and promoting high-efficiency LPG stoves (R-LPG). The potentials of energy savings and CO_2 emission reductions are presented in Fig. 2 and 3. These two interventions would reduce the energy demand of 587 ktoe in 2020 and 1,255 ktoe in 2030. They are expected to reduce 2,603 $ktCO_2$ and 4,868 $ktCO_2$ in 2020 and 2030, respectively.

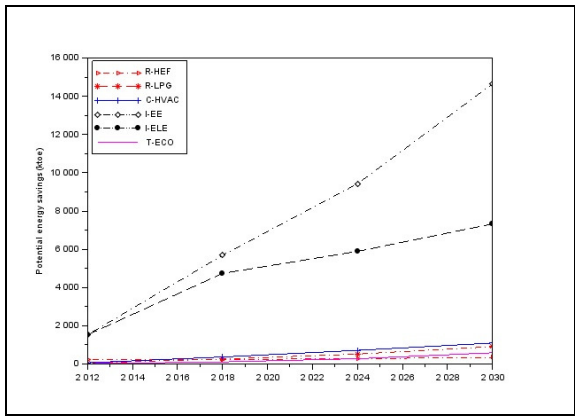

Fig. 2. Potential energy savings under energy efficiency case (ktoe)

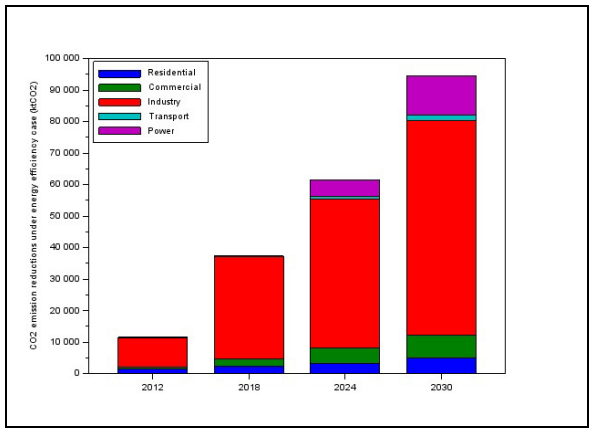

Fig. 3. CO_2 emission reductions under energy efficiency case by sectors ($ktCO_2$)

Generally, commercial sector constributes less percentage share in total final energy demand. However, this sector has high potential for emission reductions. The policy intervention in this sector includes promoting efficient HVAC systems (C-HVAC). This could lead to reduce energy demand of 504 ktoe in 2020 and 1,096 ktoe in 2030, resulting in emission reductions of 3,340 $ktCO_2$ and 7,267 $ktCO_2$.

Industrial energy demand plays a crucial role in terms of managing total energy demand and CO_2 mitigation. The improvement of industrial energy efficiency (I-EE) is expected to reduce energy demand of 6,790 ktoe in 2020 and 14,646 ktoe in 2030, equivalent to emission reductions of 21,061 $ktCO_2$ and 45,431 $ktCO_2$ in the same year. These reductions come from energy

efficiency improvements in boiler and steam, compressed air and lighting systems. In the improvement of efficient electricity end-use devices (I-ELE), the energy savings are expected to be 5,092 ktoe in 2020 and 7,323 ktoe in 2030. CO_2 emission reductions would be 15,796 ktCO_2 and 22,716 ktCO_2 in 2020 and 2030.

Transport sector is expected to play an important role in the reduction of fossil fuels. In this study, only promoting eco-cars (T-ECO) in passenger car is examined. Results show that T-ECO could lead to total energy savings of 153 ktoe in 2020 and 587 ktoe in 2030. These would lead to emission reductions of 438 ktCO_2 in 2020 and 1,685 ktCO_2 in 2030.

Power sector accounts for a large growing share of CO_2 emissions. Increasing efficiency in power plants would lead to emission reductions of 12,602 ktCO_2 in 2030. The results emphasize the significant role of energy efficiency improvments in CO_2 mitigation in the power sector.

4. CONCLUSION

The decarbonizing energy system can be achieved through a combination of strategies. The role of energy efficiency improvements has been examined through energy modeling exercise. The study shows that under the BAU case, the projections of total energy demand and CO_2 emissions from the demand and power sectors would be 170,964 ktoe and 521 MtCO_2 in 2030. In residential sector, significant opportunity exists to reduce energy demand. The two interventions would reduce the energy demand of 1,255 ktoe in 2030, equivalent to CO_2 emissions of 4,868 ktCO_2. The improvement of HVAC system is a significant area in the commercial sector. The C-HVAC could lead to reduce energy demand of 1,096 ktoe in 2030, resulting in emission reductions of 7,267 ktCO_2. The improvement of industrial energy efficiency (I-EE) is expected to reduce energy demand of 14,646 ktoe and reductions of 45,431 ktCO_2 in 2030. In the I-ELE, the potentials of energy savings and CO_2 emission reductions are expected to be 7,323 ktoe and 22,716 ktCO_2 in 2030. Promoting eco-cars (T-ECO) is expected to reduce energy demand of 587 ktoe and emission reductions of 1,685 ktCO_2 in 2030. The power sector is heavily dependent on fossil fuels. Therefore, energy efficiency is an important measure for addressing CO_2 mitigation as well as enhahcing energy security. Increasing efficiency of power plants would reduce emissions of 12,602 ktCO_2 in 2030. With implementation of all energy efficiency improvements, Thailand could reduce the energy demand approximately 25 Mtoe and CO_2 emissions of 95 MtCO_2 in 2030 compared to the BAU projections.

5. REFERENCES

[1] U.S. Energy Information Administration. International Energy Statistic Database: World energy related carbon dioxide emissions: 1980-2010. [online] 2012. Available from: http://www.eia.gov/lies2012.

[2] T. Foran, P.T. du. Pont, P. Parinya, and N. Phumaraphand, "Securing energy efficiency as a high priority: Scenarios for common appliance electricity consumption in Thailand," *Energy Efficiency*, 2010, Vol. 3, No.4, pp. 347-364.

[3] H. Geller, P. Harrington, A. Rosenfeld, S. Tanishima, and F. Unander, "Policies for increasing energy efficiency: Thirty years of experience in OECD countries," *Energy Policy*, 2006, Vol. 34, pp. 556-573.

[4] Stockholm Environment Institute. Handbook on Mitigation Assessment for Non-Annex I Parties. [online] (n.d.) Available from: http://unfccc.int

[5] Energy Policy and Planning Office. Thailand Power Development Plan 2012-2030 (PDP 2010: Revision 3). [online] (n.d.). Available from: http://www.eppo.go.th/power/index.html.

[6] National Economic and Social Development Board and World Bank. Thailand: Clean Energy for Green Low-Carbon Growth. [online] 2011. Available from: http://documents.worldbank.org.

[7] National Economic and Social Development Board. Population Projections for Thailand 2000-2030. [online] 2007. Available from: http://social.nesdb.go.th.

[8] King Mongkut's University of Technology Thonburi. Survey of Residential Energy Consumption, Research Report, Bangkok, Thailand, 2003.

[9] S. Tanatvanit, B. Limmeechokchai, and S. Chungpaibulpatana, "Sustainable energy development strategies: implications of energy demand management and renewable energy in Thailand." *Renewable and Sustainable Energy Reviews*, 2003, Vol. 7, pp. 367-395.

[10] R.M. Shrestha, S. Malla, and M.H. Liyanage, "Scenario-based analyses of energy system development and its environmental implications in Thailand." *Energy Policy*, Vol. 35, pp. 3179-3193.

[11] Thailand Research Fund. Research Programme on Policy Research for Promoting the Development and Utilisation of Renewable Energy and the Improvement of Energy Efficiency in Thailand. [online] 2008. Available from: http://elibrary.trf.or.th.

[12] P. Winyuchakrit, B. Limmeechokchai, Y. Matsuoka, K. Gomi, M. Kainuma, J. Fujino, and M. Suda, "Thailand's low-carbon scenario 2030: Analyses of demand side CO2 mitigation options." *Energy for Sustainable Development*, 2011, Vol. 4, pp. 460-466.

[13] Ministry of Transport. Vehicle Registered in Thailand 1989-2010. [online] (n.d.). Available from: http://apps.dlt.go.th/statistics_web/statistics.html.

[14] N. Chollacoop, P. Saisirirat, T. Fukuda, and A. Fukuda, "Scenario Analyses of Road Transport Energy Demand: A Case Study of Ethanol as a Diesel Substitute in Thailand. *Energies*, 2011, Vol.4, pp. 108-125.

[15] U.S. Agency for International Development. Energy Trends in Developing Asia: Priorities for a Low-Carbon Future. [online] 2011. Available from: http://lowemissionsasia.org/content/energy-trends-developing-asia-priorities-low-carbon-future.

The 7th International Conference on Engineering and Technology
ICET-2015, Phuket, June 19-20, 2015
Prince of Songkla University, Faculty of Engineering
Hat Yai, Songkhla, Thailand 90112

Effects of Sugar Cane Bagasse Ash with High LOI Value on Basalt Aggregate Concrete Properties

Yongmanee R. , Tonnayopas D.*
Geotechnical and Innovative Construction Materials Research Unit (GICMRU),
Faculty of Engineering, Prince of Songkla University, Hat Yai, Songkhla, 90112, Thailand
E-mail of corresponding author: danupon.t@psu.ac.th

Abstract: *Effects of sugar cane bagasse ash (SCBA) with high loss on ignition value on basalt aggregate concrete (BAC) properties was investigated. Ordinary Portland cement, Type I was replaced partially by 15, 20 and 25wt.% SCBA in concrete samples. Water to cementitious material ratio is maintained at 0.4 throughout this study. The specimens were water cured for 7, 28 and 56 days. Bulk density, water absorption, and compressive strengths of hardened concrete were determined. Test results of the BAC incorporated 15% SCBA provided the best performance for high strength concrete.*

Keywords: ***Sugar Cane Bagasse Ash/ Basalt Aggregate/ Mineral Admixture/ High strength concrete***

1. INTRODUCTION

Basaltic rocks are one type widely used as construction materials including aggregates for Portland cement concrete and asphaltic concrete, rock fill for dams and breakwaters, material for railroad ballast and highway base courses [1]. The aggregates quality mainly depends on the rock mass types properties. A number of literature reviews such as Hong et al. [2], Lees and Kennedy [3], Fookes [4], Korkanç and Tuğrul [5], Kazi and Al-Mansour [6] have explained the several geological parameters such as petrographical composition, texture, particle shape, roughness, pores, etc. that influence the mechanical degradation of aggregates. Regarding the texture of a rock is an importance and complex factor affecting strength. Moreover, effect of mineral composition and texture variations of basalt on physico-mechanical properties as aggregate indicate that these rock types improve quality and strength of concrete [7, 8]. On the other hand, basaltic rocks largely have higher bulk density than other rock types. They cause segregation and therefore difficulty in pumping of concrete [9, 10]. Bell [11] indicated that basaltic rocks tend to produce angular rock fragments in crushing.

In almost regions of Thailand are exposed volcanic rocks except the southern [12]. Basaltic rocks are largly the alternative source for crushed rock aggregate in Lower Northeastern Thailand area (Nakhon Ratchasima, Surin, Ubon Ratchatani, Buri Ram, Si Sa Ket). The use of basalts as aggregate material and building stones is widespread in Thailand for long ago. The late of the volcanic eruptions in the area have generally been basic and high sulfur in composition and the Tertiary age of Buri Ram basalt was used in this study [12].

In near future, a part of the Lower northeastern to the Upper northeastern mortorway and high speed railway section of the Asean Transportation Hub (ATH) is proposed passing through several regions of Thailand. Therefore, there is a need for crushed rock for concrete, embankments, granular, ballast and cemented base, etc.

2. MATERIALS AND METHODS

The study was classified into three categories, involving petrographical and chemical characteristics of basalt aggregate and SCBA, the basalt aggregate properties and concrete properties.

2.1. Materials used

Basalt sample was collected as irregular lumps from a quarry in Buriram province. It was fresh to slightly weathered. The basalt aggregate produced from the laboratory jaw crusher. Ordinary Portland cement (OPC) conforming to Thailand standard code TIS 15-12547 [13] was used. Graded river sand passing through 1.18 mm sieve with fineness modulus of 3.34 and specific gravity of 2.56 was used as fine aggregate.

Beside the SCBA used in this study was collected at a local sugar factory in the Nakhon Ratchasima province, Thailand. The SCBA is a waste producted from control burnt in boilers at temperatures varying from 700 to 900°C, depending on the moisture content of the bagasse. The SCBA was ground less than 45 μm or determined by laser particle sie analyser (LPSA) was in in range of 0.869-46.43 μm or 23.84 μm mean grain size before it was used as a cementitious material.

2.2. Experiment procedures

Aggregate properties of the Thai basalt was determined by a various laboratory tests. The specimens were prepared and tested generally in accordance with the standard methods suggested by ASTM, BS and ISRM. Investigated aggregate properties included surface texture of the basalt was observed by using visual, dry specific gravity, water absorption, size and shape based on ASTM C33 [14]. Point load strength index converted to uniaxial compressive strength values and were evaluated on the basis of the ISRM [15] classification. Moreover, the studied basalt sample was broken into smaller pieces by hammer. Standard (10-14 mm) and nominal (6.3-10 mm) size aggregate fractions were provided from the smaller pieces using a laboratory jaw crusher and then cone crusher. The aggregate tests undertaken included flakiness and elongation indices were determined according to the procedures given by BS 812-105.1 [16] and BS 812-105.2 [17], oven-dried specific gravity, water absorption was determined according to the ASTM C C127-12 [18], loose and dense bulk density was also determined in accordance with ASTM C29/C29M-09 [19], aggregate impact value (AIV) test [20] and Los Angeles abrasion value [21]. At least three tests were carried out for each property and the average values were obtained.

2.3. Mix proportions and casting of specimens

SCBA blended cements were prepared by replacing OPC with different amounts of SCBA (15, 20 and 25 wt.%) in dry condition. The mixtures were thoroughly homogenized and kept in polythene bottles before use. Four different proportions of concrete mixes varied from 15 to 25wt.%SCBA, including the control mix were prepared with a water to cementitious material ratio 0.40 which kept constant throughtout in this study. The mix proportions are summarized in Table 1. For all mixes concrete of 100 mm × 100 mm × 100 mm dimension were cast from each batch of all testing. After casting for 24 h. the specimens were then demoulded and transferred to moist curing room until the time of testing.

Table 1. *Ingredients of basalt aggregate concrete sample*

Proportion / Item	Content (kg/m^3)			
	0	15%	20%	25%
OPC, Type I	350	295	280	265
SCBA	0	55	70	85
Basalt aggregate	1080	1080	1080	1080
Sand	830	830	830	830
Water	140	140	140	140

2.4. Characterization of OPC and SCBA

Chemical composition of the SCBA major element oxides were determined by X-ray fluorescence (XRF) method. The results of the chemical analyses were given in Table 2. The total Fe_2O_3 content is low. MgO and SO_3 contents are also too low. But loss on ignition value is rather high 21.01%. This means that SCBA contained high unburnt carbon [22]. Particle size distribution of SCBA was analysed using Coulter LS 230 particle size analyzer and shaped likely OPC. Specific surface area (SSA) of SCBA was obtained using Blain's air permeability method larger than SSA's OPC.

Table 2. *Chemical compositions of cementitious materials in basalt aggregate concrete by XRF*

Chemical composition	OPC (wt.%)	SCBA (wt.%)
SiO_2	70.12	62.76
Al_2O_3	14.34	3.19
Fe_2O_3	0.41	3.89
CaO	6.72	7.00
MgO	1.99	1.47
SO_3	0.98	0.68
LOI	0.51	21.01
Specific surface area (m^2/g)	-	46.612
Void volume (ml/g)	-	0.00344

3. RESULTS AND DISCUSSIONS

3.1. Aggregate properties

The results are summerized in Table 3. Coarse aggregate was crushed basalt fragmented lump, passing through 12.5 mm sieve and retained on 9.5 mm sieve with fineness modulus of 6.67 and specific gravity of 2.72. It found that the flakiness index of the basalt aggregate ranges between 30.71% and 43.70%, and the elongation index ranges between 14.07% and 30.90%. According to BS 882 [14], the flakiness index in crushed stone should be maximum 40%. The basalt aggregate fulfils this requirement. The toughness aggregate varies from 5.63% to 8.40%, presented in Table 3. The loose relative density and compact relative density of the basalt is 1,400 and 1,700 kg/m^3, respectively. Water absorption values range between 0.30% and 1.35% and can be classified as low to high according to the IAEG [23].

Table 3. *Properties of basalt aggregate sample used*

Property test	Test value
Bulk specific gravity	2.68-2.70
Saturated specific gravity	2.39-2.47
Apparent specific gravity	2.71-2.72
Water absorption, %	0.30-1.35
Point load strength index, MPa	3.98-4.63
Modulus of fineness, %	7.03-7.49
Coefficient of uniformity	3.8-6.52
Coefficient of curvature	1.57-2.07
Flakiness index, %	30.71-43.70
Elongation index, %	14.07-30.90
Loose dry density, kg/m^3	≈1,400
Compact dry density, kg/m^3	≈1,700
Los Angeles abrasion wear, %	17.76-22.92
Uniformity factor	0.22-0.24
Impact value, %	5.63-8.40

3.2. Effect of basalt aggregate on concrete

Water absorption is a useful property in assessment durability of different rocks as concrete aggregates. Shakoor et al. [24] has been concluded that rocks with absorption values greater than 3% are subject to freeze–thaw damage. According to test results obtained, basalt has lower water absorption values than 3% (Fig. 1). The

porosity is an important factor in geomaterial strength in those voids reduces the integrity of the material [1,4,11]. As far as frost susceptibility is concerned, the porosity plays an important role [11]. Increase porosity and pore size appears decrease less than 0.004 mm can be caused to reduce the freeze–thaw durability of concrete [9]. Dense basalts are used in production of concrete having high wearing resistance [9]. The strength of a rock is an intrinsic characteristic, but the effective strength of an aggregate particle is modified by its shape and size [3].

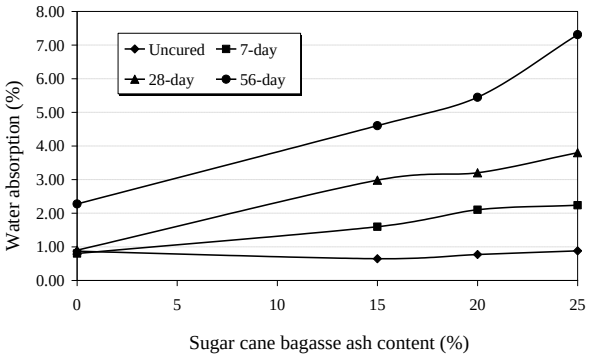

Fig. 1 *Effect of SCBA contents on water absorption of BAC for different curing periods*

Although the correlation between the performance of the geomaterial and the aggregate form is not consistent [8], production of concrete with high compressive strength mainly depends on strength of aggregate. The point load strength of the basalt, having matrix composed certainly of vesicular and amygloidal texture with calcite fill and those affected from basalt magma intrusion in the eastern Thailand. Permissible limit for coarse aggregate is ≤4% [14]. This is also mainly governed by the fracture pattern within a rock mass [5]. Olaleye [25] indicates that some rock aggregates crushed by jaw crusher have higher flakiness and elongation index values. Angular fragments may produce a mix which is difficult to work. Inside, it is rarely self-compacting concrete and offers workability hardly. Nevertheless, angular particles are produced a denser concrete (Fig. 2). In general, strong and hard or brittle rocks produce a higher proportion of flakes than weak rocks, although the latter generate more fines in crushing [5]. The inherent texture affects frictional properties and intertransition zone between unbound aggregate and the adhesion of cementitious material. In concrete, surface roughness is required for an interfacial bond strengh between aggregate and cement or asphalt. In construction use, flakes lead to an increase in the specific surface of the aggregate and control the packing pattern and, therefore, porosity and permeability in the unbound conditions. The flakiness index and elongation index values of the basalt exhibited differences in non significance. It was revealed that the mechanical properties increased with increases in the roughness of a coarse aggregate surface, but the increment decreased on regular plane surface [2]. A rough surface creates a good bond, whereas a smooth surface is poor [11]. This is due to influence of mineral composition, size and percentage of phenocrysts, size and distribution of microlitic plagioclases, size of pores, and microfractures.

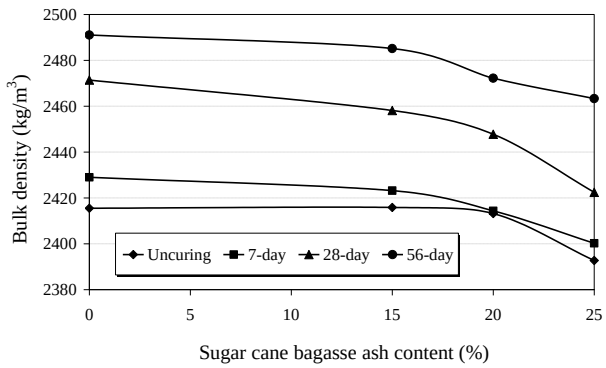

Fig. 2 *Effect of SCBA contents on bulk density of BAC for different curing periods*

3.3. Effect of SCBA on concrete

The highest compressive strength and the pozzolanic activity index of concretes were derived using 15%SCBA of different curing periods (7, 28 and 56 days). As anticipated, strengths increase or decrease with appropriate pozzolanic reactivity of SCBA and curing time (Fig. 3). However, the replacement of OPC by certain amounts of SCBA resulted in a decrease in compressive strength, compared to the control concrete, due to the negative effect resulting from OPC replacement by SCBA with high LOI value. It is continually declined by the increase of SCBA amounts. In accordance to statistical analysis, high significant difference exists in compressive strength of the SCBA-BAC prepared using 15-25%SCBA, comparison uncuring and 7 days of curing. The whole batchs present different values of compressive strength, but increasing with curing periods. After 28 days of curing, all concrete samples given significantly different strengths, base on this experiment, with the exception of 15%SCBA and 20%SCBA batchs, which are similarly equal value. After 56 days, it can be observed that the 15%SCBA and 20%SCBA concretes are nearly same compressive strength development (Fig. 3).

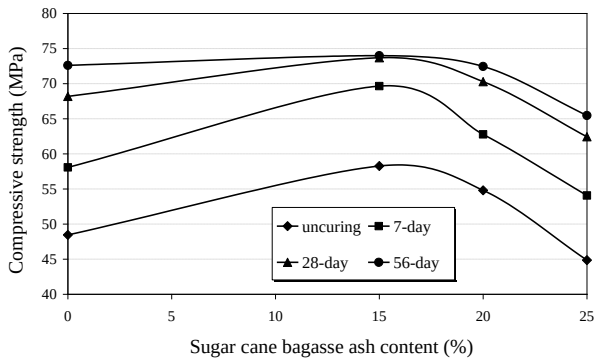

Fig. 3 *Effect of SCBA contents on compressive strength of BAC for different curing periods*

The results indicated the production of concrete with high cement replacement 20%SCBA with the same compressive strength of control concrete was possible. The reactivity of SCBA with OPC was formed large amounts of calcium silicate hydrate (C–S–H) in the hydration time of SCBA [26]. This can be well observed by comparing compressive strengths and SCBA-BAC for

different periods of curing. After 7 days, the strength of SCBA-BAC is about 13% higher than that of the BAC control (Fig 3). Nevertheless, the results obtained after 28 and 56 days of curing are statistically equal, which represent a rise not associated with the filler effect. Especially, the increase in strength between 7 and 56 days is more significant for 15%SCBA and 20%SCBA, when compared to the other batchs with SCBA. The effect of SCBA contents and curing periods on the compressive strength of the BAC are illustrated clearly in Fig. 3.

4. CONCLUSIONS

The investigation results of the effects of the basalt aggregate properties and mineral admixture of SCBA on the BAC samples allowed concluding that a correlation between the water absorption, bulk density and compressive strength of BAC containing SCBA and the curing periods. On the other hand, the compressive strength of BAC containing over 15%SCBA is inversely proportional to SCBA's content. The pozzolanic activity of SCBA was established from the comparison with compressive strength at the same curing period. After more than 28 days of curing, the compressive strength of BAC with 15%SCBA was about 5% higher than the strength of control concrete. Thus, the results suggested that the SCBA with high LOI value displays physico-chemical properties capable for its use as mineral admixture.

5. REFERENCES

[1] R. E. Goodman, "Engineering Geology: Rock in Engineering Construction," Wiley, New York. 1993, 432 pp.

[2] L. Hong, X. Gu, and F. Lin, "Influence of aggregate surface roughness on mechanical properties of interface and concrete," *Constr Build Mater*, 2014, Vol. 65, pp. 338-349.

[3] T. A. Engidasew and G. Barbieri, "Geo-engineering evaluation of Termaber basalt rock mass for crushed stone aggregate and building stone from Central Ethiopia," *J. African Earth Sci*, 2014, Vol. 99, Part 2, pp. 581-594.

[4] Fookes, P.G., "Geomaterials," *Quarterly J Engin Geol*, 1991, Vol. 24, pp. 3-16.

[5] M. Korkanç and A. Tuğrul, "Evaluation of selected basalts from Niğde, Turkey, as source of concrete aggregate," *Eng Geol*, 2004, Vol. 75, Issues 3-4, pp. 291-307.

[6] A. Kazi, and Z. R. Al-Mansour, "Influence of geological factors on abrasion and soundness characteristics of aggregates," *Eng Geol*, 1980, Vol. 15, pp. 195-203.

[7] W. S. Tasong, C. J. Lynsdale, and J.C. Cripps, "Aggregate-cement paste interface: II. Influence of aggregate physical properties," *Cem Concr Res*, 1998, Vol. 8(10), pp. 1453-1465.

[8] D. Tonnayopas, T. Wongwiriyasakul, W. Sae-Toy, and C. Aidpan, "Influence of coarse aggregate type on properties of concrete," *The 6th PSU Engineering* [*Conference*, 8-9 May 2008, Songkhla, pp. 68-73. (in Thai).

[9] P. G. Fookes, "An introduction to the influence of natural aggregates on the performance and durability of concrete," *Quarterly J. Engin Geol*, 1980, Vol. 123, pp. 207- 229.

[10] A. M. Neville, "Properties of Concrete," 4th ed. Pitman, London. 1995, 844 pp.

[11] F. G. Bell, "Engineering Geology and Construction," 1st ed., Spon Press, London, 2006, 807pp.

[12]D. Tonnayopas, "Minerals and Rocks," 1st ed., Dept. of Mining and Materials Engineering, Prince of Songkla University, 2010, 344 p. (in Thai)

[13] TIS 15-1-2547, "Portland cement: Part 1 Specification," Thai Industrial Standard Institute, 1995. (in Thai)

[14] ASTM C33/C33M, "Standard specification for concrete aggregates," West Conshohocken, 2013.

[15] ISRM, "The Complete ISRM Suggested Methods for Rock Characterization, Testing and Monitoring:1974-2006", R. Ulusay and J.A. Hudson (eds.), 2007.

[16] BS 812: Section 105.1:1989, "Testing aggregates. Methods for determination of particle shape: flakiness index," British Standard Institution, 2000.

[17] BS 812: Section 105.2:1989, "Testing aggregates. methods for determination of particle shape: elongates index," British Standard Institution, 2000.

[18] ASTM C127–12, "Standard test method for density, relative density (specific gravity), and absorption of coarse aggregate," West Conshohocken, 2012.

[19] ASTM C29/C29M-09, "Standard test method for bulk density ("unit weight") and voids in aggregate," West Conshohocken, 2009.

[20] BS EN 1097-2, "Test for mechanical and physical properties of aggregates. Method for the determination of resistance to fragmentation," British Standard Institution, 2010.

[21] ASTM C131/C131M-14, "Standard test method for resistance to degradation of small-size coarse aggregate by abrasion and impact in the Los Angeles machine," West Conshohocken, 2014.

[22] G.C., Cordeiro, R.D., Toledo Filho, L.M. Tavares, and E.M.R. Fairbairn, "Ultrafine grinding of sugar cane bagasse ash for application as pozzolanic admixture in concrete", *Cem Concr Res*, 2009, Vol. 39(2), pp. 110–115.

[23]IAEG, "Classification of rocks and soils for engineering geological mapping. Part 1, rock and soil materials," *IAEG Bulletin*, 1979, Vol. 19(1), pp.364-371.

[24] A. Shakoor, T.R. West, and C. F. Scholer, "Physical characteristics of some Indiana argillaceous carbonates regarding their freeze–thaw resistance in concrete,"*IAEGBulletin*,1982, Vol. 19(4), pp.371–384.

[25] B.M. Olaleye, "Influence of some rock strength properties on jaw crusher performance in granite quarry mining," *Science and Technology (China)*, 2010, Vol. 20(2), pp. 204-208.

[26] N. B. Singh, V. D. Singh, and R. Sarita, "Hydration of bagasse ash-blended Portland cement," *Cem Concr Res*, 2000, Vol. 30(9), pp. 1485-1488.

The 7th International Conference on Engineering and Technology
ICET-2015, Phuket, June 19-20, 2015
Prince of Songkla University, Faculty of Engineering
Hat Yai, Songkhla, Thailand 90112

Analytical Solution of Temperature Fields and Effectiveness of Multi-Pass Cross-Flow Heat Exchanger

Dušan Gvozdenac*
University of Novi Sad, Faculty of Technical Sciences, Novi Sad, Serbia
*Email of corresponding author: dusan.gvozdenac@gmail.com

Abstract: *A method for analytical solving the mathematical model of cross-flow heat transfer problem with both fluids unmixed in a multi-pass heat exchanger is presented. The fluid with lower heat capacity rate is considered mixed between passes. Assuming that the temperature distribution of this fluid at the entrance is an arbitrary multi-pass function and specifying the order of coupling the passes in identic order, the corresponding temperature fields, mean mixed exit temperatures and the heat exchanger effectiveness are obtained. These close form solutions are convenient for practical engineering use.*

Key Words: ***Heat Exchangers/Multi-Pass Cross-Flow***

1. INTRODUCTION

In a large number of technical problems, there are mathematical difficulties to find an accurate solution. When heat exchangers are concerned, these difficulties are particularly pronounced for cross flows in case when fluid flows are not mixed perpendicularly to the flow. Such exchangers are discussed in this paper. From a practical engineering standpoint, the greatest importance is attributed to the determination of the exchanger's effectiveness as the function of the number of transfer units (NTU), thermal capacity rate ratio (ω) and flow arrangement. This requires the knowledge of temperature fields by solving the corresponding system of partial differential equations of the first order for a special class of boundary conditions. The presented method enables unique approach not only to solving single-pass cross flow heat exchanger (both fluids unmixed) but also to finding temperature fields, mean mixed outlet temperatures and the effectiveness of some of multi-pass cross-flow heat exchangers.

According to our information, this problem has been considered only in [3]. However, the solutions there are given only in a formal expression that significantly complicates practical application. The solutions presented here are not burdened with this deficiency and they are in a general form suitable for practical use.

The paper [1] considers the same problem, but the solution presented here are more suitable for practical use.

The opportunities provided by numerous numerical methods and available software do not allow the possibility of maintaining physical essence of a mathematical problem. Only an analytical solution maintains the physical basis of a studied problem and this is an advantage of the proposed procedure in relation to numerical ones.

2. PROBLEM DEFINITION

The drawing of a cross-flow heat exchanger which is used for mathematical analysis is shown in Fig. 1. It contains the necessary system of designation and coordinates which will be used in this paper. The fluid 1 flows in the X direction and the fluid 2 in the Y direction. The fluid flows are not mixed perpendicularly to their flows. Making the usual asssumptions for any heat exchangers [2,4,5] and applying them to this problem, the following two partial differential equations are obtained:

$$-\frac{\partial\theta_1(x,y)}{\partial x} = \theta_1(x,y) - \theta_2(x,y) \tag{1}$$

$$\frac{\partial\theta_2(x,y)}{\partial y} = \theta_1(x,y) - \theta_2(x,y) \tag{2}$$

Common boundary conditions imply constant inlet temperatures. However, the problem is resolved here for the case when inlet temperature profile of the fluid flow "1" is an arbitrary function and of the flow "2" it is constant. In a dimensionless form, boundary conditions are:

$$\begin{aligned}\theta_1' &= \theta_1(0,y) = \phi_1(y)\\ \theta_2' &= \theta_2(x,0) = 0\end{aligned} \tag{3}$$

The problem formulated in this way enables finding out temperature fields for both single-pass and multi-pass heat exchangers.

3. PROBLEM SOLUTION FOR SINGLE-PASS CROSS-FLOW HEAT EXCHANGER

To resolve the defined boundary problem, Laplace integral transforms can be used. Differentiation of the

equation (1) along "y" and substitution of $\partial\theta_2/\partial y$ from the equation (2) and θ_2 from the equation (1) generates a hyperbolic partial differential equation:

$$\frac{\partial^2\theta_1(x,y)}{\partial x\cdot\partial y}+\frac{\partial\theta_1(x,y)}{\partial x}+\frac{\partial\theta_1(x,y)}{\partial y}=0 \tag{4}$$

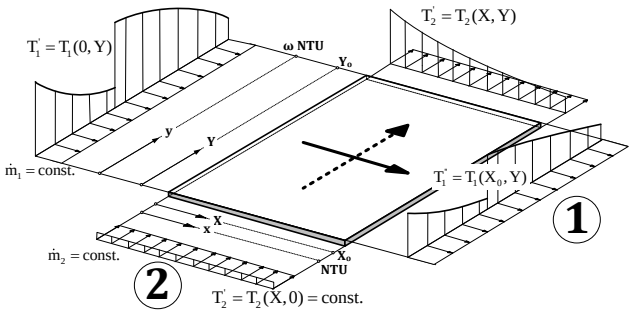

$X \in [0, X_0]$; $Y \in [0, Y_0]$ $\quad x \in [0, A]$; $y \in [0, B]$

Figure 1. Scheme of the Cross-Flow Heat Exchanger

By Laplace transform of this equation along "y", a non-homogenous common differential equation is obtained. Solving this equation by using the first of the boundary conditions (3) gives:

$$\begin{aligned}\mathbb{L}_y\{\theta_1(x,y)\} &= \theta_{1L}(x,s)\\ &= \phi_{1L}(s)\cdot\exp\left[-\frac{x\cdot s}{s+1}\right]\end{aligned} \tag{5}$$

and, by its inverse Laplace transform, it follows that:

$$\theta_1(x,y)=\mathbb{L}_y^{-1}\left\{\phi_{1L}(s)\cdot\exp\left[-\frac{x\cdot s}{s+1}\right]\right\} \tag{6}$$

The temperature filed of the flow 2 is determined from the equation (1) buy means of the determined $\theta_1(x,y)$:

$$\theta_2(x,y)=\theta_1(x,y)+\frac{\partial\theta_1(x,y)}{\partial x} \tag{7}$$

The equations (6) and /7) define required temperature fields of fluid flows. The example of a single-pass cross-flow exchanger with a constant inlet temperature of the flow "1" will be used to demonstrate the procedure for determining temperature fields and exit temperatures. Since $\theta_1(0,y)=\phi_1(y)=1$ from the equation (6), it follows that:

$$\theta_1(x,y)=\mathbb{L}_y^{-1}\left\{\phi_{1L}(s)\cdot\exp\left[-\frac{x\cdot s}{s+1}\right]\right\} \tag{8}$$

The exponential function can be expresses as an endless series and the expression (8) becomes:

$$\theta_1(x,y)=\mathbb{L}_y^{-1}\left\{\frac{1}{s}\cdot\sum_{k=0}^{\infty}(-1)^k\cdot\frac{x^k}{k!}\cdot\left(\frac{s}{s+1}\right)^k\right\} \tag{9}$$

and, since:

$$\frac{1}{s}\cdot\left(\frac{s}{s+1}\right)^k=\sum_{i=0}^{\infty}(-1)^i\frac{(k+i-1)!}{(k-1)!\cdot i!}\cdot\frac{1}{s^{i+1}}\quad \text{for } k\geq 1 \text{ and } s>0 \tag{10}$$

determination of inverse Laplace transform becomes very simple. It follows that the temperature field of the flow "1" is:

$$\begin{aligned}\theta_1(x,y) &= F_1(x,y)\\ &= 1\\ &+\sum_{k=1}^{\infty}\sum_{i=0}^{\infty}(-1)^{k+i}\\ &\cdot\frac{(k+i-1)!}{(k-1)!\cdot i!}\cdot\frac{x^k}{k!}\cdot\frac{y^i}{i!}\end{aligned} \tag{11}$$

The temperature field of the flow "2" is obtained by the equation (7) and by performing simple mathematical operations on the equation (11). Thus, the following is obtained:

$$\theta_2(x,y)=F_1(x,y)-F_0(x,y) \tag{12}$$

where

$$\begin{aligned}F_0(x,y) &= -\frac{\partial F_1(x,y)}{\partial x}\\ &= \sum_{k=1}^{\infty}\sum_{i=o}^{\infty}(-1)^{k+i-1}\\ &\cdot\frac{(k+i-1)!}{(k-1)!\cdot i!}\cdot\frac{x^{k-1}}{(k-1)!}\cdot\frac{y^i}{i!}\end{aligned} \tag{13}$$

The mean exit temperature of the flow "1" is obtained with the integration of the exit temperature profile along the outlet edge of the exchanger:

$$\bar{\theta}_1''=\frac{1}{B}\int_0^B\theta_1(A,v)\cdot dv=\frac{1}{B}\cdot F_2(A,B) \tag{14}$$

where

$$\begin{aligned}F_2(x,y) &= \int_0^y F_1(x,v)\cdot dv\\ &= y\\ &+\sum_{k=1}^{\infty}\sum_{i=o}^{\infty}(-1)^{k+i}\\ &\cdot\frac{(k+i-1)!}{(k-1)!\cdot i!}\cdot\frac{x^k}{k!}\cdot\frac{y^{i+1}}{(i+1)!}\end{aligned} \tag{15}$$

The effectiveness of any heat exchanger is $\varepsilon=1-\bar{\theta}_1''$. In case of the single-pass cross-flow exchanger, it is $\varepsilon=1-F_2(A,B)/B$. The equation that exit temperature of the fluid "2" is $\bar{\theta}_2''=\omega\cdot\varepsilon$ is also valid.

4. PROBLEM SOLUTION FOR MULTI-PASS CROSS-FLOW HEAT EXCHANGER

Connecting several single-pass cross-flow exchangers so that the flow "2" does not mix perpendicularly on its way and the flow "1" is led to an arbitrary section and after passing without perpendicular mixing upon leaving the section goes into the second pass produces a multi-pass heat exchanger (Figure 2).

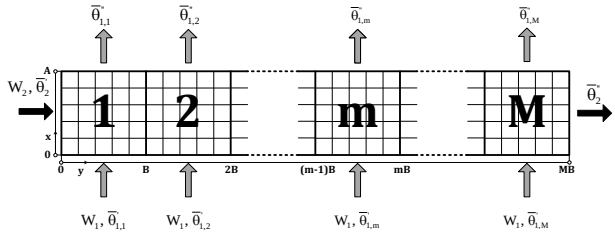

Figure 2. Multi-Pass Cross-Flow Heat Exchanger

Such a heat exchanger can be observed as a single-pass one with the discrete distribution inlet temperature profile of fluid "1". Boundary conditions of this exchanger are as follows:

$$\phi_1(y) = \begin{cases} 0 & y < y_1 \\ \bar{\theta}'_{1,m}=\text{const.} & y_m \le y \le y_{m+1} \\ 0 & y > y_{M+1} \end{cases} \quad (m = 1,2,\dots,M) \qquad \bar{\theta}'_2 = 0 \tag{16}$$

If number of transfer units of all multi-pass heat exchangers is NTU and the number of passes is M, then for each pass, it will be $A = NTU/M$; $B = \omega \cdot NTU/M$, and independent variables will be changed in intervals $x \in [0, NTU/M]$ and $y \in [0, \omega \cdot NTU/M]$.

Since

$$\phi_{1,L} = \mathbb{L}_y\{\phi_1(y)\} = \sum_{j=1}^{M} \frac{\bar{\theta}'_{1,m} - \bar{\theta}'_{1,m-1}}{s} \cdot \exp(-s \cdot y_m) \quad (m = 1,2,\dots,M) \tag{17}$$

the temperature field of the flow "1" will be (Eq. 6):

$$\theta_{1,m}(x,y) = \mathbb{L}_y^{-1}\left\{\sum_{j=1}^{m} \frac{\bar{\theta}'_{1,j} - \bar{\theta}'_{1,j-1}}{s} \cdot \exp(-s \cdot y_j) \cdot \exp\left(-\frac{x \cdot s}{s+1}\right)\right\} \quad (j = 1,2,3,\dots m) \text{ and } (m = 1,2,3,\dots M) \tag{18}$$

The inverse Laplace transform gives:

$$\theta_{1,m}(x,y) = \sum_{j=1}^{m}\left(\bar{\theta}'_{1,j} - \bar{\theta}'_{1,j-1}\right) \cdot \begin{cases} 0 & y < y_1 \\ F_1(x, y - y_j) & y_j \le y \le y_{j+1} \\ 0 & y < y_m \end{cases} \quad (j = 1,2,3,\dots m) \text{ and } (m = 1,2,3,\dots M) \tag{19}$$

The application of this equation is conditioned by the knowledge of inlet temperatures of the flow "1" ($\bar{\theta}'_{1,m}$), and they are dependent upon the flow "1" entry into the exchanger and the sequence of its pass through the section. The temperature field of the flow "2"is obtained from the equation (7).

5. EXAMPLE

If the inlet section of the flow "1" is divided into three equal sections (Figure 3), it is possible to obtain six different flow schemes depending on the sequence of the flow "1" entry and the manner of connection of inlet flows. Below the graphical presentation, there is a mathematical expression for the conditions of the fluid flow's "1" connection.

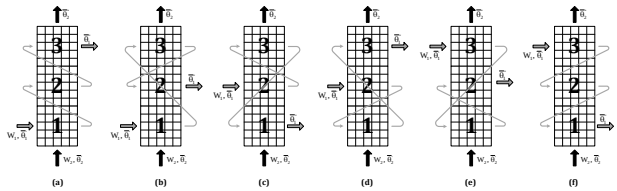

(a) $\bar{\theta}'_1 = \bar{\theta}'_{1,1} = 1$ $\bar{\theta}''_{1,1} = \bar{\theta}'_{1,2}$ $\bar{\theta}''_{1,2} = \bar{\theta}'_{1,3}$ $\bar{\theta}''_{1,3} = \bar{\theta}''_1$	**(b)** $\bar{\theta}'_1 = \bar{\theta}'_{1,1} = 1$ $\bar{\theta}''_{1,1} = \bar{\theta}'_{1,3}$ $\bar{\theta}''_{1,3} = \bar{\theta}'_{1,2}$ $\bar{\theta}''_{1,2} = \bar{\theta}''_1$	**(c)** $\bar{\theta}'_1 = \bar{\theta}'_{1,2} = 1$ $\bar{\theta}''_{1,2} = \bar{\theta}'_{1,3}$ $\bar{\theta}''_{1,3} = \bar{\theta}'_{1,1}$ $\bar{\theta}''_{1,1} = \bar{\theta}''_1$
(d) $\bar{\theta}'_1 = \bar{\theta}'_{1,2} = 1$ $\bar{\theta}''_{1,2} = \bar{\theta}'_{1,1}$ $\bar{\theta}''_{1,1} = \bar{\theta}'_{1,3}$ $\bar{\theta}''_{1,3} = \bar{\theta}''_1$	**(e)** $\bar{\theta}'_1 = \bar{\theta}'_{1,3} = 1$ $\bar{\theta}''_{1,3} = \bar{\theta}'_{1,1}$ $\bar{\theta}''_{1,1} = \bar{\theta}'_{1,2}$ $\bar{\theta}''_{1,2} = \bar{\theta}''_1$	**(f)** $\bar{\theta}'_1 = \bar{\theta}'_{1,3} = 1$ $\bar{\theta}''_{1,3} = \bar{\theta}'_{1,2}$ $\bar{\theta}''_{1,2} = \bar{\theta}'_{1,1}$ $\bar{\theta}''_{1,1} = \bar{\theta}''_1$

Figure 3. Possible Combinations of the Three-Pass Cross-Flow Exchanger

The equation (19) for M=3 determines three temperature fields and for x=A, three exit profiles of the flow "1", as well. Mean temperatures of the flow "1" after each pass are obtained by the integration of these profiles in boundaries [0,B]. These temperatures are:

$$\begin{aligned} \bar{\theta}''_{1,1} &= \frac{1}{B} \cdot \bar{\theta}'_{1,1} \cdot F_2(A,B) \\ \bar{\theta}''_{1,2} &= \frac{1}{B} \cdot \left(\bar{\theta}'_{1,2} - \bar{\theta}'_{1,1}\right) \cdot F_2(A,B) + \frac{1}{B} \cdot \bar{\theta}'_{1,1} \cdot [F_2(A,2B) - F_2(A,B)] \\ \bar{\theta}''_{1,3} &= \frac{1}{B} \cdot \left(\bar{\theta}'_{1,3} - \bar{\theta}'_{1,2}\right) \cdot F_2(A,B) + \frac{1}{B} \cdot \left(\bar{\theta}'_{1,2} - \bar{\theta}'_{1,1}\right) \cdot [F_2(A,2B) - F_2(A,B)] + \frac{1}{B} \cdot \bar{\theta}'_{1,1} \cdot [F_2(A,3B) - F_2(A,2B)] \end{aligned} \tag{19}$$

Calculation results of exit temperatures of the flow "1" and their mean value between steps are shown in the Table 1. In addition, the effectiveness of the heat exchanger is presented. The outlet temperature of the flow "2" is obtained from the general relation $\bar{\theta}''_2 = \omega \cdot \varepsilon$. In this example, the NTU = 4 and ω = 1. As it is expected, the most efficient is the scheme f that is a combination of a counter-flow and a cross-flow exchanger.

Table 1. Results of Calculation

Scheme a			
Inlet		*Outlet*	
$\theta'_{1,1}$	1,000	$\theta''_{1,1}$	0,463
$\theta'_{1,2}= \theta''_{1,1}$	0,463	$\theta''_{1,2}$	0,492
$\theta'_{1,3}=\theta''_{1,2}$	0,492	$\boldsymbol{\theta''_{1,3}}$	**0,498**
ε=0,502			
Scheme b			
Inlet		*Outlet*	
$\theta'_{1,1}$	1,000	$\theta''_{1,1}$	0,463
$\theta'_{1,2}=\theta''_{1,3}$	0,493	$\boldsymbol{\theta''_{1,2}}$	**0,506**
$\theta'_{1,3}=\theta''_{1,1}$	0,463	$\theta''_{1,3}$	0,493
ε=0,494			
Scheme c			
Inlet		*Outlet*	
$\theta'_{1,1}=\theta''_{1,3}$	0,674	$\boldsymbol{\theta''_{1,1}}$	0,312
θ'1,2	1,000	$\theta''_{1,2}$	0,650
$\theta'_{1,3}=\theta''_{1,2}$	0,650	$\theta''_{1,3}$	0,674
ε=0,688			
Scheme d			
Inlet		*Outlet*	
$\theta'_{1,1}=\theta''_{1,2}$	0,641	$\theta''_{1,1}$	0,297
$\theta'_{1,2}$	1,000	$\theta''_{1,2}$	0,641
$\theta'_{1,3}=\theta''_{1,1}$	0,297	$\boldsymbol{\theta''_{1,3}}$	**0,506**
ε=0,494			
Scheme e			
Inlet		*Outlet*	
$\theta'_{1,1}=\theta''_{1,3}$	0,635	$\theta''_{1,1}$	0,294
$\theta'_{1,2}=\theta''_{1,1}$	0,294	$\theta''_{1,2}$	0,312
$\theta'_{1,3}$	1,000	$\boldsymbol{\theta''_{1,3}}$	**0,635**
ε=0,688			
Scheme f			
Inlet		*Outlet*	
$\theta'_{1,1}=\theta''_{1,2}$	0,470	$\boldsymbol{\theta''_{1,1}}$	**0,218**
$\theta'_{1,2}=\theta''_{1,3}$	0,733	$\theta''_{1,2}$	0,470
$\theta'_{1,3}$	1,000	$\theta''_{1,3}$	0,733
ε=0,782			

6. CONCLUSION

In this paper, the analytical solution of the heat exchanger between the fluid "1" flows in the X direction and the fluid "2" flows in the Y direction separated with a tin wall is presented. The fluid flows are not mixed perpendicularly to their flow. The fluid "1" is mixed between passes for multi-pass heat exchanger. Assuming that inlet temperature of the fluid "1" is a discrete distribution function and assigning the sequence of passes of this flow through individual steps generates corresponding temperature fields, mean exit temperatures and effectiveness of multi-pass cross-flow heat exchangers. Shown analytical solutions are suitable for practical application as they are easily programmable.

Nomenclature

A = NTU/M
B = ω NTU/M
F heat transfer area, [m^2]
h heat transfer coefficient between fluid and exchanger wall, [W/(m^2 K)]
m mass flow rate, [kg/s]
M number of passes
NTU = UF/W_1, number of transfer units, dimensionless
T temperature, [K]
U overall heat transfer coefficient, [W/(m^2 K)]
$F_0(x,y)$; $F_1(x,y)$; $F_2(x,y)$ = functions defined in Eqs. (13, 11 and 15)
W thermal capacity rate, M c_p, [W/K]
ε $=(T_1' - T_1'')/(T_1' - T_2')$, effectiveness of the heat exchanger, dimensionless
ω = W_1/W_2, thermal capacity rate ratio, dimensionless
θ $=(T - T_1'')/(T_1' - T_2')$, dimensionless temperature
$\bar{\theta}$ dimensionless mean mixed fluid temperature
ξ = x/A, dimensionless coordinate
η = y/B, dimensionless coordinate

Subscripts
1 refers to fluid with (M $c_p)_{min}$
2 refers to fluid with (M $c_p)_{max}$
A refers to the pass A
B refers to the pass B
i, j, k integers

Superscripts
' at exchanger inlet
" at exchanger outlet

REFERENCES

[1] B. S. Bačlić B S and D. D. Gvozdenac, "Exact Explicit Equations for some Two- and Three-Pass Cross-Flow Heat Exchangers Effectiveness", *NATO Advance Study Institute on Heat Exchangers – Heat Transfer & Fluids Flow Fundamentals*, Istanbul, 4-15 Aug 1980.

[2] D. Gvozdenac, "Analytical Solution of Dynamic Response of Heat Exchanger", *Chapter 2 in Heat Exchanger-Basic design Application, Ed. Jovan Mitrović, INTECH*, 2012 (www.intechopen.com)

[3] A. E. Jampol'skij, "Temperaturtnye polja v mnogohodovyh perekrestno-točnyh teploobmenikah s nepremešivajušćomisja teplonositeljami", *Teploenergetika*, No 7, 1980, pp 53-56

[4] W. Nusselt, "Der Wärmeübergang im Kreuzstrom", *VDI-Z*, Vol 55, 1911, pp. 2021-2024

[5] W. Roetzel and Y. Xuan, "Dynamic Behaviour of Heat Exchangers", *Developments in Heat Transfer*, Volume 3, WITpress/Computational Mechanics Publications, 1999

The 7th International Conference on Engineering and Technology
ICET-2015, Phuket, June 19-20, 2015
Prince of Songkla University, Faculty of Engineering
Hat Yai, Songkhla, Thailand 90112

Simulation model of haulage system(Shovel and trucks) at Mae Moh Lignite mine Lampang,Thailand

Siwarin Kanthik[1]*, Manoon Masniyom[2]
[1]Prince of Songkla University, Faculty of Engineering, Thailand
[2]Prince of Songkla University, Faculty of Engineering, Thailand
*Email of corresponding author: sine.siwarin@gmail.com

Abstract: *This research is aimed to study the Mae Moh Lignite open pit mine truck- shovel haulage systems using computer simulation approach. The lignite mining were operated principally by the state-owned Electricity Generating Authority of Thailand (EGAT)in Lampang ,Thailand. Haulage system data gathered from South – East Pit of Mae Moh's Lignite mine. The data that we apply for created the model have to reference the statistic data from real working area.*
Firstly, the data is set of shovel and truck from the activities collected at Mae Moh's Lignite mine on October 2012 to September 2013. The compile data had feature by SPOT1 , Loading , Traveling loaded (TVL) , SPOT2 , Dumping and Traveling empty (TVE). Secondly, the statistic data was analysis to find the mean and standard deviation (S.D.) for adapt to the model. In this study, the model had made to find the number of trucks (Model , Hitachi EUCLID EH 1700 truck capacity 100 tons.) that suitably for shovel – Demag H185S (Bucket capacity 14 Cu.m.) and shovel – Demag H95 (Bucket capacity 7.5 Cu.m.) which differend haulage distance. The result that hearing by % utilization of loading more than 90%.
In case of, loading by Demag H185S have to using 3 trucks and the percentage for maximum's haulage distance is 400 meter , using 4 trucks for 1,300 meter. In case of, loading by Demag H95 have to using 2 trucks for haulage distance is 200 meter and 3 trucks for haulage distance 1,000 , 1,300 , 1,600 meter the percentage for maximum.

Key Words: *Simulation / haulage system*

1. INTRODUCTION

The Mae Moh lignite mine were operated principally by the state-owned Electricity Generating Authority of Thailand (EGAT) in Lampang,Thailand.(Fig.1)
The Lignite from mine had haulage to stock pile by conveyor system and then it will be delivered to power plant. Mae Moh power plant have to used lignite from Mae Moh mine around 15-17 million tons / year.
So the haulage system is very importance for production. Simulation model from Arena simulation program can increase the percentage for utilization.

Fig. 1. Mae Moh Lignite mine location

The truck have to waiting in coal area for loading, using shovel Demag H185S or shovel Demag H95.(Fig.2and 3)

Fig. 2. Loading by Demag H185S

Fig. 3 Loading by Demag H95

Each fully loaded the truck must be weighed to record. After that the truck is traveling to EGAT crusher, where the coal must be dumped. Then the empty truck will returns to coal area and starts the cycle over again.
(Fig.4)

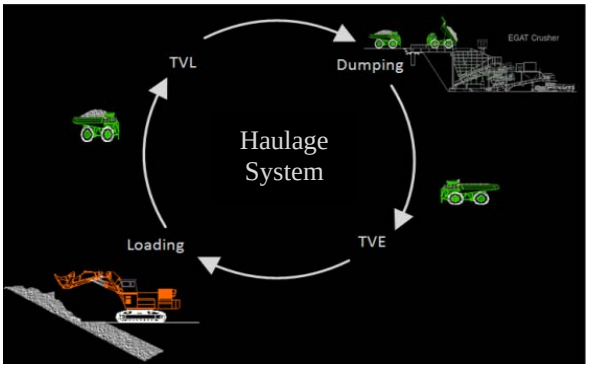

Fig. 4. Coal haulage cycle

2. METHODOLOGY

2.1. Field data

The data is set of shovel and truck from the activities collected at Mae Moh's Lignite mine on October 2012 to September 2013.The compile data is feature by the process time such as SPOT1 , Loading , Traveling loaded (TVL) , SPOT2 , Dumping and Traveling empty (TVE).(Table.1)

Table 1. *Field cycle time data*

Date : 15/12/12					
Shovel: H95					
Material: Coal					
Haulage distance:1,600 m.					
Cycle time (minute)					
SPOT1	Loading	TVL	SPOT2	Dumping	TVE
0.42	4.27	4.46	0.58	1.04	2.55
0.53	4.33	4.38	1.22	0.56	2.58
0.48	4.15	4.13	0.44	1.01	2.30
1.02	4.28	4.33	0.59	0.58	2.57
0.33	4.23	4.26	1.04	0.54	2.42
0.28	4.14	4.17	0.50	0.57	3.02
0.46	4.32	4.11	0.45	1.02	2.44
0.55	4.41	4.22	0.52	0.52	2.56
0.51	4.30	4.27	0.59	1.09	2.51
1.13	4.18	4.34	0.48	1.01	2.59

2.1. Statistical analysis

The compile data had analyzed for evaluate mean and standard deviation (S.D.) of SPOT1 , Loading , Traveling loaded (TVL) , SPOT2 , Dumping and Traveling empty (TVE)by the function Input Analyzer on Arena programe. (Fig.5)

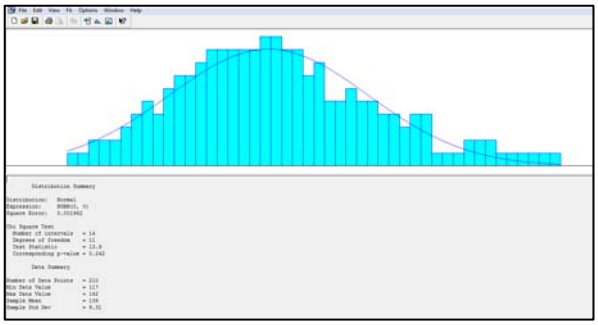

Fig. 5. Input Analyzer on Arena simulation programe

2.3. Simulation model

After the statistical analysis, the data were prepared for the simulation model on Arena simulation programe. The simulation model had made to fine the appropriate number of haulage system. (Fig.6)

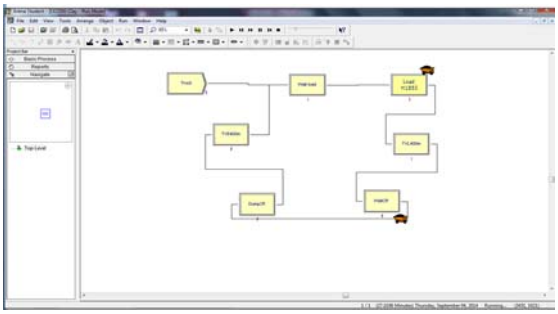

Fig. 6. Simulation model by Arena programe

3. RESULT

3.1. Statistical analysis

The compile data had analyzed for evaluate mean and standard deviation (S.D.) by the function Input Analyzer on ARENA SIMULATION programe. (Table.2,3 and 4)

Table 2. *Mean and Standard deviation of loading*

Shovel	Mean (Sec.)	Standard deviation (S.D.)
Demag H185S	220	9.28
Demag H95	357	14.30

Table 3. *Mean and Standard deviation of TVL and TVE*

Haulage Distance (Meter)	Traveling Loaded		Traveling Empty	
	Mean (Sec.)	S.D.	Mean (Sec.)	S.D.
200	47	6.43	43	4.95
400	110	3.07	63.5	6.98
600	119	6.53	89.9	13.1
800	145	10.7	121	8.81
1,000	163	7.15	144	6.28
1,300	244	9.73	175	9.97
1,600	270	9.87	216	7.83

Table 4. *Mean and Standard deviation of dumping*

	Mean (Sec.)	S.D.
Dumping	38.1	6.02

3.2. Simulation model

The simulation model of haulage system, whitch loading by Demag H185S and Demag H95can working 10 Hrs./shift. The simulation model of haulage system, whitch the maximum for loading of Demag H185S (Bucket capacity 14 Cu.m.) are 166 trips (80 tons per trip) and 99.92 % utilization. (In Table.5) And loading by Demag H95 (Bucket capacity 7.5 Cu.m.) are 102 trips (80 tons per trip) and 99.92 % utilization. (In Table.6)

Table 5. *Simulation results, loading by Demag H185S*

Haulage Distance (Meter)	Number of trucks	Number of trips (Loading)	% utilization of shovel
200	2	153	93.50
400	3	166	99.92
600	3	165	99.60
800	3	162	97.86
1,000	3	155	93.79
1,300	4	166	99.92
1,600	4	162	97.42

Table 6. *Simulation results, loading by Demag H95*

Haulage Distance (Meter)	Number of trucks	Number of trips (Loading)	% utilization of shovel
200	2	101	99.92
400	2	100	99.25
600	2	98	97.17
800	2	92	91.74
1,000	3	102	99.92
1,300	3	102	99.92
1,600	3	102	99.92

4. CONCLUSION

The appropriate number of trucks in the haulage system , loading by Demag H185S (Bucket capacity 14 Cu.m.) for haulage distance 200 meter have to using 2 trucks (truck capacity 100 tons.), 400 meter - 1,000 meter have to using 3 trucks and 1,300 meter - 1,600 meter have to using 4 trucks. And for loading by Demag H95 (Bucket capacity 7.5 Cu.m.) for haulage distance 200 meter - 800 meter have to using 2 trucks and 1,000 meter - 1,600 meter have to using 3 trucks.

5. REFERENCES

[1] Krause A. and Musingwini C. , " Modeling Open Pit Shovel-truck SystemsUsing the Machine Repair Model," *The Journal of The Southern African Instituteof Mining and Metallurgy*, 2007, pp.469-476.

[2] Cetin N., Erarslan I.C., Okuducu A., " Computer Simulation of Truck/Shovel System at Tuncbilek Coal Mine Using GPSS/H," *International Mining Congress and Exhibition of Turkey :IMCET 2001*,June 19-22,2001, pp.715-718.

[3] Leelasukseree C. and Rujittawiwat W. , "Coal haulage simulation of Truba Indo Coal Mine. *The 10 th International Conference on Mining ,Materials and Petroleum Engineering:PSU-IC 2012* ,May 9-11,2012.

The 7th International Conference on Engineering and Technology
ICET-2015, Phuket, June 19-20, 2015
Prince of Songkla University, Faculty of Engineering
Hat Yai, Songkhla, Thailand 90112

A low cost, rapid prototyping of microfluidic device: an approach to separate blood plasma

Cheewarak Rodniam, Somyot Chirasatitsin*
Prince of Songkla University, Faculty of Medicine, Institute of Biomedical Engineering, Thailand
*Email of corresponding author: somjot.c@psu.ac.th

Abstract: *This study applied a low-cost and rapid fabrication technique using a cutting plotter to address the prototype of microfluidic device for blood plasma separation. Microchannels were carved into commercial clear plastic films made from polyvinylchloride with plasticizer and polyethylene terephthalate. The results revealed the capability to create negative microchannels whose sizes less than 100 µm on to the films. The channel distortion occurred on the horizontal cutting axis more than the vertical one. The final microfluidic device established the drift or cell-free layer (CFL) enhanced at downstream channel about 10 µm thick, which provided the region to separate blood plasma.*

Key Words: ***Microfluidics / Rapid Prototyping / Cutting plotters / Cell-free layer***

1. INTRODUCTION

The development of microfluidics has grown rapidly over the past decade. Microfluidic devices (µF) have been widely applied in many fields including scientific, industrial, and biomedical fields. Most of the microfluidic devices are made from the method based on a microelectronic fabrication technique, called photolithography, on materials like glass, quartz, or silicon and poly(dimethylsiloxane) (PDMS). However, this technique is quite complicated and required expensive apparatus.

For developing countries, the major challenge is how to fabricate the devices in a rapid, simple, and inexpensive way. Numerous of unconventional low cost fabrication techniques have been presented, such as patterning SU-8 photoresist and wax onto papers[1], x-y desktop plotting[1] and xurography[2]–[4], to address these challenges. Some drawbacks, *e.g.*, less precise, unsmooth surface, low resolution, appeared among the fabrication methods. Xurographic prototyping is a useful and inexpensive research tool to focus on the microfluidic device development before moving to higher qualitative techniques[2]. The hardware resolution is specified by the resolution of motors, while the software resolution is limited with the resolution down to 25 µm of step size[2]. Craft cutting plotters, with thin cutting blade, are presented to carve microchannels directly to the surface of various materials[2]. This easy–to–prototype, inexpensive, method enhances the microchannel fabrication without clean room facilities.

This study applied the low-cost fabrication technique using a cutting plotter with inexpensive materials of transparent plastic films to address the microfluidic device for blood plasma separation. Because blood samples are usually separated into blood plasma before performing blood tests, separating plasma on microfluidic devices would be a challenge. Many researches

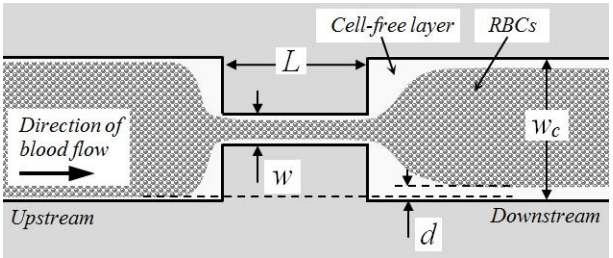

Fig. 1. Layout of microchannel for the microfluidic cell focusing device., where w_c is the width of the main channel upstream and downstream. The length (L) and width (w) were geometry of rectangular constriction channel.

reported that manipulating geometry of microchannel affected the hydrodynamic separation of red blood cells (RBCs) and plasma. Faivre *et al.* presented the manipulatation in width (*w*) and length (*L*) of the rectangular constriction channel shown in Fig.1 to enhance CFL or drift *d* at downstream[5]. Then, the enhanced CFL was applied to separate blood plasma in microfluidic devices[6]. This passive techinque was possible to extract plasma 10-25% out of the injected volume, with an excellent purity, low contamination rate, even for 1:10 and 1:20 diluted blood[6], [7]. For this study, the microchannel based on the xurographic technique was investigated. Finally, the prototype of the microfluidic device for enhancing the CFL thinkness, which provided the region to separate blood plasma, was developed.

2. MATERIALS AND METHODS

2.1. Choice of materials

Two types of clear plastic films, Polyvinylchloride with plasticizer (PVC) and Polyethylene terephthalate (PET) were selected for carved material in this study. Their advantages also include lightweight, flexibility,

smooth surface, good optical transparency and inexpensive material. The A4 sheet of the films which normally used for presentation and laser printing were purchased from OfficeMate Co., Ltd. Thailand (~$10 per 100 sheets). Although the nominal thicknesses of both films are ~100 µm, other mechanical properties are different. Young's modulus of PVC and PET films are 25-1600 MPa and 2100-3100 MPa, respectively. Moreover their thermal properties are also different.

2.2. Fabrication of clear plastic microfluidic devices

The craft cutting plotter (Silhouette Cameo™, Silhouette America Inc.), with commercial thin cutting blade and cutting met, was introduced to carve micro-channels directly onto the surface of the plastic films. Computer-aided design software (Solid Edge 2D Drafting ST6 Free License, Siemens Product Lifecycle Management Software Inc.) was used to design the layouts of microchannels. The layouts were saved as the DXF file format and imported to the plotter software of Silhouette Studio® V3 for cutting control. The plotter software has the ability to assign cutting parameters such as cutting speed, cutting force, cutting style and etc. The rapid fabrication processes from carving the designed layout to the completed chip have shown in Fig. 2. A piece of plastic film was adhered onto a recyclable cutting met and then carved the designed layout. After peeling off the layer from the met, the layer was sealed using double layers of thermal laminating films (Laminating pouch film 125 µm thick, Value Choice®, OfficeMate Co., Ltd.) with pre-cut inlets and the outlets to finish the microfluidic chip. A roller thermal laminator was preheated at 140°C before the chip bonding. Finally, a custom acrylic chip holder, with tubing connectors and rubber plugs of continuous ink supply systems (CISS) for an inkjet printer, polyethylene tubing (I.D. 0.58 mm, O.D. 0.965 mm), was used to connect the fabricated microfluidic chip to a syringe (1 mL, Terumo Inc.) during experiments.

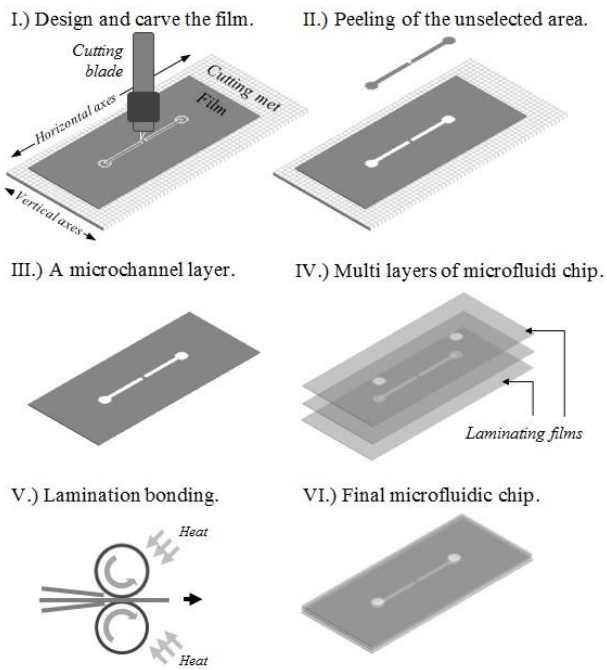

Fig. 2. Illustration of the microfluidic fabrication

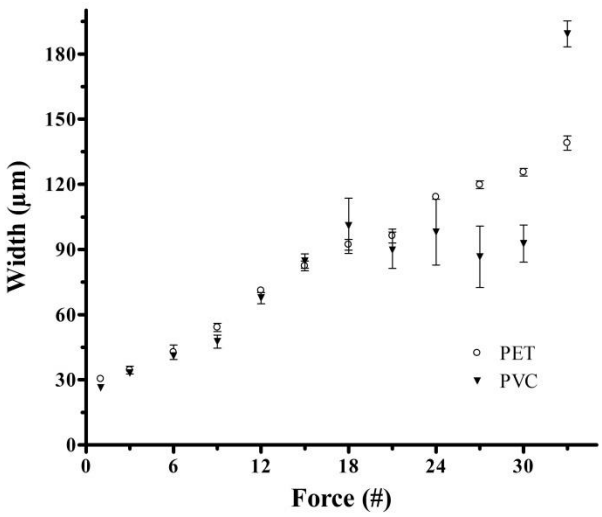

Fig. 3. Plot of microchannel width specified by different cutting forces on to both plastic films.

2.2. Blood sample preparation

Blood sample used in the experiments was obtained from a healthy hamster in EDTA tubes (Vacutainer, BD). The hematocrit percentage of blood sample was 41%. The sample was diluted to 1:10 by normal saline solution (NSS) with heparin (IP, 1000 USP/mL). Experiments were conducted on the same day of blood collection.

2.3. Experimental procedures

2.3.1. Characterization of microchannels

To investigate microchannel feature size, the straight-carving lines of 10-mm-long at various applied forces (Level 1 to 33 as maximum cutting force of 210 gf) and the rectangular-carving patterns of 10 mm long and 100 µm to 1000 µm width were cut onto the surface of both types of plastic films. The microstructures on the surfaces were captured using a CCD camera (D90, Nikon) attached to a light microscope (CKX41, Olympus). Finally, the feature size was measured, at the microchannel positions of 2.5, 5.0 and 7.5 mm length, using the image processing software of ImageJ.

2.3.2. Enhancement of the downstream CFL after the constriction

The layout of the microfluidic cell focusing device has shown in Fig. 1. This device geometry and drift parameter *d* were reported by Faivre *et al*.[5] as shown in equation (1) below. The following layout: L=300 µm, w_C=500 µm, w=100 µm was designed with the predicted drift d more than 10 µm using equation (1). The channel height was 100 µm.

$$d = 0.26 + 0.24\frac{Lw_c}{w^2} \qquad (1)$$

The fluid flow in microchannels was controlled by a standard motor-driven pump (Harvard 33 Twin Syringe Pump, Harvard Apparatus) with constant flow rate of 10 µL/min. Movies and images were taken with the CCD camera.

3. RESULTS AND DISCUSSION

The rapid fabrication steps from carving the designed layout to the completed chip was able to be finished less than ten minutes like previous study[4]: Step-I, a complete carving of individual microchannel layer can be done in a minute. Step-II, approving the microchannel layer with light microscope and image processing software would take ~5 min, and Step-III, the assembly and bonding of the final device spent ~1 min. Though, this low cost microfluidic chip could be achieved simply and rapidly, channel distortion and dimensional variation were typically occurred during the fabrication process.

The smallest feature size of negative microchannel was obtained, approximately 30 µm both on PVC and polyester films, by the minimum nominal applied force of level 1. As shown in Fig. 3, numerous feature size of microchannel occurred when applied the different cutting forces. The feature size was low deviation, when half cutting (not carving through out the thickness of materials). Die-cutting (carving through out) the PVC and PET films occured when the applied force more than level 20 and 30, respectively. The different Young's modulus of plastic films affected the variability of

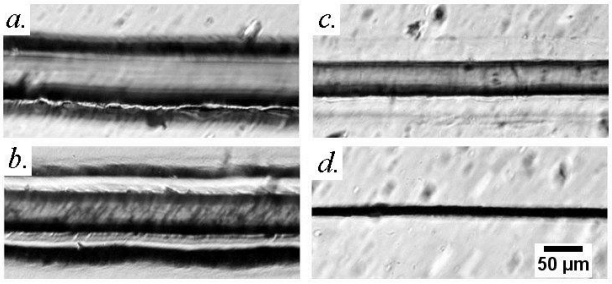

Fig. 4. Light microscope image of microchannel: the microchannels were obtained with an apply force level 9 onto the surface of PET(a) and PVC(b). Size of the microchannels on PET(c) and PVC(d) have changed after bonding with thermal lamination film.

feature size. However, this results have shown the capability to create negative microchannel whose size less than 100 µm onto the PVC and PET.

The negative microchannel size close to 50 µm was found in PET and PVC shown in Fig. 4(a) and Fig. 4(b), respectively. Some roughness on the channel edge of both materials was appeared. It would be a key factor of the change in velocity profile as a result of increasing in average velocity[8]. Moreover, the laminated channels after bonding were narrower than the channels after cutting. This could be the bonding temperature of 140°C was higher than the glass transition temperature (70-80°C) so that the channels were creep during pressed. Despite these size changes, the laminated PET channel width in Fig. 4(c) was less deviated than that of PVC shown in Fig. 4(d). The thermal expansion property of the PET films promoted the stability over the PVC. The other bonding technique with glue[9] should be more suitable for the PVC. Although chip bonding with thermal laminating films affect the channel width on plastic, this technique provide rapid bonded in a minute.

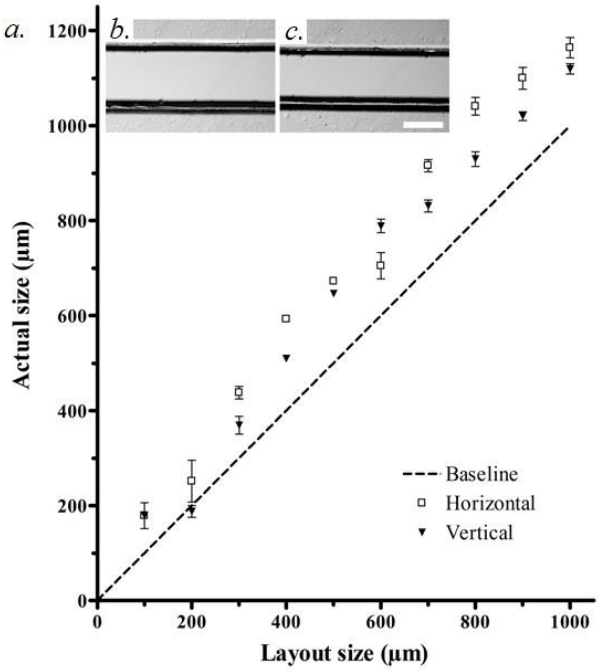

Fig. 5. A compareation of actual microchannel width from horizontal and vertical cutting axes; (a) Plot of the drawing versus actual sizes of microchannels and the light microscope images of 400-µm-wide microchannel by die-cutting in (b) horizontal and (c) vertical axes, respectively. The scale bar is 400 µm.

The other cutting study was the die-cutting 10 mm long of rectangular channels with varying the width sizes. Fig. 5(a) shows the comparison of the actual sizes and the drawing sizes of the rectangular channels. The baseline (dash line) was the target width. However, the carved channels were overcut. It was found that the width of carved channels was about 10% more than which of the drawing. Because of the certain overcut, therefore drawing a layout 10% smaller than the target size could fit the final target width.

The carving directions of rectangular channels were also examined, *i.e.* along the horizontal and vertical axes of the plotter. The plot of varies target channels on horizontal (opened square dots) and vertical cutting (rigid triangular dots) has also shown in Fig. 5(a). The phase contrast images in Fig. 5(b) and Fig. 5(c), were carved from 400 µm layouts on PET films along the horizontal and vertical axes, respectively; however, the target channels were different. It found that cutting along the vertical axis was occurred less distorted than the horizontal one. Therefore, the more accurate channel size to the drawing would run in the vertical. This issue may cause by the different motion control system and motor drives on the horizontal and vertical or x-y axes. Normally, the cutting plotters work with different motion control system on x-y axes. For this study, the cutting plotter was a motion shaft control system on x-axis and a machine rollers system on y-axis. It was noticed that the channel distortion occurred on a single cutting plotter. It may provide the distortion less than 10% if working with other resolution plotters or higher grade cutting plotter.

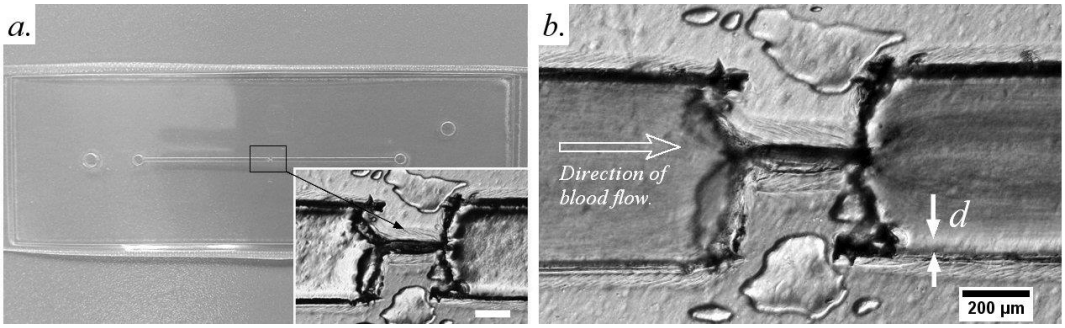

Fig. 6. The final microfluidic chip for cell focusing(a) and the light microscope image of the microfluidic chip between blood flowing(b) through the channel. All scale bars are 200 µm.

For approaching to a microfluidic device for blood plasma separation, the sample channel geometry reported by Faivre *et al.*[5] was chosen. Although the designed was very small constriction channel at 15 µm, this research extended the constriction to 25 - 100 µm like previous research[6] with the predicted drift *d* more than 10 µm. The final device with the constriction area was shown in Fig. 6(a). The geometry of laminated micro-fluidic device was measured as L=396 µm, w_C=558 µm, and w=78 µm as shown in small figure of Fig. 6(a). The constriction channel was slightly deformed at the end of the channel. As shown in Fig. 6(b), the picture of 1:10 diluted blood at the flow rate of 10 µL/min was captured. The thin layer of CFL or the drift *d* of ~10 µm, occurred clearly on a side of the downstream channel. The single side CFL could be affected by the deformation at the end of the constriction channel. However the channel deformation could not be control during the thermal lamination process. The uncontrollable channel deformation would possibly be improved by eliminating the surface roughness of the channel before bonding process.

4. CONCLUSION

The microfluidic fabrication processes from the drawing layout to the final device could be finish within ten minutes by xurography with thermal lamination films. The small negative microchannels, from 100 µm to 30 µm width, were fabricated with line carving. To fabricate bigger channels more than 100 µm, die-cutting along the vertical axis was applied to obtain more accurate feature sizes than the horizontal one. However the actual microchannels were distorted 10% more than the drawing ones. The cell focusing chip using this fabrication technique was presented. Despite the uncontrollable channel deformation, the enhanced CFL at downstream was ~10 µm thick. For the future works, the channel geometry to get the appropriate enhancement of CFL for blood plasma separation would be varied as well as an improvement of surface roughness of the constriction channel.

5. ACKNOWLEDGMENTS

We would like to acknowledge the Cardiovascular Engineering Research Laboratory: CERL for providing blood sample and Asst. Prof. Dr. Warakorn Limbut for suggestions. This research was supported by Faculty of Medicine, Prince of Songkla University and NSTDA funding.

6. REFERENCES

[1] H. Sharma, D. Nguyen, A. Chen, V. Lew, and M. Khine, “Unconventional Low-Cost Fabrication and Patterning Techniques for Point of Care Diagnostics,” *Ann. Biomed. Eng.*, vol. 39, no. 4, pp. 1313–1327, Dec. 2010.

[2] D. A. Bartholomeusz, R. W. Boutte, and J. D. Andrade, “Xurography: rapid prototyping of microstructures using a cutting plotter,” *J. Microelectromechanical Syst.*, vol. 14, no. 6, pp. 1364–1374, Dec. 2005.

[3] J. Do, J. Y. Zhang, and C. M. Klapperich, “Maskless writing of microfluidics: Rapid prototyping of 3D microfluidics using scratch on a polymer substrate,” *Robot. Comput.-Integr. Manuf.*, vol. 27, no. 2, pp. 245–248, Apr. 2011.

[4] A. C. Glavan, R. V. Martinez, E. J. Maxwell, A. B. Subramaniam, R. M. D. Nunes, S. Soh, and G. M. Whitesides, “Rapid fabrication of pressure-driven open-channel microfluidic devices in omniphobic RF paper,” *Lab. Chip*, vol. 13, no. 15, p. 2922, 2013.

[5] M. Faivre, M. Abkarian, K. Bickraj, and H. A. Stone, “Geometrical focusing of cells in a microfluidic device: An approach to separate blood plasma,” *Biorheology*, vol. 43, no. 2, pp. 147–159, Jan. 2006.

[6] J. Marchalot, Y. Fouillet, and J.-L. Achard, “Multi-step microfluidic system for blood plasma separation: architecture and separation efficiency,” *Microfluid. Nanofluidics*, vol. 17, no. 1, pp. 167–180, Jul. 2014.

[7] E. Sollier, H. Rostaing, P. Pouteau, Y. Fouillet, and J.-L. Achard, “Passive microfluidic devices for plasma extraction from whole human blood,” *Sens. Actuators B Chem.*, vol. 141, no. 2, pp. 617–624, Sep. 2009.

[8] S. Prentner, D. M. Allen, L. Larcombe, S. Marson, K. Jenkins, and M. Saumer, “Effects of channel surface finish on blood flow in microfluidic devices,” *Microsyst. Technol.*, vol. 16, no. 7, pp. 1091–1096, Jan. 2010.

[9] R. Arayanarakool, S. Le Gac, and A. van den Berg, “Low-temperature, simple and fast integration technique of microfluidic chips by using a UV-curable adhesive,” *Lab. Chip*, vol. 10, no. 16, pp. 2115–2121, 2010.

The 7th International Conference on Engineering and Technology
ICET-2015, Phuket, June 19-20, 2015
Prince of Songkla University, Faculty of Engineering
Hat Yai, Songkhla, Thailand 90112

Passive Micromixer of a Microfluidic Chip Fabricated by the Xurographic Technique

Mahdee Samae, Somyot Chirasatitsin*
Prince of Songkla University, Faculty of Medicine, Institute of Biomedical Engineering, Thailand
*Email of corresponding author: somjot.c@psu.ac.th

Abstract: *This paper presents the designs of passive micromixers in microfluidic chips. Three different geometries: Line-, W- and circular-micromixes were fabricated by the xurographic method using a cutting plotter for carving microstructures on polyvinyl chloride (PVC) lamination films. Liquid red and green food colors were used for evaluating the mixing performance. It was found that the W- and circular micromixers provided intimately the mixing efficiency ~70% at the flow rate of 1000µl/min. Moreover, integrated W- and circular micromixer obtained ~80% mixing efficiency. The passive micromixer designs, proposed in this study could be easily applied to micro total analysis systems.*

Key Words: ***Microfluidic chip / Passive micromixer / Cutting plotter / Low-cost technique***

1. INTRODUCTION

The Micro Total Analysis Systems (µTAS), which is aimed at miniaturization and integration of biochemical analysis, has recently applied in biomedical research and medical microdevices[1]. For microsystems such as lab-on-a-chips for biological microreactors and for complex chemical synthesis, well mixing of fluids is very important[2]. Because of the difficulty to mix fluids at microscopic scale with very low Reynold numbers, particular designs of micromixers are usually used to improve the mixing peformance. They can normally be classified as the active and passive micromixers. The active micromixer uses external energy to enhance mixing process. While the passive one does not require external energy but rely completely on diffusion. Thus, rapid mixing in passive micromixer can be accomplished by increasing the contact surface area between different fluids and decreasing the diffusion path to improve diffusion rate[3]. Furthermore, Mengeaud *et al.* demonstrated that sharp corners in the zigzag channel caused complete mixing due to turbulent flow[4]. Yung-Chiang Chung *et al.* proposed the design of a passive micromixer that utilizes the self-circulation of the fluid in the mixing chamber[5]. The results indicated that the self-circulation could enhance the mixing efficiency even at low Reynold numbers. Jiang *et al.* also reported that a channel comprising four circular arcs and two straight inlet and outlet sections improve mixing performance[6]. Design layout of microchannels plays an important role in enhanceing mixing efficiency. However complex layouts require qualified microchannel fabrications.

Currently, most of the microfluidic fabrications, such as PDMS molding, micromilling, and laser cutting, are time consuming and required expensive facilities. However, Bartholomeusz *et al.*[7] reported rapid prototyping of microstructures by xurography. This technique uses a cutting plotter, traditionally used for cutting graphics in adhesive vinyl films, to carve microchannels. A craft cutting plotter is inexpensive compared with other equipments such as photolithography equipment, laser cutting machine, and micro-milling machine. However it provides rapid prototyping of microfluidic chips with certain resolution.

In the present study, passive micromixers of three simple designs; Line-, W-, and O-microchannels were fabricated by the xurographic technique. Two food coloring solutions (red and green) were used for investigating mixing efficiency.

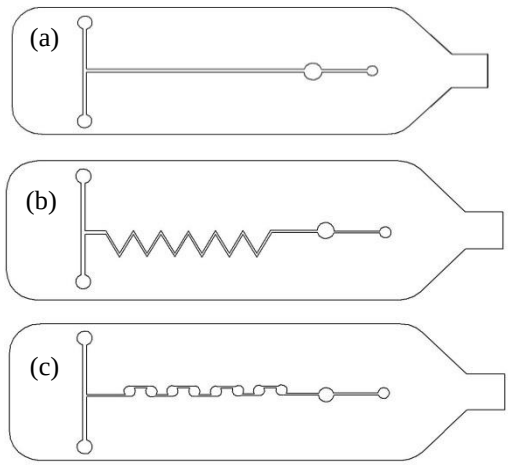

Fig.1 Schematic diagram of the three types of mixers. (a) The Line-microchannel; (b) The W-microchannel; (c) The circular mixer.

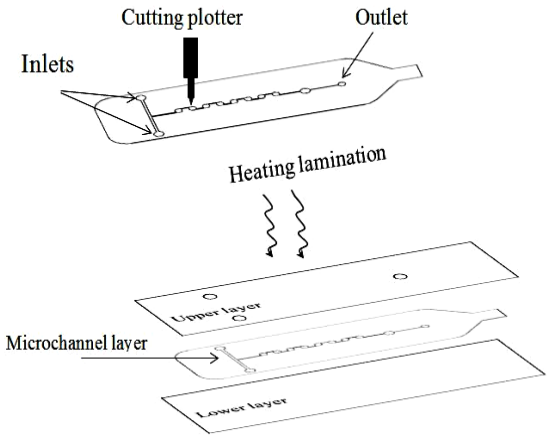

Fig. 2 Fabrication processes of the microfluidic chip

2. EXPERIMENTAL DETAILS

2.1 Device design and Fabrication

Three patterns of micromixer were designed, such as the Line microchannel or LM (Fig.1a), the W-microchannel or WM (Fig.1b) and the circular or O-microchannel or OM (Fig.1c). All of the microchannels was 125 µm height; however, other dimensions were different from each design. The LM was 250 µm width, and 20 mm long. The WM consisted of 11 sharp corners of 60° angle with 250 µm width, and totally 45 mm long. The OM comprised 8 circular chambers of 1500 µm in diameter and connecting microchannels of 250 µm width assymmetrically about the center of the chambers. As a result, the aspect ratio of the width of the construction channel to the chamber diameter was 1/6. After the micromixer zone, there was a chamber of detection or detection zone with 2 mm in diameter.

Fig. 2 illustrates the fabrication processes of the microfluidic devices. They were made from PVC thermal laminating pouch flims (VALUE CHOICE®, OfficeMate, Thailand). The cutting plotter (Silhouette CAMEO®, Silhouette America, Inc.) was used for cutting the channels. The device was fabricated by three layers. The upper layer was cut three holes of 2 mm diameter for 2 inlets and one outlet. The design patterns were carved on the middle layer, meanwhile the lower layer was sealed forming complete microchannels. The patterns were designed using a CAD software (Solid Edge 2D Drafting ST6 Free License, Siemens Product Lifecycle Management Software Inc.) After that the pattern files was transfered to the plotter software of Silhouette Studio® V3 for cutting control. Then the carved flims were bonded layer-by-layer at 160 °C using a laminator (FGK-320 laminating machine).

2.2 Experimental setup

The schematic of the experimental setups has shown in Fig.3. The flow rate is controlled accurately by a motor-driven syringe pump (Harvard 33 Twin Syringe Pump, Harvard Apparatus). The solutions of 1% food coloring (red and green) (Best Ordour Co., Ltd., Thailand) in water were used for the mixing tests. The inverted microscopes (CKX41, Olympus) was applied with phase contrast filter to capture images during the tests. The mixing images were recorded by a digital camera (D90, Nikon).

2.3 Evaluation of mixing efficiency

To quantify the mixing efficiency, the standard deviation of the concentration of the coloring solution was calculated by a custom Javascript in ImageJ. Brieftly, The captured images were split into 8-bit grayscale images of red, green, and blue components. The red component was only used for measuring the intensities pixel-by-pixel via the detection zone. A standard curve relating intensities and concentrations was established. After converting the intensities to the concentrations, the homogeneity was represented by the standard deviation of the concentration over the detection area:

$$\sigma = \sqrt{\frac{1}{N}\sum_{i=1}^{N}(Ci-\overline{C})^2} \qquad (1)$$

where C_i is the concentration of pixel i, N is the number of pixel over detection zone, and $\overline{C}$ is the ideally average concentration at well-mixing which is equal to 50% of the initial concentration. The standard deviation will be 0 for well-mixing. The mixing efficiency was defined as in Eq. (2):

$$\eta = 1-\sqrt{\frac{1}{N}\sum_{i=1}^{N}\left(\frac{Ci-\overline{C}}{\overline{C}}\right)^2} \qquad (2)$$

The efficiency is therefore between $0 < \eta < 1$. When $\eta = 0$ means the highest variation of concentration, *i.e.* no mixing. While $\eta = 1$ is well-mixing.

3. RESULTS AND DISCUSSION

3.1 Microchannel fabrication

The microchannels in the three mixers were designed in the free software of Solid Edge 2D Drafting ST6 and then cut by a plotter of Silhouette CAMEO® (cost ~$600USD). The microchannel materials was PVC thermal laminating films cost ~$0.1USD per A4 sheet, which one A4 sheet can produce 10 microfluidic chips. As one chip used 3 peices of the cut films, thus one chip cost ~$0.03USD or less than 1Baht per chip. However, this price was still in laboratory scale. As a result, the

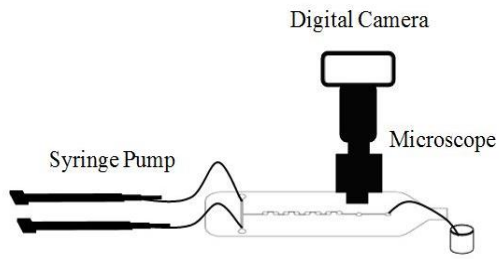

Fig.3 Schematic setup for mixing experiments

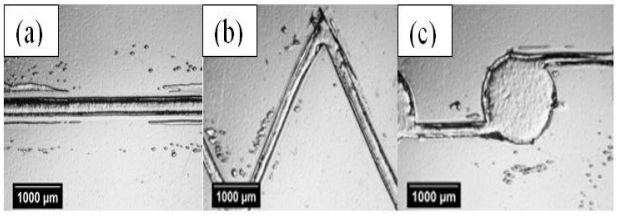

Fig. 4 Three patterns of micromixer on the chips: (a) The Line-microchannel (b) The W-microchannel and (c) The circular mixer.

cost would possibly be reduced significantly in the mass production. Fig. 4 shows the microchannels of each design via a light microscopy with phase contrast filtering. The differences between the cut microchannels and the design ones was about 5%, mainly due to the limitation of the cutting plotter. This was probably due to differences between the cutting patterns and the material feeding motors on the cutting plotter. In addition, The edge of channel walls was rough, (the microscopic images not shown here) which could be the effects of mechanical properties of carved materials and the blade[7]. However, the plotter was approximately able to cut on the same spot if the cutting adhesive mat was sticky enough. For the fabrication cycle time, the overall was less than 10 minutes. These clearly demonstrated that laboratories, without accessing to the clean room microfabrication facilities, could quickly build up, and test the conceptual design of microfluidic devices, especially flow behavior investigation.

3.2 Standard curve of the mixing solution

To relate the intensity with the corresponding concentration, the standard curve was evaluated. The preparation was used the concentration of 1 % liquid food dye (red and green) solution. In Fig. 5 shows the standard curve relate to concentrations and intensities of red color. To cover the concentration range from 0 – 1%, the standard curve was fit by a 2nd degree polynomial.

3.3 Mixing efficency of the three designs.

The mixing efficiencies η of the three micromixers were presented at different flow rates from 500–1000 µl/min, shown in Fig.6. However the Reynold numbers of these experiments were lower than 1. The LM, as expected, obtained very low performance of mixing due to the decrease in the contact area of the fluids and laminar flow. The WM and OM were almost the same mixing efficiencies, especially at high flow rates of 800–1000 µl/min, *i.e.* 65-70%. The OM at 1000 µl/min however was slightly higher efficient than the WM, *i.e.* 71% and 65%, respectively. The OM's efficiency increased from 40% to 71% by the formation of recirculation inside the circular chamber caused by inertial forces. Consequently, a disturbance in the flow field was produced resulting in enhancing mixing performance. Fluids entering circular chambers were a smooth flow along the side wall of the chamber. After that they flowed into the out let, and hence enhanced mixing. This phenomena was reported by Afroz *et al.*[8]. While in WM the laminar recirculation induced by the

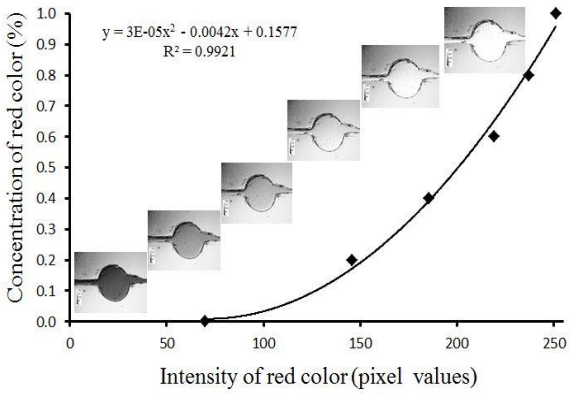

Fig. 5 Schematic of standard curve relating between intensity and concentration

WM angles[4]. The recirculations inducing transverse component of the velocity spread out species from the interface to the walls. Consequently, at high flow rates, the mixing was enhanced by both diffusion and laminar recirculation processes.

In addition, the WM combined with OM which consisted of 2 sharp corners of WM before OM chambers (the design graphic not shown). The performance of WM combine with OM design as shown in Fig.7, increased to 80% due to the contact area increasing. The WM at the early of the mixer improved the efficieny by 10% before entering OM zone. Therefore overall efficiency of WM combined with OM was also about 10% increasing from which of OM only. At flow rate of 1000 µl/min, the well-mixed has therefore been manifested at ~80%, as recommended by [9] (80%-100%).

3.4 Outlook

As shown in the results above, the WM and OM designs provided fully mixing. However, the mixing elements could be changed, for examples, barriers embedded in circular chambers ,increasing numbers of sharp corners of WM and variation of corners' angles.

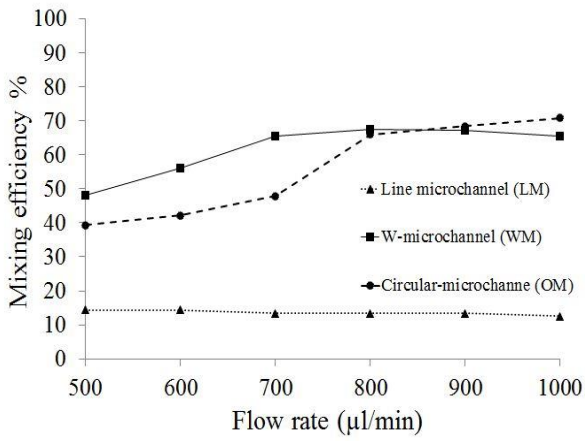

Fig. 6. Variations of mixing efficiency with flow rate at the exit of the detection zone for different design micromixers.

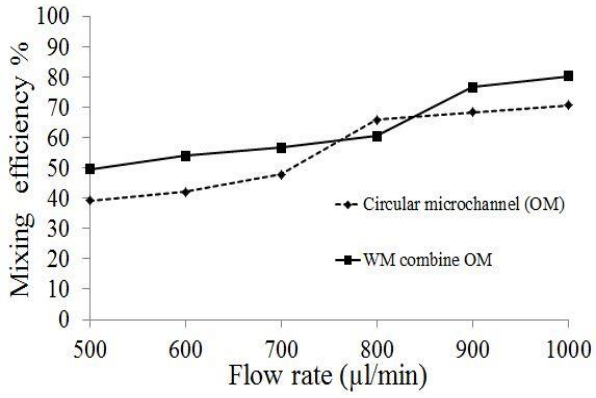

Fig. 7. Variations of mixing efficiency of W-channel with circular mixer design

4. CONCLUSION

The passive micromixers of three designs of Line-, W- and O-micromixers were fabricted by a low cost technique of xurography, providing ~$0.03USD per chip in laboratory scale and spending less than 10 min. as truly cheap and rapid prototyping method for microchannel fabrication. The Circular-micromixer have almost the same mixing efficiency with W-microchannel and higher than line-micromixers. Specifically,circular-micromixer mixing efficiency 71% at 1000 µl/min. Moerover the WM integrated with OM increased the efficiency up to 80%.

5. ACKNOWLEDGMENT

The authors would like to thank Mr. Cheewarak Rodniam for suggestions in Javascripts of ImageJ. We also gratefully acknowledge Asst. Prof. Dr. Warakorn Limbut for suggestions and the funding from the Faculty of Medicine, Prince of Songkla University, Thailand.

6. REFERENCES

[1] S. A. Rahim, T. N. T. Ibrahim, A. A. Ma'Radzi, and M. M. A. Jamil, "Design and development of oblique groove micromixer for laminar blood reagent mixing," 2013, pp. 547–550.

[2] D. S. Kim, S. W. Lee, T. H. Kwon, and S. S. Lee, "A barrier embedded chaotic micromixer," *J. Micromechanics Microengineering*, vol. 14, no. 6, pp. 798–805, Jun. 2004.

[3] H. M. Xia, S. Y. M. Wan, C. Shu, and Y. T. Chew, "Chaotic micromixers using two-layer crossing channels to exhibit fast mixing at low Reynolds numbers," *Lab. Chip*, vol. 5, no. 7, p. 748, 2005.

[4] V. Mengeaud, J. Josserand, and H. H. Girault, "Mixing Processes in a Zigzag Microchannel: Finite Element Simulations and Optical Study," *Anal. Chem.*, vol. 74, no. 16, pp. 4279–4286, Aug. 2002.

[5] Y.-C. Chung, Y.-L. Hsu, C.-P. Jen, M.-C. Lu, and Y.-C. Lin, "Design of passive mixers utilizing microfluidic self-circulation in the mixing chamber," *Lab. Chip*, vol. 4, no. 1, p. 70, 2004.

[6] F. Jiang, K. S. Drese, S. Hardt, M. M. Küpper, and F. Schönfeld, "Helical flows and chaotic mixing in curved micro channels," *AIChE J.*, vol. 50, no. 9, pp. 2297–2305, Sep. 2004.

[7] D.A. Bartholomeusz, R. W. Boutte, and J. D. Andrade, "Xurography: rapid prototyping of microstructures using a cutting plotter," *J. Microelectromechanical Syst.*, vol. 14, no. 6, pp. 1364–1374, 2005.

[8] A. Alam and K.-Y. Kim, "Mixing performance of a planar micromixer with circular chambers and crossing constriction channels," *Sens. Actuators B Chem.*, vol. 176, pp. 639–652, Jan. 2013.

[9] M. Nimafar, V. Viktorov, and M. Martinelli, "Experimental comparative mixing performance of passive micromixers with H-shaped sub-channels," *Chem. Eng. Sci.*, vol. 76, pp. 37–44, Jul. 2012.

The 7th International Conference on Engineering and Technology
ICET-2015, Phuket, June 19-20, 2015
Prince of Songkla University, Faculty of Engineering
Hat Yai, Songkhla, Thailand 90112

Analysis of Active Filter Circuit Basic using MATLAB-GUI for Electrical Engineering Education

Sommart Khamkleang
Program of Industrial and Technology, Faculty of Industrial Technology, Songkhla Rajabhat University
160, Moo 4, Tambon Khoa-Roob-Chang, Muang District, Songkhla, Thailand 90000
E-mail: khamkleang@gmail.com

Abstract: *This paper presents an analysis of active filters circuit with graphical user interface developed for electrical engineering studies. Four modules included in the package are low-pass filter circuit, high-pass filter circuit, band-pass filter circuit, and band-rejection filter circuit. The design environment of this program is based on the m-file of Matlab that provides the drawing function and the graphical user interface development environment, GUIDE. The simulated results obtained through the presented methodology have shown close agreement with experimental results thus validating the performance of this software tool.*

Key Words: ***MATLAB, graphical user interface, active filter***

1. INTRODUCTION

A comparison of passive filters and active filters as follows: the advantages of each filter type, passive filter are, no power supply required, can handle large currents and high voltages, very reliable, least number of components for given filter, noise arises from resistances only, no bandwidth limitation, and active filter are, no inductors, easier to design, high impedance input and low impedance output for minimal loading, can produce high gains, generally easier to tune, and small in size and weight. The disadvantages of each filter type, passive filter are, inductors large for lower frequencies, some inductors (non-toroidal) may require shielding, limited standard sizes, often requiring variable inductors and therefore tuning, low tolerance inductors (1-2%) very expensive, must be designed with consideration to input and output loading, generally not amenable to miniaturization, no power gain possible, no voltage gain, and active filter are, power supply required, susceptible to intermodulation, oscillations, susceptible to parasitic from DC output offset voltage and input bias currents, op amp gain bandwidth constrained, op-amp slew rate constrained, can require many components [1]. The advantages and disadvantages mentioned above. It's as difficult for students to understand. The solution Wythe One popular use today is the implementation of computer-aided analysis and design models.

Computer-aided circuit analysis has been a powerful and widely used assistant tool of circuit analysis and design accompanied with the development of modem electrical technology and computer. MATLAB has already been a powerful tool in developing circuit analysis calculation software, which can process scientific calculation, sign calculation and graphic process. Meanwhile it can figure out some peculiar problems which are out of the ability of Multisim. But now, circuit analysis calculation of MATLAB mainly aims at particular problems, not for all. From the trends of software development, it is can be seen that friendly user interface has been basic interactive portal. The graphic user interface design tool of MATLAB GUIDE, which supports GUI, can design easily-manipulated and convenient interface with menus and controls [2-4].

Considerable research efforts are reported on developed of MATLB-GUI in the electrical engineering, highlighting the simplicity and friendly of this system [5-9]. Compared with C and Labview, Matlab is easier to understand, convenient for image display and benefits for system optimization, because of its strong numerical calculation and various integrated image processing and instrument control toolboxes [10]. Therefore, Matlab provides an alternative approach to passive and active filter design, which will be discussed of detail in the section, so on.

2. BACKGROUND CONCEPT OF THE PROGRAM

The developed software package includes four modules. Theoretical background of each module is briefly described below [11-13].

2.1 Low-Pass Filters

The transfer function of a single stage is:

$$A_i(s) = \frac{A_0}{1 + a_i s + b_i s^2}. \quad (1)$$

For a first-order filter, the coefficient b is always zero (b_1=0), thus yielding:

$$A(s) = \frac{A_0}{1 + a_1 s}. \quad (2)$$

The first-order and second-order filter stages are the building blocks for higher-order filters. Often the filters operate at unity gain (A_0=1) to lessen the stringent demands on the op-amp's open-loop gain.

Fig.1 shows the cascading of filter stages up to the sixth order. A filter with an even order number consists of second-order stages only, while filters with an odd order number include an additional first-order stage at the beginning.

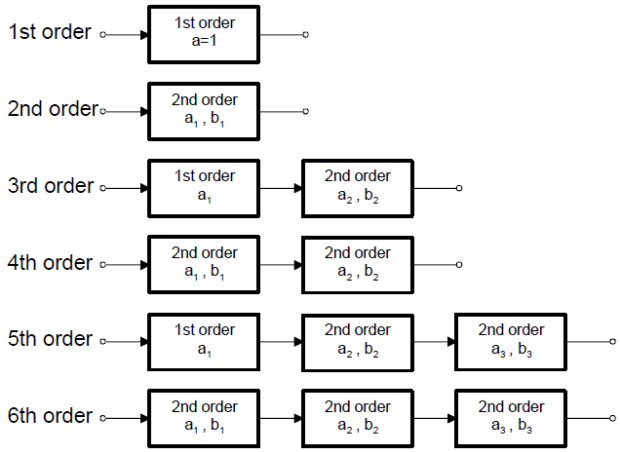

Fig.1. Cascading filter stages for higher-order filters

2.2 High-Pass Filters

By replacing the resistors of a low-pass filter with capacitors, and its capacitors with resistors, a high-pass filter is created in show Fig.2.

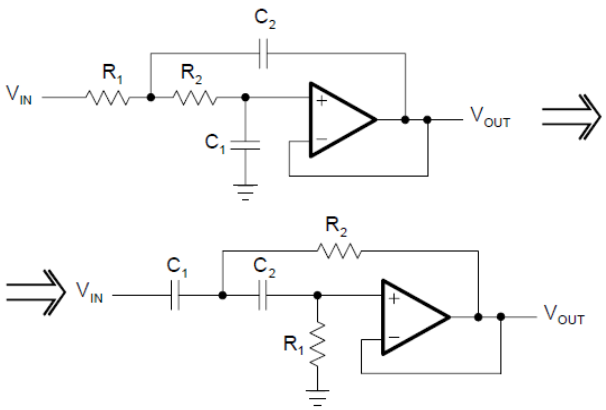

Fig.2. Low-pass to High-pass transition through components exchange

The general transfer function of a high-pass filter is then:

$$A(s) = \frac{A_\infty}{\prod_i (1 + \frac{a_1}{s} + \frac{b_1}{s^2})}. \quad (3)$$

With A_∞ being the passband gain.

Since Equation (3) represents a cascade of second-order high-pass filters, the transfer function of a single stage is:

$$A_i(s) = \frac{A_\infty}{(1 + \frac{a_1}{s} + \frac{b_1}{s^2})}. \quad (4)$$

With b=0 for all first-order filters, the transfer function of a first-order filter simplifies to:

$$A(s) = \frac{A_0}{1 + \frac{a_1}{s}}. \quad (5)$$

2.3 Band-Pass Filter

In Section 2.2, a high-pass response was generated by replacing the term *S* in the low-pass transfer function with the transformation 1/s. Likewise, a band-pass characteristic is generated by replacing the S term with the transformation:

$$\frac{1}{\Delta\Omega}\left(s + \frac{1}{s}\right). \quad (6)$$

In this case, the pass-band characteristic of a low-pass filter is transformed into the upper pass-band half of a band-pass filters. The upper pass-band is then mirrored at the mid frequency, f_m (Ω=1), into the lower pass-band half (Fig.3).

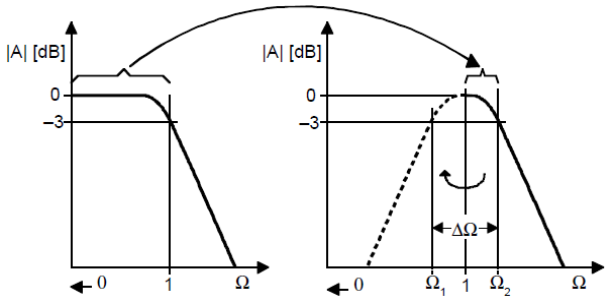

Fig.3. Low-pass to Band-pass transition

The corner frequency of the low-pass filter transforms to the lower and upper –3 dB frequencies of the band-pass, Ω_1 and Ω_2. The difference between both frequencies is defined as the normalized bandwidth $\Delta\Omega$:

$$\Delta\Omega = \Omega_1 - \Omega_2. \quad (6)$$

The normalized mid frequency, where Q = 1, is:

$$\Omega_m = 1 = \Omega_2 \Omega_1. \quad (7)$$

In analogy to the resonant circuits, the quality factor (Q) is defined as the ratio of the mid frequency (f_m) to the bandwidth (B):

$$Q = \frac{f_m}{B} = \frac{f_m}{f_2 - f_1} = \frac{1}{\Omega_2 - \Omega_1}.$$

$$Q = \frac{1}{\Delta\Omega}. \quad (8)$$

The simplest design of a band-pass filter is the connection of a high-pass filter and a low-pass filter in series, which is commonly done in wide-band filter applications. Thus, a first order high-pass and a first-order low-pass provide a second-order band-pass, while a second-order high-pass and a second-order low-pass result in a fourth-order band-pass response.

2.4 Band-Rejection Filter

A band-rejection filter is used to suppress a certain frequency rather than a range of frequencies.

Two of the most popular band-rejection filters are the active twin-T and the active Wien-Robinson circuit, both of which are second-order filters.

To generate the transfer function of a second-order band-rejection filter, replace the S term of a first-order low-pass response with the transformation in (9):

$$\frac{\Delta\Omega}{s+\frac{1}{s}} \tag{9}$$

Which gives:

$$A(s)=\frac{A_0(1+s^2)}{1+\Delta\Omega\cdot s+s^2}. \tag{10}$$

Thus the pass-band characteristic of the low-pass filter is transformed into the lower pass-band of the band-rejection filter. The lower pass-band is then mirrored at the mid frequency, f_m (Ω=1), into the upper pass-band half (Fig.4).

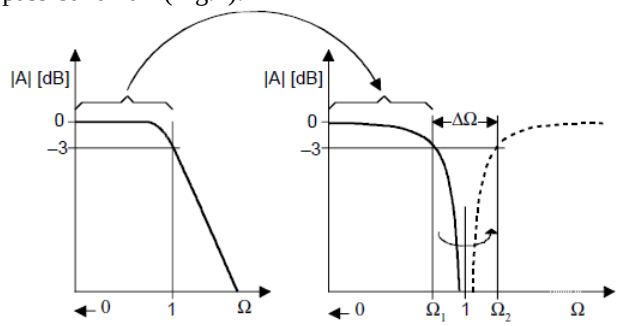

Fig.4. Low-pass to Band-rejection transition

The corner frequency of the low-pass transforms to the lower and upper –3dB frequencies of the band-rejection filter Ω_1 and Ω_2. The difference between both frequencies is the normalized bandwidth $\Delta\Omega$:

$$\Delta\Omega=\Omega_{max}-\Omega_{min}. \tag{11}$$

Identical to the selectivity of a band-pass filter, the quality of the filter rejection is defined as:

$$Q=\frac{f_m}{B}=\frac{1}{\Delta\Omega}. \tag{12}$$

Therefore, replacing $\Delta\Omega$ in Equation (10) with 1/Q yields:

$$A(s)=\frac{A_0(1+s^2)}{1+\frac{1}{Q}\cdot s+s^2}. \tag{13}$$

3. FLOWCHART AND GUI OF THE DEVELOPED PROGRAM

The proposed active filter circuit analysis program is developed under Matlab environment, where the merits of universal and effective computation capabilities of MATLAB, user-friendly GUIDE, and the convenient drawing function provided by m-file are adopted in the development. The purpose of this program is to facilitate the user's understanding of active filters circuit studies. Peculiar features and prominent functions of this program include

1. Simple displays.
2. Flexible input data format.
3. Output results are easily understood.

Fig. 5 depicts the flowchart of the developed program. As the user accesses the main screen, the input data format must be determined first. The input data can be expressed as an existent circuit selected of the active filter circuits under study, after providing data input, the user can select one of the four modules in the program and performs studies.

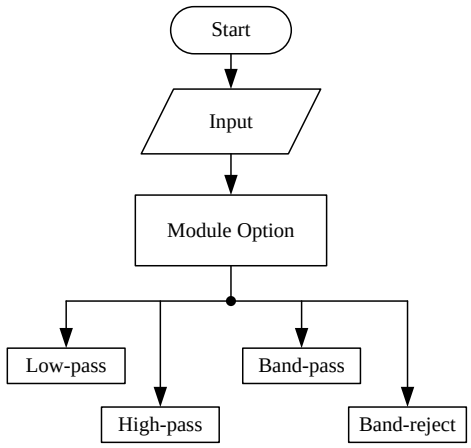

Fig. 5. Flowchart of the construction of the developed software.

4. EXECUTION DISPLAY OF THE DEVELOPED PROGRAM

Fig. 6 shows the main display for execution control of the program. When the main display is brought up, the user must select the input data format. The data contained in the input file includes the low-pass filter, high-pass filter, band-pass filter and band-rejection filter.

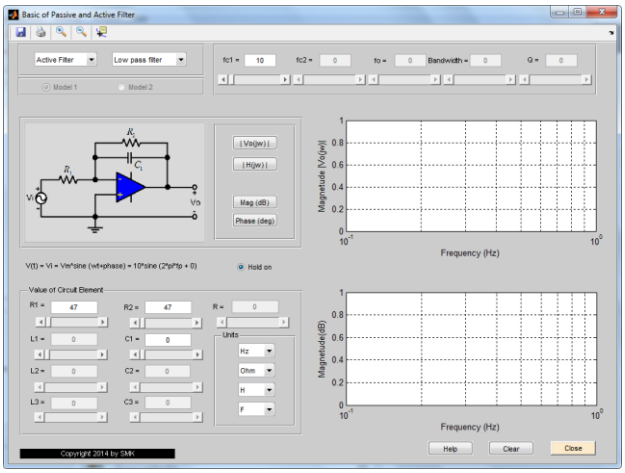

Fig. 6. Main display for execution control of the program.

To have a better understanding for users about the developed program, a band-pass filter test is demonstrated in the applications (Fig.7). When the user chooses to band-pass filter analysis, this program will open a set of value in GUI (Value of circuit element) as follows; $V(t)=10\sin(2\pi f+0^\circ)$, $R_1=R_2=47\Omega$, and $C_1=1\mu F$, $f_1=10H_Z$, $f_2=100H_Z$, and can be calculated, $R=1591.55\Omega, C_2=0.1\mu F$, $f_m=31.62H_Z$, bandwidth = 90 H_Z and Q = 0.351 as shown in Fig. 8.

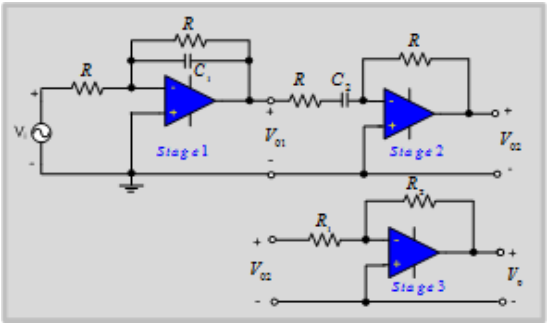

Fig.7. Band-pass filters circuit at test.

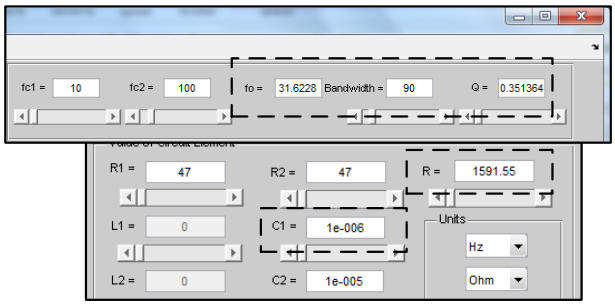

Fig.8. The design parameters of $f_0 = f_m$, bandwidth and quality factor (Q) using program.

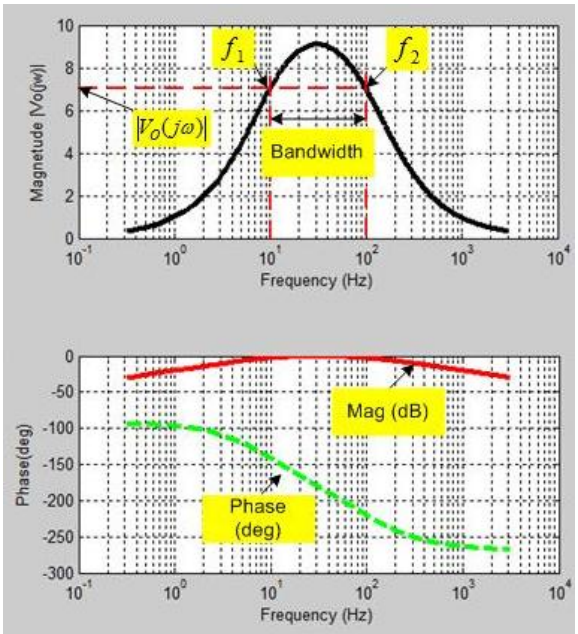

Fig.8. Response of the band-pass filters circuit of the program.

The analysis of the circuit of Fig. 9 shows that the response of the output voltage ($|V_O(j\omega)|$) at the cut-off frequency (f_1, f_2) = 7.07 V. Considering of bode plot, the size of the cut-off frequency response (f_1, f_2) = -3.0 dB, the angle response the range -92 to -268 degrees, when considering the middle frequency (f_m) with an angle of -180 degrees, and the frequency (f_1) is equal to the angle of -141 degrees and the frequency (f_2) is equal to the angle of -219 degrees.

5. CONCLUSION

This paper presents a User-friendly education-oriented active filter circuit simulation tool developed under Matlab/ m-file and GUI environments. At present, main modules of the software package include low-pass filter, high-pass filter, band-pass filter, and band-rejection filter. This package can be used in the classroom or by practicing engineers. The simulation results are in accordance with theory.

6. REFERENCES

[1] http://www.schematica.com/active_filter_resources /comparison_of_active_and_passive_filters.html

[2] Jingxiu Lee, and Weijuan Zhang, "Development of Visual Circuit Calculation Software Based on MATLAB GUI," 2nd International Conference on Education Technology and Computer (ICETC), 2010, pp.113-115.

[3] S. S. Murthy and Rajesh Kr Ahuja. "Design and Analysis of Three Phase Self Excited Induction Generators using MATLAB Graphical User Interface Based Methodology" IEEE International Conference ICPCES-2010, Nov.28-Dec.1, 2010 at Allahabad, India.

[4] Y. N. Anagreh and I. M. Al-Refae'e. "Teaching the self excited induction generator using Matlab", Intl. Journal of Electrical Engineering Education, vol. 40, no.1, Jan. 2003,pp. 55-65.

[5] Zhenxing Liu, Biao He, Bin Cai. "Teaching software development of Electrical Machinery & Towage based on MATLAB GUI". Multimedia Technology (ICMT), 2011 International Conference on , 26-28 July 2011, pp.5572-5574.

[6] S. Khamkleang and S. Akatimagool. "Microwave Planar Circuit Design Tool in the teaching of Microwave Engineering". Electrical Engineering / Electronics, Computer, Telecommunications and Information Technology, 2009. ECTI-CON 2009. 6th International Conference, Volume 2,May 2009, pp.830-833.

[7] Aliane N. "A Matlab/Simulink-Based Interactive Module for Servo Systems Learning". Education, IEEE Transactions on, Vol: 53, Issue: 2, 2010, pp. 265 - 271.

[8] Eroglu A. "Complete Modeling of Toroidal Inductors for High Power RF Applications". Magnetics, IEEE Transactions on, Vol: 48 , Issue: 11, 2012, pp. 4526 - 4529.

[9] Hacivelioglu F. Uslu M.A. Sevgi L. "A MATLAB-Based Virtual Tool for the Electromagnetic Wave Scattering from a Perfectly Reflecting Wedge ". Antennas and Propagation Magazine, IEEE Vol: 53 , Issue: 6, 2011, pp. 234 - 243.

[10] Tadej TASNER, Darko LOVREC, Francisek TASNER, Jorg EDLER. "Comparison of LabVIEW and MATLAB for Scientific Research". ANNALS of Faculty Engineering HUNEDOARA - International Journal Of Engineering, 2012, pp. 389-394.

[11] Thomas Kugelstadt. Active Filter Design Techniques. Texas Intrument, 2008.

[12] William H. Hayt. Jr, Jack E. Kemmerly and Steven M. Durbin."Engineering Circuit Analysis, Seventh Edition". McGraw-Hill, 2007.

[13] Allan H. Robbins,Wilhelm C. Miller."Circuit Analysis Theory and Practice, 5th edition". Cengage Learning, 2013.

The 7th International Conference on Engineering and Technology
ICET-2015, Phuket, June 19-20, 2015
Prince of Songkla University, Faculty of Engineering
Hat Yai, Songkhla, Thailand 90112

Set-point Optimization Using Kálmán Filter for Vertical Filling Weighing System

Sakkarin Sinchai*, Jeerasuda Koseeyaporn, Paramote Wardkein
Faculty of Engineering, King Mongkut's Institute of Technology Ladkrabang
Ladkrabang, Bangkok, 10520, THAILAND
*Email: s6601262@kmitl.ac.th

Abstract: *In any measuring system, a vertical filling weighing system used in this work, if a sensor is delayed to sense the desired weight, the measured weight is, of course, more than the desired value because the excess of weight is added. Hence, compensation must be made. However, the surplus is inconstant because of some random noises. To answer this problem, Kálmán filtering is employed to optimally compensate the set-point to satisfy the target weight. To achieve convergence of Kálmán filtering, the process and measurement models are consistently designed. To validate the efficiency of the proposed approach, it is experimented using a practical machine at the target quantity of 3505 grams. The results have revealed that the percentage mean error of measured weight is fairly low, only 0.08%.*

Key Words: ***Approximation / Estimate /Filling weighing system / Kálmán filter / Surplus of weight***

1. INTRODUCTION

Undeniably, controlling system has become involved in humans' daily life in many systems such as automatic lighting for cars, boiling systems, room temperature controlling and so on. These given examples, including any other controlling schemes, have something in common is a set-point [1]. From this point of view, it can be said that the set-point is an assigned value to be a constraint to operate any system to produce a desired response. However, a value of set-point might be set by two situations as depicted in Fig. 1. Both Fig. 1(a) and 1(b) are vertical filling weighing systems, consisting of a discharge gate, a container and a sensor, which is a measuring system employed to weigh a substance during filling process to a desirable quantity. The weighing system in Fig. 1(a) is mostly for liquid [2] but the weighing system in Fig. 1(b) is for both liquid and solid [3-4]. As can be seen, the difference between Fig. 1(a) and 1(b) is that the sensor in the former is mounted at the discharge gate; in contrast, the sensor in the latter is installed under the container. Hence, the way in which both sensors sense the value is distinct. The sensor in Fig. 1(a) can sense the value suddenly when the substance is released through the discharge gate which is unlike the sensor in Fig. 1(b) has to wait until the substance hits its body in order to sense the value. Of course, by the time the sensed value of both sensors equals to the desired quantity, for Fig. 1(b), there is some quantity not sensed yet left in the air. As a result, when weighing finishes, the obtained quantity in Fig. 1(a) equals to the desirable quantity whilst the obtained quantity in Fig. 1(b) is greater than the desired quantity as illustrated in Fig. 2. Because of the delay in reading the value in Fig. 1(b) makes the excess occur, therefore, the measured quantity is consisted of the desired quantity and the excess. Undoubtedly, in each weighing, the surplus varies from time to time. In other word, the excess is not constant due to some factors might interfere in weighing process. For this reason, this is a challenging task for this work to estimate an appropriately compensated set-point to satisfy the oscillating excess in vertical filling weighing system which the sensor is fixed beneath the container as shown in Fig. 1(b). In Fig. 3, albeit the set-point is in the controlling point axis (x-axis), this set-point is directly related to the value in the value axis (y-axis). Thus, the set-point is referred to the value in the value axis. According to this work concerning about weight, the value aforementioned is used in the unit of weight. Hereafter, the set-point will be expressed in the unit of weight as well.

A proper set-point for weighing system is significant because an inappropriate set-point, a set-point is not adjusted to an excess, can lead to either over-target-amount or under-target-amount. In case of the former, a

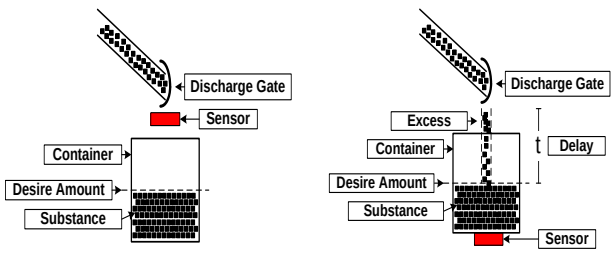

(a) Sensor mounted at the top (b) Sensor installed at the bottom

Fig. 1. Different situations of set-point setting.

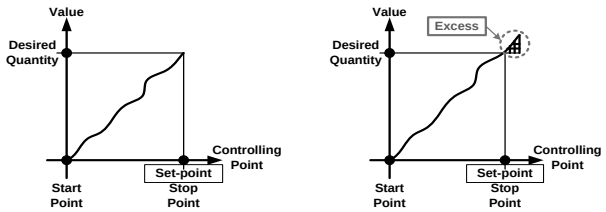

(a) Amount given by Fig. 1(a) (b) Amount given by Fig. 1(b)

Fig. 2. Illustration of desired quantity obtained by Fig. 1(a) and 1(b).

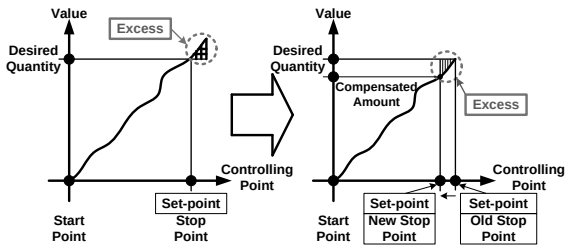

Figure 3. Set-point compensation.

producer is just a giveaway to customers which means that it loses an opportunity to increase a capacity to trade. For the latter case, a producer may not appreciate because it gets complained from customers or even gets fined by legal stipulation. Neither over-desired-quantity nor under-desired-quantity is good [2]. This is the motivation why several works have contributed to develop an approach to estimate an appropriate set-point. In [5], a moving average method is presented to compensate the set-point. The recompense is first done by collecting surplus-weight samples within a required amount of samples and calculating the average of surplus-weight samples. Then, the average excess is deducted from the weight target so the set-point is acquired. By employing this method, the set-point obtained is not adjusted in an instant manner because adjusting is based on the number of collected surplus samples. In [6], the technique circumvents a mathematical model using fuzzy logic. Even though it is simple to implement, many set-point conditions for fuzzy logic must be made to cover as many patterns as possible to cope with the surplus which may arise.

Thence, in this work, a new scheme which is simpler and more robust than the approaches [5-6] in terms of parameters used and tweaked is introduced. To make the proposed technique approximate the optimum of set-point, an estimator using a minimum mean-squares error (MMSE) criterion is employed. Also, to verify that this proposed scheme can be utilized in a real application, it is experimented using a practical machine.

The rest of this paper is constructed as follows. Section 2 explains the recompense design of the presented technique. The simulation and experimental results of optimizing the set-point are given in Section 3. Lastly, Section 4 is devoted to the conclusion.

2. RECOMPENSE DESIGN

In this section, the set-point compensation design is explained in details how it is adapted to the vertical filling weighing system as rendered in Fig. 1(b). The proposed recompense is simply illustrated as the block diagram shown in Fig. 4.

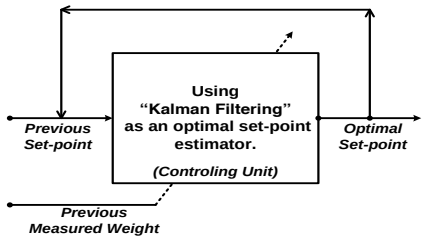

Fig. 4. The proposed design block diagram.

2.1. Proposed technique

For more than 50 years, Kálmán filter has been established, it is still useful nowadays. In Kálmán filtering [7], it is supposed that the current state at time $\boldsymbol{n}$ is succeeded to the preceding state at time $\boldsymbol{n}-1$ as explicitly revealed in the following equation,

$$\boldsymbol{x}[\boldsymbol{n}] = \boldsymbol{A}\boldsymbol{x}[\boldsymbol{n}-1] + \boldsymbol{B}\boldsymbol{u}[\boldsymbol{n}] + \boldsymbol{w}[\boldsymbol{n}] \tag{1}$$

where $\boldsymbol{x}[\boldsymbol{n}]$ is a linear summation of its prior state value $\boldsymbol{x}[\boldsymbol{n}-1]$, a control input and a process noise. $\boldsymbol{u}[\boldsymbol{n}]$ is the control input to the system and $\boldsymbol{w}[\boldsymbol{n}]$ is the process noise referred to the random noises of the system. $\boldsymbol{A}$ is the state transition coefficient and $\boldsymbol{B}$ is the control input coefficient. Also, in favor of predicting the optimal state, the measurement $\boldsymbol{z}[\boldsymbol{n}]$ of the system is necessarily modeled as,

$$\boldsymbol{z}[\boldsymbol{n}] = \boldsymbol{H}\boldsymbol{x}[\boldsymbol{n}] + \boldsymbol{v}[\boldsymbol{n}] \tag{2}$$

where $\boldsymbol{H}$ is the transformation coefficient and $\boldsymbol{v}[\boldsymbol{n}]$ is the measurement noise. Besides, the noises $\boldsymbol{w}[\boldsymbol{n}]$ and $\boldsymbol{v}[\boldsymbol{n}]$ are presumed to be zero-mean Gaussian with variances $\boldsymbol{Q}$ and $\boldsymbol{R}$ respectively.

To perform Kálmán filtering, consistent modeling (1) and (2) to the system, the vertical filling weighing system as mentioned, is necessary. Since the proposed technique does not require an external input to bias the system, the control input coefficient $\boldsymbol{B}$ is not needful to be modeled, thus, it is set to zero so is $\boldsymbol{u}[\boldsymbol{n}]$. Therefore, only coefficients $\boldsymbol{A}$ and $\boldsymbol{H}$ are modeled, respectively.

The state transition coefficient $\boldsymbol{A}$ is modeled under the assumption that the next set-point would be increased if the measured weight was under the desired weight. Similarly, the next set-point would be decreased if the measured weight was over the weight target. To satisfy this assumption, $\boldsymbol{A}$ is simply modeled in (3).

$$\boldsymbol{A} = \boldsymbol{Tg}(\boldsymbol{z}[\boldsymbol{n}-1]^{-1}) \tag{3}$$

From (3), assigning $\boldsymbol{Tg}$ as a weight target which is constant and $\boldsymbol{z}[\boldsymbol{n}-1]$ is a prior measured weight.

To model the transformation coefficient function $\boldsymbol{H}$, the practical machine weighing detergent powder as displayed in Fig. 5 is introduced. Its weighing range is valid from 3000grams to 5000grams. In this work, the target weight values of 3005grams, 3305grams, 3505grams, 4005grams and 5005grams are selected to

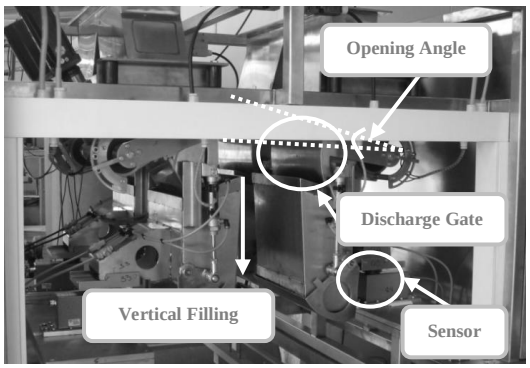

Fig. 5. The practical machine.

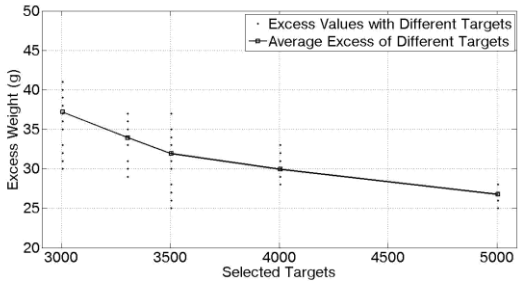

Fig. 6. The relation of the targets and the excess values.

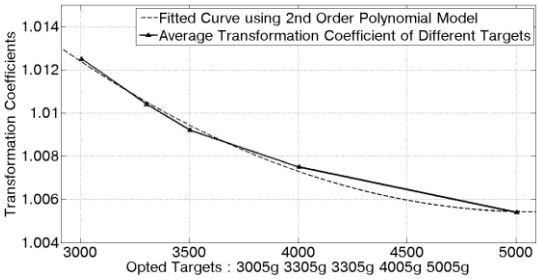

Fig. 7. The transformation coefficient as a function

form the representative function of the transformation coefficient. To do so, each target is collected 40 samples. The total samples (200) are computed their excess values to determine the relation of the weight target and the excess values as illustrated in Fig. 6. By using the information provided in Fig. 6, at each opted weight target, the set-point is obtained by deducting the mean surplus from the opted weight value. Also, excess variance of the average excess is computed. Hence, $\boldsymbol{H}$ is formed by calculating the ratio of the selected target and the set-point, as listed in Table 1. To formulate $\boldsymbol{H}$, the relationship betwixt each selected target and $\boldsymbol{H}$ is plotted in Fig. 7. From Fig. 7, the line joining the triangle-symbols is fitted using a second order polynomial model to extract the transformation coefficient function as rendered in (4).

$$\boldsymbol{H} = 1.613\boldsymbol{e}^{-9}(\boldsymbol{Tg})^2 - 1.638\boldsymbol{e}^{-5}(\boldsymbol{Tg}) + 1.047 \tag{4}$$

2.2. Recursive Kalman filtering

Since the Kálmán filtering cannot directly obtain the true value of the set-point, the measurement is used as a feedback control to accomplish the optimum of the set-point. To get the set-point optimized, the Kálmán filtering entailing two main steps has to run recursively. Both two main steps are the prediction update and the

Table 1. *Transformation Coefficients and Targets*

	Selected Targets				
	3005g	**3305g**	**3505g**	**4005g**	**5005g**
Mean Surplus	37g	34g	32g	30g	27g
Set-point	2968g	3271g	3473g	3975g	4978g
Transformation Coefficient	1.0125	1.0104	1.0092	1.0075	1.0054
Excess Variance	$17.6567g^2$				

correction update which can be detailed by the following equations.

2.2.1. Prediction Update

$$\boldsymbol{x}[\boldsymbol{n}\,|\,\boldsymbol{n}-1] = \boldsymbol{A}\boldsymbol{x}[\boldsymbol{n}-1\,|\,\boldsymbol{n}-1] + \boldsymbol{w}[\boldsymbol{n}-1] \tag{5}$$

$$\boldsymbol{P}[\boldsymbol{n}\,|\,\boldsymbol{n}-1] = \boldsymbol{A}\boldsymbol{P}[\boldsymbol{n}-1\,|\,\boldsymbol{n}-1]\boldsymbol{A}^{\boldsymbol{T}} + \boldsymbol{Q} \tag{6}$$

where $\boldsymbol{x}[\boldsymbol{n}\,|\,\boldsymbol{n}-1]$ is the predicted set-point at time $\boldsymbol{n}$, given corrected set-point at time $\boldsymbol{n}-1$, $\boldsymbol{x}[\boldsymbol{n}-1\,|\,\boldsymbol{n}-1]$. $\boldsymbol{P}[\boldsymbol{n}\,|\,\boldsymbol{n}-1]$ is the predicted error variance at time $\boldsymbol{n}$, given corrected estimate of error variance at time $\boldsymbol{n}-1$, $\boldsymbol{P}[\boldsymbol{n}-1\,|\,\boldsymbol{n}-1]$.

2.2.2. Correction Update

$$\boldsymbol{K}[\boldsymbol{n}] = \boldsymbol{P}[\boldsymbol{n}\,|\,\boldsymbol{n}-1]\boldsymbol{H}^{\boldsymbol{T}}(\boldsymbol{H}\boldsymbol{P}[\boldsymbol{n}\,|\,\boldsymbol{n}-1]\boldsymbol{H}^{\boldsymbol{T}} + \boldsymbol{R})^{-1} \tag{7}$$

$$\boldsymbol{x}[\boldsymbol{n}\,|\,\boldsymbol{n}] = \boldsymbol{x}[\boldsymbol{n}\,|\,\boldsymbol{n}-1] + \boldsymbol{K}[\boldsymbol{n}](\boldsymbol{z}[\boldsymbol{n}] - \boldsymbol{H}\,\boldsymbol{x}[\boldsymbol{n}\,|\,\boldsymbol{n}-1]) \tag{8}$$

$$\boldsymbol{P}[\boldsymbol{n}\,|\,\boldsymbol{n}] = (\boldsymbol{I} - \boldsymbol{K}[\boldsymbol{n}]\boldsymbol{H})\boldsymbol{P}[\boldsymbol{n}\,|\,\boldsymbol{n}-1] \tag{9}$$

where $\boldsymbol{K}[\boldsymbol{n}]$ is Kálmán gain, $\boldsymbol{x}[\boldsymbol{n}\,|\,\boldsymbol{n}]$ is the corrected set-point at time $\boldsymbol{n}$, and $\boldsymbol{P}[\boldsymbol{n}\,|\,\boldsymbol{n}]$ is the corrected estimate of error variance at time $\boldsymbol{n}$.

3. SIMULATION AND EXPERIMENT

3.1. MATLAB simulation

In MATLAB simulation, the set-points estimated by the proposed method, and the techniques of [5] and [6] are compared to show their performances. Additionally, the desired target $\boldsymbol{Tg}$ is simulated only 3505 grams.

Before simulating the proposed technique, some parameters need to be assigned as follows. $\boldsymbol{Q}$ is 1. $\boldsymbol{H}$ calculated by (4) is 1.0094. As a matter of fact, in practice, the excess variance, $\boldsymbol{R}$, is not constant. Hence, the variable $\boldsymbol{R}$ is sought using an exhaustive search method to make the predicted set-points more robust (not to swing as much as the actual variance occurred). $\boldsymbol{R}$ is forced to 1. Owing to the next set-point is evolved from the previous set-point, $\boldsymbol{x}[0\,|\,0]$ is determined to 3473g (from Table 1) and $\boldsymbol{A}$ is initially set to 1, and $\boldsymbol{P}[0\,|\,0]$ is firstly assigned to 1.

To illustrate the efficiency of approximating the set-point, a set of pre-generated 50 measured weight values is randomly generated. The simulation results are depicted in Fig. 8 and the statistical data of the simulated results are concluded in Table 2. Obviously, the set-points optimized by the proposed technique do not

oscillate as much as the results of the method of [6]. In addition, the set-point results obtained by the method of [5] gradually decrease toward a constant value, however, the constant value may not be an optimal set-point.

3.2. Experiment employing the practical machine

In the experiment, it is experimented with the practical machine depicted in Fig. 5. In accordance with the simulation results, not only the proposed technique outperforms the approaches of [5] and [6], but also the computational complexity of the proposed method is less than the methods of [5] and [6] using Big-O criterion. Therefore, only the presented technique is performed. The desired target of 3505 grams is conducted in which 100 samples are collected as shown in Fig. 9. Also, the parameters implemented are set as same as the simulation.

The information of the results obtained from Fig. 9 is summarized in Table 3, including the accuracy calculation. The accuracy of the observed weight values is computed using mean absolute percentage error (MAPE) as expressed by the following equation,

$$\%\boldsymbol{M} = \frac{1}{\boldsymbol{n}}\sum_{i=1}^{n}\left|\frac{\boldsymbol{Tg}-\boldsymbol{MW}_i}{\boldsymbol{Tg}}\right| \text{x}100 \qquad (10)$$

where $\boldsymbol{MW}$ is a measured weight value, $\boldsymbol{n}$ is the total samples and $\%\boldsymbol{M}$ is the mean absolute percentage error (MAPE). In addition, by employing the proposed method, the set-point is converged to the optimal value

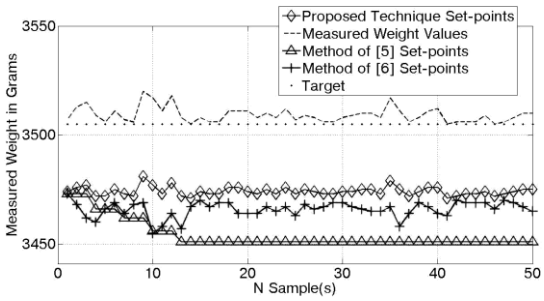

Fig. 8. Simulation results of the proposed technique, method of [5] and [6].

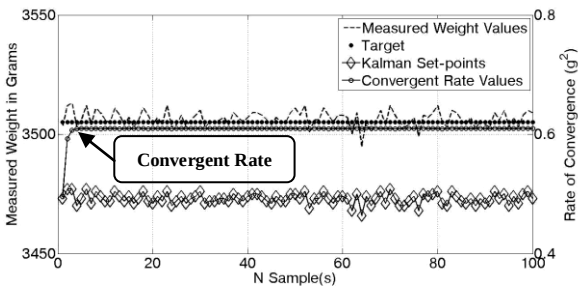

Fig. 9. Experimental results with the practical machine.

Table 2. *Statistical Data of Set-point (Simulation)*

Compensation Method	Av.M	Avg.SP	Ex	Var	STD	Big -O
Proposed Method	3509g	3470g	35g	5.01	2.24	1
Method of [5]		3454g	51g	42.03	6.48	**N**
Method of [6]		3466g	39g	13.24	3.64	**M**

Av.M-Average Measured Weight, **Avg.SP**-Average Set-point, **Ex**-Average Excess, **Var**-Variance of Set-point, **STD**- Standard Deviation of Set-point, **N** is the order of moving average **O(3)** and **M** is the amount of fuzzy logic rules **O(32)**

Table 3. *Statistical Data of Set-point and Accuracy Calculation (Experiment)*

Compensation Method	Av.M	Avg.SP	Ex	Var	STD
Proposed Method	3507g	3473g	34g	4.78	2.19

	Variance of the sensed weight	Standard Deviation of the sensed weight	%M
Proposed Method	10.29	3.21	0.08

fairly fast, after three iterations as shown in Fig. 9. Thus, this rate of convergence is fast enough for this application because, in practical, at least 5-10 iterations are adjusted before running the machine continually.

4. CONCLUSION

In this paper, the new technique for compensating the set-point in a vertical filling weighing system is presented. The technique optimizes the set-point based on Kálmán filtering in which its process equation and measurement equation are consistently designed to the vertical filling weighing system. The proposed scheme is tested its performance not only in the simulation but also in the practical machine. In both simulation and experiment, they have resulted in the same way. Also, it is found that, in experimenting using the practical machine, the fresh technique provides good accuracy of measured weight. Moreover, it is suggested that this proposed method may be applicable for a practical system.

5. ACKNOWLEDGMENT

The authors would like to thank Lion Corporation (Thailand) Limited for supporting an experimental setup.

6. REFERENCES

[1] J. Li, and L. Zhou, "Improved satisfactory predictive control algorithm with fuzzy setpoint constraints," *Proceedings of the 6th World Congress on Intelligent Control and Automation*, Dalian, June 2006, pp. 6274-6278.

[2] M. Wheatley, "Filling time," *IET Journals & Magazines*, vol. 5, pp. 54-56, November-December 2010.

[3] D. Combeau, J.B. Rey, J.E. Fontan, Ph. Arnaud, and F. Brion, "Evaluation of a filling system for binary pediatric solutions," *Pharm World Sci*, vol. 20, pp. 32-37, 1998.

[4] R.C. Rodrigues de Oliveira, and C. Garcia, "Simulator for a packing and weighing system of granulated powders," *ISA Transactions*, vol. 52, pp. 672-683, 2013.

[5] *F701-C Weighing Controller Operation Manual.*, Unipulse Corporation., Tokyo 103-0005, August 2012, pp. 82-84.

[6] Z. Dejun, W. Haochen, and L. Chunmei, "The application of fuzzy control in high accurate automatic powder dosing system," *Electric Information and Control Engineering. (ICEICE)*, Wuhan, April 2011, pp. 1771-1774.

[7] S.M. Kay, *Fundamentals of Statistical Signal Processing, Vol. I: Estimation Theory.* New Jersey, US: Prentice Hall, 1993, pp. 419-478.

The 7th International Conference on Engineering and Technology
ICET-2015, Phuket, June 19-20, 2015
Prince of Songkla University, Faculty of Engineering
Hat Yai, Songkhla, Thailand 90112

Determination of Mean Values of Common Distributions in Civil Engineering from the Specifications for Mass Production

Kong Kamollertvara*and Winai Ouypornprasert
Rangsit University, College of Engineering, Pathumthani, Thailand
* kong@asiagroup1999.com

Abstract: *The objective of this technical paper was to propose an approach to determine the mean values for mass production based on statistical data available in the factory. The mean values were determined from the specified values, the coefficient of variation and the chance that the values of the variable would be less than the specifications. Distribution functions and the corresponding shape parameters as well as calculation procedures were summarized for 11 functions commonly used in civil engineering. The authors also showed an example to determine suitable mean values of the compressive strength of concrete for the corresponding specifications.*

Keywords: Mean Value, Specification, Goodness-of-Fit Test, Continuous Distribution, Non-normal Distribution, Mass Production

1. INTRODUCTION

For the mass production in a factory products have to be conforming to specifications. To avoid rejection of products, the mean value for each engineering property has to be at least equal to the corresponding specification. Usually a good quality control will lead to a lower value of cov (the **c**oefficient **o**f **v**ariation) of the property involved. The lower the cov, the lower the corresponding mean value required. Although actual engineering data showed some skewness [1], normal distributions could be applied conservatively [2]. Fortunately best fitted distributions could be obtained as suggested in [3]. Based on this the most suitable mean value for each specification for mass production could be further inversely determined from existing engineering data using the formulations proposed.

In this technical paper the determination of mean values from the given specifications for non-normal distributions will be discussed. Section 2 will begin with the prediction of expected values of engineering properties for the normal distribution. Then a numerical example will be demonstrated in Section 3. Finally the summary will be given in Section 4.

2. DETERMINATION OF MEAN VALUES FROM SPECIFICATIONS

2.1 General Remarks

Let x be the value of a basic variable X with the mean (μ) and the standard deviation (σ), $f_X(x)$ and $F_X(x)$ be pdf (the **p**robability **d**ensity **f**unction) and df (the **d**istribution **f**unction), respectively. The relationship between $f_X(x)$ and $F_X(x)$ can be shown in the following:

$$f_X(x) = \frac{dF_X(x)}{dx} \tag{1}$$

$$F_X(x) = \int_{-\infty}^{x} f_X(x)dx \tag{2}$$

Furthermore Ω is the **c**oefficient **o**f **v**ariation (cov) defined in form of:

$$\Omega = \frac{\sigma}{\mu} \tag{3}$$

For the sake of further discussions let define a and b as the lower bound and the upper bound of a bounded distribution, respectively, x_{spec} as the specified value of X and p as the non-exceedance probability. All formulations summarized in the

following subsections are based on the assumptions that both Ω and p be given.

2.2 Determination of mean values for Normal Variables

$$f_X(x) = \frac{1}{\sqrt{2\pi}\cdot\sigma}\cdot e^{-\frac{1}{2}\left(\frac{x-\mu}{\sigma}\right)^2} \quad (4)$$

$$F_X(x) = \int_{-\infty}^{x} \frac{1}{\sqrt{2\pi}\cdot\sigma}\cdot e^{-\frac{1}{2}\left(\frac{x-\mu}{\sigma}\right)^2} dx \quad (5)$$

For the value of the standard normal variable (Z) with the mean equal to zero and the standard deviation equal to 1 is defined as

$$z = \frac{x-\mu}{\sigma} \quad (6)$$

Then the corresponding df ($\Phi(z)$):

$$\Phi(z) = F_Z(z) = \int_{-\infty}^{z} \frac{1}{\sqrt{2\pi}}\cdot e^{-\frac{1}{2}z^2} dz \quad (7)$$

p can be calculated from Eq. (8) and (9), respectively.

$$z = \Phi^{-1}(p) \quad (8)$$

$$x = \mu + \sigma\cdot\Phi^{-1}(p) \quad (9)$$

Since Ω is the result from the quality control, it is better to determine σ in term of Ω. Substituting z from Eq. (8) and σ into Eq. (9) yields

$$x = \mu + \Omega\cdot\mu\cdot\Phi^{-1}(p)$$

Then

$$\mu = \frac{x_{spec}}{1+\Omega\cdot\Phi^{-1}(p)} \quad (10)$$

The values of $z = \Phi^{-1}(p)$ for p in the range of 0.01 – 0.05 are summarized in Table1.

Table 1 z-Scores and Non-Exceedance Probability

p(%)	1	2	3	4	5
$z = \Phi^{-1}(p)$	-2.326	-2.054	-1.881	-1.751	-1.645

2.3 Determination of mean values for non-normal variables

2.3.1 General

Besides the normal distribution the other 10 types of distributions will be discussed. Shape parameters related to basic statistical properties are referred to [1]. Only the formulas for determining shape parameters and mean values for mass production and will be summarized here. For more details it is referred to [3] and [4], respectively.

2.3.2 Uniform Distribution

$$F_X(x) = \int_{-\infty}^{x} \frac{1}{b-a} dx; a \le x \le b \quad (11)$$

$$a = \frac{c\cdot x_{spec}}{p + c\cdot(1-p)} \quad (12)$$

$$c = \left(\frac{1-\sqrt{3}\cdot\Omega}{1+\sqrt{3}\cdot\Omega}\right) \quad (13)$$

$$b = \frac{x_{spec} - a(1-p)}{p} \quad (14)$$

$$\mu = \frac{a+b}{2} \quad (15)$$

2.3.3 Shifted Exponential Distribution

$$F_X(x) = \int_{-\infty}^{x} \lambda e^{-\lambda(x-a)} dx; \quad x \ge a \quad (16)$$

where λ is the shape parameter.

$$\mu = \frac{x_{spec} + \ln(1-p)}{1-\Omega} \quad (17)$$

2.3.4 Rayleigh Distribution

$$F_X(x) = \int_{-\infty}^{x} \frac{x-a}{\alpha^2}\cdot\exp\left(-\frac{1}{2}\cdot\left(\frac{x-a}{\alpha}\right)^2\right); x \ge a \quad (18)$$

where α is the shape parameter.

$$\alpha = \frac{\Omega\cdot x_{spec}}{2 - 0.5\pi + \Omega\cdot\left(\sqrt{0.5\pi} - \sqrt{-2\ln(1-p)}\right)} \quad (19)$$

$$\mu = \alpha\cdot\sqrt{\frac{\pi}{2}} + a \quad (20)$$

2.3.5 Gumbel - Type I - Largest Distribution

When the tail of mother distribution $F_X(x)$ is an exponential function, then the distribution of the largest value y takes the form:

$$F_Y(y) = \exp\left[-e^{-\alpha(y-u)}\right]; -\infty < y < \infty \quad (21)$$

where u is the mode and α is the shape parameter.

$$\mu = \frac{-c\cdot x_{spec}}{\ln(-\ln(p)) + \gamma - c} \quad (22)$$

where γ is an Euler constant with the value of 0.5772156 and $c = \pi/(\sqrt{6}\cdot\Omega)$.

2.3.6 Gumbel - Type I - Smallest Distribution

When the tail of the mother distribution $F_X(x)$ is an exponential function, the distribution of the smallest value y takes the form:

$$F_Y(y) = 1 - \exp\left[-e^{\alpha(y-u)}\right]; -\infty < y < \infty \quad (23)$$

where u is the mode and α is the shape parameter.

$$\mu = \frac{c \cdot x_{spec}}{\ln\left(-\ln\left(1-p\right)\right)+\gamma+c} \quad (24)$$

where γ is an Euler constant with the value of 0.5772156 and $c = \pi/(\sqrt{6}\cdot\Omega)$.

2.3.7 Lognormal Distribution

$$f_X(x) = \frac{1}{\sqrt{2\pi}\zeta x}\exp\left[-\frac{1}{2}\left(\frac{\ln x-\lambda}{\zeta}\right)^2\right]; x>0 \quad (25)$$

where λ and ζ are shape parameters related to μ and σ as followed:

$$\mu = \exp\left(\lambda+\frac{1}{2}\zeta^2\right) \quad (26)$$

$$\sigma^2 = \mu_X^2\left(e^{\zeta^2}-1\right) \quad (27)$$

$$\mu = \frac{x_{spec}}{\exp\left(\zeta\cdot\Phi^{-1}\left(p\right)\right)} \quad (28)$$

2.3.8 Gamma Distribution

$$f_X(x) = \frac{\nu(\nu x)^{k-1}e^{-\nu x}}{\Gamma(k)}; x\geq 0 \quad (29)$$

where ν and *k* are shape parameters. Γ(·) is the value of the gamma function.

$$\Gamma(k) = \int_0^\infty x^{k-1}e^{-x}dx; k>0 \quad (30)$$

$$\mu = \frac{k}{\nu} \quad (31)$$

$$\sigma = \frac{\sqrt{k}}{\nu} \quad (32)$$

$$\mu = \frac{x_{spec}}{\Omega^2\cdot\nu x_{spec}} \quad (33)$$

2.3.9 Fréchet - Type II - Largest Distribution

When the tail of the mother distribution $F_X(x)$ is a polynomial function, the distribution of the largest value y takes the form:

$$F_Y(y) = \exp\left[-\left(\frac{w}{y}\right)^m\right]; m>0, w>0, y>0 \quad (34)$$

Where *w* and *m* are shape parameters. *w* determines the size and *m* determines the shape.

$$\mu = w\Gamma(1-\frac{1}{m}) \quad (35)$$

$$\left(\frac{\sigma}{\mu-\varepsilon}\right)^2 = \frac{\left\{\Gamma\left(1-\frac{2}{m}\right)-\Gamma^2(1-\frac{1}{m})\right\}}{\Gamma^2(1-\frac{1}{m})}; m>2 \quad (36)$$

$$\mu = \frac{x_{spec}}{\left(-\ln\left(p\right)\right)^{\frac{1}{m}}}\cdot\Gamma\left(1-\frac{1}{m}\right) \quad (37)$$

2.3.10 Weibull – Type III – Smallest Distribution

When the mother distribution $F_X(x)$ is define in range of $\varepsilon \leq x < \infty$.

$$F_X(x) = a(x-\varepsilon)^m; \quad -\infty<x<\infty, x\geq\varepsilon \quad (38)$$

The distribution of the largest value *y* takes the form:

$$F_Y(y) = 1-\exp\left[-\left(\frac{y-\varepsilon}{v-\varepsilon}\right)^m\right]; y\geq\varepsilon, m>0, v\geq\varepsilon \quad (39)$$

where *v* and *m* are shape parameters. w determines the size and m determines the shape.

$$\mu = \varepsilon+(v-\varepsilon)\Gamma(1+\frac{1}{m}) \quad (40)$$

$$\left(\frac{\sigma}{\mu-\varepsilon}\right)^2 = \frac{\left\{\Gamma(1+\frac{2}{m})-\Gamma^2(1+\frac{1}{m})\right\}}{\Gamma^2\left(1+\frac{1}{m}\right)}; m>0 \quad (41)$$

$$\mu = \frac{x_{spec}}{\left(-\ln\left(1-p\right)\right)^m}\cdot\Gamma\left(1+\frac{1}{m}\right) \quad (42)$$

2.3.11 Beta Distribution

$$f_X(x) = \frac{1}{B(q,r)}\frac{(x-a)^{q-1}(b-x)^{r-1}}{(b-a)^{q+r-1}}; a\leq x\leq b \quad (43)$$

where q and r are shape parameters and $B(q,r)$ is the beta function:

$$B(q,r) = \int_0^1 x^{q-1}(1-x)^{r-1}dx = \frac{\Gamma(q)\Gamma(r)}{\Gamma(q+r)} \quad (44)$$

$$\mu = a+\frac{q}{q+r}\left(b-a\right) \quad (45)$$

$$\sigma^2 = \frac{qr}{\left(q+r\right)^2\left(q+r+1\right)}\left(b-a\right)^2 \quad (46)$$

Shape parameters can be determined by solving the system of non-linear equations [3] as shown:

$$\left(\frac{\sigma}{\mu-a}\right)^2 = \frac{r}{q\cdot(q+r+1)} \quad (47)$$

$$r = q\cdot\left[\frac{\left(b-a\right)}{\left(q+r\right)\cdot\left(\mu-a\right)}-1\right] \quad (48)$$

However, iterative procedures must be used to solve for the mean by assuming known shape parameters considered from existing data of similar classes.

3. EXAMPLE

For the production the compressive strength of concrete at the age 1 day and 7 days should be not less than 250 ksc and 350 ksc, respectively and the non-exceedance probability should be 5% (p =

0.05). With the current production processes cov of the compressive strength of concrete has been 0.20. By improving production processes we can lower the value of the cov of the compressive strength of concrete to 0.12. The calculated mean values for the compressive strength of concrete for $\Omega = 0.20$ and $\Omega = 0.12$ for 11 types of distributions are summarized in Tab. 2 and Tab. 3, respectively.

Table 2 Mean Values for $\Omega = 0.20$

Type Distr.| Spec.	250 ksc	350 ksc
Normal	372.6	521.6
Uniform	363.3	508.6
Exponential	312.4	437.4
Rayleigh	298.1	417.3
Gumbel Largest	338.3	473.7
Gumbel Smallest	398.8	558.4
lognormal	346.3	484.8
gamma	359.6	503.4
Fréchet	320.1	448.2
Weibull	386.4	541.0
beta	310.7	435.0

Table 3 Mean Values for $\Omega = 0.12$

Type Distr.| Spec.	250 ksc	350 ksc
Normal	311.5	436.1
Uniform	307.5	430.5
Exponential	284.0	397.7
Rayleigh	283.2	396.4
Gumbel Largest	296.4	415.0
Gumbel Smallest	322.1	451.0
lognormal	304.3	426.1
gamma	308.2	431.5
Fréchet	291.1	407.6
Weibull	319.9	447.8
beta	283.2	396.5

At the early stage of production the compressive strength of concrete might be assumed normal. Thus the mean values at the ages 1 day and 7 days should be not less than 372.6 and 521.6 ksc respectively.

Later on, the producer has collected statistical data, and discovered that the best fitted type of distribution for the compressive strength of concrete was lognormal. Therefore the producer can reduce the mean values of the compressive strength at the ages 1 day and 7 days to not less than 346.3 and 484.8 ksc, respectively (reduction of 7.06%).

By improving production processes, producer can lower the cov of the compressive strength to not greater than 0.12. The producer can further adjust the mean values of the compressive strength at the ages 1 day and 7 days to not lesser than 304.3 and 426.1 ksc, respectively (reduction of 18.3%).

4. RESULT AND SUMMARRY

In this technical paper, the authors

1) concluded 11 types of distributions commonly used in civil engineering including shape parameters and necessary formulas for considering mean values from specified values and the coefficients of variation with the given non-exceedance probability,
2) demonstrated an example for considering minimum mean values suitable for concrete production and showed how to reduce the production cost by using the suitable types of distributions of the existing data and the production technology for reducing the variability of product properties.

5. ACKNOWLEDGEMENT

We would like to thank Asia Group (1999) Co., Ltd. for the full research fund.

6. REFERENCES

[1] Achintya Haldar and Sankaran Mahadevan, Probability, Reliability, and Statistical Methods in Engineering Design, John Wiley & Sons, New York, 2000.

[2] M.L. Gambhir, Concrete Technology, 5th Ed., McGraw Hill, 2013, 774 pages.

[3] W. Ouypornprasert, Goodness-Of-Fit Tests for Common Distributions in Civil Engineering, in Proceedings of the Conference on Computational Mathematics and Modeling (CMM2002), Organized by Mahidol University and Curtin University of Technology, Bangkok, 2002.

[4] Kong Kamollertvara, Probability-Based Concrete Mix Design, Master Thesis, Submitted for Partial Fulfillment of Master Degree in Civil Engineering, Rangsit University, 2015.

The 7th International Conference on Engineering and Technology
ICET-2015, Phuket, June 19-20, 2015
Prince of Songkla University, Faculty of Engineering
Hat Yai, Songkhla, Thailand 90112

The Dynamic Behavior of the Speed Variator with Unpredictably Changing Mode of Operation

Miodrag Zlokolica[1*], Maja Čavić[2], Milan Kostić[3]
Faculty of Technical Sciences, University of Novi Sad, Novi Sad, Serbia
[*]Email of corresponding author: mzlokolica@uns.ac.rs

Abstract: *Variable-speed drives, contained in many complex systems of modern technique, can be recognized as nonholonomic mechanical systems. This type of transmission has the connections of differential character between transmission elements. The aim of this paper is to give general approach to dynamical description of the behavior of the variable-speed drive as nonholonomic system, estimating its functional stability for changeable working regime. For dynamical description of the mechanical nonholonomic system, Appell`s differential equations are used. By numerically solving differential equations of motion an answer concerning the working stability as well as the dynamical and kinematics behavior of observed system is obtained. Results can be used in choosing optimal parameters for the synthesis of such kind of power transmissions.*

Key Words: ***Dynamics, Nonholonomic System, Power Transmissions, Variable-speed Drive***

1. INTRODUCTION

Different kinds of variable-speed drives (variators) are commonly met as a part of complex machine systems with changeable working regime. They are used for changing speed in agricultural machines, cutting machines, machine for foil streching, carpet and paper industries, mining machines, automotive industry etc [1], [2]. Having in mind variable-speed drives such a large use of mechanical variations in contemporary industry it is important to develop a general procedure for the dynamic analysis of this class of mechanical systems.

Variable-speed drives are nonholomic mechanical systems, because the connections between its links are differential -connections between kinematic parameters in nonholomic systems are described by differential equations which cannot be integrated in order to deduce geometric characteristics. This is the basis of nonholonomic mechanics and gives the difference from holonomic mechanics where all connections have geometric characteristic and there are no limits of speed and acceleration for the system [3]. The theoretical considerations as well as the case studies of some simple mechanical nonholonomic systems are presented in [4], [5].

In this paper a variable-speed drive with two half balls, disc and Watt`s regulator will be analyzed. The nonholonomic connection occurs in the points of physical contact between the half balls and disc which performs a complex spatial motion. Watt`s regulator is added to this system for regulation of the variable transmission relation between input and output elements. A damper is added for motion stabilizing. Appell`s equations will be used for the dynamical analysis. As a result differential equations of motion which describe the variator as the complex, spatial, mechanical and nonholonomic system are obtained. Commonly it is not possible to solve these differential equations analytically so they will be solved on computers using numerical methods.

2. METHOD FOR DYNAMIC ANALYSIS OF NONHOLONOMIC SYSTEMS

Appell`s equations, which are very suitable for nonholonomic dynamic analysis are given in the form [6],[7],[8]:

$$\frac{\partial S^*}{\partial \ddot{q}_\nu} = Q_\nu^* \quad (\nu = 1,2,\ldots,p) \tag{1}$$

where:

S^* - energy of acceleration (a function of $\ddot{q}$ only);

$\ddot{q}$ - generalized acceleration

Q_ν^* - generalized force

Following relation gives the energy of acceleration:

- for the material point:

$$S = \frac{m\bar{a}^2}{2} = \frac{1}{2}m\left(\ddot{\bar{r}}\right)^2 = \frac{1}{2}m\left(\ddot{x}^2 + \ddot{y}^2 + \ddot{z}^2\right) \tag{2}$$

where:

$\ddot{\bar{r}}_j$ - acceleration of material points j with mass m_j

- for body performing spatial motion

$$S = \frac{m\vec{a}_C^2}{2} + \tilde{S} =$$
$$\frac{1}{2}m\left(\ddot{x}^2 + \ddot{y}^2 + \ddot{z}^2\right) + \frac{1}{2}\left(J_\xi\dot{\omega}_\xi^2 + J_\eta\dot{\omega}_\eta^2 + J_\zeta\dot{\omega}_\zeta^2\right) +$$
$$\left(J_\eta - J_\xi\right)\omega_\xi\omega_\eta\dot{\omega}_\zeta + \left(J_\zeta - J_\eta\right)\omega_\zeta\omega_\eta\dot{\omega}_\xi +$$
$$+\left(J_\xi - J_\zeta\right)\omega_\zeta\omega_\xi\dot{\omega}_\eta + \tilde{S} \qquad (3)$$

where:

$\vec{a}_C$ - acceleration of the center of the mass (point C)

m - mass of thr body

$\omega_\xi, \omega_\eta, \omega_\zeta, \dot{\omega}_\xi, \dot{\omega}_\eta, \dot{\omega}_\zeta$ - angular velocities and accelerations of the body in coordinate system $C\xi\eta\zeta$ (ξ, η, ζ axes are coincident with principle axes of inertia of the body)

J_ξ, J_η, J_ζ - moments of the inertia of the body in coordinate system $C\xi\eta\zeta$

$\tilde{S}$ - term that does not contain angular accelerations

Generalized force isgiven as:

$$Q_\nu^* = \sum_{j=1}^{N} \vec{F}_j \vec{A}_{j\nu} \qquad (3)$$

where:

$\vec{F}_j$ - external force in material point j

$\vec{A}_{j\nu}$ - Appell`s vector

For this class of problems generalized forces can be found in a more simple manner - using principle of virtual work [6], [7],[8].

3. VARIABLE-SPEED DRIVE AS NON-HOLONOMIC SYSTEM

The frictional variable-speed drive with half balls and disc is shown in Fig. 1. Variation of angular speed by this variable-speed drive is performed due to a change of position of contact points A and B caused by rotation of the element 4 in one or other direction. In this way the distances between the contact points and rotating axes of 1 and 2 is changed thus giving the variable transmission ratio between elements 1 and 2.

The closed automatic regulation is made through action of the slider 8 which is integrated in the mechanism at the point D. This type of variable-speed drive is good for large ranges of regulation.

Symbols in Fig.1 are:

R_1 and R_2 - radii of guiding and guided half balls elements 1 and 2

R_4 - radius of segment gear 4

r - radius of gear 3

x and x_o - position and start position of slider D of regulator

α and α_o - angle and start angle of gear 3, measured around the axis O_4

δ - position angle of regulators bar

J_{o3} - inertial moment of frictional disc 3 with respect to the axis O_3

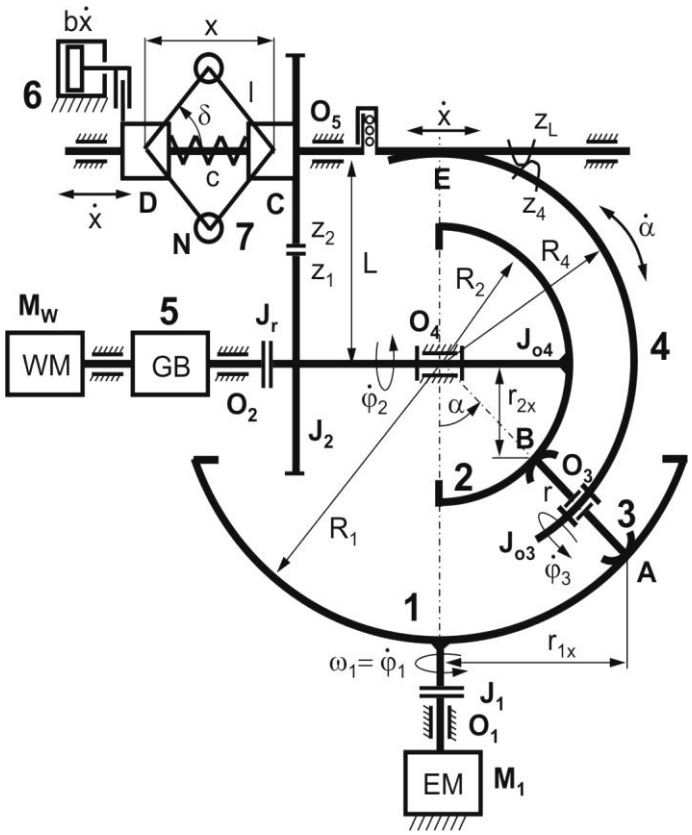

Fig. 1. Closed mechanical regulating system with variable-speed drive

J_r - reduced inertial moment of all rotating masses of working elements on the axis O_2 of element 2, inertias of gears z_1 and z_2 incorporated also

J_{o43} - inertial moment for axis O_4 of the disc 3

J_{o44} - inertial moment for axis O_4 of the segment gear 4

$$J_{04} = J_{043} + J_{044} \qquad (4)$$

J_1 - inertial moments of the guiding half ball 1

J_2 - inertial moments of the guided half ball 2

M_1 - torque on the element 1

$$M_1 = M_{EM} \qquad (5)$$

M_2 - torque on the element 2

$$M_2 = M_W\, i_r \qquad (6)$$

M_W - torque on the working machine

i_r - transmission ratio of gear-box 5, between shaft O_2 and working machine

i_{12} - transmission ratio between half balls 1 and 2 with radii R_1 and R_2

$\dot{x}$ - speed of regulation, change of position for slider D

$\Delta\ell$ - start load of elastic element

c - spring coefficient

z_1, z_2, z_4 and z_L - number of teeth of the gears and the lathe

$\dot{\phi}_1, \dot{\phi}_2, \dot{\phi}_3, \dot{\alpha}$ - angular speeds of: guiding half ball 1(around axisO_1), guided half ball 2 (around axis O_2) , disc 3 (around axis O_3), and segment gear 4 (around axis O_4)

m_D - mass of the slider in point D

m_N - mass of the regulator ball

b - damping coefficient

Dynamical analysis will be done by Appell's equations for non-holonomic systems. This system has three generalized coordinates ϕ_1, ϕ_2 and x. Nonholonomic connection is:

$$\dot{\phi}_1 - i_v \dot{\phi}_2 = 0 \tag{7}$$

where:

$$i_v = \frac{r_{2x}}{r_{1x}} = \frac{R_2 \cos\alpha}{R_1 \sin\alpha} = i_{12}\, ctg\alpha \;; \qquad i_{12} = \frac{R_2}{R_1} \tag{8}$$

so there will be two independent generalized coordinates - $\ddot{x}$ as the first one and $\ddot{\varphi}_2$ which will be adopted as the second one.

The general form of Appell's equations is:

$$\frac{\partial S}{\partial \ddot{\phi}_2} = Q_{\phi_2} \qquad \frac{\partial S}{\partial \ddot{x}} = Q_x \tag{9}$$

where:

S - energy of acceleration (function of independent generalized accelerations, velocities and coordinates)

$\ddot{\phi}_2, \ddot{x}$ - generalized accelerations

Q_{ϕ_2}, Q_x - generalized forces (function of independent generalized coordinates and speeds).

Energy of acceleration for the whole system is given as:

$$S = S_1 + S_2 + S_3 + S_4 + S_D + 2S_N \tag{10}$$

where:

- S_1 - energy of acceleration of the element 1

$$S_1 = \frac{1}{2} J_1 \ddot{\varphi}_1^2 + \tilde{S}_1 \tag{11}$$

Connection between $\ddot{\phi}_1$ and $\ddot{\phi}_2$ is obtained by differentiating nonholonomic connection (7):

$$\ddot{\phi}_1 = i_v \ddot{\phi}_2 + \frac{di_v}{dt}\dot{\phi}_2 \;; \qquad \frac{di_v}{dt} = i_{12}\frac{\dot{\alpha}}{\sin^2\alpha} \tag{12}$$

- S_2 - energy of acceleration of the element 2

$$S_2 = \frac{1}{2} J_2 \ddot{\varphi}_2^2 + \tilde{S}_2 \tag{13}$$

- S_3 - energy of acceleration of the element 3

$$S_3 = \frac{1}{2} m (R_2 + r)^2 \dot{\alpha}^2 + \frac{1}{2} m (R_2 + r)\ddot{\alpha}^2 + \frac{1}{2} J_3 \ddot{\varphi}_3^2 + \frac{1}{2} J_{o43}\ddot{\alpha}^2 + \tilde{S}_3 \tag{14}$$

$$S_3 \approx \frac{1}{2} J_3 \ddot{\varphi}_3^2 + \frac{1}{2} J_{o43}\ddot{\alpha}^2 + \tilde{S}_3$$

First component of the angular velocity and acceleration of element 3 can be expressed as:

$$i_{32} = \frac{\dot{\varphi}_3}{\dot{\varphi}_2} = \frac{r_{2x}}{r} = \frac{R_2 \cos\alpha}{r} = i_2 \cos\alpha$$

$$\dot{\varphi}_3 = \dot{\varphi}_2\, i_2 \cos\alpha; \qquad \ddot{\varphi}_3 = \ddot{\varphi}_2\, i_2 \cos\alpha - \dot{\varphi}_2\, i_2\, \dot{\alpha} \sin\alpha \tag{15}$$

As for generalized coordinates x and α, geometrical connection is:

$$x - x_o = (\alpha - \alpha_o)\, r_4 \tag{16}$$

Differentition gives:

$$\dot{\alpha} = \frac{\dot{x}}{r_4}; \quad \ddot{\alpha} = \frac{\ddot{x}}{r_4} \tag{17}$$

- S_4 - energy of acceleration of the element 4

$$S_4 = \frac{1}{2} J_{o44}\ddot{\alpha}^2 + \tilde{S}_4 \tag{18}$$

- S_D - energy of acceleration the slider D

$$S_D = \frac{1}{2}\ddot{x}^2\, m_D$$

- S_N - energy of acceleration of the regulator ball N

$$S_N = \frac{1}{2} a_N^2\, m_N; \qquad \vec{a}_N = \vec{a}_{pN} + \vec{a}_{pT} + \vec{a}_{rN} + \vec{a}_{rT} + \vec{a}_K \tag{19}$$

where:

$\vec{a}_{pN}, \vec{a}_{pT}$ - normal and tangential transmission acceleration of point N

$\vec{a}_{rN}, \vec{a}_{rT}$ - relative normal and tangential acceleration of point N

$\vec{a}_k$ - Coriolis's acceleration

$$a_{pN} = \ell\dot{\phi}_2^2 \sin\delta; \; a_{rN} = \ell\dot{\delta}^2; \qquad a_K = 2\ell\dot{\delta}\dot{\phi}_2; \qquad a_{pT} = \ell\ddot{\phi}_2 \sin\delta; \; a_{rT} = \ell\ddot{\delta} \tag{20}$$

Square or acceleration for point N is:

$$a_N^2 = \left(a_{pN}\sin\delta + a_{rN}\right)^2 + \left(a_{rT} - a_{pN}\cos\delta\right)^2 + \left(a_{pT} + a_K\right)^2 \tag{21}$$

Geometrical connection between x and δ is:

$$\cos\delta = \frac{x}{2\ell} \tag{22}$$

Differentiation of eq. (22) gives:

$$\dot{\delta} = -\frac{\dot{x}}{2\ell\sin\delta} = -\frac{\dot{x}}{\left(4\ell^2 - x^2\right)^{1/2}}; \qquad \ddot{\delta} = -\frac{\ddot{x}}{\left(4\ell^2 - x^2\right)^{1/2}} - \frac{\dot{x}^2 x}{\left(4\ell^2 - x^2\right)^{3/2}} \tag{23}$$

Now it can be written for S_N:

$$S_N = \frac{1}{2} m_N a_N^2 = \frac{1}{2} m_N \ell^2 \left[\dot{\varphi}_2^2\left(1 - \frac{x^2}{4\ell^2}\right) + \frac{\dot{x}^2}{4\ell^2 - x^2}\right]^2 + \ell^2\left[-\frac{\ddot{x}}{\left(4\ell^2 - x^2\right)^{1/2}} - \frac{\dot{x}^2 x}{\left(4\ell^2 - x^2\right)^{3/2}} - \dot{\varphi}_2^2 \frac{x}{2\ell}\left(1 - \frac{x^2}{4\ell^2}\right)^{1/2}\right]^2 + \ell^2\left[\ddot{\varphi}^2\left(1 - \frac{x^2}{4\ell^2}\right)^{1/2} - 2\dot{\varphi}_2 \frac{\dot{x}}{\left(4\ell^2 - x^2\right)^{1/2}}\right]^2 \tag{24}$$

Generalized forces are defined from virtual work and potential energy.

$$\delta A = M_1\,\delta\phi_1 - M_2\,\delta\phi_2 - b\,\dot{x}\,\delta x = \\ = Q_{\phi 2}\,\delta\phi_2 + Q'_x\,\delta x \tag{25}$$

and:

$$Q_{\phi 2} = M_1\,i_v - M_2\,; \quad Q'_x = -b\,\dot{x} \tag{26}$$

where:

$$M_1 = A - B\,\dot{\phi}_1\,,\ M_2 = i_r\,(D - Ct) \tag{27}$$

If the change of positions for elastic element is described as $\Delta\ell + [x - x_0]$ potential energy can be written in the following form:

$$\Pi = \frac{1}{2}c[\Delta\ell + x - x_0]^2 \tag{28}$$

Generalized force including damping force is:

$$Q_x = -c[\Delta\ell + x - x_0] - b\dot{x} \tag{29}$$

Finally, differential equations of motion are:

$$\left[J_1 i_v^2 + J_3\cos^2\alpha\, i_2^2 + J_2 + J_r + 2\,\ell^2\, m_N\left(1 - \frac{x^2}{4\,\ell^2}\right)\right]\ddot{\phi}_2 +$$

$$+\left[J_1\, i_v\,\frac{di_v}{dt} + J_3\,\frac{\dot{x}\cos\alpha}{r_4}\sin\alpha\, i_2^2 + 2\,m_N\,\ell\,\dot{x} + B\,i_v^2\right]\dot{\phi}_2 =$$

$$= A\,i_v - i_r\,(D - C\,t)$$

and:

$$\left[J_{o4}\,\frac{1}{r_4^2} + m_D + \frac{2\,\ell^2\,m_N}{(4\,\ell^2 - x^2)}\right]\ddot{x} + \frac{2\,\ell^2\,m_N}{(4\,\ell^2 - x^2)}\,\dot{x}\,x +$$

$$+ b\cdot\dot{x} + \frac{1}{2}\dot{\phi}_2^2\cdot x\cdot m_N + c\cdot(x - x_0) = -c\cdot\Delta\ell \tag{30}$$

Putting $\dot{x} = V$ and $\dot{\phi}_2 = \omega_2$ and solving the system of non-linear differential equations (30) on electrical computer using numerical method of integration it is possible to denote the parameters *x, V* and ω_2 in function of time t.

4. EXAMPLE

For example depicted on Fig. 1 values of parameters are:

$J_1 = 0.04$; $J_2 = 0.09$; $J_3 = 0.12$; $J_r = 0{,}5$; $J_{03} = 0.2$ (kg m^2);
$m_N = 0.04$; $m_D = 0.2$ (kg);
c = 57 (N/m); b = 4000 (Ns/m);
$\Delta\ell = 8$; $\ell = 200$; L =45; $R_4 = 45$; $R_1 = 60$; $R_2 = 30$ (mm);
$z_1 = z_2$; z_4=45;
$M_1 = A\text{-}B\,\dot{\phi}_1$; A = 557,9 (Nm); B = 5.33 (Nms); $i_r = 5$;
$M_2 = M_w\cdot i_r = i_r\,(D\text{-}C\cdot t)$; D = 10 (Nm); C = 0.524 (Nm/s);
$t_0 = 0$(s); $\alpha_o = 45^o$; $\omega_{20} = 20$ (s^{-1}); $x_o = 0.20$ (m);

On Fig. 2. Time histories of *x*, $\dot{x} = V$ and $\dot{\phi}_2 = \omega_2$ in function of the time t are presented.

It an be seen on the Fig. 2 that the motion becomes stable after 20 seconds. Presented mechanical nonholonomic system is very good for regulation of unpredictably changing mode of working process.

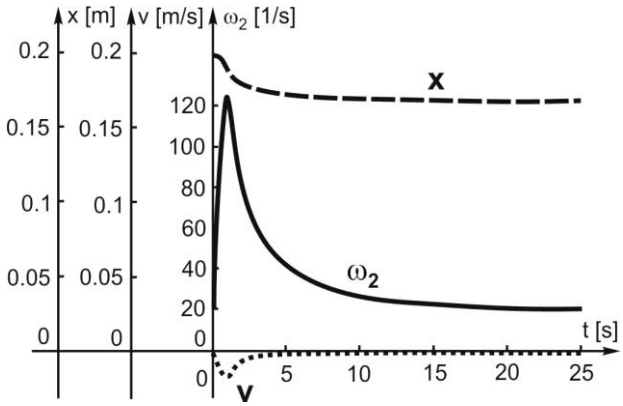

Fig. 2. Time histories of *x*, $\dot{x} = V$ and $\dot{\phi}_2 = \omega_2$

5. CONCLUSION

Using frictional variable-speed drive with two half balls and disc with contact in point an answer about the behavior of this mechanical nonholonomic system is got. Appell`s equations were used in the process. Solving the system of differential equations (29),(30) it is possible to determine the parameters x, V, ω_2 as ω_1 too, in function of time t. Then it is possible very simple to denote the stability of this system. The motion often becomes stable in few seconds (see Fig. 2). This example is very good for presentation of dynamical behavior of nonholonomic mechanical transmission as regulation system.

6. REFERENCES

[1] ESINENKO YA. I., Mechanical Speed Varitors, 1961, Kiev

[2] H NAUNHEIMER, B. BERTSCHE, J. RYBORZ, W. NOVAK, AUTOMOTIVE TRANSMISSIONS: FUNDAMENTALS, SELECTION, DESIGN AND APPLICATION, SPRINGER, 2011.

[3] DOBRONRAVOV V. V., Osnovi mechaniki negolonomnih system, 1970, MOSKVA

[4] ARTOBOLEVSKIJ I. I.; ZINOVIEV V. A.; UMNOV V. N. The Equation of Motion For a Mechanical System With a Variator, Journal of Mechanisms, Vol. 3.,1967, PP 269-274.

[5] MURINOVA G.. M. Issledovanije dinamiki frikcionnogo variatora s učetom negolonomnych svjazej sistemy, Trudy TIITa Transport, 1970, vyp. 317.

[6] ZLOKOLICA Miodrag; VLADIĆ Jovan; ČAVIĆ Maja; KOSTIĆ Milan, DYNAMIC OF POWER TRANSMISSIONS WITH NONHOLONOMIC CHARACTER IN AUTOMOTIVE ENGINEERINGS, FISITA Proc. of World Automotive Congress, Seoul, S. Korea, Vol. 12, 2000.

[7] ZLOKOLICA Miodrag; VLADIĆ Jovan; ČAVIĆ Maja; KOSTIĆ Milan. About Dynamic Characteristics of Nonholonomic Transmision, The Scientific Journal of the Vibration Institut of India, Advances in VIBRATION ENGINEERING, Vol.2, No.2 , 2003, PP151-158

[8] ZLOKOLICA Miodrag; ČAVIĆ Maja; KOSTIĆ Milan. General Approach to the Dynamical Behavior of Power Transmission as Nonholonomic System, International Conference on Motion and Power Transmissions MPT2009-Sendai JSME, 2009, PP371-374

The 7th International Conference on Engineering and Technology
ICET-2015, Phuket, June 19-20, 2015
Prince of Songkla University, Faculty of Engineering
Hat Yai, Songkhla, Thailand 90112

Formal Verification of Gearman Framework based on PHP

Warush Leekasem[1]*, Denduang Pradubsuwun[2]
Thammasat University, Computer Science, Thailand
[1]leekasem@live.com, [2]denduang@cs.tu.ac.th

Abstract: *Gearman based on PHP is an open source web application framework that provides ability to excute program in concurrency. Since it is hard to predict all possible cases of concurrent processes to ensure the correctness and reliability of web application that run with Gearman. Therefore, a formal verification is required. In this paper, we proposed method to applied timed trace theory with temporal constraints to verify safety and timing failures of Gearman based on PHP. Experimenting it with application shows that our proposed approach is effective.*

Key Words: ***concurrent computing / time Petri net / formal verification***

1. INTRODUCTION

Nowadays, web applications provide several services for multiple users. Performance and reliability are needed to fulfill the user requirement. Therefore, concurrent computing is required to increase performance of web applications. One of the popular web programming language is PHP. However, PHP does not support concurrency. Therefore, Gearman [1] is needed to provide concurrent computing ability for it.

Gearman are applied into various systems to improve system performance [2]. But it still lacks verifiability. Up until now there is no research papers which propose the verification of Gearman thus, we applied timed trace theory to verify it with temporal constraints. Timed trace theory has been presented to verify asynchronous microprocessor. It is such kind of a concurrent system. It is the same as Gearman. Thus, we propose a verification method for Gearman based on PHP by using timed trace theory. This paper is organized as follows. The section 2 describes Gearman briefly. The section 3 summarizes the idea of timed trace theory. The propose method is illustrated in the section 4. The experimental results is shown in the section 5. Finally the conclusion and our futures work is in the section 6.

2. A GEARMAN FRAMEWORK

Gearman provides an application framework to execute program with multiple processes or machines. It allows applications to complete tasks in concurrent computing. It can be used in a variety of programming languages such as PHP, C, and Perl. Gearman consists of three parts including client, job server and worker as shown in the Figure 1.

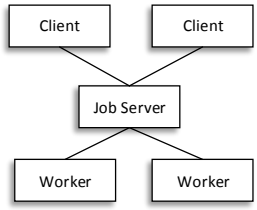

Figure 1. Gearman structure.

Client is used to send tasks to the job server. Job server is to find a suitable worker which can run the task and assign the task on it. Worker is for executing the task requested by the client and sends a response to the client through the job server. Gearman APIs handle with all communications between client and worker via TCP sockets. Hence, programmers do not need to deal with networking or mapping of tasks.

In this paper, some of Gearman and PHP command are chosen. They are enough to develop such kind of a concurrent program. They are shown as follows.

Here is Gearman commands.

- *doNormal* is used to execute a single task and then return a result.
- *doBackground* is used to run a task in the background.
- *addServer* is used to add a job server to the client.
- *addTask* is used to add a task to be run in concurrent.
- *runTasks* is used to run a list of all of tasks in concurrent.

Next, PHP commands are shown as follows.

- *break* is used to finish executing of the current structure.
- *continue* is used to skip the rest of the current loop and continue to condition at the beginning of the next iteration.
- *echo* is used to show an output.
- Conditional and iterative commands include *if-else*, *while*, *do-while*, *for*, *switch*
- *variable action* commands is for initializing and returning the value of variables.

An example of a Gearman application based on PHP is shown in the Figure 2 [4]. This application is for reversing two strings concurrently. The reversed strings will then be displayed as an output. For example, two input strings are “Hello World!” and “!dlroW olleH”. After finish executing the application, the string “!dlroW olleH” and “Hello World!” are produced.

```
1: <?php
2: # create our gearman client
3: $gmclient= new GearmanClient();
4: # add the default job server
5: $gmclient->addServer();
6: # set a function to be called when the work is complete
7: $gmclient->setCompleteCallback("complete");
8: # add a task to perform the "reverse" function on the string
"Hello World!"
9:  $gmclient->addTask("reverse", "Hello World!", null, "1");
10:  # add another task to perform the "reverse" function on the
string "!dlroW olleH"
11:  $gmclient->addTask("reverse", "!dlroW olleH", null, "2");
12:  # run the tasks
13:  $gmclient->runTasks();
14:  function complete($task)
15:  {
16:    echo "COMPLETE: " . $task->unique() . ", " . $task-
>data() . "\n";
17:  }
18: ?>
```

Figure 2. An example of a Gearman application based on PHP.

3. TIMED TRACE THEORETIC VERIFICATION

This section we summarize the concept of timed trace theoretic verification. The implementation and specification are respectively modeled by module and semi-module.

A *module* M consists of three tuples denoted by $M = (O, I, N)$ where I is a set of input transitions, O is a set of output transitions and N is a time Petri net. The time Petri net N consists of six tuples denoted by $N = (P, T, B, F, M0, Time)$ where P is a finite nonempty set of *places*, T is a finite set of *transitions* ($P \cap T = \emptyset$), B is the backward incidence function $P \times T \rightarrow N$ or *input arc* flow relation from place to transition, F is the forward incidence function $T \times P \rightarrow N$ or *output arc* flow relation from transition to place, M_0 is an *initial marking* of the net, *Time* is delay function. Let $Q+$ denotes the set of positive rational numbers $T \rightarrow Q+ \times Q+ \cup \{\infty\}$ such that $T = [a_i, b_i]$; a_i, and b_i represent the static bound for the *earliest* and *latest firing times* of transitions respectively, satisfying $ai(t) \leq bi(t)$ for all $t \in T$;

A *semimodule* of module M is a mirror of module M denoted by $M^{sm} = (O,I,N)$. The definition of *timed trace structure* is not the same as *module*.

A *timed trace structure* of a module M, denoted by T(M) consists of four tuple (I, O, S, F) where S is called success trace set and F is called failure trace set, contains a trace $y(w, \tau) \notin S$, as show in this equation $y \in F$, or $y \in S$, $\tau \leq TL(y, N)$, $w \in I$, or $y \in S$, $\tau > TL(y, N)$, limit $(y, N) \subseteq I$. $TL(y, N)$ is the latest time until when the firing of all enabled transitions in N can be postponed after y. limit (y, N) is the set of wires that correspond to the enable transitions which determine $TL(y, N)$.

To verify the correctness between a module M_1 and a module M_2, we considering on the time trace structure of $T_1 = (I_1, O_1, S_1, F_1)$ and $T_2 = (I_2, O_2, S_2, F_2)$ such that $I_1 \cup O_1 = I_2 \cup O_2$, intersection of T_1 and T_2 denoted by $T_1 \cap T_2$, is a timed trace structure.

According to the equation $(I_1 \cap I_2, O_1 \cup O_2, S_1 \cap S_2, (P_1 \cap F_2) \cup (F_1 \cap P_2))$, $T(M_1)$ *conforms to* $T(M_2)$ when $(P_1 \cap F_2) \cup (F_1 \cap P_2) = \emptyset$. This conformation implies that the module M_2 fully implements the module M_1 with any environment as shown in a Theorem 1.

Theorem 1: $\{M_1,\ldots, M_{k-1}, MK_1,\ldots, M_{km}, M_{k+1},\ldots, M_n\}$ conforms to M_s, if $\{ M_{k1},\ldots, M_{km}\}$ conforms to M_k, and $\{ M_1,\ldots, M_{k-1}, M_k, M_{k+1}, \ldots , M_n \}$ conforms to M_s

Note that the implementation may compose of several modules including $M_1,\ldots, M_{k-1}, M_{K1},\ldots, M_{km}, M_{k+1},\ldots,M_n$ thus, $M_k = \{M_{k1},\ldots, M_{km}\}$ and module M_s is represented of the specification.

Using the timed trace theory, such kinds of two design errors will be detected including *safety failure* and *timing failure*. *Safety failure* will happen when an output produced by a *module* or *semimodule* cannot be accepted by some other *module* or *semimodule*. *Timing failure* is a subset of liveness failures. It will take place when an input expected by a *module* or *semimodule* cannot be given in time by other *module* or *semimodule*.

4. THE PROPOSED METHOD

The perspetive of the propose method is shown in the Figure 3.

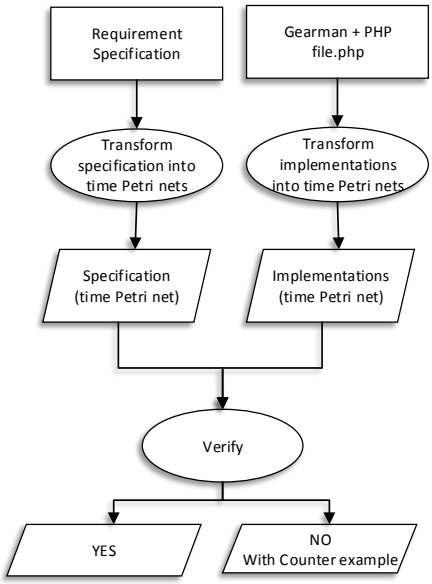

Figure 3. Perspective of the proposed method

In order to verify a Gearman application based on PHP by timed trace theory, a source code of a Gearman application based on PHP or an implementation must firstly be transformed into the time Petri net by the Algorithm1. Let us demonstrate how it works with the example in the section 2.

Step 1: The source code of a Gearman application based on PHP is read line by line.

Step2: Check the type of statements. Each statements will be transformed into the corresponding time Petri net as shown in the Table 1 and Table 2.

Step3: Check the total number of *addtask* and *runTask* command in the source code. This is used to identify the number of concurrency flows. The time Petri net in the step 2 is refined in order to increase the concurrency flows in the net.

Step4: The time Petri net of the implementation is derived as shown in the Figure 4(a). The time constraints of the implementation is assigned at this point.

Next, the time Petri net of a specification is given in the design phase. For this example, its specification is shown in the Figure 4(b). Afterwards, the conformation relation between the implementation and specification are checked by a verification tool [3].

Algorithm 1 Transform Gearman base on PHP into time Petri net

Input : Gearman and PHP client source code
Output : time Petri net $N(P, T, B, F, M_0, Time)$
begin
1: *Structural* ← if-else ∪ while ∪ do-while ∪ for ∪ switch
2: *task* = 0;
3: Read input from php file line by line in php tag
4: **for** each *command[i]* **do**
5: **if** *command[i] = Structural* **then**
6: call transform_time_Petri_net(*command[i], start, end*);
7: Check inside *Structural* for *commands*;
8: **endif**
9: **if** *command[i] = addTask* **then**
10: *task* + 1;
11: **else if** *command[i] = runTask* **then**
12: call transform_time_Petri_net(*command[i], i, task*);
13: *task* = 0;
14: **else**
15: call transform_time_Petri_net(*command[i], i, i*);
16: **endfor**
17: transform_time_Petri_net(*command, start, end*)
18: {
19: Initial state by M_0.
20: Map each *command* to *T*.
21: Map each system state to *P*, punctuate with *T*.
22: Message or variable is represented by *token*.
23: The control flow between t_i, t_j are represented *B* or *F* arc.
24: Temporal constraints of t_i are managed by $[a_i, b_i]$
25: }
end

Table 1. *Model of Gearman command in time Petri net*

Command	time Petri net
doNormal	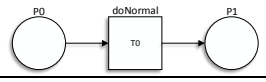
doBackground	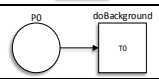
addServer	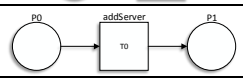
addTask	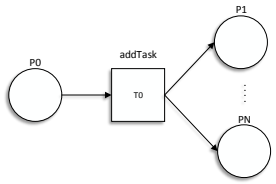
runTasks	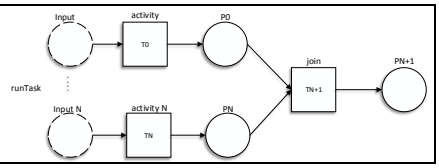

Table 2. *Model of PHP command in time Petri net*

Command	time Petri net
if-else	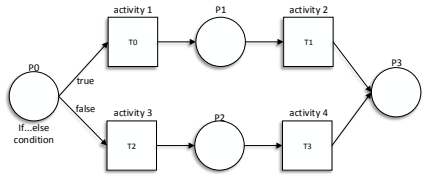
while	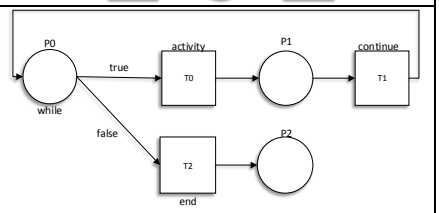
do-while	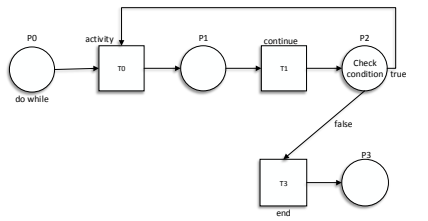
for	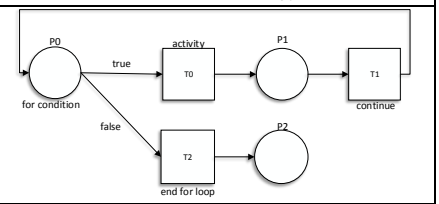
break	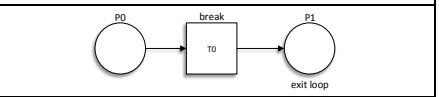
continue	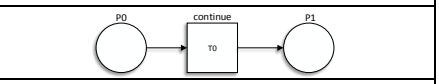
switch	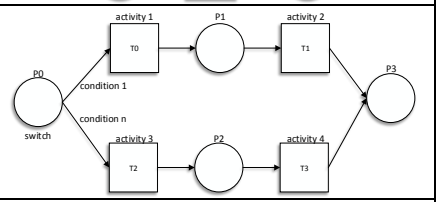
echo	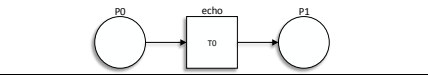
variable action	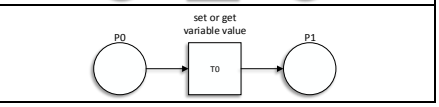

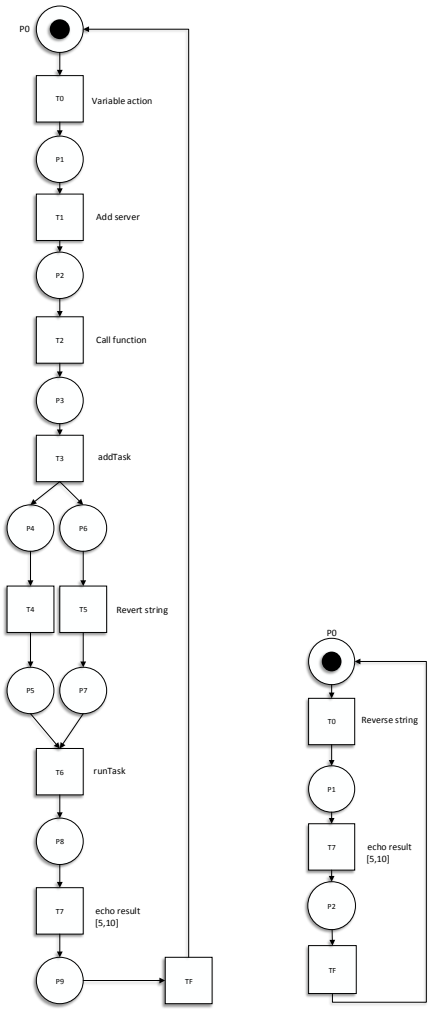

(a) (b)

Figure 4. Implementation (a) and specification (b) in time Petri net model**.**

5. EXPERIMENTAL RESULTS

To show the effectiveness of the proposed method, an application for reversing strings as shown in the Figure 2 is verified. It is a Gearman application based on PHP. Thus, it is such kind of a concurrent program. Conformance between its implementation in the Figure 4(a) and its specification in the Figure 4(b) are checked. Here, the experiment has been done on a 3.30 GHz Intel corei5-2500 with 12 gigabytes of memory. The result shows that no failure occurs. Hence, a Gearman application based on PHP in the Figure 2 does fully implement its specification.

6. CONCLUSION AND FUTURE WORK

In this paper, we have proposed a method to verify correctness of a Gearman application based on PHP by using timed trace theory. Also, the algorithm for transforming the source code of a Gearman application based on PHP into the time Petri net is proposed. We have shown the experimental results for a trivial example. It shows the effectiveness of the proposed method. In the futures, we are planning to verify more practical systems for expressing the usefulness of the proposed method.

7. REFERENCES

[1] Gearman [Gearman Job Server].(n.d.), Retrieved from http://gearman.org

[2] C. Haen, E. Bonaccorsi, N. Neufeld, (2011). Distributed Monitoring System Based on ICINGA. ICALEPCS. France.

[3] Denduang Pradubsuwun, Tomohiro Yoneda and Chris Myers, “Partial Order Reduction for Detecting Safety and Timing Failures of Timed Circuits. IEICE vol. E88-D No.7, Japan, July 2005.

[4] PHP: GearmanClient::addTask - Manual. (n.d.), Retrieved from http://php.net/manual/en/gearmanclient.addtask.php

The 7th International Conference on Engineering and Technology
ICET-2015, Phuket, June 19-20, 2015
Prince of Songkla University, Faculty of Engineering
Hat Yai, Songkhla, Thailand 90112

Peak Vehicle Lateral Acceleration at Obstacle Evasive Manoeuvre

Zoran Papić[1]*, Vuk Bogdanović[1], Milan Simeunović[1], Nenad Saulić[1]
[1]University of Novi Sad, Faculty of Technical Sciences, Novi Sad, Serbia
*Email of corresponding author: njele@uns.ac.rs

Abstract: *The vehicle lateral acceleration during the evasive lane change manoeuvre is in the functional correlation with the speed at which the manoeuvre is carried out and its longitudinal and lateral displacement. This value is changeable and has the maximum at points where the curvature is with the smallest radius, which is the consequence of centrifugal force effects. Considering the importance of lateral acceleration value for longitudinal displacement calculation, the experimental research was carried out, where peak values were measured. The measurement results were analysed and presented in the form of recommended values, which can be used in longitudinal displacement calculations.*

Key Words: ***lateral acceleration / vehicle / obstacle /evasive manoeuvre***

1. INTRODUCTION

A driver, as a traffic participant, has to undertake manoeuvres all the time, for the purpose of his vehicle speed or direction. These changes can be voluntary or planned actions, but they can also be caused by dangerous situations. A direction change with the lateral displacement of a vehicle is usually undertaken in regular operating regime for the purpose of traffic lane change, overtaking or bypassing. However, in certain situations in traffic, a driver is forced to operate the steering system abruptly, trying in this way to avoid the accident by a lateral evasive lane change manoeuvre.

At the beginning of an evasive manoeuvre the vehicle changes its movement from rectilinear to curvilinear. The vehicle centre of gravity path which is made at the beginning of the manoeuvre is of changeable curvature radius in relation to the momentary rotation pole, with the tendency of its reducing. Owing to the described movement, lateral inertial, that is, centrifugal force starts to act, and it gradually rises with the curvature radius path reducing, giving:

$$F_{c\max} = \frac{m \cdot V^2}{R_{\min}} \qquad (1)$$

Simultaneously, the maximal value of the centrifugal force is the result of the multiplication of the vehicle mass and maximal lateral acceleration:

$$F_{c\max} = m \cdot a_{y_{\max}} \qquad (2)$$

If expressions (1) and (2) are equated, it can be concluded that maximal lateral acceleration is directly proportional to the square value of the speed, and inversely proportional to the minimal curvature radius of the movement path.

$$a_{y\max} = \frac{V^2}{R_{\min}} \qquad (3)$$

The minimal curvature radius of the vehicle centre of gravity trajectory depends on the model which is used for its describing.

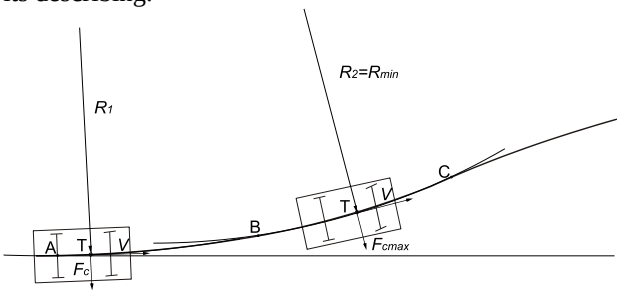

Fig. 1. Effects of centrifugal force during entering evasive manoeuvre

Most mathematical models of the vehicle lane change trajectory are based on certain approximations, such as the constant input speed into maneuver or medium lateral acceleration in the first and the second phase of the manoeuvre. Sledge and Marshek [1] presented analytical analysis of the lane change trajectory forms of vehicles and their mutual comparison. All mathematical models as a basic parameter in the process of vehicle lane changing treat lateral acceleration that occurs during the manoeuvre. The lane change distance necessary for the realization of manoeuvre in most mathematical trajectory models has the form:

$$x_e = V_0 \cdot C_x \sqrt{\frac{y_e}{a_Y}} \qquad (4)$$

The values of the coefficient C_x in theoretical models vary in the range of 2.51, for trajectory model described by a ramp sinusoidal function [2] [3], to 2.82, for reverse circular arcs model [4]. Based on empirical models

defined by experimental research the values of coefficients were 2.6 [3], and 2.7 [5].

Peak values of the vehicle lateral acceleration during the evasive manoeuvre have not been the subject of much research. Considering the importance of this value in the course of traffic accidents expertise, an experimental study has been outlined, with the aim of determining maximal values of lateral acceleration during evasive lane change manoeuvre, up to a certain sample, whose statistic data processing could give some recommendations for its application in the process of traffic accidents expertise or autonomous vehicle design, when it is necessary to analyse the minimal path length needed for the manoeuvre.

2. EXPERIMENTAL RESEARCH OF LATERAL ACCELERATION IN OBSTACLE AVOIDANCE MANOEUVRE

2.1. Experiment Design

The experiment was carried out on the newly built traffic artery with asphalt carriageway covering of high quality, without intensive traffic. The carriageway is 6.6 metres wide and it is divided into two traffic lanes of equal width by a longitudinal lane line. On the right side of the carriageway, viewed in the direction of the vehicle movement, there is an earthen verge, about one metre wide, and after it, there is a drain channel about 0.8 metres deep. On the left side of the carriageway, there is a verge overgrown with low vegetation. The length of the section available for the research was about 400 metres, while the length of the runway was 150 metres.

The experimental research of lateral vehicle displacement was carried out in accordance with the procedure given in the standard ISO 3888-2 (Passenger cars – Test track for a severe lane-change manoeuvre – Part 2: Obstacle avoidance) [6]. This part of the ISO 3888 defines the dimensions of the test track for the closed-loop, severe lane-change manoeuvre and is applicable to passenger cars and light commercial vehicles up to gross vehicle mass of 3.5 t. Regarding the subject matter, a modification of the testing ground was done for this experimental research needs, so that the testing track was shortened giving the total length of 36.5 metres, while the section width depended on the vehicle width. The test track was formed by the traffic cones, according to the lengths of certain sections. The schematic outline of a modified test track used for this experimental research is shown in the Fig. 2, while the dimensions with the track section lengths are given in the table 1.

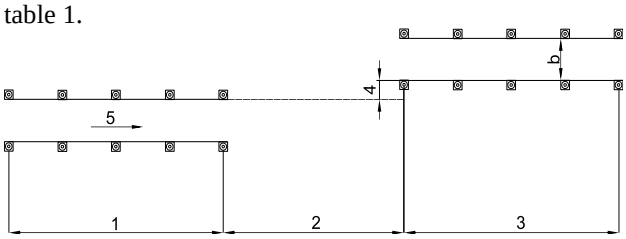

Fig. 2. The outline of the modified test track for a severe lane change maneuver

This manoeuvre test for avoiding hitting an obstacle by lane change implies a vehicle shifting from an entry gate into the next, that is to its parallel one, at a possibly maximal speed, without any track lines crossing, that is, without having the traffic cones fallen. The aim is that the vehicle alternately reaches high values of lateral acceleration for the purpose of its dynamic and stability characteristics assessment. This experimental research covered small vehicles (up to 3.5 metres long), middle-length vehicles (3.5-4.0 metres long) and longer cars (4.0-4.5 metres long).

Table 1. The dimensions of a modified test track for a severe lane change manoeuvre

Track section	Length (m)	Shift (m)	Width b (m)
1	12	-	1.1 x car shift* + 0.25
2	13.5	-	-
3	11	1	car shift + 1
* width is taken without side mirrors			

Fig. 3. One of the vehicles during the test

Performance Box Sport is a small GPS device which can record speed, momentary paths, lateral and longitudinal acceleration, direction and many other data relevant for the analysis of lateral lane change manoeuvre for avoiding hitting an obstacle. All recorded data are archived on the memory card inside the device. The measurement is done at the frequency of 10 Hz. This device does not have its own display so that the analysis of the recorded data must be done by means of the accompanying computer software Performance Tools Software or by their input into MS Excel.

2.2. Research Results

The speed at which the manoeuvre of lateral displacement is carried out is the key factor and the intensity of lateral acceleration depends on it. The maximal manoeuvre entry speed mostly depends on subjective driver's characteristics. Although the drivers were given instructions that the manoeuvre of lateral displacement should be carried out at a maximum possible speed, the first trials were the slowest, whereas with the increased number of trials the speed kept gradually increasing, up to the speed value at which the manoeuvre could not be carried out without having a traffic cone fallen.

During the study of the entry speed influence on lateral acceleration intensity in the manoeuvre of lateral displacement there were 65 test rides altogether. Seeing that it had been previously established that overall dimensions of vehicles do not significantly influence the

lateral acceleration intensity, this part of study does not include any vehicle type categorization but heterogeneous sample which contains small, middle-sized and big vehicles. The entry speed classification was done within the class ranging to 5kph. At the beginning of the test ride the entry speed was up to 60 kph so that lower limit of the range covered by the test ride of vehicle lateral displacement for avoiding hitting an obstacle was 55kph. Speeds lower than 55kph caused lower values of lateral acceleration and they are covered in a special research [7].

The entry manoeuvre into the testing ground at the speed of 55-60 kph was recorded with six test rides. Most of the test rides, 38, that is 58.5% of the studied sample, were done at the speed ranging 60-65kph. At the speed higher than 65 kph, for having traffic cones fallen, the number of successfully carried out test rides significantly dropped and the number was only 14. At speeds ranging 70-75 kph the manoeuvre was successfully completed only 7 times. Histogram which shows the distribution of entry speeds at the obstacle avoidance manoeuvre has been shown in the Fig. 4.

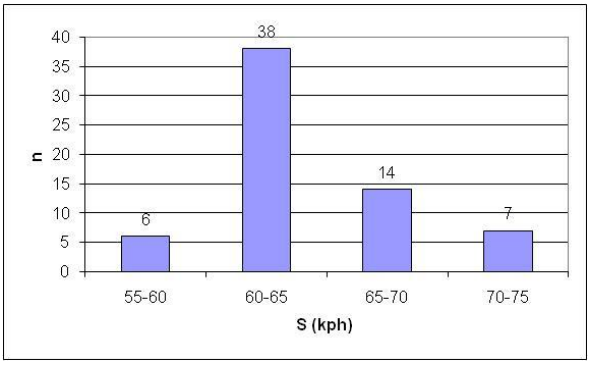

Fig. 4. Histogram of entry speeds in vehicle lateral displacement test rides

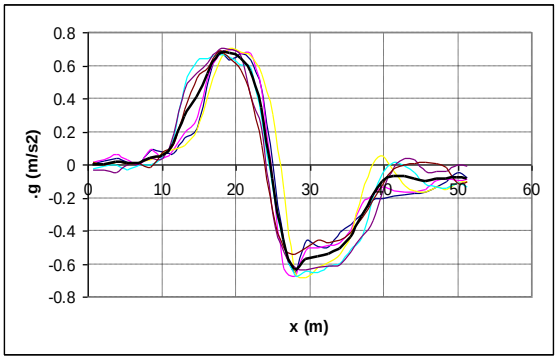

Fig. 5. Diagrams of lateral acceleration intensity at entry speeds 55-60 kph

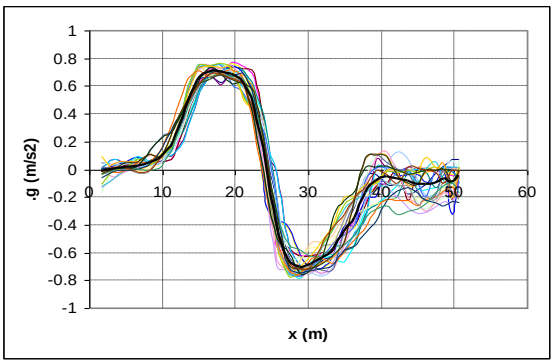

Fig. 6. Diagrams of lateral acceleration intensity at entry speeds 60-65 kph

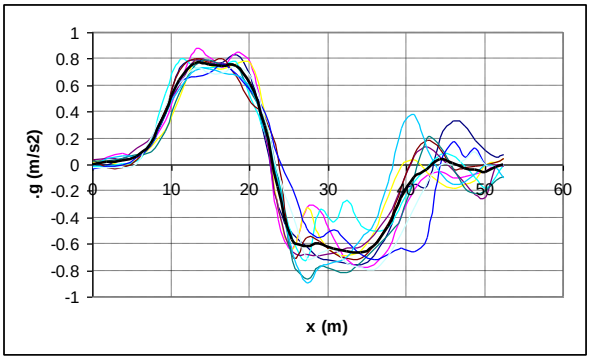

Fig. 7. Diagrams of lateral acceleration intensity at entry speeds 65-70 kph

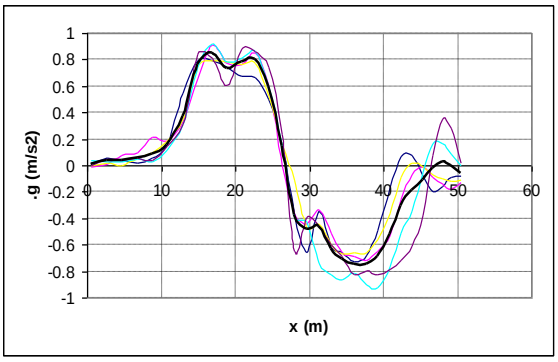

Fig 8. Diagrams of lateral acceleration intensity at entry speeds 70-75 kph

Mean maximal values of lateral acceleration, by entry speeds, and standard deviations, at the vehicle entrance and exit manoeuvres of lateral displacement are shown in the table 2 and table 3.

Table 2. Mean maximal values of lateral acceleration at entry speeds for entrance manoeuvre

Entry speed (kph)	Entrance manœuvre values (g)	
	Mean	SD
55-60	0.68929	0.016832
60-65	0.726988	0.028299
65-70	0.791855	0.043118
70-75	0.863483	0.061999

Table 3. Mean maximal values of lateral acceleration at entry speeds for exit manoeuvre

Entry speed (kph)	Exit manœuvre values (g)	
	Mean	SD
55-60	-0.64179	0.051771
60-65	-0.72372	0.041914
65-70	-0.75911	0.072865
70-75	-0.77154	0.103845

3. DISCUSSION

Within this study, most of the test rides were successfully completed at the speed ranging 60-65kph. The speed itself at which the manoeuvre was most often carried out successfully is not of great significance for it depended in the given situation on the very testing ground form. For drawing relevant conclusions, it is more important, in any case, to consider manoeuvre lateral acceleration accomplished in most of successfully carried out test rides. In this regard, the study showed that the mean value of peak lateral accelerations, at the sample of successfully carried out test rides at the entry speeds of the manoeuvre (60-65kph), was 0.727g, with the standard deviation of 0.028g. Taking into account the fact that the purpose of this study is in connection with traffic accidents expertise, as a recommendation relating to vehicle lateral acceleration intensity in analysis of displacement manoeuvres for avoiding hitting an obstacle, peak values reached in this research certainly cannot be taken for their incidence was low. The mean value of peak lateral acceleration in the biggest sample of successfully carried out manoeuvres at the speed of 60-65 kph, which reduced for the standard deviation is about 0.7g, is very close to the mean peak lateral acceleration carried out at speeds of 55-60kph. Taking into consideration this fact, lateral acceleration of 0.7g can be recommended as a maximal value which can be useful in the study of the length of the track in lane change manoeuvre for avoiding hitting an obstacle.

The study showed that in displacement manoeuvres even high values of lateral acceleration can be carried out, where the maximal value in successfully carried out test rides was 0.92g. In this way it has been established that these high values of lateral acceleration intensity, which did not cause any significant vehicle skid, are technically possible, but they cannot be used in analysis of real traffic situations in case of traffic accidents expertise. The values of lateral acceleration over 0.7g can be possibly used in analyses of traffic situations where a vehicle after the carried out displacement manoeuvre cannot remain on the carriageway surface, that is, it cannot re-establish the direction parallel to the one at the beginning of the manoeuvre. The vehicle lateral acceleration intensity at the manoeuvre exit is slightly weaker than the one at the manoeuvre entrance. In the diagrams (Fig.5-Fig.8) it can be seen that when the manoeuvre speed rises, the deviation in relation to the mean acceleration curve also rises. The greatest deviation relating the mean value can be seen in the final phase of the manoeuvre and they are the consequence of different driving techniques, that is, of undertaking certain corrective steering actions with the aim of endeavouring to stabilise the vehicle at the exit direction.

4. CONCLUSION

Lateral acceleration in a vehicle displacement manoeuvres is a factor which influences the distance length necessary for having this manoeuvre carried out. The experimental research of the lateral acceleration intensity during lane change was carried out by a test whose procedure is defined by ISO 3888-2 standard. In that way it was possible to repeat the test more times under the same conditions, with the endeavour to drive at a maximal speed in the testing ground without having its boundaries (traffic cones) fallen. The research carried out with more different vehicles steered by different drivers showed that that masses, dimensions and driving and dynamic characteristics do not significantly influence the success of a manoeuvre carrying out, that is, it is to the greatest extent in the domain of the subjective driver's characteristics. This conclusion and obtained results of the research allowed criteria establishing in connection with peak values of a vehicle lateral acceleration, which can be used in the traffic accident expertise proceedings with the analysis of the possibility of avoiding hitting an immobile obstacle during an evasive lane change manoeuvre.

5. REFERENCES

[1] Sledge, N, Marshek, K, Comparision of Ideal Vehicle Lane-Change Trajectories, SAE Technical Paper Series 971062, International Congress & Exposition, Detroit, Michigan, 1997.

[2] Zellner, J.W., Weir, D.H., et al., Development of Handling Test Procedures for Motorcycles, Motorcycles Dynamics and Rider Control, SP-428, SAE, Warrendale, PA, SAE 780313, 1978.

[3] Limpert, R., Motor Vehicle Accident Reconstruction and Cause Analysis, 4th Edition, The Michie Company, Charlottesville, VA, 1994.

[4] Daily, J., Fundamentals of Traffic Accident Reconstruction , Chapter 6, Derivation of the Lane-Change Maneuver Formula, IPTM, University of North Florida, 1988.

[5] Araszewski,M., Toor, A., Lane Change Maneuver Modeling for Accident Reconstruction Applications, SAE Technical Paper Series 2002-01-0817, SAE 2002 World Congress, Detroit, Michigan, 2002.

[6] International Standard, ISO 3888-2, Reference number ISO 3888-2-2002(E), Geneva, 2002.

[7] Papić, Z., The Contribution of Lane Change Manoeuvre Research for the Purpose of Traffic Accident Expertise, Ph.D. Thesis, University of Novi Sad, Faculty of Technical Sciences, Novi Sad, 2010.

The 7th International Conference on Engineering and Technology
ICET-2015, Phuket, June 19-20, 2015
Prince of Songkla University, Faculty of Engineering
Hat Yai, Songkhla, Thailand 90112

Traffic Conditions Influence on Critical Headway at Unsignalized Intersections

Vuk Bogdanović[1]*, Zoran Papić[1], Valentina Basarić[1], Nenad Ruškić[1]
[1]University of Novi Sad, Faculty of Technical Sciences, Novi Sad, Serbia
*Email of corresponding author: vuk@uns.ac.rs

Abstract: Capacity and level of service of unsignalized intersections, besides the conflict flow intensity, largely depend on the critical headway. This paper presents the results of the research that included several unsignalized intersections in several cities and towns. The research results confirm the fact that the type of minor movement largely affects the value of the critical headway. Analysis of the research results showed that the city size affects the size of the critical headway. The difference in critical headway length which is accepted by the drivers in small compared to big cities differs by nearly one second. In addition, the measured value of the critical headway is significantly different from that recommended in the manual HCM.

Key Words: ***Unsignalized Intersection, Critical Headway, Capacity***

1. INTRODUCTION

Intersections where the traffic is regulated by priority signs or unsiglized intersection are the most common type of intersections in Europe, as well as many other countries [2]. The most common of these intersections in Europe are TWSC (Two Way Stop Controlled) intersections, but in the world are often in use AWSC (All Way Stop Controlled) intersections.

At unsignalized intersections of TWSC type there are two characteristic types of approach, which are different in traffic regulation type, and in traffic conditions:

- *minor street approach* - secondary street approach where vehicles are obliged to give right-of-way to vehicles on the main road and,
- *major street approach* or the main road where vehicles have right-of-way regarding vehicles on minor streets. Also, vehicles which turn left from the major street are obliged to give right-of-way to vehicles passing through from the opposite direction.

For traffic regulation on minor street approaches at unsignalized intersections traffic signs used are “Yield” and ”Stop”, while the main road uses the sign “Priority Road”

The basic characteristic of unsignalized intersections is “self-regulation”, because vehicles from a minor street don’t have information when it is safe to leave the approach, and make maneuver through the intersection [1]. Because of the absolute priority of streams which are on higher place in the hierarchy level, some maneuvers carried out from minor streets demand high attention from drivers.

Drivers on the minor street approaches to unsignalized intersections, according to their perception, knowledge and experience, estimate the possibility of carrying out the desired maneuver by estimation of the headway between vehicles on the main road. In theory, the period, or interval that drivers on minor streets used to perform maneuver is called the critical interval of following vehicles ("*critical headway*" or "*critical gap*").

In our region, most commonly used methodology for the analysis of capacity and level of services is HCM (Highway Capacity Manual). Values of parameters recommended in the HCM methodology are based on the research of traffic flow within the standards and regulations to regulate traffic. Traffic conditions in which this research was conducted are often different from the local European conditions, so before applying the recommended settings from HCM, a local measurement of parameters are proposed to check their values in the local conditions and to make possible corrections.

2. UNSIGNALIZED INTERSECTIONS CAPACITY

The analysis of methodologies for calculating the capacity of the unsignalized implies that the calculation of the unsignalized intersections capacity is based on the classical mass queuing system models. The input of mass queuing system, in this case intersection is, a complex mass queuing system. In this system vehicles on minor street wait for the appearance of free critical headway on the main road, to carry out their maneuver.

Capacity of unsignalized intersections is calculated for each minor movement and it is the maximal number of vehicles which in a definite period carry out the named minor movement. Within the last decade there are two most common used models for minor movement capacity calculation. Those are “Siegloch” and “Harders” model. Capacity of minor movement according to “Siegloch” model, is calculated as follows:

$$C_{p,x} = \frac{3600}{t_f} \cdot e^{-\frac{(\sum_x V_{c,x}) \cdot t_0}{3600}} \quad [PA/h] \tag{1}$$

$$t_0 = t_{c,x} - t_{f,x}/2 \tag{2}$$

According to "*Harders*" model, capacity of minor movement is calculated as follows:

$$C_{p,x} = V_{c,x} \cdot \frac{e^{-V_{c,x} \cdot t_{c,x}/3600}}{1-e^{-V_{c,x} \cdot t_{f,x}/3600}} \quad [PA/h] \tag{3}$$

Where:

- x – minor movement,
- $C_{p,x}$ – potential capacity of minor movement "x",
- $V_{c,x}$ – conflicting flow rate for movement "x",
- $t_{c,x}$ – critical headway for minor movement "x",
- $t_{f,x}$ – follow-up time for minor movement "x".

As in previous relationships it can be seen, the capacity of minor movements at an unsignalized intersection depends on the intensity of conflict flow, the size of the critical headways in the main flow and the size of the critical headway in the minor movement. Intensity of the conflict flow is a measured input parameter that does not change values depending on the applied methodology. The size of the headways in the secondary flow $t_{f,x}$ is a parameter whose values do not vary too much. For this reason, the capacity of minor movement at an unsignalized intersection largely depends on the adopted value of the critical headway.

2.1. Significance of critical headway for minor movements capacity

Back in the early sixties the importance of free headways in the main course was analyzed, which is acceptable for drivers from a minor street for the execution of the desired maneuvers. These "headways" in the mainstream are defined as the minimum acceptable following intervals in the main road ("minimum acceptable major street headway") and it was used in the formulas for capacity calculation [8].

Almost all the methods, after Tanner, J.C, demonstrated in his paper [2] took into consideration the size of the acceptable critical headways as one of the most important input parameters in the process of calculating the capacity of the unsignalized intersections.

The minimum acceptable intervals on the main road for drivers carrying out minor movements are defined as critical gap or critical headways. Critical headways on the main road is defined as the minimum required size of the follow interval on the main road which allows one vehicle to pass through the intersection from a minor street [3], [4], [5]. The number and distribution of critical headways which can be used for the execution of the desired maneuver for vehicles from a minor street, primarily depends on the intensity of flow on the main road. Previous research studies have shown that the size of the critical headway also affects the number of traffic lanes on the main road, type of traffic sign in a minor street and the allowed vehicle speed.

For drivers, critical headway is the minimum time that can be accepted for the safe carrying out the desired movement. In practically ideal conditions, the drivers from the minor street approach would reject any headway that is less than critical, and accept each interval equal to and larger than the critical headway. So, drivers from minor streets would accept all headways in the main street greater than a defined critical headway. In real conditions, drivers individually assess the traffic situation, which means that the acceptance of headway for performing the desired movement are the drivers estimation that he forms on the basis of their knowledge, skills and performance of the cars he drive. For that reason, in the real conditions, it could happen that drivers refuse the headway greater than critical, and to accept the intervals less than critical. Possibility that the environment has the influence on developing of driver's capability cannot be excluded.

Because of this and the fact that the time changes drivers' habits and vehicle performance, the size of the acceptable critical headway is constantly being changed. As the structural characteristics and performance of all categories of motor vehicles improve day by day, and drivers are more capable to assess a complex traffic situation due to modern life and the everyday presence in the traffic, so it is reasonable to expect that the values of critical headways are getting smaller [1]

In many countries, research of critical headway has been carried out in a variety of conditions. They are mostly analysed effects of the traffic sign type ("Yield" or "Stop") and the type of minor movement. HCM manuals for the calculation of the capacity recommend local measurements when calculating the capacity of the each intersection in order to determine capacity more accurately.

It is known that intersections geometry or its environment can affect the behaviour of drivers, which directly affects the size of the critical headway. Results of conducted research studies show that the values of critical headways can be significantly different, indicating the need for a permanent research. The following table provides results of some research which were carried out to define the size of the critical headway.

Table 1. *Some recommendations for* $t_{c,x}$

Method	Sign type	Critical headway - $t_{c,x}$			
		Left major	Right minor	Through minor	Left minor
HCM '85	II–1	5.0	5.0	5.5	6.0
HCM '85	II–2	5.0	5.5	6.0	6.5
HCM '94	II–2	5.0	5.5	6.0	6.5
DanKap '99*	II-1	5.5	5.5	6.0	7.0
DanKap '99	II–2	-	6.5	7.0	8.0
HCM '00	II-1	4.1	6.2	6.5	7.1
SNRA '01*	II–1	4.8	5.0	5.1	5.3
SNRA '01	II–2	6.7	7.5	7.6	7.8
Finland '04	II–1	5.9	6.1	–	6.4
HCM '10	II-1	4.1	6.2	6.5	7.1

The previous table shows that the critical headways vary depending on the location of the measurement and the type of controls on the minor street.

Research of this kind has not been made in the SEE (South-Eastern Europe) region, and the recommended values are accepted by default without specific testing. All this may cause wrong conclusions about the capacity capabilities of transport network.

3. RESEARCH

Critical intervals were measured and investigated on 3-leg and 4-leg intersections in the cities, which can be classified by the number of people living in it, into three categories: large, medium and small cities. The research was conducted in several cities in SEE region [1].

In the present, there are about 30 methods for assessing the critical headway, which have been published around the world [7].

In addition, unrealistically large headways were excluded from analysis, as well as the intervals that were measured in a situation when a driver from a minor street forced a driver on the main road to change their driving direction, or motion mode, or when, for some reason, a driver from the main road let the driver from the minor street to perform his movement.

At intersections in large cities, or in situations where the intersection has an intensive flow, the appearance of measurable headways in the main stream is larger. However, in larger cities, there were many irregularities which could not be considered. Also, there was a significant number of situations that can be characterized as "jump-in" in the main stream when the drivers from the main street had to brake or slow down their vehicle to avoid a collision. In addition, there were frequent situations when the vehicles on the main and minor approaches were interfered with pedestrians.

In large towns and cities of medium size the headways over 8.0s were not taken into consideration, and in smaller towns over 8.5 s, as well as all those where greater changes in the speed of vehicle movement were observed in priority conflict flows.

Beside measuring the critical headways, classical traffic count was carried out on all approaches, in order to determine the dependence between the intensity of flow in the major and minor street and the headways between vehicles.

4. RESEARCH RESULTS

Tables, figures, diagrams, block schemes and other research was made on the sample of 4,403 headways, while the total flow on the main stream was 48,566 vehicles, and on the minor street were 16,428 vehicles. Headways have been classified by movement type into four main basic minor movements:

- left turn from the major street,
- right turn from the minor street,
- through movement from the minor street,
- left turn from the minor street.

Analysis of the results of the conducted research has shown that the size of critical headways depends on the size of the city, where the research was made. Variations of the parameter value can be significant depending on the size of the city. Results of the conducted analysis showed that drivers in large cities used significantly smaller intervals in the main street.

The following tables show the headways in big and small cities as well as differences in their average values.

Table 2. *Research results*

Maneuver	Small city		Big city		HCM 2010
	Sample	$t_{c,x}$	Sample	$t_{c,x}$	$t_{c,x}$
Left from major app.	442	5.4	330	4.6	4.1
Right from minor app.	885	5.4	933	4.6	6.2
Through from minor app.	293	5.7	402	5.9	6.5
Left from minor app.	610	5.5	512	4.7	7.1

A previous table shows that in smaller cities and towns, drivers use the critical headways, which are almost 1.0 s larger than those used by drivers in big cities. Further, values of critical headway are significant different from HCM 2010 values.

Analysing the results of the presented research it was concluded that the greatest similarity in the determined critical headways is with the value determined by research in Scandinavian countries.

5. DISCUSSION

For all types of maneuvers that research was done for, there were considerably different results obtained for the intersections in big cities and small cities and populated places, despite the fact that in smaller places the chosen intersections were with a significant traffic flow. These results can be explained only by different driving habits and driving methods of drivers in major cities. In larger cities, the intensity of traffic flow on major roads, as a rule, is significantly higher, and the number of suitable headways that can be used to perform the desired maneuver is significantly lower. If a driver fails to use suitable headway, waiting for the appearance of an appropriate headway may be a few dozen of seconds. For this reason, drivers in big cities are more concentrated and aggressive. Using faster response and sharper driving, they use all available headways, even those which are refused as too small by the drivers in smaller cities.

Headways that are determined by measurement and analysis are significantly different from the suggested in the procedures used in engineering practice. The largest difference occurs compared to HCM-2010 procedure, which is commonly used in the region for calculating the capacity of roads and intersections. Local measurements which were carried out showed that drivers in our region use significantly smaller headways.

Using the values of the critical headways obtained by local measurements in the process of HCM-2010 would give realistic capacity of unsignalized intersections. Implementing the process in the proposed way of calculating the capacity of unsignalized intersections would be in accordance with real conditions.

The following figures have shown the value of different critical headway impact on potential capacity for all minor maneuvers at unsignalized intersection.

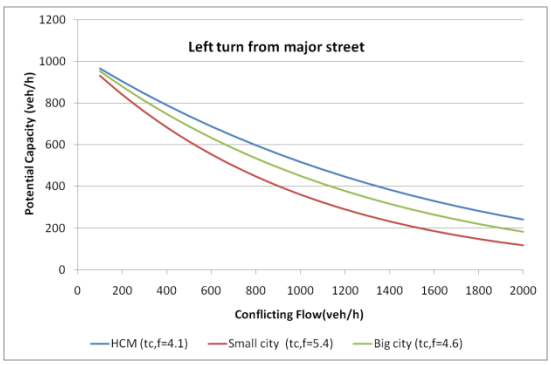

Figure 1. Potential capacity of left turn maneuver on the major street

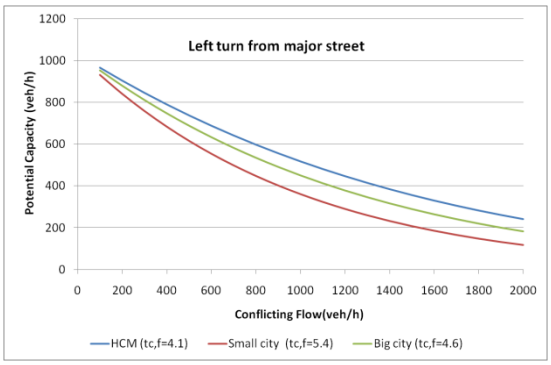

Figure 2. Potential capacity of right turn maneuver on the minor street

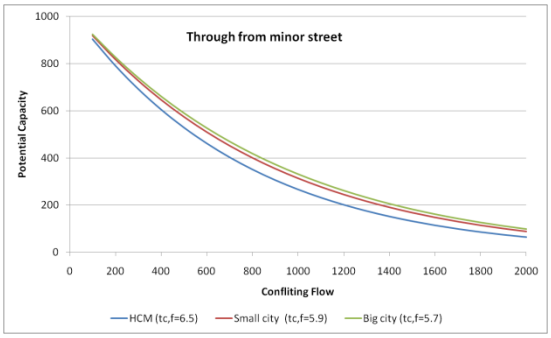

Figure 3. Potential capacity of through movement on the minor street

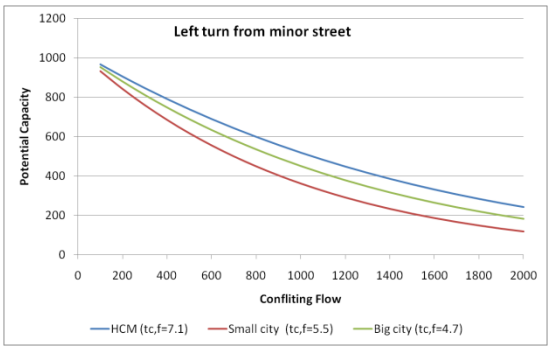

Figure 4. Potential capacity of left turn maneuver on the minor street

5. CONCLUSIONS

Unsignalized intersections are the most common type of road and street crossings, therefore, more attention should be paid to the procedures for calculation of capacity of this type of intersections. One of the parameters that can easily be determined by local measurements is the critical headway in the major street. The size of the critical headway significantly affects the size of the unsignalized intersection approach capacity. For this reason, it is very important to determine the appropriate size of this parameter in order to properly determine the capacity. Analysis of the results of the research presented in this paper shows that the value of the critical headway is significantly smaller than the value recommended by the HCM-2010, which is most commonly used for calculation of the unsignalized intersections capacity. Analysis showed that the determined value of the critical headway has the greatest similarity with the results of the research that was conducted in Scandinavian countries, especially in Finland.

The research results presented in this paper show that there are significant differences in the size of the critical headway in less populated areas compared to large cities.

Determining the actual value of the critical headway is a key data for calculating the unsignalized intersection capacity in real conditions. More reliable data on the size of the critical headway can be obtained by local measurements compared to the value given in the recommendations and in this way to determine the real value of the capacity of unsignalized intersections. This way of determining the capacity can contribute in the process of selecting the optimal regulation method.

6. REFERENCES

[1] Bogdanović, V., Contribution to Study of Capacity And Service Level on Priority Roundabouts and T–Intersections, PhD thesis, University of Novi Sad, 2005.

[2] Đorđević, T., Bogdanović, V., The capacity of road and street crossroads – priority intersection (new concept), Faculty of Technical Sciences, University of Novi Sad, 2002.

[3] Highway Capacity Manual, Chapter 10, Special Report, TRB, Washington D.C. 1994.

[4] Highway Capacity Manual, Chapter 17, TRB, Washington D.C. 2000.

[5] Highway Capacity Manual, Chapter 19, TRB Washington D.C. 2010.

[6] Interim Materials on Unsignalized Intersection Capacity TRB, No 373, 1994.

[7] Brilon, W., König, R., Troutbeck, R.: Useful Estimation [Procedures for Critical Gaps. Proceedings of the 3rd International Symposium on Intersections without Traffic Signals, Portland Oregon, pp. 71 – 87, July 1997

[8] Research on Road Traffic, Chapter 6 Traffic Capacity, Department of Scientific and Industrial Research, London 1965.

The 7th International Conference on Engineering and Technology
ICET-2015, Phuket, June 19-20, 2015
Prince of Songkla University, Faculty of Engineering
Hat Yai, Songkhla, Thailand 90112

Effects of US-EDM-Complex Vibration on Machining of WC-Co

Chaiya Praneetpongrung[1]*, Sakchai Chantasri[1] and Paitoon Poolsukho[1]
[1]Rajamangala University of Technology Thanyaburi, Faculty of Engineering, Thailand
*Email of corresponding author: chaiya.p@en.rmutt.ac.th

Abstract: *The ultrasonic vibration assisted electrical discharge machining (US-EDM) is an innovative technique that helps to improve material removal rate (MRR) of work piece. Many researchers have been experimented on the ultrasonic vibration assisted EDM on tool electrode vibration and workpiece vibration. The past experimental used the vibration only one axis vibratory. In this study, a new innovative technique of ultrasonic vibration which a tool electrode vibrates on longitudinal and bending (US-EDM-complex vibration) was purposed. The material removal rate(MRR), tool wear rate (TWR), and surface roughness (SR) of the new technique were investigated. The experimental results were compared with normal EDM, ultrasonic assisted EDM with longitudinal vibration (US-EDM-longitudinal) and ultrasonic assisted EDM with bending vibration (US-EDM-bending). The results showed that the new technique gave a high material removal rate more than normal EDM.*

Key Words: ***EDM /Ultrasonic /WC-Co/Machining***

1. INTRODUCTION

Due to its very high hardness and excellent wear resistance over a wide range of temperature, tungsten carbide cobalt (WC-Co) is an important material to use in producing cutting tools, die, and other special tools and components [1]. However, these characteristics cause the machining of this material to be very difficult by using conventional machining technique and being expensive.

To overcome this problem, special machining methods are employed. Among many special techniques, electrical discharge machining (EDM) has been the most favorable. EDM is the thermal erosion process in which metal is removed by series of recurring electrical discharges between a cutting tool as an electrode and a conductive workpiece, in the presence of dielectric fluid. This discharge occurs in a voltage gap between the electrode and workpiece. Heat from the discharge vaporizes minute particles of workpiece material, which are then washed from the gap by the continuously flushing dielectric fluid.

In the present date, researchers try to develop new techniques to expand the EDM application. Among many new techniques, the EDM assisted ultrasonic vibration (US-EDM) is one of the applications. The study of the effects on ultrasonic vibration of the electrode on EDM has been undertaken since mid 1980s. The higher efficiency gained by employment of ultrasonic vibration is mainly attributed to the improvement in dielectric circulation which facilitates the debris removal and creation of a large pressure change between the electrode and the workpiece, as an enhancement of molten metal ejection from the surface of the workpiece [2].

The effects of ultrasonic vibration on the EDM electrode were studied by some researchers[3-9]. From the literatures review, most researchers studied on EDM assisted ultrasonic vibration on longitudinal direction. This research focused on investigation the effect of parameters that affects the machining properties of the US-EDM-complex vibration method. Material removal rate (MRR), relative wear ratio, and the surface topography were investigated and comparing the results with normal EDM.

2. METHOD AND MATERIALS

The experiments are performed on a die-sinking EDM machine (VX-20, Mitsubishi Co., Ltd.). The schematic of the experiment represents in Fig. 1.

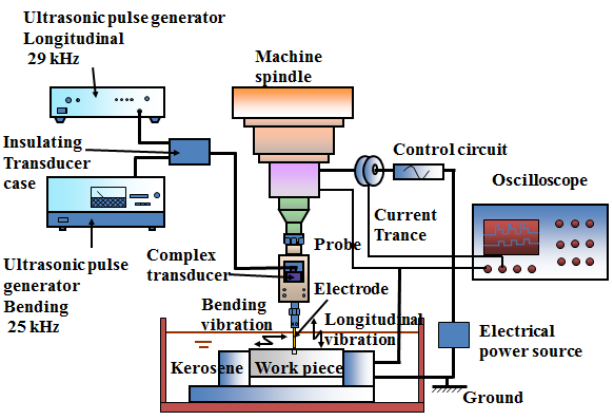

Fig. 1. Illustration of the schematic of the experiment

The ultrasonic transducer is fixed in housing and attached to the machine spindle. The ultrasonic pulse generator on longitudinal vibration 29 kHz and bending vibration 25 kHz are connected to the ultrasonic transducer.

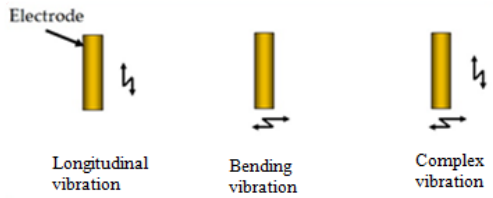

Fig. 2. Illustration of vibration directions

The frequency and amplitude of ultrasonic vibration were measured by a laser machine. The laser machine was mounted at the tip of the electrode for measuring the amplitude and frequency on longitudinal vibration. For the bending vibration, the laser machine is mounted on a side of the electrode. Table 1 and 2 summarize the elemental composition of the workpiece and the electrode. Other experimental conditions considered in the tests are given in Table 3.

Table 1. *Workpiece (WC-Co) material properties*

Composition	W 68.40%,Co 30.63%, Cr 0.97%
Density (g/cm^3)	14.1
Hardness (HRA)	89.0
Tensile strength (kg/mm^2)	148
Compressive strength (kg/mm^2)	4,750
Young modulus (× 10^{4}kg/cm^2)	5.7

Table 2. *Copper tungsten electrode material properties*

Composition	75%WC,25%Cu
Density (g/cm^3)	14.3
Melting point (ºC)	3500
Electrical resistivity (μΩ cm)	5.5
Hardness	HB200

Table 3. *Experimental conditions*

Condition	**Description**
Ultrasonic amplitude - Longitudinal vibration	27μm
- Bending vibration	4 μm
- Complex vibration	Longitudinal 26 μm + bending 11 μm
Ultrasonic frequency - Longitudinal vibration	29 kHz
- Bending vibration	25 kHz
Workpiece material	WC-Co
Electrode material	CuW ∅ 3 mm
Discharge currents	2, 5, 35 A
Open circuit voltage	80, 150, 220, 320 V
On time	2, 8, 32 μs
Duty factor	33.3%, 50%
Tool polarity	-, +
Dielectric	Kerosene
Jet flushing	0.06 MPa

The experiments were carried out on the effects of ultrasonic vibration on MRR and relative wear ratio. The MRR represents the average volume of material removed from the workpiece per unit time. In the EDM process, both tool and workpiece are eroded during discharge. The Tool wear rate (TWR) is calculated as the volume of material eroded from the tool electrode per unit time divided by the volume of material eroded from a workpiece in the same time. The weigh different of workpiece and electrode before and after undergoing the EDM process was weighed by weighing machine within precision 0.0001 gram. Duty factor (DF.) is a percentage of the pulse duration relative to the total cycle time.

Generally, a higher duty factor means increased cutting efficiency. It is calculated in percentage by dividing pulse duration by the total cycle time (on-time + off-time). Rarely is spark on and off times equal in actual EDM operations. To determine average machining amperes, and calculate the ratio of spark on to off time by using Equation (1) to find the duty factor

Dutyfactor (DF.,%) = te/(te+ti) (1)

Where:

te = spark on time in microseconds

ti = spark off time in microseconds

3. RESULTS AND DISCUSSION

The experiments were carried out on the effects of jet flushing on material removal rate (MRR). The EDM parameters are pulse current (Ip), pulse on time (te), pulse off time (ti), and the gap voltage (Vg) while the machining responses in concern are the material removal rate and the electrode wear.

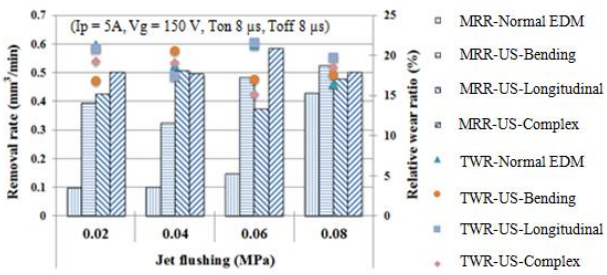

Fig. 3. Illustration of the effects of thejet flushing on MRR

The effects of the jet flushing on MRR of normal EDM, ultrasonic assisted EDM which is vibration on horizontal direction (US-EDM-bending), ultrasonic assisted EDM which is vibration on longitudinal direction (US-EDM-longitudinal), ultrasonic assisted EDM wich is vibration on both direction (US-EDM-complex) and the electrode wears are shown in Fig. 3.

The results indicate that the highest of MRR are obtained at the jet pressure 0.06 MPa of US-EDM-complex vibration because of the improvement in dielectric circulation, which facilitates the debris removal and the creation of a large pressure change between the electrode and the workpiece, as an enhancement of molten metal ejection from the surface of the workpiece. In this research, all experiments were carried out by using a jet flushing at 0.06 MPa.

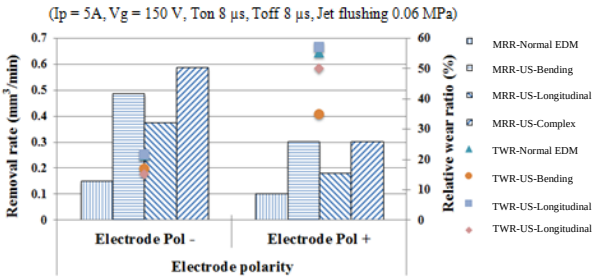

Fig. 4. Illustration of the effect of electrode polarity

Fig. 4 shows the MRR and TWR results with positive and negative electrode polarities. The MRR of the negative polarity was higher than the positive polarity, and the TWR of the negative polarity was smaller than the positive under the finishing machining condition. These results indicate that the MRR of EDM polarity could be obtained at the negative polarity and better than the positive polarity. In this research, all experiments were carried out by using a negative electrode polarity.

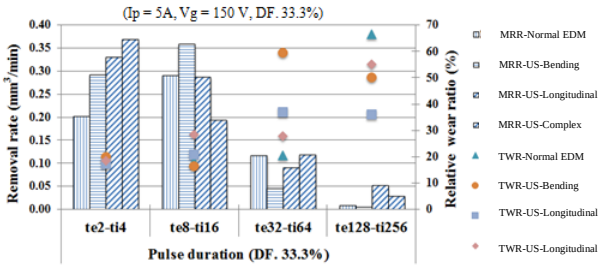

Fig. 5. Illustration of the effects of pulse time DF.33.3% on MRR

Effects of pulse time DF.33.3% on MRR show in Fig. 5. When increased the pulse time, the material removal rates decreased. The results of MRR were contrary with electrode wear rate. The results indicate that the long pulse of DF. 33.3% were not suitable for machining because the MRR values were low.

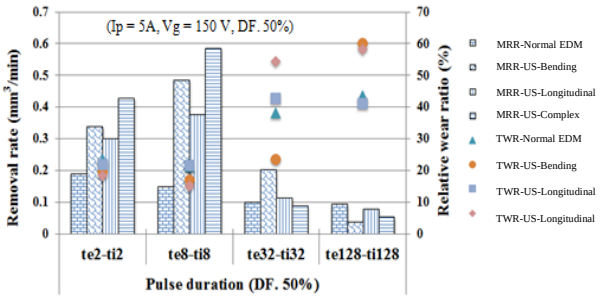

Fig. 6. Illustration of the effects of pulse time DF.50% on MRR

Effects of pulse time DF.33.3% on MRR show in Fig. 6. The highest MRR obtained at the te and te 8 µs of US-EDM-complex vibration. When the pulse times increased the MRR values were decreased. The results of MRR were contrary with electrode wear rate.

The MRRs of DF. 50% were higher than the DF. 33.3%. In this research, all experiments were carried out using the DF. 50% of te and te 8 µs.

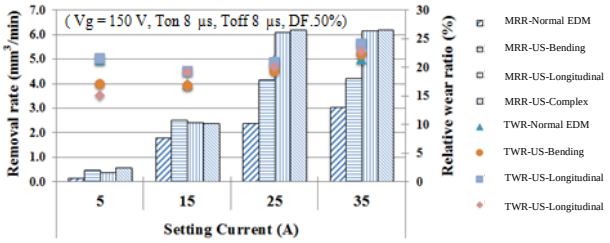

Fig. 7. Illustration of the effects of current on MRR

Effects of current show in Fig. 7. When increased the discharge current, the MRRs were increased. The highest of MRRs obtained at the current 35A. of US-EDM longitudinal vibration and US-EDM complex vibration. The MRR values were higher than normal EDM about three times.

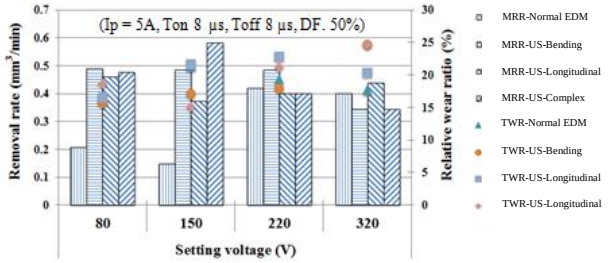

Fig. 8. Illustration of the effect of voltage on MRR

Effects of voltage on MRR and electrode wear were showed in Fig. 8. The highest MRR obtained at the voltage 150 V. of US-EDM-complex vibration. In this research, all experiments were carried out by using the voltage 60V.

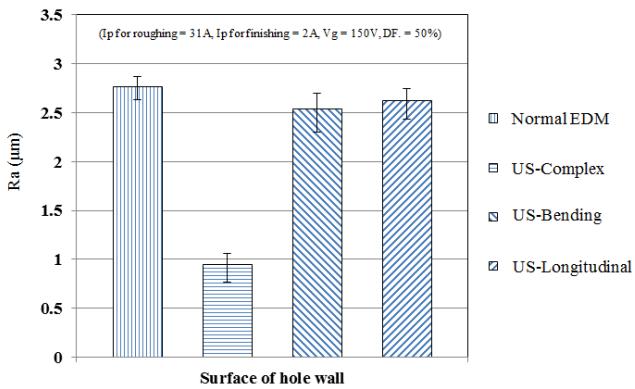

Fig. 9. Illustration of the effects of ultrasonic amplitude on surface roughness of hole wall

The surface of hole walls was measured by using stylus surface roughness machine. The Ra results show in Fg. 9. The results indicated that the US-EDM-complex gave the lowest roughness of hole wall.

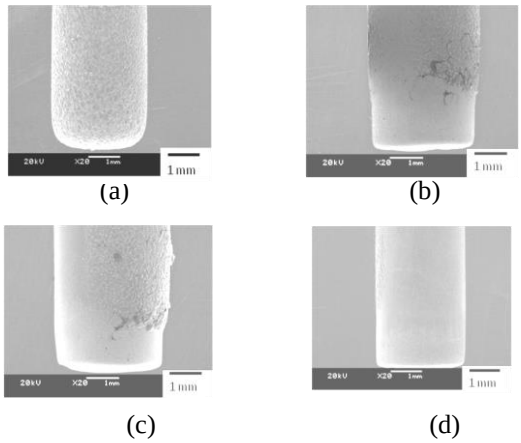

(a) (b)

(c) (d)

Fig. 10. Illustration of the cross section surface and shape of holes, (a) Normal EDM, (b) US-EDM-longitudinal, (c) US-EDM-bending, and (d) US-EDM-complex

The best shape of hole could be obtained from (d) US-EDM-complex vibration. The hole shape of normal EDM was round at the corner due to the electrode wear.

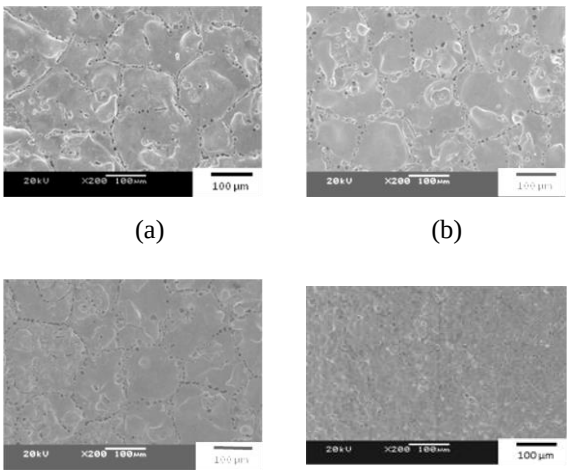

(a) (b)

(c) (d)

Fig. 11. Illustration of the side hole surfaces, (a) Normal EDM, (b) US-EDM-longitudinal, (c) US-EDM-bending, and (d) US-EDM-complex

The side hole surfaces show in Fig, 11. The photographs were taken by digital microscope . The cracks were occurred at (a) Normal EDM, (b) US-EDM-longitudinal, and (c) US-EDM-bending but small amount of cracks were observed from US-EDM-complex.

4. CONCLUSIONS

1. The US-EDM-Complex system gave higher removal rate than the other. The complex vibration made a high pumping force of ejecting the debris out of discharge gap cause the removal rate increasing.
2. On the negative electrode polarity, the MRR could be obtained and better than the positive polarity.
3. The best of surface roughness values of hole walls obtained at the complex vibration method.
4. The best shape of hole could be obtained from the US-EDM-complex.
5. The long pulse durations did not suitable for US-EDM.

5. REFERENCES

[1] R.A., Mahdavinejad and A. Mahdavinejad, “ED machining of WC-Co,” *J. Mater. Process. Tech.*, 2005, Vol. 162-63, pp. 637-643.

[2] N. M., Abbas, D. G. Solomon and Md. F., Bahari, “A review on current research trends in electrical discharge machining (EDM),” *Int. J. Mach. Tool Manu*., 2007, Vol. 47, pp. 1214-1228.

[3] S. H., Yeo and L. K., Tan, “Effects of ultrasonic vibrations in micro electro-discharge machining of microholes,” *J. Micromech. Microeng*., 1999, Vol. 9, pp. 345-352.

[4] B.H., Yan, A.C., Wang, C.Y., Huang and F.Y. Huang, “Study of precision micro-holes in borosilicate glass using micro EDM assisted with micro ultrasonic vibration machining,” *Int. J. Mach. Tool Manu*., 2002, Vol. 42, pp. 1105-1112.

[5] J. W. Mwangi, B. W. Ikua, G. N. Nyakoe, H. Zeidler and S. K. Kabini, “Effect of low frequency vibration in electrical discharge machining of AlSiC metal matrix composite,” *JSRE.*, 2014, Vol. 1(2), pp. 45-50.

[6] Z. Wansheng, W. Zhenlong, D. Shichun, C. Guanxin and W. Hongyu, “Ultrasonic and electric discharge machining to deep and small hole on titanium alloy,” *J. Mater. Process. Tech.*, 2002, Vol. 120, pp. 101-106.

[7] J. H., Zhang, T. C., Lee, W. S., Lau and X., Ai, “Spark erosion with ultrasonic frequency,” *J. Mater. Process. Tech.*, 1997, Vol. 68, pp. 83-88.

[8] T. B., Thoe, D. K., Aspinwall and N., Killey, “Assisted ultrasonic and electrical discharge machining of ceramic coated nickel alloy,” *J. Mater. Process. Tech.*, 1999, Vol. 92-93, pp. 323-328.

[9] M., Ghoreishi and J., Atkinson, “A comparative experimental study of machining characteristics in vibratory, rotary and vibro-rotary electro-discharge machining,” *J. Mater. Process. Tech.*, 2002, Vol. 120, pp. 374-384.

The 7th International Conference on Engineering and Technology
ICET-2015, Phuket, June 19-20, 2015
Prince of Songkla University, Faculty of Engineering
Hat Yai, Songkhla, Thailand 90112

Effect of Gas Metal Arc Welding Speed on Tensile Properties of SUS304 Stainless Steel and SS400 Carbon Steel Butt Joint

Pramote Poonnayom[1]*, Paiboon Yaemphuarn[2], Kittipong Kimapong[3]
[1,2,3]Rajamangala University of Technology Thanyaburi (RMUTT), Faculty of Engineering,
Department of Industrial Engineering, Thailand
*Email of corresponding author: ppoonnayom@yahoo.com

Abstract: *This paper aimed to apply a gas metal arc welding process for welding the butt joint between SUS304 stainless steel and SS400 carbon steel and study of welding speed variaction affecting the joint properties. Welding parameters in this study was a welding speed of 300-450 mm/min, a welding current of 110 A, and a mixed shielded gas of 95%Ar5%He. The summarized results are as follows. The welding speed affected to decrease the tensile strength of the joint and showed the maximum tensile strength of 520MPa with the welding speed of 350 mm/min. Fracture characteristic of the maximum tensile strength joint showed a large deformation at the location that was closely the fracture location that implied a ductile behavior. Increase of the welding speed affected to increase the average grain size at the HAZ where the fracture path was found and was caused by the increase of the GMAW heat input. The dissimilar SUS304/SS400 metals joint showed a low hardness base metal, a higher hardness HAZ and a highest hardness weld metal. The maximum hardness of 300 and 320 HV, was found at the fusion line for SS400 and SUS304 sides, respectively.*

Key Words: ***SUS304/ SS400/ Butt Joint/ Dissimilar Metals Joint/ Tensile Strength***

1. INTRODUCTION

Dissimilar metals joint between stainless steel and carbon steel is widely applied in various industries such as a food industry because of a requirement of a corrosion resistance and a cost reduction. High corrosion resistance of the part that contacts the humidity could be found when stainless steel was selected as a structure but its cost was expensive. To reduce the cost and keep the strength of the structure, the low carbon steel is replaced the stainless steel at the part that was not contacted the corrosive media such as food or some humidity [1, 2].

However, the fusion welding for producing the sound weld that suggested the high tensile strength was still investigated and developed. Recently, various papers reported the welding of the stainless steel and the low carbon steel that could prepare useful information for this study. There were a gas metal arc welding (GMAW) of 18G2A carbon steel/austenitic 1H18N10T stainless steel butt joint [3], a gas metal arc welding of AISI403/ AISI304L(N) stainless steels butt joint [4], a gas tungsten arc welding (GTAW) of AISI304 stainless steel/st37 carbon steel butt joint [5], a shielded metal arc welding (SMAW) of X5CrNi18-10 austenitic stainless steel/ X20CrMo13 martensitic stainless steel butt joint [6].

However, the gas metal arc welding of the dissimilar stainless steel/carbon steel showed insufficient results for applying in various works. So, this work aimed to apply GMAW for welding the dissimilar SUS304 stainless steel/SS400 carbon steel butt joint and investigate the joint properties such as a tensile strength, hardness and microstructure of the joint.

2. EXPERIMENTAL PROCEUDRE

The base metals used in this study were SUS304 stainless steel and SS 400 carbon steel. The chemical compositions of the base metals are listed in Table 1. The specimen plates were cut to be a rectangular shape. A dimension of the plates was a width of 75 mm, a length of 150 mm and a thickness of 3 mm. The plates were firmly clamped in a jig for preparing a butt joint with an opening gap of 1.2 mm.

Table 1 Chemical compositions of base materials (wt%)

Composition	SUS304	SS400	ER309L
C	0.020	0.050	0.034
Mn	1.320	0.200	1.520
P	0.045	0.007	0.021
S	0.002	0.009	0.080
Si	0.440	0.010	0.490
Cr	18.670	0.050	23.520
Ni	8.040	0.017	13.860
Mo	0.020	0.020	-
Fe	balance	balance	-

A gas metal arc welding was used for joining the dissimilar SUS304/SS400 metals joint by one pass of AWS A5.9 ER309L stainless steel solid wire electrode.

The welding process parameters were a flat position, a welding electrode dia-meter of 1.2 mm, a mixed shielded gas of 95%Ar5%He, a welding current of 110 A, a welding speed of 300-450 mm/min.

The welded joints were cut by a micro-cutter with the lubrication and then machined by a milling machine to be a tensile strength test specimen as shown in Fig. 1. The tensile strength test was conducted using a strain rate of 1 mm/min.

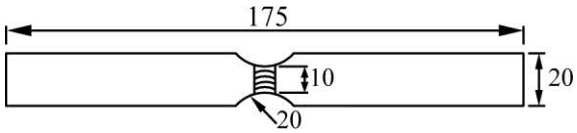

Fig. 1 Schematic of the tensile strength test specimen.

Metallographic samples for a light optical microscope (LOM) were prepared from a cross-section at the middle of the plate that was perpendicular to the welding direction. The cross-sections were mechanically polished using the #150-1000 emery papers and then followed by 1 micron in diameter of the diamond paste until the surface was a mirror-like. The mirror-like surfaces were etched by a solution of 50 mL of HCl+50 mL of H_2O for SUS304 stainless steel and a solution of 5 mL of HNO_3+95 mL of H_2O for SS400 low carbon steel. After etching step, the etched surfaces were examined for revealed the grain detail of the base metal, the heat affected zone (HAZ) and the weld metal (WM).

The micro-hardness test was carried out on the etched surface of the metallographic specimen with the test load of 100 gf and the holding time of 10 sec. The test was performed at the center of the plate cross-section with the test distance between the points of 0.5 mm as shown in Fig. 2.

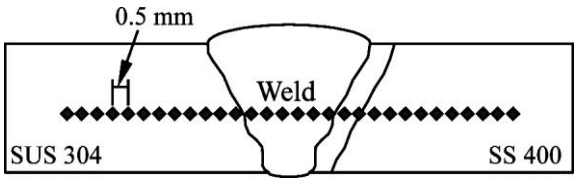

Fig. 2 Hardness measurement location.

3. RESULTS AND DISCUSSION

Fig. 3 shows the macrostructures of the butt joint that were welded by the welding current of 300 A and the welding speed of 300-345 mm/min. The macrostrucutres showed no defect in the weld metal and the interface between the weld metal and the base metals. When the welding speed was increased, the convex surface bead and the welded bead width of the joints were slightly increased. The fusion area of the welded metal was larger when the welding speed was increased.

Before tesnsile strength testing, the convex bead surface of the joint was removed by a grinding machine and then prepared mechanically to be a tensile strength test specimen. Fig. 4 shows the joint tested results of the tensile strength and the elongation that were welded by the welding speed of 300-450 mm/min and the welding current of 110 A. Most tensile strength of the joint was lower than that of the tensile strength of the base metals that was 750 MPa and 460 MPa for SUS304 stainless steel and SS400 carbon steel, respectively. The welding speed that produced the maximum tensile strength of 520 MPa was 350 mm/min. The tensile strength of the joint also showed that the welding speed that increased to be 400-500 mm/min, decreased slightly the tensile strength of the joint. Compared with the variation of the tensile strength, the elongations of the tested specimens that were produced by the welding speed of 300-450 mm/min were slightly changed between 5.0-5.8%.

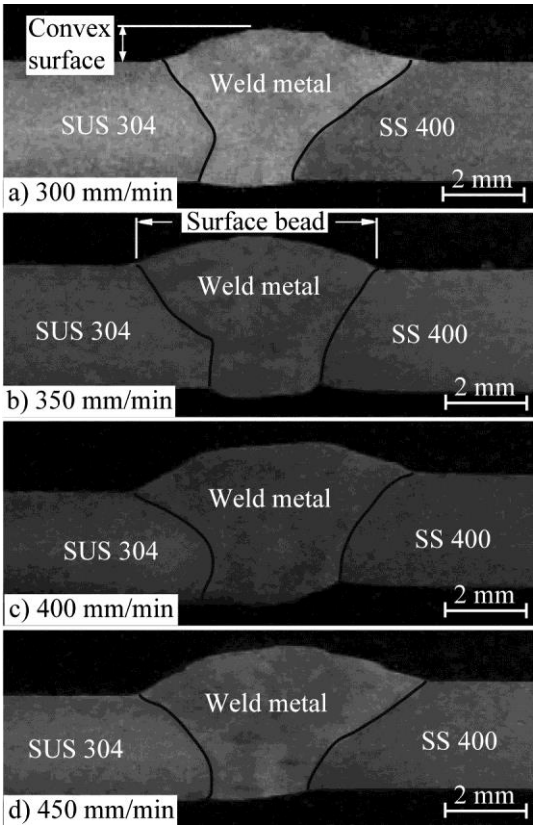

Fig. 3 Macrostructure of the dissimilar SUS304 stainless steel/SS400 carbon steel joint.

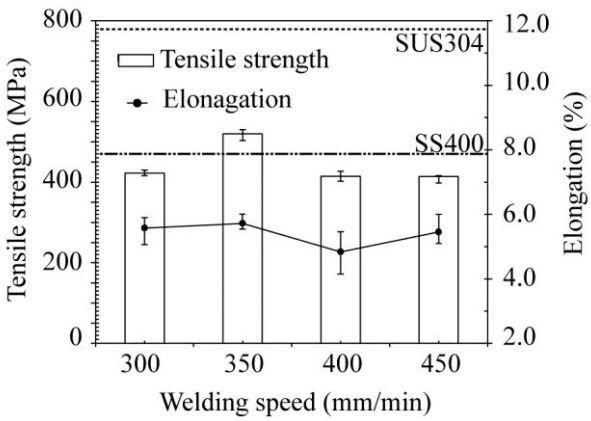

Fig. 4 Relation of the tensile strength, the eleongation and the welding speed.

Fracture characteristic of the tensile strength tested specimens that were welded by the welding speed of 300-450 mm/min was shown in Fig. 5. The figure shows the top view (as first column in fig. 5) and the side view (as second column in fig. 5) of the tested specimens at the welding speed of 300-450 mm/min. The fracture

locations and the fracture paths were different when the welding speed was increased. The fracture location of the tested specimen was occurred at the HAZ area of SS400 steel side of the joint. All fracture paths seemed to be initiated at the HAZ area and propagated to the fusion area at the bottom of the joint. Comparing the side view of the test specimen, it was found that the fracture paths of 300, 400 and 450 mm/min welding speed were at 45 degrees with the loaded direction of the test. The 350 mm/min welding speed fracture path that showed the maximum tensile strength among the investigated welding speed, showed the larger deformation of the tested specimen. The fracture specimen as shown in the side view of Fig. 5 (b) also showed that the joint thickness was decreased around the fracture path and the rough surface of fracture could be found.

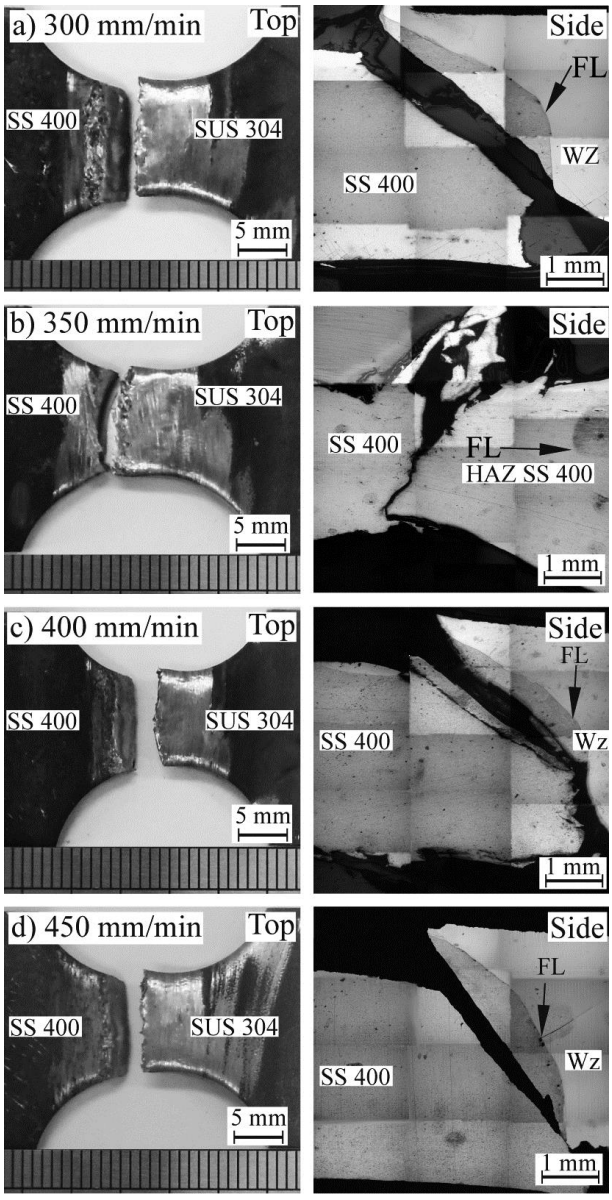

Fig. 5 Fracture location of the tensile strength tested specimens. (WZ=weld zone, FL=fusion line)

To compare the relation between the tensile strength and the fracture location of the joint, the microstructure of the HAZ area at SS400 steel side where the fracture was found (Location I in Fig. 6 (a)), was investigated and shown in Fig. 6 (b) and (c). The microstructure of the HAZ area of the 350 mm/min that gave that maximum tensile strength showed a fine equi-axed grain that had an average grain size of 4.6733 um as shown in Fig. 6 (b). The equi-axed grain was also found at the HAZ area of the 450 mm/min as shown in Fig. 6 (c) but the grain was larger than that of the 350 mm/min.

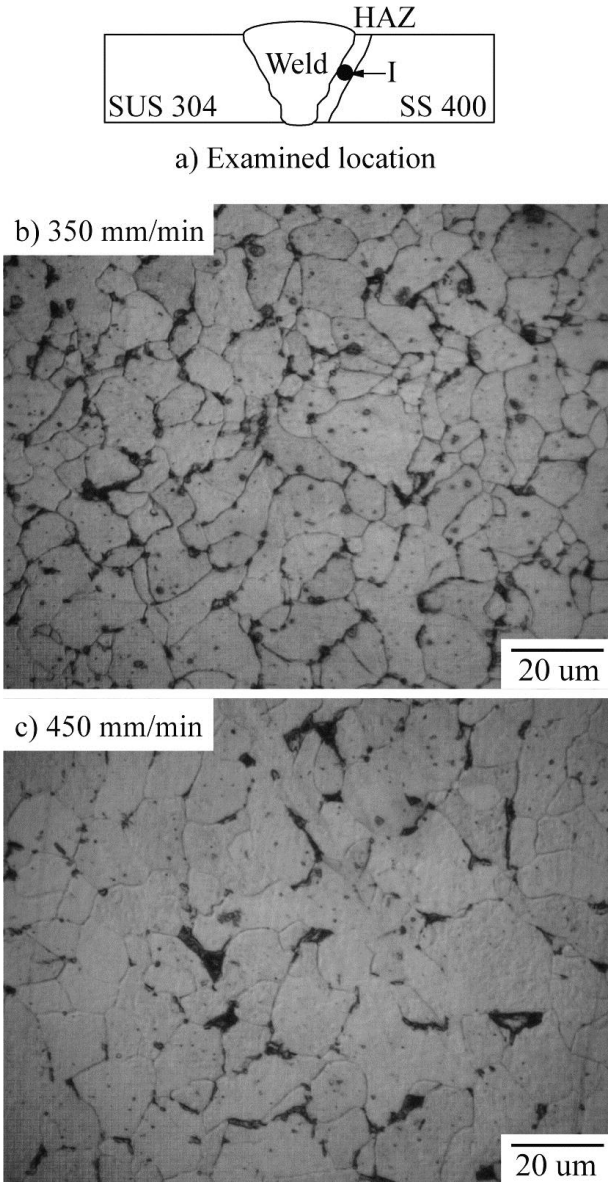

Fig. 6 microstructure of HAZ area: (a) 350 mm/min and 450 mm/min welding speed.

Fig. 7 shows the relation of the average grain size at the HAZ area of SS400 side (Location I in Fig. 6 (a)) and the welding speed. It was found that the lower welding speed, the grain size of the HAZ area was small as 7.7067 and 4.6733 um for the welding speed of 300 and 350 mm/min, respectively. The grain size of the HAZ area of the joint could be larger if the welding speed was increased to be 400 and 450 mm/min. The larger average grain size of the HAZ area was caused of the increase of the GMAW heat input that was applied to the joint with the increase of the welding speed and was caused of the tensile strength decreasing [7].

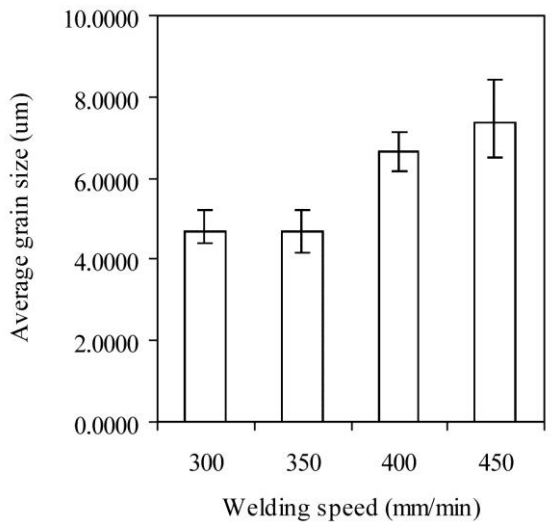

Fig. 7 Relation of the welding speed and the grain size average of HAZ.

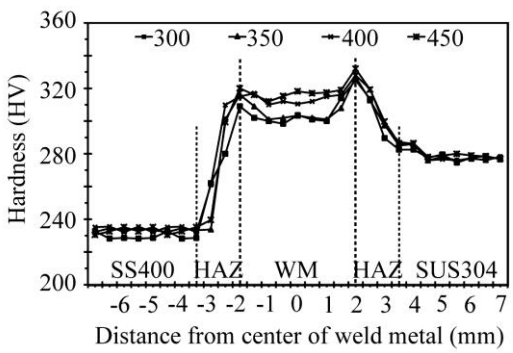

Fig. 8 Microstructure profile of the weld joint produced by various welding speeds.

Fig. 9 shows the relation of the hardness profile, the measurement location that was designed as shown in Fig. 2 and the welding speed. The hardness profile showed clearly the boundary of the weld that was consisted of the SS400 base metal, the SS400 HAZ area, the weld metal, the SUS304 HAZ area and the SUS304 base metal. The hardness measurement results also showed that the SS400 base metal and the SUS304 base metal indicated a hardness of about 230 and 280 HV, respectively. The hardness of the joint was increased when the measured location was in the HAZ caused by the formation of the fine equi-axed grain as shown in Fig. 7. Increase of the hardness was found when the location was closely the fusion line of the weld where showed the highest hard-ness of 300 and 320 HV for SS400 and SUS304 sides, respectively. The weld metal hardness was slightly decreased to be 320 HV but was still higher than that of the HAZ and the base metals. Considering the slope of the hardness variation from the fusion line to HAZ, it was found that the hardness slope at the SS400 side was higher than that of the SUS400 side and might be one of factor that the fracture was occurred in SS400 side [8].

4. CONCLUSION

This study applied the gas metal arc welding process for welding the butt joint between SUS304 stainless steel and SS400 carbon steel and studied of welding speed variaction affecting the joint properties. The summarized results are as follows.

4.1 The welding speed affected to decrease the tensile strength of the joint and showed the maximum tensile strength of 520MPa with the welding speed of 350 mm/min.

4.2 Fracture characteristic of the maximum tensile strength joint showed a large deformation at the location that was closely the fracture location that implied a ductile behavior.

4.3 Increase of the welding speed affected to increase the average grain size at the HAZ where the fracture path was found and was caused by the increase of the GMAW heat input.

4.4 The dissimilar SUS304/SS400 metals joint showed a low hardness base metal, a higher hardness HAZ and a highest hardness weld metal. The maximum hardness of 300 and 320 HV, was found at the fusion line for SS400 and SUS304 sides, respectively.

ACKONWLEDGEMENT

Authors would like to thank Rajamangala University of Technology Thanyaburi for its financial support.

5. REFERENCES

[1] D. Brandon and W. D. Kaplan, *Joining Processes, An introduction*. Great Britain: John Wiley & Sons Ltd., 1997.

[2] R. Paventhan, P. R. Lakshminarayanan, and V. Balasubramanian, "Fatigue behaviour of friction welded medium carbon steel and austenitic stainless steel dissimilar joints," *Materials & Design*, 2011, vol. 32, pp. 1888-1894..

[3] P. Sędek, J. Brózda, L. Wang, and P. J. Withers, "Residual stress relief in MAG welded joints of dissimilar steels," *International Journal of Pressure Vessels and Piping*, 2003, vol. 80, pp. 705-713.

[4] C. R. Das, A. K. Bhaduri, G. Srinivasan, V. Shankar, and S. Mathew, "Selection of filler wire for and effect of auto tempering on the mechanical properties of dissimilar metal joint between 403 and 304L(N) stainless steels," *Journal of Materials Processing Technology*, 2009, vol. 209, pp. 1428-1435.

[5] A. Celik and A. Alsaran, "Mechanical and Structural Properties of Similar and Dissimilar Steel Joints," *Materials Characterization*, vol. 43, 1999, pp. 311-318.

[6] R. Kaçar and O. Baylan, "An investigation of microstructure/property relationships in dissimilar welds between martensitic and austenitic stainless steels," *Materials & Design*, 2004, vol. 25, pp. 317-329.

[7] Y. Shi, D. Chen, Y. Lei, and X. Li, "HAZ microstructure simulation in welding of a ultra fine grain steel," *Computational Materials Science*, 2004, vol. 31, pp. 379-388.

[8] E. Gharibshahiyan, A. H. Raouf, N. Parvin, and M. Rahimian, "The effect of microstructure on hardness and toughness of low carbon welded steel using inert gas welding," *Materials & Design*, 2011, vol. 32, pp. 2042-2048.

The 7th International Conference on Engineering and Technology
ICET-2015, Phuket, June 19-20, 2015
Prince of Songkla University, Faculty of Engineering
Hat Yai, Songkhla, Thailand 90112

Fracture Strength and Failure Location of GMAW Lap Joint between SS400 Carbon Steel and SUS304 Stainless Steel

Sakchai Chantasri[1]*, Kittipong Kimapong[2]
[1.2]Rajamangala University of Technology Thanyaburi (RMUTT), Faculty of Engineering,
Department of Industrial Engineering, Thailand
*Email of corresponding author: sakchai.c@en.rmutt.ac.th

Abstract: *Lap joint of dissimilar metals between SS400 carbon steel and SUS304 stainless steel was welded by a gas metal arc welding (GMAW). The lap joint properties evaluation such as tensile shear strength, fracture location and microstructure was performed. The summarized results are as follows: Increase of the welding current affected to increase tensile shear strength of the lap joint and showed the maximum fracture load of 15,570 N at the welding current of 100 A. Higher welding current produced the larger welding bead and the larger weld leg but decreased the weld penetration. Larger secondary dendrite arm spacing that was produced by the higher welding current caused the lap joint was bent. Higher hardness of the weld metal affected to show higher tensile shear strength and resisted the weld metal to occur at the boundary of the fusion line/weld metal.*

Key Words: ***lap joint/ dissimilar metals/ fracture load***

1. INTRODUCTION

Sugar production industry is one of important industries for agriproduct processing in Thailand. In sugar production process, a mechanical squeezing step that extracts a molasses from a sugar cane requires machine's parts that could withstand acting load, wear and corrosion during the process. However, if a production process's strucutre is designed to support those factors, a structure cost migh be heavy and expensive. Therefore, a flexible structure that was composed by various metals such as dissimilar metals was introduced to replace structure's part in the process.

Dissimilar metals joint might complicate for fusion welding because of the different in the metal properties. However, some reports suggested a good combination of metals and implied a sufficient joint strength. Those reports are as follows. Arivazhagan *et al.* [1] joined AISI304 stainless steel to AISI 4140 low alloy steel using 3 different welding processes. The experimental results showed the joint strength was 681, 635 and 494 MPa for the electron beam welding (EBW), the gas tungsten arc welding (GTAW) and friction welding (FW), respectively. The enrichment of chromium, nickel and carbon on the EBW weldment was the key factor to show the maximum tensile strength in their work. Wang *et al.* [2] joined the dissimilar metals joint between 2205 duplex stainless steel and 16MnR low alloy high strength (HSLA) steel by shielded metal arc welding (SMAW) and gas tungsten arc welding. The results showed that the mechanical properties of the joints that were produced by 2 welding process were highly satisfied. This carbon diffusion from HSLA side to weld metal affected to produce more metal carbide in the weld metal. This effect also raised the weld metal hardness but decreased impact toughness of the weld metal. The results also suggested that GTAW was suited to weld this dissimilar metal than that of SMAW. The GTAW process [3] also produced the ductile properties and high tensile strength of the weld metal when it applied to weld dissimilar metals between AISI347 stainless steel and A335 low alloy steel with the filler metals of ER309L and ERNiCr-3. Another fusion welding process that could produce the sound joint of dissimilar metals bet-ween low carbon steel and stainless steel was laser weld-ing [4]. The relation between laser mean power and fusion area was key effect to vary the joint strength. Increasing of laser mean power affected directly to increase the peak load of the joint.

The above reports showed that the selection of the welding process for joining the dissimilar metals of the ferrous metals was interestingly important. So, the development and the investigation for the suit welding process for dissimilar metals are still performed. In this present work, the effect of GMAW current on dissimilar metals SS400 carbon steel and SUS304 stainless steel lap joint properties was studied. The evaluation of the joint properties such as tensile shear strength, joint displacement and microstructure was performed.

2. EXPERIMENTAL PROCEDURES

Materials in this study were rolled plates of SS400 carbon steel and SUS304 stainless steel that had chemical compositions as listed in Table 1. The plates (100 mm. wide, 200 mm. long and 3 mm. thick) were

firmly clamped in a jig and set up to be a lap joint as shown in Fig. 1 (a).

Table 1. *Chemical composition of experimental materials*

Element (wt%)	SUS304	SS400	ER309L
C	0.02	0.05	0.034
Mn	1.32	0.20	1.52
P	0.045	0.07	0.021
S	0.002	0.09	0.08
Si	0.44	0.01	0.49
Cr	18.67	0.05	23.52
Ni	8.04	0.017	13.86
Mo	0.02	0.02	-

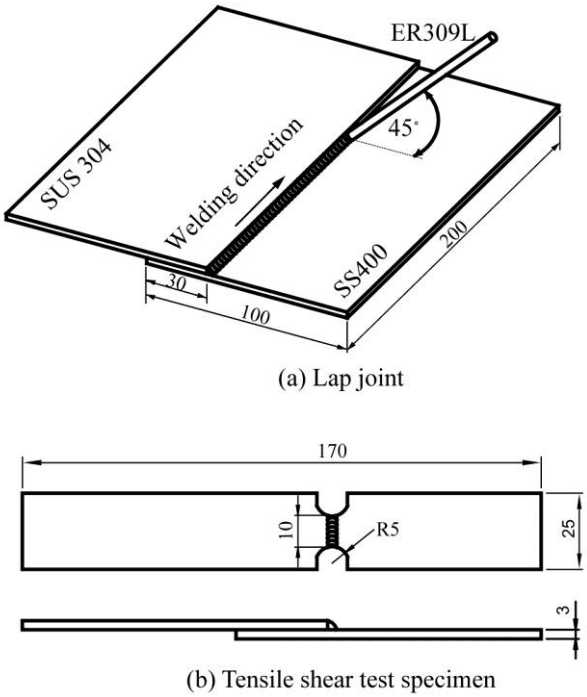

Fig. 1 Schematic of the lap joint and (a) and dimension of tensile shear specimen (b).

Gas metal arc welding was applied to weld the lap joint with various welding parameters that were the welding current of 90-120 A, the welding speed of 200 mm/min, and the welding angle of 45 degree. The welding wire using in this experiment was ER309L electrode that showed the chemical composition as listed in Table 1. A shielding gas was a mixture of 95%Ar and 5%He.

After welding, the lap joints were mechanically prepared and investigated for the joint properties such as tensile shear strength, hardness and microstructure. The tensile shear test specimen with a configuration as shown in Fig. 1 was carried out and calculated for a fracture load, a fracture location and a joint displacement.

Macro and micro structure examination specimens were prepared as a section part that was perpendicular to the welding direction at middle of the welding line. The mirror-like polished specimen was chemically etched by 5%Nital for SS400 side and the solution of 45%HCl+ 15%HNO_3+40%H_2O for SUS304 side. Light optical microscope was the tool for observation the microstructure of the lap joint.

3. EXPERIMENTAL RESULTS AND DISCUSSION

Fig. 2 shows cross sections of the lap joint that was prepared perpendicularly to welding direction at middle of welding line. The cross sections of the lap joint that were welded by minimum and maximum welding currents showed the weld metal with complete fusion area. The weld defect such as an undercut defect or an overfill defect could not be observed in these weld area. These characterizations also found in the cross sections of the lap joints that were welded in the welding current of 90-110 A.

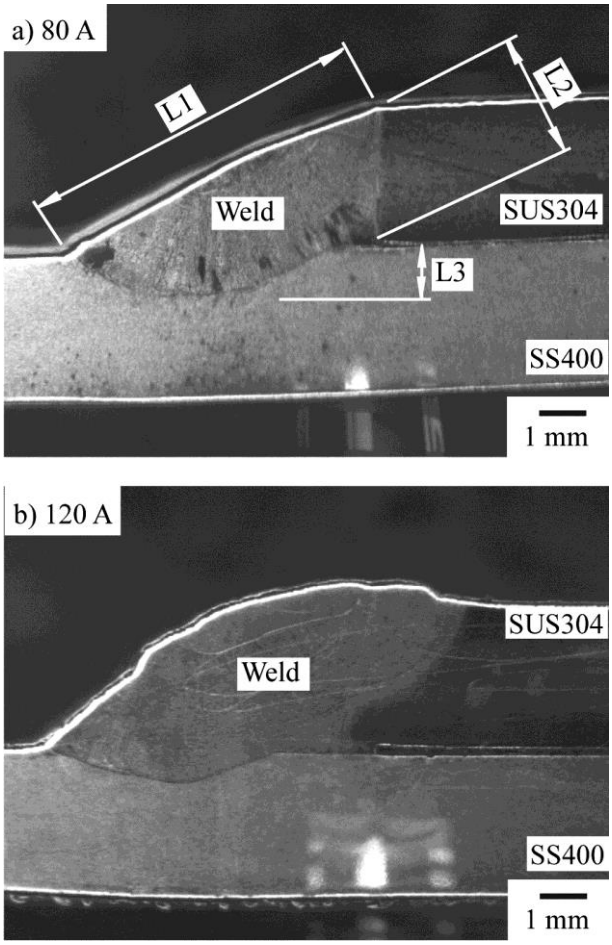

Fig. 2 Macrostructure of the lap joint. (L1=weld width, L2=actual throat, L3=penetration depth)

However, when comparing the feature of the lap joint cross section such as the weld bead size, the leg size and the penetration depth, it was found that the increase of the welding current affected to change this feature as shown in Fig. 3. Increase of the welding current affected to increase the weld bead size and the leg size but decreased the penetration depth of the weld metal. The larger size of the weld bead and leg was caused by the higher heat input that applied to the joint with higher welding current [5].

Increasing the welding current also increased the penetration depth of the weld to the SUS304 stainless steel lower plate of the joint when the welding current increased from 80 to 100 A but if the welding current was higher than that of 110 A, the penetration depth was slightly decreased. This increase of penetration depth was still not cleared for this work but when compared to

the fracture as shown in Fig. 4, it seem to relate to the fracture load of the lap joint that fracture load was highest at the welding current of 100 A and decreased slightly when the welding current increased from 110-120 A. In this work, an optimum welding current was 100 A.

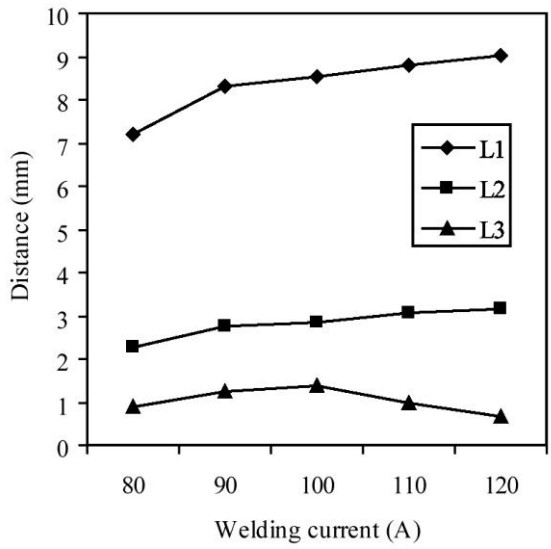

Fig. 3 Relation of the weld configuration and the welding current.

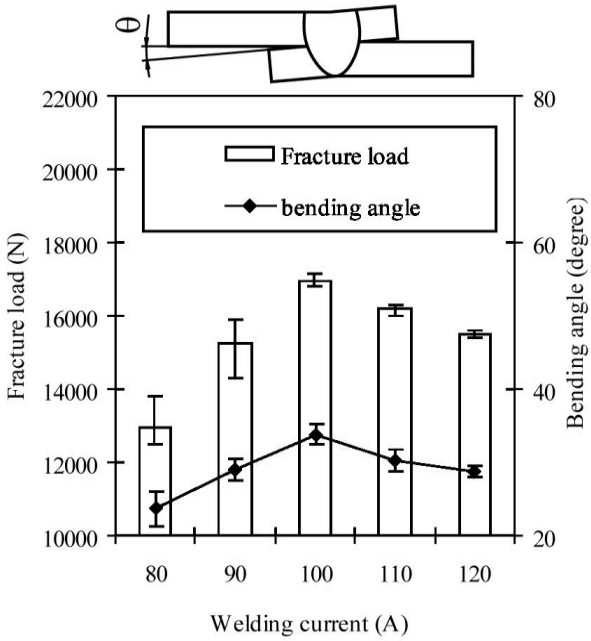

Fig. 4 Relation of fracture load, bending angle of test specimen and welding current.

Variation of the fracture load when the welding current was increased, related directly to the deformation of the tensile shear test specimen. When the specimen was pulled, the upper and lower plate of the lap joint was separated and bent to be a bending angle (θ) as shown in Fig. 5. This bending angle was increased when the welding current increased as shown in Fig. 4. Most fracture locations of the test specimen were occurred at HAZ zone at SUS304 stainless steel side as shown in Fig. 5 (a). The fracture paths were perpendicular to loading direction (Type I). The fracture location of the specimen that showed the maximum fracture load and showed maximum bending angle, was occurred at the HAZ zone and showed the fracture path that was not perpendicular to the loading direction (Type II) as shown in Fig. 5 (b). The larger bending angle that increased as the increase of fracture load might be caused by the fine dendrite structure at the fracture location at the HAZ zone as shown in Fig. 6. Secondary dendrite arm spacing (SDAS) [5] of the fracture location that welded by various welding currents suggested that the fine dendrite structure was formed at the lower welding current. These SDAS was about 4.8974, 8.5641, 10.4102, 10.2131 and 10.2212 μm for the welding current of 80, 90, 100, 110 and 120 A, respectively.

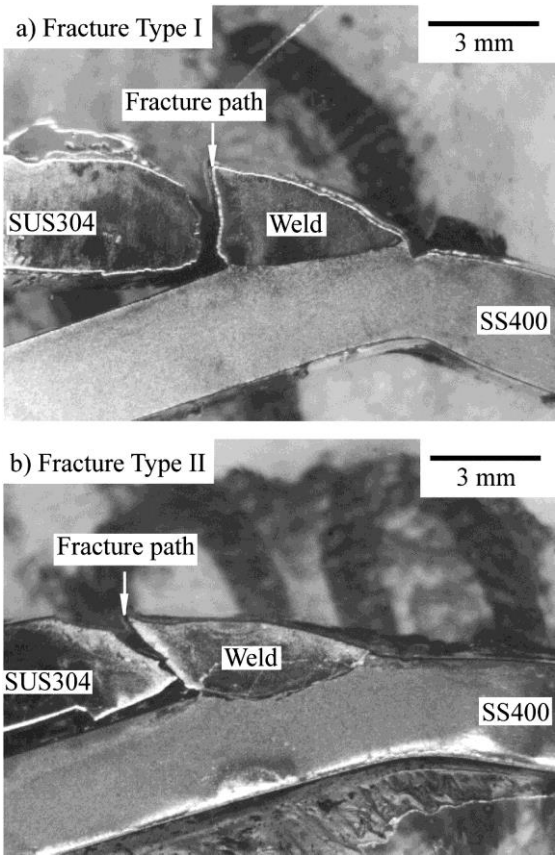

Fig. 5 Fracture location of lap joints.

The hardness comparison of the lap joint produced by the welding current of 80 A that showed the minimum fracture load and the lap joint produced by the welding current of 100 A that showed the maximum fracture load was shown in Fig. 6. The hardness was measured at 3 locations on the polished cross section surface of the lap joint. The measured locations were at the fusion boundary of SUS304/the weld metal, the weld metal and the fusion boundary of SS400/the weld metal. The hardness of 3 points along the measurement locations was investigated and averaged. The hardness measurement results showed that the hardness of the fusion boundary /the weld metal was higher than that of the weld metal. The lower hard-ness of the weld metal when compared to the fusion boundary/the weld metal might be caused the

tensile shear test specimen to be bent easily and initiated the fracture during the test.

Comparing the hardness of the different welding current, it was found that the weld metal hardness of the 100 A welding current was higher than that of the 80 A welding current. The results also showed that higher hardness of the weld metal resisted the failure along the weld metal and caused the failure path occurred along the boundary of fusion line/the weld metal as shown in Fig 5 (b).

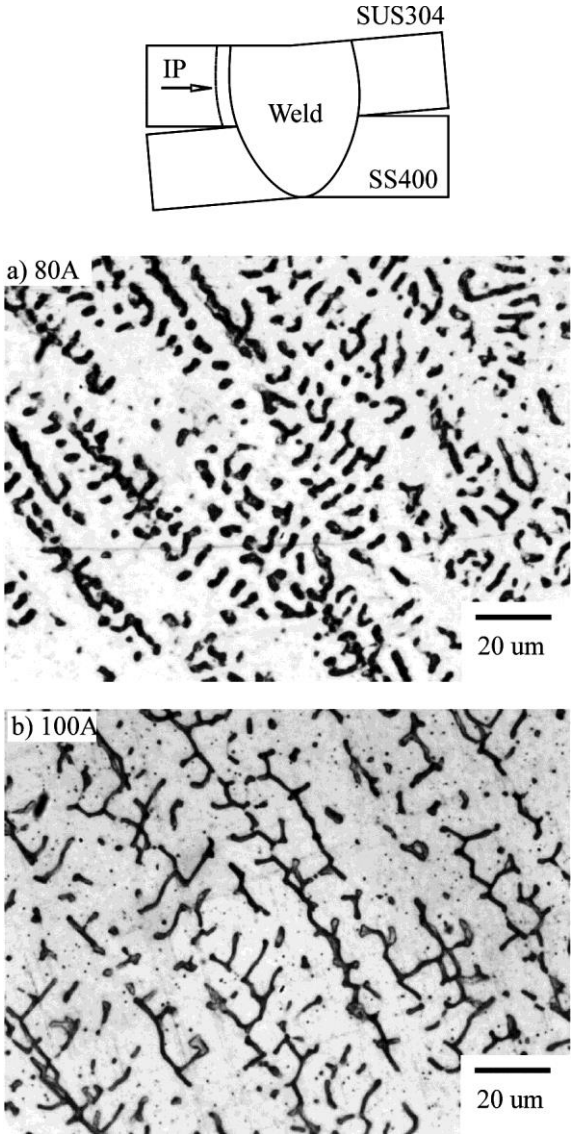

Fig. 6 Microstructure of fracture location.

5. CONCLUSION

5.1 Increase of the welding current affected to increase tensile shear strength of the lap joint and showed the maximum fracture load of 15,570 N at the welding current of 100 A.

5.2 Higher welding current produced the larger welding bead and the larger weld leg but decreased the weld penetration.

5.3 Larger secondary dendrite arm spacing when the higher welding current was applied caused the lap joint was bent and showed higher tensile shear strength.

5.4 Higher hardness of the weld metal affected to show higher tensile shear strength and resisted the weld metal to occur the boundary of the fusion line/weld metal.

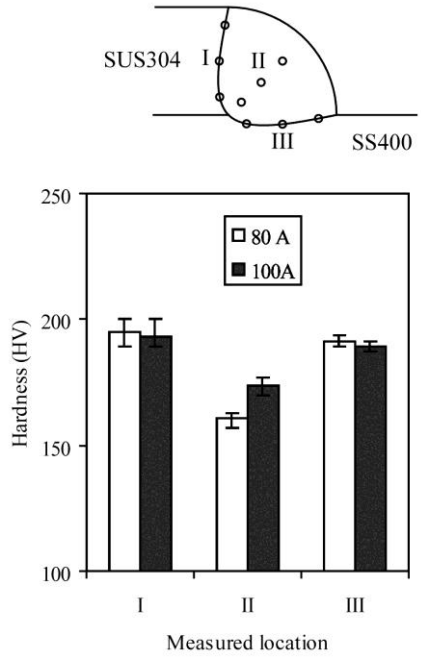

Fig. 6 Micro-vickerse hardness of weld metal.

ACKNOELEDGEMENT

Authors would like to thank Rajamangala University of Technology Thanyaburi for its financial support. This work was technically supported by Mr. Amornsak Mayai and Mr. Jessada Keawvijit. Authors also would like to thank for thier kind.

REFERENCES

[1] N. Arivazhagan, S. Singh, S. Prakash, and G. M. Reddy, "Investigation on AISI 304 austenitic stainless steel to AISI 4140 low alloy steel dissimilar joints by gas tungsten arc, electron beam and friction welding," *Materials & Design*, 2011, vol. 32, pp. 3036-3050.

[2] S. Wang, Q. Ma, and Y. Li, "Characterization of microstructure, mechanical properties and corrosion resistance of dissimilar welded joint between 2205 duplex stainless steel and 16MnR," *Materials & Design*, 2011, vol. 32, pp. 831-837.

[3] I. Hajiannia, M. Shamanian, and M. Kasiri, "Microstructure and mechanical properties of AISI 347 stainless steel/A335 low alloy steel dissimilar joint produced by gas tungsten arc welding," *Materials & Design*, 2013, vol. 50, pp. 566-573.

[4] M. J. Torkamany, J. Sabbaghzadeh, and M. J. Hamedi, "Effect of laser welding mode on the microstructure and mechanical performance of dissimilar laser spot welds between low carbon and austenitic stainless steels," *Materials & Design*, 2012, vol. 34, pp. 666-672.

[5] M. P. Groover, *Fundamentals of Modern Manufacturing: Materials, Processes, and Systems*, 3 ed.: John Willey & Sons (Asia) Pte. Ltd., 2007.

The 7th International Conference on Engineering and Technology
ICET-2015, Phuket, June19-20, 2015
Prince of Songkla University, Faculty of Engineering
Hat Yai, Songkhla, Thailand 90112

Automatic Onset Time Detection for a SEMG Measurement System

Chaiwat Lersviriyanantakul*, Apidet Booranawong, Pornchai Phukpattaranont and Nattha Jindapetch
Department of Electrical Engineering, Faculty of Engineering,
Prince of Songkla University, Hat Yai, Songkhla 90112, Thailand
*Email of corresponding author: chaiwat-l@bunga.pn.psu.ac.th

Abstract: *A surface electromyography (SEMG) measurement for any applications consists of three parts: an onset time detection for finding the first point of movement, a feature extraction, and a feature classification. For an automatic system, the onset time detection is one of the important part that influrences the accuracy of the other parts. In this paper, a new automatic and simple algorithm for onset time detection is prsented. There are two main processes in the proposed algorithm; a smoothing process for reducing the noise of the measured SEMG signal and an automatic threshold calculation process for determining the onset time. The experimental results show the performance evaluation of the proposed algorithm to detect the SEMG onset time in various smoothing-threshold equations. Our findings reveal that using a simple square interal (SSI) equation with the given SEMG signals gives the best performance for onset time detection.*

Key Words: ***SEMG/ Smoothing/ Onset Time Detection***

1. INTRODUCTION

The SEMG is the electrophysiological signal generated from the brain to control muscle activities. Currently, the SEMG signal is wildly used in many fields such as, a robotic control [1, 2], patient rehabilitation [3], Parkinson's disorder recognition [4], prosthesis devices controlling for disable people [5, 6] and improving the quality of life for the disabled and elderly people [7].

The whole method to process the SEMG data consists of an onset time detection, a feature extraction and a feature classification. We found that most of publications as preseted in the research literature focus on the feature extraction and the feature classification parts; they still do not consider how to get the onset time in the onset time detection process [5, 8, 9]. Additionally, the manual onset time detection is not suitable for the automatic SEMG measurement system.

According to the literature review, there are some publications propose onset time detection techniques. For examples, Teager-Kaiser Energy Operator was applied for locating the onset time of a muscal avtivity [10]. Reference [11] developed a new algorithm to determine the onset time for measuring the SEMG signal in an inspiratory event. In reference [12], an Autoregressive-Generalized Autoregressive Conditional Heteroscedastic (AR-GARCH) model was used to detect the onset and offset times, and it also gave the performance better than a double-threshold detection technique. Reference [13] proposed a novel algorithm for real-time onset time detection using the Quasi-Tension technique to detect wrist movement. In [14], the P&WND method was compared with the traditional Di Fabio's method to detect the EMG signal for a segmentation process. Finally, in [15], the Maximum Likelihood method is applied with an adaptive threshold technique to estimate the onset and offset times of muscle contraction.

However, the algorithms for detecting the onset time of the SEMG signal from those publications as mentioned above are tested on the computer. They use the complex algorithms, which are not appropriate for an embedded system. By this reason, we try to design a simple algorithm which is suited to implement in an embedded hardware.

In this paper, we use six smoothing-threshold equations including standard derivative (STD), root mean square value (RMS), mean average value (MAV), wave form length (WL), simple square integral (SSI) and integrated EMG (IEMG) to smoothen the measured SEMG signal and to detect the onset time by determining the threshold. The threshold value is also calculated from these equations. The experimental results indicate that using SSI for both smoothing and thresholding (i.e. called SSI-SSI) with 50 points window size is suitable for detecting the onset time of the given SEMG data. Therefore, for further work of our research, we plan to implement SSI in an embeded hardware for the onset time detection.

2. METHODOLOGY

2.1. Data acquisition

The EMG signals were acquired from both muscles Flexor carpi radialis and Extensor carpi radialis longus using Ag-AgCl Red-Dot surface electrodes (3M, 2237) [16]. The electrodes were placed lengthwise at the same

muscle. The displacement between each one is 20-30 mm, as show in Fig.1. The ground electrode was placed on the other wrist. All SEMG signals were recorded by using Mobi6-6b (TMS International BV, Netherlands) [17]. The band-pass filter is in the range 10-500 Hz, and sampling frequency is 1,000 Hz. The hand motions consist of one motionless (i.e. rest) and six types of the movement i.e. wrist flexion, wrist extention, hand colose, hand open, pronation and supination, as show in Fig.2. Each movement performs for 0.5 second and rests for 4 second in the duration.The process was repeated for ten times. The example of SEMG data from both muscles is shown in Fig.3.

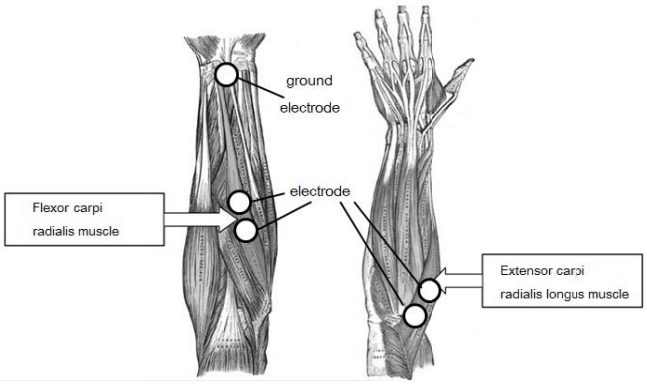

Fig.1. Target muscles and electrode placement positions; note that in our experiment, the ground electrode is placed on the other hand [18, 19]

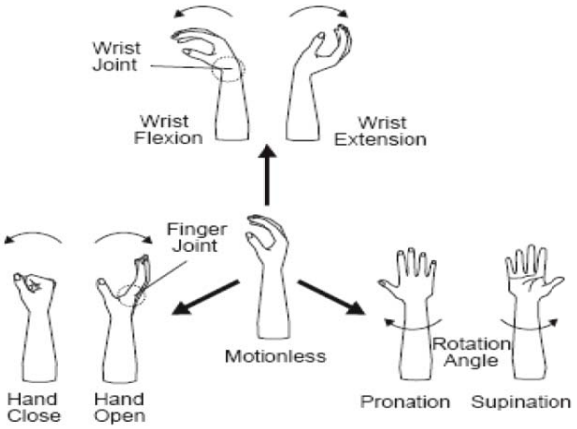

Fig.2. Seven types of hand movement [20]

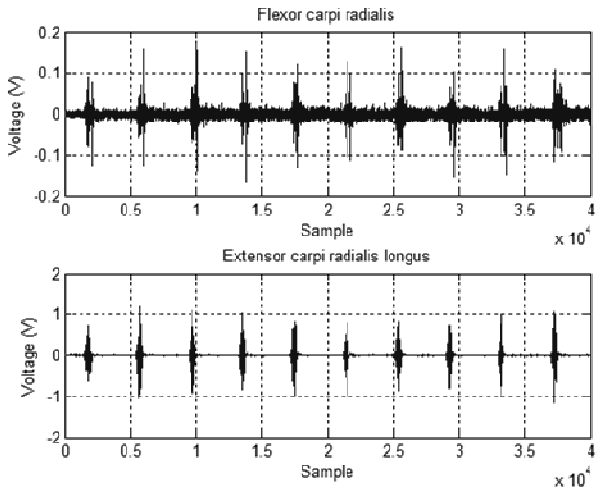

Fig.3. The example of SEMG signals from both muscles

2.2. Onset time detection

The onset time detection algorithms consist of two processes: smoothing and threshold calculations. Both processes use the same smoothing-threshold equation to calculate the SEMG signals. Six smoothing-threshold equations uses in this paper are shown in equations (1)-(6). Where N is the number of SMEG signals, x_n is the SEMG value at the nth point and $\bar{x}$ is the average value of the SEMG signals.

$$STD = \left(\frac{1}{N-1} \sqrt{\sum_{n=1}^{N} (x_n - \bar{x})^2} \right) \tag{1}$$

$$RMS = \left(\frac{1}{N} \sqrt{\sum_{n=1}^{N} (x_n - \bar{x})^2} \right) \tag{2}$$

$$MAV = \frac{1}{N} \sum_{n=1}^{N} |x_n| \tag{3}$$

$$WL = \sum_{n=1}^{N-1} |x_{n+1} - x_n| \tag{4}$$

$$SSI = \sum_{n=1}^{N-1} |x_n|^2 \tag{5}$$

$$IEMG = \sum_{n=1}^{N-1} |x_n| \tag{6}$$

The method to discover the onset time of the SEMG uses the intersection point between the smoothing and threshold process. We use twelve types of the algorithm for testing the data. The notation smoothing-threshold is used to represent each method i.e. STD-STD, STD-RMS, STD-MAV, RMS-STD, RMS-RMS, RMS-MAV, MAV-STD, MAV-RMS, MAV-MAV, WL-WL, SSI-SSI and IEMG-IEMG. The threshold is determined by 500 points of SEMG data during the first motionless. This threshold is used throughout the data set. The smoothing process is calculated by shifting the window size from the starting point of SEMG data point by point until the end point of the data. When the first intersection between the threshold and the smoothing process at each window size is found, the position is recorded. Then, the window size is moved out of the SEMG data for 1500 points to find the next onset time position from the next SEMG signal. The example of using SSI-SSI at the window size 50 point written in the Pseudo code is provided below.

VARIABLES: *window_size, starting_point, endding_point, Smoothing, Threshold*
BEGIN
(1) // Initial value
(2) *Window_size* = 50;
(3) *Starting_point* = 1;
(4) *Endding_point* = number of SEMG data;
(5) // Main process
(6) Calculate *Threshold* from SSI at 1-500 points of the first motionless
(7) **FOR** *i* = *Starting_point* to *Ending_point*
(8) **FOR** *n* = *Starting_point* to *Window_size*
(9) Calculate *Smoothing* from SSI at this *Window_size*;
(10) **END**

```
IF Smoothing > Threshold THEN
    Record onset time position;
/*Move the consider point n and Window_size 1500 Point*/
    n = n + 1500;
    Window_size = Window_size +1500;
END IF
ELSE
/*Move the consider point n and Window_size to next Point*/
    n = n + 1;
    Window_size = Window_size + 1;
END
END
```

3. RESULTS AND DISCLIUSIONS

In order to demonstrate the performance of the onset time detection algorithm, we calculate the distance error between a manual detection and an automatic detection using the proposed algorithm. For the manual detection, we observed the signal value by zoom in the SEMG data and recorded the onset time position. For the automatic detection, six smoothing-threshold equations are used to smoothen the SEMG data and to calculate the threshold value for determining the onset time position. The distance error is calculated by using the difference between the manual and the automatic detection positions of each technique and each movement.

From the experiment results, we observed that the STD, RMS and MAV can be used as the smoothing and the threshold calculation to compare between each other in the same method, because the output values after we do the smoothing and the thresholding by these equations have the same range. Nevertheless, for example, WL and RMS cannot be used in the same method. This is because the value from each equation is not in the same range. Such as using WL as smoothing process gets the value in range 10^5 while using RMS as thresold process gets the range less than 10. Thus, both values cannot be used in the same smoothing and the threshold process to give the good result.

From the test, the example of finding onset time position in SEMG data is shown in Fig.4. Fig.5 shows the displacement error from twelve algorithms in each hand movement of window size 50 points. The results show that SSI-SSI gives the best result to detect the onset time position.

We also investigated the displacement error while varying the window sizes. 50, 100, 200, 300 and 500 points of the window sizes were selected. The result shows that using SSI-SSI (i.e. smoothing-threshold) at the window size 50 points gives the least error forthe onset time detection, as shown in Fig.6.

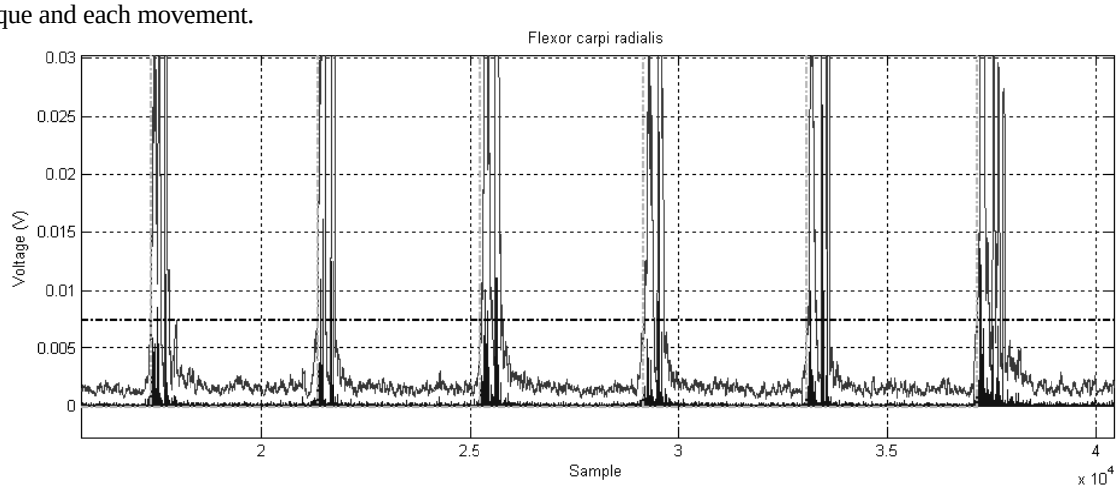

Fig.4. The example of onset time detection movement

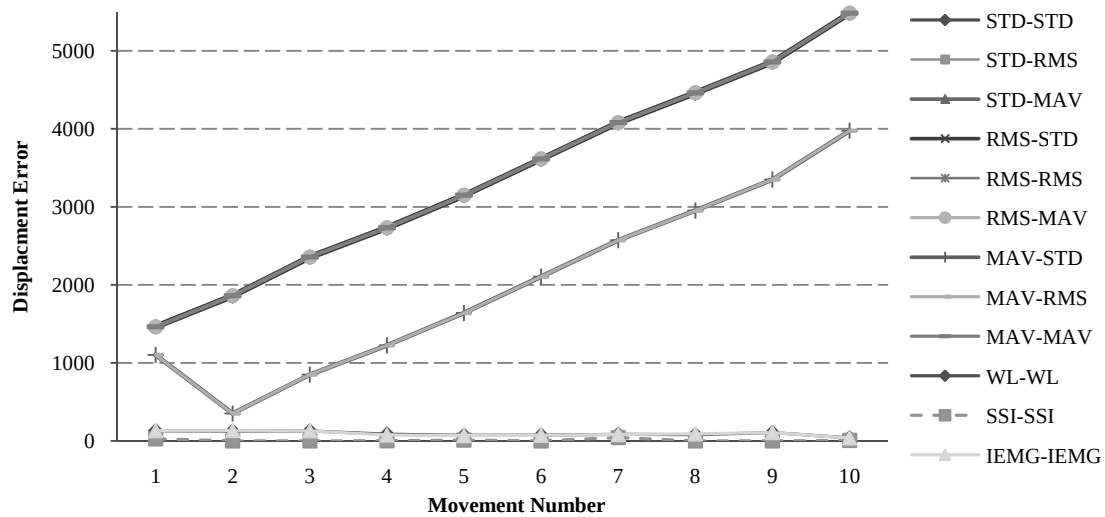

Fig.5. Displacement error from each number of movement in wrist extension motion

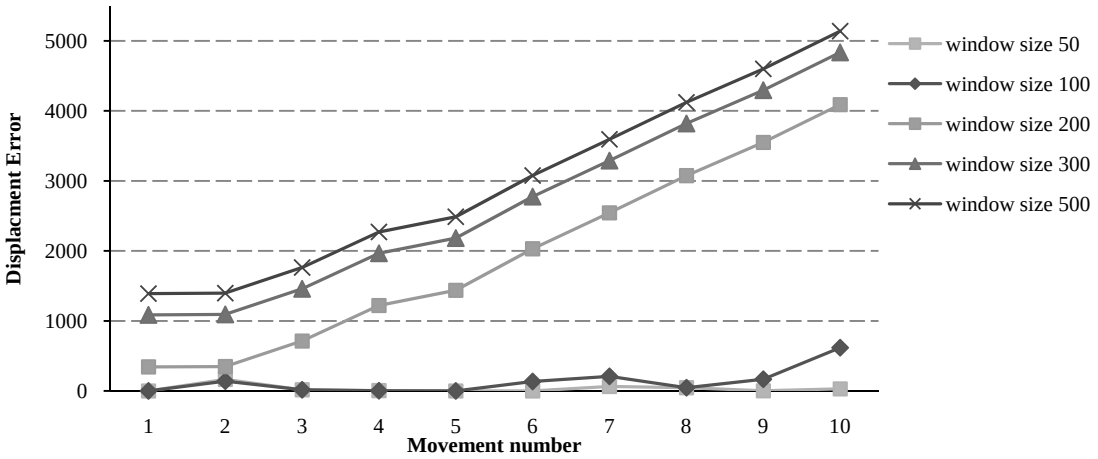

Fig.6. Displacement error using SSI-SSI for window 50 points of extensor muscle and wrist flexion movement

4.CONCLUSIONS

The new algorithm using the correlation between smoothing data and threshold has been proposed for the onset time detection. The performance evaluation shows that using SSI for both smoothing and threshold processes with 50 points windows size gives the best result. However, the whole process is proved by only the given data set. If we chang the input SEMG signal, the result may change; SSI-SSI may not give the best performance.

5. ACKNOWLEDGMENT

This research was supported by the Ministry of Science and Technology and the Faculty of Engineering, Prince of Songkla University, Thailand.

6. REFERENCES

[1] M. Yoshikawa, M. Mikawa and K. Tanaka, "A Myoelectric Interface for Robotic Hand Control Using Support Vector Machine,"*in Proc. IEEE/RSJ International Conference on Intelligent Robots and Systems*, pp. 2723-2727, 2007.

[2] H. Kang, K. Rhee, K. J. You and H. C. Shin "Intuitive Robot Navigation Using Wireless EMG and Acceleration Sensors on Human Arm," *in Proc. of International Symposium on Intelligent Signal Processing and Communication System* (*ISPACS*), pp. 1-4, 2011.

[3] S. Guangji, W. Li, M. Dengrong and F. Fan, "The Design of a Rehabilitation Training System with EMG Feedback," *in Proc. of the International Conference on Biomedical Engineering and Biotechnology* (*iCBEB*), pp. 917-920, 2012.

[4] P. Kugler, C. Jaremenko, J. Schlachetzki, J. Winkler, and B. Eskofier,"Automatic Recognition of Parkinson's Disease Using Surface Electromyography During Standardized Gait Tests,"*in Proc. of the 35th Annual International Conference of the IEEE EMBS*, pp. 5781-5784, 2013.

[5] R. Boostani and M. H. Moradi, "Evaluation of the Forearm EMG Signal Feature for the Control of a Prosthetic Hand," *Physiological Measurement*, vol. 24, pp. 309-319, 2003.

[6] A. H. Al-Timemy, G. Bugmann, J. Escudero and N. Outram, "Classification of Finger Movement for The Dexterous Hand Prosthesis Control with Surface Electromyography,"*IEEE Journal of Biomedical And Health Informatics*, vol.17, no.3, pp. 608-618, 2013.

[7] M. R. Ahsan, M. I.Ibrahimy and O. O.Khalifa, "Advance in Electromyogram Signal Classification to Improve the Quality of Life for the Disabled and Aged People," *Journal of computer Science*, vol. 6, pp. 705-715, 2010.

[8]A. Phinyomark, S. hirunviriya, A. Nuidod, P. Phukpattaranont and C. Limsakul, "Evaluation of EMG Feature Extraction for Movement Control of Upper Limb Prostheses Based on Class Separation Index, *in Proc. of the International Conference on biomedical Engineering IFMBE Proceedings*, vol. 35, pp. 750-754, 2011.

[9] A. Subasi, "Classification of EMG Signals Using Combined Features and Soft Computing Techniques," *Applied Soft Computing*, vol. 12, pp. 2188-2198, 2012.

[10] X. Li and A. Aruin, "Muscle Activity Onset Time Detection Using Teager-Kaiser Energy Operator," *in Proc. of the 27th Annual International Conference of the Engineering in Medicine and Biology* (*IEEE-EMBS*), pp. 7549-7552, 2005.

[11] E.D. Dow, A.M. Petrilli, C.B. Mantilla and W.Z. Zhan, "Electromyogram-Triggered Inspiratory Event Detection Algorithm," *in Proc. of the IEEE Soft Computing and Intelligent Systems* (SCIS), pp. 789-794, 2012.

[12] R. Ghulam, B. Nidhaland I. Kamran,"Muscle Activity Detection from Myoelectric Signal Based on the AR-GARCH Model," *in Proc. of the IEEE Statistical Signal Processing Workshop*, pp. 420-423, 2012.

[13] Y. Kuroda, I. Nisky, Y. uranishi, M. Imura, A.M. Okamura and O. Oshiro, "Novel Algorithm for Real-Time Onset Detection of Surface Electromyography in Step-Tracking Wrist Movements. *in Proc. of the 35th Annual International Conference of the IEEE Engineering in Medicine and Biology Society*, pp. 2056-2059, 2013.

[14] S. Lei and W. Qiang, "A Novel Method of SEMG Signal Segmentation,"*in Proc. of the 9th International Conference on Mobile Ad-hoc and Sensor Networks*. pp. 515-520, 2013.

[15] X. Qi, Y. Lei and H. Jiping,"An Adaptive Algorithm for the Determination of the Onset and Offset of Muscle Contraction by EMG Signal Processing,"*IEEE TransactionOn Neural System and Rehabilitation Engineering*, vol. 21 no.1, pp. 65-73, 2013.

[16] Available online: http://solutions.3m.com/wps/portal/3M/en_US/IPD-NA/3M-Infection-Prevention/products/catalog/~/3M-Red-Dot-Foam-Monitoring-Electrodes-2237?N=5640900+4294957412&rt=d (Accessed on 30 January 2015).

[17] Available online: http://www.tmsi.com/products/systems/item/mobi(Accessed on 30 January 2015).

[18] Available online: http://en.wikipedia.org/wiki/Flexor_carpi_radialis_muscle (Accessed on 30 January 2015).

[19] Available online: http://en.wikipedia.org/wiki/Extensor_carpi_radialis_longus_muscle (Accessed on 30 January 2015).

[20] M. Yoshikawa, M. Mikawa, and K. Tanaka, "Real-Time Hand Motion Estimation Using EMG Signals with Support Vector Machines," *in Proc. of the International Joint Conference SICE-ICASE*, pp. 593-598, 2006.

The 7th International Conference on Engineering and Technology
ICET-2015, Phuket, June 19-20, 2015
Prince of Songkla University, Faculty of Engineering
Hat Yai, Songkhla, Thailand 90112

Perceptions of Distributive Justice Among Employees in Country in Transition: The case of the Republic of Serbia

Srecko Stamenkovic[1]*, Biljana Ratkovic Njegovan[2]
[1] University of Novi Sad, Faculty of Technical Sciences, Novi Sad, Serbia
[2]University of Novi Sad, Faculty of Technical Sciences, Novi Sad, Serbia
*Email of corresponding author: srecko@ihrms.rs

Abstract: *This paper discusses the importance of distributive justice in the distribution of the resources of the organization, as well as the perception of employees about the fairness of decisions of managers in that distribution. The paper is based on a survey of the entire territory of the Republic of Serbia, with 4208 respondents, which are divided into two subsamples according to gender female and men, seven subsamples based on age, four subsamples according to the level of the working position, six subsamples according to the number of employees in the organization and two subsamples based on ownership of the company.*
Key Words: ***Distributive Justice / Employees / Job Satisfaction / the Republic of Serbia***

1. INTRODUCTION

To achieve the correct way of managing people in organizations and increase competitiveness, designed by organizational procedures and structure of human resources management system, it is not enough only way to do that. Necessary ethical aspirations of the organization's management to establish justice and equitable climate based on such moral character. This was the main argument to conduct research on the impact of distributive justice on the employees in organizations in Serbia, as well as an understanding of distributive justice with instrumental and moral side of people management in the organization. Distributive justice and the proper management of human resources, unfortunately for employees in Serbians organizations is still far below the level at which it could be described as satisfactory. The implementation of satisfactory distributive justice in Serbia faces a lot of problems, both of objective and subjective nature. Some of the objective issues are a large number of our companies is undergoing transition changes, a certain number of them is preparing for it, in some companies the changes are not on the way, and hence such a situation, including the foreign-owned companies or companies established with a foreign capital, enables a great variety of attitudes, application and values on the distributive justice in Serbia [10]. The reasons for such a situation can be found in the fact that the changes on the labor market are always late compared to changes in economic activities. Yet, it is typical in all countries that after the crisis and lower economic activities follow the stagnation period in employment. Despite the real needs for new job openings, employers wait a certain time to fulfilling those needs. One of the reasons for such a behavior are also the cost of employing new workers, which is a burden for entrepreneurs. Economic growth analysis point to the fact that is necessary to wait for minimum one quarta1 to see the real situation. If it is for any consolation, the situation is the same in the neighboring countries and also in EU countries.

The question of distributive justice and the perception of fairness in the allocation of organizational resources in Serbian theoretical corpus rarely investigated [1]. More or less this is a problematic issue in the organizations themselves and among employees, however, mostly in small companies, but not unusual even in medium-sized companies. How to Serbia in its transition path opted for a sharp neo-liberal concept of economic development, the current economic (dis)advantages encourage debates on issues of justice and fairness in business relationships. Justice and fair treatment as a standards work morale has special significance: it implies a higher moral standard than they do right and regulation, given that equity, except legal, contains the economic dimension, but also the dimension of morality in business [2].

If justice, especially distributive justice in the organization is perceived as injustice, it could negatively affect the morale and employee behavior, for which there is a popular local saying “No one can pay me as low as little I can do”.

2. DISTRIBUTIVE JUSTICE AND JOB SATISFACTION

Distributive justice and represents the perceptions of employees about the fairness of decisions managers in

relation to the distribution of evaluation results, such as salaries, promotions, etc. [5]. Distributive justice recognizes geometric equality, and the rights and obligations allocated according to criteria established by a higher authority.

The most important of all is the attitude of employees attitude towards their work. This position is referred to as job satisfaction and we can define it as "the cognitive, affective and evaluative responses of the individual to his job" [6]. Job satisfaction is, therefore, a complex attitude which involves certain assumptions and beliefs about the job (cognitive component), feelings towards work (affective component) and assessment work (evaluation component). Job satisfaction is one of the most researched topics in the field of human behavior in organizations. The reason for this is certainly rooted belief that a satisfied worker is a productive worker and that the organization's success can not be achieved with disgruntled employees.

Bearing in mind the importance of distributive justice is responsible for organizational behavior, employee loyalty, their attitudes, etc., Conducted a study on the relationship between perceived distributive justice and job satisfaction, which started from the basic assumption that distributive justice contributes to the increase employees job satisfaction.

3. METHODOLOGY

Data processing was planned and implemented in accordance with the objectives of the research and complete research plan. Statistical analysis was performed in MANOVA program for processing data from univariate methods applied to Roy's test. To avoid losing information by finding the finest links and information on nonparametric sizes, scaling is performed on the data tables of contingency. This procedure, based on the frequency, each class a real number. The fact that the scaled values of possible application procedures related to the scale of the situation shows that in this way leads to new discoveries in research, that can not be obtained using methods and procedures related to the non-parametric scales. Scaling the data do not exclude the use of nonparametric tests. Based on the above it is evident that the scaled data possible application of multivariate analysis (MANOVA), discriminant analysis and other parametric procedures and methods. From the univariate procedures shall be implemented Roy's test, Pearson's coefficient of contingency (χ), multiple correlations coefficient (R).

3.1. Sample

Using a self-administered questionnaire, 4208 employees were randomly selected and surveyed. The participants were selected from organizations which represented a wide range of industries. The study included respondents with valid answers, which are divided into 2 subgroups according to gender (female and male), 7 subsamples based on age, 4 subsamples according to the working position (junior, midlevel, top management, basic level), 6 subsamples according to the number of employees in the organization and 2 subgroups according to the type of company ownership. The respondents were representing top, middle and bottom levels of management in different types of organization.

Table 1. *The Description of the Study Sample*

Gender		Age		Job level		Number of employees in org.		Type of ownership	
Male	2140	-18	429	J	2338	-20	1356	P	3480
Female	2068	19-25	1399	ML	1169	21-50	658	S	728
		26-30	1020	TM	411	51-100	599		
		31-35	586	BL	290	101-500	819		
		36-40	349			501-1000	263		
		40-	357 + 68			1000+	513		

3.2. Measures

For the measurement of perceptions of distributive justice is used adopted a six-item distributive justice scale based on previous works. [4]. The measure was assessed on a 5- point scale ranging from 0 “strongly disagree” to 4 “strongly agree”. The Cronbach alpha for the six items was 0.918. The six items were related to distributive justice (alpha value 0.786). Scale items for measuring distributive justice is:

1. How fair has the organization been in rewarding you when you consider the amount of effort that you have put forth?
2. How fair has the organization been in rewarding you when you consider the responsibilities that you have?
3. How fair has the organization been in rewarding you when you consider the stresses and strains of your job?
14. How fair has the organization been in rewarding you when you take into account the amount of education and training that you have?
5. How fair has the organization been in rewarding you when you consider the work that you have done well?
6. How fair the organization been in rewarding you when you consider the amount of experience that you have?

This is presented distributive justice is analyzed in relation to the variable: "I work with satisfaction for my organization."

4. RESULTS

Processing data was planned and implemented in accord with the research goals and the full research concept. For checking the validity of the questionnaire on distributive justice, applied, was the factor analysis,

with the oblique angle Promax rotation. To reduce the variables used was the main components method, and thus the replies from the people surveyed were reduced to the first main component of the suitable subscale. Hence, in addition to descriptive statistics, used was the factor analysis, canonic correlational analysis, t-test, variance analysis and multiple regression analysis.

Table 1. *Influence of distributive justice on job satisfaction*

	χ	r	f	p	k.dsk
Q 1	.043	.032	.896	.466	.003
Q 2	.142	.136	16.140	.000*	.021
Q 3	.079	.059	3.013	.018*	.005
Q 4	.072	.057	2.763	.027*	.006
Q 5	.066	.057	2.827	.024*	.002
Q 6	.090	.068	3.917	.004*	.002

Legend: k.dsk *is the coefficient of discrimination*

Using the enter method, Table 1. gives information for the use of questions to determine the relationship between measured variables of distributive justice and job satisfaction. All questions except question 1 use for distributive justice showed significant predictor of job satisfaction and that is because p <.1 accepts that there is a significant difference between modalities of the measured variables.

5. DISCUSSION

This research was conducted in the Republic of Serbia and covered the entire territory. Also, this research examined the influence of distributive justice on job satisfaction in the Republic of Serbia. The results showed that distributive justice has a significant impact on job satisfaction, and the influence of distributive justice is more pronounced in the less developed areas of the Republic of Serbia than in more developed. The study also shows, that in all the subjects who showed greater satisfaction with justice in the organization, and expressed greater job satisfaction.

Justice as a basis for understanding the employees and their job satisfaction is very dependent on cultural standards, norms and values of organizations and its people [8]. The norms and values of people differ due to the different tradition and cultural backgrounds. Leung and Morris [9] have argued that people's perception of justice may depend on their culture or ethnicity.

5.1. Limitations and Future Research Directions

The measurement instruments were complicated in that they contained numerous scales that had to be cross-correlated for purposes of the study. It is recommended that further research in this area includes more detailed research into the relationship between the demographic variables of employees and distributive justice. Extending similar research to other specific industries and type of ownership of the company (private sector or public sector).

5.2. Implications

The interaction between distributive justice and employees relationship in the organization takes place in the network of relationships between power, desires, demands, needs, organizational structure, organizational and individual goals. A fair and equitable treatment of employees in an organization is considered solely from a legal point of view. That may be one of the reasons why this treatment is not successful in Serbia. Organizations often do not focus on how employees are treated in the workplace. There are no regulations or laws set for regulating humanity of employment. Despite employers having the option of using government funded benefits to improve the treatment of employees, often top management, supervisors, directors or managers ruin the success of initiatives in treating employees poorly. One way of ensuring that employees are treated fairly is to reach and maintain a high level of distributive justice which would entail showing respect and understanding towards employees, to ensure employee participation in solving problems that directly involve them, as well as to ensure employees have enough information and to encourage active participation in creating distributive justice, especially the part that deals with humane and fair relationships between employees.

6. CONCLUSION

Some main conclusions in this first study about distributive justice in the Republic of Serbia can be made. First of all, employees' justice perceptions are a very important predictor of their motivation. This is consistent with the view that distributive justice is associated with a variety of positive work attitudes and behavior. Second, different perceptions of justice by employees, causing a variety of reactions. The direct consequence is reflected in the level of job satisfaction of employees and their view of the decisions of the organization, the way decisions were made and the quality of communication among employees. Third, perception of distributive justice is an important impeller of the organization's staff. If employees are treated fairly they will strive to be more productive at work and their sense of belonging to the organization, will be stronger.

5. REFERENCES

[1] B. Mirković, "Psihometrijska provjera i validacija skale organizacijske pravde na srpskom uzorku" ["Psychometric testing and validation of the scale of organizational justice on the Serbian sample"],

Primjenjena psihologija, 2014, Vol. 7, No. 4, pp. 599–619.

[2] B. R. Njegovan, *Poslovna etika*, [*Business Ethics*], 2013, Faculty of Technical Sciences, Novi Sad.

[3] Fernandes, C. & Awamleh, R. (2006). "Impact of Organizational Justice in an Expatriate Work Environment," Management Resources News, 29 (11), 701- 712.

[4] Curry, J. P., Wakefield, D. S., Price, J. L., Mueller, C. W. (1986). On the causal ordering of job satisfaction and organizational commitment. Academy of Management Journal, 29, 847-858.

[5] J. Greenberg, "The seven loose can(n)ons of organizational justice", in J. Greenberg and R. Cropanzano, R. (Eds.), *Advances in Organizational Justice*, 2001, Stanford University Press, Stanford, CA, pp. 245–271.

[6] K. Leung and M. W. Morris, "Justice through the lens of culture and ethnicity", in J. Sanders and V. L. Hamilton (Eds), *Handbook of Justice Research in Law*, 2001, Springer, US, pp. 343–378.

[7] Rad AM, Yarmohammadian MH (2006). A study of relationship between managers leadership style and employees job satisfaction. Leadership and Health Service. 19(2): xi – xxviii.

[8] R. Folger, M. A. Konovsky, "Effects of distributive and procedural justice on reactions to pay raise decisions", *Academy of Management Journal*, 1998, Vol. 32, No. 1, pp. 115–130.

[9] Richard L. Oliver, "Cognitive, Affective, and Attribute Bases of the Satisfaction Response", *Journal of Consumer Research*, Vol. 20, No. 3 (Dec., 1993), The University of Chicago Press, pp. 418-430.

[10] S. Stamenkovic, "Organizaciona pravda kao pokazatelj kvaliteta upravljanja ljudskim resursima u organizacijama u Srbiji", ["Organizational justice as an indicator of quality of human resources management in organizations in Serbia"], *Megatrend Revija*, 2/2013, Vol.10, No. 2, pp. 249–270.

The 7th International Conference on Engineering and Technology
ICET-2015, Phuket, June 19-20, 2015
Prince of Songkla University, Faculty of Engineering
Hat Yai, Songkhla, Thailand 90112

Dual Mode Impedance Controller for Safe Human-Robot Interaction

Srđan Savić, Branislav Borovac, Mirko Raković, Milutin Nikolić
University of Novi Sad, Faculty of Technical Sciences.
* Email of corresponding author: savics@uns.ac.rs

Abstract *This paper presents the dual mode control algorithm, based on impedance control, for safe human-robot interaction. Proposed algorithm guarantees accurate trajectory tracking during free space motion and safe and compliant behavior in contact tasks, during human-robot interaction. Two control modes of the robot controller have been proposed: joint space impedance control with redundancy resolution for unconstrained motion and controlled gravity compensation for operating in the vicinity of humans. Performance of the proposed control has been verified through a numerical simulation of 7 DOFs (Degrees Of Freedom) robot arm movements.*

Key Words: ***assistive robot/ impedance control/ compliant control/controlled gravity compensation***

1. INTRODUCTION

Physical human-robot interaction and cooperation has become a topic of increasing importance and of major focus in robotics research [1]. A lot of effort has been made to incorporate the robots and humans in a coexisting environment and to provide their cohabitation. It is a challenging task to design an appropriate control algorithm for robot motion, witch will guarantee the safety of the humans in the robot's surrounding during contact tasks and physical interaction. Interaction control has been the research topic for more than 30 years. A survey of robot interaction control schemes, based on static and dynamic model-based compensations is given in [2]. Another survey on robot-environment dynamic interaction, with a historical perspective on interaction control is given in [3]. The idea of impedance control was presented a long time ago [4]. In this paper dual mode controller for compliant and safe human robot interaction, based on impedance control, is proposed. The idea is to use the joint space impedance control with redundancy resolution for unconstrained motion, which allows accurate trajectory tracking in unconstrained directions and compliant behavior in the constrained one. Controlled gravity compensation is used for constrained motion in interaction with humans. In gravity compensation mode, current position is permanently taken as the desired one, while the desired velocity and acceleration are zero. This allows the human user to move the compliant robot arm in the space and provides safe interaction.

2. MOTION PLANNING AND REDUNDANCY RESOLUTION

Motion planning, used in simulation, is based on setting the desired target point in the workspace to which the robot hand is supposed to move rectilinear. The direction of the desired TCP (Tool Center Point) velocity vector is such that vector points towards the target position in each time instant [5]. Desired velocity profile used in our simulation is based on the way how reaching task is realized by humans. Movement of a human's hand is approximately rectilinear, fast in the beginning and slower when it approaches the target [6].T here are three different phases of motion: acceleration phase, cruising phase with constant velocity and deceleration phase. Velocity profile is generated as S-shaped spline-based curve. Generated TCP velocity profile (scalar value) is multiplied with unit vector of the position error vector, which points from current TCP position towards target point, in order to obtain operational space velocity vector $\dot{\mathbf{x}}_d$. More details about trajectory generation can be found in [5].

Once the profile of the desired operational space velocity $\dot{\mathbf{x}}_d(t)$ is known, it is necessary to determine the vector of desired joint velocities $\dot{\mathbf{q}}_d$ as:

$$\dot{\mathbf{q}}_d = \mathbf{J}^{\dagger}\mathbf{v} + \left(\mathbf{I} - \mathbf{J}^{\dagger}\mathbf{J}\right)\dot{\mathbf{q}}_h, \qquad (1)$$

where $\mathbf{J}^{\dagger} = \mathbf{J}^T\left(\mathbf{J}\mathbf{J}^T\right)^{-1}$ is the right pseudo-inverse of the Jacobian matrix. Vector $\dot{\mathbf{q}}_h$ is projected into the null space of Jacobian and enables us to exploit system redundancy to solve the additional constraint, which is in our case avoiding joint mechanical limits. Vector $\dot{\mathbf{q}}_h$ can be chosen in the following way:

$$\dot{\mathbf{q}}_h = k_0\left(\frac{\partial\omega(\mathbf{q})}{\partial\mathbf{q}}\right)^T, \ \omega(\mathbf{q}) = -\frac{1}{2n}\sum_{i=1}^{n}\left(\frac{\mathbf{q}_i - \bar{\mathbf{q}}_i}{\mathbf{q}_{iMAX} - \mathbf{q}_{iMIN}}\right) \qquad ,(2)$$

where k_0>0 and $\omega(\mathbf{q})$ is the secondary objective function which maximizes the distance from joint mechanical

limits. Vectors $\mathbf{q}_{iMAX}$, $\mathbf{q}_{iMIN}$ and $\bar{\mathbf{q}}_i$ are maximum and minimum joint limits and middle values of the joint ranges, respectively [7]. Desired angular positions and accelerations are obtained by integrating and differentiating desired velocity, respectively.

3. CONTROL ALGORITHM

Two control modes have been proposed for possible robot applications. First mode covers free motion where impedance control behaves in the same way as the inverse dynamics control and provides trajectory tracking, under the assumption that the dynamic model is known, and constrained motion during object manipulation where impedance controller parameters are chosen to provide good positioning accuracy in unconstrained directions and small contact forces in direction of contact. Stereo vision should provide information in which direction the contact is expected. It is assumed in this case that force/torque measurement is provided. Second control mode is controlled gravity compensation [8]. The controller switches to this mode when the robot is in the close vicinity of a human being in order to provide safe human-robot interaction and prevent generation of large impact forces during contact with a human being.

3.1 Impedance control

Humanoid robot is highly nonlinear, coupled and multivariable system and its dynamic model is given with:

$$\mathbf{H}(\mathbf{q})\cdot\ddot{\mathbf{q}}+\mathbf{C}(\mathbf{q},\dot{\mathbf{q}})+\mathbf{G}(\mathbf{q})=\boldsymbol{\tau}+\mathbf{J}^T\mathbf{F}_{ext}, \qquad (3)$$

where $\boldsymbol{\tau}$ is vector of driving torques, $\mathbf{q}$ is vector of generalized coordinates, $\mathbf{H}(\mathbf{q})$ is symmetric, positive-definite inertia matrix, $\mathbf{C}(\mathbf{q},\dot{\mathbf{q}})$ is vector of torques due to Coriolis and centrifugal forces, $\mathbf{G}(\mathbf{q})$ is vector of torques caused by gravitational forces, $\mathbf{J}$ is Jacobian matrix and $\mathbf{F}_{ext}$ is vector of external force, exerted by the environment on the robot's end effector.

Under the assumption of known dynamic model, feedback linearization has been used in order to cancel system nonlinearities and reduce the original system to a system of double integrators. Control torque is chosen in the following way:

$$\boldsymbol{\tau}=\mathbf{H}(\mathbf{q})\mathbf{a}+\mathbf{C}(\mathbf{q},\dot{\mathbf{q}})+\mathbf{G}(\mathbf{q})-\mathbf{J}^T\mathbf{F}_{ext}, \qquad (4)$$

where $\mathbf{a}$ is the new control input. Substituting (4) into dynamic model (3), system dynamics is now reduced to the system of double integrators $\ddot{\mathbf{q}}=\mathbf{a}$.

Control input $\mathbf{a}$ should be appropriately chosen to provide the desired dynamic relation between the contact force and displacement error, described by the impedance model. Operational space impedance is described with the following differential equation:

$$\mathbf{H}_m(\ddot{\mathbf{x}}-\ddot{\mathbf{x}}_d)+\mathbf{D}_m(\dot{\mathbf{x}}-\dot{\mathbf{x}}_d)+\mathbf{K}_m(\mathbf{x}-\mathbf{x}_d)=\mathbf{F}_{ext}. \qquad (5)$$

Matrices $\mathbf{H}_m, \mathbf{D}_m$ and $\mathbf{K}_m$ are desired inertia, desired damping and desired stiffness, respectively. These matrices have to be Hurwitz matrices to provide the stability of the system and convergence of displacement error to zero, in case of free motion, or to some equilibrium value, in case of contact with the environment. These matrices are also diagonal, which means that impedance is decoupled for each operational space direction.

Under the assumption that manipulator velocities are small, Jacobian derivative can be neglected, because it will have a small value. In order to provide joint space impedance model following kinematic and static relations are used:

$$d\mathbf{x}=\mathbf{J}(\mathbf{q})d\mathbf{q}, \quad \dot{\mathbf{x}}=\mathbf{J}(\mathbf{q})\dot{\mathbf{q}},$$
$$\ddot{\mathbf{x}}=\mathbf{J}(\mathbf{q})\ddot{\mathbf{q}}+\dot{\mathbf{J}}(\mathbf{q},\dot{\mathbf{q}})\dot{\mathbf{q}}\approx\mathbf{J}(\mathbf{q})\ddot{\mathbf{q}}, \quad \boldsymbol{\tau}_{ext}=\mathbf{J}^T\mathbf{F}_{ext}, \qquad (6)$$

If the displacement error, in the joint space, is denoted with $\tilde{\mathbf{q}}=\mathbf{q}-\mathbf{q}_d$ than Substituting (8) in (5) joint space impedance model is obtained:

$$\mathbf{J}^T\mathbf{H}_m\mathbf{J}(\ddot{\mathbf{q}}-\ddot{\mathbf{q}}_d)+\mathbf{J}^T\mathbf{D}_m\mathbf{J}(\dot{\tilde{\mathbf{q}}})+\mathbf{J}^T\mathbf{K}_m\mathbf{J}(\tilde{\mathbf{q}})=\mathbf{J}^T\mathbf{F}_{ext}, \qquad (7)$$

If the acceleration is expressed from (9), an expression for new control input $\mathbf{a}$ is obtained which will provide the system to behave according to the impedance model:

$$\mathbf{a}=\ddot{\mathbf{q}}_d+\mathbf{J}^{\dagger}\mathbf{H}_m^{-1}\left(\mathbf{J}^{\dagger}\right)^T\left[\mathbf{J}^T\mathbf{D}_m\mathbf{J}\dot{\tilde{\mathbf{q}}}+\mathbf{J}^T\mathbf{K}_m\mathbf{J}\tilde{\mathbf{q}}+\mathbf{J}^T\mathbf{F}_{ext}\right]. \qquad (8)$$

It can be noticed that inertia, damping and stiffness are constant in Cartesian space ($\mathbf{H}_m, \mathbf{D}_m$ and $\mathbf{K}_m$) but variable and configuration dependent in joint space. When there is no external force $(\mathbf{F}_{ext}=0)$ impedance controller actually becomes pure inverse dynamics controller and achieves trajectory tracking. When there is a contact between robot and environment, external force is not zero, and tracking error in the constrained direction increases. Elements of matrices $\mathbf{H}_m, \mathbf{D}_m$ and $\mathbf{K}_m$ are appropriately chosen to provide small contact forces in the constrained direction. Substituting (8) into (4) gives the final expression for torque control input.

3.2 Controlled gravity compensation

During the therapy robot should never get in physical contact with human being, but for safety reasons, compliant robot behavior must be provided. Hence, when the stereo vision system detects human being in the close vicinity of the robot, motion controller switches to the gravity compensation mode. In this case impedance control is used to actively imitate the behavior of robot with pure gravity compensation. Due to a compliance of an impedance controller, user is able to move the robot arm through physical interaction. The idea is to take the current robot position as a reference, desired position for the impedance controller in each time instant. Desired velocity and acceleration are zero, since the robot should keep its current position when there is no external force.

$$\mathbf{q}_d(t)=\mathbf{q}(t),\ \dot{\mathbf{q}}_d(t)=0,\ \ddot{\mathbf{q}}_d(t)=0, \qquad (9)$$

Substituting (11) into (10) control input $\mathbf{a}$ is obtained, which provides behavior similar to pure gravity compensation:

$$\mathbf{a}=\mathbf{J}^{\dagger}\mathbf{H}_m^{-1}\left(\mathbf{J}^{\dagger}\right)^T\left[\mathbf{J}^T\mathbf{D}_m\mathbf{J}(-\dot{\mathbf{q}})+\mathbf{J}^T\mathbf{F}_{ext}\right]. \qquad (10)$$

Damping term on the right hand side of (10) prevents position drift when the external force disappears. Substituting (10) into (4) gives the final expression for torque control input.

4. SIMULATION RESULTS

Performance of the impedance controller for two different control modes has been verified through a numerical simulation. Both simulations have been performed only for the 7 DOFs robot arm while the robot torso was fixed. The robot arm is modeled using software we have already developed and used for modeling. The software is capable of forming dynamic model of humanoid robots [9] and simulating robots with one or more open and closed kinematic chains. Segments are connected with joints having one rotational degree of freedom, each.

First simulation shows scenario where robot is in contact with the environment. Robot is writing a square on a board in front of itself. Stick diagram of simulated contact task is shown in Figure 5.

The board is modeled as an elastic element with high stiffness. Contact force is given with the following expression

$$\mathbf{F}_{ext} = \mathbf{K}_A\left(\mathbf{x}_e - \mathbf{x}\right), \mathbf{K}_A = diag\left\{k_x, k_y, k_z\right\}, \quad k_x = 10^4 \text{ N/m}, k_y = 0 \text{ N/m}, k_z = 0 \text{ N/m} \quad (11)$$

where $\mathbf{x}_e$ is the undeformed environment rest position, and $\mathbf{K}_A$ is environment stiffness matrix. Following parameters have been chosen for the impedance model:

$$\mathbf{H}_m = diag\left\{10,100,100\right\}, \quad \mathbf{K}_m = diag\left\{250,2500,2500\right\}, . \quad \mathbf{D}_m = diag\left\{500,500,500\right\} \quad (12)$$

Since impedance model (5) is linear, second order system, following relationship can be established between parameters of the impedance model and damping coefficient ξ and undamped natural frequency ω_n in constrained direction (X-axis) and unconstrained directions (Y and Z-axes):

$$\xi_x = \frac{d_{m_x}}{2\sqrt{h_{m_x}\left(k_{m_x} + k_x\right)}} = 0.78, \ \omega_{n_x} = \sqrt{\frac{k_{m_x} + k_x}{h_{m_x}}} = 32, \quad (13)$$

$$\xi_y = \xi_z = \frac{d_{m_x}}{2\sqrt{h_{m_x} k_{m_x}}} = 0.5, \ \omega_{n_y} = \omega_{n_z} = \sqrt{\frac{k_{m_x}}{h_{m_x}}} = 5. \quad (14)$$

Since damping coefficient has value between 0 and 1, the system will be damped with a small overshoot but with a faster response. The environment in the simulation was modeled as very stiff ($k_x = 10^4$ N/m). Therefore, the controller stiffnes was reduced in the direction of contact (X-axis) in order to obtain compliant behavior of the robot.

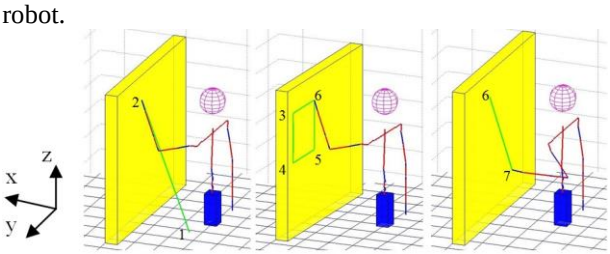

Fig. 5 *Stick diagrams of simulated arm movements: robot arm approaching the board (left); Writing a square while in contact with the board (middle); Robot arm detaching from the board (right)*

In the direction of free motion accurate trajectory tracking, without overshoot, has been achieved and robot successfully follows the desired square path in the Y-Z plane. Robot TCP trajectory and desired TCP positions in Y and Z direction are shown in Figure 6. Robot successfully achieves trajectory tracking in the unconstrained directions and keeps the contact force bounded in the constrained directions by decreasing the desired positioning accuracy.

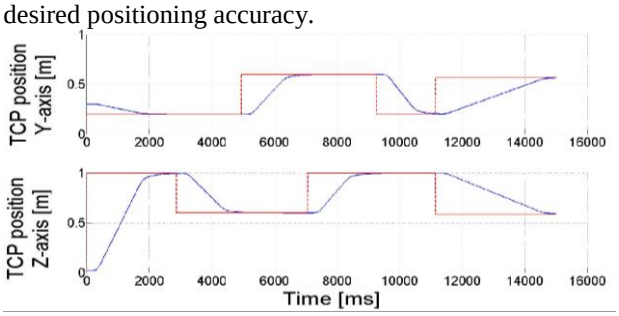

Fig. 6 *Actual position of the robot TCP (blue) and desired TCP position (red) for Y and Z axes*

Friction between the robot arm and board was neglected in the robot dynamics model. Since the motion in Y-Z plane is unconstrained, and tangential component of the friction force is zero, there is no contact force in Y and Z direction. Contact force in the X direction depends on the board deformation, and it is shown in Figure 7.

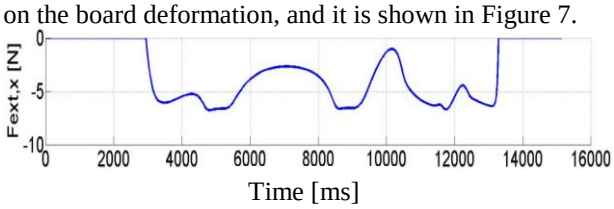

Fig. 7 *X component of the contact force*

It can be seen from Fig. 7 that contact force, exerted by the environment, in the X-axis direction is bounded and has a small amplitude value between -6 N and -7 N. In the approaching and detaching phase robot is not in contact with the board, so the contact force is zero.

In the second simulation controlled gravity compensation mode of the controller, for achieving safe and compliant robot behavior in presence of humans, has been tested. Stick diagram of the simulated movement is shown in Figure 8. At the beginning of simulation robot arm is in free motion and follows the desired rectilinear trajectory using impedance control. At approximately half of the trajectory, external force $\mathbf{F}_{ext1}$ starts acting on the robot hand in negative Z direction and robot controller switches to the controlled gravity compensation mode. In this phase, motion of the arm is driven by the external force. After $\mathbf{F}_{ext1}$ becomes zero, robot arm stops and keeps the current position for two seconds. Then external force $\mathbf{F}_{ext2}$ starts acting in negative Y direction and drives the arm in a new position. When $\mathbf{F}_{ext2}$ decreases to zero robot arm keeps the current position for two more seconds and than continuous to move towards the desired target point in the workspace. First external force vector is defined as $\mathbf{F}_{ext1} = \begin{bmatrix} 0 & 0 & -f_1 & 0 & 0 & 0 \end{bmatrix}^T$ and the second one as

$\mathbf{F}_{ext2} = [0 \quad -f_2 \quad 0 \quad 0 \quad 0 \quad 0]^T$, where the profile of f_1 is shown in Figure 8. Profile of f_2 is the same as f_1, but it acts between 4 s and 5 s.

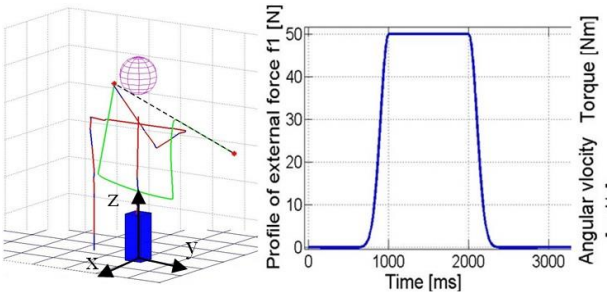

Fig. 8 *Stick diagram of robot motion in controlled gravity compensation mode: desired trajectory- dashed line, real trajectory-green line (left); Profile of the external force f_1 (right)*

Velocity and torque of the elbow joint are shown in Figure 9 and it can be noticed that after 2 s, when external force decreases to zero, there is a short transient period where the damping term is decreasing the velocity to zero. So, the damping term from (12), prevents the joint from drifting, after the external force vanishes. Torque at the elbow joint, in the time range where external force $\mathbf{F}_{ext1}$ acts, has slightly higher value than in the range of action of $\mathbf{F}_{ext2}$. This is due to the robot configuration in these two specific time ranges. In the time range between 1-2s robot configuration is such that the elbow joint is under a significant influence of gravity and external force while between 4-5s gravity force is more compensated by other joints.

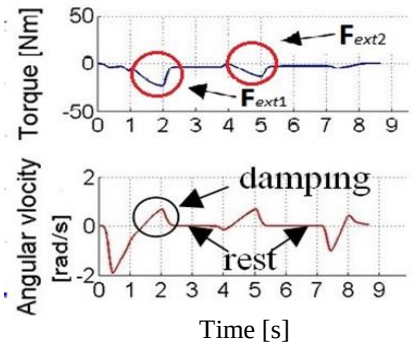

Fig. 9 *Graphic of angular velocity and torque for elbow joint (right)*

After transient, robot arm keeps the current position until the external force $\mathbf{F}_{ext2}$ starts acting on the system. Results show that impedance controller is capable of achieving compliant behavior similar to the gravity compensation. In the presence of an external disturbance robot arm motion is compliant and driven by the external force. In the absence of the external force robot arm keeps the current position.

5. CONCLUSIONS

In this paper dual mode control algorithm for safe human-robot interaction, based on joint space impedance control, was presented. Performance of the impedance control was tested through numerical simulations for two different operating modes. First case is constrained motion, where robot is in contact with its environment. Results have shown that robot with impedance controller is able to achieve accurate trajectory tracking in unconstrained directions while containing the contact force bounded. Second simulation tested the performance of the impedance controller in controlled gravity compensation mode, which should be used when robot is in contact or in a close vicinity of a human. Results have shown that controlled gravity compensation provides safe and compliant behavior, where the robot motion is driven by the action of external force.

6. REFERENCES

1. Haddadin S., Albu-Schäffer A., Hirzinger G.: Safe Physical Human-Robot Interaction: Measurements, Analysis & New Insights, Robotics Research: Springer Tracts in Advanced Robotics, Vol. 66, pp. 395-407, (2011)
2. Chiaverini S., Siciliano, B. ; Villani, L.: A survey of robot interaction control schemes with experimental comparison, IEEE/ASME Transactions on Mechatronics, Vol. 4, Issue 3, pp. 273-285, (1999)
3. Vukobratovic M.: Robot-environment dynamic interaction survey and future trends, Journal of Computer and Systems Sciences International, Vol. 49, Issue 2, (2010)
4. Hogan N.: Impedance Control: An Approach to Manipulation: Part II—Implementation, J. Dyn. Sys., Meas., Control, Vol. 107, Issue 1, (1985)
5. Savić S., Raković M., Nikolć M. and Borovac B.: SVM Regression-Based Computed Torque Control of Humanoid Robot Reaching Task. In Proceedings of IcETRAN 2014, Vrnjacka Banja, Serbia, 04.-07. June, (2014)
6. Konczak J. and Dichgans J.: The development toward stereotypic arm kinematics during reaching in the first 3 years of life. Exp Brain Res, vol. 117, no. 2, pp. 346–354, (1997)
7. Sciavicco L. and Siciliano B.: Modelling and Control of Robot Manipulators, 2nd ed. London, Great Britain, Springer-Verlag, (2005)
8. Wrede S., Emmerich C., Grünberg R., Nordmann A., Swadzba A. and Steil J.: A User Study on Kinesthetic Teaching of Redundant Robots in Task and Configuration Space. Journal of Human-Robot Interaction, Vol. 2, No. 1, (2013)
9. Potkonjak V., Vukobratović M., Babković K. and Borovac B.: General model of dynamics of human and humanoid motion: feasibility, potentials and verification. Int. Jour. of Humanoid Robotics, Vol. 3, No. 2, pp. 21-48, (2006)

The 7th International Conference on Engineering and Technology
ICET-2015, Phuket, June 19-20, 2015
Prince of Songkla University, Faculty of Engineering
Hat Yai, Songkhla, Thailand 90112

Air Quality modeling: Case study Novi Sad

Bogdana Vujic[1]*, Milan Pavlovic[1], Aleksandar Tomovic[1],
[1]Universityof Novi Sad , Technical Faculty "Mihajlo Pupin", Zrenjanin, Serbia
*bogdana.vujic@tfzr.rs

Abstract: *Air quality assessment is very important task considering the the fact that air pollution is significant in terms of human health and the environment. For that purpose, in this paper, simulation of NO_2 dispersion, using the ADMS Urban software, has been conducted. NO2 emission from the heating station which produces thermal energy for households heating in Novi Sad and in whose surroundings are facilities for individual and collective housing, hospitals, schools, hotels etc. were used.*

Pollution dispersion of three typical meteorological scenarios for the given period show the most common directions, intensity of the dispersion as well as the most frequent concentration levels of NO_2.

Key Words: ***Air quality /Modeling /Pollution dispersion***

1. INTRODUCTION

Air pollution is one of the most serious environmental threats in the global world. 71% of the world s cities nitrogen dioxide emissions, often associated with automobile use exceeded WHO maximums [1]. One of the dominant characteristics related to air quality in urban areas it's changing in character and intensity at different time scale and mostly depends on the emissions from individual sources, the number and density of emission sources, topography and atmospheric and meteorological conditions. Therefore, air quality assessment is very important task considering the fact that air pollution is still significant in terms of human health and the environment. Because of the complex influence of many factors on the air quality, for determining ambient air quality, different methods of measurement, mathematical calculations, predictions or assessments (modeling) are being usedThe most significant pollutants in urban areas are particulate matter, NO_x, VOC, CO, O_3. [2]. Anthropogenic activities, such as traffic, industrial combustion processes as well as thermal energy production, contribute to high concentrations of nitrogen oxides in urban areas. [4]. Regardless of whether viewed as a primary or a secondary pollutant, NO_2 certainly affects human health. Epidemiological studies have shown that symptoms of bronchitis in asthmatic children increase in association with long-term exposure to NO_2. Reduced lung function growth is also linked to NO_2 at concentrations currently measured (or observed) in cities of Europe and North America [5]. The effects of short-term exposure are still unclear, but continued or frequent exposure to concentrations that are typically much higher than those normally found in the ambient air may cause increased incidence of acute respiratory illness in children [3].

In order to protect human health, limit values are set for different time scales (Table 1)

Table 1- Limit values (LV) for NO2 defined by Sebian legislation [6], WHO[7], and USEPA[5]..

	Serbia	WHO	USEPA
LV (1h)	*150 µg/m^3	200µg/m^3	100ppb
LV (24h)	85 µg/m^3	-	-
LV(Year)	40 µg/m^3	40 µg/m^3	53ppb

*Must not overreach 18 times in a calendar year

Like any urban environment, Novi Sad (335 701 inhabitants [8]) with the presence of heterogeneous sources of emissions, is facing a variety of challenges in terms of air quality management.The traffic has enormous impact on air quality, but during the winter months the emissions from the heating station system significantly contribute to the total NO_2 concentration. The greater part of the Novi Sad urban area are collective residences that are connected to the district heating system, while the suburbs are mainly oriented towards individual housing and individual heating. Technical heating station system consists of six heating plants that use gas as the main energy source [9]. This paper considers the emission from heating plant in Novi Sad, which has the largest capacity and supplies the biggest town surface with heat energy. H eating season officially starts from 15th of October until the 15th of April and lasts 13 hours per day (7am-8pm). However, in extreme weather conditions or when temperatures are very low (a few degrees below zero), inhabitants are supplied with heating for 24 hours. Continuous production of heat energy in combination with other sources, such as traffic in combination with adverse weather conditions can lead to the accumulation of pollution.

NO_2 concentrations in urban areas are monitored for nearly two decades in the network of measurement stations in Serbia [10]. Although the results show that the average annual values of NO_2 for Novi Sad are below the LV [11,12], its impact on pollution should not be ignored.

In this paper, using ADMS Urban software, simulation of the NO_2 dispersion from the local heating plant has been conducted. Simulation was performed for several scenarios that represent different weather conditions typical for the winter period.

2. MATERIAL AND METHODS

2.1. Study area

The simulation was carried out in part of the town, which in its neighborhood has residential buildings for individual and collective housing, hospital, primary school and hotel (Figure 1).

Figure 1- Illustration of the study area

2.2. Modeling

The ADMS-Urban (Atmospheric Dispersion Modelling System) is a multiple-source Gaussian dispersion model developed by Cambridge Environmental Research Consultants, which have ability to describe in detail what happens on a range of scales, from the street scale to the city-wide scale, taking into account the whole range of relevant emission sources: traffic, industrial, commercial, domestic and other less well-defined sources [13].

2.3. Input data

Meteorological data

The data required for modeling include two sets of meteorological data: surface heat flux variables (year/day/time/cloud cover or sufrace sensibile heat flux) and obligatory paramers (boubdary layer height, surface temperature, lateral spred, relative humidity). For this simulation following meteo parameters were used : year/day/time/cloud cover, surface temperature, wind speed and direction, as well as relative huidity [14,15,16]

Emission data

Data about the source of emissions (height and width), averaged annual data of waste gases (speed, volume, temperature) as well as the annual average NO_2 concentrations were obtained from a competent company whose business is supplying citizens with thermal energy.

3. RESULTS AND DISCUSSION

One of the important factors that influence dispersion and distribution of pollutants is meteorological data. In this study a detailed analysis of meteorological data (2011- 2013) for the winter months (the heating season) have been made. The analysis of meteorological parameters that are important for modeling have been presented hereinafter.

Meteorological data (2011-2013) show that the lowest temperatures are more often in February (Table 2.)

Table 2. Average temperature during the winter months

	January			February		
	2011	2012	2013	2011	2012	2013
Min	-3,1	-1,3	-0,5	-3,0	-8,6	3,2
Max	3,6	5,5	5,8	3,5	-1,8	9,5
Average	0,1	1,7	2,3	-0,2	-4,9	4,8
	March			November		
	2011	2012	2013	2011	2012	2013
Min	1,2	1,2	1,2	-0,9	5,2	5,1
Max	11,0	15,6	10,3	7,5	14,1	13
Average	6,0	8,1	5,4	2,8	9,1	8,4
	December					
	2011	2012	2013			
Min	1,2	-2,3	-1,8			
Max	8,0	3,4	5,9			
Average	4,2	0,3	1,6			

During the winter months fluctuations in air temperature are very frequent, so that only in a few days the temperature changed for more than 10 ° C can be recorded. The graph shows temperature fluctuations for the period of 17th-21st of January 2011, when in only a few of days temperature changed for 15°C (Graph1).

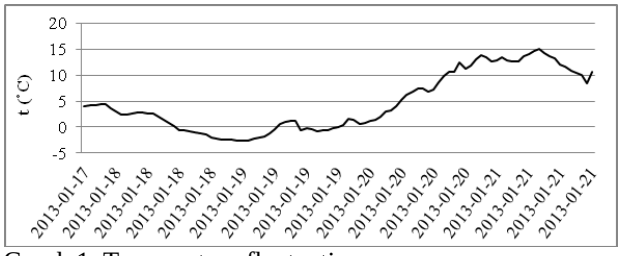

Graph 1. Temperature fluctuations

Meteorological data analysis showed that the dominant winds in the winter season are western (W), eastern (E), with the most common speed in the class up to 2.1 m / s, followed by east-north-east (NE) west-north-west (NW) with the most common speed in the class up to 2.1 m / s, as well as east-south east (ESE) with equal speed level up to 2.1m / s and 3.6m / s (Graph 2).

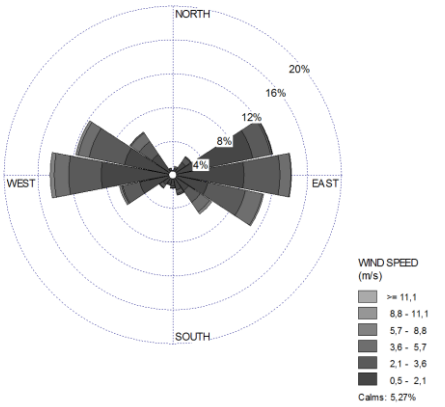

Graph 2. Dominant wind direction (˚) and speed (m/s) [17]

It is certain that the weather conditions greatly affect dispersion and movement of pollutants. Therefore, this paper will present simulation for several scenarios of meteorological conditions that are typical for the winter period. Those are:

Scenario1: simulation for the day when the recorded temperatures were below zero, at the highest cloudiness and relatively low eastern wind speeds in the class up to 2.1 m / s (Figure 2).

Scenario 2: simulation for the day with low temperatures, cloudiness and relatively high eastern wind speeds, in the class of 5.5-8.8m / s (Figure 3).
Scenario3: simulation for the day when the temperature was above the average for that time of the year with relatively clear sky and low eastern wind speeds (Figure 4).

Simulations for pollutant dispersion at different heights were conducted, starting from the source height. The figures show the concentration on 1.5 m, which is taken as the inhalation height.

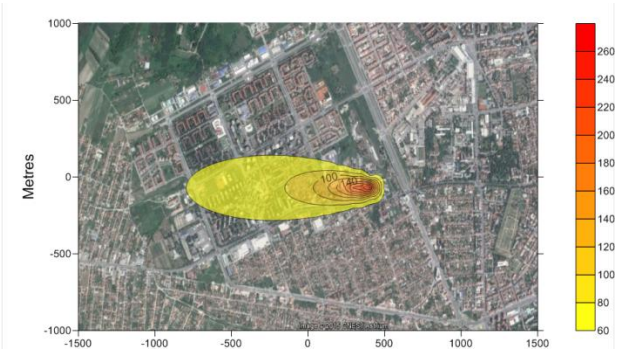

Figure 2 - Pollutant dispersion for meteorological data of Secnario 1

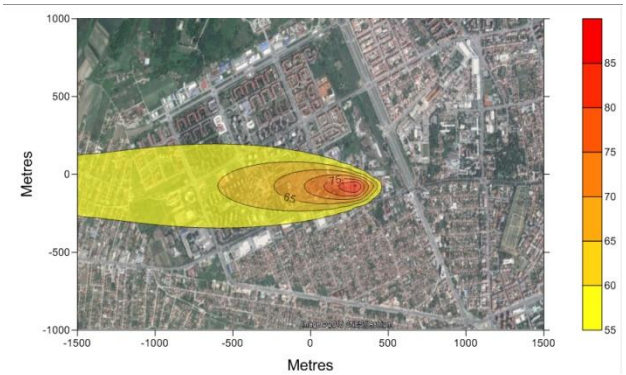

Figure 3. - Pollutant dispersion for meteorological data of Secnario 2

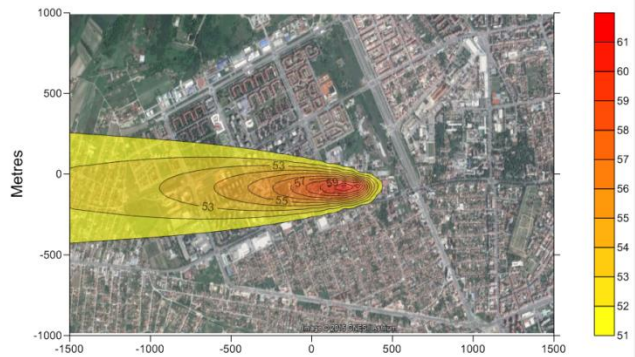

Figure 4. - Pollutant dispersion for meteorological data of Secnario 3

Based on the conducted simulations it can be concluded that the dispersion of pollution from the observed sources is the most intense during the days that are characterized as cold (-5˚C), cloudy (8/8octas) and with relatively low wind speeds (up to 2.1 m/s) (Scenario 2). Meteorological conditions that are characterized as above the average for the winter period, i.e. the day with less cloud cover (2/8octas) relatively high temperature (10°C) and with relatively low wind speeds (up to 2.1 m/s) (Scenario 3) also show significant pollutant dispersion, but less compared to the Scenario 2. As the most favorable scenario, i.e. meteorological conditions in which the smallest surface area is affected by pollution, is Scenario 1. Those are meteorological conditions with relatively low temperatures of (5˚C), the high wind speeds (up to 8.8m/s) and total cloudiness (8/ 8octas).

Regardless of the dispersion intensity, the concentration of NO_2 in the modeled plumes is approximately 50 µg/m^3, which is below the LV (1hr) (Table 1).

4. CONCLUSION

Based on the results obtained by simulation, it can be concluded that the pollution dispersion from observed sources is the most intensive in Scenario 2. Meteorological conditions in Scenario 3 also show significant pollutant dispersion, but less compared to Scenario 2. Meteorological condition, in which the smalest urban area is under influence of the pollution plume, ie. when the dispersion of NO_2 is the smallest, is

Scenario 1. Modeled NO_2 concentration levels are below the LV (1h) for all three scenarios.

Air quality assessment is a very important task given the fact that air pollution is still significant in terms of human health and the environment. Modeling is a complex process that involves a series of procedures which among other things include careful selection and analysis of input data whether it is the data about the emissions source, pollution carasteristic or concentration or meteorological conditions. For verificarion of the modeling results it is desirable to have background concentrations of observed pollutant.

4. REFERENCES

[1] World Bank, World Development Indicators : Some World watch calculation based on data, 2003, Pages 168-169 (Washington, DC: 2003)

[2] J. Fenger , Urban Air Quality, *Atmospheric Environment* 1999,Vol.33, pp. 4877-4900

[3] Unated States Environmental Agency, www. usepa.gov

[4] Europes Environment: *The Third Assessment. Environmental Assessment Report*, Copenhagen, Denmark , EEA, 2003: www.eea.europa.eu/publications/environmental_assessment_report_2003_10

[5] Health Aspects of Air Pollution with Particulate Matter Ozone and Nitrogen Doixide Report on a WHO Workong Group, 2003, Bonn, Germany.

[6] Bylow on air quality monitoring requirements (Official Gazette RS No11/10)

[7] World Health Organisation, www.who.org

[8] Popis stanovnistva, domacinstava i stanova u Republici Srbiji 2011. - Republički zavod za statistiku

[9] http://www.nstoplana.rs/

[10] B.Vujić, V. Kerleta: The development of ambient air quality monitoring on APV territory, 2. International Conference "*Ecology of urban areas 2012*", Zrenjanin, 15 Oktobar, 2012, pp. 45-52, ISBN 978-86-7672-172-6

[11] Annual Raport on air Quality in Republic of Serbia 2012, www.sepa.gov.rs

[12]Annual Raport on air Quality in Republic of Serbia 2013, www.sepa.gov.rs

[13] CERC, 2001. ADMS-Urban: Urban Air Qualita` Management System. User Guide. Version 3.4. CERC Limited, Cambridge,/www.cerc.co.uk.

[14] Meteorological yearbook- climatological data 2011, www. hidmet.gov.rs

[15] Meteorological yearbook- climatological data 2012, www. hidmet.gov.rs

[16] Meteorological yearbook- climatological data 2013, www. hidmet.gov.rs

[17] WRPLOT VIEW, Wind Rose Plots for Meteorological Data, 1998-2011 Lakes Environmental Software, Version 7.0

The 7th International Conference on Engineering and Technology
ICET-2015, Phuket, June19-20, 2015
Prince of Songkla University, Faculty of Engineering
Hat Yai, Songkhla, Thailand 90112

Implementing Augmented Reality in Disassembly Process

Srdjan Tegeltija[1], Milovan Lazarevic[2], Stevan Stankovski[3], Gordana Ostojic[4*]
[1]University of Novi Sad, Faculty of Technical Sciences, Novi Sad, Serbia
[*]Email of corresponding author: goca@uns.ac.rs

Abstract: *The purpose of the paper is to introduce possibilities of implementation of augmented reality (AR) concept in disassembly process. Basic concept of AR implementation in various applications, as well as developed concept in disassembly system is presented. Also, in this paper the experimental setup of developed concept in disassembly system for AC water pumps that was conducted in laboratory conditions is shown, and conclusions are presented.*

Key Words: ***disassembly sequence, human-machine interaction, marker***

1. INTRODUCTION

Disassembly process has become one of the major aspects of life cycle engineering and environmental protection issues. When an End-Of-Life (EOL) product is disassembled and recycled, all hazardous substances must be identified and safely removed in order to comply with the Waste Electric and Electronic Equipment (WEEE) directive [1].

The main purpose of disassembly process is to revalorize EOL products by a methodical separation of their parts and materials for recycling, remanufacturing and reuse [2]. When defining disassembly sequences several issues must be considered simultaneously—geometric constraints, safety, economy, and environmental impacts. Also in order to assure the competitiveness of disassembly lines, the line designers have to deal with the uncertainty that characterizes EOL products and to be able to determine the level of disassembly for which the revenue obtained from retrieved parts is higher than disassembly cost [3].

Since disassembly sequences are different for each type of product it is essential to supply disassembly workers with relevant information as efficiently as possible at the corresponding location and at the right time. Several methods and technologies have been used to achieve this goal like: Petri net [4], Monte Carlo method [3], barcode, RFID [5] and others. Augmented Reality (AR) is a new concept that can also help in suppling workers with relevant information in real time. In this paper a strategy of implementation of augmented reality in disassembly proces in order to asist workers by suggesting adequate technological procedure for disassembly operation will be presented.

2. AUGMENTED REALITY

Augmented reality allows a combination of real world elements, captured through a camera, with multimedia elements such as text, images, video or 3D models and animations. AR environment allows the user to see the real world with virtual computer-generated objects superimposed or merged with real surroundings. In terms of used technology, AR can be said to require the following three characteristics: it combines the real and virtual, it is interactive in real time, and registered in 3D.

Today, implementation of augmented reality has being implemented in several nonindustrial fields [6] like: medicine [7], architecture [8], aerospace [9], education [10], construction [11], etc. There are also industrial applications in which augmented reality can be applied in all phases of product life cycle. In the product development phase, esthetic designing has become an essential process that can be effectively assessed by using AR without making a real physical prototype, and which reflects the immediate feedback of evaluators [12]. Also, evaluation of the effectiveness of technical maintenance assisted with interactive augmented reality instructions has been presented in [13] and integrating of AR into the planning process of manual assembly stations is presented in [14].

In order to enable AR in any process there is a need for implementation of four hardware components: sensors, processor, display and input devices [15].

Sensors in AR are responsible for collecting information about the environment. The most commonly used sensor in AR is camera, which is used for taking pictures of the actual world. The processor is responsible for processing images from the camera, and its enrichment with additional information. The display is used to display the results of image processing, or the image of the real world enriched with additional useful information. There are various technologies for displaying information such as optical projection systems, monitors, hand held devices, glasses, and display systems worn on one's person (HMD, Head

Mounted Displays). Input devices are used for commands which affect information processing and displaying. Modern mobile computing devices like smart phones and tablet computers contain these elements which often include a camera and MEMS (Microelectromechanical systems) sensors such as accelerometer, GPS (Global Positioning System), and solid state compass, making them suitable AR platforms [16].

There are two primary types of AR implementations: MARKER-Based and Markerless [17]. Marker-based implementation utilizes some type of image as a marker to produce a result when it is sensed by a reader, typically a camera on a mobile phone. Markerless AR is often more reliant on the capabilities of the device being used such as the GPS location, velocity meter, etc. Both Marker-based and Markerless AR requires AR specific software or browsers to function. On the market there are available a large number of ready-made software solutions and platforms to work with AR.

To implement interactive instructions with the AR in most cases Marker-based AR is used, which can show videos, 2D and 3D animations. These instructions can be used both in non-industrial and industrial systems (instructions for home appliances, maintenance manuals for machines).

Using interactive instructions can have multiple advantages. Example advantages in assembly systems are next: no need for training of workers; lost assembly time is minimal; possibility for product callback due to assembly mistakes is minimal [18]. Using some of the devices (mobile device, glasses, ..) user take picture of the marker, and device process that picture to get orientation of marker, i.e. virtual local coordinate system in which 3D model or 3D animation is drawn and shown on the display. Mobile phones (and tablets) because of the large number of built-in functionality are suitable AR platform. On the market there are a very large number of different types of products, different models and different manufacturers, and it is not possible to realize a universal application that would encompass all possible products. The solution to this problem is that the marker provides details about the product. Dedicated application detects marker, read information about product from marker and access to the database using that information, and retrieve the data related to the product (instructions in the form of images, 2D or 3D animation, video files) [19]. After retrieving, this information would be shown on the screen on devices display. Database can be local (example factory database with instructions for products assembly) or database can be on internet (manufacturers database with instruction for using their products).

3. DISASSEMBLY PROCESS

Disassembly is one of the processes in the life cycle of a product, which has a key role in remanufacturing, recycling of products and disposal. This is due to ecological and economical reasons.

The execution of disassembly process consists of a series of sequences that need to be done in order to take apart the product of elementary components, which then need to be distributed to the appropriate material flows for further processing in order to optimize their life cycle.

A typical disassembly work place (Fig. 1) includes the basic elements, such as: tools, fixtures, containers for part selections, part holders and measurement instruments.

Fig. 1. Disassembly work place

Disassembly sequence includes the following activities:

1. taking the product from pallet,
2. determination of variant and types of products,
3. description of the disassembly technology procedure,
4. execution of disassembly sequences,
5. determination of the condition of disassembled component (condition analysis),
6. diagnosed component condition,
7. component selection according to component condition and placing in adequate container.

It must be emphasized that in some cases the description of the disassembly technology procedure can be modified, i.e. some actions can be completely eliminated (when processing well known product).

Each of mentioned activities (1-6) requires a certain time for accomplishment. However, in most cases the product information is completely missing and thus disassembly activities can unnecessarily last for too long. These cases represent a loss for the system. For example, the determination of variants and types of products lasts often several times longer than necessary.

The result of this situation is reduce of the labor utilization degree, reduce of the machines and devices, used for the disassembly process, degree of utilization, reduced productivity, low quality materials that are obtained in the process of product disassembling, prolonged treatment products, etc. Result of all these problems is a reduction in the efficiency and effectiveness of the disassembly process, and the core of these problems is lack of information.

In order to efficiently deal with lack of information AR can be used for delivering interactive instructions for disassembly process in the shortest time (Fig. 2). These instructions include:

- a detailed instructions on how to perform the disassembly sequence,
- a detailed instructions on how to perform analysis and diagnosis on component condition,

- a detailed instructions on how to perform component selection according to component condition.

Fig. 2. AR interactive instructions for disassembly sequence

3.1. Methodology for AR concept implementation

When developing methodology for AR concept implementation one important thing was taken into account and that was to be easily implemented this concept in existing disassembly systems, meaning that it is not necessary to change the spatial structure of the existing system in order to implement concept. Disassembly system with implemented AR concept is represented in Fig. 3. Block "collected products" represents an input buffer for disassembly facility. In this buffer all products, that will be disassembled, are stored. Examples of products can be different household appliances (washing machines, dishwashers, mixers, irons, televisions, stereos ...).

These products are then transferred sequentially to the work place where the trained worker defines a disassembly strategy for each specific product. In order to do that efficiently he or she communicates with server with database where the data about used materials as well as the process of disassembling and instructions for disassembly sequence for each specific product is located (represented as block “server with database”, Fig. 3). Instruction for disassembly sequence can be in different forms like: video files, simplified 2D or 3D animations. These data and animations can be created also by the manufacturer for each type and model of the product. Beside this information, in the database, there is a marker with a unique mark for each product.

When worker, who needs to define disassembly strategy, gets product her or she firstly checks if the product information is in the database. If the product information is not in the database it is necessary for the worker to generate a marker with unique label for that product and obtain, from the manufacturer, data and instructions for disassembly process. If manufacturer data are not available he or she needs to suggest adequate instructions for disassembly sequence. If product information is in the database, worker prints marker for that product and attaches it to the product or to the pallet on which the product is transported and then send product to disassemble line (block “disassembly”, Fig. 3).

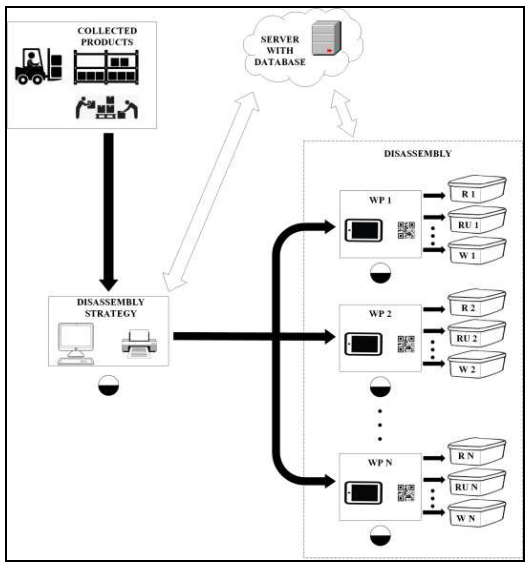

Fig. 3. Disassemble system with implemented AR concept

At disassemble line worker at work place (WP, Fig. 3) takes product with marker and then scans marker with mobile device (mobile phone, tablet,...) and dedicated application. After scanning marker, data and instructions for product disassembly sequences are retrieved from the database on a server. After downloading needed information, instructions for specific product are displayed on the mobile device screen at work place in form of: video files, 2D or 3D animation. According to displayed information worker can perform the disassembly sequence, perform analysis and diagnosis on component condition and perform component selection according to component condition. After component selection worker puts each component in adequate container, Fig. 3. e.g.:

- Re-use of used products (RU);
- Redesign of used products (R);
- Use of used products for spare parts (USP);
- Recycling with disassembly (RWD);
- Recycling without disassembly (RWOD);
- Dumping of used products (W).

After completion of disassembly process worker, using mobile device, can generate report and write in database specific result of work that was done. In that way gathered information can be used for analyzing the efficiency of disassembly process.

3.2. Experimental system

Experimental testing of AR implementation in disassembly system was conducted in laboratory conditions. AC water pumps were used as products for disassembly process simulation (Fig. 2). Disassembly system was set according to concept shown in Fig. 3.

In case of AC water pump disassembly process instructions for disassembly sequences were generated as a number of image files (Fig. 2). Server with database, which acts as FTP server, was used. Each product was labeled with marker in form of QR code with coded name of product. Android mobile phone was used as device, for showing interactive instructions. Dedicated application is developed by using Zxing library for

scanning QR codes and MetaioSDK as library for Augmented Reality.

The procedure that was used at work place was next: worker takes product with marker from pallet and activate dedicated application on mobile device. This applications is then used to scan QR code and decode name of product. After decodng name of product applications get zipped file, which contains instruction for disassembly process, from PC. Same QR code is used as marker for drawing instruction as Augmented Reality. According to diagnosis on component condition worker puts disassembled parts in apropriate container.

4. CONCLUSION

The implementation of AR in the area of disassembly systems can lead to improvements of overall disassembly process. These improvements can be characterized by the following:

- Shortening duration of the procedure of disassembly,
- Shortening time needed for component condition analysis,
- Shortening time needed for component condition diagnosis,
- Shortening time of appropriate material flow selection for disassembled components.

In experimental system, represented in paper, Marker-based AR for showing interactive instructions was used. Marker-based AR is currently the most prevalent and easiest to accomplish, and that is the reason for using it in this application.

The problem that has been observed during the experiment is related to the positioning of markers, so in further research the Markerless AR will be used.

5. REFERENCES

[1] WEEE Directive 2002/96/EC of the European Parliament and of the Council of 27 January 2003 on waste electrical and electronic equipment (WEEE), 2002.

[2] A. Gungor and S. M. Gupta, "Issues in environmentally conscious manufacturing and product recovery: a survey," *Comput. Ind. Eng.*, 1999; Vol. 36, pp. 811–853.

[3] M. L. Bentaha, O. Battaïa and A. Dolgui, "Disassembly Line Balancing and Sequencing under Uncertainty," Proc. of 21st CIRP Conference on Life Cycle Engineering, Procedia CIRP, 2014, Vol. 15, pp. 239 – 244.

[4] T. C. Kuo, "Waste electronics and electrical equipment disassembly and recycling using Petri net analysis: Considering the economic value and environmental impacts," *Comput. Ind. Eng.*, 2013, Vol. 65, Iss. 1, pp. 54-64.

[5] D. Vukelic, G. Ostojic, S. Stankovski, M. Lazarevic, B. Tadic, J. Hodolic and N. Simeunovic, "Machining fixture assembly/disassembly in RFID environment," *Assembly Automation*, 2011, Vol. 31, No 1, pp. 62-68.

[6] A. B. Craig, "Augmented reality applications," In A. B. Craig & M. Kaufmann (Eds.), *Understanding augmented reality*, 2013, pp. 221–254, USA: Boston.

[7] I. Cabrilo, A. Sarrafzadeh, P. Bijlenga, B.N. Landis and K. Schaller, "Augmented reality-assisted skull base surgery," *Neurochirurgie*, 2014, Vol. 60, Iss. 6, pp. 304-306.

[8] T. Fukuda, T. Zhang and N. Yabuki, "Improvement of registration accuracy of a handheld, augmented reality system for urban landscape simulation," *Frontiers of Architectural Research*, 2014, Vol. 3, Iss. 4, pp. 386-397.

[9] A. L. Gorbunov, "Stereoscopic augmented reality in visual interface for flight control," *Aerospace Science and Technology*, 2014, Vol. 38, pp. 116-123.

[10] T. Jerabek, V. Rambousek and R. Wildova, "Specifics of Visual Perception of the Augmented Reality in the Context of Education," *Procedia - Social and Behavioral Sciences*, 2014, Vol. 159, pp. 598-604.

[11] C. Koch, M. Neges, M. Konig and M. Abramovici, "Natural markers for augmented reality-based indoor navigation and facility maintenance," *Automation in Construction*, 2014, Vol. 48, pp. 18-30.

[12] M. K. Park, K. J. Lim, M. K. Seo, S. J. Jung and K. H. Lee, "Spatial augmented reality for product appearance design evaluation," *Journal of Computational Design and Engineering*, 2014, doi:10.1016/j.jcde.2014.11.004

[13] M. Fiorentino, A. E. Uva, M. Gattullo, S. Debernardis and G. Monno, "Augmented reality on large screen for interactive maintenance instructions," *Computers in Industry*, 2014, Vol. 65, Iss. 2, pp. 270-278.

[14] G. Reinhart, C. Patron, "Integrating Augmented Reality in the Assembly Domain - Fundamentals, Benefits and Applications," CIRP Annals - Manufacturing Technology, 2003, Vol. 52, Iss. 1, pp. 5–8.

[15] J. Jeon, S. Kim, S. Lee,"Considerations of Generic Framework for AR on the Web", In W3C's AR on the Web Workshop, 2010, Vol. 6.

[16] Augmented Reality Ar Is A Live Media Essay, [online], http://www.uniassignment.com/essay-samples/media/augmented-reality-ar-is-a-live-media-essay.php [10 January 2015].

[17] Augmented Reality: About AR, [online], http://researchguides.dartmouth.edu/AR [10 January 2015].

[18] R. Radkowski, "Augmented Reality to Supplement Work Instructions", Model-Based Enterprise Summit2013, [online], www.nist.gov/el/msid/upload/2Radkowski_AugmentedReality.pdf, [10 January 2015]

[19] M. Hakkarainen, C. Woodward, M. Billinghurst, "Augmented assembly using a mobile phone", In 7th IEEE/ACM Int. Symp. on Mixed and Augmented Reality (ISMAR 2008), 2008, pp. 167-168.

[20] G. Ostojic, M. Lazarevic, S. Stankovski, I. Cosic, Z. Radosavljavic, "Radio Frequency Identification Technology Application in Disassembly Systems," *Strojniški vestnik - Journal of Mechanical Engineering*, 2008, Vol. 54, Iss. 11, pp. 759-767.

The 7th International Conference on Engineering and Technology
ICET-2015, Phuket, June 19-20, 2015
Prince of Songkla University, Faculty of Engineering
Hat Yai, Songkhla, Thailand 90112

The Choice of Muscles Impacts the Linear Relationship between the Probability Density Function of Surface EMG Signal and the Level of Contraction Force

Sirinee Thongpanja[1]*, Angkoon Phinyomark[2], Franck Quaine[3], Chusak Limsakul[1], Pornchai Phukpattaranont[1]
[1]Prince of Songkla University, Faculty of Engineering, Thailand
[2]University of Calgary, Faculty of Kinesiology, Canada
[3]University Joseph Fourier, GIPSA Laboratory, SAIGA Team, France
*Email of corresponding author: sirinee.th@gmail.com

Abstract: *A linear relationship between the probability density function (PDF) of surface electromyography (EMG) signal and the level of contraction force has been found in many previous investigations. However, only few muscles have been studies while differences between muscles in anatomical and physiological properties are ackowledged. Therefore, the purpose of the present study was to examine the relationship between the PDF of EMG from three different forearm muscles: flexor carpi radialis (FCR), flexor pollicis longus (FPL), and extensor digitorum (ED), and the level of contraction force on individual subjects. Kurtosis and negentropy were used to measure the non-Gaussianity level of EMG. The results showed that as the FCR muscle's contraction force increases the PDF of EMG tends to a Gaussian distribution, i.e., a negative linear relationship, which is consistent with literature. Conversely, the PDF of EMG tends to a Laplacian distribution as the FPL and ED muscles's contraction force increases, i.e., a positive linear relationship. To our knowledge, this is a novel finding and also suggests that the choice of muscles impacts the linear relationship between the PDF of EMG and the level of contraction force.*

Key Words: ***Electromyography Signal / Gaussianity Tests / Higher-Order Statistics***

1. INTRODUCTION

Surface electromyography (EMG) is a non-invasive technique for measuring the electrical manifestation of neuromuscular activities and produces a record called electromyogram. EMG signals are stochastic complex signals which are dependent on various factors involving anatomical and physiological properties of the muscles. Therefore, to classify movements from EMG patterns of information, a method to transform the original EMG signals into a reduced representation set of variables referred to as feature extraction is needed [1]. The extracted features are supposed to contain the relevant information from EMG for motion pattern classification.

It has long been assumed that the EMG signal records during constant-force, constant-angle and non-fatiguing contraction can be modelled as a zero-mean, correlation-ergodic and random process, referred to as a Gaussian density [2]. Therefore, traditionally feature extraction methods have been developed based on the Gaussian model, such as root mean square (RMS) and principal component analysis (PCA) methods [3-4]. Although the probability density function (PDF) of the EMG signal is frequently assumed to be Gaussian distributed, recently several experimental studies show that the PDF of EMG recorded during some levels of isometric contraction is more peaked near zero than the Gaussian distribution and could be modelled with the Laplacian distribution [2, 5-8]. Thus, feature extraction methods developed based on the non-Gaussian model, such as mean absolute value (MAV) and independent component analysis (ICA), have been proposed and successful to classify movement patterns associated with surface EMG signals [3, 9].

However, many previous studies on EMG pattern classification system have not selected feature extraction methods based on a data distribution type examined by the Gaussianity tests [10-11]. Gesture and muscle types selected for a specific recognition system proposed in these studies may involve both Gaussian and Laplacian EMG PDFs. Consequently, the best feature subset that was selected through an experimental comparison may depend on the proportion of the Guassian and Laplacian PDFs of EMG in the study. For instance, if the average PDF of EMG is closer to a Laplacian density, the MAV feature (i.e., the optimal maximum likelihood estimation (MLE) of the EMG amplitude based on the Laplacian model) would provide a better classification accuracy compared to the RMS feature (i.e., the optimal MLE of the EMG amplitude based on the Gaussian model) [3].

Based on kurtosis and negentropy analyses, previous studies [5-8] demonstrate that as the level of contraction force increases, on average the PDF of EMG tends towards the Guassian distribution. Although this linear relationship is useful for helping reseachers to design the pattern recognition system of human gestures associated with surface EMG, only few muscles have been studies [5-8] while differences between muscles in anatomical and physiological properties are ackowledged. Therefore, the purpose of the present study was to examine the relationship between the PDF of EMG measured from three different muscles: flexor carpi radialis (FCR), flexor pollicis longus (FPL), and extensor digitorum (ED), and the level of contraction force on individual subjects. We hypothesized that the choice of muscles impacts the linear relationship between the PDF of EMG signal and the level of contraction force. It is important to note that the FCR muscle has been studied before while the FPL and ED muscles have never been studied.

2. EXPERIMENTS AND METHODS

2.1. Data collection

EMG signals were measured from three different forearm muscles involving FCR, FPL, and ED, using bipolar surface electrodes (H124SG, Kendal ARBO) with an inter-electrode distance of 20 mm. Another electrode (2237, 3M) was placed on the wrist to provide a common ground. All the EMG signals were recorded by the EMG data acquisition system (Mobi6-6b, TMS International B.V.) with a gain of 19.5x and a sampling rate of 1024 Hz. Movement artifact (<20 Hz) and high-frequency noise (>500 Hz) were removed using a band-pass equiripple FIR filter.

Six able-bodied young subjects participated in the present study: four males (20.5±0.6 yrs) and two females (21.0 yrs). Participants were asked to perform five levels of isometric contraction by lifting the external absolute load: 1, 2, 3, 4, and 5 kg at 90° of elbow flexion for 5 s in each trial. Each participant performed 5 trials per day on 4 separate days, i.e., 20 trials in total for each weight.

2.2. PDF of EMG signal

For measurement of the non-Gaussianity, measured EMG signals were normalized to have zero mean and unit variance (x). To estimate the non-Gaussianity level of EMG, the kurtosis and negentropy approaches were used [5-8]. Kurtosis or *kurt* is one of the classical higher-order statistics which is defined as the fourth-order cumulant of the normalized data x:

$$kurt = \left[N^{-1} \sum_{i=1}^{N} x_i^4 \Big/ \left(N^{-1} \sum_{i=1}^{N} x_i^2 \right)^2 \right] - 3 . \quad (1)$$

Negentropy is a measure of the difference in entropy between the distribution measured and the Gaussian distribution. This approach is less sensitive to outlier as compared to the kurtosis approach by using a non-quadratic function G instead of a higher power function. In this study, where v is a Gaussian random variable with zero mean and unit variance and a was set at 1, the approximation of negentropy (J) is defined as

$$J = \left[N^{-1} \sum_{i=1}^{N} G(x) - N^{-1} \sum_{i=1}^{N} G(v) \right]^2 ; \quad (2)$$

$$G(x) = a^{-1} \log \cosh(ax) . \quad (3)$$

It should be noted that the Gaussian distribution has a kurtosis of 0 as well as a negentropy of 0, while the Laplacian distribution has a kurtosis of 3 and a negentropy of 0.0013.

2.3. Level of contraction force

For estimating muscle's contraction force, measured EMG signals were normalized using the submaximal voluntary isometric contraction (sub-MVIC). For each trial, EMG signals were rectified and low-pass filtered using a Butterworth filter with a cut-off frequency of 6 Hz to produce a linear envelop and then the average of linear envelop amplitude at 5 kg was computed to obtain the reference level (100% sub-MVIC). Subsequently, measured EMG signals at other load levels (1-4 kg) were normalized as the %sub-MVIC.

2.4. Data analysis

The mean and standard deviation of the kurtosis and negentropy values were calculated for each level of contraction force. In order to measure the degree of linear relationship between the PDF of EMG via the kurtosis or the negentropy and the level of contraction force as %sub-MVIC, the correlation analysis was performed. The correlation coefficients (r) present the direction and strength of the linear relationship. The sign of the r coefficient (+, -) defines the direction of the relationship, either a positive linear relationship (+) and a negative linear relationship (-). The absolute value of the r coefficient defines the strength of the relationship. In this study, the $0.68 \leq |r| \leq 1.00$ indicates a strong linear relationship, $0.36 \leq |r| \leq 0.67$ as a moderate linear relationship, and $|r| \leq 0.35$ as a weak linear relationship [12]. To be easily observed from the figures the strong and the moderate *negative* linear relationships were shown by the *red* solid and dashed lines, respectively. On the other hand, the strong and the moderate *positive* linear relationships were shown by the *blue* solid and dashed lines, while *no* or low linear relationship was shown by the *black* solid line in the figures. In addition to the quantitative measures of EMG PDF using the kurtosis and negentropy values the PDF of EMG was confirmed by visually inspecting the 1001-bin histogram. Further, the effect of the number of levels of sub-MVIC on the strength of the linear relationship was investigated by increasing the number of levels from 5 levels (i.e., one %sub-MVIC level for each load level by averaging across all the trials) to higher number of levels (i.e., one level with either an interval of 1% or 10% by averaging all the trials within the same interval).

3. RESULTS

In Fig. 1, the perfect linear correlation (r = 0.996) between the external absolute load holding by the participants and the level of muscle's contraction force as %sub-MVIC is shown. The results obtained from the kurtosis and negentropy were similar, therefore only the results of the kurtosis were shown in remaining. The

relationships between the PDF of EMG via the kurtosis values and the level of contraction force with five %sub-MVIC levels for the FCR, FPL, and ED muscles are respectively shown in Figs. 2(a)-2(c). The normalized experimental PDF of EMG measured from the ED muscle is shown in Fig. 3 using the histograms. The relationships between the PDF of EMG and the level of contraction force with the 1% and 10% intervals of %sub-MVICs are shown in Fig. 4.

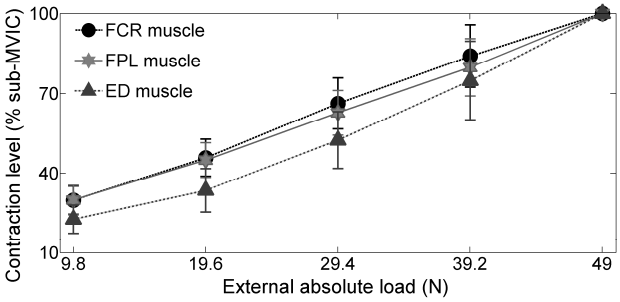

Fig. 1. The mean and standard deviation of the %sub-MVIC values for all subjects at five different external absolute load levels for the FCR, FPL, and ED muscles.

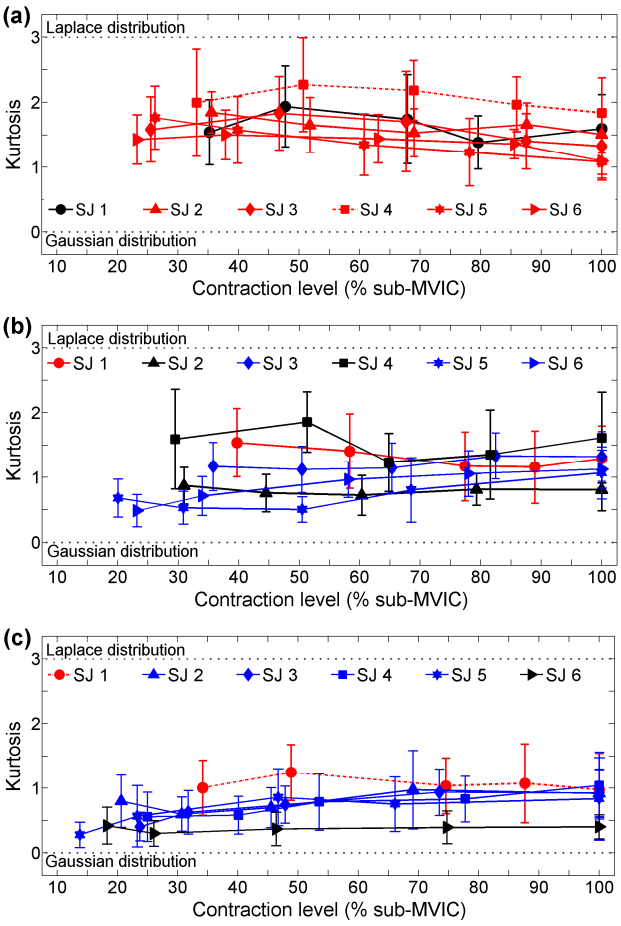

Fig. 2. The mean and standard deviation of the kurtosis values for all subjects at five different %sub-MVIC levels for the (a) FCR, (b) FPL, and (c) ED muscles. The grey dotted lines at the top of the sub-figures indicate the theoretical Laplacian value of kurtosis and at the bottom indicate the theoretical Gaussian value of kurtosis.

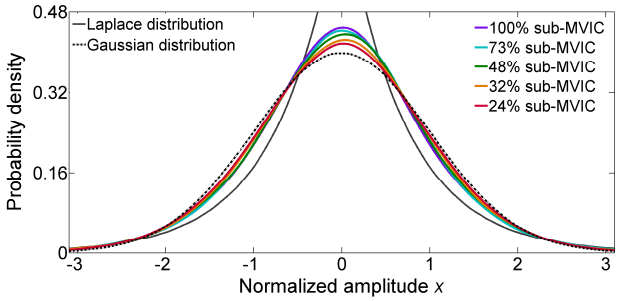

Fig. 3. Normalized experimental PDF of EMG measured from the ED muscle at five different contraction levels (24%-100% sub-MVIC) from Subject #4.

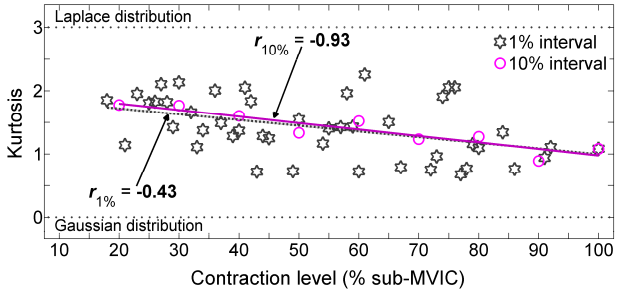

Fig. 4. The mean of the kurtosis values at the 1% and 10% intervals of the %sub-MVIC levels for the FCR muscle from Subject #5 and their correlation coefficients *r*.

4. DISCUSSION AND CONCLUSIONS

The purpose of the present study was to examine the relationship between the PDF of EMG measured from three different muscles: FCR, FPL, and ED, and the level of contraction force on individual subjects. In support of our hypothesis, the choice of muscles impacts the linear relationship between the PDF of EMG and the level of contraction force. Specifically, in support of Nazapour et al.'s findings [5], for the FCR muscle as the contraction force increases the PDF of EMG tends to a Gaussian distribution, i.e., a negative linear relationship. As shown in Fig. 2(a), the strong and the moderate negative linear relationships were found for 5 subject (83% of the population), while only one subject showed no linear relationship between the EMG PDF and the contraction force. This relationship has been found in several muscles such as abductor pollicis brevis [5], flexor digitorum supificailis (FDS) [6], and biceps brachii [7, 8].

While only the negative linear relationship has been found in previous available studies on a limited number of muscles, the evidence in the present investigation has clearly shown that the experimental PDF of EMG measured from the FPL and ED muscles tends to a Laplacian distribution at higher levels of contraction force, i.e., a positive linear relationship. As shown in Fig. 2(b), the strong positive linear relationships were found for 3 subjects (50% of the population) for the FPL muscles, while for the ED muscle the strong positive linear relationships were found for 4 subjects (67% of the population). Further, the linear relationships examined by the kurtosis and negentropy values were confirmed by visual inspection of the histogram in Fig. 3. Therefore,

the present results suggested that the choice of muscles impacts the linear relationship between the PDF of EMG and the level of contraction force and the relationship is also dependent on individual subjects due to human physical variation [13]. Specifically, the reason may be the differences in muscle fiber compositions and distributions of the muscles, i.e., the anatomical factor.

In future works, this linear relationship can be used to choose a group of gestures that their PDFs of EMG can be modelled either with the Gaussian or non-Gaussian distribution, and then to select the optimal subset of feature extraction methods based on that data distribution type. For instance, in the study of Naik et al. [9] the RMS feature can correctly estimate the force of finger flexion only when the level of the FDS muscle's contraction force is high (>50% of maximum voluntary contraction, MVC). Because, the PDF of EMG for the FDS muscle tends to the Gaussian distribution as the contraction force increases [6] and the RMS feature is also the optimal EMG amplitude estimator for the Gaussian model [2, 3]. Therefore, to correctly estimate the force of finger flexion when the level of the FDS muscle's contraction force is low (20% MVC), the MAV feature should be used rather than the RMS feature, as suggested in [2, 3], or applying ICA method for the pre-processing of EMG signals before extracting feature, as suggested in [9]. Future studies involving muscles other than previously investigated [5-8] are necessary.

Limitations to the current study and also previous related studies are acknowledged. First, usually only four to six levels of muscle's contraction force were included in the investigations [5-8]. However, if the number of levels of contraction force increased the strength of the linear relationship computed from the correlation analysis may be decreased, as shown in Fig. 4 (from r = -0.93 based on 10% interval to r = -0.43 based on 1% interval). Hence, the interpretation and comparison of the results from different studies should be careful. A large number of EMG data sets for each contraction force are also needed in future investigations. Second, in this study the EMG data was normalized to activation levels during sub-MVIC. Although this normalization technique can be used to compare patterns of muscle activation, the reference value used in this technique cannot represent the maximum capacity of the muscle. Therefore, at 100% of the maximum muscle capacity, the PDF of EMG may be close to either the Gaussian or Laplacian distribution more than the results presented in Fig. 2.

In summary, the PDF of EMG from the FCR muscle tends to be more Gaussian at high contraction force levels, whereas the PDF of EMG from the FPL and ED muscles tends to be more Gaussian at low levels of contraction force. Therefore, the results of the present investigation suggested that the choice of muscles impacts the linear relationship between the PDF of surface EMG signals and the level of contraction force.

5. ACKNOWLEDGEMENTS

This work is jointly funded by Prince of Songkla University and Thailand Research Fund through the Royal Golden Jubilee Ph.D. Program (Grant No. PHD/0155/2554).

6. REFERENCES

[1] A. Phinyomark, F. Quaine, S. Charbonnier, C. Serviere, F. Tarpin-Bernard, and Y. Laurillau, "EMG feature evaluation for improving myoelectric pattern recognition robustness," *Expert Syst. Appl.*, 2013, Vol. 40, No. 12, pp. 4832-4840.

[2] E. A. Clancy and N. Hogan, "Probability density of the surface electromyogram and its relation to amplitude detectors," *IEEE Trans. Biomed. Eng.*, 1999, Vol. 46, No. 6, pp. 730-739.

[3] A. Phinyomark, F. Quaine, Y. Laurillau, S. Thongpanja, C. Limsakul, and P. Phukpattaranont, "EMG amplitude estimators based on probability distribution for muscle-computer interface," *Fluctuation Noise Lett.*, 2013, Vol. 12, No. 3, 1350016.

[4] A. Phinyomark, H. Hu, P. Phukpattaranont, and C. Limsakul, "Application of linear discriminant analysis in dimensionality reduction for hand motion classification," *Meas. Sci. Rev.*, 2012, Vol. 12, No. 3, pp. 82-89.

[5] K. Nazarpour, A. H. Al-Timemy, G. Bugmann, and A. Jackson, "A note on the probability distribution function of the surface electromyogram signal," *Brain Res. Bull.*, 2013, Vol. 90, No. 100, pp. 88-91.

[6] G. R. Naik, D. K. Kumar, and S. P. Arjunan, "Kurtosis and negentropy investigation of myo electric signals during different MVCs," *Proc. of ISSNIP Biosignals and Biorobotics Conf.*, 2011, pp. 1-4.

[7] S. Thongpanja, A. Phinyomark, C. Limsakul, and P. Phukpattaranont, "Probability density of electromyography signal for different levels of contraction of biceps brachii," *Proc. of 10th Inter. Conf. on Electr. Eng./Electron., Comput., Telecommun. and Info. Technol.*, 2013, pp. 1-5.

[8] K. Nazarpour, A. R. Sharafat, and S. M. Firoozabadi, "Negentropy analysis of surface electromyogram signal," *Proc. of IEEE/SP 13th Workshop on Statistical Signal Processing*, 2005, pp. 974 –977.

[9] G. R. Naik, D. K. Kumar, and S. P. Arjunan, "Pattern classification of myo-electrical signal during different maximum voluntary contractions: a study using BSS techniques," *Meas. Sci. Rev.*, 2010, Vol. 10, No. 1, pp. 1-6.

[10] M. A. Oskoei and H. Hu, "Myoelectric control systems-A survey," *Biomed. Signal Process. Control*, 2007, Vol. 2, No. 4, pp. 275-294.

[11] A. Phinyomark, P. Phukpattaranont, and C. Limsakul, "A review of control methods for electric power wheelchairs based on electromyography (EMG) signals with special emphasis on pattern recognition," *IETE Tech. Rev.*, 2011, Vol. 28, No. 4, pp. 316-326.

[12] R. Taylor, "Interpretation of the correlation coefficient: a basic review," *J. Diagn. Med. Sonogr.*, 1990, Vol. 6, pp. 35–39.

[13] A. Phinyomark, F. Quaine, S. Charbonnier, C. Serviere, F. Tarpin-Bernard, and Y. Laurillau, "A feasibility study on the use of anthropometric variables to make muscle-computer interface more practical," *Eng. Appl. Artif. Intell.*, 2013, Vol. 26, pp. 1681–1688.

The 7th International Conference on Engineering and Technology
ICET-2015, Phuket, June 19-20, 2015
Prince of Songkla University, Faculty of Engineering
Hat Yai, Songkhla, Thailand 90112

ENERGY INDICATORS OF PUBLIC BUILDINGS IN AP VOJVODINA WITH FOCUS ON HOSPITALS, SCHOOLS AND ADMINISTRATIVE BUILDINGS

Jovan Petrović[1]*, Milovan Medojević[1], Milana Perić[1], Igor Mujan[1]
[1]University of Novi Sad, Faculty of Technical Sciences, Novi Sad, Serbia
*Email of corresponding author: medojevicmilovan@gmail.com

Abstract: *Bearing in mind that building sector represents one of the biggest energy consumers in European countries, the facilities in the public sector have been in the focus of attention when it comes to energy consumption with annually increasing energy demand and absence of proper energy management. The aim of this paper is to present the research results and to point out the current state and future needs of energy systems in buildings in relation to its users. Three major parts of public building sector in Autonomus Province of Vojvodina (APV) were observed: 22.6% of Educational facilities, 67.1% of Medical facilities and 58% of the Administrative sector (municipalities). This paper provides a quick look at the vast disparity between the Ordinance on energy efficiency of buildings issued in 2011 and the real energy consumption in public sector as well as problems influenced by outdated energy systems and their improper utilization.*

Key Words: ***Energy consumption, energy efficiency, indicators, public buildings, energy systems.***

1. INTRODUCTION

According to the study conducted by World Bank [1], estimated savings potential in public buildings is Serbia amounts about 39 - 44% of current energy consumption. Energy efficiency (EE) in the public buildings sector can be mandated more easily than in the private buildings sector, which directly indicates that the public sector is, therefore, often a good place to start EE programs. In addition, the results of this study are based upon collected data from 27 hospitals and 11 schools with a heated area of 104,969 m^2 which were renovated. Specific building heat consumption dropped from 266 kWh/ m^2/annum to 162 kWh/ m^2/annum. Annual energy consumption could be reduced by more than 39% at investment costs of around 35 €/m^2. Hospitals specific heat consumption could be reduced from average 329 kWh/m^2/annum to 210 kWh/m^2/annum in general. Excluding two hospitals which had only minor works done, annual energy demand for space heating was reduced by 43.8% through investments with costs ranging from 21.1 to 58.8 €/m^2. Most energy savings derived from roof insulation and new windows and doors. When it comes to public school buildings, similar results could be achieved, respectively average energy demand for space heating could be reduced by 43.4%. Overall energy savings based on programs and audits of 11 school buildings and 27 hospital buildings, are presented in Table 1.

Table 1. Energy savings in public buildings in Serbia

Institutional Buildings	Energy savings (as % of heating energy)	Heating energy (as % of total energy)	Energy savings (as % of total energy)
Schools			
District-heated	43.8	70	30.7
Fuel Oil	56.3		39.4
Coal	10.0		7.0
Hospitals			
District-heated	11.7	70	8.2
Fuel Oil	49.3		34.5
Coal	20.5		14.4

In the short- to medium-term, prospects are slim for major, sustainable EE programs in country with low energy prices and high commercial losses. Good EE equipment prices tend to be at world market levels or higher, so payback periods would be too long because consumers typically apply high discount rates to these investments, for example, up to 20% for households and up to 50% for industry [2]. But public-sector programs for schools, hospitals, and administrative buildings can promote comfort, health, as well as energy savings that will increase over time as energy prices rise. The Serbia Energy Efficiency Project is an excellent example of this [3]. Municipal governments have strong incentives for EE investments due to the scale of their public facilities

and street lighting systems, and substantial subsidies for district heating systems and heat consumers; however, funding often needs to come from central government. EE could also be a cost-effective contribution to the social safety net for the poor [4-6].

2. METHODOLOGY

Realization of project "*Energy systems in public buildings*" during the first year covered the data analysis about the current state in the educational and medical facilities. Both medical and educational facilities were separated into categories. Medical facilities categorized into: general hospitals, special hospitals, institutes, health clinics, health centers, medical offices; while the educational facilities were split into: elementary schools, secondary schools and mixed schools. In the second year of the project realization, administrative buildings were included into the research process and additional data were collected for the healthcare sector of APV. In addition, an analysis was made on the basis of all gathered information while estimations were made on the total and specific energy consumption in these facilities. Research and data collection was carried out in the following steps. First, a survey was made ("Current state in energy sector, Energy and fuel consumption with building and equipment characteristics in education, healthcare and administration"). Next, the public building sector database was collected in the APV governmental institution and surveys were sent accordingly in electronic form while the responsible people were contacted to supervise and oversee the results. Thereafter, surveys were completed and collected (electronically or by visit) and analysis was carried out. The new database was made to systematize the gathered information while always being susceptible to change. Lastly, all of the criteria for determining the specific indicators (kWh_e/m^2, kWh_h/m^2, and kWh/pupil) were formed. These indicators served as a primary tool for analysis and comparison of the current state of observed facilities.

3. RESULTS

Previous results are classified into three categories according to the type of the facility utilization.

3.1. School facilities

Gathered sample consists of 122 schools (22,6%) of the total number 540 (100%) in APV, which was then taken as a representative school sample because of the inability to analyze all of the schools. To properly determine the correct ratio of the results, it is important to know the amount of surveyed school by categories: C1: 99 elementary (81%), C2: 17 secondary (14%) and C3: 6 mixed schools (5%). The following table (Table 2.) shows that energy indicators from the analyzed schools are far higher than those anticipated by the Ordinance on energy efficiency of buildings issued by the State. According to the Ordinance, already exiting educational facilities should not exceed 75 kWh/m^2 of heat consumption. Having this in mind, immediate interventions are needed on the building envelopes as well as on existing energy systems.

Table 2. Energy indicators for school facilities

Energy indicators	C1	C2	C3
Total heat energy consumption [GWh]	42.6	1.6	13.7
Total energy consumption (not including heat) [GWh]	4.4	0.14	2
Average heat energy consumption [MWh]	430.2	267	809
Average electrical energy consumption (not including heat) [MWh]	44.2	22.9	122
Average heat energy consumption per pupil [MWh/pupil]	1.17	1.27	0.99
Average heat energy consumption per building area [MWh/m^2]	0.2	0.23	0.23
Average electrical energy consumption per pupil (not including heat) [MWh/pupil]	0.12	0.1	0.15
Average electrical energy consumption per building area (not including heat) [kWh/m^2]	21	20	35

Summarized average values for energy indicators (electricity and heat) in mixed schools according to the previous table are 249 kWh/m^2 and 1,374 kWh/pupil. Average values for energy indicators in elementary schools are 222 kWh/m^2 and 1,289 kWh/pupil. Average values for energy indicators in secondary schools are 264 kWh/m^2 and 1,142 kWh/pupil [7,8].

3.2. Administrative buildings

From the total number (45 in APV) of administrative (municipal) institutions which received the survey, 26 municipalities filled in the survey with sufficient data. Some municipalities sent the data for several buildings in their possession. Therefore the total number of analyzed administrative buildings is 63. Administrative buildings were also built during the beginning and the middle of the last century. The majority of buildings consumes natural gas as a heating source or is connected to the district heating system thereby paying on a yearly basis per m^2 of heated surface. However, municipalities use other energy sources for heating such as coal, oil, electricity and geothermal. Several municipalities use two energy sources for heating while majority uses electricity for reheating, if needed. Administrative buildings are separated into groups based on their analyzed data and cross-reference to the Serbia's Ordinance on EE of buildings (Table 3.). From the total of the administrative buildings that were analyzed first group consists of 52%, second from 19% and the third from 29%. In the first group are the buildings with energy indicators that fall in the realm of expected results given by the Ordinance and experience from the researchers. Second group is made up from types that are charged for heating energy per m^2 and the prices are in the range from 0.49 to 2.34 €/m^2 depending on the municipality. Third group (exception group) consists of buildings that have energy consumption either too high

or too low from what was expected as well as buildings that rely on electricity as a primary heating source. Cause for the high energy consumption is the age of the buildings, poor energy infrastructure, bad envelope insulation, nonexistent energy management and inadequate use of the facility and its energy systems. Cause for the low energy consumption indicators are unconscionably filled surveys, bad recording systems and the lack of data, irregular readouts and payments for the consumed energy or subventions made by the government. The fact that this group consists of 29% administrative buildings, clearly points out that the introduction of energy management is absolutely necessary in order to improve current state of energy consumption in these facilities [7,8].

Table 3. Energy indicators for administrative building

Energy indicators for administrative buildings	Group 1 - Annual payment per usage			Group 2 - Annual set price for m^2			Group 3 - Exceptions		
	Min	Average	Max	Min	Average	Max	Min	Average	Max
Electricity [kWh/m^2]	20.4	63.3	174	14	62	101	2	55	257
Electricity [kWh/user]	437	2,651	20,899	402	2,340	10,230	128	1,616	6,633
Annual electricity cost [€/m^2]	1	4	11	1.2	4.3	8.3	0.13	3.3	15
Annual electricity cost [€/user]	18	166	1,292	27	169	754	15	100	361
Heating [kWh/m^2]	90	194	407	/	/	/	0	313	4,284
Heating [kWh/user]	1,302	8,646	48,938	/	/	/	0	6,415	37,117
Annual heating cost [€/m^2]	3.4	7.3	17	7.5	15	24	0	5.4	26
Annual heating cost [€/user]	62	278	1,024	124	549	1,503	0	252	1,918
Total energy [kWh/m^2]	127	257	581	/	/	/	6	367	4,541
Total energy [kWh/ user]	186	11,298	69,836	/	/	/	755	8,030	39,342
Annual total energy cost [€/m^2]	4.8	11	27	9	19	26	0.4	8.6	41
Annual total energy cost [€/user]	88	441	1,711	189	718	2,257	47	352	2,009

3.3. Hospitals and Helthcare facilities

From the total number of healthcare facilities in APV (82) to whom the survey was sent, 45 surveys were collected. However some facilities cover several separate institutions and the data was actually collected from 52 institutions (63%). Furthermore, 3 major hospitals were added by collecting data locally. Therefore, the data presented here includes 55 institutions in total. It is important to mention the fact that some of the facilities were built during the beginning and the middle of the last century and that the envelope and energy system revitalization is necessary but complex. Most of the energy systems are outdated in terms of function and EE which contributes massively to the inconsistency among the current energy consumption and aforementioned Ordinance, where, similarly to the values for schools, for the already exiting healthcare facilities anual heat energy consupmtion should not exceed 120 kWh/m^2. Indicators for heltcare facilities are listed in Table 4 [7,8].

Table 4. Energy indicators for healthcare facilities

Energy indicator for healthcare facilities	Health center	General Hospital	Special Hospital	Institute	Health Clinic	Health Office	Average (area share)
Healthcare surface area share [%]	23	39.5	12.2	11.4	11.3	2.6	-
Electricity [kWh/m^2]	125	152	142	103	250	101	149
Electricity [kWh/user]	2,923	4,483	8,597	1,868	6,392	2,654	4,497
Annual electricity cost [€/m^2]	6.9	5.5	7	6.8	8.3	6.1	6.5
Annual electricity cost [€/user]	160	147	347	118	175	154	174
Heating [kWh/m^2]	244	392	534	297	422	182	362
Heating [kWh/user]	5,950	11,026	32,580	5,342	7,907	5,321	11,350
Annual heating cost [€/m^2]	8.8	13	18	9.5	16	6.4	12.4
Annual heating cost [€/user]	196	334.2	1,102	165	289	181	368
Total energy [kWh/m^2]	368	544	676	399	672	283	511
Total energy [kWh/ user]	8,873	15,509	41,177	7,210	14,300	7,974	15,847
Annual total energy cost [€/m^2]	16	19	25	16	24	13	19
Annual total energy cost [€/user]	356	481	1,449	283	465	335	543

3.4. Current state of existing energy systems

During the research period it was concluded that majority of energy production is done by the public facilities themselves. Most boilers and related equipment, which are currently in use are more then 25 years old and have not been changed since the time the building was built. When the maintenance crew was interviewed the consensus was that there were not enough funds to improve the EE. Seldom are the cases of boiler replacement due to total breakdowns or donations by the government or foreign stakeholders. In addition, the current outdated heat energy generating equipment has no economizers to increase EE. The water treatment plants for water softening are not working optimally and the large scale sedimentation is present. Boiler heating tubes need to be maintained constantly which increases the maintenance costs and stops the heat production. Hot water distribution pipes and heat exchangers were also examined. The common problem with the distribution pipelines is the fact that they lack insulation. Even in places where the insulation was put during the system assembly, after repairs and modifications or vandalism it was not put back which ensures massive energy losses. Also, in large healthcare institutions the pipelines are underground and highly inaccessible for maintenance. In some instances where the steam is still used, major losses occur due to corrosion damage while the facility loses over 10 m^3 of treated and softened water on a daily bases. The majority of building regardless whether they have educative, healthcare or administrative purpose are heated buy hot water which is exchanged through radiators inside the rooms. The radiator type is the cast iron. Radiators have not been changed since the buildings were built. As well as less efficient over time and not being dimensioned properly for the current state of the buildings the user has no way to interact with the radiators and properly set the room temperature. There are no thermostat heads or whatsoever temperature monitoring and regulation system. The common occurrence is that the rooms in buildings closer to the boiler plant are overheated. This is unacceptable and is one of the main factors in the total energy consumption problem. On the other hand, the cooling is ether non-existent in the current public buildings or is primarily accomplished by the split system units with low seasonal COP. The majority of examined rooms have high inadequate temperatures during the summer where some reaching as high as 34°C. The users rely on shading surfaces to help in decreasing the temperature or use electric fans to circulate the air inside the rooms. The problem arises at the large complexes were the team encountered up to 720 separate split system units on total of 8 buildings. The collective initial, operating and maintenance costs of such arrangement highly surpasses the one of a centralized system. The further downside is user inability to control the humidity and fresh air intake inside the room. Furthermore, the split systems also create problems with reactive energy and need additional equipment to compensate it or the facility faces increased electricity bills because of the electricity grid destabilisation. Only the healthcare facilities have the luxury of centralized systems. Though, there is seldom occurrence of modern centralized air conditioning units (operating hospital blocks). In the outdated centralized system there is evident lack of modern automatic control system. The chilling compressors are mostly as old as the buildings themselves. In the common case of HVAC system with a screw compressor chiller with the refrigerant (R-22) is used to transfer heat from the evaporator to the condenser. By utilization over a long period of time, damages occur on the compressor blades and cause leakage and back-flow which causes the lower coefficient of performance (COP). Lastly, the chiller compressors capacities are usually much higher than needed which affects EE additionaly [7,8].

4. CONCLUSION

Within this study, a wide range of factors was considered when analyzing the energy consumption indicators for specific public facilities, which were based on an aforementioned sample in Vojvodina. The ultimate objective of this study was to introduce accurate and reliable data about the current state of the public building sector which should be an important foundation for the Serbia's long-term energy consumption reduction planning and devising of measures to improve EE.

5. REFERENCES

[1] Document of the World Bank, "Status of Energy Efficiency in the Western Balkans - A Stocktaking Report", June 15, 2010

[2] IEA, World Energy Outlook 2007. World Bank, Infrastructure in Europe and Central Asia: Approaches to Sustainable Services, 2006. McKinsey Global Institute, Curbing Energy Demand Growth: The Energy Productivity Opportunity, 2007.

[3] World Bank, Serbia Energy Efficiency Project, 2004 (first credit) and 2007 (additional financing).

[4] M. Perić, M. Medojević, "Energy efficient building stock regulation in European union and Serbia", *44th International Congress & Exhibition on Heating, Refrigeration and Air Conditioning (KGH)*, Smeits, Belgrade 2013, ISBN: 978-86-81505-69-4.

[5] M. Medojević, M. Perić, "The current state in Serbian energy sector with focus on barriers to energy efficiency", *IEEP 2013*, *Društvo termičara Srbije*, Divčibare, ISBN 978-86-7877-023-4.

[6] M. Medojević, M. Perić, "Energetics of Serbia – Current state and potential of renewable energy sources, *World Students Summit for Sustainability 2012*, Multimedia University College, Nairobi, Kenya from 12th – 17th November, 2012.

[7] I. Mujan, J. Petrović, M. Perić, A. Anđelković, M. Klajić, "Energy indicators in public sector in Autonomous Province of Vojvodina", *IEEP 2013*, *Društvo termičara Srbije*, Divčibare, ISBN 978-86-7877-023-4.

[8] I. Mujan, A. Anđelković, J. Petrović, M. Kljajić, "Energy Systems and Their Use in Public Sector in Autonomous Province of Vojvodina", *16th Symposium on Thermal Science and Engineering of Serbia – SIMTERM*, Sokobanja, 22-25 October, 2013, pp. 588-594, ISBN 978-86-6055-043-1

The 7th International Conference on Engineering and Technology
ICET-2015, Phuket, June 19-20, 2015
Prince of Songkla University, Faculty of Engineering
Hat Yai, Songkhla, Thailand 90112

Model selection for minimal daily pavement temperatures at Awbari in Libya

Hassan Awadat Salem*[1], Zagorka Lozanov-Crvenković[2]
Emilija Nikolić-Đorić[3], Bojan Matić[4]
[1]University of Novi Sad, Faculty of Technical Sciences, Novi Sad, Serbia
[2]University of Novi Sad, Faculty of Sciences, Novi Sad, Serbia
[3]University of Novi Sad, Faculty of Agriculture, Novi Sad, Serbia
[4]University of Novi Sad, Faculty of Technical Sciences, Novi Sad, Serbia
*Email of corresponding author: has712002@yahoo.co.uk

Abstract: *This paper presents a part of the research undertaken to develop models to predict high and low asphalt pavement temperatures at Awbari, Libya. Regression analysis is used to develop models for minimal daily pavement surface temperature, using minimal daily air temperature, day of the year, wind speed and solar radiation as predictors. Several criteria were used for selection of the best model. Results were compared with existing SHRP and LTPP models.*

Key Words: ***Pavement temperature, model selection, Cross-validation, Mallow's Cp,*** R^2 ***adjusted.***

1. INTRODUCTION

Temperature can contribute to certain common types of asphalt pavement distresses such as permanent deformation or rutting (typically associated with high temperature environments), bleeding, and thermal cracking (associated with low temperature environments). The Strategic Highway Research Program (SHRP) established the Long Term Pavement Monitoring Program (LTPP) program in 1987 to support a broad range of pavement performance analyses leading to improved engineering tools to design, construct, and manage pavements [3]. Libya in general, has a different environment from that of the North America and Gulf area, and therefore, the applicability of the recent SHRP and LTPP developments in the US to Libya's environmental conditions needed to be evaluated. Monitoring stations were set-up at eight locations in Libya to collect data on air temperature, wind speed, solar radiation and pavement temperatures at various depths.

Here we presents a part of this research, namely the model selection for prediction of minimal daily temperatures of the surface of the pavement, using minimal daily air temperature, day of the year, wind speed and solar radiation, based on data from Awbari, one of the eight locations where data were collected. Awbari is situated in desert part of Libya, latitude 26°46'N and longitude 12°57'E. The temperature data used in analysis were collected in the period from 1th of January 2012 to 31th of December 2012. The temperatures of the air and pavement were registered each 15 seconds, as well as the wind speed and solar radiation. Minimal daily temperatures of the air and pavement were extracted for each day of observed period. Based on these data, using regression analysis, models for minimal daily pavement surface temperatures were obtained. Similar research was done in [1] for Al Kufrah region in Libya, and in [5] for pavement temperatures in Serbia. Here we discuss the selection of the best regression model, applying six criteria. Data were analyzed using the R programming language (R 3.1.2), and the statistical package Statistica 12 (StatSoft Inc., Tulsa, OK, USA), university license for Novi Sad University.

2. DATA ANALYSIS

Prior to discussing the temperature models, a brief summary of the air and pavement temperature data is presented. In table 1 the descriptive statistics for minimal daily temperatures for the Awbari location are given, including the mean, 95% confidence interval (CI), minimum, maximum, standard deviation (St.Dev), skewness (Skew.) and kurtosis (Kurt.)

Table 1: Awbari minimal daily air and pavement surface temperatures

Min temp	Mean	-95%CI	95%CI	Min
Air	15.81	15.038	16.58	0.31
Surf.	18.53	17.73	19.32	4.16
Min temp	Max	St.Dev	Skew.	Kurt.
Air	29.73	7.49	-0.21	-1.19
Surf.	30.99	7.72	-0.21	-1.33

In figure 1 the scatter plot of minimal daily temperatures of the surface of the pavement against minimal daily air temperatures showing linear relationship. Thus, the first variable in the model is

minimal daily air temperature. Figure 2 presents minimal daily pavement surface temperature and air temperatures during study period (1.1.2012. - 31.12.212), showing non linear dependance on the day of the year, therefore time - day of the year, denoted by t, was included in the model as t and t^2. To establish the periodicity in behaviour of the minimal daily pavement surface temperatures we calculated periodogram [2] and singled out the harmonic component that has the highest contribution to the mean of the total sum of squares of time series. Therefore, time t - day of the year, was included in the model as sin($2\pi t/182$) and cos($2\pi t/182$). Days of the year were coded with codes: 0 for 1.1.2012, up to 366 for 31.12.2102.

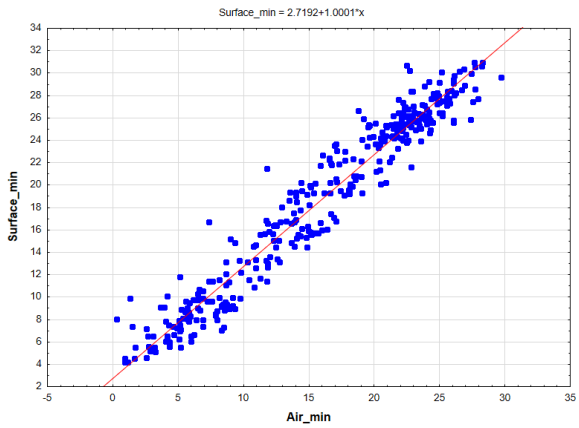

Fig. 1. Minimal daily surface pavement temperature against minimal daily air temperatures

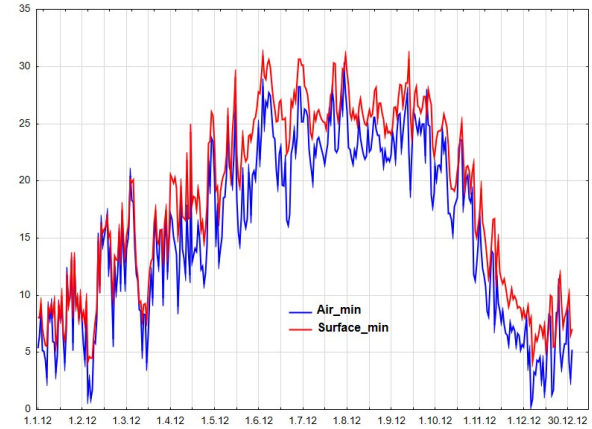

Fig. 2. Minimal daily surface pavement temperature against minimal daily air temperatures

Since daily minimal daily surface pavement temperature is affected by factors other than daily minimal air temperature and day of the year, other parameters were considered in order to improve the model, namely wind speed (m/s) and solar radiation (W/m^2). In table 2 all considered models are listed.

In order to select the best model, six criteria were applied. Adjusted R^2, Mallow's Cp, Akaike's information criterion (AIC), Bayesian information criterion (BIC), as well as two algorithms for cross-validation: leave one out cross-validation and 15-fold cross-validation. The split of 364 observations into 15 groups was done randomly with 100 replications. All criteria except Adjusted R^2 are based on balancing model complexity against quality of model's fit. The results are given in table 3. The values in bold denote the best model according to corresponding criteria

Table 2. *List of all considered models*

No.	Predictors
1	Air_min, t, t^2, $\sin\left(\frac{2\pi t}{182}\right)$, $\cos\left(\frac{2\pi t}{182}\right)$.
2	Air_min, t, t^2, WS, $\sin\left(\frac{2\pi t}{182}\right)$, $\cos\left(\frac{2\pi t}{182}\right)$.
3	Air_min, t, t^2, SR, $\sin\left(\frac{2\pi t}{182}\right)$, $\cos\left(\frac{2\pi t}{182}\right)$.
4	Air_min, t, t^2, $\cos\left(\frac{2\pi t}{182}\right)$.
5	Air_min, t, t^2, WS, SR, $\sin\left(\frac{2\pi t}{182}\right)$, $\cos\left(\frac{2\pi t}{182}\right)$.
6	Air_min, t, t^2, WS, $\cos\left(\frac{2\pi t}{182}\right)$.
7	Air_min, t, t^2, SR, $\cos\left(\frac{2\pi t}{182}\right)$
8	Air_min, t, t^2, WS, SR, $\cos\left(\frac{2\pi t}{182}\right)$
9	Air_min, t, t^2, $\sin\left(\frac{2\pi t}{182}\right)$
10	Air_min, t, t^2, WS, $\sin\left(\frac{2\pi t}{182}\right)$

Legend: Air_min – minimnal daily air temperature, t – day of the year, SR – solar radiation, WS – wind speed.

Table 3. *The best models, according to six criteria*

No	Mallows' Cp	Adj. R^2	AIC	BIC	CV1	CV15
6	**5.88**	0.9650	**1308.27**	**1335.55**	2.1184	2.1202
2	6.07	**0.9651**	1308.43	1339.61	**2.1179**	**2.1201**
8	7.87	0.9649	1310.26	1341.44	2.1293	2.1319
5	8.00	0.9650	1310.35	1345.43	2.1295	2.1325
1	12.30	0.9644	1314.75	1342.03	2.1566	2.1587
3	14.25	0.9643	1316.69	1347.88	2.1688	2.1716
4	14.94	0.9641	1317.35	1340.74	2.1749	2.1767
7	16.78	0.9640	1319.19	1346.47	2.1852	2.1878
9	19.60	0.9636	1321.92	1345.30	2.2001	2.202
10	21.27	0.9635	1323.60	1350.88	2.2108	2.2127

Legend: CV1 – leave on out cross-validation, CV15 - 15-fold cross-validation

For repeated 15-fold cross-validation the empirical distributions of CV-test criterion for applied methods may be obtained and compared (Figure 3).

Table 4. *Coefficients of the best model to predict minimal daily surface pavement temperature*

N=364	Residual standard error: 1.444 on 358 degrees of freedom Multiple R-squared: 0.9655, Adjusted R-squared: 0.965 F-statistic: 2005 on 5 and 358 DF, p-value: < 2.2e-16			
	b	Std.Err. of b	t(356)	p
Intercept	1.132758	0.242404	4.673	<0,01
Air_min	0.759659	0.019343	39.273	<0,01
t	0.088008	0.005708	15.417	<0,01
t^2	-0.000228	0.000015	-14.858	<0,01
WS	-0.096520	0.029012	-3.326	<0,01
$\cos(2\pi t/182)$	0.597117	0.133887	4.459	<0,01

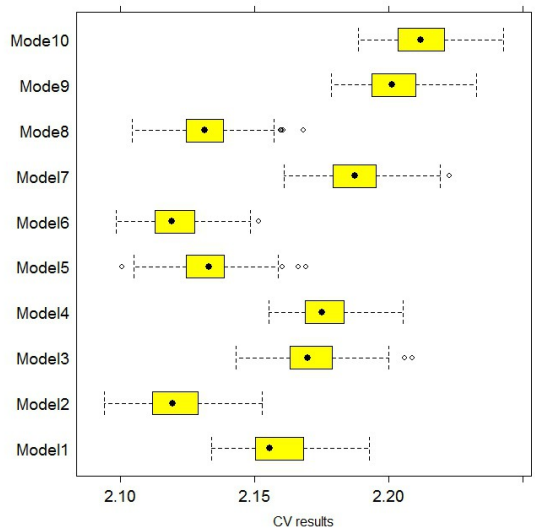

Fig. 3. Distribution of repeated 15-fold CV with 100 replications

2.1 Comparison of minimal daily pavement temperatures models

In order to compare our model and SHRP and LTPP low temperature prediction models for pavement surface temperature, we consider the SHRP model,

$$T_{surf}^{\min} = 0.859 * T_{air}^{\min} + 1.7 \quad (1)$$

and LTPP model

$$T_{surf}^{\min} = -1.56 + 0.72 * T_{air}^{\min} - 0.004 * Lat^2 + 6.26 \log_{10}(25) \quad (2)$$

where $T_{surf}^{\min}$ is the daily minimum pavement surface temperature, and $T_{air}^{\min}$ is minimum daily air temperature in °C and *Lat* is latitude for Awbari and is equal to 26.767 (26°46'N). The predicted models and collected data are presented in figure 4. It can be seen that the predicted minimal daily surface pavement temperatures by SHRP model are lower than both the measured values and the minimal daily surface pavement temperature predicted by the best model. The LTPP model underestimate high minimal daily surface pavement temperatures both for the measured values and for predicted temperatures by the best model.

3. CONCLUSIONS

Regression models for predicting minimal daily pavement surface as a function of minimal daily air temperature, day of the year, wind speed and solar radiation are considered. The best model was selected using adjusted R^2, Mallows' Cp, AIC, BIC and cross-validation. The comparison of the best model with SHRP and LTPP models indicates that the latter models would estimate lower minimal daily surface pavement temperatures for Awbari, Libya. Therefore, these models would be conservative in the selection of Performance Grade (PG) binders.

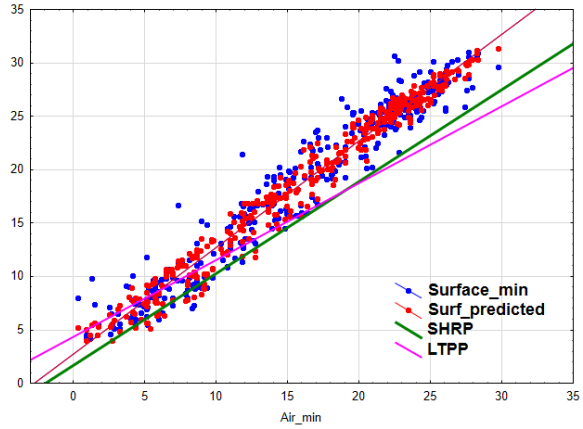

Fig. 4. Comparison between the best selected model for predicting minimal daily surface pavement temperature and SHRP and LTPP models.

4. ACKNOWLEDGMENTS

This paper was realized as a part of the Projects No.43007 and No.174019 financed by the Ministry of Education, Science and Technological Development of the Republic of Serbia.

5. REFERENCES

[1] Awadat Salem, H., Uzelac, Dj., Lozanov-Crvenković, Z., "Development of a model to predict pavement temperatures for Alkufrah region in Libya", *Journal of Society for Transportation and Traffic Studies (JSTS)* (2014) Vol.5 No.4

[2] Box, G.E.P., Jenkins, G. M., Reinsel, G.C., 2008, "Time Series Analysis, Forecasting and Control", fourth ed. John Wiley & Sons, Inc., Hoboken, New Jersey.

[3] Diefenderfer, B.K., Al-Qadi, I.L., Reubush, S.D. and Freeman, T.E., 2002, "Development an Validation of A Model to Predict Pavement Temperature Profile," Presented at Transportation Research Board 82ndAnnual Meeting, Washington DC

[4] Hassan, H.F., Al-Nuaimi, A.S., Taha R., Jafar, T.M.A. "Development of Asphalt Pavement Temperature Models for Oman" *The Journal of Engineering Research* Vol.2, No. 1 (2005) 32-42

[5] Matić, B., Matić, D., Radović , N., "Model for pavement temperature prediction in Serbia"

Building Materials and Structures 54 (2011) 4 (55-66)

[6] R Core Team. R: A language and environment for statistical computing. R Foundation for Statistical Computing. Vienna, **R version 3.1.2**; 2014. Available from: http://www.R- project.org/

[7] StatSoft Inc. STATISTICA (data analysis software system), v.12; 2012. Available from: www.statsoft.com

The 7th International Conference on Engineering and Technology
ICET-2015, Phuket, June 19-20, 2015
Prince of Songkla University, Faculty of Engineering
Hat Yai, Songkhla, Thailand 90112

Experimental Research on the Surface Roughness of Creep-Feed Grinding Process

Marin Gostimirovic[1]*, Pavel Kovac[1], Ildiko Mankova[2], Borislav Savkovic[1], Milenko Sekulic[1]
[1]University of Novi Sad, Faculty of Technical Sciences, Novi Sad, Serbia
[2]Technical University of Kosice, Faculty of Mechanical Engineering, Kosice, Slovakia
*Email of corresponding author: maring@uns.ac.rs

Abstract: *The creep-feed grinding process is a widely used manufacturing method in state of engineering products. By realizing needs of manufacturers, creep-feed grinding parameters must be carefully selected in order to maintain an high surface quality and optimum productivity. Surface roughness is generally accepted as an important indicator in creep-feed grinding process. In this study, effects of creep-feed grinding parameters* (*workpiece feed speed and depth of cut*) *to surface roughness parameters* (*roughness average, mean roughness depth, maximum roughness depth and profile bearing length ratio*) *were experimentally investigated. It was determined that the creep-feed grinding process gives an excellent surface quality.*

Key Words: ***Creep-feed Grinding / Surface Roughness Parameters / Conditions Machining***

1. INTRODUCTION

The grinding process is considered as one of the most important machining methods in the manufacturing of engineering products. The major advantages of grinding process are high precision and surface quality. In the recent period, besides the conventional multi-pass grinding, there has been a introduction of high performance grinding technology. These high performance grinding applications use larger cutting speeds and/or depths of cut in order to increase the low productivity which has been considered the main drawback of conventional grinding. However, the increase of conditions machining considerably changes kinematics of grinding process [1].

Creep feed grinding is a highly productive and accurate method of the machining intricate forms in a wide variety of materials. In creep-feed grinding, very slow (creep) workpiece feed speeds and extremely large depths of cut are used. Creep feed grinding process is characterized by a lower tool wear and surface roughness. At the same time, a prolonged time of contact wheel with workpiece material, results in the generation of more intensive heat load on the surface layer of the workpiece material [2, 3].

Based on the previous discussion, it is evident that creep-feed grinding process cause the specific surface integrity, i.e. surface topography and surface layer characteristics [4]. The topography is characterized by the waviness and surface roughness. The surface layer characteristics include local plastic deformation, microstructure phase changes, microhardness, residual stresses, burned surfaces and cracks [5, 6].

Surface roughness is represented by a large number of irregularities on the surface incurred during material remove by grinding wheel [7, 8]. Surface roughness during grinding process is dependent of the grinding granule abrasion orientation and the depth of cut. Fig. 6 shows mechanism of the surface roughness formation during grinding.

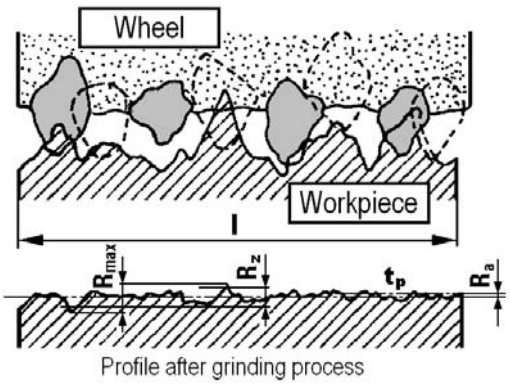

Fig. 1. Mechanism of the formation of surface roughness in grinding

In the present work, since the main task of the creep-feed grinding is to achieve satisfactory part quality with as large productivity as possible, special attention is focused on the effect that conditions machining have on the change of surface roughness. If the workpiece feed speed and depths of cut are poorly chosen, the overall effect can substantially diminish exploitation features of the finished part. Therefore, in order to enable machining of parts high surface quality, it is necessary to investigate the effects of the cutting conditions of creep-feed grinding on the workpiece surface roughness.

2. EXPERIMENTAL PROCEDURES

Experimental investigation was conducted on a surface creep-feed grinding machine »Majevica« type CF 412 CNC with 50 kW power (Fig.2). Fort the test used was a porous aluminium oxide wheel »Norton« type 32 A54 FV BEP, size 400×80×127 mm. Water-based cutting fluid (emulsion 6 %) was used during the grinding test with a flow rate of 175 l/min.

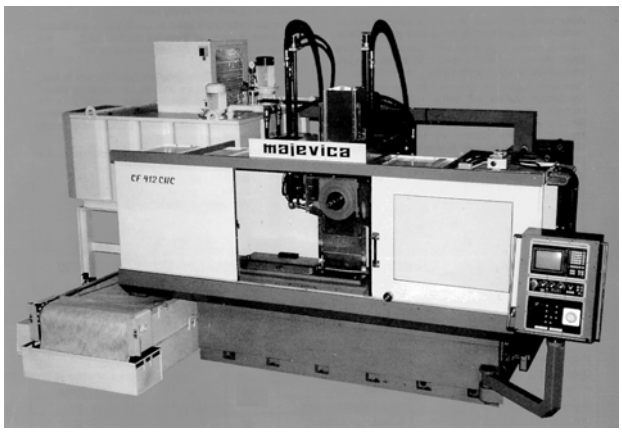

Fig. 2. CF 412 CNC surface creep-feed grinding machine

The workpiece material used in the experiment was high speed steel (HSS), B.S. BM 42. The chemical composition of the tested samples was as follows: 1,08% C; 0,22% Si; 0,23% Mn; 0,014% P; 0,019% S; 4,1% Cr; 1,5% W; 9% Mo; 1,1% V and 8% Co. The microstructure of investigated steel was martensite with fine globular cementite and hardness 66±1 HRc (Fig.3). Shape and dimensions of specimens used were 40×20×16 mm.

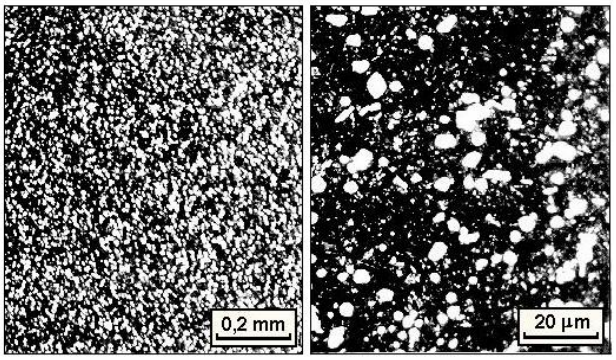

Fig. 3. Microstructure of high speed steel, B.S. BM 42

The machining conditions included variable workpiece feed speed and depth of cut. The range of the workpiece feed speed was v_w = 1; 2,5; 5; 10; 25 and 50 mm/s, while the depth of cut was a = 0,05; 0,1; 0,25; 0,5 and 1 mm. The wheel speed was held constant v_s = 30 m/s.

The experiment was conducted according to the specified experimental plan [9]. Input parameters were varied and the resulting surface roughness of creep-feed grinding process were monitored and recorded. Surface roughness measurements were conducted using surface profilometer »Form Talysurf« of the Rank Taylor Hobson Ltd (Fig.4).

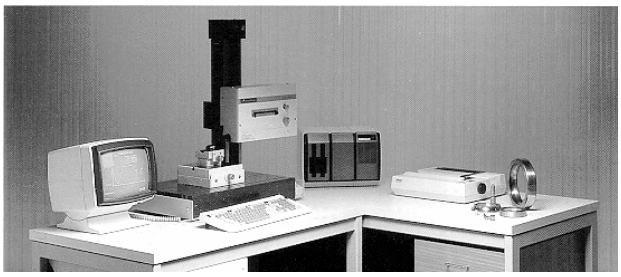

Fig. 4. Profilometer »Form Talysurf«

Surface roughness cannot be accurately characterized by using a single parameter. Instead, a set of surface roughness parameters is defined. In this testing measured were parameters (ISO 4287/1): arithmetic mean deviation of the assessed profile (Roughness Average R_a), mean height value of five local maxima and local minima (Mean Roughness Depth R_z), maximum height of the profile (Maximum Roughness Depth R_{max}) and description of the material portion in the roughness profile (Profile Bearing Length Ratio t_p). These parameters are the most widely utilized in different applications of surface topography.

3. RESULTS AND ANALYSIS

In order to identify the influence of creep-feed grinding on the surface roughness, a set of workpiece surface roughness parameters under different machining conditions were determined. Surface roughness were measured at various places the contact surface of the wheel/workpiece.

In Fig. 5 is shown experimentally obtained dependence between the surface roughness parameters (roughness average R_a, mean roughness depth R_z, maximum roughness depth R_{max} and profile bearing length ratio t_p) and the depth of cut, for a constant workpiece feed speed. The diagram shows a slight increase of surface roughness parameters with the increase of the depth of cut.

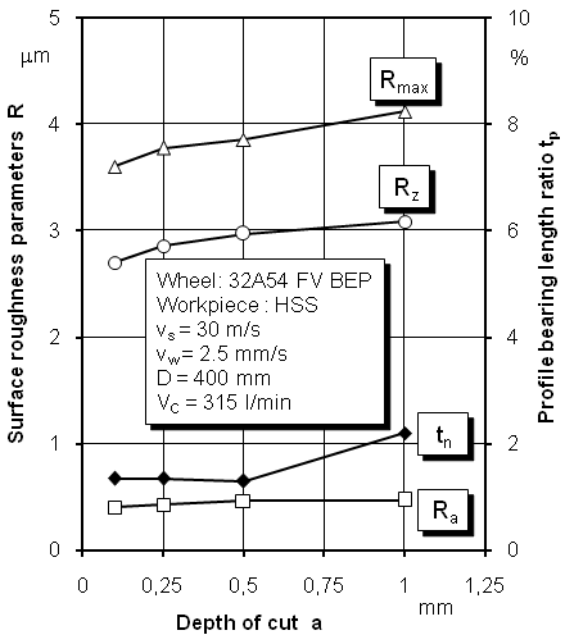

Fig. 5. Influence of the depth of cut on surface roughness parameters

In Fig. 6 is shown an experimentally obtained dependence between the surface roughness parameters and the workpiece feed speed, for a constant depth of cut. The diagram shows a slight decline of surface roughness parameters with the increase of the workpiece feed speed.

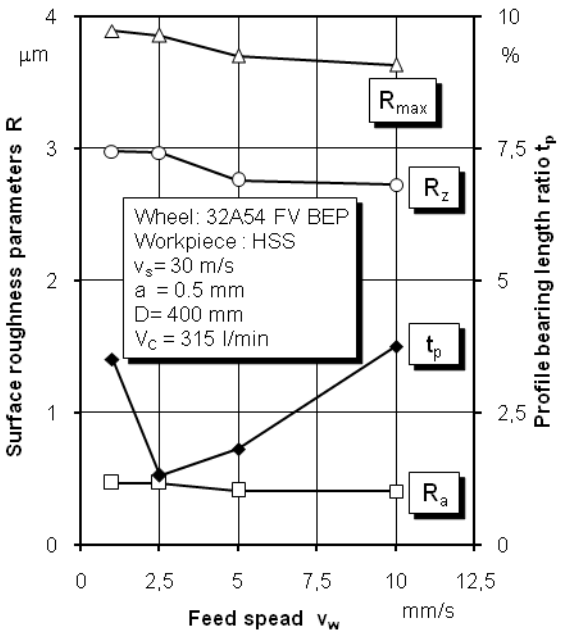

Fig. 6. Influence of the workpiece feed speed on surface roughness parameters

The increase of the surface roughness parameters with increasing the depth of cut is obvious primarily because of increased chip thickness and higher friction between the workpiece and the grinding granule. On the other hand, when the workpiece feed speed is increasing, due to the decrease of the contact time on the workpiece material and the faster flow of coolant to the grinding surface, the surface roughness parameters are decreasing. However, the results of experimental investigation show that the decrease of workpiece feed speed and depth of cut have negligible influence on surface roughness parameters. But it is evident that the creep-feed grinding process gives an excellent surface quality N5.

Further on, Fig. 7 shows the influence of the cutting conditions (workpiece feed speed and depth of cut) on the surface roughness parameters, for a constant specific productivity Q'_w. The diagram shows that there exists an optimal specific productivity ($Q'_w = v_w \cdot a = 2{,}5$ mm^3/mm s) which results in minimum values of the surface roughness parameters.

4. CONCLUSIONS

Based on this experimental investigation, the following conclusions can be made:

- Considering of the ever increasing requirements in terms of productivity and surface quality, the role of creep-feed grinding becoming more and more important in comparison to conventional grinding;

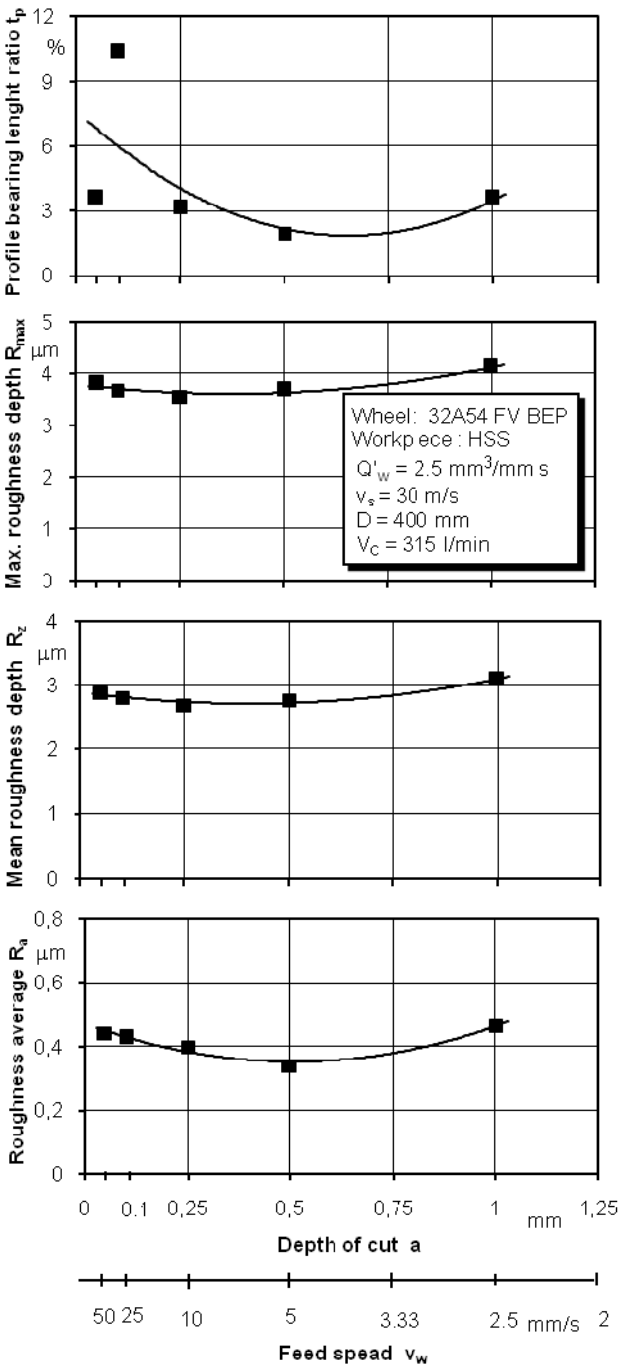

Fig. 7. Dependence of surface roughness parameters on cutting conditions for a constant specific productivity

- Increasing the depth of cut leads to a slight increase of surface roughness parameters, primarily because of the increased friction length between the wheel and the workpiece material;
- With decreasing the workpiece feed speed, the surface roughness parameters are increasing, due to the increased time in which the grinding process influence the workpiece material;
- In the creep-feed grinding there exists an optimal cutting conditions (specific productivity) which results in minimum values of the surface roughness parameters;

- Due to the low feed speed, creep-feed grinding workpieces impress with better surface roughness, i.e. workpieces have a glossy surface quality.

5. REFERENCES

[1] J. Kopac, and P. Krajnik, "High-performance grinding - A review", *Journal of Materials Processing Technology*, 2006, Vol. 175, No 1-3, pp. 278-284.

[2] M. Gostimirovic, M. Sekulic, J. Kopac, and P. Kovac, "Optimal control of workpiece thermal state in creep-feed grinding using inverse heat conduction analysis", *Journal of Mechanical Engineering*, 2011, Vol. 57, No 10, pp. 730-738.

[3] J. S. Kim, J. D. Hwang, and Y. G. Jung, "Development of twin wheel creep-feed grinding machine using continuous dressing for machining of aircraft rotary wing", *Journal of Central South University of Technology*, 2011, Vol. 18, No 3, pp. 704-710.

[4] P. Krajnik, J. Kopac, and A. Sluga, "Design of grinding factors based on response surface methodology", *Journal of Materials Processing Technology*, 2005, Vol. 162, pp. 629-636.

[5] M. Gostimirovic, P. Kovac, D. Jesic, B. Skoric, and B. Savkovic "Surface layer properties of the workpiece material in high performance grinding", *Metalurgija*, 2012, Vol. 51, No 1, pp. 105-108.

[6] S. Guo, and S. Malkin, "Analytical and experimental investigation of burnout in creep-feed grinding", *Annals of the CIRP*, 1994, Vol. 43, pp. 283-286.

[7] R. L. Hecker, and S. Y. Liang, "Predictive modeling of surface roughness in grinding", *International Journal of Machine Tools and Manufacture*, 2003, Vol. 43, No 8, pp. 755-761.

[8] X. Zhou, and F. Xi, "Modeling and predicting surface roughness of the in grinding process", *International Journal of Machine Tools and Manufacture*, 2002, Vol. 42, No 8, pp. 969-977.

[9] P. Kovac, I. Mankova, M. Gostimirovic, M. Sekulic, and B. Savkovic "A reviews of machining monitoring systems", *Journal of production engineering*, 2011, Vol. 14, No 1, pp. 1-6.

The 7th International Conference on Engineering and Technology
ICET-2015, Phuket, June 19-20, 2015
Prince of Songkla University, Faculty of Engineering
Hat Yai, Songkhla, Thailand 90112

Small Project Examination Timetabling Assignment with Multi-level Penalty Values

Trirat Soemsap
Udon Thani Rajabhat University, Faculty of Science, Thailand
Email: Treerat54@hotmail.com

Abstract: *A memetic algorithm was used for exam timetabling in this study with 16–22 time slots, comprising 3 hard and 5 soft constraints. Multi-level penalty values were used to find the fitness values. Three types of penalty values were used, with some similarities between the second and third. In the first type, penalty values were in the form of linear equations; the other types utilising linear equations which increased into the large values at the high penalty level. The findings suggest that the experiments employing the second and third penalty values yield better results than the first, in terms of time taken to find the best solution with the lowest number of violations of the soft constraints with a high-score penalty. None of the three experimental types violated the hard constraints.*

Key Words: ***timetable / local search / memetic algorithm / project examination timetable / multi-level penalty values***

1. INTRODUCTION

Most studies of timetabling utilise the number of constraint violations to determine the appropriateness of a timetable. This research aimed to investigate how to organise the timetable to more effectively meet the various needs of those involved. The examination timetabling for the projects of computer science and information technology majors in Udon Thani Rajabhat University has been a challenging task, and therefore the researcher decided to use this situation as a case study for testing students' projects, using the dual criteria of having to pass Project 1 and Project 2 courses and also that the examinations committee should have sufficient expertise and interest in their work to provide useful comments and recommendations for subsequent improvement.

The study divides the experimental procedures into three types in order to find the optimum, as discussed in section three. Section two discusses related studies and relevant theories, section four the experimental results , section five discusses the experiment and section six presents the conclusion.

2. THEORIES AND RELATED RESEARCH

2.1 Related studies

Studies pertaining to institutional academic timetabling may be categorised into course timetabling [2], [3], [5], examination timetabling [6], [7], and master thesis timetabling [8], all of which use algorithms such as the genetic algorithm [2], [3], [9], local search [10], [11], particle swarm optimisation [7], [12] and the memetic algorithm [1]. With regard to penalty values, the number of violations occurring determines increase in these values in most studies. In actual fact, penalty values comprise multiple levels of expertise, interest and importance of the task. Many studies, therefore, including this research, have employed such values [2], [3], [4], [13].

2.2 The Memetic algorithm

The memetic algorithm is derived from the genetic algorithm in order to facilitate achievement of a result. In its operation, the genetic algorithm is analogous to the biological natural selection of genes, adopting terms such as '*chromosomes*' and '*chromosome selection for the next generation*.' With respect to timetabling, therefore, a timetable is regarded as a chromosome, which should, as far as possible, accommodate hard and soft constraints. In addition, the operations of strain include crossover and mutation, rendering them different from the original chromosomes, which may have more or less fitness. The memetic algorithm adds a local search component to enable access to a wider variety of chromosomes. Finally it uses the replacement function which replace the old chromosomes with the best and the selected chromosomes. These steps are continually repeated to enable expression of the desirable chromosomes in accordance with the constraints . [1]

2.3 Multi-level penalty values

The fitness of chromosomes is determined from each event within the timetable. If they frequently violate many constraints, they accumulate many penalty values, resulting in a suboptimal timetable. Chinnasri [3] designed penalty values by using a constant divided by 2^n. In the study [2], [4], [13], the fuzzy sets were used to

calculate the penalty values of the soft constraints which had consumed more time.

2.4 Related system

Data for the experiments were extracted from 79 projects conducted in 2012 involving 18 lecturers, 5 rooms and 21 time slots, each being one hour in length. Each examinatiion employed an advisor and two concerned lecturers. At present, all examination timetabling has been performed manually, which has the disadvantages of being both time consuming and unable to satisfy everyone's requirements.

3. THE EXPERIMENTS

3.1 Data

The database used consisted of tables such as time slots, room-time slots, rooms, lecturers, lecturers' expertise and busy periods, projects, project types, project classification, chromosomes and chromosome details.

3.2 Constraints

An important issue in scheduling is defining the most desirable scheduling characteristics, in other words determining the constraints, which may be described as hard and soft. Whenever values were set or changed within the experimental procedures, this was done in accordance with the hard constraints, enumerated as follows:

H1: In one time slot, a lecturer can attend only one examination, and has a single responsibility;

H2: A group of students can take an examination only once;

H3: A room in one slot can be used for only one examination.

The soft constraints involved during the timetabling process were addressed as follows:

S1: Schedule the timetable recognising the importance of the time slots of the concerned advisor and lecturers;

S2: Consider the lecturers' level of interest in the project types;

S3: Schedule the lecturers' timetables equally, except in the case of those having previous commitments, and who therefore are only available for fewer timetables;

S4: The standard deviation of the amount of variation between the number of examinations and of the scheduled examinations is at a minimum;

S5: Consideration of the number of 16–22 time slots for timetabling in this study to provide alternatives for the users.

Table 1 *The weight value of soft constraints*

WType	W1	W2	W3	W4
1	150	167	0	2000
2	100	167	1000	4000
3	565	470	1000	1335
4	300	167	267	1000
5	300	167	267	500

Table 2 *Penalty values of the soft constraint S1*

Penalty levels	Type1	Type2	Type3
No	0	0	0
Little	1	5	5
Middle	2	30	30
Much	3	1000	1000

Table 3 *Penalty values of the soft constraint S2*

Penalty levels	Type1	Type2	Type3
0-6	0-6	0-6	0-6
7-13	7-13	7-13	7-13
14-19	14-19	14-19	14-19
20, 21, 22	20, 21, 22	60, 63, 66	512,724,1024
23, 24	23, 24	69, 72	1448, 2048

Table 4 *Penalty values of the soft constraint S3, S4*

Penalty levels	Type1	Type2	Type3
|difference|<5	|difference|	|difference|	|difference|
|difference|≥5	|difference|	$\|difference\|^3$	$\|difference\|^4$

	Time slot 1			**Time slot 2**			**…**	**Time slot T**		
	room 1	room 2	room 3	room 1	room 2	room 3	…	room 1	room 2	room 3
Trno	1	2	3	4	5	6	…	3T-2	3T-1	3T
Pno							…			
TnoA							…			
Tno1							…			
Tno2							…			

Fig. 1. *Example of a chromosome with 3 rooms*

3.3 Parameter Setting

The weight values in Table 1 were obtained from the openion survey of the concerned lecturers. Table 2 demonstrated the different panalty values resulting from the timetabling being unable to meet the involved party's requirements. Unlike other studies which adopted the yes - no penalty scale, this contained three levels of penalty: little, middle and much. Table 3 indicated the values of indifference toward the assigned topics in each level. Table 4 illustrated the penalty values resulting from the difference in the number adjusted for the committee and the original one.

3.4 Chromosomes

Fig. 1 demonstrates the behaviour of a chromosome in the case of three rooms and T time slots. Trno represents the room-time slot number, Pno the project number, TnoA the advisor, Tnol the first lecturer and Tno2 the second lecturer.

The initial number was 50 chromosomes, commencing with random numbering of the room-time slots from one project to another. Any room-time slots without the project examination were filled with 0, the values of the advisor being read from a database in memory and entered in TnoA, with those of the first and second lecturers entered by randomly to Tno1 and Tno2, respectively.

3.5 Fitness

During the processing, violation of the hard constraints was controlled, so that the fitness values could then be calculated from those resulting from violation of the soft constraints using the following equation:

$$Fitness(n) = \sum_{i=1}^{4} w_i p_i \qquad (1)$$

Equation (1) was employed to find the fitness values of the nth chromosome. Those with the lower values were considered to be better. W_i was the weight of the ith soft constraint whereas P_i was the sum of the average penalty value of the ith soft constraint.

The experiments were partitioned into three types: Type 1, Type 2 and Type 3, each using five sets of weights, the last being used to summarise the results. The penalty values of the soft constraints are shown in Tables 2–4.

3.6 Methods

The process of creating examination timetables involved the following sequence of steps:

(1) Read the related table from the database into the memory and created 50 chromosomes as mentioned in section 3.3;

(2) Generate three times as many chromosomes by changing the examination committee in all room-time slots randomly for 40 % of the room-time slots;

(3) Generate three times as many chromosomes by switching the examination committee in the same time slots randomly for 40% of all time slots;

(4) Generate three times as many chromosomes by randomly switching 40% of the time slots;

(5) Find the fitness values from Steps (1)–(4) chromosomes;

(6) Select the best five chromosomes;

(7) Select the chromosomes remaining from (6) by using the roulette wheel technique [14], yielding 45 chromosomes;

(8) Confirm whether fifty rounds of the processes from Steps (2)–(7) have been performed and the best five chromosomes recorded at completion of the processes and then create 50 new chromosomes, entering those in Steps (6)–(8) together, or if not, those in Steps (6) and (7) should be entered together; and

(9) Verify whether 5,000 rounds of all processes had been accomplished. If so, select the best 100 chromosomes. If not, repeat the process in Step (2).

4. RESULTS

The four weight sets and seven types of time slots were used for each experiment type. Data processing was performed four times with 5,000 rounds for each experiment. To enable comparisons of each experiment type, 100 of the best chromosomes from each experiment were selected and passed through the 5th set of weight values and penalty values of the soft constraints of Type1. Table 5 indicates that, when 5,000 rounds had been completed, Types 2 and 3 yielded marginally better fitness values. Table 6 displays the time (in seconds) at which the optimum chromosomes were found and the average time in seconds taken for identification of the best chromosomes in each experiment in Table 5. Experiment Types 2 and 3 yielded the best answers for all experiments, and the best of each of these was faster than that of Type 1.

Table 7 shows the minimum fitness values after a 10–minute processing time. The fitness values occurring after 5,000 rounds and ten-minute rounds are not dissimilar. Fig. 2–4 suggest that the Type 2 and Type 3 experiments were 92% better than Type 1.

Table 5 *The fitness after 5000 rounds*

Experiment	Type 1	Type 2	Type 3
Minimum	2439	2392	2417
Average	3184.60	3144.94	3156.77

Table 6 *The time at which the best was found*

Experiment	Type 1	Type 2	Type 3
Second	8137	7403	3034
Average second	6848.04	4155.21	3744.71

Table 7 *The fitness after 10 minutes*

Experiment	Type 1	Type 2	Type 3
Minimum	2665.83	2603.72	2633.33
Average	3382.61	3363.11	3460.12

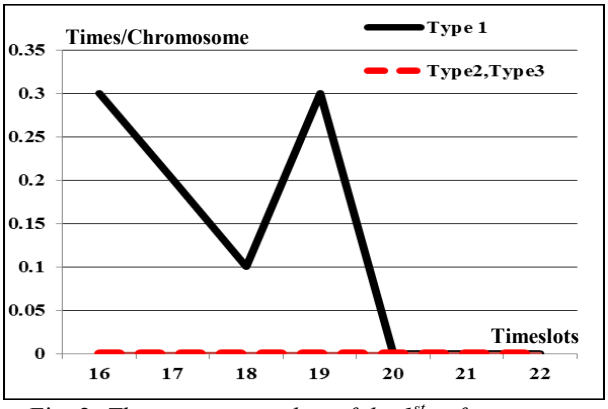

Fig. 2. *The average number of the 1st soft constraint violating with the highest penalty level*

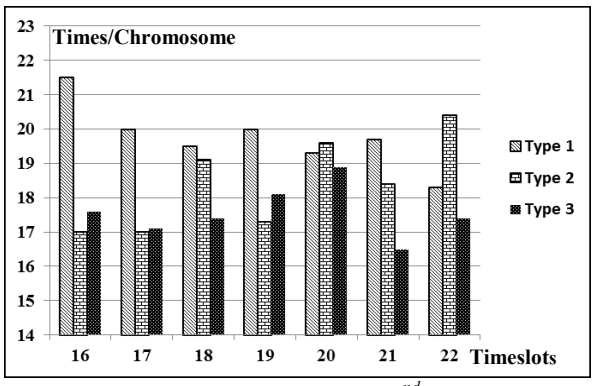

Fig. 3. *The average number of the 2nd soft constraint violating with a penalty level of more than 19*

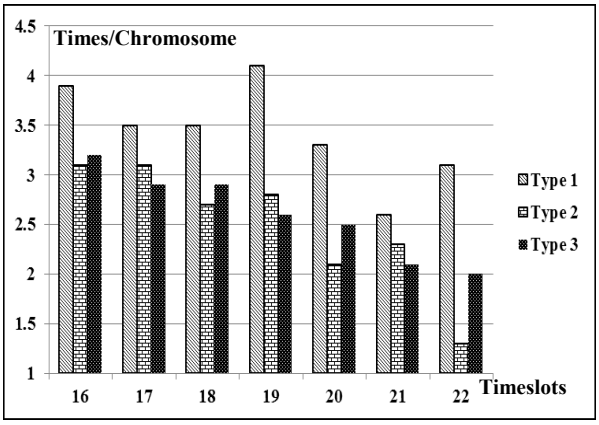

Fig. 4. *the average number of the 3nd soft constraint violating with a penalty level of more than 4*

5. DISCUSSION

The fact that the second and third experiments yielded the better results in terms of the speed and the number of the soft restraint violation with the high penalty value probably resulted from the fact that the high penalty value used in the former was a little higher than that utilized in the latter. The high-valued chromosomes might be selected as the parental ones, but in the two experiments such chromosomes were rapidly extracted.

6. CONCLUSION

The research procedures in examination timetabling for undergraduate projects aimed to compare the effectiveness of two methods; one applying a linear equation, the other a linear equation increasing into the large values at the high penalty level. The study, which employed a memetic algorithm and 'roulette wheel' techniques for chromosome selection, found that the optimum fitness values of the latter two types produced superior results. However, the time intervals in which the best chromosomes were found, and the average times in which the best chromosomes for each experiment were identified were superior to those for Type 1. With respect to violation of the soft constraints with high scoring penalty values in all experiments, the latter two types resulted in a 92% lower value than the first type.

ACKNOWLEDGMENT

This research was supported by Udon Thani Rajabhat University.

REFERENCES

[1] M. A. Ahandani and M. T. V. Baghmisheh. 2011. Memetic Algorithms for Solving University Course Timetabling Problem . 2011 1st International Conference on Computer and Knowledge Engineering (ICCKE), Mashhad, Iran, Oct. 13-14, 2011: 40-44.

[2] M. S. Kohshori, M. S. Abadeh and H. Sajedi. (2011). A Fuzzy Genetic Algorithm with Local Search for University Course Timetabling. Data Mining and Intelligent Information. 2011 3rd International Conference on Data Mining and Intelligent Information Technology Applications (ICMiA 2011), Macao, Chaina, Oct. 24-26, 2011: 250–254.

[3] W. Chinnasri. 2012. The Optimal Genetic Algorithm Design for University Time-tabling Problem. Thesis for the Degree of Doctor of Philosophy, Computer Education, King Mongkut's University of Technology North Bangkok, Bangkok, Thailand. (in Thai)

[4] R. Perzina and J. Ramik. 2013. Timetabling Problem with Fuzzy Constraints: A Self-Learning Genetic Algorithm. International Journal of Engineering and Innovative Technology (IJEIT), 3(4), 105-113.

[5] S. Yang and S. N. Jat. 2011. Genetic Algorithms With Guided and Local Search Strategies for University Course Timetabling. IEEE Transactions on Systems, Man, and Cybernetics—Part C: Applications and Review, 41(1): 93-106.

[6] S. K. Jha. 2014. Exam Timetabling Problem using Genetic Algorithm. Journal of Research in Engineering and Technology, 3(5): 649-654.

[7] N. R. Sabar, M. Ayob, G. Kendall and R. Qub. 2012. A Honey-bee Mating Optimization Algorithm for Educational Timetabling Problems. European Journal of Operational Research, 216: 533–543.

[8] H. T. T. Binh, P. Q. Dung and P. D. Dat. 2012. Genetic Algorithm for Solving the Master Thesis Timetabling Problem with Multiple Objectives. The 2012 Conference on Technologies and Applications of Artificial Intelligence, Tainan, Taiwan, Nov. 16-18, 2012: 74-79.

[9] S. Innet. 2013. A Noval Approach of Genetic Algorithm for Solving Examination Timetabling Problems. 2013 13th International Symposium on Communication and Information Technologies(ISCIT), Surat Thani, Thailand, Sep. 4-6, 2013: 233-237.

[10] A. Abuhamdah, M. A. G Kendall and N. R. Sabar. 2014. Population Based Local Search for University Course Timetabling Problems. Applied Intelligence, 40(1): 44-53.

[11] A. Schaerf. 2002. Local search techniques for large high school timetabling problems. Systems, Man and Cybernetics, Part A: Systems and Humans, IEEE Transactions, 29(4): 368 – 377.

[12] M. Nandhini and S. Kanmani. 2012. Comparison of Memetic Algorithm and PSO in Optimizing Multi Job Shop Scheduling. International Journal of Advanced Research in Computer Engineering & Technology, 1(5): 256-261.

[13] D. Lei. 2012. Co-evolutionary Genetic Algorithm for Fuzzy Flexible Job Shop Scheduling. Applied Soft Computing, 12: 2237–2245.

[14] W. Chinnasri and N. Sureerattanan. 2010. Comparison of performance between different selection strategies on genetic algorithm with course timetabling problem. Advanced Management Science (ICAMS), 2010 IEEE International Conference. Chengdu, China, Jul. 9-11, 2010: 105-108.

The 7th International Conference on Engineering and Technology
ICET-2015, Phuket, June 19-20, 2015
Prince of Songkla University, Faculty of Engineering
Hat Yai, Songkhla, Thailand 90112

Factors Influencing the Implementation of NFC Smart Posters

Wasinee Noonpakdee*, Patchareerat Mitchorb
Thammasat University, Collage of Innovation, Thailand
*Email of corresponding author: wasinee@citu.tu.ac.th

Abstract: *Near Field Communication (NFC) is regarded as one of the recent ICT developments that has attracted great interest from research communities and industries. Smart posters are NFC applications which provide an easy way to access the benefits of NFC. This paper presents a framework for implementing NFC smart posters, and explores the various factors influencing the implementation of NFC smart posters in a city in Thailand. An empirical study is applied by conducting in-depth interviews. The results indicate significant factors which influence the implementation of NFC smart posters from the prospective of city, content provider, and user.*

Key Words: ***NFC, Smart Posters, Success factors, Acceptance Model***

1. INTRODUCTION

Near Field Communication (NFC) is a short-range half duplex communication, which provides simple and secure communication based on Radio Frequency Identification (RFID) communication [1]. NFC depends on inductive coupling between transmitting and receiving devices, and has been adopted as a basic configuration of the system on many smart phones [1, 2]. The communication range is within few centimeters with 13.56 MHz operating frequency. A wide variety of NFC applications have been subsequently developed over the past few years [1-5].

Smart posters are one of the promising applications of NFC technology due to user-friendly feature, as they provide some information to users without a considerable amount of user interaction [6]. Moreover, smart posters are easy to implement in large volumes, flexible in size and usage, readily updateable, and low in cost compared with other forms of dynamic display [7].

Smart posters can come in many forms such as simple posters, billboards, magazines, and even three-dimensional objects. Smart Posters are attractive to retailers, transport agencies, health care providers, and any entities which have information to share [7, 8]. Examples for NFC smart posters include a poster with some tourist information and directions, a timetable displayed at a bus stop, coupons inserted in a magazine for marketing campaigns, movie promotions, parking, shops and restaurants, maps, taxi ordering, and information provided for education [7-9].

This paper proposed a framework for implementing NFC smart posters in a city in Thailand to provide tourist information and maps, and to support shops and restaurants for coupons and promotions. The factors influencing the implementation of NFC smart posters are studied through literature reviews and in-depth interviews.

The rest of this paper is organized as follows. In Section 2, the system model is provided. Section 3 presents system implementation and factors influencing the implementation of NFC smart posters. Finally, Section 4 concludes the paper.

2. SYSTEM MODEL

To implement NFC smart posters, we adapted the model described in [7]. Our proposed system model consists of three entities: city, content provider, and user as illustrated in Figure 1.

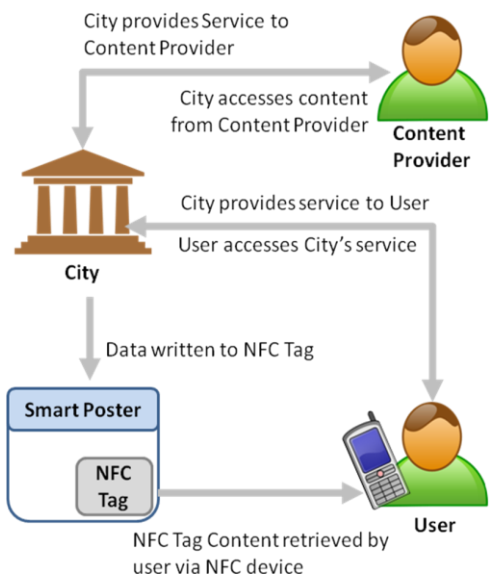

Fig. 1. Illustration of a model for implementing NFC smart posters (Adapted from [7])

From Figure 1, the city is responsible for providing the NFC service and platform as well as overall management of NFC smart posters system. The content provider could be a hotel, restaurant, shop, tourist site, museum, or an advertising agency. The content provider has to register to be a member of the system. Then, the content provider can access the service and provide some contents to the city. The city puts these contents to NFC tag, and the contents are retrieved by user through NFC device when user touches smart posters. User of this system could be customer, tourist, or local people who live in the city.

NFC Smart Posters can be located almost anywhere depending on city's plan. With NFC smart posters, users are able to engage in the services offered in an active way.

When applied in tourism, this system helps reduce the number of printed brochures used in the tourist industry while providing users with interactive and real-time information through the simplicity of touch. Moreover, if the system is introduced in a museum, users could access more detailed information, including further text, photos, audio, and video content [7].

For hotels, shops, and restaurants, smart posters could be applied for location-based personalized coupons and promotions. Users can download coupons and discount relevant to each person's location and personal profile which were store in their mobile [7]. Furthermore, the city could act as a content provider that provides some information to local people such as city services, maps, or events calendar.

3. RESULT & DISCUSSION

In this section, we study factors influencing the implementation of NFC smart posters in a city in Thailand. From the framework shown in Figure 1, the entities related to the implementation are city, content provider, and user.

We conducted an empirical study by reviewing literatures and in-depth interviewing a content provider, two city's top management persons, and four users.

From city and content provider's prospective, the success factors in project implementation are considered [10-14]. From user's perspective, technology adoption model is reviewed [6, 7, 15]. The result from literature reviews and in-depth interviews illustrates factors influencing the implementation of NFC smart posters as show in Table 1.

Table 1. Factors influencing the implementation of NFC smart posters

Aspects	Factors	Sub-Factors
City and Content provider 's perspective (Success factors)	Top management support	Government Support
		City’s top management support
		Financial support
		Vision / strategy
		/ policy
	Management	Project managemnt
		Change management
		Partner and supplier management
		Risk management
		Stakeholder management
	People	Education and training
		Project Manager Competencies
		Staff Competencies
		User skills
		Stakeholders involvement
	Technology	NFC Technology
		Infrastructure
		Technological change
	Communications	Public Relations
		Communication Management
	Project monitoring, evaluation, and control	Quality control
		System maintenance
		Continuous monitoring, evaluation, and control
User's perspective	Technology adoption	Perceived usefulness
		Perceived ease-of-use
		Security and privacy
		Attractive contents
		Updated contents
		Compatibility with user's Lifestyle

According to the in-depth interviews, from city and content provider's perspective, the most significant factors influencing the implementation of NFC smart are Government and city's top management support. Similar to any other new technology adoption project [14], the

support and commitment of top management is influential in the adoption decision and the success of the NFC smart posters implementation. Moreover, the support of top management, especially financial support, makes the implementation process smoother. Other significant factors are stakeholder management, smart posters' project public relation, and project management.

From user's perspective, the most significant factors are perceive ease of use, perceive usefulness, updated content, and compatibility with user's lifestyle.

4. CONCLUSION

A Framework for implementing NFC smart posters is proposed in a city in Thailand in order to provide people an easy way to access the benefits of NFC technology. The NFC smart posters application could provide tourist information, coupons and promotions, maps, and city events calendar. Furthermore, the factors influencing the implementation of NFC smart posters are studied not only from city and content provider's prospective but also from user's prospective.

The results of this research can be applied for an actual implementation of NFC smart posters for providing various attractive services to users to enhance their experience. Moreover, this paper can be a guideline for other ICT project implementations.

5. REFERENCES

[1] V. Coskun, B. Ozdenizci, and K. Ok, "A Survey on Near Field Communication (NFC) Technology," *Wireless Personal Communications*, vol. 71, pp. 2259-2294, 2013.

[2] J. Ma and J. E, "An NFC-based Scenic Service System " *Journal of Networks*, vol. 9, 2014.

[3] M. S. AlZuhair, A. B. Najjar, and E. Kanjo, "NFC based applications for visually impaired people - A review," in *Multimedia and Expo Workshops (ICMEW), 2014 IEEE International Conference on*, 2014, pp. 1-6.

[4] J. Fischer, "NFC in cell phones: The new paradigm for an interactive world [Near-Field Communications]," *Communications Magazine, IEEE*, vol. 47, pp. 22-28, 2009.

[5] A. Juntunen, S. Luukkainen, and V. K. Tuunainen, "Deploying NFC Technology for Mobile Ticketing Services- Identification of Critical Business Model Issues," in *Mobile Business and 2010 Ninth Global Mobility Roundtable (ICMB-GMR), 2010 Ninth International Conference on*, 2010, pp. 82-90.

[6] K. Boes, L. Borde, and R. Egger, "Information and Communication Technologies in Tourism 2015," in *The Acceptance of NFC Smart Posters in Tourism* ed: Springer, 2015.

[7] *Smart Posters: How to use NFC tags and readers to create interactive experiences that beneft both consumers and businesses*: NFC Forum, 2011.

[8] P. C. Garrido, G. M. Miraz, I. L. Ruiz, and M. Á. Gómez-Nieto, "A Near Field Communication Tool for Building Intelligent Environment using Smart Posters " *Internaitonal Journal of Computers and Communications*, vol. 4, pp. 9-16, 2010.

[9] D. Volland, K. Noyen, O. Kayikci, L. Ackermann, and F. Michahelles, "Switching the Role of NFC Tag and Reader for the Implementation of Smart Posters," in *Near Field Communication (NFC), 2012 4th International Workshop on*, 2012, pp. 63-68.

[10] M. A. AlSuwaidi and A. V. Rajan, "E-government failure and Success Factors Rank Model an extension of Heeks Factor Model," in *Current Trends in Information Technology (CTIT), 2013 International Conference on*, 2013, pp. 161-165.

[11] D. Handayani, R. B. Abdullah, M. A. Abdulgani, and A. Rahman bin Ahmad Dahlan, "Critical success factors for IS project implementation in Malaysian institutions of higher learning," in *Information and Communication Technology for the Muslim World (ICT4M), 2010 International Conference on*, 2010, pp. E40-E47.

[12] O. S. Ogunleye and J. P. Van Belle, "Exploring the success, failure and factors influencing m-Government implementation in developing countries," in *IST-Africa Conference Proceedings, 2014*, 2014, pp. 1-10.

[13] D. Ronggui and W. Yanwei, "An Empirical Study on Critical Success Factors Based on Governance for IT Projects in China," in *Wireless Communications, Networking and Mobile Computing, 2008. WiCOM '08. 4th International Conference on*, 2008, pp. 1-7.

[14] E. W. T. Ngai, D. C. K. Chau, J. K. L. Poon, A. Y. M. Chan, B. C. M. Chan, and W. W. S. Wu, "Implementing an RFID-based manufacturing process management system: Lessons learned and success factors," *Journal of Engineering and Technology Management*, vol. 29, pp. 112-130, 2012.

[15] C. Yu, "Understanding Technology Adoption through System Dynamics Approach: A Case Study of RFID Technology," in *Embedded and Ubiquitous Computing (EUC), 2011 IFIP 9th International Conference on*, 2011, pp. 366-371.

The 7th International Conference on Engineering and Technology
ICET-2015, Phuket, June 19-20, 2015
Prince of Songkla University, Faculty of Engineering
Hat Yai, Songkhla, Thailand 90112

DECCE - Development of Engineer's Competencies by Changes in Education

Dušan Kovačević*, Leposava Grubić-Nešić, Aco Antić, Slavica Mitrović. Jelena Nikolić
University of Novi Sad, Faculty of Technical Sciences, Novi Sad, Serbia
*email: dusan@uns.ac.rs

Abstract: *This paper is a short review about the DECCE project proposed in the framework of Erasmus+ EU development program. Basic efforts in our investigation will be directed on the improvement of out-of-date concept of engineering education and make of circumstances for "New status of engineer's profession". DECCE proposal has international character and importance because such kind of problems is obvious even in many well organized and developed state environments.*

Key Words: Engineering Education, Technical Knowledge, Real Competencies

1. INTRODUCTION

The current education in the engineering field is slightly overloaded by facilities that are unnecessary and sometimes hide the essence of engineering application. Explanation is the fact that those who impose only a theoretical approach are not engineers, but only trainers, educators and/or professors. This circumstance is particularly pronounced in well-established university environments.

The principal idea of our project DECCE (Development of Engineer's Competencies by Changes in Education) is increasing of attractiveness of engineering studies in West Balkan Countries (WBC) universities, through innovative, entrepreneurial and soft-skill oriented educational concept, according to principles of European Higher Education Area (EHEA).

Goal of the proposed research are reasonable changes in the education concept which will be the base of a new professional profile of a graduated engineer: with enthusiasm and advanced competencies. In that sense we plan to formulate a design of "New kind of engineer" - oriented towards resolving a wide area of technical and non-technical problems that feature today's social environment. As a positive consequence we will achieve a "New status of engineer's profession" - status of a dedicated with increased motivation and effectiveness for impact on a wide range of matters.

2. ACTUAL CIRCUMSTANCES IN ENGINEER'S EDUCATION

Why is "attractiveness" the key thing? Because of the fact that many successful scholars enroll in non-technical studies. Why this is so important? Because of strict real-world rule: good enough scholars are a foundation for quality students and future well established and competent engineers. What is the reason of mentioned unattractiveness? It is evident that for a long time, all education systems (in the technical field, especially) produced "graduated students" instead of graduated engineers. The main reason for such is the formal character of transfer and testing of knowledge characteristic of an "old fashioned" concept in university education. Unfortunately, even after numerous changes in curriculums, situation remains the similar, because the anachronous education concept had now become the "weakest link" in the chain: "science-technology-professors-education-students".

Following illustration shows actual misunderstanding about character of engineers education an it is the old joke about how things can be analyzed (different professions in train observe cow in the field, Fig. 1).

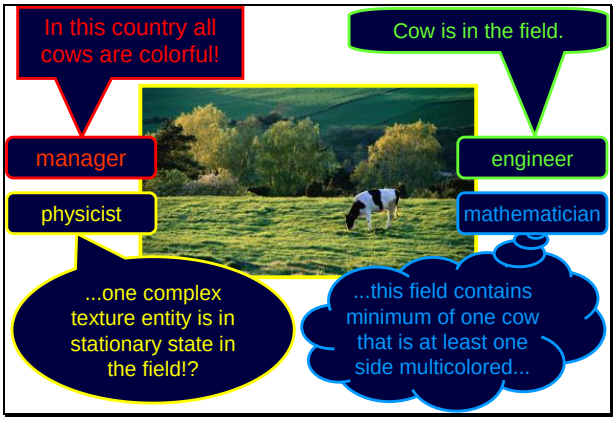

Fig. 1. Different views about same thing

During time, a question of quality of education concept escalates. In addition to high knowledge and competency in the primary technical profession (mechanical, electric, civil engineering, technology, agriculture...) sophisticated knowledge from fields which are usually indicated as "basic technical culture sciences" (physics, chemistry, mathematics, software design,

information technology - IT...) is also needed. Additionally, mentioned escalation strengthens the importance of knowledge in so-called "lateral skills" (psychology, sociology, soft-skills, entrepreneurial, marketing and public relations...).

For these reasons, all project members are confident that each technically oriented university should make the mentioned concept in education possible.

Education and, especially, examination of the real state of student knowledge in the primary profession should be adapted, first of all, to facilitate a complete understanding of the essence of engineering issues. Gaining "encyclopedia like" knowledge by studying many methods for analysis possibly provides wide education and contributes to the some kind of "technical culture", but it takes away attention and energy and ruins enthusiasm of students. Such "out of time" and "ex cathedra" given knowledge is inadequate for practical use and could be disruptive if the rest of the education is based on CATE (Computer Aided Teaching and Education) which is applied in a competent manner. In that sense, need of introduction of various IT instruments in all subjects is obvious.

Another problem is the conceptual "out-of-date" state of technical regulations which brings the developers, designers, distributors and users into an absurd situation where even good knowledge is used with unnecessary difficulties. Regulations should, thus, be harmonized with the most important heritage of the introduction of modern science and technology: elimination of tiring and monotonous manual operations, and thus making more time for the creative work.

3. PLANNED ACTIVITIES AND COOPERATION

In the framework of DECCE project we expect to investigate and solve following specific topics:

- How to increase interest of over-than-average high-school scholars for studying of engineering sciences.
- How to introduce innovative teaching concepts according to actual needs on engineering knowledge market of Program Countries by increasing of sophisticated-pragmatically oriented educational concept.
- How to promote components of entrepreneurial attitude which is needed for increasing the competence of students of engineering sciences.
- How to develop soft-skills of teaching personnel, with respect to better implementation of the new educational and working concept.

In Partner Countries (Albania, Bosnia and Herzegovina and Serbia) we have received many very interesting additional suggestions which are a real proof that our project proposal could be successful for the region as a whole, considering same or similar situation in other countries of region in higher education of engineering profession.

Also, our colleagues in Program Countries (Croatia, Slovenia and Austria) gave us inspirational support and encouragement for our future research deeply oriented in proposed direction, on bases of certain signs that described issues could be present in their countries.

The DECCE project is inspired by many suggestions of our colleagues from various engineering universities. Some of them are invited for the cooperation in the framework of our project. All their opinions are matched in a joint attitude: engineering education must be reorganized due to appearance of a new kind of student which enrolls technical studies and changed needs on the market of engineering knowledge.

Very similar thinking is presented in everyday conversation with our business partners, which are from technical field or which have requests for technical assistance. Their common opinion is that universities give excellent education only for excellent students, which mainly continue their carriers at development offices or research laboratories, although there is a urgent need for creative engineers "in situ".

4. SETTING-UP THE CONSORTIUM

Structure of proposed Consortium of Program and Partner Countries is created on the basis of circumstances of different or similar levels of economic and education levels and almost same attitudes about possibly the most competitive value of small countries - well educated community in a whole.

Long-term political instability and wars in former Yugoslavia caused crisis in all societal areas and decreased or stopped almost any kind of development in all counties in a region, especially in Serbia, Bosnia and Herzegovina, as well as in Albania. Because of specific circumstances our partners in Slovenia and Croatia reached higher level in the educational field and together with partner from Austria will be very helpful logistic and program support to our efforts in improvement of described modest status.

Our countries were in political separation for a time, which disabled cooperation and transfer of information in the right time. Therefore, it is now important to enable permanent cooperation with Europe, international cooperation as well and further exchange of knowledge and experience between countries in our region. Our advanced theoretical and practical experiences make the cooperation with foreign experts for support in realization of our future plans possible.

All Balkan partners in this project are potential members of EU. One of the requirements for their membership is reform of studies curricula, according to well-known Bologna principles. These reforms passed through a beginning and middle phase, with some moderate results.

Some changes were performed on the level of study curriculums, but that may be the easier part. Probably the harder part was the cooperation with EU universities. Balkan countries didn’t make enough progress in this field. The exceptionally important thing is achieving a permanent cooperation with institution which for a long time founded progressive processes. In that sense, permanent entry of the information and knowledge about accomplishments in the field of engineering and positive changes in curricula is possible. This is possible in case of more established countries, with bigger entry of grants and funds and with a longer tradition in application of Bologna concept.

In spite of different level of political, economic and democratic development as well as living quality, general decrease in technical education quality manifested itself in all countries. Deficiency and disability to invest in education caused it's degradation in all segments, and higher education is not an exception. Reforms in the high education (Bologna process) are manifested mainly formally. All aforementioned issues result in a constant deterioration of expert and basic knowledge of graduate engineers, in spite of increasing number of passed exams and shorter period of studying.

Upon first contact, it is necessary to assure Europe in our competence and our desire to catch up with it. It is necessary to encourage foreign professor visits, student exchanges, projects, making allied teams for common goals, etc.

5. EUROPEAN ADDED VALUE

The DECCE project is inspired by many suggestions from our colleagues from universities in neighboring countries (Bulgaria, Romania, Hungary, Slovenia, Austria, Croatia) as well as non-EU countries of Western Balkan (Albania, FYR Macedonia, Montenegro, Bosnia and Herzegovina).

We could perform this type of project without the cooperation of others but in that case we would be faced with an "issue of global importance and solution with local character". This annoying situation was completely unacceptable, whereof our potential partners had same impression. Very interesting is the detail that our expert colleagues from Program countries (Austria, Slovenia and Croatia) have perception that the whole European educational space has the same or problem of similar character.

Since we all share the same ideas regarding the questions "what is the basic problem" and "what is an optimal solution" in the engineering sense, these ideas are transformed in the allied project proposal.

6. INNOVATIVE CHARACTER

Main innovation in our DECCE project is effort in direction of harmonization of strategy of transfer and examination of technical knowledge, according to actual circumstances on the market of engineering knowledge, actual attitudes about education in student's community and actual relation between engineers and other professions. In comparison with previous work in this field, we offer relatively rapid and simple synchronization of technical knowledge with real needs and conditions. It is important to emphasize that this synchronization will certainly be in a satisfying sense of an organization of "new status of engineering studies".

Next innovative thing is our attitude on "changes without revolution, but only by evolution" which is a better basis for success of a project. Namely, even in academic environment high positioned members have a resistance against changes which need complete reorganization and expensive efforts. Our proposal can be performed "in the walk", without changes in curriculums, but only in harmonization of inadequate attitudes about the dilemma of "what is good education" with actual circumstances in science and technology.

One of the most efficient techniques for acquiring new knowledge from various areas is Internet use but not just as a source of various information but also as a possible platform for interconnection type of courses in many different fields of engineering science. A great advantage of such approach is that the lecturer or lecturers as well as listeners can be at distant locations e.g. in different countries and still have needed level of communication in real time visually and audibly. That would result in a considerably faster and easier exchange of information.

This approach has a great influence on cutting cost of regular course i.e. costs of organization in a traditional way which means that all participants have to meet in one place, there must be accommodation, space for work etc.

7. SUSTAINABILITY

The principal goal of our project DECCE is simultaneously the basic advantage of such kind of project: reasonable changes in the engineering education concept during the light adaptation on the environment and circumstances of real requested engineering knowledge. We believe in the existed spontaneous and enthusiastic affinity of teaching personnel for everyday development of lifetime learning which will be carried to students.

Once time begins, sort of "chain reaction" of acquiring of knowledge is unstoppable. All structural elements of community will be interested for person who is with well-adjusted performance in intellectual, emotional and ethical field. In that sense, technical culture and technical knowledge, even in case of non-technical professions, add some kind of new dimension for their everyday and advanced tasks.

About sustainability our target group is leading technical staff on working level - "in situ" and on higher hierarchy level in some system (company, state, etc.). These categories will be active interested for conditions of whole-life acquiring of knowledge which is important for common progress and financial matters.

After the first impressions and exact proofs that mentioned "new kind of engineer" is "large step for the person as well as great leap for the system" all members of technical and management staff will request that successful concept would be additionally developed. As a consequence we expect constant and pragmatic efforts and investment of community. The most interest fact and comparative advantage of our proposal is that once started process is self-sustain.

Additional improvement of teaching process is practically impossible without introduction of teaching innovations with unique goal: make the education attractive in comparison with other lifestyles. Here the most important role has educational concept as well as technical covering of education.

Basic advantage of our project in comparison with alternatives in this field is increasingly emphasized motivation for lifetime learning and a limitless need for knowledge will be one of our keywords.

8. FINAL REMARKS

As a positive consequence we will achieve a "new status of engineer's profession" - with increased motivation and effectiveness for impact on a wide range of matters. Proposed changes are possible "in passing", without any significant variations in curriculums and will be efficiently performed.

Work on proposed project will be performed through following phases:

- Study visits to EU and WBC universities with consultative meetings and allied DECCE Memorandum in the form of "Letter to Intent" with detailed description of our goal, method of research and lifetime sustain of our results.
- Developing the new teaching concept and training of teaching staff according to concept.
- Development of guidelines for development of enhanced learning technology aimed to increase attractiveness of engineering studies in EU and WBC.
- Improvement of teaching process by obtaining of equipment for use in demonstration educational purposes and increasing of engagement of students for acquiring of sophisticated knowledge.

ACKNOWLEDGEMENT

The work reported in this paper is a part of the research in the project "Development and Application of Contemporary Procedures for Design, Construction and Maintenance of Buildings", granted by Department for Civil Engineering and Geodesy, Faculty of Technical Sciences, Novi Sad.

9. REFERENCES

[1] European Commission, An Agenda for new skills and jobs: A European contribution towards full employment, COM (2010) 682 final, Strasbourg, 23.11. 2010, internet: http://eur-lex.europa.eu/LexUriServ/LexUriServ.do?uri=COM:2010:0682:FIN:EN:PDF

[2] European Council, Presidency conclusions, Lisbon, 23-24 March, 2000, internet: http://www.europarl.europa.eu/summits/lis1_en.htm. http://ec.europa.eu/archives/growthandjobs_2009

[3] European Commission, Europe 2020 – Background Information for the Informal European Counci, 11.2. 2010, http://ec.Europa.eu/commission_2010-2014/president/news/statements/pdf/20100210_3_en.pdf

[4] European Commission, The European Platform against Poverty and Social Exclusion: A European framework for social and territorial cohesion, COM (2010) 758 final, Brussels, 16.12. 2010, http://eurlex.europa.eu/LexUriServ/LexUriServ.do?uri=COM:2010:0758:FIN:EN:PDF

The 7th International Conference on Engineering and Technology
ICET-2015, Phuket, June 19-20, 2015
Prince of Songkla University, Faculty of Engineering
Hat Yai, Songkhla, Thailand 90112

Procedure for Development and Testing of Power Electronics Control Systems Based on HIL Technology

Marko Vekic, Stevan Grabic, Zoran Ivanovic, Vlado Porobic, Vladimir Katic
University of Novi Sad, Faculty of Technical Sciences, Novi Sad, Serbia
*Email of corresponding author: vekmar@uns.ac.rs

Abstract: *This paper proposes procedure of development of Power Electronics control systems based on the Hardware – In – the – Loop technology. Procedure was presented through development and testing of one complex control algorithm for the connection of the permanent magnet synchronous generator to the electrical grid. Development steps were explained in detail and appropriate scenarios proposed.*

Key Words: ***PMSG/ HIL/ Synchronization / Development / Algorithm***

1. INTRODUCTION

Electrical drives and Power Electronics based system in general consist of two main parts: the Power Stage and the Controller Stage. The Power Stage includes Power Electronics converters, electrical machines, sources (electrical grid, batteries, PV panels), filters, etc, while the Controller Stage is composed of digital controller and a PWM unit.

The cost of the Controller Stage is just a tiny part of the overall drive investment. However it presents its crucial part, responsible for the safety and the overall performance. The number of tested operation points is severely limited with safety and resource constraints as well as with the market pressure at the other side. For instance, it would be prohibitively expensive and time consuming to test the wind turbine operation under all severe grid disturbances and / or short circuits. At the other side, errors and oversights which occur due to the lack of comprehensive testing might be extremely expensive. All this implies that procedures and processes should be established to compromise the two opposite goals: the goal for exhausting testing, in all operational points of interest and predefined strict deadlines at the other side.

It is very difficult to fulfil such rather heavy task with usual procedures based on testing in the high – voltage lab. Therefore in this paper the approach which combines classical processes with the state of the art Hardware – In – the – Loop (HIL) technology [1] will be presented. The proposed approach will be illustrated in detail through development of one non-standard algorithm [2] for connection of Permanent Magnet Synchronous Generator (PMSG) to the electrical grid. Implementation of the proposed algorithm directly in the 2 MW prototype would be extremely difficult. Therefore such example is an excellent case study to illustrate the proposed procedure for development and testing of PE control systems. Before the development and testing procedure itself is to be explained, we will deal shortly with so called Active damping algorithm [3] which presents the theoretical background of PMSG synchronization.

2. ACTIVE DAMPING ALGORITHM

It is well known from literature and practice that connection of the synchronous machine to the grid is more complex process than connection of the induction machine because the vector of electromotive force (emf) has to be identical to the vector of grid voltage. Even if frequencies are the same, but there is still the difference between phase angles, significant oscillations in torque may occur. Oscillations are only lightly damped due to the small stator resistance. Our aim is therefore to find a way to effectively damp the oscillations so that synchronization could be succesfully achieved at some arbitrary instant of time when appropriate vectors do not match. To achieve such a goal, so called PMSG Cascade (Fig. 1) will be employed. The concept is described in detail in [4] - [6].

If we apply the algorithm developed in [6], called the Active Damping, oscillations due to the rapid load change will be damped which can be concluded from the following equation:

$$m_{el} = \frac{\sin\theta}{x_S}\left(1 - \frac{u_{SC}^{r}}{\sqrt{2\cdot(1-\cos\theta)}}\right) \qquad (1)$$

where m_{el} is the electrical torque, x_s is synchronous reactance, θ is the angle difference between vectors (phasors) of emf and voltage, while u^r_{SC} stands for the reactive voltage component injected by series converter. The first part of (1) is well known expression which

describes (in [p.u.]) the PMSG with rounded rotor connected to the ideal grid.

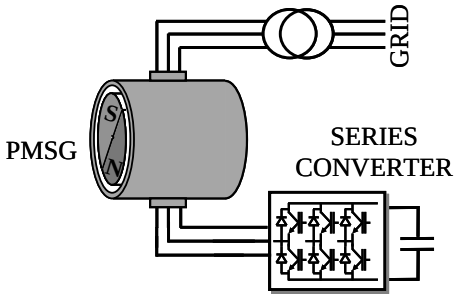

Fig. 1. PMSG Cascade

Generally this equation defines the power flow between two voltage sources connected through the reactance (x_s here). However, the second part of the equation depends on the injected voltage of series converter, u^r_{SC}. Controlling this voltage, the electrical torque m_{el} can be modulated and hence, this modulated torque could bring the damping ability. Using the electro-mechanical analogy, it can be shown [13] that the voltage u^r_{SC} should be generated as follows:

$$u^r_{SC} = -k_{dmp} \cdot \frac{d\theta}{dt} \cdot \mathrm{sgn}(\theta) \qquad (2)$$

where k_{dmp} is the damping factor and θ is the angle difference between the grid voltage and induced PMSG emf.

However, we need to modify such algorithm in order to damp oscillations during the synchronization process. The development of algorithm will be presented through several steps of the proposed Procedure. Before the explaining Procedure itself, a short overview of employed development and testing tools will be presented. Matlab simulation is used for obtaining the feasibility study, while Typhoon HIL400 emulator is used for the purpose of verification and testing.

3. EVALUATION TOOLS

Fig. 2 shows the HIL setup for evaluation of the proposed synchronization algorithm. Dspace dS1104 is employed as the controller stage, while HIL400 platform is used to emulate the power stage.

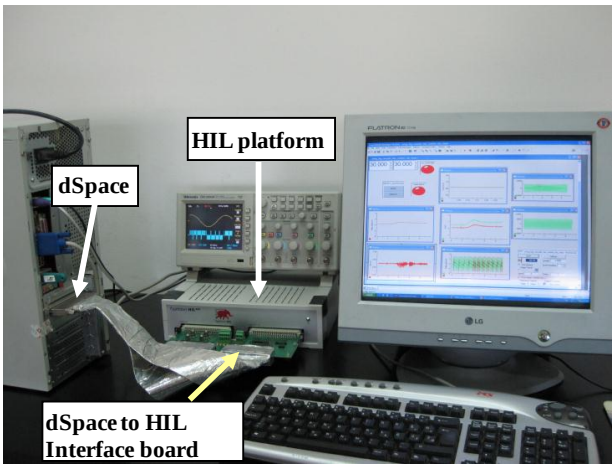

Fig.2: HIL emulation of PMSG drive

All necessary elements, series converter, PMSG, passive elements as well as electrical sources (electrical grid) are chosen from the HIL400 library and arranged in the Schematic Editor to represent the PMSG drive with the series cascade (Fig. 3).

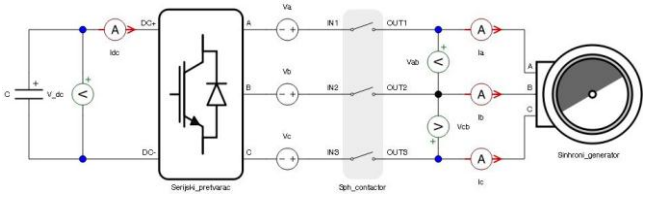

Fig.3: PMSG drive in the HIL Schematic Editor

In order to check the fidelity of emulation, the test results are initially compared with the real drive (test bench) operation (Fig. 4)

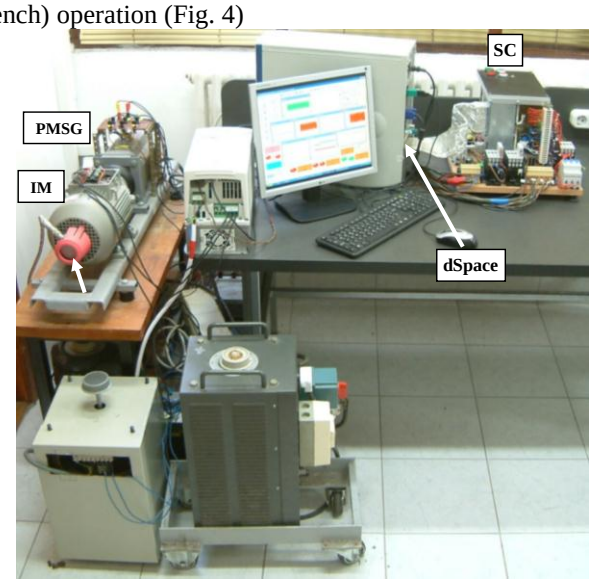

Fig.4: Laboratory test bench

4. DEVELOPMENT AND TESTING PROCEDURE

Here procedure of development the Modified Active Damping Algorithm will be presented step by step using theory analysis, simulation and emulation tools described in the previous chapter. The modified algorithm is based on one described in the second chapter under the following assumptions:

- PMSG is connected to electrical grid (synchronized with) employing series converter (Fig. 1) with rated power of 0.2 [p.u.].
- PMSG is accelerated by some external driving machine or turbine (like wind turbine) which provides an arbitrary input mechanical torque in the range of 0.1 to 1 [p.u.] during the acceleration as well as after synchronization.
- Series converter injects reactive power only

Required algorithm will be derived, developed and tested in the following steps.

A. Step 1: Theory analysis

The described control law (2) has to be modified, because in the case of the synchronization it cannot be assumed that PMSG speed is nominal, i.e. $n \neq 1$ [p.u.]. Therefore, PMSG speed appears in the further consideration as a variable which also implies variable

$U_{EMF} = n \cdot \psi$, where ψ is permanent magnets flux. Following these modifications, the equation (1) becomes:

$$m_{el} = \frac{\psi}{n \cdot x_s} \cdot \sin\theta - \frac{\psi}{n \cdot x_s} \cdot \sin\theta \cdot \frac{U_{SC}^r}{\sqrt{1 + n^2 \cdot \psi^2 - 2 \cdot n \cdot \psi \cdot \cos\theta}} \quad (3)$$

Accordingly, the control law is given by:

$$U_{SC}^r = -\frac{a}{2} \cdot n \cdot (n-1) \cdot \frac{\sqrt{1 + n^2 \cdot \psi^2 - 2 \cdot n \cdot \psi \cdot \cos\theta}}{\sin\frac{\theta}{2}} \quad (4)$$

In the upper equation a is the damping coefficient instead of k_{dmp} from (2). The torque expression (1) now becomes:

$$m_{el} = \frac{\psi}{x_s} \cdot \frac{\sin(\theta)}{n} + a \cdot \frac{\psi}{x_s} \cdot (n-1) \cdot \cos\left(\frac{\theta}{2}\right) \quad (5)$$

In order to complete the control law, the coefficient a has to be determined. The control structure is given at the Fig. 5.

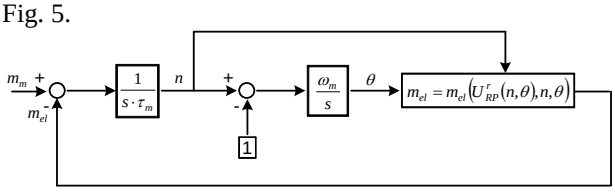

Fig. 5. Synchronization control scheme

Although this control diagram looks pretty simple, the block which represent torque calculation is non-linear as (8) clearly shows. Therefore, in order to obtain coefficient a the linearization around the operation point has to be performed. It is justified to adopt the PMSG nominal value (n = 1 [p.u.]) for operation point because the process of synchronization should start when the speed approaches grid (nominal) speed. The linearized control diagram is presented on Fig. 6.

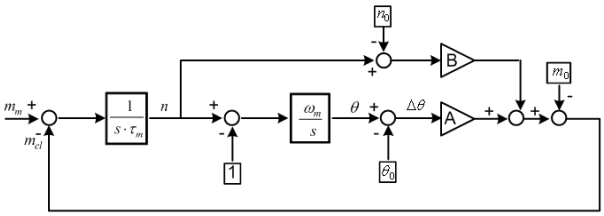

Fig. 6. Linearized synchronization control scheme

B. Step 2: Algorithm feasibility

Simulations will be employed here to determine validity of theoretical assumptions. Keeping in mind that series converter is rated to 0.2 [p.u.] and injects reactive power only as defined by assumptions, it is obvious that proposed Modified Active Damping algorithm has its certain limits. To determine those limits, a detailed simulation model was developed in order to find the range of the input mechanical torque M_m, initial angle difference θ_{init} and initial speed at the beginning of synchronization n_{init}, for which the synchronization is possible. The simulation results are shown at the Fig. 7.

Results from the Fig. 7 are obtained under assumption that the initial PMSG speed at the moment of synchronization was n_{init} = 0.98 [p.u.], while the power angle (the difference between the grid and PMSG angle) and input mechanical torque are arbitrary values. It can be concluded that synchronization is possible for any value of the mechanical input torque in the range of [0.1,..,0.9, 1] when the initial power angle θ_{init} is in the range of -30º to 100º. These boundaries are essentially the consequence of the limited series converter voltage (13).

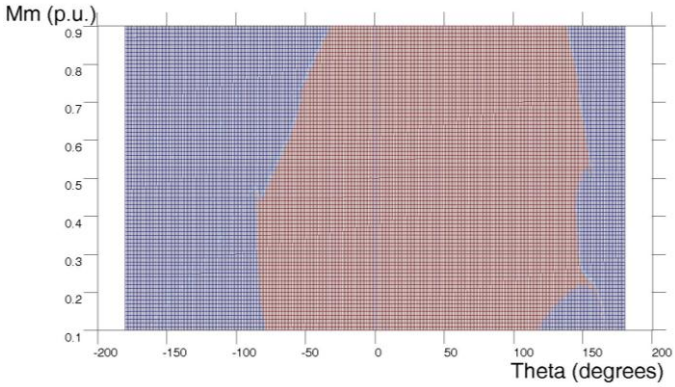

Fig. 7. The area where synchronization is possible

C. Step 3: Development and testing

In order to check the control law and its borders, we need to perform tests in all operation points, particularly on border area (Fig. 9) itself and a little beyond. For that purpose HIL emulator (Fig) will be employed. Tests were performed for 40 points of interest (different imput torques and initial valyes). Here two characteristic results will be presented, one from the inside of the area (Fig. 8) and the another from the outside of the safe area (Fig. 9).

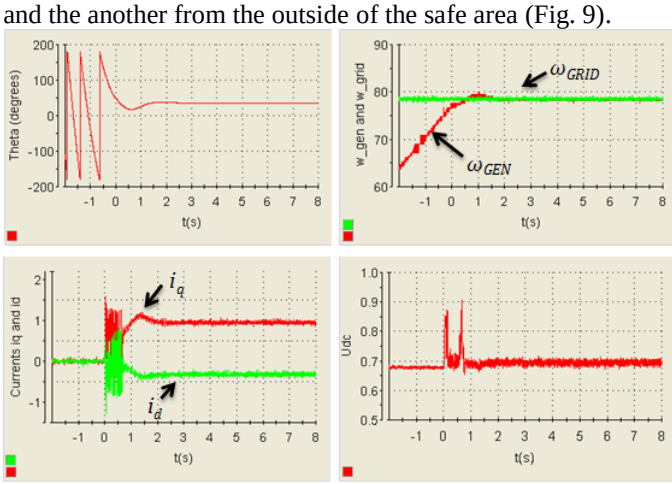

Fig. 8. PMSG Synchronization when M_m=1.0 [p.u] and θ_{init}= 45º

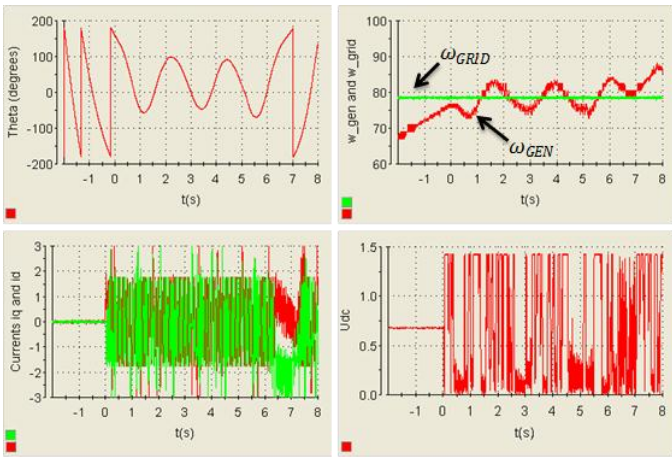

Fig. 9. PMSG Synchronization when M_m=0.6 [p.u] and θ_{init}=160 º

According to expectations, the system response is very clear and smooth in the case from Fig. 8 However, Fig. 9 clearly shows that the synchronization to the grid is impossible when the initial angle difference is significantly displaced from the pre-defined boundaries. Further tests showed that the PMSG connection to the grid is still possible slightly beyond borders of the area defined by Fig. 7.

5. DEVELOPMENT SCENARIOS

Based on the presented procedure steps, several scenarios or algorithms for PE control systems development can be proposed [7]. For the sake of clarity, the algorithm of classical development will be given the first (Fig. 10).

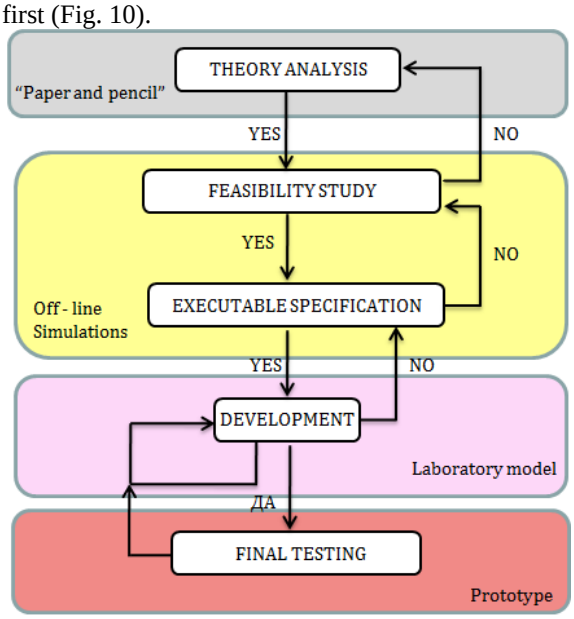

Fig. 10. Classical development algorithm

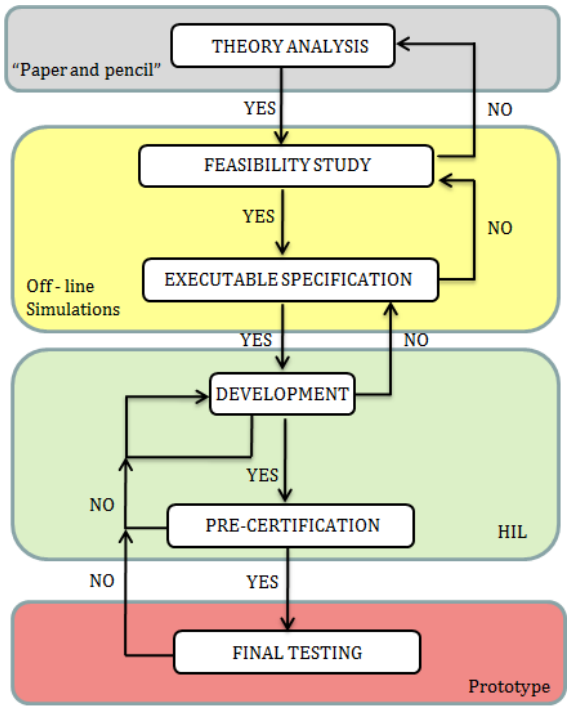

Fig. 11. Development algorithm based on HIL

The key role in the scenario from Fig. 10 has the step which is performed on the laboratory model (test bench). The main drawback of such approach is a very long time constant in the inner development loop.

Employing HIL technology leads to the algorithm depicted by Fig.11. Development time constants are here very short and the whole process is much more efficient.

6. CONCLUSION

Development of PE control systems was demonstrated through several steps: theory analysis, feasibility, as well as development and testing. As a case study one new control strategy for connection of PMSG to electrical grid was chosen, implemented and tested according to the proposed procedure. More efficient scenario for development based on HIL technology was presented.

7. APPENDIX

This research was partially co-funded by the Ministry of Education, Science and Technological Development of Republic of Serbia under contract No. III 042004 and by the Provincial Secretariat for Science and Technological Development of AP Vojvodina under contract No. 114-451- 3508/2013-04.

8. REFERENCES

[1] M. Vekic, S. Grabic, D. Majstorovic, N. Celanovic, V. Katic, "Ultralow Latency HIL Platform for Rapid Development of Complex Power Electronics Systems", IEEE Trans. on Pow. El. vol.. 27, no. 11, Nov 2012, pp. 4436-4444.

[2] Marko Vekic, Milan Rapaic, Stevan Grabic Nikola Celanovic, VladimirKatic, "HIL Evaluated New Control Algorithm For PMSG Grid Connection", 17th International Symposium on Power Electronics - Ee 2013, Novi Sad, Serbia, October 30th-November 1st, 2013 Paper No. Sps-1.5, pp 1-5, ISBN: 978-86-7892-550-4

[3] S. Grabic, N. Celanovic, V. A. Katic, "*Permanent Magnet Synchronous Generator Cascade for Wind Turbine Application*", IEEE Trans. on Pow. Electron. vol.. 23, no. 3, May 2008, pp. 1136-1142.

[4] J. Xu, S. Xie, T. Tang, " Active Damping-Based Control for Grid-Connected LCL-Filtered Inverter With Injected Grid Current Feedback Only", IEEE Trans. Ind. Electronics, vol. 61, no. 9, pp. 4746-4758, Sept. 2014.

[5] X. Wang, F. Blaabjerg, M. Liserre, Z. Chen, J. He, Y. Li, "An Active Damper for Stabilizing Power-Electronics-Based AC Systems", IEEE Trans. Power Electron., vol. 29, no. 7, pp. 3318–3329, Jul. 2014.

[6] S. Grabic, N. Celanovic, and V. Katic, "Series converter stabilized wind turbine with permanent magnet synchronous generator," in Proc. IEEE 35th Annu. Power Electron. Spec. Conf., Aachen, Germany, 2004, pp. 464–468.

[7] Marko Vekic, "New real time emulation based procedure for Power Electronics controllers development", PhD thesis, Faculty of technical sciences, Novi Sad, February 2014, in Serbian

The 7th International Conference on Engineering and Technology
ICET-2015, Phuket, June 19-20, 2015
Prince of Songkla University, Faculty of Engineering
Hat Yai, Songkhla, Thailand 90112

Wind Turbine integration into the smart grid in case of unbalanced voltage conditions

Zoran Ivanović*, Marko Vekić, Evgenije Adžić, Vlado Porobić, Vladimir Katić
University of Novi Sad, Faculty of Technical Sciences, Novi Sad, Serbia
*Email of corresponding author: zorani@uns.ac.rs

Abstract: *This paper deals with control of wind turbine connected to the smart grid through the back-to-back converter in case of unbalanced grid voltages. The motivation for this research has been found in recent transmission and distribution grid code, which demand modern wind turbines to stay connected to the grid and supply the highest possible apparent power during the grid disturbances. In order to comply with these requirements we proposed improved dual vector current controller to deal with the unbalance imposed by the electrical grid. Proposed control algorithm is validated using hardware-in-the-loop emulation platform, while controller is based on TMS320F2812 DSP.*

Key Words: ***Smart grid/ Wind turbine/ Back-to-back converter /Dual vector current controller***

1. INTRODUCTION

The need for integration of renewable and distributed energy sources into existing power system requires a lot of new software and control solutions to stabilize the grid at all levels. Such an intelligent grid is nowadays called smart grid [1]–[3]. Distributed generation (DG) units play very important role as a means of achieving increased power system stability. One of the most commonly employed types of DG unit is wind turbine (WT) [4].

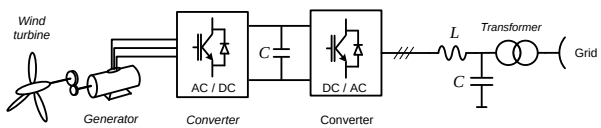

Fig. 1. Wind turbine connected to the grid

Wind turbine is usually connected to the grid through the power electronics converter. One complete solution is shown in Fig. 1. Wind turbine equipped with induction machine generator is connected to the grid through the back-to-back converter. In the past there were no strong grid code requirements for a WT to stay connected to the grid during the fault or grid disturbances [5]. The main focus was on protection of WT unit itself. In the recent time, increaseing integration of wind energy systems lead to fast establishment of variety of grid codes, which define behavior of WT during disturbances. Grid code requirements vary from country to country. One of the most commonly used, implemented by the company E.ON Netz, is shown in Fig. 2. According to this grid code, WT should stay connected to the grid and inject active and reactive power to the grid even in case of very strong disturbances [6]–[8].

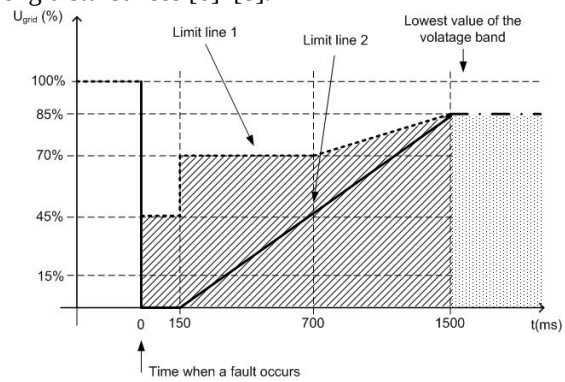

Fig. 2. E.ON grid connection requirements

In this paper we proposed control algorithm to meet grid-code requirements in severely unbalanced grid conditions. In order evaluate its performance we used Hardware-in-the-loop (HIL) based emulation platform to represent power stage, while the controller is realized using a control platform based on the TMS320F2812 DSP. The entire power stage is emulated in real time on an FPGA platform with a fixed simulation time step of 1 µs.

2. SYSTEM MODELING

An unbalanced system of the three phase-voltages (u_a, u_b, u_c) could be represented with its positive and negative sequence components, as given by:

$$u_{\alpha\beta} = e^{j\omega t} u_{dq}^{p} + e^{-j\omega t} u_{dq}^{n} \qquad (1)$$

where $u_{\alpha\beta} = \sqrt{2/3}\left(u_a + u_b e^{j2\pi/3} + u_c e^{-j2\pi/3}\right)$ is the grid voltage vector expressed in the stationary reference frame and ω is the angular grid-frequency [9]. In the same manner, unbalanced grid currents could be

represented in terms of positive and negative sequence current components, similarly to (1):

$$i_{\alpha\beta} = e^{j\omega t} i_{dq}^{p} + e^{-j\omega t} i_{dq}^{n} \tag{2}$$

where ($i_{dq}^{p} = i_{d}^{p} + j i_{q}^{p}$) and ($i_{dq}^{n} = i_{d}^{n} + j i_{q}^{n}$).

One case of unbalanced grid-voltages in the original and synchronously rotating reference frame is shown in Fig. 3. It should be noted that in the positive sequence reference frame, a positive component appears as DC, whereas a negative component oscillates at twice the grid frequency. In the negative reference frame, it is the opposite, which is explained thoroughly in [10].

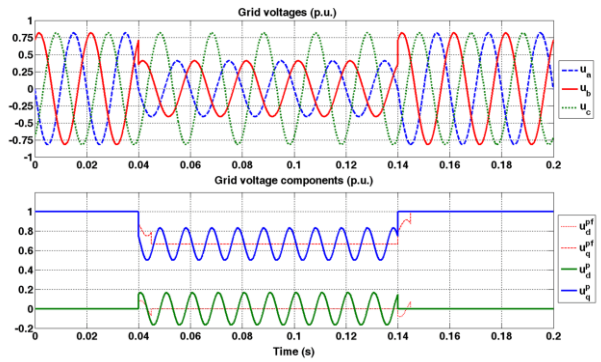

Fig. 3. Unbalanced grid voltages representation

The representation of a two-level VSC, used as a power electronic block in WT application, could be described by differential equations in the dq reference frame:

$$v_{dq}^{p} = L\frac{di_{dq}^{p}}{dt} + Ri_{dq}^{p} + j\omega L i_{dq}^{p} + u_{dq}^{p} \tag{3}$$

$$v_{dq}^{n} = L\frac{di_{dq}^{n}}{dt} + Ri_{dq}^{n} - j\omega L i_{dq}^{n} + u_{dq}^{n} \tag{4}$$

With regards to this, instantaneous apparent power could be expressed as:

$$s = u_{\alpha\beta} i_{\alpha\beta}^{*} = p(t) + jq(t) \tag{5}$$

where active power $p(t)$ and reactive power $q(t)$ are:

$$p(t) = P_0 + P_{c2}\cos(2\omega t) + P_{s2}\sin(2\omega t) \tag{6}$$

$$q(t) = Q_0 + Q_{c2}\cos(2\omega t) + Q_{s2}\sin(2\omega t) \tag{7}$$

Terms P_0 and Q_0 designate the value of the average power, while P_{c2}, P_{s2}, Q_{c2} and Q_{s2} are the magnitudes of the power oscillations caused by the unbalance. Matrix expression of terms in equations (6) and (7) are given here:

$$\begin{bmatrix} P_0 \\ Q_0 \\ P_{C2} \\ P_{S2} \end{bmatrix} = \begin{bmatrix} u_d^p & u_q^p & u_d^n & u_q^n \\ u_q^p & -u_d^p & u_q^n & -u_d^n \\ u_q^n & -u_d^n & -u_q^p & u_d^p \\ u_d^n & u_q^n & u_d^p & u_q^p \end{bmatrix} \begin{bmatrix} i_d^p \\ i_q^p \\ i_d^n \\ i_d^n \end{bmatrix} \tag{8}$$

3. CONTROL STRUCTURE DEVELOPMENT

The complete control scheme is represented in Fig. 4. There are two separate control structures. During the normal system operation WT side inverter is in charge of controlling WT torque and speed using vector control technique, while grid side inverter is in charge of controlling active and reactive power and DC bus voltage.

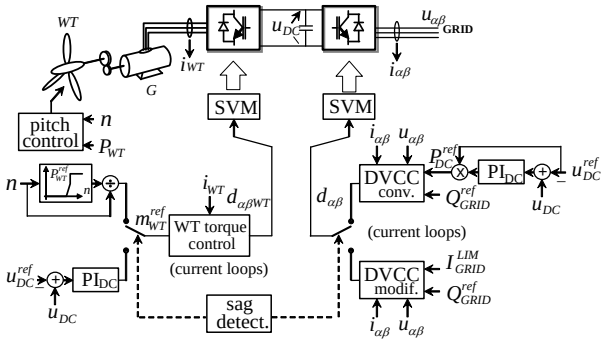

Fig. 4. WT control structure

In normal grid conditions torque reference m_{WT}^{ref} for WT controller is obtained based on optimal turbine power characteristic $P_{WT}^{ref} = f(n)$ [11]. At the grid side, in normal conditions conventional DVCC is used (Fig 5.). There, power transfer reference command P_{DC}^{ref} comes from the output of DC voltage controller and reference average reactive power is set to $Q_0 = Q_{GRID}^{ref} = 0$.

After the voltage sag has been detected, control structure has to be altered so that modified DVCC imposes current limit in the output current and WT side converter takes over DC voltage control. Obviously, power flow through the back-to-back converter would be reduced. Therefore, the WT mechanical input has to be restricted by means of the pitch control [5]. The control structure completes sag detector that manipulates the switching between the two control objectives.

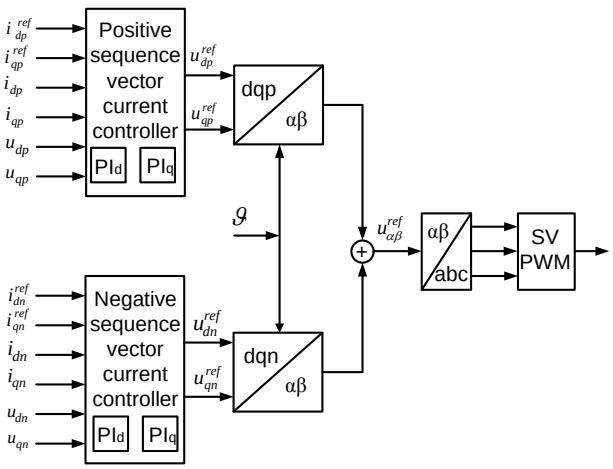

Fig. 5. Dual vector current controller

Current references are extract form the following equation:

$$\begin{bmatrix} |I_{GRID}|^2 \\ Q_0 \\ P_{C2} \\ P_{S2} \end{bmatrix} = \begin{bmatrix} I_{LIM}^2 \\ 0 \\ 0 \\ 0 \end{bmatrix} = \begin{bmatrix} i_d^{pref} & i_q^{pref} & i_d^{nref} & i_q^{nref} \\ u_q^p & -u_d^p & u_q^n & -u_d^n \\ u_q^n & -u_d^n & -u_q^p & u_d^p \\ u_d^n & u_q^n & u_d^p & u_q^p \end{bmatrix} \cdot \begin{bmatrix} i_d^{pref} \\ i_q^{pref} \\ i_d^{nref} \\ i_q^{nref} \end{bmatrix} \tag{9}$$

First row in the equation (9) is current limiting condition imposed by the grid side inverter.

4. EXPERIMENTAL SETUP

Tests on modern smart grids are difficult and costly to carry out on real systems due to the high power rating of the hardware, system complexity and difficulties associated with emulating grid disturbances [12]. Instead of that we commonly use HIL based emulation platform. This principle is illustrated in Fig. 6. Power stage is usually executed in real time on a FPGA based platform, while the controller is real [13].

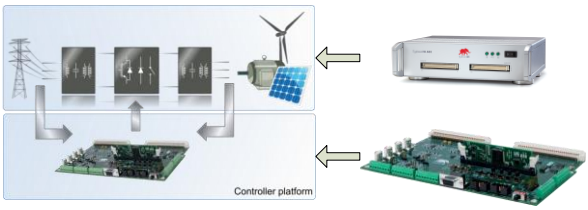

Fig. 6. HIL principle illustration

Power stage of the emulated electrical system (Fig. 7) is comprised of electrical grid, power transformer, voltage sag emulator, grid side converter, machine side converter (back-to-back) and induction generator. It is executed on the FPGA based platform with 1μs latency.

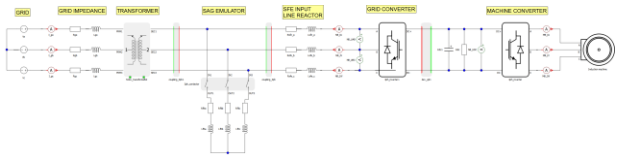

Fig. 7. Schematic diagram of WT connected to the grid

The hardware and setup is shown in Fig. 8. On the right side, we can see the HIL emulator box and on the left side we can see the DSP-based control board. We used TMS320F2812 DSP controller for control code generation.

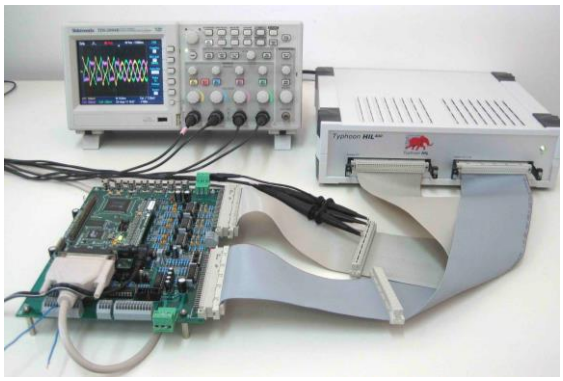

Fig. 8. Experimental setup

5. EXPERIMENTAL RESULTS

HIL experimental results given in Figs. 9 – 13 show system's response to unbalanced voltage sag, where two phase voltages fall to 49% of nominal value while third phase voltage remain the same (type E voltage sag). Voltage sag is introduced using RL impedance and contactor. With the proper selection of R and L we can chose the depth of voltage sag.

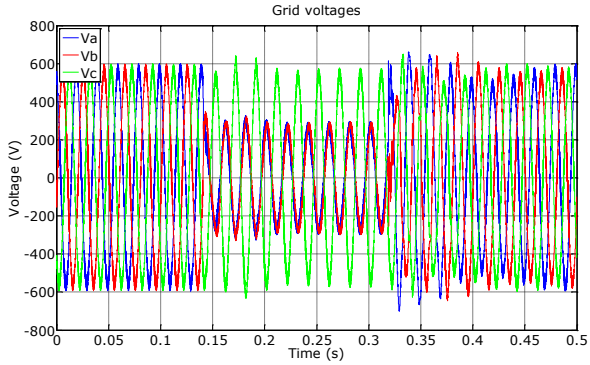

Fig. 9. Grid voltages – voltage sag type E

During the voltage sag grid currents are higher than nominal, but they are limited in accordance to the grid side converter protection. Current ripple is due to swathing frequency which is chosen to be 2 kHz. A lower grid voltage and limited grid current imply a decrease in active power flow from the generator to the grid.

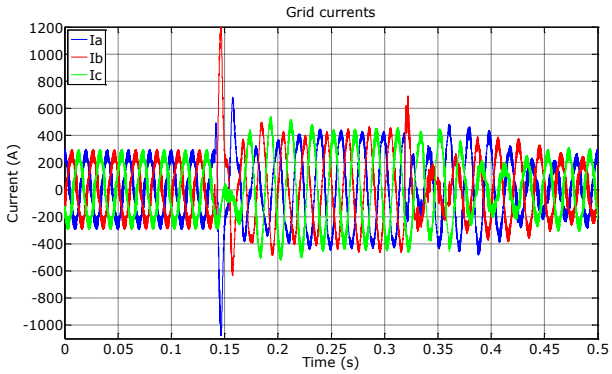

Fig. 10. Grid currents – voltage sag type E

In order to keep power flow balance it is necessary to reduce energy production of the distributed generator. This is achieved by proper reduction of torque reference. We can see in Fig. 12 that electrical torque during the voltage sag is reduced. In accordance with that generator currents are also reduced. DC bus voltage is still stable, except during transient, where we have a little deviation. DC bus stability is indicator that the power flow is correctly managed.

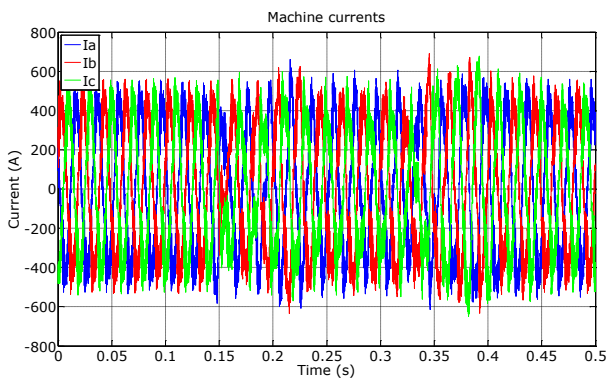

Fig. 11. Machine currents – voltage sag type E

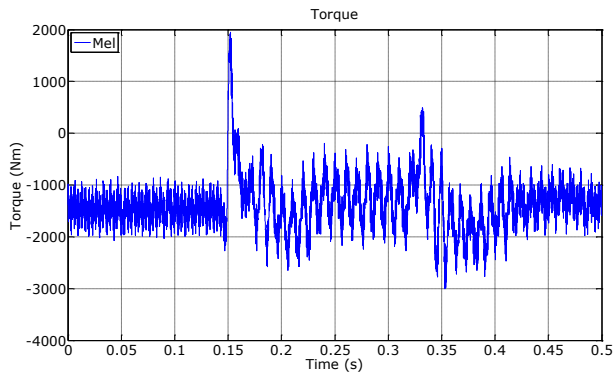

Fig. 12. Machine torque – voltage sag type E

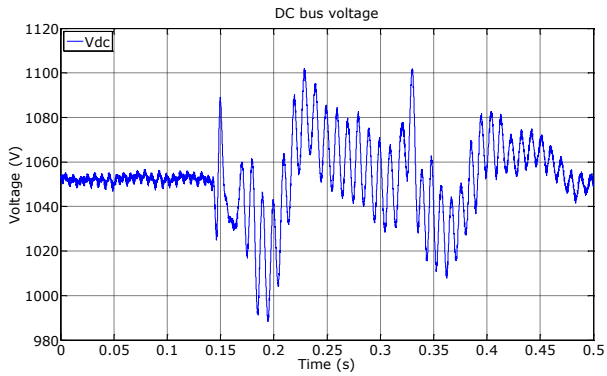

Fig. 13. DC bus voltage – voltage sag type E

6. CONCLUSION

This paper proposed novel power flow control strategy for wind turbine integrated into the smart grid through the back-to-back converter. The algorithm was implemented on a TMS320F2812DSP and its performance is verified by means of HIL emulator.

Implemented control algorithm show significant improvement over solution proposed in literature. New way of current references calculation is introduced which in effective way limit inverter currents. During the voltage sags constant active power is produced and delivered to the grid, according to grid code requirements.

7. ACKNOWLEDGEMENT

This research was partially co-funded by the Ministry of Education, Science and Technological Development of Republic of Serbia under contract No. III 042004 and by the Provincial Secretariat for Science and Technological Development of AP Vojvodina under contract No. 114-451- 3508/2013-04.

8. REFERENCES

[1] F. Li, W. Qiao, H. Sun, H. Wan, J. Wang, Y. Xia, Z. Xu, P. Zhang, "Smart transmission grid: vision and framework," *IEEE Trans. Smart Grid*, Aug. 2010., vol. 1, issue 2, pp. 168–177.

[2] F. S. Bifaretti, P. Zanchetta, A. Watson, L. Tarisciotti, J. C. Clare, "Advanced power electronic conversion and control system for universal and flexible power management," *IEEE Trans. Smart Grid*, May 2011., vol. 2, issue 2, pp. 231–243.

[3] *IEEE Guide for Smart Grid Interoperability of Energy Technology and Information Technology Operation with the electric Power System and End-Use Applications and Loads, IEEE Standard P2030.1.*

[4] *IEEE Standard for Interconnecting Distributed Resources with Electric Power Systems, IEEE Standard P1547.2, 2008.*

[5] Z. Ivanovic, M. Vekic, S. Grabic, V. Katic, "Control of multilevel converter driving variable speed wind turbine in case of grid disturbances," *Proc. 12th IEEE EPE-PEMC, Portoroz, Slovenia*, Aug./Sept. 2006, pp. 1569–1573.

[6] C. Ng, L. Ran, "Unbalanced-grid-fault ride-through control for a wind turbine inverter," *IEEE Trans. Ind. Appl.*, May/Jun. 2008 vol. 44, no. 3, pp. 845–856.

[7] F. Wang, J. L. Duarte, M. Hendrix, "Pliant active and reactive power control for grid interactive converters under unbalanced voltage dips", *IEEE Trans. Power Electron.*, May. 2011., vol. 26, no. 5, pp. 1511–1521.

[8] X. Guo, W. Wu, "Improved current regulation of three-phase grid-connected voltage source inverter for distributed generation systems," *IET Renewable power generation*, Sep. 2009., vol. 4, iss.2, pp. 101–115.

[9] J. Hu, Y. He, "Modelling and control of grid-connected voltage-sourced converters under generalized unbalanced operating conditions," *IEEE Trans. Energy Convers.*, Sep. 2008, vol. 23, no. 3, pp. 903–913.

[10] H. Song, K. Nam, "Dual current control scheme for PWM converter under unbalanced input voltage conditions," *IEEE Trans. Ind. Electron.*, Oct. 1999., vol. 46, no. 5., pp. 953–959,

[11] Y. Suh, Y. Go, D. Rho, "A comparative study on control algorithm for active front-end rectifier of large motor drives under unbalanced input," *IEEE Trans. Ind. Appl.*, May/Jun. 2011,vol. 47, no. 3, pp. 1419–1431.

[12] W. Li, G. Joos, and J. Belanger, "Real-time simulation of a wind turbine generator coupled with a battery supercapacitor energy storage system," *IEEE Trans. Ind. Electron.*, Apr. 2010, vol. 57, no. 4, pp. 1137–1145.

[13] Z. Ivanović, E. Adzić, M. Vekić, S. Grabić, N. Čelanović, V. Katić, "HIL evaluation of power flow control strategies for energy storage connected to smart grid under unbalanced conditions," *IEEE Trans. Power electron.*, Nov. 2012. USA, vol. 27, no. 11, pp. 4699–4710.

The 7th International Conference on Engineering and Technology
ICET-2015, Phuket, June 19-20, 2015
Prince of Songkla University, Faculty of Engineering
Hat Yai, Songkhla, Thailand 90112

Sensorless vector control of induction motor with current reconstruction method

Evgenije Adžić, Vlado Porobić, Zoran Ivanović, Marko Vekić, Stevan Grabić
University of Novi Sad, Faculty of Technical Sciences, Novi Sad, Serbia
*Email of corresponding author: evgenije@uns.ac.rs

Abstract: *This paper deals with sensorless induction motor drive control method which uses minimal number of sensors, providing only dc-link current measurement as a feedback signal. Improved dc-link current sampling scheme and modified asymmetrical switching pattern cancel characteristic waveform errors which exist in all three reconstructed line currents. Proposed control algorithm is validated using hardware-in-the-loop test platform and TMS320F2812 digital signal processor.*

Key Words: ***Induction motor drive/ Vector control/ Sensorless control /Single current sensor***

1. INTRODUCTION

Controlled induction motor drives are used in a wide range of industry applications where they significantly contribute to improved efficiency and reliability of automation processes. Due to economical and reliability reasons most automation systems use induction motor drives where motor torque and speed are controlled without shaft-sensor [1]. Speed information is then determined indirectly, by measuring terminal currents and voltages [1-3]. Industry trends to provide more robust and reliable drives operation imposed necessity for drives with minimal number of sensors.

This paper proposes solution for induction motor control, where number of sensors is reduced to minimum. Only one sensor which measures the dc-link current of the converter is used [4]. Control algorithm includes method for motor terminal current reconstruction in a way to achieve motor current and speed control. Analysis of recent relevant literature, confirms that most of the problems are recognized and solved in a way which allows their application in low-performance drives [4]-[9]. In this situation, authors usually do not consider quality and performance of implemented control algorithms.

Application of the current reconstruction method in a vector controlled induction motor drives proves to be significantly lower in quality and performances compared to drives using direct line current measurement. This is mainly consequence of the usual inaccuracy in reconstructed current waveforms, which is explained in details in [10]. Application of the conventional current reconstruction mechanism with two dc-link current samples in different time instants during the same switching period in combination with PWM current ripple generates error reflected in abrupt changes in reconstructed line current waveforms. This error reflects further in dq-current components in vector control algorithm, which can be observed in increased torque and speed oscillations. Moreover, in shaft-sensorless drives, accuracy in estimated speed is significantly reduced. Stability is seriously jeopardized in situations when current and speed controllers are tuned in optimal way characteristic for high-performance drives.

This paper presents original solution for conventional current reconstruction method improvement, which avoids dynamic reduction, but in the same time eliminates the error and contributes to better control characteristics.

2. PROPOSED CURRENT RECONSTRUCTION METHOD

The basic idea suggested in this paper represents an improvement of the method proposed in [5], which used the line-currents measured in both halves of the naturally symmetrical PWM switching period. The method proposed in [5] is based on sampling of the dc-link current in the center of the active voltage vectors four times during one PWM period and calculation of the two available line-current values by averaging the samples from two matching vector pairs.

This approach provides synchronous measurement of all three line-currents, referred to the center of a PWM period. It effectively cancels error due to current ripple in the reconstructed line-currents and eliminates the current samplesô mutual phase-shift. Besides its simplicity, this method is completely insensitive to machine parameter variances. However, in [5] the critical cases of a reference voltage vector passing between the six possible active vectors or with a low modulation index are neglected and not considered. This would cause unstable drive operation.

Considering the high PWM switching frequencies, up to 20 kHz, and usually employed electrical motors, one can conclude that there is no need for the very high current control-loop sampling rate at the PWM level. This fact allow us to record line-current information on the lagging (right) side of one PWM period and then on the leading (left) side of the subsequent PWM period and calculate the available line-currents by simple averaging of the corresponding recorded values. In this way, all three estimated line-currents would be referred to the same instant reflecting the average current value in two consecutive PWM periods. The proposed method enables us to improve the PWM pattern control in order to account for critical cases. PWM pattern is modified where under critical conditions, the lagging half-pulse width is shifted to the right and the leading half-pulse width in the subsequent PWM period is shifted to the left in order to create sufficient sampling windows for current measurement (Fig. 1b).

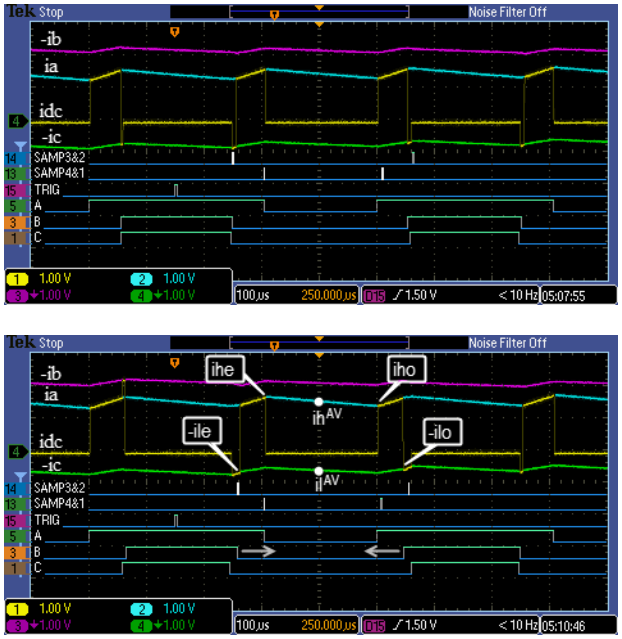

Fig. 1. a)Proposed dc-link current (i_{dc}) sampling scheme (SAMP3&2, SAMP4&1), and b) modified PWM pattern (A, B, C) for improved line current (i_a, i_b, i_c) reconstruction

Fig. 1 shows the dc-link current (i_{dc}) and motor line currents (i_a, i_b, i_c) during two consecutive PWM periods and details related to the proposed method. Sampling signals *SAMP1* and *SAMP4* are triggers for measurement of dc-link current in two consecutive PWM periods during matching active voltage vectors defined with only one inverter switch turned-on (here, with PWM signal *A*). *SAMP1* samples dc-link current at the beginning of the active voltage vector, and *SAMP4* at the end of the active vector. Similar, sampling signals *SAMP2* and *SAMP3* are triggers for measurement of dc-link current at the beginning and at the end of matching active voltage vectors defined with two upper switches turned-on (here, with PWM signals *A* and *B*), respectively.

The line currents at the time instant representing average values in two consecutive PWM periods, can be obtained using simple calculation:

$$i_l^{AV} = -\frac{i_{dc}(SAMP2)+i_{dc}(SAMP3)}{2} = -\frac{i_{lo}+i_{le}}{2}$$

$$i_h^{AV} = \frac{i_{dc}(SAMP1)+i_{dc}(SAMP4)}{2} = \frac{i_{ho}+i_{he}}{2} \qquad (1)$$

$$i_m^{AV} = -\left(i_l^{AV} + i_h^{AV}\right)$$

It remains to assign the resultant currents i_h^{AV}, i_m^{AV} and i_l^{AV} to motor line-currents i_a, i_b and i_c depending on the actual sector number as in conventional case [4].

Proposed current reconstruction algorithm is integrated in the sensorless control structure for induction motor drive, which is illustrated in the Fig. 2. Key blocks that improve control quality and performances are proposed current sampling block *F281X_IDC4*, *AVERAGING* block for finding inputs for conventional line current reconstruction which uses only two dc-link current samples *IABC_RECONS*, and proposed modified voltage modulator *SVGEN_AB4* that generates proposed modified PWM switching pattern and overcomes critical cases in the reconstruction mechanism. Used flux estimator consists of two models: simple $i_s - \omega_r$ open-loop current model defined in field coordinates which has to provide correct estimation in the low speed range, and adaptive $u_s - i_s$ model obtained in stator coordinates for precise estimation in wide speed range [11]. Determination of rotor flux vector position is done using phase-locked-loop structure implemented in rotating reference frame. Rotor speed is estimated in open-loop, based on estimated rotor flux frequency from PLL block and calculated slip frequency which is directly proportional to the motor electromagnetic torque.

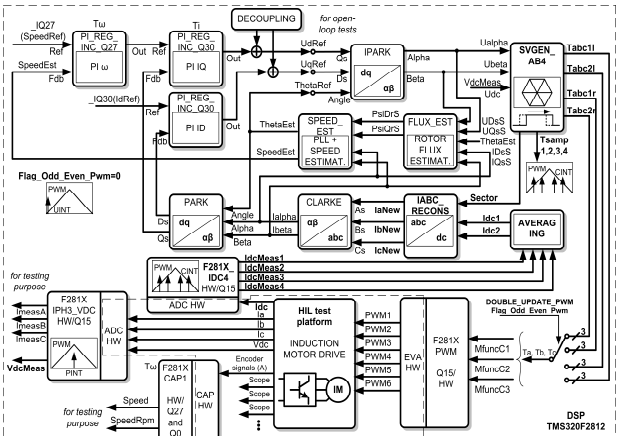

Fig. 2. DSP implementation structure of sensorless induction motor drive with proposed current reconstruction algorithm

3. EXPERIMENTAL SETUP

In order to validate effectiveness and reliability of the proposed control algorithm, hardware-in-the-loop (HIL) emulator was used for representing the power stage of induction motor drive. The core of the HIL platform is programmable FPGA based processor dedicated for processing power electronics circuits, with fast

analog/digital input/output interface and supporting software tool-chain. Beside schematic configurator and compiler, software tool-chain includes oscilloscope function for observing desired system variables and flexible debugging of the connected controller.

This approach provides real-time execution with *0,5 μs* emulation time-step and digital signals (e.g. PWM) sampling period of *20 ns* for more accurate system emulation. This feature allows the connection of real hardware controller. Controller interfaced with the HIL system is based on TMS320F2812 digital-signal processor. In all performed experiments, PWM frequency was set to *2 kHz*. Fig. 3 shows the experimental setup used for evaluation of the induction motor drive with minimal number of sensors.

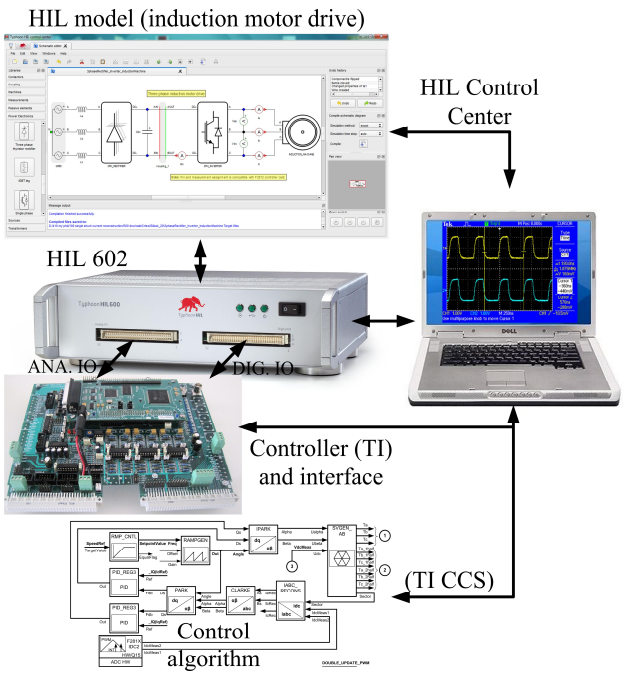

Fig. 3. Experimental setup for algorithm verification

4. EXPERIMENTAL RESULTS

The first improvements in the reconstructed line-current waveform can be observed for a steady-state operation with ω_r^{REF} = *0,4 p.u.* (*1200 rpm*), T_{load} = *1,5 Nm* (20% of nominal) and closed-loop operation with proposed current feedbacks, in Fig. 4. Fig. 4a shows actual (measured) line current values, i_a, i_b, and i_c, compared to the reconstructed line currents by proposed scheme, i_a^{NEW}, i_b^{NEW}, and i_c^{NEW}, and by conventional scheme, i_a^{REC} (only phase-*a* current is shown for clarity). Improved reconstructed currents do not include characteristic abrupt changes in its waveforms due to the passing reference voltage vector between SVPWM sectors. Proposed current reconstruction reduces presence of third and sixth harmonic terms in dq-current components by factor of 3, but also the offset from actual values which are noticeable especially in d-current component (Fig. 4b).

Improvements can be observed in motor torque and speed, not only in the steady-state, but also in transient intervals, where dynamic response is more stable. Figs. 5 and 6 show dynamic response of motor speed, electromagnetic torque, and stator line currents in the transient operating conditions: speed step reference ω_r^{REF} = *0,1-0,4 p.u.* and T_{load} = *1,5 Nm*.

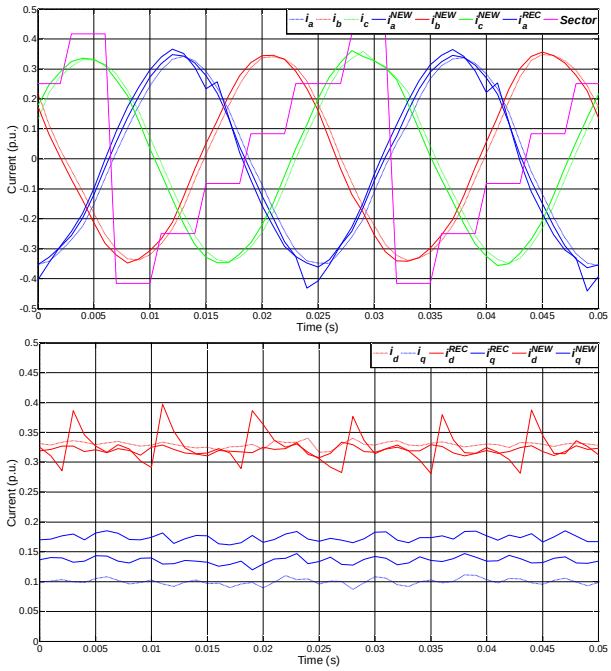

Fig. 4. Steady-state response: a) actual and reconstructed line currents, b) actual and reconstructed dq-currents with proposed (^{NEW}) and conventional reconstruction method (^{REC})

Oscillations are less reduced for low speed reference *0,1 p.u.* because there are more frequent requirements for application of asymmetrical PWM signals due to the low reference voltage amplitude. However, comparing results in Figs. 5 and 6 verify that proposed method provide more stable stationary and dynamic response compared to the conventional current reconstruction method. This is specially noticable in the developed motor torque and stator line currents.

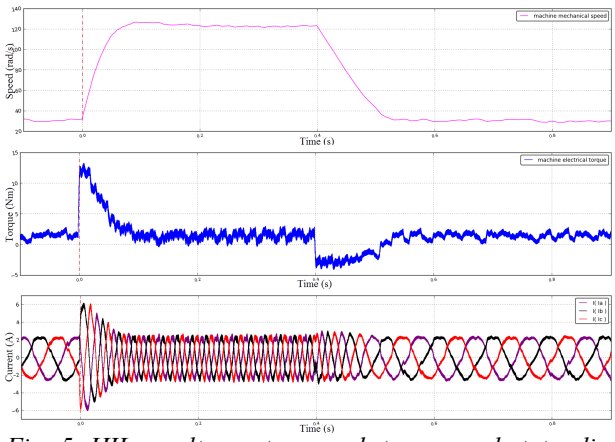

Fig. 5. HIL results: motor speed, torque and stator line currents transient response for speed step reference – conventional current reconstruction method

Fig. 7 shows stable dq-current response in the case when control algorithm uses proposed reconstructed currents as feedback signals.

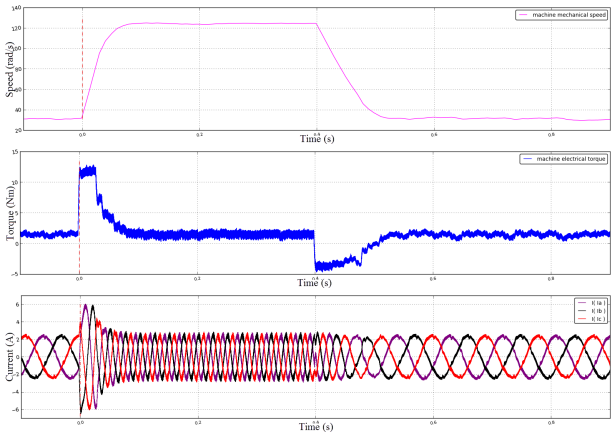

Fig. 6. HIL results: motor speed, torque and stator line currents transient response for speed step reference – proposed current reconstruction method

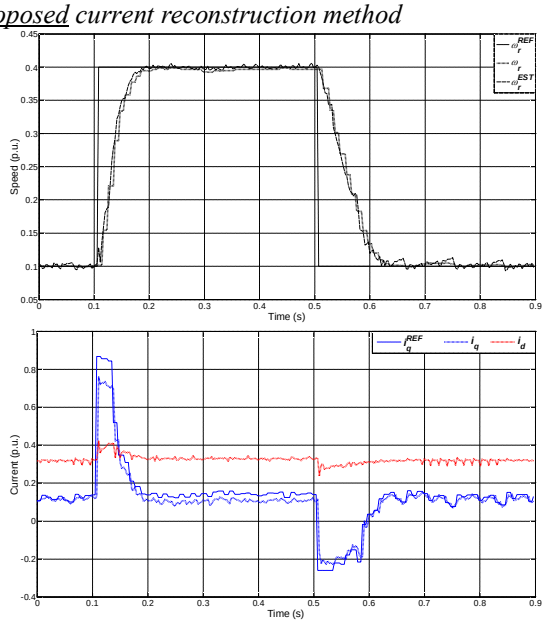

Fig. 7. DSP results: motor speed and dq-currents transient response for speed step reference

5. CONCLUSION

This paper proposes novel current reconstruction algorithm which is suitable for integration in the standard sensorless vector control induction motor drives. Proposed solution is completely independent on the machine model and parameters. It uses averaging of totally four dc-link current samples in two consecutive PWM periods, which significantly reduces the phase error and characteristic harmonics in the dq-current components. Average dc-link samples are referred to the same time instant which yields to the reconstructed line current waveforms which are almost the same as actual measured values.

Obtained results verifies that proposed method reduces motor current, torque and speed oscillations to the acceptable level in the case when only one current sensor is used, and in the conditions where all controller and estimator parameters are set for high performance response.

6. ACKNOWLEDGMENT

This research was partially co-funded by the Ministry of Education, Science and Technological Development of Republic of Serbia under contract No. III 042004 and by the Provincial Secretariat for Science and Technological Development of AP Vojvodina under contract No. 114-451- 3508/2013-04.

7. REFERENCES

[1] J. Holtz, ñSensorless control of induction machinesð With or without signal injection?ò *IEEE Trans. Ind. Electron.*, Feb. 2006., vol. 53, no. 1, pp. 7ï 30.

[2] P. Vas, *Sensorless Vector and Direct Torque Control*. New York: Oxford University Press, Inc., 1998.

[3] C. Lascu, I. Boldea, F. Blaabjerg, ñA Class of Speed-Sensorless Sliding-Mode Observers for High-Performance Induction Motor Drives,ò *IEEE Trans. on Ind. Electron.*, vol. 56, no. 9, Sept. 2009.

[4] T. C. Green and B. W. Williams, ñDerivation of motor line-current waveforms from the DC-link current of an inverter,ò in *Proc. Inst. Elect. Eng. B—Elect. Power Appl.*, Jul. 1989, vol. 136, no. 4, pp. 196ï 204.

[5] F. Blaabjerg, J. K. Pedersen, U. Jaeger, P. Thoegersen, ñSingle Current Sensor Technique in the DC Link of Three-Phase PWM-VS Inverters: A Review and a Novel Solution,ò *IEEE Trans. Ind. Appl.*, Sept./Oct. 1997, vol. 33, no. 5, pp. 1241-1253.

[6] H. Kim, T. M. Jahns, ñPhase Current Reconstruction for AC Motor Drives Using a DC Link Single Current Sensor and Measurement Voltage Vectors,ò *IEEE Trans. Power Electron.*, Sept. 2006, vol. 21, no. 5, pp. 1413-1419.

[7] J. I. Ha, ñVoltage Injection Method for Three-Phase Current Reconstruction in PWM Inverters Using a Single Sensor,ò *IEEE Trans. on Power Electron.*, Mar. 2009, vol. 24, no. 3.

[8] Y. Gu, F. Ni, D. Yang, H. Liu, ñSwitching-State Phase Shift Method for Three-Phase-Current Reconstruction With a Single DC-Link Current Sensor,ò *IEEE Trans. on Ind. Electron.*, Nov. 2011, vol. 58, no. 11.

[9] C. Zhang, F. Lin, ñA Single Current Sensor Control Technique for Induction Motors,ò *Proc. Of PowerCon 2002,* 2002, vol. 4, pp. 2290-2293.

[10] D. Marcetic, E. Adzic, ñImproved Three-Phase Current Reconstruction for Induction Motor Drives With DC-Link Shunt,ò *IEEE Ind. Electron.,* July 2010, vol. 57, no. 7, pp. 2454-2462.

[11] C. Lascu, I. Boldea, F. Blaabjerg, ñA Modified Direct Torque Control for Induction Motor Sensorless Drive,ò *IEEE Trans. on Ind. Electron.*, vol. 36, no. 1, Jan./Feb. 2000.

The 7th International Conference on Engineering and Technology
ICET-2015, Phuket, June 19-20, 2015
Prince of Songkla University, Faculty of Engineering
Hat Yai, Songkhla, Thailand 90112

Seasonal Asphalt Concrete Surface Pavement Temperature Models Using Neural Networks

Bojan Matić[1]*, Vlastimir Radonjanin[1], Mirjana Malešev[1], Nebojša Radović[1], Siniša Sremac[1]
[1]University of Novi Sad, Faculty of Technical Sciences, Novi Sad, Serbia
*Email of corresponding author: bojan.matich@gmail.com

Abstract: *Many regression models have been developed to predict the temperature of an asphalt concrete (AC) layer using air temperature with some other input parameters. Some of these models are aged and cannot be applied to diverse site locations with accuracy. This paper presents models to predict surface pavement temperature depending on the days of the year using neural networks. Four annual periods are defined and new models are formulated for each period. Models are formed on the basis of data gathered on the territory of the Republic of Serbia and are valid for that territory.*

Key Words: ***pavement, temperature, model, predicting, artificial neural networks (ANN)***

1. INTRODUCTION

Authors all around the world have provided models to predict pavement temperature both on local and on global level.

Several models predicting the pavement temperature have been analysed, and it has been determined that the best predicting models are the ones formed using databases for the territory where they are intended to predict pavement temperature.

Pavement temperature can be influenced, apart from latitude and other factors, by seasons as well, and by time of a day.

Until today, many authors have formed models using statistical data analysis to predict the surface pavement temperature.

Table 1. *An overview of models for predicting pavement temperatures using regression analysis [1,2,3,4,5,6]*

Author	The publishing year	Statistical data analysis
Strategic Highway Research Program (SHRP)	1987	Yes
Mohseni A.	1998	Yes
Lukanen et al.	1998	Yes
Bosscher et al.	1998	Yes
Ovik et al.	1999	Yes
Park et al.	2001	Yes
Marshall et al.	2001	Yes
Denneman E.	2007	Yes

Abo-Hashema, M. (2013) discusses the feasibility of applying artificial neural network (ANN) technology in predicting the AC layer temperature. In his paper, the neural network is trained and tested using NeuroSolutions 5.0 software through the actual field data obtained from Long-Term Pavement Performance (LTPP), Seasonal Monitoring Program (SMP) - DataPave3.0 software.

Results indicate that the developed ANN-based pavement temperature prediction models can be used in predicting AC layer temperature with high accuracy in comparison to the measured values.

This outcome is considered crucial to the pavement design, especially followed by the second ANN model where some input parameters may not be available [7].

B. Matić et al., (2014) formulate a new model for predicting pavement temperatures at specified depth using neural networks, depending on the surface pavement temperature and depth.

Based on the correlation coefficient, standard model deviation and mean absolute error (MAE), it could be concluded that these models could be utilized with the adequate accuracy for predicting maximal and minimal pavement temperature at depth; yet, the model for predicting minimal pavement temperature at certain depth provides a somewhat more accurate result.

Also, it can be concluded that the models formed by ANN predict pavement temperatures with higher accuracy than models formed by the regression analysis [8].

2. EXPERIMENTAL PART

2.1. Instrumentation and data

Data used for analyzing and forming the model for pavement temperature prediction were taken from the pilot project by the public company (JP)"Putevi Srbije" and the Government of Sweden.

Surface pavement temperature, as well as air conditions, were monitored using modern meteorological stations (Road Meteorological Information System) on six locations during the part of 2010, the entire 2011 and the part of 2012 for winter road maintenance.

The plan was to monitor temperature in winter months only.

Fig. 1. Road meteorological stations [9]

However, following the insistence and demand by the Faculty of Technical Sciences in Novi Sad, Serbia to monitor temperature during the entire year for the purpose of scientific research, JP "Putevi Srbije" granted the monitoring in other months as well.

The acquisition of all meteorological data in the base, including temperature, was performed every 30 minutes.

Following values were measured: air temperature, air humidity, dew point temperature, type of precipitation, surface pavement temperature, and max wind speed [9].

3. RESULTS AND DISCUSSION

3.1. Methodology and anticipated results

The model developed with the objective of predicting surface pavement temperature is based on the neural networks analysis. Models are formed to predict maximum and minimum surface pavement temperatures, depending primarily on the maximum and minimum air temperature and depending on the days of the year.

3.2. Model validation

The paper formulates new models for predicting maximum and minimum pavement surface temperatures using ANN, in dependence on the ambient air temperature.

The former predicts maximum surface pavement temperatures based on maximum air temperature, as seen in Table 2. Mean Average Error (MAE) for this model is 3.82937757 ^{o}C.

The latter predicts minimum surface pavement temperatures based on minimum air temperature, as observed in Table 3. Mean Average Error (MAE) for this model is 1.40998219 ^{o}C.

Table 2. *Model predicting maximum surface pavement temperature based on maximum air temperature by ANN*

Index	Net. name	Training perf.	Test perf.	Training error	Test error	Training algorithm	Error function	Hidden activation	Output activation
1	MLP 1-5-1	0.944463	0.815718	0.004626	0.015968	BFGS 111	SOS	Logistic	Exponential

Table 3. *Model predicting minimum surface pavement temperature based on minimum air temperature by ANN*

Index	Net. name	Training perf.	Test perf.	Training error	Test error	Training algorithm	Error function	Hidden activation	Output activation
1	MLP 1-5-1	0.974493	0.972041	0.001555	0.001618	BFGS 44	SOS	Logistic	Tanh

Table 4. *Table overview of MAE of models predicting max and min surface pavement temperature by ANN*

Mean Average Error, MAE, ^{o}C	
maxTk	minTk
3.82937757	1.40998219

Based on previously completed research and developed models using regression analysis, it is concluded that models that predict the minimum and maximum surface pavement temperature provide better results in comparison to the models using ANN [10].

Furthermore, the paper formulates the models for predicting surface pavement temperature for diverse periods during a year based on air temperature, day of the year and humidity by ANN. The Mean Average Errors (MAE) of these models are shown in Table 5.

Table 5. *Table overview of models predicting surface pavement temperature for diverse periods during a year by ANN*

Independent Variables	**Mean Average Error, MAE, ^{o}C**			
	January-March	April-Jun	July-September	October-December
Air temperature, day of year	**0.894487**	**2.226435**	1.690075	0.869849
Air temperature, day of year, humidity	1.033865	2.470103	**1.683501**	**0.852367**

If we use humidity as one of the input variables in the model for predicting the surface pavement temperature, the MAE will not be less for all models. For some models MAE will be increased.

Accordingly, it can be concluded that the model for predicting surface pavement temperature using ANN for the first two periods of the year (from January to March and from April to June) is better without humidity as an input variable (i.e. model where the input variables are air temperature and day of the year). For the other two periods (from July to September and October to December) a better model is with humidity as an input variable.

The tables below present the ANN models that predict seasonal asphalt concrete surface pavement temperature with the highest accuracy using ANN for four different periods of the year (Tables 6, 7, 8, 9).

Table 6. *Model predicting surface pavement temperature by ANN based on air temperature and day of the year for period January-March*

Index	Net. name	Training perf.	Test perf.	Training error	Test error	Training algorithm	Error function	Hidden activation	Output activation
1	RBF 2-63-1	0.895316	0.889872	0.002	0.0021	RBFT	SOS	Gaussian	Identity

Table 7. *Model predicting surface pavement temperature by ANN based on air temperature and day of the year for period April-Jun*

Index	Net. name	Training perf.	Test perf.	Training error	Test error	Training algorithm	Error function	Hidden activation	Output activation
1	MLP 3-6-1	0.946513	0.964050	0.002701	0.003905	BFGS 47	SOS	Logistic	Logistic

Table 8. *Model predicting surface pavement temperature by ANN based on air temperature and day of the year for period July-September*

Index	Net. name	Training perf.	Test perf.	Training error	Test error	Training algorithm	Error function	Hidden activation	Output activation
1	MLP 3-3-1	0.961315	0.955025	0.00	0.002	BFGS 50	SOS	Tanh	Identity

Table 9. *Model predicting surface pavement temperature by ANN based on air temperature and day of the year for period October-December*

Index	Net. name	Training perf.	Test perf.	Training error	Test error	Training algorithm	Error function	Hidden activation	Output activation
1	MLP 3-4-1	0.978898	0.972124	0.000711	0.000916	BFGS 70	SOS	Exponential	Logistic

4. CONCLUSION

The paper formulates new models for predicting minimum and maximum pavement surface temperatures using ANN, in dependence on the ambient air temperature.

Also, the paper formulates new models for predicting day surface pavement temperature, including seasonal influences by ANN.

Furthermore, model validation has been conducted.Based on the mean absolute error (MAE) and standard deviation of error (SDE) between measured and predicted pavement temperatures, it can be concluded that the models formed with two variables (air temperature and day of the year) by ANN predict pavement temperatures for period January-March and April-Jun with better accuracy than the models formed by regression analysis.

Likewise, it can be concluded that the models formed with three variables (air temperature, day of the year and humidity) by ANN predict pavement temperatures for period July-September and October-December with higher accuracy than the models formed by two variables.

Table 10. *Table overview of models predicting surface pavement temperature for diverse periods during a year by regression analysis and ANN*

Independent Variables	**Type of analysis**	**Mean Average Error, MAE, ^{o}C**			
		January-March	April-Jun	July-September	October-December
Air temperature, day of year	Regression analysis [3]	1.284492	2.799148	2.158237	1.123356
	ANN	**0.894487**	**2.226435**	1.690075	0.869849
Air temperature, day of year, humidity	Regression analysis [3]	1.283519	2.613486	2.162538	1.082358
	ANN	1.033865	2.470103	**1.683501**	**0.852367**

Acknowledgment

The authors acknowledge the support of the research project TR 36017, funded by the Ministry of Science and Technological Development of Serbia.

5. REFERENCES

[1] T. Kennedy, G. Huber, E. Harrigan, R. Cominsky, C. Hughes, H. V. Quintus, J. Moulthrop, "Superior Performing Asphalt Pavements (Superpave): The product of the SHRP Asphalt Research Program", National Research Council, Washington, DC, (1994).

[2] A. Mohseni, M. Symons, "Effect of Improved LTPP AC Pavement Temperature Models on SuperPave Performance Grades", Proceedings of 77th Annual Meeting, Transportation Research Board, Washington, DC, (1998b).

[3] E. O. Lukanen, H. Chunhua, E.L. Skok, "Probabilistic Method of Asphalt Binder Selection Based on Pavement Temperature", Transportation Research Record, Transportation Research Board, 1609 (1998), 12-20.

[4] P. J. Bosscher, H.U Bahia, S. Thomas, J.S. Russel, "Relationship Between Pavement Temperature and Weather Data: Wisconsin Field Study to Verify SuperPave Algorithm", Transportation Research Record, 1609 (1998), 1-11.

[5]C. Marshall, R. Meier, M. Welch, "Seasonal Temperature Effects on Flexible Pavements in Tennessee", Transportation Research Record, 1764 (2001), 89-96.

[6] E. Denneman, "The application of locally developed pavement temperature prediction Algorithms in Performance Grade (PG) Binder Selection", The Challenges of Implementing policy-SATC 2007: The 26th Annual Southern African Transport Conference and Exhibition, Pretoria, South Africa, (2007), p.10.

[7] Abo-Hashema M., "Modeling Pavement Temperature Prediction Using Artificial Neural Networks". Airfield and Highway Pavement, 2013, pp. 490-505.

[8] B. Matić, D. Matić, Đ. Ćosić, S. Sremac, G. Tepić, P. Ranitović, "A model for the pavement temperature prediction at specified depth", Metallurgy, 52 (2013) 4, 505-508.

[9]B. Matić, "Seasonal asphalt concrete surface pavement temperature models", Contemporary Civil Engineering Practice, 2013, pp. 243-258.

[10] B. Matić et al., "Development and evaluation of the model for the surface payment temperature prediction", Journal "Metalurgija", Croatian Metallurgical Society, Zagreb, Croatia, 51(2012)3, pp. 329-332, ISSN: 0543-5846.

.

The 7th International Conference on Engineering and Technology
ICET-2015, Phuket, June 19-20, 2015
Prince of Songkla University, Faculty of Engineering
Hat Yai, Songkhla, Thailand 90112

A Conceptual Framework transforms The Player into Buyers on Mobile Applications: A Case Study of Mobile Social Network Games

Metawat Kavilkrue*, Witchakon Khuankaew
North – Chiang Mai University, Faculty of Engineering, Chiang Mai, Thailand
*metawat@northcm.ac.th, mcnmmcnm@gmail.com

Abstract: *In this paper, It focuses on the elements that make to transform the player into buyers of mobility social network games on smart phone. It is based on very popularity social network games and top charts categories in app/play store. This research finds a conceptual framework or conceptual model from the comparison of the case study. This conceptual framework might shows the root problem of the player or the development business of the creator. The experiment results can indicate the decision of the player*

Key Words: ***Social Network Games, Mobile Applications, Internet Marketing, Conceptual Framework, Smart Phone***

1. INTRODUCTION

Mobile phones have grown rapidly in the current economic situation. Currently, the Mobile phones have gained popularity and acceptance is a smart phone for virtually every country in the smart phone. It can meet the needs of users. It provides a convenient means of communication with the user to provide entertainment to users. The most important thing is second from the operating system of the smart phone is applications.

Application with many existing categories such as games, entertainment, news, photography, social, sports, etc. which are one type that has been very popular on the mobile phone or tablet is games application. Social network games are growing up that fuel of audience who spends revenue to social network game merchant. Current, applications games organized in the smart phone and tablet have tremendous soon the game will feature a unique and unlike any other game for prominence of that game but at least those hypothesized that must have many parts that look the same in a game application called co-factors which we can find common factors of similarity of features and game applications available for study comparison based on the principles of internet marketing, nature or characteristics of the games and type of users.

2. REVIEW

2.1 Pirate Kings

Pirate king is a 3D game in which players must create an island for a residential area of the characters that players can choose from. Format, the player must rotate the pie plate with the press of a button and has a limited rotation. One round will be rotated to match the topics contained in the circular plate. Circular plate are formed in 10 channels which form the plate consists of Cash Steal, Spins Defend and Attack when they stop sign and arrow pointing at a Steal Spins, Defend and Attack when stopped at the position of these players can be different. Follow these instructions by which the player can Steal the money looted from the island of the enemy. The money will be randomly drawn from the islands of the other players, and will select the 3 islands for the player to choose, and if a player chooses a player can rob your money for the full amount of the players choose not to pay you less. When stopped at the Spins can stop the rotation allows players to rotate an additional 10 rounds. Revolutions have a maximum of 50 rounds and 1 hour to the rotation increments of 5 rounds. When a player can Defend against the barrier islands of the players. The first barrier is to prevent attacks to 3 other players who are attacking the player, and can protect up to 3 channels. And stopped the Attack, players can attack the island of other players. once In the attack, the player can choose to attack the island of the other players have. Whether it is an island of the island of friends or other players of the game was randomly selected for the players themselves by attacking one can choose from 5 types of attack including attack on the island, pirate attacks, homes attack,Attack island decor items and silly to attack the statue. When a player has enough money, players can upgrading island, upgrading the ship, Homes upgrading, upgrading island decor items, and upgrading sacred statues. The price of the upgrade will cost more in the order given to the game and when the island is full and then upgrade. The game will be moved to the new island and the island of players play money upgrading to

the new format is a beautiful island and better. The more players there are many islands island upgrading better the players get more stars only. Stars in the game, meaning the player's level. Players will use the stars on the level with your friends or other players in the game. The more players there are many stars to the level of the players are amongst the highest in comparison to other players or friends of the players. The game will allow players to accumulate money to rebuild the island for the better and more beautiful. The players get money from the players roll a stop sign at the Cash, Which will be a lot less, respectively, each channel. The other is from a robbery in a Steal. And by attacking the other players in the attack. Another way is to use outside money to buy in-game currency. You will have to buy a five-level sort order from cheap to expensive and ascending.

2.2 Cookie Run

Cookie run game in 2D designed to run through each state, each state will have Gold, Silver and cookies to collect to finish the stage that played by the player must choose a character to run in the state it. that the game has been given, and when the player will be a button to press two buttons is a button to jump to the slide and when the character is running away with the energy of the run is limited and will decline steadily on. We ran forward If the player runs through obstacles in each state will be greatly reduced vitality. If a player falls to the bottom to make the characters of the play dead. During the run, each state will have to collect all the bonuses to the players to score more. The more players the more score It gives the player an advantage in the ratings compared to other players and it's a race to get the most points in each state itself. The game will have the bigger the star, the star level, it would mean we play a lot more experience itself. Later, as a diamond With the purchase of in game accessories such as a help in the running of the character. Later, a Coins can buy it on sale in the shops of the game and coins can be collected from each state to state, running through the heart is indicative of a character's life. To run one state to use One Heart. When I run out of time to get to the heart from the fact that all five planets and invite your friends to play the game and send it to heart each day. Character of the game is free to choose the players to start the game. But if a player wants to buy additional character that has the power to run and beauty of the animal to run after us and ordered us to collect the items in each state can be obtained by incubating the eggs, which hatch in. using diamond pet hatching out. Characters and pets can not upgrade that use coins to upgrade. Players must collect coins to buy and to upgrade. But if the coins does not have to be bought with money from the outside. Some characters use coins to buy. Others can buy a diamond. Diamonds are available from the outside even in the game and bought with money.

2.3 Let's Get Rich

Let's get king is a 3D game that takes place in a channel on the board. The province name land-based casinos including the outer space The board will consist of one 32 channel and the class has 5 levels: beginner-level, intermediate-level, high-level, professional-level, and super professional-level. Each class will be used to play different. Gait patterns each use 2 dice to determine the number of characters of the player's own pace. The ball rolled on the dice have the same number of dice rolled, the player can have one around. When players stop a channel on the board, players will be able to act in the place such as Buy land, Build Houses and Cities. The Kate player is "land mark build" the game will determine compete with one another and can be played with in one board with a number of players up to 4 people on board, let's get king to issue an order requiring the user. Play action name in various activities. Each board shall order and different activities away. The area is said to double the toll twice as much at the start of play, the player will receive a lump sum based on the creation of a pick. And when the dice determines the character of the passage of each player. Each player must manage the money of the building assigned to the board. Whether buying land Buying a home of another player already created and players can build a house out of the house, we bought a house occupied by buying other players will have to pay twice that a lot of building at home that is generating much more money from tolls. The purchase of the building of the other players can buy it if the player has created a building that is not a "Land Mark" making the buildings in the area of the players as "Land Mark" to take home all three, each will have. Sizes vary from small, medium and large rear respectively, and when it rolled to a stop in the 4 round and has built homes. Players will be building a "Land Mark" occupied. The board also has the risk of random cards. The gold card, both cards to give luck to the players or the card fine. When a player gets a card system condemned to walk on the taxpayers. The more players lot building. Will allow players to pay more taxes. The money is only when another player rolled to a stop at the house that we own. That will cause another player to stop this waste of money. The more players there are in the building is very expensive. To make more tolls along the same time. In order to be exchanged with expensive construction. To get money to buy By the fact that players have to win games to play one of the board. The loser was the same, but not less. And the loser will lose the experience as well. The amount of money a player can be purchased in shops such. Dice to roll The pitching is the number of the characters, more accurate, and can upgrade the dice, using gold and diamond card, the card players can compete in the board cards have several examples guard. The purchase of a building that we built into the game. Guard to pay a toll to stop at the place of the other players are winning players on the amount of administration to 0 will cause the player to lose the game immediately. The game is scheduled for players to go into place as scheduled on each board. If the players went into that place at all. The player has won and will automatically make the players get gold. Amount of gold and diamonds in the game can be purchased in stores. Of the store where purchased for a coder to join the board with dice, playing with others. When gold and diamonds, the player is not enough. Must buy gold and diamond using external funds for the purchase. This will enable players to spend more in stores and to make the characters, the player has an advantage over others.

3. COMPARATIVE STUDY

In table 2, we try to limit the scope of the main factors affect the decision of the player. The classification into 4 categories thus game engine, mobile operating system, internet marketing and mobile social networking. First, we'll give respondents prioritize the main factors that most infuence the decision in descending. From table 1, shows the percentage of main factors affect the decision of the player into the buyer. This process does not interest in the games.

Table 1. *Main Factors*

Main Factors	Percentage
	%
Game Engine	5.40
OS & Application	3.20
Internet Marketing	75.80
Mobile Social Networking	15.60

In table 1, we have notes that internet marketing has the most impact as 75.80% from results. For the main factors that impact is minimal as OS & Application because the players don't feel the difference. Both operating sustems are supports games that it's not affect the decision of the players.

Table 2. *Requirement of Surveys*

Requirement of Survey	Levels					
	5	4	3	2	1	0
Characters						
Life Time						
Score						
Tools						
Round Time						
Ranking						
Money						
Funny						
Competition with yourself						
Competition with other						
Graphic						
Continuation						
Diversity & Novelty						
Social Stream						

In table 2, we propose a part of queries of this research that how do we collect information from users? The inquiry will focus on the factors involved in the decision of the user. The query will have a score to the end user. And to determine the percentage And the weight of each factor Then compare the factors had little effect on the decision. Then summarize the results in the graph. Including queries that users enter in other factors. The research presented is not comprehensive.

From research [1] presents comparative study of internet marketing on mobility social network game. We observed factors to consider the internet marketing and do not include other factors, according to the authors, more research on the factors that affect the players. We analyze of the number of player, applications and popularity games. From original research comparison of the 3 case studies that we have to put the game out more to complete in table 3, and the difference is clear. The previous paper compares various internet marketing techniques which attract a player for transform to buyer.

Table 3. *Comparative Study of factors transforms Player into Buyer of Social Network Game*

Game / Factors	Pirate King	Let's Get Rich	Cookie Run
Characters	✓	✓	✓
Life Time	-	-	✓
Score	✓	✓	✓
Tools	✓	✓	✓
Round Time	-	✓	-
Ranking	✓	✓	✓
Money	✓	✓	✓
Competition with yourself	✓	-	-
Competition with other people	✓	✓	✓
Graphic	✓	✓	✓
Continuation	✓	✓	✓
Diversity & Novelty	✓	✓	✓
Social Stream	✓	✓	✓

From table 3, internet marketing factors has 13 elements are that include character, life time, score, tools, round time, ranking, money, competitiom with yourself, competition with other people, graphic, continuation, diversity & novelty and social stream. From questions that arise from factors other than the internet marketing and have an impact on the decision of the player or not?. Because internet marketing that it does not cover all the factors that will change the player to a buyer immediately. The author believes that there must be other factors or elements. Related understanding In purchasing decisions that the survey was conducted. The players selected to the 1,000 persons were then compared to the three game to see the difference and make the results more clearly in terms that are relevant to internet marketing, which turns out that the factors that affect the players trading decisions, as shown in table 3. In addition to internet marketing are aware that other factors that transform players into buying it. There are many these factors have a greater impact on the internet marketing. It's has many factors such as Characters, Life Time, Score, Tools, Round Time, Ranking, Money, Funny, Competition with yourself, Competition with other, Graphic, Continuation, Diversity & Novelty and Social Stream.

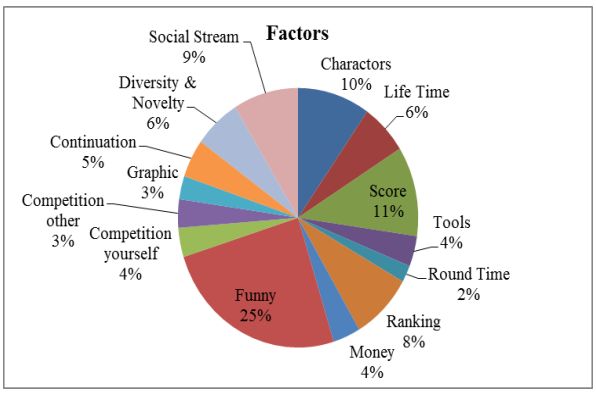

Fig. 1. Results of internet marketing factors on mobility social network game

4. EVALUATIONS

From Fig. 2, the difference of two conceptual frameworks is the numbers of transformation system, we will consider only three factors are not. Because of the survey the entire game is on different operating systems such as iOS or Android, even if the number of players, it affects the decision as well. We provide co-factors in addition to internet marketing. Thus, the authors concluded that the conceptual framework.

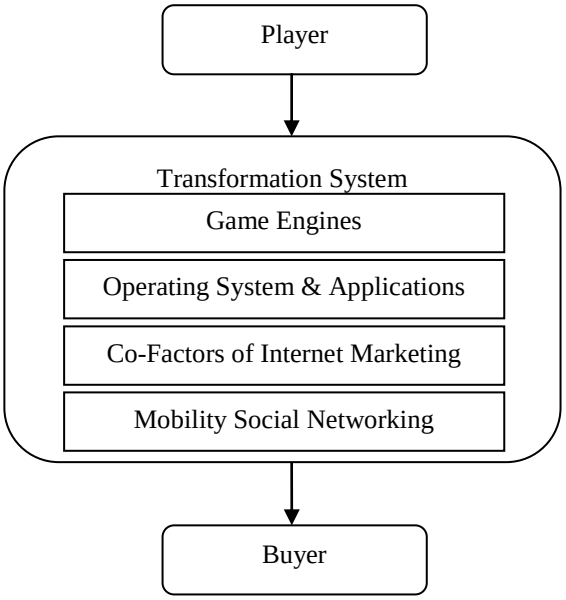

Fig. 2. Conceptual Framework of Co-Factors Transform Player into Buyer of Social Network Game

5. CONCLUSION

Of the doubt and with great attention to the author, for the case of transform players into a buyer of play games on mobile applications for smart phones. The previous research has concluded a framework that brings the internet marketing analysis, but since the author did more research on the person using the actual number of 1,000 peoples showed that the theory of internet marketing available but not all. It also includes other factors Involved in the decision of many players. In conclusion, as a percentage of section 3 and 4 depict that other factors are actually involved in the decisions of the players, so factor that is identical or similar to the internet marketing cofactors. We have presented a conceptual framework transform the players into the buyers on mobile application that covering more. Researchers can also use this case study to other research. The proposed framework and can be a contributing factor to meet the transitional period.

6. REFERENCES

[1] Sarawut Ramjan, “Comparative Study of Internet Marketing on Mobility Social Network Game”, May 2014, Vol 2, P.240-247.

[2] Metawat Kavilkrue, “Comparatine Study of Co-factors transforms Player into Buyer of Social Network Game on Mobile Application,” *Proc. of PSU-PIC Inter. Conf. on Eng. and Envir. 2014 :PSU-PIC 2014*, Nov 13-14, 2014, pp..

[3] Ivashkin & Mishurova. (2013). The Internet Advertising as a Tool of Personified Impact on the buyer. Bulletin of PNU. 2013, Vol. 31 Issue 4, P.171 – 178.

[4] AI-Weshah et al. (2013). Electronic Networks and Relationship Marketing: Qualitative Evidence from Jordanian Travel Agencies. Journal of Relationship Marketing. 2013, Vol. 12, Issue 4, P.261 – 279.

[5] Siegler, MG (June 11, 2008). Analyst: There’s a great future in iPhone apps. Venture Beat.

[6] Matthias Böhmer, Brent Hecht, Johannes Schöning, Antonio Krüger, and Gernot Bauer. 2011. Falling asleep with Angry Birds, Facebook and Kindle: a large scale study on mobile app usage. In: Proceedings of the 13th International Conference on Human Computer Interaction with Mobile Devices and Services (MobileHCI '11). ACM, New York, NY, USA, 47-56.

[7] Chu Eric (13 February 2009). Android Market Update Support.

[8] Leppäniemi, Matti, “Mobile marketing communications in consumer markets”, Faculty of Economics and Business Administration, Department of Marketing, University of Oulu, 2008, p. 21.

[9] Karjaluoto Heikki and Leppäniemi Matti, “Factors influencing consumers’ willingness to accept mobile advertising: a conceptual model”, Int. J Mobile Communications, Vol 3, No. 3, 2005, p. 198.

[10] D. Quercia, Ilias Leontiadis, Liam McNamara, Cecilia Mascolo, Jon Crowcroft (2011). SpotME If You Can: Randomized Responses for Location Obfuscation on Mobile Phones. IEEE ICDCS.

The 7th International Conference on Engineering and Technology
ICET-2015, Phuket, June 19-20, 2015
Prince of Songkla University, Faculty of Engineering
Hat Yai, Songkhla, Thailand 90112

The Effects of High Temperature to Read-Head Instability

Tossapon Kijpitak, Wanchai Pijitrojana, and Kasin Vichienchom

King Mongkut's Institute of Technology Ladkrabang, College of Data Storage Innovation, Thailand
Thammasat University, Department of Electrical and Computer Engineering, Thailand
King Mongkut's Institute of Technology Ladkrabang, Department of electronics, Thailand
Tossapon.kijpitak@seagate.com, pwanchai@engr.tu.ac.th, kvkasin@kmitl.ac.th

Abstract: *The head instability results in an amplitude changes, signal distortion, and/or resistance due to the output noise. The causes come from the thermal stress interaction between different material layers. This research proposes a study in the thermal stress of head gimbal assembly (HGA) to identify process factors involving a degradation of a read sensor. It is found that the thermal radiation mechanism during the curing process could largely be responsible for the damage. The important finding is that the peak temperature appear in the slider is much higher than the one that controlled from the thermocouple during the curing process.*

Key Words: ***Head Instability / Thermal Stress / Head Gimbal Assembly.***

1. Introduction

The growth of the hard disk drive (HDD) applications in the global market is increasing due to its ultra-high storage capacity and highly cost-effective investment compared to other storage devices. To improve the product yield, the HDD industry is highly increasing an effort on a process development to maintain or even reducing the cost of the manufacturing.

According to the development of the quasi static test, the transfer curve can be used to describe the instability in the tunnelling magnetoresistance (TMR) read-head [1]-[2]. The composition of the TMR includes two ferromagnetic (FM) layers separated by a thin insulating barrier layer (RL). The two FM layers are the free layer (FL) and the pinned layer (PL) as shown in Figure 1. The magnetic field induces a change in the direction of magnetic moment of the FL while the direction of the magnetic moment in the PL is fixed by the interaction between the ferromagnetic (FM) and the antiferromagnetic (AFM) layer which is also known as exchange bias effect [3]. However, if the temperature of the AFM layer exceeds its blocking temperature, the exchange bias effect will be vanished. For this reason, the magnetic instability in the TMR head is of concern at elevated temperatures.

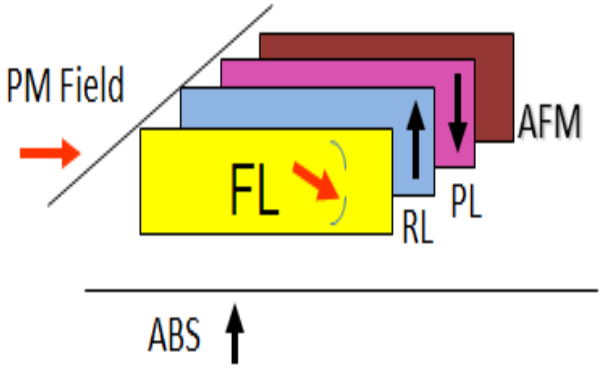

Figure 1: *The fundamental schematic of the TMR head. The two ferromagnetic, free layer (FL) and pinned layer (PL) are separated by a thin insulating barrier layer (RL). The magnetic moment in the PL is fixed by the antiferromagnetic layer (AFM) while the direction of the magnetic moment of the FL is changed by the induction of the magnetic field.*

In the manufacturing of head gimbal assembly, the curing process and the soldering process are two of the major causes of the degradation in the TMR recording heads because they directly generate the heat to the slider body. The experimental results of investigations of the reader performance were reported by Masami Miyatake in 2012 [4]. The results showed that the instability was occurred from lower blocking temperature in the PL or the magnetization on the FL was affected by the temperature. Moreover, as shown by Suttipan Aksornnium [5] on an electromagnetic (EM) curing process, the 2D simulation model resulted in the differentiation between the temperature at the slider area and the one that showed in the thermocouple control

which may cause unexpectedly excessive heat of the read layers.

2. OBJECTIVE

To investigate the instability head that effect from the thermal stress in head gimbal assembly and design the new measurement tool that literally report the heat occurrence in the TMR head.

This paper is organized as follows; Section III presents the discrimination of the transfer curve from Quasi Static tester (QST), next, the real-time temperature measurement method. Section IV shows the experimental results. Finally, the conclusion will be drawn.

3. METHODS

3.1 The discrimination of the transfer curve from Quasi Static Tester (QST).

The quasi static test has been implemented in HGA process to detect the head instability in HGA level. It also can prevent the failed part escaping to the drive operation which will impact to the product reliability.

The quasi static transfer curve is a measure of the read sensor's amplitude and the external magnetic field. It uses to describe anomalies which cause errors in HDD. Figure 2 is the transfer curve characteristics that are detected during the static test in HGA process.

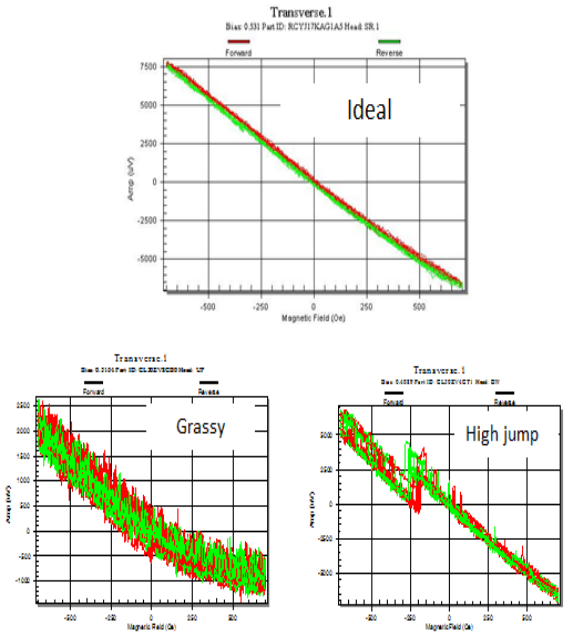

Figure 2: *The transfer curve characteristics that are detected during the static test in HGA process. The heating process might be the potential cause of these failures.*

"The Grassy" and "The High Jump" types are commonly occurred in HGA processes. The heating processes are on focus to be the causes of these failures.

3.2 Real-time temperature measurement method.

Although the machines in the HGA process line already have the functions that can control the environment temperature, but the actual temperature that originates in the slider head has not been studied yet. To identify process factors that involve in a degradation of the read sensor in the HGA line process, the new measurement tooling is designed as shown in Figure 3.

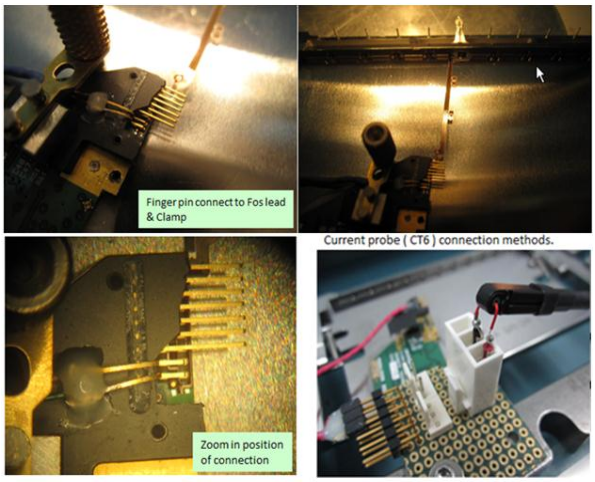

Figure 3: *Illustration of the new measurement tool design. The finger pin is connected to the FOS lead of the HGA part to detect the changing resistance which can be converted to the real time temperature during the heat process.*

The concept of this tooling is to detect the changing resistance during the operation in the heat process. The reason of this change in a resistivity can be explained by considering the flow of current through the material. When the electron is moving from one atom to another, it creates the flow of current. However, only some electrons are free to migrate, other are held so tightly to their particular atoms and will not be dislodged by an electric field. Therefore the current flowing in the material depends on the number movements of the free electron compare with those tightly bound to their atoms. The effect of heat is to make the atoms vibrate, and this vibration will make the changing in the resistivity.

4. EXPERIMENTAL RESULTS.

In the current head gimbal assembly, there are two heating processes; the Electromagnetic (EM) Oven, and the Reflow Soldering. The Electromagnetic (EM) Oven is used to cure the bonding adhesive between sliders and suspensions. The infrared lamp at wave length around 1 µm will provide the heat at specific area (slider area) as shown in Figure 4. The thermocouple is set at the slider area to control the temperature.

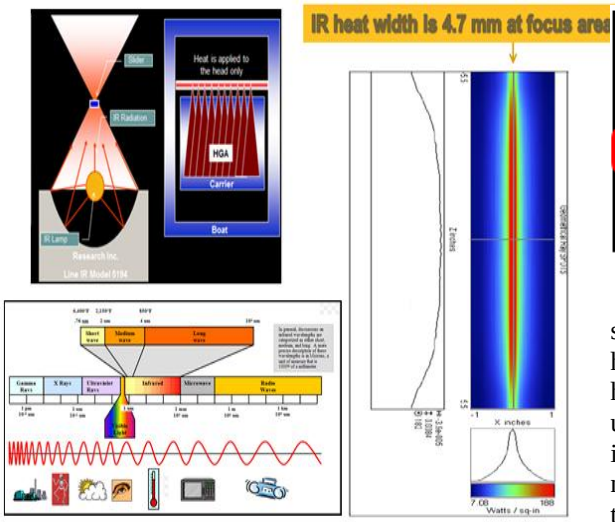

Figure 4: *The fundamental schematic of the Electromagnetic (EM) Oven machine. The infrared lamp at wave length arounf 1um will radiate the heat to the slider area.*

The other heating process is the Reflow Soldering machine. The purpose of this machine is to bond the curcuit between sliders and suspensions. The bonding material is a solder ball which has a melting point above 200 degree Celsius. The figure 5 shows the bonding steps; melting the solder ball by heat, the pad circuit is connected by solder after cooling.

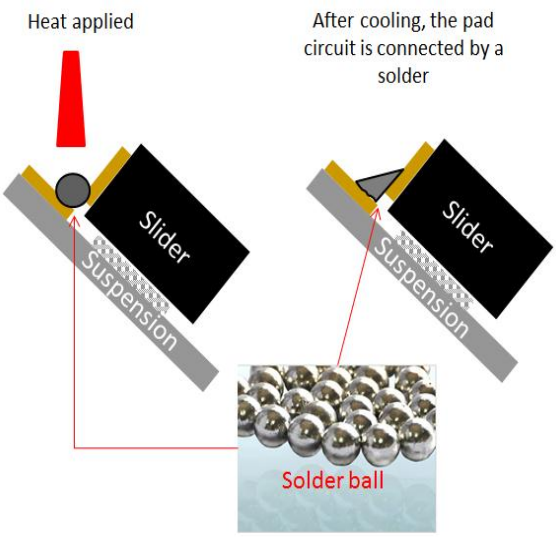

Figure 5: *The functional operation of the Reflow Soldering machine.The solder will be melt by heat at temperature above 200 degree Celsius and connect the pad circuit after cooling.*

To distingish the cause of the instability, the design of the experiment is discussed. The group has been separated into 4 groups:

Group1: Normal oven cured + Reflow soldering
Group2: Higher oven cured + Reflow soldering
Group3: Lower oven cured + Reflow soldering
Group4: No oven cured + Reflow soldering

Table1: *The head instability evaluation result.*

Head instability evaluation			
Condition	Oven temperature	Thermal Interconnected	% Instability head
Group 1	Normal temperature	Normal setting	1.50%
Group 2	High temperature	Normal setting	2.30%
Group 3	Low temperature	Normal setting	1.00%
Group 4	No curing process	Normal setting	0.50%

The evaluation result which has shown in Table 1 shows that the oven machine has potential to degrade the head sensor than the Reflow Soldering machine. The higher temperature, the higher head degraded. To understand the causes, the new measurement tool design is applied. The delta resistance that is detected from the new measurement tooling design will be converted to the temperature by using the transfer function as shown in figure6.

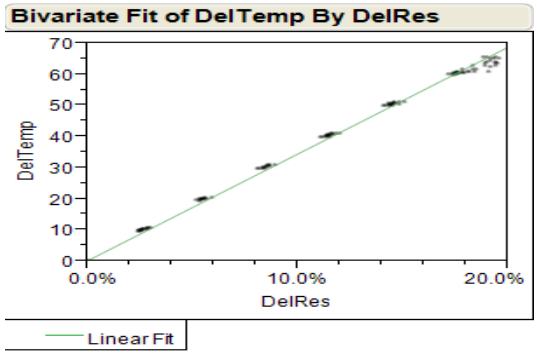

Figure6: *The transfer function of temperature and resistance.*

The result shows that the actual temperature in the slider head is much higher than the one that shows on the thermocouple in the control chart. The Figure7 shows that the actual peak temperature inside the slider head is over 200 degree Celsius. From this result the Electromagnetic (EM) Oven can be a potential cause of the instability head.

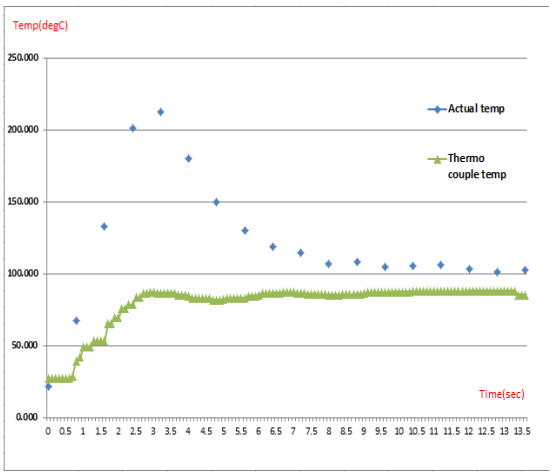

Figure7: *The actual temperature from the new measurement tooling design during the heat process in the Electromagnetic (EM) Oven shows the peak temperature over 200 degree Celsius.*

Not only the oven temperature needs to be verified, but also the Reflow Soldering temperature is required for verification. By using the new measurement tooling design, the peak temperature of the Reflow Soldering machine is 37 degree Celsius as shown in Figure 8. According to this result, the Reflow Soldering machine is not affected to the head degradation.

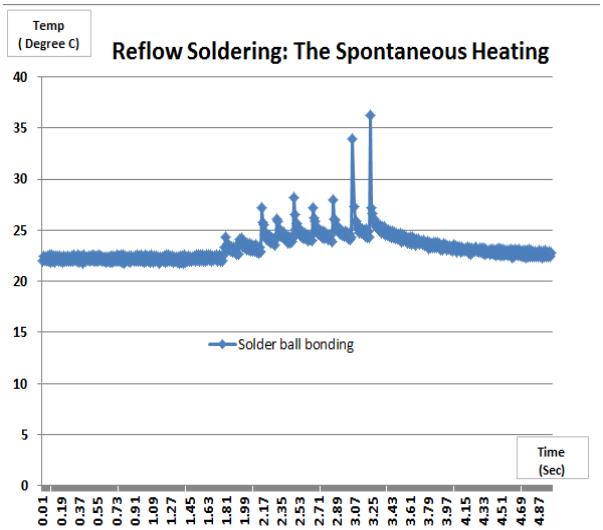

Figure8: *The actual temperature from the new measurement tooling design during the heat process in the Reflow Soldering shows the peak temperature around 37 degree Celsius.*

5. CONCLUSION

The head instability in HGA process is verified. The electromagnetic oven is the major machine for this degradation. The new measurement tooling design can capture the actual peak temperature above 200 degrees Celsius which is different from the thermocouple control in the machine. On the other hand, the Reflow Soldering machine which is using the melted solder ball at melting point above 200 degree Celsius does not affect to the degradation. The peak temperature that can be captured by the new measurement tooling design is around 37 degree Celsius. To avoid the head instability in HGA process, the temperature control system in the oven must be replaced. A measurement tooling design should be an alternative idea that can be modified or upgraded to the future control system.

6. ACKNOWLEDMENT

The authors would like to acknowledge the College of Data Storage Innovation King Mongkut's Institute of Technology Ladkrabang, The National Electronics and Computer Technology Center (NECTEC), The Technology Development Agency (NSTDA), and Seagate Technology (Thailand) Co., Ltd. for equipments and financial supports.

7. REFERENCES

[1] Junguo Xu, Masayuki Kurita, and Mikio Tokuyamad, "Thermal Analysis of a Magnetic Head," *IEEE Transaction on magnetics*, July 2004, Vol. 40, No. 4, pp 3142-3144.

[2] Wei Hua, Jianhua Li, and Bo Liu, "Modeling and simulation of nanometer spaced head disk system," DSI Technical report, data Storage Institute, Singapore, 2002.

[3] M. Rickart, A. Guedes, J. Ventura, J.B. Sousa, and P.P. Freitas, "Blocking Temperature in Exchange Coupled MnPt/CoFe Bilayers and Synthetic Antiferromagnets," J. Applied Physics, vol. 97, no. 10, 10K110, 2005.

[4] Masami Miyatake, Fumio Kugiya, and Naoki Kodama, "Read Performance Reliability in TMR Head," *IEEE Transaction on Device and Materials Reliability*, 2011, Vol. 12, Issue 1, pp 24-30.

[5] Suttipan Aksomnium, Orrathai Watcharakitchakom, and Rardchawadee Silapunt, "A Study of Radiation Heating during the Curing Process of head Gimbal Assembly," *Tencon 2011 -2011 IEEE Region 10 Conference*, Nov 2011, pp 725-728.

The 7th International Conference on Engineering and Technology
ICET-2015, Phuket, June 19-20, 2015
Prince of Songkla University, Faculty of Engineering
Hat Yai, Songkhla, Thailand 90112

Characteristics of Head Gimbal Assembly (HGA) component relate to solder joint reliability

Kanokpong Thongkorn, Monsak Pimsarn
King Mongkut's Institute of Technology Ladkrabang, College of Data Storage Innovation, Thailand
King Mongkut's Institute of Technology Ladkrabang, Faculty of Engineering, Thailand
kpmonsak@kmitl.ac.th

Abstract: *The solder joint reliability of head gimbal assembly (HGA) is key parameter of hard disc drive performance. It is directly impacted to electrical signal of hard disc drive circuit. The solder joint is the connection between slider to circuit. To understand behaviors of head gimbal design by modeling would be the advantage of HGA performance. This thesis showed the study of the HGA characteristic and comparison the difference TGA designs by using Finite Element Analysis. The stress, deformation and frequency response are the parameters that use to imply the impact of frequency from HGA cleaning process to solder joint reliability.*

Keywords: Head Gimbal Assembly (HGA) / Trace Gimbal Assembly (TGA) / Solder ball / Finite Element Analysis (FEA).

1. Introduction

The components of hard disc drive (HDD) are included with many parts. There are head, HGA, head stack assembly (HSA), print circuit board (PCB), media, motor and drive base as shown in Figure 1. Slider is key component that has function to Read and Write Data and to record the signal at Media. Slider is assembled to trace gimbal assembly (TGA) and mounted together with stainless steel to control positioning of Read and Write track on the media. The slider circuit connecting uses solder joint to connect electrical signal as shown in Figure 2. These are part of HGA assembly process. In HGA process, there is the cleaning process which has mainly purpose to remove the contamination off from HGA. The cleaning system has the ultrasonic generator in the machine. The frequency of ultrasonic has set up for optimizing the contamination removal performance. However, there is the solder joint crack is happened from this cleaning process with ultrasonic applied. Therefore this thesis is going to analyze the characteristic of HGA which can be directly impact to HGA cleaning process in order to improve the solder joint reliability.

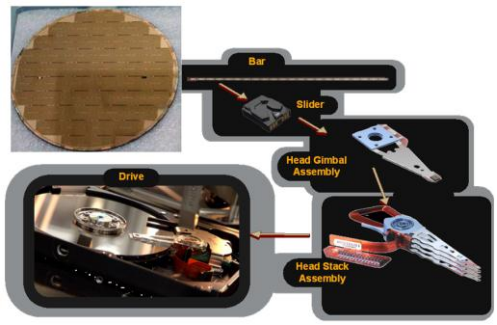

Figure 1. *Hard disc drive manufacturing flow*

A solder ball is the preferred material in the electronic industrial. The standard of solder ball material is consisted of tin, silver and copper. In this research will be studied the behavior of the HGA design by model that effects and impacts to solder joint with finite element analysis.

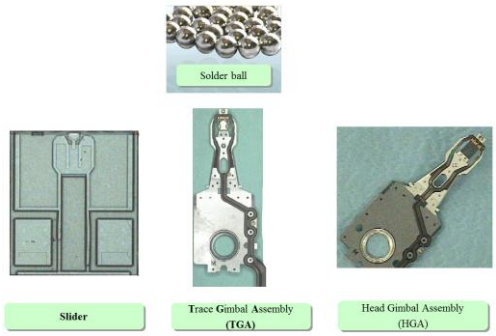

Figure 2. *Head Gimbal Assembly (HGA) components*

2. Characteristics of HGA assembly process

In the HGA, there are 3 components, TGA , slider and solder ball as shown in figure 3. Slider is assembled on the top of stainless steel. The natural frequency response shaking is directly caused solder structure deforming and cracking. This is why signal disconnecting between TGA circuit and slider itself.

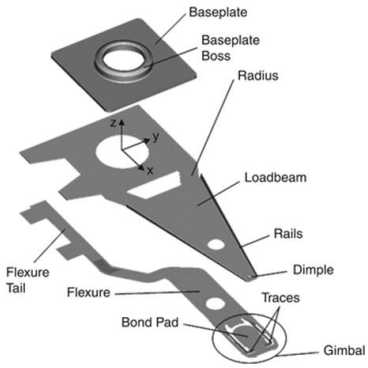

Figure 3. *TGA design*

3. Finite Element analysis

In this study, finite element analyze is performed using ANSYS, a powerful finite element software, to analyze deformation behavior of the HGA. The complication and difficulty of physical shape, material, and condition can be generated easily when using the software and performed on high performance computer to obtain results faster. Contact mechanics using implicit analysis is conducted in the FEA software. Details of these procedures and analyses are presented in the following topics.

3.1 Finite Element Model

In this analysis, the main parts of finite element model is consist of the TGA and slider. The analysis is the comparison between TGA circuit design A and B which the design A is larger gimbal shape than design B. This research would like to analyze the frequency response in each design as shown in Figure 4.

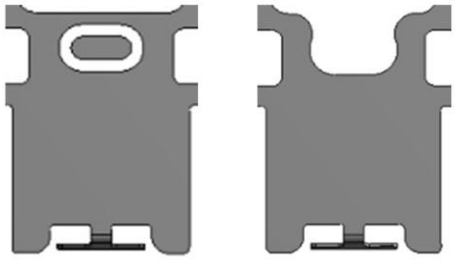

Figure 4. *Design A and design B*

3.2 Definition of interaction

Interactions in these analysis are defined as 2 types. Firstly, the friction less which contact the dimple and gimbal components of TGA. Secondly, the bonding contact which used for the interaction between trace, stainless steel layer and load beam as shown in Figure5. And the comparison gimbal profile between design A and B is shown in Figure 6.

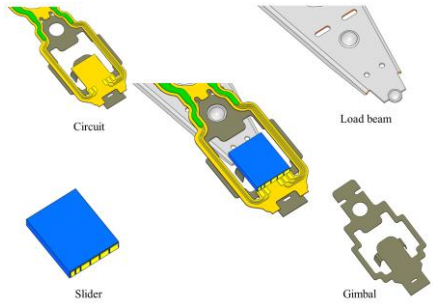

Figure 5. *Configuration of HGA*

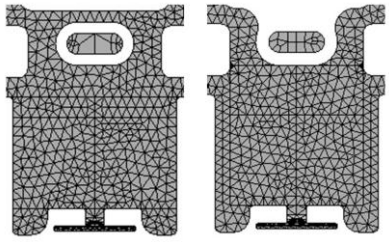

Figure 6. *Comparison Gimbal design A and B*

3.3 Boundary condition

For simplify modeling and easier analysis to understand the behavior of stress , deformation and frequency response , the fix rigid element at load beam is implied in figure 7.

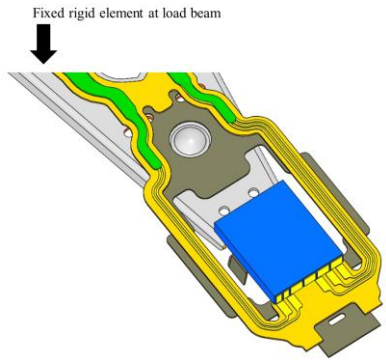

Figure 7. Boundary condition

4. Result

4.1 Simulation result

In this study is focus on the von-mises stress, deformation and resonance frequency response which these characteristics are directly impact to solder joint reliability. The highest stress is appeared on strut area on the both design A and B. And the von-mises stress values are comparable between design A and B, 142.37 and 147.24 MPa which means there is no significant impact to HGA assembly process on this design changes, as shown in Figure 8.

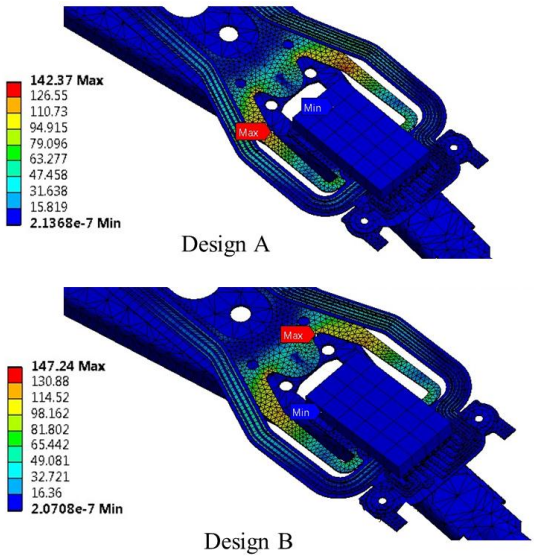

Figure 8. *Stress*

The deformation has showed the head can be held on the center of the dimple which the data of deformation in the z direction are 0.128 mm vs 0.13 mm for design A and B respectively. The result of this 2 designs are comparable as shown in figure 9 which means this analysis is proven that slider is sitting properly on center of dimple location.

Figure 9. *Deformation Design A and B*

The resonance frequency response showed the difference frequency mode between design A and design B as shown in figure 10 and 11. The mode 57 frequency response result are 133.3 and 111.1 KHz for design A and B respectively. This result can be implied that the Gimbal shape has the direct impact to resonance frequency response when gimbal design is changing. The natural frequency of design B is farther away from target of ultrasonic frequency of HGA cleaning process than design A.

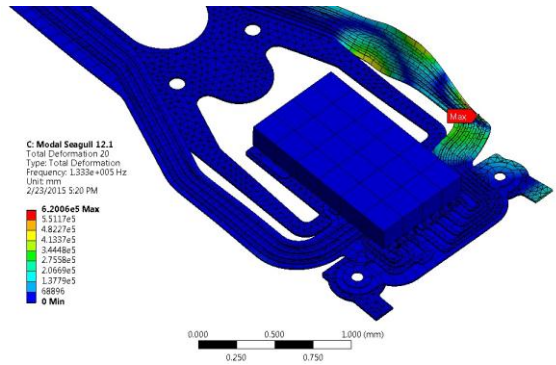

Figure 10. *Frequency response mode 57 of design A*

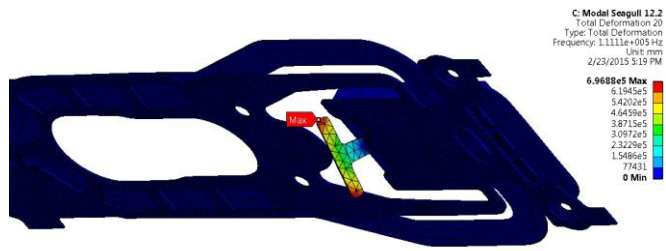

Figure 11. *Frequency response mode 57 of design B*

Table 1. *Frequency response comparison*

Frequency response	Design A (KHz)	Design B (KHz)
Mode 55	122.8	107.9
Mode 56	124.8	110.7
Mode 57	133.3	111.1
Mode 58	134.4	114.9
Mode 59	136.9	117.5

4.2 Experimental result

To validate the modeling by cleaning the HGA sample between design A and B and using HGA cleaning with ultrasonic frequency. Then post cleaning inspection at solder joint by scanning electron microscope equipment to investigate the solder joint physical quality. The result showed the design A has 80% failures of solder joint cracking and design B has no any failures as shown in table 2 and figure 12.

Table 2. *Comparison solder joint reliability*

HGA	Sample (pcs)	Failure (pcs)
Design A	10	80% (8/10)
Design B	10	0% (0/10)

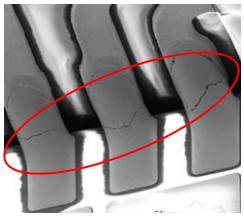

Solder joint reliability of design A

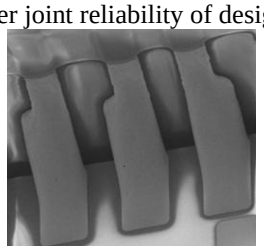

Solder joint reliability of design B

Figure 12. *Solder joint reliability by scanning electron microscope*

5. Conclusion

The analysis is comparison the main characteristic of gimbal between design A and B that are directly affected to resonance frequency response. By designing TGA to have the natural frequency response to be mismatched with frequency in HGA cleaning process is the main principle. This helps to increase the robustness the solder joint in HGA cleaning process. For the stress and deformation are also key metrics to consider the TGA design. If the stress and deformation are changing that might be impact to another parameters of HGA assembly process which can be critical to quality of the product. The experiment result showed the design A is worse than design B based on the solder joint cracking failures. This analysis can be used for guideline to choose the design of TGA, by using the modeling to analyze the several of characteristics of TGA designs. This can help to have the minimal product design candidates for HGA process validation. It can definitely reduce cost and time, also improve the quality of future product launches.

6. Reference

[1] C.F.Luk,Y.C Chan and K.C Hung, “Appilaction of adhesive bonding techniques in disk drive head assembly” Microeletronics Reliability2002 : 767-777

[2] Kilian, S., U. Zander, F.F. Talke. 2003 “Suspension Modeling and Optimization Using Finite Element Analysis” Tribology International 36:317-324.

[3] Joompon Bamrungwong , “Analysis and Design the sound Frequency of a treble Gamelan Using FEA” ME-NETT21 , 2006

[4] Thoatsanope Kamner,Surachate Chutima and Jukkraphun Parirukvijit , “The Improvement of Deformations and Characteristics of HGA During Clamping using Finite element analysis” IEEE 2008

[5] Surachet Chutima , Tossapon Kamnerdthong , Visawat Atjannakul and Kajonsak Jaidee , “A study of Behaiors After Mounted with Shipping Comb” ME-NETT23 , 2009

The 7th International Conference on Engineering and Technology
ICET-2015, Phuket, June 19-20, 2015
Prince of Songkla University, Faculty of Engineering
Hat Yai, Songkhla, Thailand 90112

Risk assessment of landfill in Serbia based on flooding potential

Dejan Ubavin[1]*, Nikola Maodus[1], Srdjan Kovacevic[1], Bojan Batinic[1] and Maja Djogo[1]
[1] University of Novi Sad, Faculty of Technical Sciences, Novi Sad, Serbia
*Email of corresponding author: dejanubavin@uns.ac.rs

Abstract: *As a consequence of undeveloped waste management system in the past, Serbia at the moment has more than 3400 wild dumps, around 150 municipal non sanitary landfills and less than 10 sanitary landfills.*
Beside sanitary landfills, which mostly fulfill regulation requirements, selection of location for all other landfills were based predominantly on distance from the settlements without taking into account other aspects.
Landfills located in potential flood zones and zones with higher level of groundwater represent a threat to surrounding areas and surface/groundwater bodies due to waste emissions and subsequent pollution, especially when landfill bodies are not designed properly, which is often case in countries with undeveloped waste management system. During the floods in May 2014 many Municipalities in Serbia suffered significant damage in the field of waste management. The main goal of this paper was to establish new risk assessment approach for determining flood risk of landfills based on hydrological aspects, which will help to establish the register of the most threatened landfills in Serbia.

Key Words: ***Flood / Landfill /Risk assessment /Groundwater***

1. INTRODUCTION

During the third week of May, record-breaking amounts of rainfall were recorded. More than 200 mm of rain fell in western Serbia which is the equivalent of 3 months of rain under normal conditions. The heavy rainfalls led to soil saturation and a rapid and substantial increase of water levels in the main rivers in western, south-western, central and eastern Serbia. Increase of water level caused significant rise of groundwater level. Overall the floods affected some 1.6 million people living in 38 municipalities, mostly located in central and western Serbia. Total value of damage and losses is estimated to the amount of EUR 1.7 to 1.8 billion [1].

Waste management practice in Serbia currently comprises of waste collection and disposal, mostly on non-sanitary landfills without treatments or control prior to disposal. In last few years there is tendency of separating some of the recyclable waste such as PET, paper, cardboard and metal. Even though some waste fractions are preselected for recycling, all other waste, including organic waste ends up on landfills which do not fulfill basic requirements for safe disposal. As a consequence of undeveloped waste management system in the past, Serbia at the moment has more than 3400 wild dumps, around 150 municipal non sanitary landfills and less than 10 sanitary landfills [2].

Due to uncontrolled waste disposal, those non sanitary landfills have been identified as one of the major threats and sources of contamination of environment in Serbia.

Landfills located in potential flood zones and zones with higher level of groundwater represent a threat to surrounding areas and surface/groundwater bodies due to waste emissions and subsequent pollution, especially when landfill bodies are not designed properly, which is often case in countries with undeveloped waste management system. The risk and its consequent emissions of chemicals or hazardous waste is higher in countries with economy in transition such as Serbia where risk mitigation measures have not been systematically implemented yet [3].

Due to potential negative influence of solid waste deposition sites, location of landfills in areas that do not have appropriate soil types (compacted clay with low hydraulic conductivity) or are in 100-year flood plains, and those that specify smallest acceptable distances between landfills and populated areas need to be avoided [4]. Even though National regulations and international standards require minimum distance of 500 m from any surface water [5,6], many landfills in Serbia are placed closer to the river banks [2].

Landfill leachates, are significant sources of groundwater pollution and pose major risks to groundwater quality [7].

Research on quality of groundwater in the vicinity of the landfill in Serbia shows high values of COD, BOD_5 and permanganate index, which indicate the high organic pollution of this water. Also high level of potassium, calcium and magnesium, in both, rainy and dry season, are recorded [8].

During a flood event it has to be assumed that the landfill body becomes water saturated and that this leads to a substantial mobilization of pollutants, since the

presence of water enhances decomposition and transport processes [9-12]. Heavy metal and organic pollutant contamination of soils is one of the major environmental problems resulting from the regular flooding of rivers in Europe [13].

Flooding of landfills not only helps propagation of pollution but also endangers landfill structure characteristics or stability. At several landfills which are located in flooded municipalities structural integrity was compromised by water that carried away 10 to 30 % of landfilled waste.

There are studies regarding risk assessment of landfills in Serbia which are based entirely on landfill distance from river bed and which primarily refer to prioritization regarding flood risk [3], as well as general environmental risk assessment based on larger number of general parameters [2] but studies based on detailed analysis from hydrological aspects are not realized by now.

The volume of disposed waste and occupied area per landfill are shown in Table 1. Landfill operational measures at all of these sites are not highly developed or working at high efficiency rate. Waste is deposited throughout landfill body without a good landfilling plan and it is compacted from time to time. Besides, the landfill body is not designed adequately so the landfill slopes become too steep and unstable or the landfill body is stretched on a large area with small waste lifts. Other measures such as leachate and landfill gas collection and treatment, and usage of daily cover are not implemented.

Table 1. Amount of disposed waste at landfills in flood affected Municipalities

Municipality	Area (ha)	Landfill volume (m^3)
Bajina Bašta	2.1	99,000
Čačak	3.0	365,000
Jagodina	5.2	1,650,000
Koceljeva	1.9	50,000
Kosjerić	0.9	50,000
Kragujevac	14.2	2,395,000
Kraljevo	7.3	970,000
Krupanj	1.4	57,000
Lazarevac	2.1	146,000
Loznica	7.9	258,000
Ljubovija	0.8	35,000
Mali Zvornik	0.7	41,000
Obrenovac	10.8	575,000
Osečina	0.8	32,000
Paraćin	5.9	482,000
Smed. Palanka	1.6	108,000
Svilajnac	2.3	205,000
Šabac	17.9	842,000
Šid	6.8	135,000
Trstenik	1.2	142,000
Ub	1.9	119,000
Valjevo	3.6	420,000
Varvarin	2.3	65,000
Velika Plana	2.3	94,000

All of landfills shown in table 1, are currently operating except the landfills in Šabac and Jagodina, which are closed recently.

2. METHODS

24 municipalities of 38 that were affected by floods sustained greater damage in the domain of solid waste management among other. In some municipalities landfills were partially or completely flooded which resulted in significant spreading of pollutants from these, mostly unregulated landfills. However there is a question of what were the consequences of adverse hydrological situation for other landfills in flood affected areas.

There is considerable number of wild dumps in considered municipalities (6 to 65 open dumps per selected municipality), beside main non sanitary solid waste landfills. These wild dump sites have extremely low amounts of deposited waste and for that reason they are not the subject of this research.

Risk assessment for municipal solid waste landfills in specified municipalities was realized taking in consideration four aspects: distance between landfill and surrounding water bodies, groundwater risk assessment, saturation of soil with water at landfill location and determination if landfill was actually flooded during the flood period in May 2014.

Two aspects of this risk assessment are directly related to flood disaster that occurred in May 2014. „Flooded landfill“ and „Compromised with water saturated soil“. On the other hand other two risk assessment aspects „distance from the water bodies “ (river basins, lakes, etc.) and „state (level) of groundwater at location of the landfill“ are not as directly related to flood disaster as two preceding aspects because groundwater levels and soil saturation can change without disaster occurrence and can be analyzed independently.

Previous research regarding landfills in Serbia included recording of landfill’s GPS coordinates and other attributes such as landfill surface or area, waste volume, waste depth etc. GPS coordinates were used for positioning of landfills in satellite imagery (SPOT6, Pleiades, Rapid Eye, TerraSar X, Copernicus and Dartmouth).

Data on landfill location from previous research was used for determination of distance to water bodies [14]. Positioning was done through exporting of landfill GPS coordinates, overlapping the coordinates with map of the river beds in Serbia and manual measuring the distance of each landfill to the nearest water body as shown on Fig 1.

Fig. 1. Distance of the landfill from the river

Determination of second risk assessment aspect was conducted by positioning landfills on the map of groundwater vulnerability in Serbia which was made for purposes of project "Monitoring of groundwater resources in Serbia" [15].

This map displays six degrees of groundwater according vulnerability which ranges from very low to very high risk of vulnerability. Degree of vulnerability was determined through analysis of following aspects: Influence of terrain slope on infiltration, influence of soil type and type of vegetative cover on vulnerability of groundwater, thickness of overlaying layer, geological i.e. hydrological characteristics of terrain and depth to groundwater level.

Determination of flooded landfills and soil saturation with water at landfill locations was conducted through export of landfill GPS coordinates and their overlapping with satellite imagery with indicated layers of flooded surfaces, and soil surfaces saturated with water. Satellite imagery used (SPOT6, Pleiades, Rapid Eye, TerraSar X, Copernicus and Dartmouth) was obtained at online service of Republic of Serbia Geodetic authority.

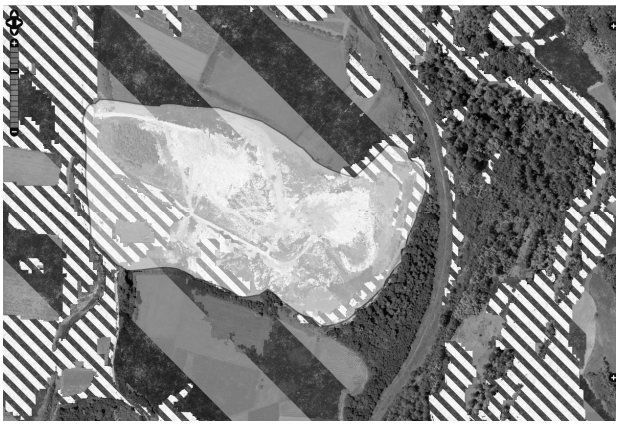

Fig. 2. Obrenovac landfill with flooded and water saturated soil layers.

The estimate of landfill vulnerability degree was based on combined usage of satellite imagery and known terrain characteristics determined during the site visits. The figure 2 shows an example of landfill marked on satellite image of the Obrenovac area where landfill surface is marked by white polygon , flooded surfaces by smaller print pattern and soil saturated with water is marked by larger print pattern.

3. RESULTS AND DISCUSSION

Risk assessment of landfills based on flooding potential was conducted in 24 Municipalities which were significantly affected by the flood.

Table 2. Municipality landfills flood risk assessment

Municipality	Status A – Flooded landfill B – Compromised with water saturated soil C – Influence on groundwater D – Less than 500 m form the water body
Bajina Bašta	A, D*
Čačak	C, D*
Jagodina	C, D
Koceljeva	C,D*
Kosjerić	C, D*
Kragujevac	C, D*
Kraljevo	C, D*
Krupanj	-
Lazarevac	-
Loznica	B, C, D*
Ljubovija	A, C, D*
Mali Zvornik	A, C, D*
Obrenovac	A, C, D
Osečina	A, D
Paraćin	B, C,D
Smed. Palanka	B
Svilajnac	B, C
Šabac	B, C, D*
Šid	B
Trstenik	-
Ub	A, C, D
Valjevo	B, C, D*
Varvarin	A, C, D
Velika Plana	B, C, D

** Less than 100 m from the water body*

Based on the results shown in Table 2, one can see that 18 out of 24 landfills are located less than 500 m from rivers although it is the minimum required safe distance. Moreover, 11 landfills are located on a distance less than 100 m from the river basins. Sixteen out of 24 landfills are placed on locations with high average groundwater levels wherein fluctuations in groundwater levels can reach deposited waste and increase dispersion of pollutants. It was determined that during the flood wave in May 2014 seven landfills were partially or completely flooded and 8 more were in the zones with water saturated soil.

All flooded landfills are located less than 500 m from water bodies. Three of the flooded landfills are located on a location which is less than 100 m and 4 of flooded landfills are located between 100 and 300 m from water bodies.

At landfills which belong to risk group from aspect of flood probability, water saturated soil and high levels of groundwater some measures as provision of alternative location for landfilling, closure and remediation of old location need to be taken in order to prevent future spreading of pollution. The method of remediation must adequately isolate landfill body which means that in combination with final top cover and bottom liner must provide sufficient level of protection in the case of high probability of high groundwater levels and water saturated soil occurrences, even though placing top cover and bottom liner is technologically and financially more demanding. Other direct measures can involve building of embankments to direct potential flood waves.

4. CONCLUSION

Looking at the results in the area of factors not directly related to disaster it can be concluded that chosen landfill locations pose high risk in the area of aquatic pollutant dispersion. Although there is law that prohibits placing landfills at such unfavorable locations, activities on remediation of several decades old landfills that are currently in use are rare. In order to improve the environment state it is necessary to be innovative and to apply existing legislation more strictly, especially in the area of prevention. Experience gained during analysis of flood consequences must result in measures that will increase flood resilience of municipal solid waste landfills.

Results obtained by this research in selected municipalities are causing for concern and it is necessary to carry out the same analysis for all landfills in Republic of Serbia and to establish the register of threatened landfills, potentially with detailed quantification of the risk.

5. REFERENCES

[1] Serbia Floods 2014 Report, Post Disaster Needs Assessment, UN, EU and WB, Belgrade 2014.

[2] Faculty of Technical Science, Novi Sad (2012) MOPRORK - Determination of contamination from landfills and monitoring models, risk assessment, determination of amount of waste with modern satellite information technology to support the implementation of legislation. Faculty of Technical Science, Novi Sad, Serbia

[3] Misato, O., Laner, D., Stanisavljevic, N., Fukuya, L., Taikan, O., Prioritization of landfills subject to flood risk in serbia, The 6th PSU-UNS International Conference on Engineering and Technology (ICET-2013), Novi Sad, Serbia.

[4] Eiselt, H.A; Marianov, V; A bi-objective model for the location of landfills for municipal solid waste, European Journal of Operational Research, Vol 235, 2014, pp 187-194

[5] The Law on Waste Management, Official Gazette of the Republic of Serbia, No. 36/09

[6] Kontos T. et al. “Siting MSW landfills with a spatial multiple criteria analysis methodology” Waste Management 2005, Vol. 25:8:818-832

[7] Christensen, T.H., Kjeldsen, P., Bjerg, P.L., Jensen, D.L., Christensen, J.B., Baun, A., Albrechtsen, H.-J., Heron, G., 2001. Biogeochemistry of landfill leachate plumes. Appl. Geochem. 16, 659–718.

[8] Djogo, M., Vujić, G., Dvornić, A., Milovanović, D., Adamović, D., Lucian, D.: „Evaluation of leachate pollution of landfill site in AP Vojvodina, Serbia“, The international conference Engineering of Environment Protection - TOP2011, Proceedings of the papers, ISBN 978-80-227-3519-3, editor: Miroslav Horvát, Bratislava, The Slovak Republic, June 14 – 16, 2011, pp. 57 – 62

[9] Laner et al. “Flooding of municipal solid waste landfills – An environmental hazard?” Sci. of the Total Envir. 2009, Vol.407:3674-3680

[10] Klink, R.,E., Ham, R.K, Effects of moisture movement on methane production in solid waste landfill samples. Resour Conserv 1982;8:29–41.

[11] Bogner J, Spokas K. Landfill CH4: rates, fates, and role in global carbon cycle. Chemosphere 1993;26:369–86.

[12] ChristensenTH, Kjeldsen P, Lindhardt B. Gas-generating processes in landfills. In: Christensen TH, editor. Landfilling of waste: biogas. London: E&FN Spon; 1996. p. 27–44.

[13] Clevers JGPW, Kooistra L, Salas EAL. Study of heavymetal contamination in river flood-plains using the red-edge position in spectroscopic data. Int J Remote Sens 2004;25:883-3895.

[14] G. Vujić, D. Ubavin, D. Milovanović, N. Stanisavljević and B. Batinić, “Identification of unsanitary landfills using GPS and determination of minimum factors for the risk assessment”, 1st International Conference on Final Sinks, 2010, Vienna, Austria, September 23-25.

[15] Milanovic S., Stevanovic, Z., Djuric, D., Petrovic T., Milovanovic, M., Mandic, M., Groundwater monitoring in Serbia – Map of Vulnerable Groundwater in Serbia, 2011, Ministry of Environment and Spatial Planning, Ministry of Agriculture, Forestry and Water Management – Directorate for Water, Serbia, Belgrade

The 7th International Conference on Engineering and Technology
ICET-2015, Phuket, June 19-20, 2015
Prince of Songkla University, Faculty of Engineering
Hat Yai, Songkhla, Thailand 90112

Modelling of Energy Efficiency Cart of Solar Energy Collectors

Pavel Kovac[1*], Vladan Petrovic [2], Vladimir Pucovski[1], Bojan Bircanin[1], Borislav Savkovic[1], Marin Gostimirovic[1], Krzysztof Rokosz[3]
[1]University of Novi Sad, Faculty of Technical Sciences, Novi Sad, Serbia
[2]Alternativna energija d.o.o. Kragujevac, Serbia
[3]Wydział Mechaniczny, Politechnika Koszalińska, Koszalin, Poland
[*]Email of corresponding author: pkovac@uns.ac.rs

Abstract: *The solution of Prof. Petrovic represents a great breakthrough in the field of energy efficiency and successful exploitation of renewable energy sources. This high-temperature storage enables the energy accumulated from the sun to be produced when necessary and continuously, 24h a day and 365 days a year. In this paper modelling of measured energy of sun insolation, energy intensity production for flat solar panel and energy intensity production of Prof. Petrovic concentrator is made with the use of genetic programming.*

Key Words: ***Energy Efficiency, Solar Energy, Collectors, Modelling***

1. INTRODUCTION

The whole world is working more on development of solar energy, but without any big success. Today there are a lot of constructed thermal solar power-plants, none of which is able to provide 24 h electricity supply during the days when the Sun shines, let alone during winter months. The biggest success is achieved by power-plants with parabolic mirrors, as well as power-plants with flat mirrors. As a temporary solution there are power-plants with a storage made of potassium and natrium salt, which can store energy for 5 - 6 h; these storages are extremely expensive with numerous technical problems. It should also be pointed out that efficiency factor of thermal solar power-plants is a big issue; they are of low efficiency because solar water steam is "low quality". Parameters like these are not present in the solar; here you can achieve pressure of about 50 bar and temperature of 350 °C. Based on these parameters, efficiency of 18 % to 20 % can be achived (Abengoa and Andasol in Spain, and solar power-plants in California).

Throughout the last couple of years it is done very little to make utilization of solar energy purposeful, and to solve energetics through solar. Various authors have made their contribution by research in this field.

Hongfei Zheng et al. [1] has conducted a study for the design of a centralized solar collection system based on combination of a light funnel concentrator with a deflector. Arzu Sencan et al. [2] conducted a theoretical modeling of an absorption heat transformer for the temperature range obtained from an experimental solar pond. Different methods such as linear regression (LR), pace regression (PR), sequential minimal optimization (SMO), M5 model tree, M50 rules, decision table and back propagation neural network (BPNN) was used for modelling the absorption heat transformer. In [3] a hybrid solar concentrator (HSC) has been fabricated by doping a rare earth complex, $Eu(TTA)_3Phen$, into a polymer optical fiber (POF). A methodological analysis to design and evaluate the technical feasibility of use a Linear Fresnel Reflector Concentrator (LFRC) as generator in an advanced absorption refrigeration system (Solar-GAX cycle) has been carried out by Velazquez et al. [4]. For this purpose, a detailed one-dimensional numerical simulation of the thermal and fluid-dynamic behavior of a LFRC. A new trapezoidal cavity receiver for a linear Fresnel solar collector is analysed and optimized via raytrace and CFD simulations in [5]. A novel geometry of a 3-D static concentrator has been designed and coined the Square Elliptical Hyperboloid (SEH) to be integrated in glazing windows or facades for photovoltaic application in [6]. Evolution algorithm has been used in mathematical model to effectively optimize the heliostat field on annual basis. [7] A beam-down solar tower (BST) system, equipped with three linear Fresnel heliostat modules, corresponding beam-down concentrators, and a central cavity receiver with a spiral tube, has been introduced, experimentally investigated and theoretically analyzed in [8]. A two-dimensional cone concentrator for sunlight was theoretically and experimentally studied by Somchai Kiatgamolchai and Ekawit Chamni [9].

Taking in consideration abovementioned research work, it was noticed the absence of genetic programming modeling procedure for energy intensity.

2. ENERGY EFFICIENCY SOLAR SYSTEMS

The solution of Prof. Petrovic represents a great breakthrough in the field of energy efficiency and successful exploitation of renewable energy sources. As it is widely known, the problem with renewable sources of energy is their constancy. Solar systems, no matter which ones, CSP or photovoltaic modules, can fulfil one third of daily needs for energy for only one single reason which is the fact that the sun shines for 8 hours a day on average. This value of insolation is taken for geographical location of Eastern Europe [10]. In order to fill in the gap of 16 hours, many companies (ABENGOA, ANDASOL, SES…), besides solar plants, installed gas power plants. There are a small number of solar power plants with heat storages based on the principle of accumulating the phase transition heat. Molten salt is utilized in this process, but such storages can ensure production of energy for only three hours more after the sunset.

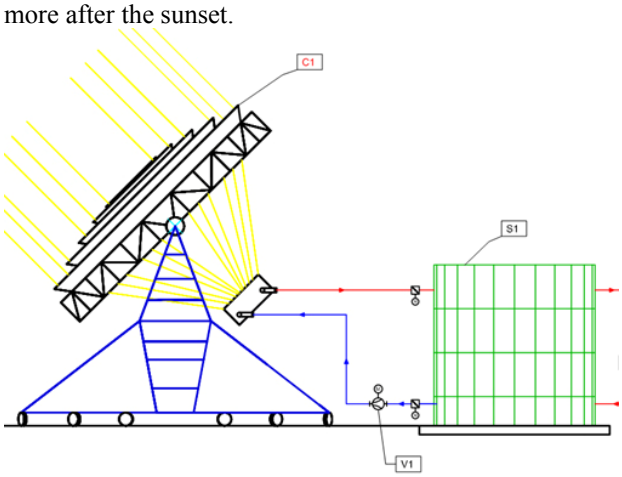

Fig. 1. Schematic of Prof. Petrovic solar system: C1-concentrator, S1-storage, V1-fan

Figure 1 presents the schematic representation of Pejovic system. Air is circulating, driven by fan V1, through pipes into the concentrator where it is heated and then stored in storage container S1.

The high-temperature storage of Prof. Petrovic enables the energy accumulated from the sun to be produced when necessary and continuously, 24h a day and 365 days a year. The storage volumetric capacity is 450 kWh/m^3, which makes it unique. Maximal temperature up to which the storage can be heated is 800 °C. The storage core insulation system is also a patent solution of Prof. Petrovic which enables heat losses to be less than 6% annually. Advantages of "Petrovic" systems:

1. Continuous production of energy from the accumulated sun energy 24h a day x 365 days

2. Accumulation capacity is 4-5 times higher than with the existing systems

3. There are no any restrictions concerning a location's selection for installing the plant.

4. The concentrator's design is composed in a special software simulation which enables the construction to withstand all atmospheric influences with considerable savings in material, unlike the similar existing systems.

Diameter of concentrator D=10 m, surface of concentrator 66.7 m^2, maximal temperature in focus 1450 °C.

3. MODELING PROCEDURE

Based on nature principle of evolution and survival of the fittest, genetic programming is one of the most used evolutionary based algorithms [11]. They use selection, crossover and mutation to yield the fittest individual. In mathematical language, genetic programming is one very capable tool for finding a suitable model function. Genetic programming is used to model membership function using available data [12, 13]. Because three independent cases are observed, number of functions generated will also be three. Operators that are included in creation process are +, -, *, /, x^2, *1/x*, and *abs*. Each generation contained 500 individuals and whole process took 3000 generations for every individual case. Whole procedure is measured in minutes and is acceptable taking in consideration average computational equipment. In this case probability for crossover was 0,7, mutation 0,1 and crossover 0,2. Number of elite individuals is 5 which mean that top five solutions from every generation will be automatically transferred into next. At the beginning of the process 6 constants (marked R_i in table 1 for insolation model, table 2 for flat solar panel and in table 3 for concentrator data model) are generated randomly and later used in creation process. As a fitness function, in this case, mean square error was used. It is found out that this type of function will yield the best results. Final function generated for insolation data is presented in equation (1), for flat solar panel in equation (2) and for concentrator in equation (3).

$$M_I=(((((R_5*R_2)-((h_i+R_2)+R_1))-((R_6\text{^}2)+((R_3-h_i)*(R_3-R_1))))*(((h_i*R_4)*(abs(h_i)))/(((R_5\text{^}2)/(h_i+h_i))+(1/(R_1/R_5)))))+((1/(((R_5-h_i)+R_1)/(R_3-(R_4\text{^}2))))+((((R_3*R_4)-(h_i+R_1))\text{^}2)/(R_5-(h_i+R_3))))) \quad (1)$$

$$M_F=((((((R_5*R_3)-(h_i+R_6))/(1/(h_i/R_6)))-R_4)*(((R_2*h_i)\text{^}2)/(((h_i+h_i)/R_6)+(1/(R_3-R_5)))))+((1/(((h_i-R_6)\text{^}2)/((R_1+R_4)-(h_i*R_1))))-((abs(((R_5\text{^}2)*(R_5/h_i))))*((R_5/(1/R_1))/((h_i\text{^}2)-(R_4+R_5)))))) \quad (2)$$

$$M_C=(((((R_1+(h_i*R_6))*(1/(h_i-R_4)))+(1/((h_i-R_3)/R_5)))+((R_3+(h_i+R_5))\text{^}2))-(abs(((((R_3+R_3)+R_5)*(R_5-h_i))*((h_i-R_6)-((1/R_5)+(R_5-R_2))))))) \quad (3)$$

Table 1. *Values of constants generated by software for insolation model*

R_1	R_2	R_3	R_4	R_5	R_6
0,79399	5,75754	0,47018	8,14488	6,44630	2,56077

Table 2. *Values of constants generated by software for flat solar panel model*

R_1	R_2	R_3	R_4	R_5	R_6
4,94484	1,16938	3,95977	8,96811	7,21380	7,37327

Table 3. *Values of constants generated by software for concentrator model*

R_1	R_2	R_3	R_4	R_5	R_6
2,25255	3,07489	7,05716	7,63340	9,75992	5,01137

where R's are constants generated on the beginning of the process and h_i are values for hour in which energy intensity is measured. Calculated modeled values for energy intensity, for every case, are shown in table 4. Average percent error is used to evaluate success of model. It is calculated using universal formula (equation 4):

$$\Delta = \sum_{i=1}^{13} \left| \frac{E_i - M_i}{E_i} \right| * 100[\%] \qquad (4)$$

where E_i is experimentally obtained energy intensity and M_i modeled value from equations (1, 2 and 3).

As shown average percent error is in acceptable range and does not exceed 15%. Results of yielded models compared with experimental, data is presented in figure 2 for insolation, figure 3 for flat solar panel and figure 4 for developed concentrator.

Table 4. *Data presentation for measured and modeled light intensity with calculated errors in deviation*

Hour	Measured energy intensity of insolation [W/m^2]	Modeled energy intensity of insolation [W/m^2]	Measured energy intensity of flat panel [W/m^2]	Modeled energy intensity of flat panel [W/m^2]	Measured energy intensity of concentrator [W/m^2]	Modeled energy intensity of concentrator [W/m^2]
6.h	0	-10,4138	0	5,59828	0	-28,9374
7.h	215	246,5715	0	-17,1758	0	21,3948
8.h	705	734,5099	105	150,8388	570	582,1298
9.h	875	800,3207	300	272,4361	695	655,419
10.h	920	884,0864	370	331,9894	740	734,2905
11.h	965	949,8995	395	370,8843	770	769,6588
12.h	975	985,4818	405	389,4068	780	835,9306
13.h	965	981,6086	395	384,7522	770	810,3476
14.h	920	929,8292	370	353,3819	740	739,6548
15.h	875	821,9597	280	291,4868	695	623,5948
16.h	705	649,9259	95	195,1341	570	462,0324
17.h	215	405,7042	0	60,32606	150	254,8894
18.h	115	81,2964	0	-116,972	0	2,117672
Average percent error [%]		**12,97**		**14,59**		**9,25**

4. DISCUSSION

As can be seen, it is possible to use genetic programming for obtaining the model function. It is mentioned that this technique offers greater flexibility and is capable of constructing function from grounds up. With an average percent error of maximum 14,6 %, yielded results are showing potential for use in this area. Observing shape of measured data dependency (figure 2, 3 and 4), one can see that its shape is fairly regular and with that in mind only basic operators were selected to take place in function creation. More improvements could be done by implementing more data and attempt to combine all data in one universal function.

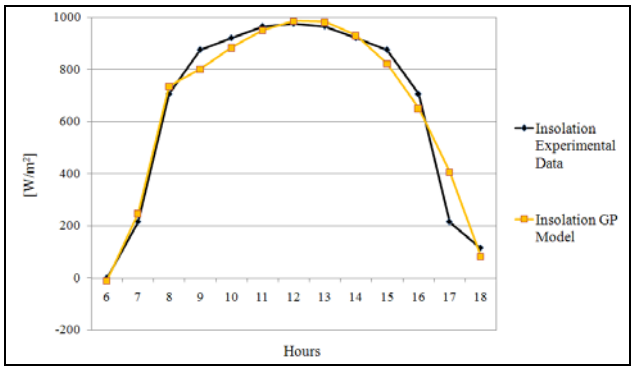

Fig. 2. Graphical comparison between measured and modelled data for insolation

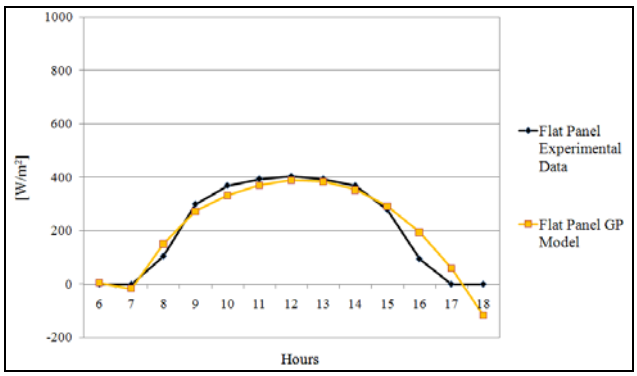

Fig. 3. Graphical comparison between measured and modelled data for flat solar panel

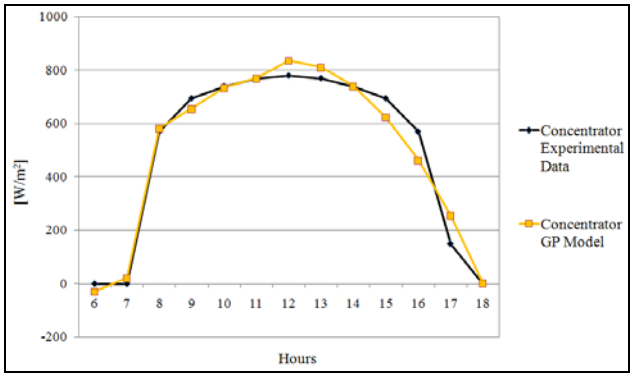

Fig. 4. Graphical comparison between measured and modelled data for developed concentrator

5. CONCLUSION

Genetic programming yielded results which gave 12,97 %, 14,6 % and 9,25 % average percent error. According to authors' opinion genetic programming offers greater flexibility without excessive prolonging computational time. More improvements could be done by implementing more data and attempt to combine all data in one universal function.

6. ACKNOWLEDGEMENT

Authors would like to thank Serbian Ministry of Education, Science and Technological Development which supported this work in form of project no. TR 35015 and Ceepus project.

7. REFERENCES

[1] Hongfei Zheng, Gang Wu, Tao Tao, Yuehong Su, Jing Dai: Combination of a light funnel concentrator with a deflector for orientated sunlight transmission, Energy Conversion and Management, 2014, Vol. 88, p.p. 785-793.

[2] Arzu Sencan, Onder Kizilkan, Nalan C. Bezir, Soteris A. Kalogirou: Different methods for modeling absorption heat transformer powered by solar pond, Energy Conversion and Management, 2007, Vol 48, p.p. 724-735.

[3] Wenxuan Wu, Tongxin Wang, Xin Wang, Si Wu, Yanhua Luo, Xiujie Tian, Qijin Zhang, Hybrid solar concentrator with zero self-absorption loss, Solar Energy, 2010, Vol. 84, p.p. 2140-2145.

[4] Velazquez, N., Garcia-Valladares, O., Sauceda, D., Beltran, R.: Numerical simulation of a Linear Fresnel Reflector Concentrator used as direct generator in a Solar-GAX cycle, Energy Conversion and Management, 2010, Vol. 51, p.p. 434-445.

[5] Jorge Facao, Armando C. Oliveira: Numerical simulation of a trapezoidal cavity receiver for a linear Fresnel solar collector concentrator, Renewable Energy, 2011, Vol. 36, p.p. 90-96.

[6] Nazimi Sellami, Tapas K. Mallick, David A. McNeil: Optical characterization of 3-D static solar concentrator, 2012, Vol. 64, p.p. 579-586.

[7] Maimoon Atif, Fahad A. Al-Sulaiman: Optimization of heliostat field layout in solar central receiver systems on annual basis using differential evolution algorithm, Energy Conversion and Management, 2015, Vol. 95, p.p. 1-9.

[8] Li, X., Dai, Y.J., Wang, R.Z.: Performance investigation on solar thermal conversion of a conical cavity receiver employing a beam-down solar tower concentrator, Solar Energy, 2015, Vol 114, p.p. 134-151.

[9] Somchai Kiatgamolchai, Ekawit Chamni: Theory and experiment of a two-dimensional cone concentrator for sunlight, Solar Energy, Vol. 82, p.p. 111-117.

[10] Pavlovic, T., Milosavljevic, D., Mirjanic, D.: Obnovljivi izvori energije, Akademija nauka i umjetnosti Republike Srpske, Banja Luka, 2013.

[11] Kovač, P., Rodić, D., Pucovski, V., Mankova, I., Savković, B., Gostimirović, M.: A Review of Artificial Intelligence Approaches Applied in Intelligent Processes, Journal of Production Engineering, 2012, Vol. 15, No. 1, p.p. 1-6.

[12] Kovac, P., Rodic, D., Pucovsky, V., Savkovic, B., Gostimirovic, M.: Application of Fuzzy Logic and Regression Analysis for Modeling Surface Roughness in Face Milling, Journal of Intelligent Manufacturing, 2012, doi: 10.1007/s10845-012-0623-z.

[13] Nagy, Ľ., Palkova, Z., Kovač, P.: Matlab Algorithms for the Lighting Control on the Constant Value, Journal of Production Engineering, 2011, Vol. 14, No. 1, p.p. 47-50.

The 7th International Conference on Engineering and Technology
ICET-2015, Phuket, June19-20, 2015
Prince of Songkla University, Faculty of Engineering
Hat Yai, Songkhla, Thailand 90112

Removal of H_2S from Biogas by $KMnO_4$ Impregnated Activated Carbon

Kawalin Prathomravee[1], Wisitsree Wiyaratn[2], and Juntima Chungsiriporn[1]*
[1]Chemical Engineering Department, Engineering Faculty, Prince of Songkla University, Thailand
[2]Faculty of Industrial Education and Technology, King Mongkut's University of Technology Thonburi, Thailand
*Email of corresponding author: juntima.c@psu.ac.th

Abstract: *Biogas, a renewable energy, has the main constituents of methane (CH_4) and carbon dioxide (CO_2). Hydrogen sulfide (H_2S) containing in biogas has the most problematic contaminants found according to malodorous gas, harmful to human health, and highly corrosive to equipments. In this study, potassium permanganate ($KMnO_4$) -impregnated activated carbons was applied as a porous adsorbent for H_2S removal in packed column. The laboratory column with 50 cm height and 4.7 cm inner diameter was set to find for optimum condition and measure % H_2S removal efficiency. Biogas containing H_2S at 1300-2000 ppmv was pumped from anaerobic digester of pig farm and fed to the packed column. The optimum condition was achieved at 5 %w/v $KMnO_4$ concentration, 6 L/min biogas flow rate, and 77 g adsorbent weight. The packed column has breakthrough time at 144 minutes with 89.95% of H_2S removal efficiency. This H_2S treatment system has effectively performed and possibly applied for the actual use in biogas system from pig farm.*

KeyWords: ***Hydrogen sulfide / Removal / Activated carbon / Impregnation / Potassium permanganate***

1. INTRODUCTION

Currently, energy shortage is one major problem for the limited natural resources. All units including household, farmer, and agriculture attempt to find clean and safe energy to use as renewable energy. One of great interesting energy is biogas, a combustible gas, produced by anaerobic digestion which microorganisms break down biodegradable material in an absence of oxygen and low-temperature. Biogas can be substituted for liquefied petroleum gas (LPG), converted to electricity for heating piglet nurseries, hot water or lighting, reduce fertilizer costs. The main constituents of biogas are methane (CH_4) and carbon dioxide (CO_2), but it also contains hydrogen sulfide (H_2S) and other impurities.

Hydrogen sulfide is a flammable and colorless gas that has smells like rotten eggs and directly effected to human health. The H_2S concentration over 200 ppmv is dangerous to respiratory failure wihtin seconds and olfactory fatigue [1]. The presence of H_2S and water make biogas very corrosive to machine contacting the gas. Its strong acid could cause internal damage of equipments. Therefore, the use of H_2S removal system is required before utilizing the biogas as a type of renewable energy.

Many methods have been developed over years for H_2S removal from biogas to obtain low concentration [2]. Activated carbon is widely used as adsorbents for air purification because their high surface area. Activated carbon contains in the packed column for H_2S adsorption. This kind of adsorbentcould be improvedthe removal capacity by impregnation with chemical solution [3]. Potassium permanganate ($KMnO_4$), an oxidizing agent and fast reaction, has been applied for H_2S removal in many system.The reactionsare given in Eq.1 for the solution pH > 7.5. [4]

$$3H_2S+8KMnO_4 \rightarrow 3K_2SO_4+2H_2O+2KOH+8MnO_2 \quad (1)$$

In this study, chemical adsorptions using activated carbonbase were evaluated for their H_2S elimination efficiency from biogas. Potassium permanganate impregnated on the activated carbon was filled in packed column and studied for the effect of biogas flow rate, concentration of $KMnO_4$, and weight of adsorbent. Optimum condition at H_2S removal efficiency higher than 80% and breakthrough time of 200 ppmv outlet H_2S concentration in biogas was observed.

2. MATERIALS AND METHODS

2.1 Materials

Granular activated coconut shell, surface area 1100 m^2/g based carbon is a commercial product purchased from Mazuma Thailand Co., Ltd. A quantity of 100 g of the activated carbon was impregnated with 150 mL of 3-9 %w/v $KMnO_4$ at room temperature for 1 hour. After that, it was dried in the oven at 60°C for 12 hours and store in a desiccator as standby.

2.2 Biogas

Biogas containing H_2S at 1300-2000 ppmv from anaerobic digester of pig farm at Thung Wang, Songkhla, Thailand.

2.3 Hydrogen sulfide removal unit

The packed bed adsorption system was designed and operated to study the removal of H_2S from biogas using the $KMnO_4$ impregnated activated carbon. A laboratory-scale apparatus was installed and run at room temperature as shown in Fig.1.

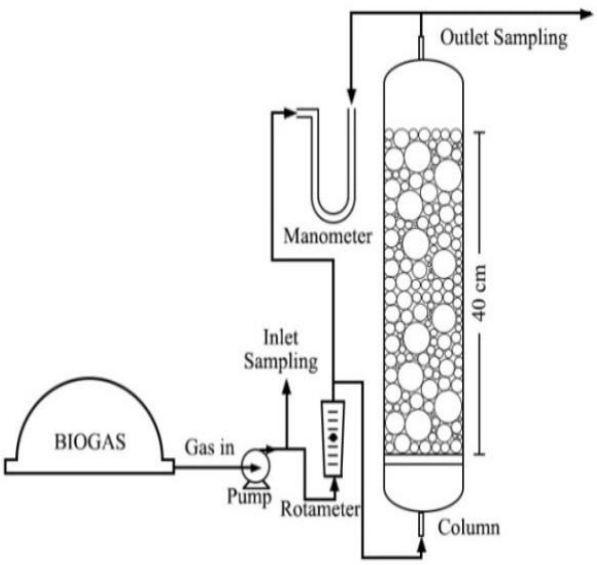

Fig.1 A schematic diagram of the H_2S adsorption unit.

Biogas containing H_2S was pumped from anaerobic digester of pig farm and fed to the bottom of the packed column. Biogas flow rate was constantly controlled by valve and measured by rotameter. The packed column is 50 cm height, 4.7 cm inner diameter, and 40 cm bed section. Pressure drop of the gas flowing through column was measure with U-tube manometer. H_2S of inlet and outlet streams were sampling during experimental passed through a midget impinger containing a cadmium sulfate ($CdSO_4$) solution which forming cadmium sulfide (CdS) as H_2S is absorbed. The concentration of H_2S was measured from amount of CdS formed by iodometric method [7]. Breakthrough time is period between the adsorbent exposure to a harmful substance breakthrough outlet H_2S concentration reach 200 ppmv. The H_2S removal efficiency was calculated according to the following equation:

$$\text{Efficiency (\%)} = \frac{[H_2S]\text{in} - [H_2S]\text{out}}{[H_2S]\text{in}} * 100$$

where $[H_2S]$in and $[H_2S]$out are inlet and outlet H_2S concentration in ppmv, respectively.

3. RESULTS AND DISCUSSIONS

3.1 Effect of $KMnO_4$ concentration

The results of biogas treatment by H_2S removal unit according to the effect of $KMnO_4$ concentration on H_2S removal efficiency and breakthrough time at 200 ppmv outlet H_2S concentration are presented in Table 1. Flow rate of biogas and weight of adsorbent were constantly controlled at 6 L/min and 63 g, respectively. The response of H_2S removal efficiency as functions of $KMnO_4$ impregnation concentration on H_2S removal efficiency is presented as a curve in Fig.2 and the response of breakthrough time at 200 ppmv outlet H_2S concentration as functions of $KMnO_4$ impregnation concentration on breakthrough time is presented as a curve in Fig.3.

Table 1. *The effect of $KMnO_4$ concentration impregnated on activated carbon on H_2S removal efficiency and breakthrough time at 200 ppmv outlet H_2S concentration.*

Run	$KMnO_4$ conc. (%w/v)	H_2S removal efficiency (%)	Breakthrough time (min)
1	3	84.7	102
2	4	86.38	114
3	5	87.17	119
4	6	87.06	118
5	7	86.06	110
6	8	84.17	95
7	9	81.39	73

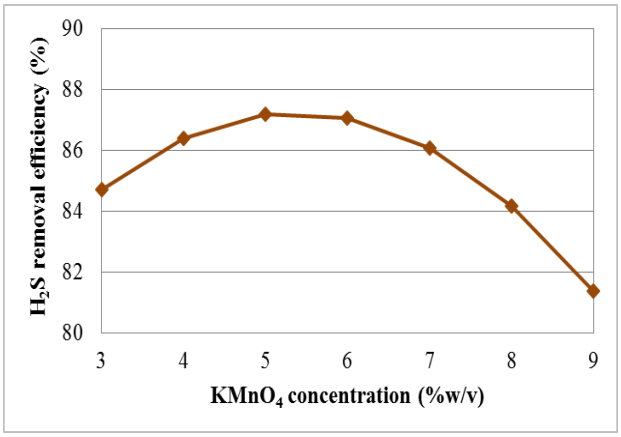

Fig.2 The effect of $KMnO_4$ concentration impregnated on activated carbon on H_2S removal efficiency at breakthrough time of 200 ppmv H_2S in biogas outlet.

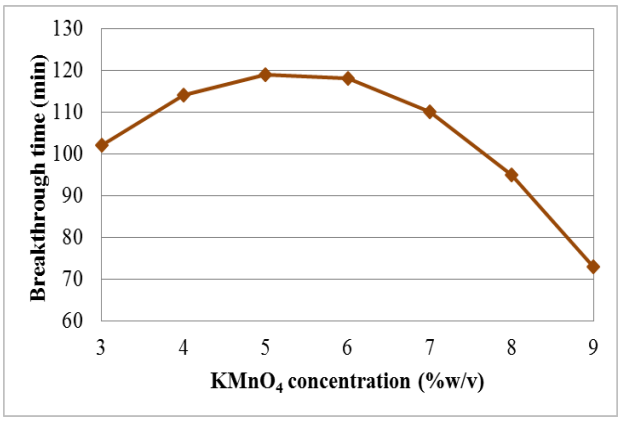

Fig.3 The effect of $KMnO_4$ concentration impregnated on activated carbon on breakthrough time of 200 ppmv H_2S in biogas outlet.

As can be seen, the maximum breakthrough time and H_2S removal efficiency were at 5 %w/v $KMnO_4$ concentration. The result indicated that breakthrough time and H_2S removal efficiency were increased by increasing $KMnO_4$ concentration in the range of 3-5 %w/v $KMnO_4$. The time and the efficiency were decreased when the concentration was increased in the range of 6-9 %w/v $KMnO_4$. This is according to the over concentration of the chemical impregnation can plugged in the pore of the activated carbon.

3.2 Effect of biogas flow rate

The results of biogas treatment by H_2S removal unit according to the effect of biogas flow rate on H_2S removal efficiency and breakthrough time at 200 ppmv outlet H_2S concentration are presented in Table 2. Concentration of $KMnO_4$ and weight of adsorbent were constantly controlled at 6 %w/v and 63 g, respectively.

Table 2. *The effect of biogas flow rate on H_2S removal efficiency and breakthrough time at 200 ppmv outlet H_2S concentration.*

Run	Biogas flow rate (L/min)	H_2S removal efficiency (%)	Breakthrough time (min)
1	4	82.43	131
2	5	86.54	126
3	6	87.06	118
4	7	83.98	107
5	8	77.31	93

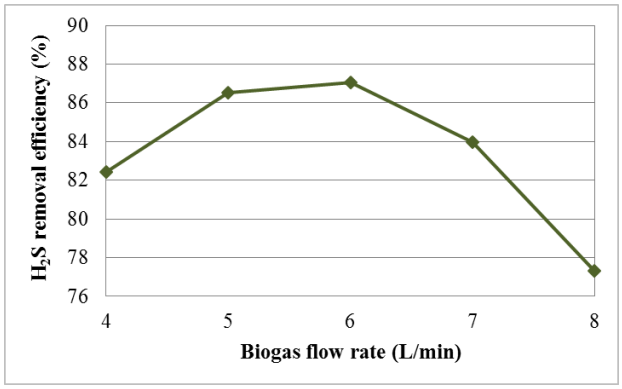

Fig.4 The effect of biogas flow rate on H_2S removal efficiency at breakthrough time of 200 ppmv H_2S in biogas outlet.

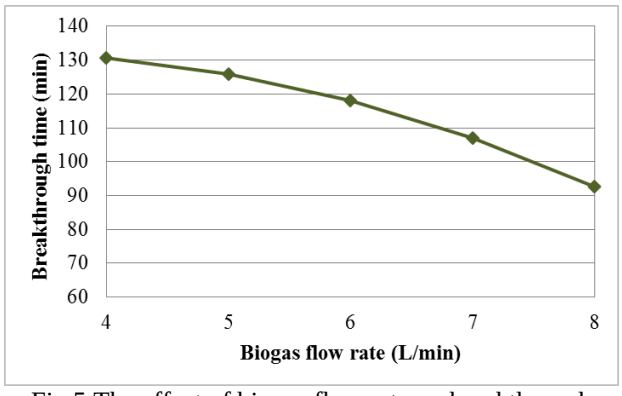

Fig.5 The effect of biogas flow rate on breakthrough time of 200 ppmv H_2S in biogas outlet.

The response of H_2S removal efficiency as functions of biogas flow rate on H_2S removal efficiency is presented as a curve in Fig.4. As can be seen, the maximum H_2S removal efficiency was at 6 L/min biogas flow rate. The result indicated that H_2S removal efficiency was increased by increasing biogas flow rate in the range of 4-6 L/min. The efficiency was decreased when the flow rate was increased in the range of 7-8 L/min. The response of breakthrough time at 200 ppmv outlet H_2S concentration as functions of biogas flow rate on breakthrough time is presented as a curve in Fig.5. As can be seen, the maximum breakthrough time was at 4 L/min biogas flow rate. The result indicated that breakthrough time was decreased by decreased biogas flow rate. Due to maximum H_2S removal efficiency different from maximum breakthrough time to choose appropriate point at 6 L/min biogas flow rate because breakthrough time different about 10 minutes but it can obtain increase gas 2 L/min. This is according to the length of time a compound is retained on a packed column. It is appropriate retention time.

3.3 Effect of adsorbent weight

The results of biogas treatment by H_2S removal unit according to the effect of adsorbent weight on H_2S removal efficiency and breakthrough time at 200 ppmv outlet H_2S concentration are presented in Table 3. Concentration of $KMnO_4$ and flow rate of biogas were constantly controlled at 6 %w/v and 6 L/min, respectively.

Table 3. *The effect of adsorbent weight on H_2S removal efficiency and breakthrough time at 200 ppmv outlet H_2S concentration.*

Run	Adsorbent weight (g)	H_2S removal efficiency (%)	Breakthrough time (min)
1	25	52.92	0
2	49	79.24	12
3	63	87.06	118
4	77	89.32	143
5	100	80.99	135

The response of H_2S removal efficiency as functions of adsorbent weight on H_2S removal efficiency is presented as a curve in Fig.6 and the response of breakthrough time at 200 ppmv outlet H_2S concentration as functions of adsorbent weight on breakthrough time is presented as a curve in Fig.7. As can be seen, the maximum breakthrough time and H_2S removal efficiency were at 77 g adsorbent weight. The result indicated that breakthrough time and H_2S removal efficiency were increased by increasing adsorbent weight in the range of 25-77 g. The time and the efficiency were decreased when the adsorbent weight was increased in 100 g. This is according to the length of time biogas contact with $KMnO_4$-impregnated activated carbon in a packed column. It is appropriate retention time.

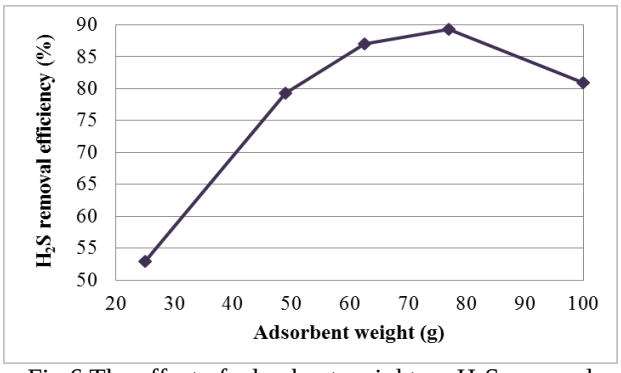

Fig.6 The effect of adsorbent weight on H_2S removal efficiency at breakthrough time of 200 ppmv H_2S in biogas outlet.

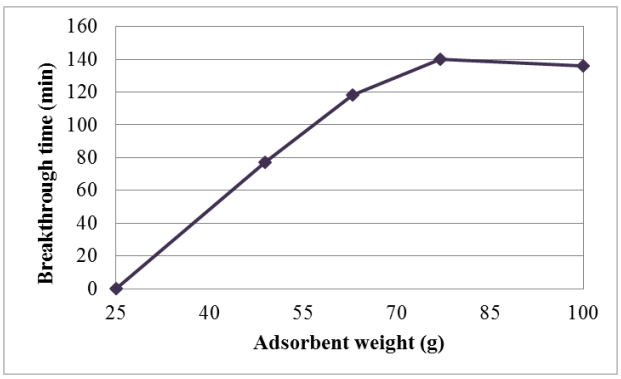

Fig.7 The effect of adsorbent weight on breakthrough time of 200 ppmv H_2S in biogas outlet.

3.4 Optimum condition

The optimization condition was achieved at 5 %w/v $KMnO_4$ concentration, 6 L/min biogas flow rate and 77 g adsorbent weight. H_2S removal efficiency is 89.95% by using constrain of outlet H_2S concentration at 200 ppmv. H_2S removal efficiency is presented in Fig. 8.

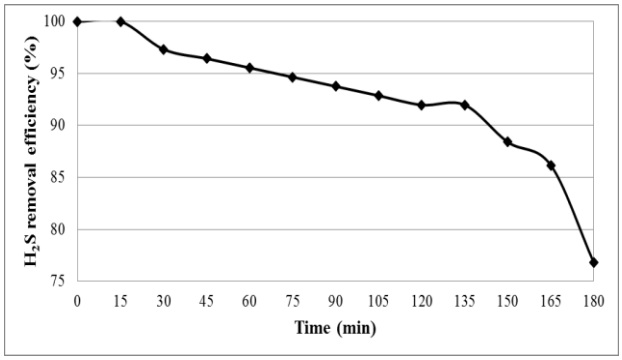

Fig.8 H_2S removal efficiency at optimum condition.

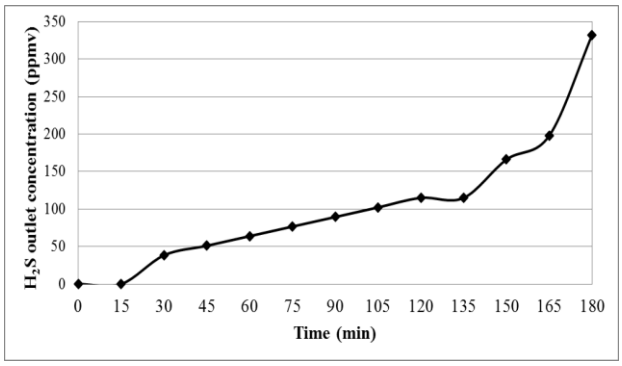

Fig.9 H_2S breakthrough curves of $KMnO_4$ impregnated activated carbon adsorption at optimum condition.

H_2S breakthrough curves for $KMnO_4$-impregnated activated carbon in packed bed column was achieved at optimum condition is presented in Fig.9. The breakthrough time measured for the adsorbent was shown at 144 minutes by using constrain of outlet H_2S concentration at 200 ppmv.

4. CONCLUSIONS

The optimum condition for the H_2S removal from biogas was achieved at 5 %w/v $KMnO_4$ concentration, 6 L/min biogas flow rate, and 77 g adsorbent weight. The packed column has the breakthrough time at 144 minutes with 89.95% of H_2S removal efficiency by using constrain of outlet H_2S concentration at 200 ppmv. This system can effectively perform for the biogas treatment by applying the impregnation on activated carbon.

5. REFERENCES

[1] Deng JF, “Hydrogen sulfide, In: Clinical Environmental Health and Toxic Exposures”, 2nd edition, John B. Sullivan, Jr., Gary R. Krieger, editors, 2001, pp. 716-722.

[2] Bunyakan Charun., Chungsiriporn Juntima, Saelee Rattana, ArunrajPattama, “A comparative study on biogas cleaning by various oxidants”, The 4th international conference on engineering technologies, 28-30 April 2009, Novi Sad, Serbian.

[3] Yonghou Xiao, Shudong Wang, Diyong Wu, Quan Yuan, “Experimental and simulation study of hydrogen sulfide adsorption on impregnated activated carbon under anaerobic conditions”, Journal of Hazardous Materials 153, 2008, pp. 1193–1200.

[4] Fernando Cadena, Robert W. Peters, “Evaluation of Chemical Oxidizers for Hydrogen Sulfide Control”, Water Pollution Control Federation, Vol. 60, No. 7 (Jul., 1988), pp. 1259-1263.

[5] JiaGuo, Ye Luo, Aik Chong Lua, Ru-an Chi, Yan-lin Chen, Xiu-ting Bao, Shou-xin Xiang, “Adsorption of hydrogen sulphide (H2S) by activated carbons derived from oil-palm shell”, Carbon 45, 2007, pp. 330–336.

[6] Yonghou Xiao, Shudong Wang, Diyong Wu, Quan Yuan, “Catalytic oxidation of hydrogen sulfide over unmodified and impregnated activated carbon”, Separation and Purification Technology 59, 2008. pp. 326–332.

[7] EPA Method 11, Determination of Hydrogen Sulfide Content of Fuel Gas Streams in Petroleum Refineries, CFR40, Part60, Appendix A

The 7th International Conference on Engineering and Technology
ICET-2015, Phuket, June 19-20, 2015
Prince of Songkla University, Faculty of Engineering
Hat Yai, Songkhla, Thailand 90112

Modification of baroreflex sensitivity in Control breathing

Isoon Kanjanasurat[1]*, Suradej Tretriluxana[1]
[1] King Mongkut's Institute of Technology Ladkrabang, Faculty of Engineering, Thailand
*Email of corresponding author: pe_win99@hotmail.com

Abstract: *This paper reveals changes in autonomic activity during the breathing control. Quantified by Baroreflex Sensitivity (BRS), this autonomic marker was evaluated during three breathing patterns; spontaneous breathing, slow breathing (6 breaths/min) and fast breathing (12 breaths/min). The Electrocardiogram (ECG) and radial artery blood pressure (BP) were simultaneously recorded from 10 healthy subjects (age: 23±2 years) in sitting position for the data analysis. Our results show that BRS during fast and slow breathing are significantly higher than BRS in normal breathing, (from 15.92 ± 13.10 to 28.49 ± 27.74 ms/mmHg, p<0.05). This finding suggests us to further investigate what cause this alteration.*

Key Words: ***Baroreflex sensitivity / Slow breathing / Controlled breathing / Spontaneous breathing***

1. INTRODUCTION

The human body is complex and also relation to each other system. Function of the cardiovascular system is heart that main organ and respiratory system have lung that main organ. The two systems are associated with transfer oxygen and carbon dioxide is produced by the metabolism.

Cardiovascular system, is controlled by autonomic nervous system, sympathetic and parasympathetic. That induces Electrocardiogram (ECG) and cardiac cycle for supply blood to the demands of daily life, including maintaining the level of a constant blood pressure to prevent harm to the body. Which blood pressure is perceived by baroreceptor [1].

Baroreceptor is a sensory nerve, which is about the recognition of changes in blood pressure, which is located in carotid sinuses and aortic arch has served as a negative feedback loop. When, there is a change in blood pressure. The firing of signal is send by Baroreceptor to brain. That compares the blood pressure. SA-node is received the firing of signal from brain by parasympathetic nerve. To reduce the heart rate, which effects of blood pressure [2 - 4]. A value that represents the function of sensory nerve is called Baroreflex sensitivity (BRS).

Baroreflex sensitivity is a value that represents the baroreceptor function as measured by a blood pressure divided by heart rate. The BRS is much that mean over time a certain range. The blood pressure remains constant, which represents the -body can maintain the balance of blood pressure. On the other hand, BRS is less means over time short. Pressure change much, which causes a disease of cardiovascular [5 - 9].

In this paper is study of the respiratory system that influence in BRS. This study on BRS in change increasing and BRS is a variation in the reduction includes both increase and decrease and uses the continuous blood pressure measurement from the radial artery, which is non-invasive method. This is an alternative method that can be used to evaluate BRS.

2. METHODS

2.1. Data acquisition

The data were acquired from 10 healthy subjects. There are 5 males and 5 females (23 ± 2 years). The experiment is completely non-invasive. Electrocardiogram (ECG) in lead 2 and Breathing by Chest strap were recorded by Biopac (BIOPAC System, Inc.) At a sampling rate of 500 Hz per channel. Continuous non-invasive blood pressure (BP) was recorded by tonometer that a device measure continuous blood pressure at radial artery as show in fig 1. The tonometer was calibrated by Omron M5 and connected to NI USB-6009 for convert analog signal to digital. Then it was recorded by program which sampling rate 500 Hz per channel, 14 bits resolution. Trigger is used to sync a signal between Biopac and tonometer.

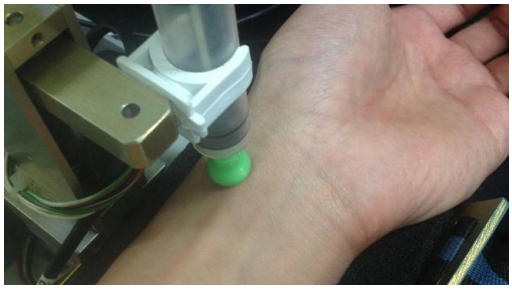

Fig 1. Measurement of non-invasive continuous blood pressure at radial arteries.

Signal is obtained from participants were abstain from coffee, tea and smoking and sitting position in room that dim lighting, Control temperature for 20 minutes of this study. Which is divided into 4 periods. In the first period, participants were spontaneous breathing. Then participants were controlled breathing at 12 cycle per minute. Next period, participants rest and spontaneous breathing again. Last period, participants were controlled breathing 6 cycle per minute. The breathing is controlled by sound.

2.2. Baroreflex sensitivity

Definition of BRS is the slope or the ratio between the RR-interval and the change in blood pressure [10-12]. That have 2 conditions to determine BRS. BRS positive sequence that Changes in blood pressure where systolic blood pressure (SBP) with an increase same RR-interval in 3 points or more consecutive and BRS negative sequence that Changes in blood pressure where systolic blood pressure (SBP) with decrease same RR-interval in 3 points or more consecutive as Then, these points that match this condition is used to calculate BRS by linear regression. BRS all is an average value between BRS positive sequence and BRS negative sequence.

Sequence to calculate BRS. First measurement of systolic blood pressure from Continuous non-invasive blood pressure signal and RR-interval from Electrocardiogram. Next, identify sequence with change in SBP and RR-interval. Then linear regression is used to estimate in BRS as mean slope of all sequence as show in fig 2.

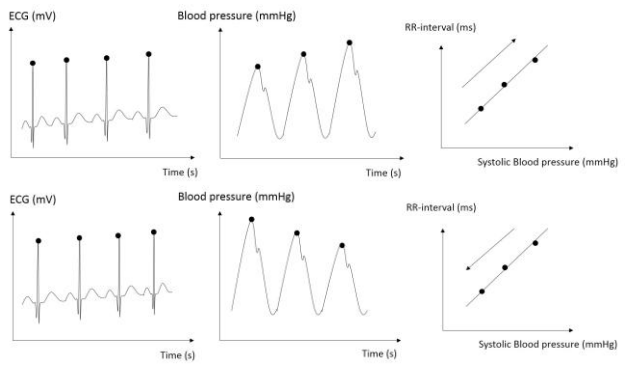

Fig 2. (Top) Baroreflex sensitivity in positive sequence that RR-interval and Systolic blood pressure increase in 3 points or more consecutive. (Bottom) Baroreflex sensitivity in positive sequence that RR-interval and Systolic blood pressure decrease in 3 points or more consecutive.

2.3 Statistical Analysis

BRS were presented as Mean ± SD and Kolmogorov – Smirnov test is used to verify normal distributions of all variable. Average value of BRS positive sequence each group is compared by paired t-test. Same BRS negative and all. Statistical significance was considered at $p<0.05$.

3. RESULTS

3.1. Baroreflex sensitivity positive sequence.

Mean value of BRS positive sequence in spontaneous is 15.43 ± 13.49 ms/mmHg and increase to 15.92 ± 13.10 ms/mmHg in breathing12 cycle/minute and increase to 28.49 ± 27.74 ms/mmHg in breathing 6 cycle/minute with significant ($p<0.05$) as show in fig 3.

3.2. Baroreflex sensitivity negative sequence.

Mean value of BRS negative sequence in spontaneous is 18.74 ± 13.49 ms/mmHg and decrease to 16.39 ± 8.92 ms/mmHg in breathing12 cycle/minute and increase to 20.32 ± 14.15 ms/mmHg in breathing 6 cycle/minute and no significant as show in fig 4.

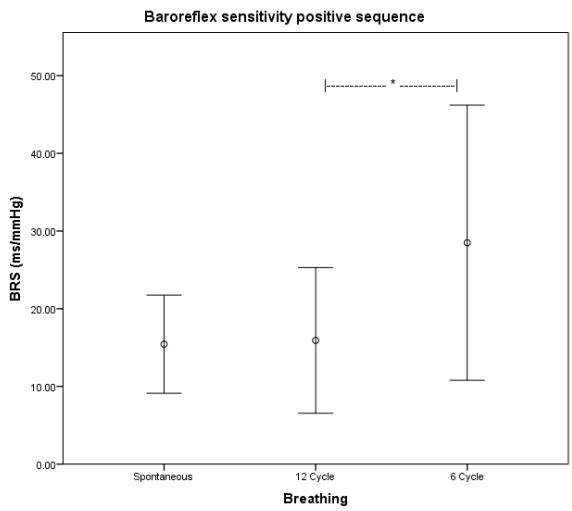

Fig 3. Baroreflex sensitivity of positive sequence in Spontaneous, Breathing 12 cycle/minute and Breathing 6 cycle/minute. *$p<0.05$, paired t test.

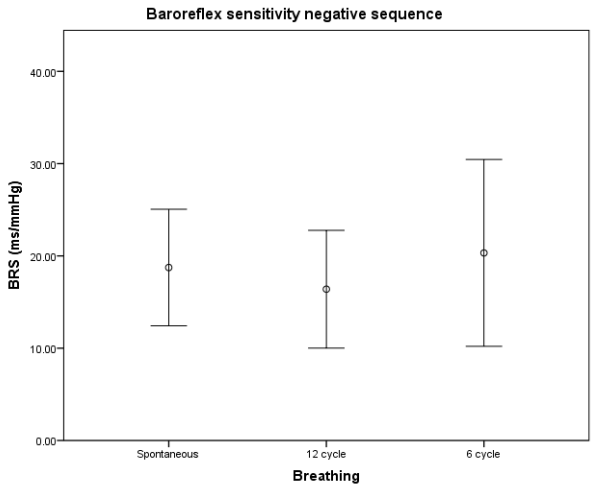

Fig 4. Baroreflex sensitivity of negative sequence in Spontaneous, Breathing 12 cycle/minute and Breathing 6 cycle/minute.

3.3. Baroreflex sensitivity positive & negative sequence.

This result compare between positive and negative sequence each group. In spontaneous breathing, BRS

positive is 15.43 ± 13.49 ms/mmHg and BRS negative is 18.74 ± 13.49 ms/mmHg. In breathing 12 cycle/minute, BRS positive is 15.92 ± 13.10 ms/mmHg and BRS negative is 16.39 ± 8.92 ms/mmHg. In breathing 6 cycle/minute, BRS positive is 28.49 ± 27.74 ms/mmHg and BRS negative is 20.32 ± 14.15 ms/mmHg. All of compare is no significant. As show in fig 5.

3.4. Baroreflex sensitivity all sequence.

Mean value of systolic blood pressure (SBP) in spontaneous breathing is 113.22 ± 9.03 mmHg and increase to 116.12 ± 10.57 mmHg in Breathing 12 cycle/ minute and increase to 116.16 ± 12.79 mmHg in breathing 6 cycle/minute and no significant in increased. as show in fig 6.

Mean value of RR interval in spontaneous breathing is 779.41 ± 91.90 ms and significant decrease to 724.04 ± 75.76 ms $p<0.01$ in Breathing 12 cycle/minute and significant increase to 796.20 ± 75.14 ms $p<0.05$ in breathing 6 cycle/minute as show in fig 7.

Mean value of BRS in spontaneous breathing is 17.08 ± 12.07 ms/mmHg and increase to 18.12 ± 12.36 ms/mmHg in breathing 12 cycle/minute and increase to 22.44 ± 15.59 ms/mmHg in breathing 6 cycle/minute and no significant as show in fig 8.

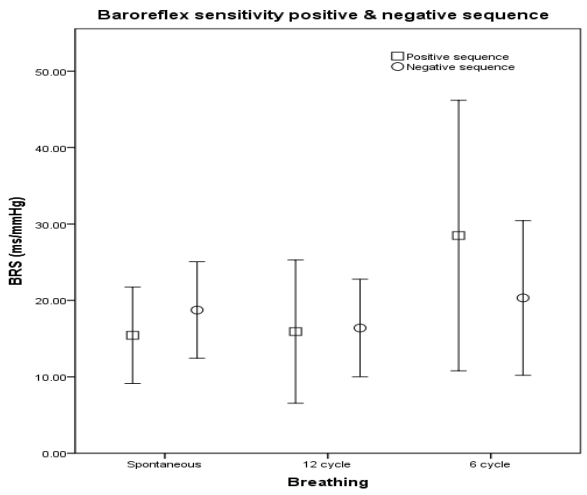

Fig 5. Baroreflex sensitivity of compare in positive and negative sequence in Spontaneous, Breathing 12 cycle/minute and Breathing 6 cycle/minute.

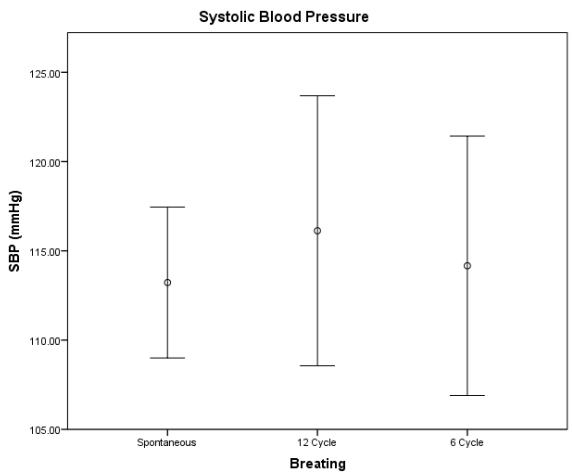

Fig 6. Systolic blood pressure in Spontaneous, Breathing 12 cycle/minute and Breathing 6 cycle/minute.

4. DISCUSSION

The result is a slow breathing improves BRS, which helps control blood pressure better than fast breathing that present in increasing of RR-interval. And there are still other factors that influence to blood pressure.

The finding BRS has increased significantly from 12 breaths per minute to 6 times per minute and changes of RR-interval significantly. Which are several possible explanations for this finding and correlated with slow breathing (6 times per minute), which is enhance to BRS that reduce blood pressure. But BRS do not show better than other research studies in hypertension [13-14].

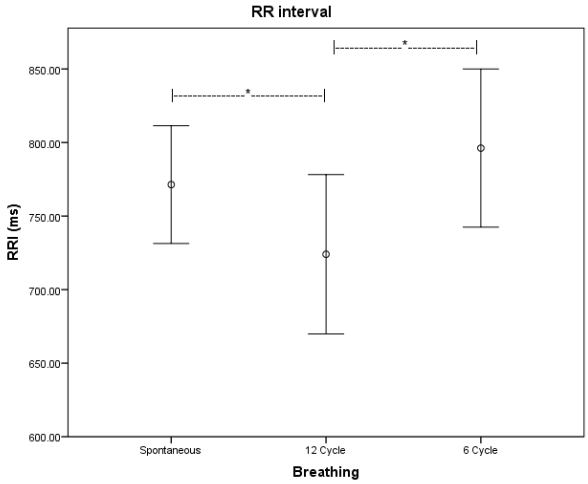

Fig 7. RR interval from ECG in Spontaneous, Breathing 12 cycle/minute and Breathing 6 cycle/minute. *$p<0.05$, paired t test.

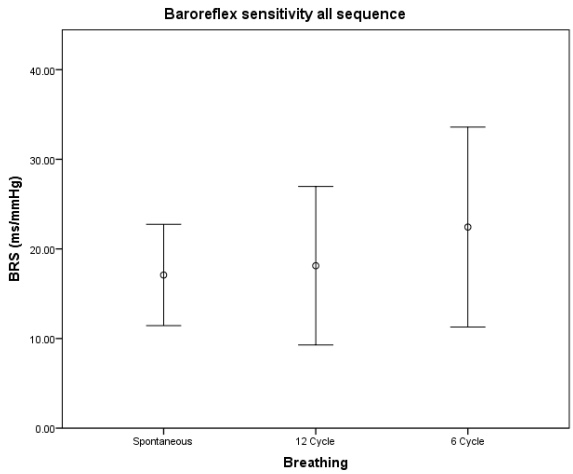

Fig 8. Baroreflex sensitivity of all sequence in Spontaneous, Breathing 12 cycle/minute and Breathing 6 cycle/minute.

In slow breathing may reduce sympathetic activity and enhanced to decrease in blood pressure and enhance to increase BRS. However, in this study can explain that BRS and autonomic nervous system are related.

In this study also had limitations in number of subject that still does not cover ages. This error occurs then influence BRS is participant to be moved, which causes blood pressure changes.

5. ACKNOWLEDGMENT

We would like to thank our participants in this study. We also grateful to ungraduated students in Information Engineering and graduate students in Biomedical Measurement and Computation Laboratory (BMCL) at King Mongkut's Institute of Technology Ladkrabang (KMITL), Bangkok, THAILAND for help and discussion.

6. REFERENCES

[1] Marek Malik, "Heart rate variability Standards of measurement, physiological interpretation, and clinical use", *European Heart Journal* ,1996, Vol 17, pp. 354–381.

[2] Maria Teresa La Rovere, "Baroreflex Sensitivity: Measurement and Clinical Implications", *Annals of Noninvasive Electrocardiology*, April 2008, Vol 13, pp. 191–207.

[3] Achilles J. Pappono, and Withrow Gil Wier. "Cardiovascular Physiology", 10th Ed. December 2012, pp. 185-193.

[4] M. Di Rienzo**,** "Computer analysis of cardiovascular signals", *Studies in health technology and informatics*, Vol 13, 1995, pp. 3-13.

[5] M. Zamir, N.S.Coverdale, C.C.Barron, C.P.Sawicki, and J.K.Shoemaker, "Baroreflex variability and "resetting": A new perspective", *Journal of Biomechanics*, 2014, Vol 47, pp. 237–244.

[6] C. A. Swenne, "Baroreflex sensitivity: mechanisms and measurement" *Neth Heart J*, 2013, Vol 21, pp. 58–60.

[7] T.Loncar-Turukalo, D. Bajic and N. Zigon, "The Evaluation of Local and Global Approaches in Assessment of Baroreflex Sensitivity using Sequence Technique", *Intelligent Systems and Informatics, 2008. 6th International Symposium*, 2008, pp. 1-4.

[8] Tomoyuki Yambe, Norihiro Sugita, and Makoto Yoshizawa, "Development of new quantitative diagnosis machine to evaluate the Baroreflex sensitivity of an artery for patients with hypertension", 31st *Annual International Conference of the IEEE EMBS*, September, 2009, pp. 888-891.

[9] Marco Di Rienzo, Gianfranco Parati, Paolo Castiglioni, Roberto Tordi, Giuseppe Mancia and Antonio Pedotti, "Baroreflex effectiveness index: an additional measure of baroreflex control of heart rate in daily life", *Am J Physiol Regulatory Integrative Comp Physiol* , 2001, pp 744-751.

[10] Marco Di Rienzo, Paolo Castiglioni,Giuseppe Mancia, Antonio Pedotti, and Gianfranco Parati, "Advancements in Estimating Baroreflex Function", *IEEE ENGINEERING IN MEDICINE AND BIOLOGY*, April 2001, pp 25-32.

[11] A. Avolio, A. Qasem, Y.J. Park, "Noninvasive Estimation of Baroreflex Sensitivity Using Pressure Pulse Amplification", *IEEE ENGINEERING IN MEDICINE AND BIOLOGY*, April 2001, pp. 53-58.

[12] Martínez-García P, Lerma C, and Infante O., "Baroreflex sensitivity estimation by the sequence method with delayed signals", *Clinical Autonomic Research*, Vol 22, pp 289-297

[13] Luciano Bernardi, Cesare Porta, Lucia Spicuzza, Jerzy Bellwon, Giammario Spadacini, Axel W. Frey, Leata Y.C. Yeung, John E. Sanderson, Roberto Pedretti and Roberto Tramarin, "Slow Breathing Increases Arterial Baroreflex Sensitivity in Patients With Chronic Heart Failure", *Journal of the American heart association*, June 2010, pp. 143-145

[14] Joseph CN, Porta C, Casucci G, Casiraghi N, Maffeis M, Rossi M, and Bernardi L, "Slow breathing improves arterial baroreflex sensitivity and decreases blood pressure in essential hypertension" *Journal of the American heart association*, 2005, Vol 46, pp.714-718

The 7th International Conference on Engineering and Technology
ICET-2015, Phuket, June 19-20, 2015
Prince of Songkla University, Faculty of Engineering
Hat Yai, Songkhla, Thailand 90112

Design of Real-Time External Force/Position Controller for Human-Robot Interaction

Paramin Neranon[1]*, Robert Bicker[2]
[1]Prince of Songkla University, Faculty of Engineering, Thailand
[2]Newcastl University, School of Mechanical and Systems Engineering, United Kingdom
*Email of corresponding author: nparamin@me.psu.ac.th

Abstract: *This paper presents the design and development of a real-time external force/position control system forhuman-robot interaction (HRI). An evaluation of the robot control system was performed to ensure its reliably and timely operational characteristics specifically for the HRI application. The ATI Gamma multi-axis force/torque sensor and ALTER real-time control path systems were evaluated to quantify their effectiveness, and the results indicated satisfactorily stable performance of the external robot force control system. In summary, the gain tuning for PI control applied to the robot's velocity and force control was implemented. Based on the results of the experiments, it can be concluded that the best performance as specified by the E_RMS of the radial force is observed with proportional and integral gains of* K_P *= 0.10 and* K_I *= 0.005, which values were subsequently implemented in the human-robot handover task.*

Key Words: ***Human-robot interaction (HRI); Robot force/position control; Proportional integral (PI) control; Virtual crank test***

1. INTRODUCTION

Control of physical human-robot interaction is a challenging area of research, and a number of research projects have proposed force-feedback control using external force control algorithms to alter the robot trajectory. These can be categorized based upon the relationship between the position and/or velocity of the robot end effector and the force applied [1], as a form of active compliance for particular applications [2]. The robot's behaviour under force control is influenced by the interactive force exerted on the system [De Schutter and Van Brussel, 1988], and it sability to control the robot simultaneously so as to respond to positional variations in the contact surface. However, the accuracy and reliability of robot force control is limited mainly by the resolution of the force sensor and the precision of robot positioning.

2. FUNDAMENTALS OF ROBOT FORCE CONTROL

The compliant behavioural motion control of robots can be categorized as: passive and active compliant motion. Passive compliance is where the robot end effector position is modified by the contact force because of the inherent compliance of the robot, whereas active compliance facilitates a programmable robot reaction using a force feedback signal, for which purpose the robot control system has been designed. Active compliance is normally used to ensure effective control and overcome the disadvantages of passive compliance.
Dombre and Khalil [3] suggest that robot force control algorithms are as follow: active stiffness control, impedance control, explicit force control, implicit position-based force control and hybrid position/force control. However, using implicit position-based force control or external force control (see Figure 1) developed by De Schutter et al. [4] is considered to offer a better solution regarding the safety constraints, simplicity and implementation efficiency [5; 6]. The key features of this technique provide reliability and stability because switching between position and force loops is avoided. Both position and force control are handled in the same Cartesian direction. This implicit position-based force control is able to be appropriately associated with simple control schemes such as robust PI or PID control, and it is also easily implemented on various types of robot controllers [7].

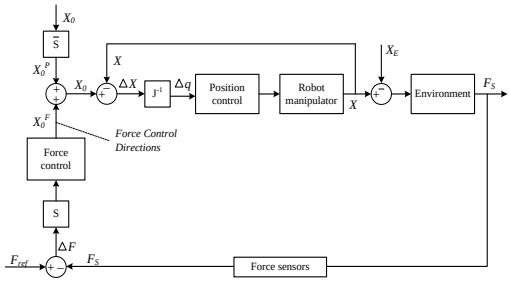

Figure 1 Position-based implicit force control or external force control [7]

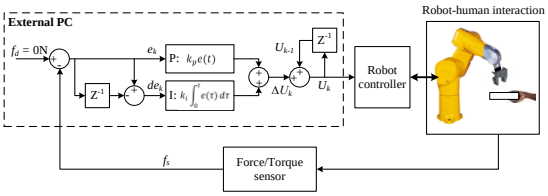

Figure 2 Schematic diagram of the force control strategy based on PI control

3. IMPLEMENTATION OF FORCE ROBOT CONTROL

It is a crucial requirement for the success of effective human-robot interaction that the HRI control system operates in real-time. Interactive force between the human and robot (via the robot end effector) is measured using a 6-axis force/torque sensor. The Stäubli robot controller communicates in real-time with an external PC via an Ethernet port using the TCP/IP protocol. The external PC (running under Linux) processes data transmitted by the sensors and generates changes in incremental position to modify the robot's path using an appropriate control algorithm.

From a review of the commercial robot and manipulator systems, a six-DOF Stäubli robot manipulator arm (TX60) with CS8C controller was chosen as it has the capability to perform real-time path control (which can be updated every 4ms) and also supports the transmission control protocol/ internet protocol (TCP/IP) interface. A 6-axis ATI Gamma force/torque sensor with a stand-alone ATI controller was used to measure the interactive force between the human participant and robot manipulator arm during joint handling of an object, and was positioned between the robot end effector and the robot gripper.

A real-time Linux PC with an Intel® Core TM 2 Duo CPU processor with a clock speed of 3GHz, which supports multi-task execution using the multi-tasking kernel to simultaneously run user programs, was used to process all sensor information, the robot force control, and the real-time updating of new targets for the modification of the robot's path.

After an extensive review of relevant academic research, it was decided to initially apply simple proportional plus integral (PI) control. The PI robot force control algorithm, as shown in Figure 2, is preferable to proportional-integral-derivative (PID) control since the derivative term is sensitive to noise and this could lead to a destabilizing effect on the HRI system. Although, the derivative gain (K_D) which gives a reduction in the system overshoot and settling time has been removed, the overshoot response can be controlled using an appropriate proportional gain [8]. As suggested by De Schutter and Van Brussel [4], Volpe and Khosla [9] and Zeng and Hemami [1], proportional integral (PI) control is appropriate for robot force/position control in order to provide the smallest possible force control error, and because this technique facilitates an increase in the accuracy and stability of the control system.

Table 1 Means and standard deviations of 3-axis force sensor readings

Mode	Fx (N)		Fy (N)		Fz (N)	
	Mean	*SD*	*Mean*	*SD*	*Mean*	*SD*
1	-0.088	0.032	-0.005	0.022	-0.068	0.065
2	-0.053	0.052	-0.049	0.054	-0.019	0.092
3	-0.006	0.032	-0.101	0.029	-0.025	0.105
4	-0.006	0.056	-0.098	0.048	0.024	0.108

An incremental discrete-time PI control algorithm with sampling time period τ and the discrete time interval k can be calculated by applying the equations 1 and 2.

$$u(k) = u(k-1) + k_P[e(k) - e(k-1)] + k_I e(k) \quad (1)$$

$$e(k) = f_d - f_s \quad (2)$$

where, $u(t)$ is PI control output,
K_P is proportional gain,
K_I is integral gain,
f_d is desired force (initially defined as 0)
f_s is the actual force

Furthermore, to filter out undesirable signal and facilitate more stability, digital finite impulse (FIR) was applied, where a 4-tap FIR filter was introduced, which is made up of 4 delay elements, 4 multipliers, 3 accumulators and the tap coefficients of h_0=0.1508, h_1=0.2230, h_2=0.2523, h_3=0.2230 and h_4=0.15080 respectively

4. EVALUATION OF FORCE ROBOT CONTROL

4.1 Evaluation of ATI Gamma Force/Torque Sensor

To ensure the reliability of force data acquisition in performing effective and accurate HRI tasks under varying conditions, the force sensor output was monitored and captured in real-time using of RT Linux. Four different modes were selected as follows:

Mode 1: Robot controller power off
Mode 2: Robot controller and arm power on
Mode 3: Robot controller and arm power on, and robot moving in the x, y and z axes with a standard moving command, and
Mode 4: Robot controller and arm power on, and robot moving in the x, y and z axes under ALTER real-time path control.

Table 1 presents the results obtained with the four modes, in which there was no significant difference between the force values recorded along the x, y and z axes. The 3-axis force values fluctuated between ±0.1N in the different modes. The maximum standard deviation for the z-axis is approximately double the x and y values at ±0.11 N, while the maximum SD values for x and y were around ±0.056 and ±0.054 N respectively.

4.2 Evaluation of ALTER Real-Time Control Path

It was necessary to evaluate the performance of the robot real-time path control in terms of its reliability and accuracy. The robot was required to move along different circular paths of 100, 150 and 200mm in diameter in a fixed time period, whereas its motion was simulated and drawn using 1500 points (N). The robot's actual positions whilst moving was compared to the desired

values, and the following data recorded and compared, namely demanded, received (through TCP/IP) and actual values. Demanded values of incremental position were used to modify the robot's path and were generated in the external real-time Linux PC and transmitted to the Stäubli CS8C controller via an Ethernet port using the TCP/IP protocol (4ms cycle interrupt). Subsequently, received data, which represent the information acquired by the controller, were computed to establish an ALTER 3-axis transformation matrix in order to enable the changes in actual robotic movements.

The results indicating the overall average and corresponding standard deviations of the x-y position errors whilst drawing the circular paths 100, 150 and 200mm in diameter are summarized. The mean errors of the x and y axes slightly increased and varied from minimum of 0.46% and 1.57% up to maximum of 2.82% and 2.64% respectively, as also shown in Figure 3. Additionally, the standard deviations of the two dimensions were in the range of 0.35-0.53mm. According to the results, it can be concluded that the performance of ALTER real-time control in path modification can be improved by decreasing the robot's velocity.

4.3 Virtual Crank-Turning Tests and Evaluation

The trial and error method based on virtual crank-turning preliminary tests were carried out to establish appropriate PI control applied to the robot's force control algorithm. The tests were undertaken by 18 participants, and they were first instructed to perform the tasks with the best of their ability and to attempt to minimize the radial forces during task execution. The procedure of the virtual crank-turning task permitted the robot to move with a constrained trajectory around the virtual crank radius, at a diameter of 200 mm, in a clockwise direction. The constrained circular path of the virtual crank was designed by assuming that F_R and F_T are radial force and tangential force respectively. The performance of the system response can be evaluated in terms of the variation in the radial forces (F_R), in which the lower the variation in radial force, the better the performance of the system.

The performance was analyzed based on the root mean square error (*E_RMS*) of the radial forces [10; 11]. The equation used to calculate the magnitude of error deviations of *E_RMS* is expressed as:

$$E_RMS = \sqrt{\frac{\sum_{i=1}^{n}(F_R - F_{De})^2}{n}} \quad (3)$$

where, n is the number of evaluated values,

F_R is the radial forces and

F_{De} is the demanded radial force (0).

To calculate the incremental change in displacement (ΔU) based on PI control, Equation 3 is used, and by using the ALTER command, an ALTER transformation matrix ($ALTER_{trsf}$) is represented as:

$$ALTER_{trsf} \begin{bmatrix} ALTER_{trsf}.x \\ ALTER_{trsf}.y \\ ALTER_{trsf}.z \end{bmatrix} \quad (4)$$

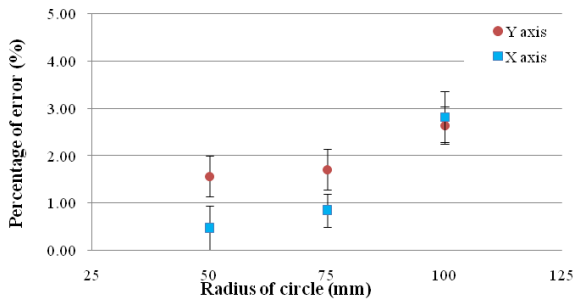

Figure 3 Means and standard deviations of percentage of error for x-y axes for x and y axes whilst drawing circular paths 100, 150 and 200mm in diameter

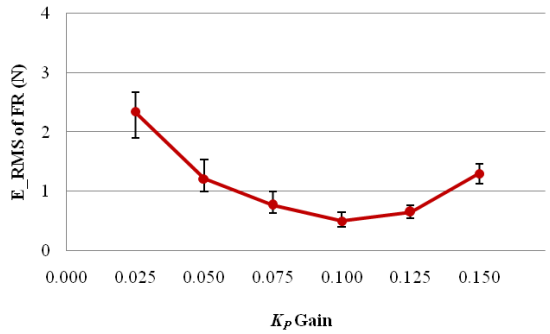

Figure 4 E_RMS of radial forces with various proportional (KP) gains applied

Figure 4 presents the performance results of the virtual crank test for different values of the proportional gain K_P ranging between 0.025–0.15 with 0.025N resolution. The system performance can be identified based on the *E_RMS* of the radial force. The best performance of this test is represented by the minimum *E_RMS* of (F_R), and was achieved at a gain K_P of 0.100, where the minimum *E_RMS* value is 0.53N with the minimum standard deviation of 0.08N. As expected, the tangential force (F_T) decreases when the gain K_P increases, and is approximately inversely proportional to the K_P gain value. It can be noted that at a value of K_P of 0.025, F_T has the largest value of 8.37N with a standard deviation of 0.34N and at K_P of 0.150 the F_T has the smallest value of 1.39N with 0.13N standard deviation. To sum up, it can be concluded that the optimized proportional gain of 0.100 shows the highest performance due to the lowest tracking error represented by the *E_RMS* of F_R.

From the experimental results showing the force profiles, it was indicated that there was small oscillation moderating in the signal; therefore the frequency domain evaluation of the force in the virtual crank tests at the six different K_P gains was determined using fast Fourier transform (FFT). To suitably identify the noise signal, a high-pass filter with a cut-off frequency at 10Hz was used. Figure 5 illustrates examples of the results of the FFT analysis (K_P=0.025, 0.075, 0.100 and 0.150). The dominant frequency is in the range between 17-20Hz with the density power spectrum is varied approximately between 450-1050N^2, and the higher frequency (28-30Hz) was clearly seen at the highest K_P. It can be highlighted that an increase in a K_P gain gives an increase in higher frequency of the system response; however, if the $K_P \geq 0.175$, the robot system has very high unstable oscillation which could damage the robot.

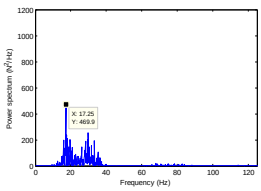

(a) $K_P = 0.025$

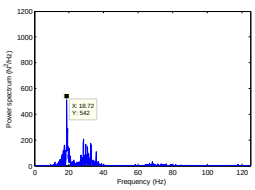

(b) $K_P = 0.075$

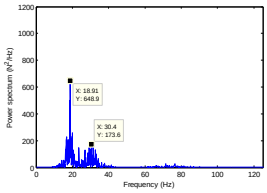

(a) $K_P = 0.100$

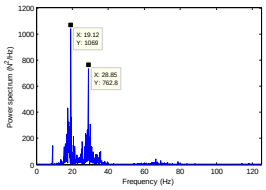

(b) $K_P = 0.150$

Figure 5 FFT analysis for virtual crank test

To optimize the integral gain (K_I), the gain K_P was set at 0.100, and then tuning of the integral gain mark by increasing K_I until the best *E_RMS* of F_R is achieved. The same procedure for the virtual crank test developed for evaluating the performance of the gain K_P was used. The same group of the participants was used to perform the assigned tests. A range of integral gains varying from 0.0025 to 0.0175 with 0.0025N resolution was selected.

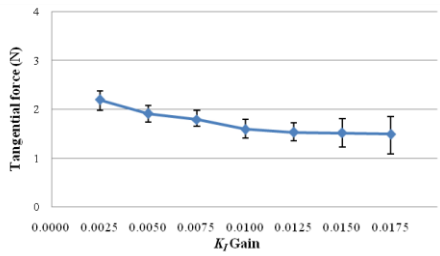

Figure 6 Effect of tangential forces (FT) from different KI gains at various speed conditions

The performance of the virtual crank test for different values of integral gain (K_I) is illustrated in Figure 6. It can be noted that the best performance of the K_I tuning test is defined as the gain K_I of 0.0050, in which the *E_RMS* value is 0.44N with a standard deviation of 0.34N. The results when the K_I was adjusted between 0.0025 and 0.0125 give low values of the *E_RMS* of F_R, which vary in the range of 0.44–0.53N with standard deviations between 0.34 and 0.70. Once the K_I was set from 0.0150 to 0.0175, the *E_RMS* of F_R significantly increased from 0.71 to 0.94N along with the standard deviations of 0.94 and 1.36N respectively. Increasing the gain K_I is accompanied by a decrease in the tangential force (F_T). The radial forces start to increase when K_I was set from 0.00125 to 0.00175, in which the standard deviations are from 0.42 to 1.50N. In summary, the gain tuning for PI control applied to the robot's velocity and force control was implemented. It can be concluded that the best performance as specified by the *E_RMS* of the radial force is observed with proportional and integral gains of $K_P = 0.10$ and $K_I = 0.005$ respectively.

5. CONCLUSIONS

This paper describes the implementation of the real-time force control system for the Stäubli TX60 robot. The real-time Linux operating system, transmit control protocol and internet protocol (TCP/IP) communication, and the multi-tasking software designed for the robot was also outlined. Outputs from the external force control system were transmitted as incremental displacements transferred to the robot CS8C controller using TCP/IP communication to modify the robot's trajectory in real-time.

The proposed HRI system has been evaluated and the criteria used for the evaluation of the real-time force sensor and real-time control path of the Stäubli robot systems have been also discussed. In particular, proportional plus integral (PI) control was applied to the robot's velocity and force control algorithms, and the gains (K_P and K_I) were experimentally tuned using a trial and error method based on a virtual crank-turning test. Based on the results of these tests, it was established that the best performance (as specified by the *E_RMS* of the radial force) is observed with proportional and integral gains of $K_P = 0.10$ and $K_I = 0.005$ respectively.

6. REFERENCES

[1] Zeng, G. and Hemami, A. (1997) 'An overview of robot force control', *Robotica*, 15, (05), pp. 473-482.

[2] Mason, M. T. (1981) 'Compliance and Force Control for Computer Controlled Manipulators', *Systems, Man and Cybernetics, IEEE Transactions on*, 11, (6), pp. 418-432.

[3] Dombre, E. and Khalil, W. (2007) 'Robot Manipulators: Modeling, Performance Analysis and Control', in HAL - CCSD.

[4] De Schutter, J. and Van Brussel, H. (1988) 'Compliant robot motion II. A control approach based on external control loops', *Int. J. Rob. Res.*, 7, (4), pp. 18-33.

[5] Degoulange, E., Dauchez, P. and Pierrot, F. (1993) Robotics and Automation, 1993. Proceedings., 1993 IEEE International Conference. 2-6 May 1993.

[6] Pierrot, F., Dombre, E., Degoulange, E., Urbain, L., Caron, P., Boudet, S., Gariepy, J. and Megnien, J. L. (1999) 'Hippocrate: a safe robot arm for medical applications with force feedback', *Med Image Analysis*, 3, (3), pp. 285-300.

[7] Farid, F. and Redouane, T. (2009) 'Dynamic External Force Feedback Loop Control of a Robot Manipulator Using a Neural Compensator-Application to the Trajectory Following in an Unknown Environment', *Int. J. Appl. Math. Comput. Sci.*, 19, (1), pp. 113-126.

[8] Stankovic, J. A. (1988) 'Misconceptions about real-time computing: a serious problem for next-generation systems', *Computer*, 21, (10), pp. 10-19.

[9] Volpe, R. and Khosla, P. (1993) 'A theoretical and experimental investigation of explicit force control strategies for manipulators', *Automatic Control, IEEE Transactions on*, 38, (11), pp. 1634-1650.

[10] Kilgus, C. C. and Gore, W. C. (1972) 'Root-Mean-Square Error in Encoded Digital Telemetry', *Communications, IEEE Transactions on*, 20, (3), pp. 315-320.

[11] Bruckner, H. P., Spindeldreier, C., Blume, H., Schoonderwaldt, E. and Altenmuller, E. *Wearable and Implantable Body Sensor Networks (BSN), 2012 Ninth International Conference.* 9-12 May 2012.

The 7th International Conference on Engineering and Technology
ICET-2015, Phuket, June19-20, 2015
Prince of Songkla University, Faculty of Engineering
Hat Yai, Songkhla, Thailand 90112

System for assistance during evacuation process

Srdjan Tegeltija[1], Branislav Tejic[1], Nikola Djukic[1], Gordana Ostojic[1*], Stevan Stankovski[1]
[1]University of Novi Sad, Faculty of Technical Sciences, Novi Sad, Serbia
[*]Email of corresponding author: goca@uns.ac.rs

Abstract: *In this paper the system for assistance in evacuation of threatened people is described. System assists persons by guiding them to safe location using UAV. UAV regulates its speed using communication device which is dropped to the person. With continuous monitoring of threatened persons, panic, injuries and casualties could be avoided. Continuous monitoring of endangered area, provides real time corrections of evacuation route.*

Key Words: ***UAV, assistance, evacuation process***

1. INTRODUCTION

Unmanned aircraft is aircraft without the presence of the pilot. In the literature unmanned aircraft most often could be found as UAV (Unmanned Aerial Vehicle). UAV can be autonomous aircraft or aircraft controlled by the operator using remote controls. For this reason, these systems can be found in the literature as the RPV (Remotely Piloted Vehicle). In the literature there are other labels have been introduced for such systems, like the Drone, ROA (Remotely Operated Aircraft), UVS (Unmanned Vehicle System).

Although originally designed and developed for military use, in recent years unmanned aircrafts have been used in the civil sector [1]. Today in the market there are UAVs designed for fun and can fit on the human palm [2], as well as commercially available unmanned aircraft that can carry large load and various equipment weight of few kilograms to a several tens of kilograms [3]. Equipment that can be mounted on UAVs is diverse such as: cameras, various sensors, clamps and many other components depending on the area of application. Examples of application of unmanned aircraft are monitoring and recording [4], the collection of data on pollution [5] [6], chemical protection and fertilization of agriculture crops (use of pesticides, herbicides, insecticides and fertilizers) [7]. UAVs are also used during natural disasters and accidents, such as monitoring the situation [8] [9], detection of persons in danger and delivery of first aid, food and water [10], mapping the terrain providing rescuers insight into the condition of the field [11]. Natural disasters or accidents caused by human error, such as floods, forest fires, or industrial accidents, often affect large populated areas, threatening the lives and well-being of the entire population. As one aspect of emergency response, evacuation can be defined as the removal of residents from the area that is considered dangerous to the security zone as quickly as possible and with the highest reliability [12]. Planning evacuation route is an important component of disaster management in order to reduce injuries and loss of life. Injuries are in this way reduced to a minimum. Aggravating circumstance that occur during the evacuation process is the panic in individuals who are in danger [13], [14]. Various studies have dealt with the two types of evacuation: evacuation of people in buildings and regional evacuation. The specificity of the evacuation of buildings is that the space for movement restricted, stairs must be used by rescuers and people in danger, various obstacles (walls, doors, smoke, fire, etc.). Papers [15] - [17] present analysis of evacuations in buildings. Specifics of regional evacuations are: it is performed on large areas, include a very large number of people (the problem of managing large crowds), weather conditions (night, rain, wind, smoke and toxic gases in case of large fires, etc.). Papers [18] - [21] present an analysis of regional evacuations.

In this paper a system for assistance during evacuation process is presented. UAV leads people from the danger zone to a safe location. After arriving to a safe location, other participants in the evacuation process takes evacuees and transports them to the hospitals or shelters. In order to avoid panic reactions it is necessary to constantly monitor evacuees. In addition, it is necessary to adjust the movement speed of UAV to the persons movement speed, as well as giving a signal to people when they need to change their movement speed in case of need (to speed up due to the rise of water in case of flooding, or intensified wind and smoke in the case of fire). To enable communication between the persons and the UAV hardware device is realized by using XBee ZB PRO Series 2 communication module.

2. SYSTEM OVERVIEW

System for assisstance during evacuation process is based on the usage of UAV. UAV leads people from the danger zone to a safe location. After arriving to a safe location, other participants in the evacuation process (medical services, military and firefighters) takes evacuees and transports them to the hospitals or shelters. Fig. 1. shows the algorithm of the system.

After obtaining the information on which location are endangered people, in order to determine optimal and safe evacuation route it is necessary to carry out photographing or the mapping of the area [22].

For the determination of the evacuation route two approaches can be applied, manual routing and automated routing. In the case of manual routing operator, who controls UAV, have to manually determine evacuation route in the dedicated software (to determine the points through UAV should pass). In the case of an automated approach for determining evacuation route dedicated software would perform processing of images and terrain mapping results, in order to determine the safe and unsafe regions. Evacuation route would go through a safe regions (existing roads, meadows, etc), while the unsafe regions should be avoided (forests, water, fire and smoke) [23] - [26]. The evacuation route could be determined by algorithms presented in [27] [28].

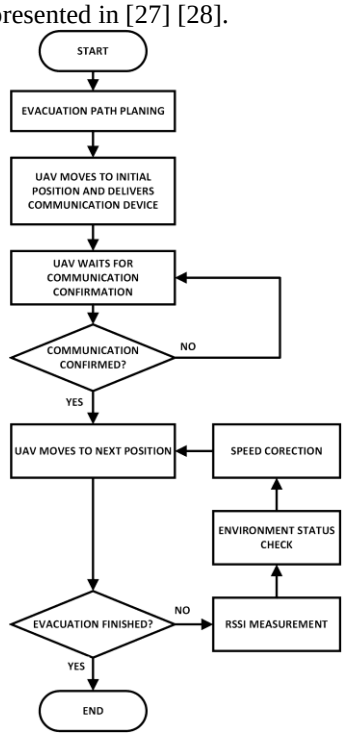

Fig. 1. Algorithm of the system

After the automated determination of the evacuation route (points through UAV should pass), it is necessary that the operator make adjustments (if needed) and confirm the evacuation route. Fig. 2. shows an example of an evacuation route. Point A represents a danger zone, point B is a safe zone. The arrows shows the path in which UAV and persons should move.

After confirming the evacuation route, UAV is positioned to the initial position. The initial position is the position where are people, who needs to be guided to a safe location, located. When came to the initial position UAV will deliver communication device to endangered people, and if necesary UAV could deliver first aid kit, water, food and instructions on how UAV will guide people to safe location. To start an evacuation process UAV waits for communication confirmation (people must press button on communication device). Management of UAVs could be performed manually by the operator or automatically using dedicated flight controller. During the flight the UAV continuously measure the RSSI between communication devices, and on the basis measured RSSI value the distance between the UAV and the people is estimated. Depending on the estimated distance correction of the UAV flying speed is performed. The UAV at the same time sends a command to the communication device for required correction of people moving speed which is shown on LED indicators and emitted as sound signal on buzzer. During the evacuation process it is necessary to constantly monitor the situation in the area. In case of an larger area one UAV could be used to lead the people and other UAV, or more of them, would be responsible for monitoring the status of that area, so that in the event of unforeseen circumstances correction of evacuation route could be made. Examples for changes in the evacuation area can be: sudden occurrence of landslides, in case of fire changes in direction and strength of the wind that could direct the fire and smoke to the evacuation route.

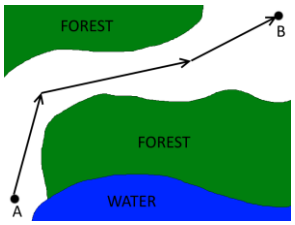

Fig. 2. Example of evacuation route

Using FPV (First Person View) system, which presents surveillance system that sends video signal from camera mounted on the UAV to the display on the operator terminal, the operator can monitor the movement of people and could, at any moment, take control over UAV in the event of an unforeseen situation (people are slowing down due to difficult conditions), in case of automated flight. When UAV brings people to a safe location evacuation process if finished. If there are more groups of people that need to be evacuated, evacuation process can be repeated.

3. UNAMNNED AERIAL VEHICLES (UAVS)

"UVS International" [29] is an international association of manufacturers of unmanned aircraft, manufacturers of subsystems and key components and related equipment for unmanned aerial vehicles, as well as companies that provide services to or for unmanned aerial vehicles. International Organization "UVS International" conducted the categorization of unmanned UAV to the range, altitude, flight autonomy and weight [30]. Depending on the type of realizations there are fixed wing UAVs and rotary wing UAVs. The wings are shaped to make air move faster over the top of the wing. When air moves faster, the pressure of the air decreases. So the pressure on the top of the wing is less than the pressure on the bottom of the wing. The difference in

pressure creates a force on the wing that lifts the wing up into the air [31]. A typical representative of UAV with fixed wings is plane. The air flow over the wings is caused by the movement of the UAVwhich is enabled by drive engine (a jet engine, the engine with the propeller). If there is no movement of the UAV there is no lift force. To fly, fixed wing UAV requires particular velocity that depends on the shape and surface of the wings, the maximum weight of the UAV, etc. For UAV with rotary wing air flow over the wing is caused by the rotating the wing (or propeller) powered by a drive engine. A typical representative of the UAV with rotary wings is a helicopter. To fly, rotary wing UAV requires a certain rotation speed of propeller, which depends on the weight of the UAV, shape and surface of propellers, etc. Both types of UAVs have certain advantages and limitations, which make them more or less suitable for different applications [32]. For this system we used rotary wing UAV, because they have possibility of vertical takeoff and landing, the ability to hover (maintain a fixed position in the air), to fly at very low speeds and perform agile maneuvering, a Tarot TL960 hexacopter is used (Fig. 3.)

Fig. 3. Tarot TL960 hexacopter

To be autonomous, it is necessary that UAV possess a dedicated flight controller. One of the most famous flight controller is "APM Autopilot Suite" [33]. "APM Autopilot Suite" is a platform that includes hardware and software used for managing unmanned aerial vehicles and vehicles on the ground. In addition to the "APM Autopilot Suite" platform, controllers for UAVs from company DJI have wide application too (Naza series, WooKong series, etc.) [34]. As flight controller Naza-M Light is used.

4. COMMUNICATION DEVICE

In order to enable the connection between UAV and endangered people two communication devices are realized, one master and one slave communication device. Master communication device is mounted on UAV, connected to UAV control unit, and consists of microcontroller and communication module. Slave communication device is similar, but in addition it consists of command buttons, LED indicators and buzzer. Master communication device take power supply from UAV, while slave communication device has a battery power supply. Fig. 4. shows slave communication device.

For powering the slave communication module a standard battery 6LR61 with nominal voltage of 9V has been used. A microcontroller is used for controlling communication modul, for reading states of buttons, for settings states of LED indicators, and to control a buzzer. For realization of communication devices a microcontroller Atmel ATmega 8 is used. Button are used for sending commands to master communication device (initial communication confirmation and start communication between master and slave device, stoping the UAV). LED indicators are used to inform people about speed of movement (speed is correct, people must speed up or people must slow down). Buzzer is used for emmiting audio signal which tells people if is speed of movement is correct, or if they must speed up or slow down.

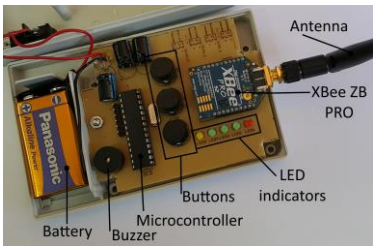

Fig. 4. Communication device

As communication modul XBee Pro ZB Series 2 module is used. XBee Pro ZB Series 2 is based on ZigBee technology. ZigBee is a wireless technology developed as an open global standard to address the unique needs of low-cost, low-power wireless M2M (Machine to Machine) networks. The ZigBee standard operates on the IEEE 802.15.4 physical radio specification and operates in unlicensed bands including 2.4 GHz, 900 MHz and 868 MHz [35]-[37]. The specification is a packet-based radio protocol intended for low-cost, battery-operated devices. The protocol allows devices to communicate in a variety of network topologies and can have battery life lasting several years. XBee-PRO ZB ZigBee modules provide cost-effective wireless connectivity to devices in ZigBee mesh networks. Utilizing the ZigBee PRO Feature Set, these modules are interoperable with other ZigBee devices, including devices from other vendors. Programmable versions of the XBee-PRO ZB ZigBee Series 2 module make customizing ZigBee applications easy, even without wireless design expertise [38].

5. CONCLUSION

In this paper the system for assistance in the evacuation process of endangered people is presented. UAV would carry out photographing or mapping of the area, in order to determine the evacuation route. During the evacuation process UAV would lead endangered people to a safe location. Depending on the situation the person would follow the UAV on foot (inaccessible mountainous terrain) or using some vehicle (boat in case of flooded area). During the evacuation process people would be constantly monitored in order to respond in a timely manner (correction of UAV speed). In addition to constantly monitoring of area status will provide changing of evacuation route if necessary.

In future work a further development of the system for assistance during evacuation process is planned. Different types of UAVs will be examined in order to realize which UAV would be optimal for evacuation process on the basis of flight speed, flight autonomy, max payload, etc. Different algorithms for image processing and segmentation for recognition of water, forest, fire, smoke, etc. will be examined, and different

algorithms for routing in order to efficiently and reliably determine evacuation routes will be examined.

6. REFERENCES

[1] http://tangosix.rs/2013/11/06/civilni-dronovi-blagoslov-prokletstvo/ (accessed February 2015.).

[2] https://droneflyers.wordpress.com/best-quadcopters-for-2014-holiday-gift-giving/cheerson-cx-10-nano-quadcopter-review/ (accessed February 2015.).

[3] http://www.schiebel.net/products/unmanned-air-systems/camcopter-s-100/system.aspx (accessed February 2015.).

[4] N. Nigam, S. Bieniawski, I. Kroo and J. Vian, "Control of multiple UAVs for persistent surveillance: algorithm and flight test results," *IEEE Trans. Control Syst. Technol.*, vol. 20(5), pp. 1236-1251, 2012.

[5] W. Zang, J. Lin, Y. Wang, and H. Tao, "Investigating small-scale water pollution with UAV remote sensing technology," In *World Autom. Congr. (WAC)*, pp. 1-4, 2012.

[6] O. Trieschmann, "Oil spill issue and the capability of monitoring the problem by remote sensing," *Compend. of Summaries*, pp. 169-176, 2008.

[7] F. G. Costa, J. Ueyama, T. Braun, G. Pessin, F. S. Osório and P. A. Vargas, "The use of unmanned aerial vehicles and wireless sensor network in agricultural applications," *In IEEE Int. Geosci. Remote Sens. Symp. (IGARSS)*, pp. 5045-5048, 2012.

[8] S. M. Adams, and C. J. Friedland, "A survey of unmanned aerial vehicle (UAV) usage for imagery collection in disaster research and management," *In 9th Int. Workshop Remote Sens. Disaster Response*, 2011.

[9] G. Zhou, C. Li, and P. Cheng, "Unmanned aerial vehicle (UAV) real-time video registration for forest fire monitoring," *In IEEE Proc. Int. Geosci. Remote Sens. Symp. (IGARSS'05)*, vol. 3, pp. 1803-1806, 2005.

[10] P. Doherty and P. Rudol, "A UAV search and rescue scenario with human body detection and geolocalization," *In AI 2007: Adv. Artif. Intell*, pp. 1-13, 2013.

[11] R. Hirokawa, D. Kubo, S. Suzuki, J. I. Meguro and T. Suzuki, T, "A small UAV for immediate hazard map generation,", *In AIAA2007-2725. AIAA Infotech@ Aerospace 2007 Conf. and Exhibit*, pp. 7-10, 2007.

[12] S. Shekhar, K. Yanga, V. M. Gunturia, L. Manikondaa, D. Olivera, X. Zhoua, B. Georgeb, S. Kimc, J. M. R. Wolffa and Q. Lua, "Experiences with evacuation route planning algorithms," *Int. J. Geogr. Inf. Sci.*, vol. 26(12), pp. 2253-2265, 2012.

[13] D. Helbing, I. J. Farkas, P. Molnar and T. Vicsek, "Simulation of pedestrian crowds in normal and evacuation situations," *Pedestrian and evacuation dynamics*, vol. 21, pp. 21-58, 2002.

[14] G. A. Frank, C. O. Dorso, "Room evacuation in the presence of an obstacle," *Phys. A: Stat. Mech. Appl.*, vol. 390(11), pp. 2135-2145, 2011.

[15] N. Pelechano and N.I. Badler, "Modeling crowd and trained leader behavior during building evacuation," *IEEE Comput. Graphics Appl.*, vol. 26(6), pp. 80-86, 2006.

[16] N. Pelechano and A. Malkawi, "Evacuation simulation models: Challenges in modeling high rise building evacuation with cellular automata approaches," *Autom. Constr.*, vol. 17(4), pp. 377-385, 2008.

[17] N. Dimakis, A. Filippoupolitis and E. Gelenbe, "Distributed building evacuation simulator for smart emergency management," *Comp. J.*, vol. 53(9), pp. 1384-1400, 2010.

[18] G. Köster, D. Hartmann and W. Klein, "Microscopic pedestrian simulations: From passenger exchange times to regional evacuation," *In Oper. Res. Proc.*, 2010, pp. 571-576, 2011.

[19] T. J. Cova and R. L. Church, "Modelling community evacuation vulnerability using GIS," *Int. J. Geogr. Inf. Sci.*, vol. 11(8), pp. 763-784, 1997.

[20] Y. C. Chiu, H. Zheng, J. A. Villalobos, W. Peacock and R. Henk, "Evaluating regional contra-flow and phased evacuation strategies for Texas using a large-scale dynamic traffic simulation and assignment approach," *J. Homeland Secur. and Emergency Manage.*, vol. 5(1), 2008.

[21] V. Pillac, P. Van Hentenryck, and C. Even, "A Path-Generation Matheuristic for Large Scale Evacuation Planning," *In Hybrid Metaheuristics*, pp. 71-84, 2014. [Proc. 9th Int. Workshop, HM 2014, Hamburg, Germany, June 11-13, 2014.]

[22] F. Remondino, L. Barazzetti, F. Nex, M. Scaioni and D. Sarazzi, "UAV photogrammetry for mapping and 3D modeling – current status and future perspectives," *Int. Arch. Photogramm. Remote Sens. and Spatial Inf. Sci.*, vol. 38(1), 2010.

[23] G. J. Hay, G. Castilla, M. A. Wulder and J. R. Ruiz, "An automated object-based approach for the multiscale image segmentation of forest scenes," *Int. J. Appl. Earth Obs. Geoinf.*, vol. 7(4), pp. 339-359, 2005.

[24] J. R. Martinez-de Dios, B. C. Arrue, A. Ollero, L. Merino and F. Gómez-Rodríguez, "Computer vision techniques for forest fire perception", *Image Vision Comput.*, vol. 26(4), pp. 550-562. 2008.

[25] J. Smeeckaert, C. Mallet, N. David, N. Chehata and A. Ferraz, "Large-scale classification of water areas using airborne topographic lidar data", *Remote Sens. Environ.*, vol. 138, pp. 134-148, 2013.

[26] P. Santana, R. Mendonça and J. Barata, "Water detection with segmentation guided dynamic texture recognition," *In IEEE Int. Conf. Rob. Biomimetics (ROBIO)*, pp. 1836-1841, 2012.

[27] T. Lozano-Pérez and M. A. Wesley, "An algorithm for planning collision-free paths among polyhedral obstacles," *Commun. ACM*, vol. 22(10), pp. 560-570, 1979.

[28] A. T. Rashid, A. A. Ali, M. Frasca and L. Fortuna, "Path planning with obstacle avoidance based on visibility binary tree algorithm," *Rob. Autom. Syst*, vol. 61(12), pp. 1440-1449, 2013

[29] UVS International, http://uvs-international.org (accessed February 2015.).

[30] http://www.insidegnss.com/auto/janfeb08-wp.pdf (accessed February 2015.).

[31] http://www.grc.nasa.gov/WWW/k-12/UEET/StudentSite/dynamicsofflight.html (accessed February 2015.).

[32] http://www.uavinsider.com/rotary-wing-vs-fixed-wing-uavs/ (accessed February 2015.).

[33] http://ardupilot.com (accessed February 2015.).

[34] http://www.dji.com/products/flight-controllers (accessed February 2015.).

[35] http://www.digi.com/technology/rf-articles/wireless-zigbee (accessed February 2015.).

[36] V. Brtka, D. Dobrilovic, Z. Stojanov, Z. Covic, and N. Bilinac, "Software application for analyses of ZigBee network performance designed for teaching and testing Wireless Sensor Networks," *In 12th IEEE Int. Symp. Intell. Syst. and Inf.(SISY)*, pp. 1-6, 2014.

[37] D. Dobrilovic, Z. Stojanov and B. Odadzic, "Teaching application development for RFID/ZigBee networks using open source hardware," *In 10th IEEE Int. Symp. Telecommun. (BIHTEL)*, pp. 1-6, 2014.

[38] http://www.digi.com/pdf/ds_xbeezbmodules.pdf (accessed February 2015.).

The 7th International Conference on Engineering and Technology
ICET-2015, Phuket, June 19-20, 2015
Prince of Songkla University, Faculty of Engineering
Hat Yai, Songkhla, Thailand 90112

Comparison of PI and Fuzzy Logic Controllers in Human-Robot Handover Task

Paramin Neranon[1]*, Robert Bicker [2]
[1]Prince of Songkla University, Faculty of Engineering, Thailand
[2]Newcastl University, School of Mechanical and Systems Engineering, United Kingdom
*Email of corresponding author: nparamin@me.psu.ac.th

Abstract: *This paper presents the design and development of an appropriate set of behaviours in a control strategy of human-robot interaction (HRI) by learning and understanding how human-human interaction (HHI) can be used to establish a framework for a behaviour-based approach.*

A set of preliminary tests using a single DOF human-human handover task was carried out to investigate the kinematics and dynamics of the human behavioural characteristics used to develop force/position controller of the robotic system in a HRI task, in which a handler dexterously transfers an object to a receiver in a timely and natural manner, similar to passing the baton in a relay race. The fast Fourier transform (FFT) is used to evaluate the performance of the proportional integral and fuzzy logic force/position control algorithms. As shown in FFT results, it can be concluded that the qualitative performance in terms of stability of the robot force control using fuzzy logic control (FLC) provides more effective in giving enhanced stability and greater overall dynamic performance and moderation in the interactive force signals than proportional integral (PI) control over a wide operational range.

Key Words: ***Human-human interaction (HHI); Human-robot interaction (HRI); Robot force/position control; Proportional integral (PI) control; Fuzzy logic control (FLC)***

1. INTRODUCTION

Interest in human-robot interaction has tended to increase significantly. Various human-robot cooperative technologies, which are used to enable unskilled workers to be able to directly teach intelligent robots, have been extensively developed. HHI behaviour is an important requirement in developing a functional HRI behaviour based framework, which facilitates natural and effective HRI in a shared workspace.

To fully understand the kinematic and dynamic HHI behaviour in attempting to carry out an effective coordinative task, it is necessary to design and develop an appropriate set of behaviour strategies to facilitate a robust, behaviour based, human-robot interactive architecture. There have been many researchers working in this area such as Ikeura and Inooka [1], Rahman et al. [2], Reed et al. [3], Bakar et al. [4] and Neranon and Bicker [5]. The current trend is for HRI to be improved by enhancing the capabilities of robots to work with humans as partners and to combine the advantages of workers and robot manipulators. Suda and Kosuge [6] proposed impedance control of a robot system whilst handling an object with a human based on the intentional force/moment. Lenz et al. [7] designed the concept of a smart working system between humans and industrial robots to assemble industrial products using the model of the architecture of joint action for humans and industrial robots (JAHIR). Also Kosuge and Hirata [8] developed effective HRI using interactive force information from a robot body force/torque sensor in order to control a dance robot partner.

The following sections explain how the control which enables the robot manipulator arm to effectively interact with the human to facilitate the dextrous transfer of objects in a safe/speedy manner can be developed.

2. A ONE DOF OF HHI HANDOVER TASK

2.1 System Design

As mentioned that it is crucial to understand the kinematics and dynamics of HHI behaviour in order to design and develop an appropriate set of force control strategies for robust, therefore a set of preliminary one DOF human-human handover experiments have been undertaken to investigate how the handler and receiver behave whilst performing the interactive tasks.

Two human participants were randomly selected to perform the one DOF human-human object handover tasks. Whilst executing the interactive task, the interactive forces f_x, f_y and f_z were measured and collected in real-time using the ATI mini40 force/torque sensor. In addition, a DE-ACCM accelerometer was used to estimate the velocity of the object by integrating an output signal from the sensor. The QNX Neutrino real-time operating system v6.4.0 supporting the implementation of the multi-tasking system was adopted to communicate with a power PDL-ME DAQ card, which furnishes six channels of analog inputs and offers the precise quantification of the strain gauge signals transmitted from the IFPS box and the acceleration data.

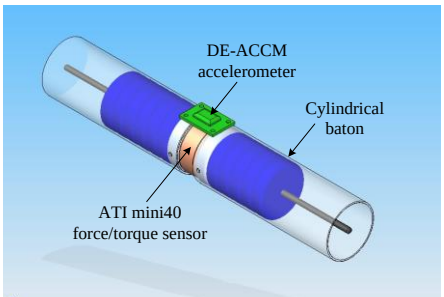

Figure 1 Design of a baton used in a one DOF HHI task

2.2 Test Procedure

The handler is requested to pass the object, as shown in Figure 1, to the receiver similarly to passing the baton in a relay race at diferent demanded velocities (10, 50 and 100mm/s). There are 18 participant pairs required to perform the object handover tasks. The workspace of the human-human handover task is that the distance from the start to end points and transfer zone were defined as 500 and 300mm in length respectively. HHI dynamics and kinematics including maximum interactive force (f_{max}), transfer time (T_{trf}) and work done (W) were used to develop an appropriate set of force/position control strategies to facilitate a robust, behaviour based, human-robot interactive architecture.

3. ROBOT FORCE/POSITION CONTROL

3.1 Fundamentals

The conceptual design of the human-robot interactive control system was developed to meet the above requirements as follows: a six DOF Stäubli robot manipulator arm (TX60) with CS8C controller was chosen and a six-axis ATI gamma force/torque sensor was used to measure the external force signal. A real-time Linux PC with an Intel UPC ouD 2 MT eroC ®processor with a clock speed of 3GHz was used.

De Schutter and Van Brussel [9] presented that a fundamental requirement for the success of human-robot cooperation is the capability of the robot to handle the physical contact between the robot and the human. The most crucial aspect in this control method applied to the HRI task is to achieve a suitable compromise between the system response and stability, where the response time was required to be as short as possible. Nevertheless, it should be noted that the system oscillations will be introduced when the control gains are too high.

It is important to develop the effective control for the Stäubli robot. After an extensive review of relevant academic research, it was finally decided to initially apply simple proportional integral (PI) in the handover task. However, optimized proportional integral control is normally employed to complete a specific task with satisfactory performance, and also provides disadvantages, i.e. high starting overshoot, sensitive to controller gains and steady-state error [10]. According to the complicated dynamic nature of human behaviour, fuzzy logic control (FLC), which has higher capability dealing with non-linear dynamic applications and does not rely on complicated mathematical models, was therefore adopted in this handover task.

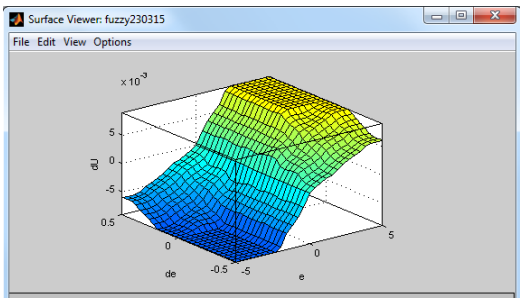

Figure 2 Surface viewer with two inputs e and de and one output ΔU

3.2 Proportional Integral (PI) Control

De Schutter and Van Brussel [9], concluded that the force trajectory tracking can be accomplished with the PI control method because it facilitates increasing accuracy and stability in the force control system. Correspondingly, the study carried out by Zeng and Hemami [11] demonstrated that PI control was appropriate for system position and force control in order to provide the smallest possible force control error. For the significant reasons mentioned above, proportional integral (PI) control was adopted and implemented for robot-force control in this study. The incremental PI algorithm is defined by:

$$u(k) = u(k-1) + k_P[e(k) - e(k-1)] + k_I e(k) \quad (1)$$

$$e(k) = f_d - f_s \quad (2)$$

where $U(k)$ is PI control output;
k_P is proportional gain;
k_I is integral gain;
$e(k)$ is difference between the desired and actual values.

Finally, the gain tuning for PI control applied to the robot's force control was implemented based on results of virtual crank tests. It can be concluded that the best performance as specified by the minimum root mean square error of the radial force is observed with proportional and integral gains of K_P = 0.10 and K_I = 0.005, and which were subsequently implemented in the human-robot handover task.

3.3 Fuzzy Logic Control

Fuzzy logic control (FLC) introduced by Zadeh [12] is normally used to control non-linear or complex systems based on 'IF-THEN' rules. It is a useful control method due to its ability to capture human qualitative control into control algorithms for the fuzzy rules. The fuzzy inputs were initially required to be identified in terms of the external force error (e) and change in the error (de), as shown in the following equations, where f_s and f_d are the mesured and desired forces respectively. Here f_d was defined as '0'.

$$e_k = f_d - f_s \quad (3)$$

$$de_k = e_k - e_{k-1} \quad (4)$$

The fuzzy logic toolbox in Matlab was used to design the FLC robot force control. Figure 2 illustrates the surface viewer with two inputs e and de and one output ΔU (incremental displacement), where for the evaluation of the fuzzy outputs based on this rule base using Mamdani fuzzy inference systems, the centroid defuzzification method was used to calculate the centroid of the output area.

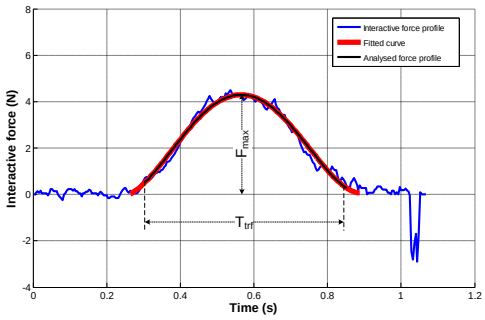

Figure 3 Actual velocity and interactive force profiles of a human-to-robot handover task based on PI control

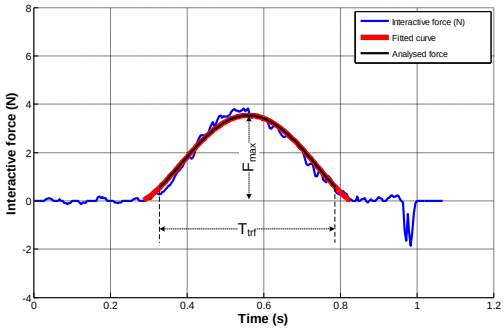

Figure 4. Actual velocity and interactive force profiles of a human-to-robot handover task based on FLC

4. FREEQUENCY ANALYSIS OF HRI HANDOVER TASK

Eighteen participants were again employed in the human-robot handover tasks. Each of the tests was repeated 5 times to ensure that the results met the requirements of statistical significance.

The test results based on both the proportional integral (PI) and fuzzy logic control (FLC) algorithms demonstrated dexterous human-human like object handovers, where the robot was able to successfully transfer the baton object to the human in smooth, safe and reliable manner. It can thus be concluded that both PI and FLC robot control strategies provide effective performance and reliability of the robot-to-human handover procedure. However, careful observation of the interactive force and velocity graphs for FLC revealed that these profiles are moderately smoother than the PI implementation (see Figures 3-4). This also supports the conclusion that using FLC has a significant advantage when controlling non-linear systems, and is more insensitive than PI control to variations in small external force disturbances, which is an important requirement in robot force/position control schemes.

5. FREEQUENCY ANALYSIS OF HRI HANDOVER TASK

In this section, frequency domain analysis, by way of the fast Fourier transform (FFT), is used to determine the performance of the robot force control implemented for the HRI tasks. The FFT analysis technique was first used by Cooley and Tukey [13].

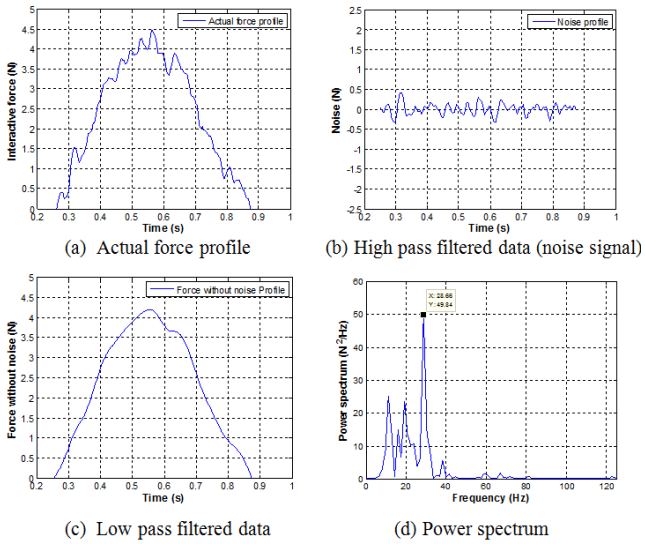

(a) Actual force profile (b) High pass filtered data (noise signal)

(c) Low pass filtered data (d) Power spectrum

Figure 5 FFT analysis for HRI using PI control

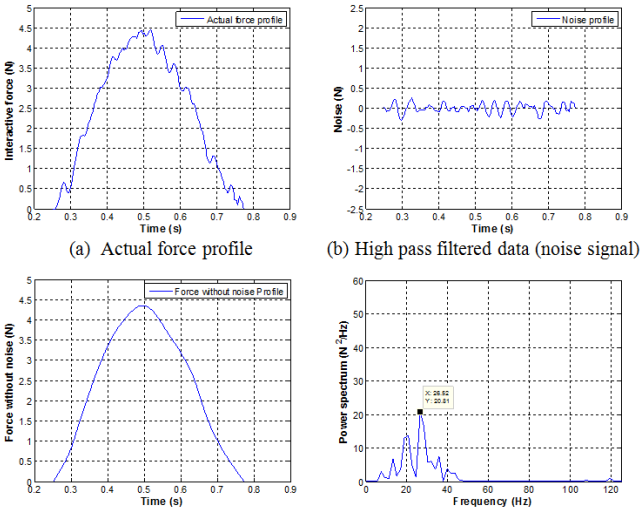

(a) Actual force profile (b) High pass filtered data (noise signal)

(c) Low pass filtered data (d) Power spectrum

Figure 6 FFT analysis for HRI using FLC

In this study, FFT was employed to identify changes in the power spectrum of the system when the Stäubli robot manipulator was controlled using PI and FLC force control schemes. From the experimental results (Figures 5 and 6) showing the interactive force profiles of the HRI, it was observed that there was small oscillation moderating in the force signals. The FFT was applied to extract the noise frequencies, which were used to compare and evaluate the qualitative performance of the robot based on the PI and FLC force control schemes at the three object transfer speeds.

Examples show how the performance in terms of the robot force control can be evaluated using FFT analysis where the robot was used to pass the object to the human at a velocity of 100mm/s. Figure 5(a) illustrates the actual interactive force trajectory during the transfer phase using PI force control. To appropriately identify the noise signal, a high-pass filter (HPF) with a cut-off frequency at 10Hz was used to filter the data (see Figure 5(b)).

Table 1 Qualitative performance measurement from FFT analysis in the HRI handover tasks

Velocity (mm/s)	Robot-to-human handover task					
	PI			FLC		
	Mean (N^2)	SD (N^2)	Frequency (Hz)	Mean (N^2)	SD (N^2)	Frequency (Hz)
10	7.7	3.3	15.5 - 30.1	5.4	3.1	17.6 - 33.2
50	34.7	12.6	17.5 - 28.6	24.3	7.4	18.2 - 27.3
100	42.5	14.3	16.7 - 32.1	28.6	9.0	18.7 - 31.3

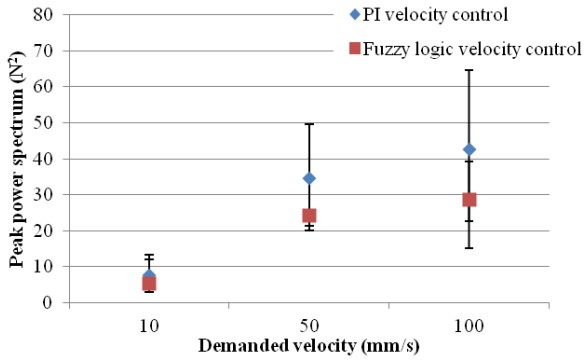

Figure 7 Comparison of the power spectral densities of robot using PI and FLC at velocities of 10, 50 and 100mm/s in robot-to-human handover tasks

The results of the FFT analysis are plotted in Figure 5(c), where the maximum power spectral density is approximately 49.84N^2 at a frequency of 28.66Hz. In addition, when the robot was controlled using FLC, a corresponding set of results shown in Figures 6(a)-(d) can be seen reduce the magnitudes of the filtered noise signal in the system, as depicted in Figure 6(b). Also, the maximum peak of the power spectrum is reduced to 20.81N^2 at the frequency of 26.52Hz.

The evaluation of the robot performance for all demanded velocity conditions in the robot-to-human handover tasks based on PI and fuzzy logic control algorithms is summarised in Table 1 and Figure 7. The results are expressed as the frequencies of the maximum power spectral densities delivered according to the proposed conditions, which varied slightly in the range of approximately 14-35Hz. The magnitudes of the maximum power spectrum of the filtered data were examined to determine the oscillations of the noise signal for each scenario. Fuzzy logic force control provided better qualitative performance of the robot in all robot-to-human handover tasks. A comparison of the power spectral densities using FLC and PI control shows that the values of power spectrum were respectively 5.4, 24.3 and 28.6N^2 for FLC, and 7.7, 34.7 and 42.5N^2 for PI control. It can be concluded that the fuzzy logic force control method is more effective in giving enhanced stability and greater overall qualitative performance in the robot force/position control system.

6. CONCLUSIONS

This research has highlighted the development of the robot external force control scheme using PI and FLC, which was implemented in the object handover tasks. The results of HHI were successfully used to design and develop an appropriate set of robot force control strategy and permit the robot manipulator arm to interact with a human so as to facilitate the dexterous transfer of objects in an effective manner.

The experimental results based on the FFT analysis have confirmed that the performance whilst using FLC in the robot-to-human handover tests is superior to that of proportional control. This is due to advantageous of FLC in dealing with non-linear systems and significantly improves the effective dynamic performance and robustness in the system. However, the performance of the fuzzy logic control method depends on the design and development of its control rule base, and is sensitive to the membership function of the fuzzy logic's inputs and output variables.

7. REFERENCES

[1] Ikeura, R., Moriguchi, T. and Mizutani, K. (2002) 'Optimal variable impedance control for a robot and its application to lifting an object with a human', *Robot and Human Interactive Communication, 2002. Proceedings. 11th IEEE International Workshop on.* 2002. pp. 500-505.

[2] Rahman, M. M., Ikeura, R. and Mizutani, K. (2002) 'Investigation of the impedance characteristic of human arm for development of robots to cooperate with humans', *Jsme International Journal,* 45, pp. 510-518.

[3] Reed, K. B., Patton, J. and Peshkin, M. (2007) 'Replicating human-human physical interaction', *Proceedings of the 2007 Ieee International Conference on Robotics and Automation, Vols 1-10,* pp. 3615-3620.

[4] Bakar, S. A. B. U., Ikeura, R., Handa, Y., Yano, T., Mizutani, K. and Sawai, H. (2010) 'Communication during the Cooperative Motion in the Task of Carrying an Object between Two Humans', *Journal of Biomechanical Science and Engineering,* 5, (2), pp. 104-118.

[5] Neranon, P. and Bicker, R. 'Human-human interaction using a behavioural control strategy', *Technologies for Practical Robot Applications (TePRA), 2013 IEEE International Conference on.* 22-23 April 2013. pp. 1-6.

[6] Suda, R. and Kosuge, K. (2002) 'Handling of object by mobile robot helper in cooperation with a human using visual information and force information', *Intelligent Robots and Systems, 2002. IEEE/RSJ International Conference on.* 2002. pp. 1102-1107 vol.2.

[7] Lenz, C., Nair, S., Rickert, M., Knoll, A., Rosel, W., Gast, J., Bannat, A. and Wallhoff, F. (2008) *Robot and Human Interactive Communication, 2008. RO-MAN 2008. The 17th IEEE International Symposium on.* 1-3 Aug. 2008.

[8] Kosuge, K. and Hirata, Y. (2004) 'Human-robot interaction', Robotics and Biomimetics, 2004. ROBIO 2004. IEEE International Conference on. IEEE, pp. 8-11.

[9] De Schutter, J. (1987) Robotics and Automation. Proceedings. 1987 IEEE International Conference on. Mar 1987.

[10] Khuntia, S. R., Mohanty, K. B., Panda, S. and Ardil, C. (2009) 'A comparative study of PI, IP, fuzzy and neuro-fuzzy controllers for speed control of DC motor drive', *International Journal of Electrical Systems Science and Engineering,* 1, (1)

[11] Zeng, G. and Hemami, A. (1997) 'An overview of robot force control', *Robotica,* 15, (05), pp. 473-482.

[12] Zadeh, L. (1956) 'On the Identification Problem', *Circuit Theory, IRE Transactions on,* 3, (4), pp. 277-281.

[13] Cooley, J. W. and Tukey, J. W. (1965) 'An algorithm for the machine calculation of complex Fourier series', *Mathematics of computation,* 19, (90), pp. 297-301.

The 7th International Conference on Engineering and Technology
ICET-2015, Phuket, June 19-20, 2015
Prince of Songkla University, Faculty of Engineering
Hat Yai, Songkhla, Thailand 90112

Evaluation of a Map Matching Algorithm for Indoor Localization with OpenStreetMap

Levent Bayındır
Department of Computer Engineering, Ataturk University, Turkey
levent.bayindir@atauni.edu.tr

Abstract: *This paper analyzes the problem of pedestrian localization in indoor environments using a dead reckoning approach. By taking into account information from the environment where the pedestrian is located, with a map matching technique, the inherent limitations of pure dead reckoning systems can be overcome. Implementation of an existing localization method with map matching based on particle filtering is described, and its performance is assessed in a real-world scenario. Experimental results show that varying a parameter of the map matching algorithm localization performance is improved.*

Key Words: ***Indoor Localization / Pedestrian Dead Reckoning / Inertial Sensors / Step Model / Map Matching / Particle Filter***

1. INTRODUCTION

Automatic localization of a person in indoor environments is a challenging problem due to the lack of coverage of global navigation systems (e.g. GPS). One of the approaches most studied for indoor localization is dead reckoning, in which the position of a moving object at a given time is determined by applying a displacement function (calculated from data measured with sensors carried by the moving object) to its position at a previous time. Pedestrian Dead Reckoning (PDR) denotes dead reckoning methods applied to localization of pedestrians.

Pure read reckoning systems suffer from cumulative errors caused by noise and drift of sensor measurements; to mitigate this problem, digital maps can be used to complement sensor readings, with a technique known as *map matching*. For example, indoor maps can contain information on what positions may or may not be occupied by users inside a building and what transitions are or are not allowed.

In this paper, a map matching technique is analyzed using an open standard (OpenStreetMap) to represent the indoor environment. Section 2 briefly describes some approaches to map matching that have been used in previous studies. Section 3 analyzes how sensor measurements from a mobile device can be used for pedestrian dead reckoning. Section 4 describes the map matching algorithm utilized in this study. Section 5 reports results of experiments conducted to evaluate the performance of the algorithm, while the last section contains some considerations on those results.

2. RELATED WORK

To increase the accuracy of dead reckoning and tackle the problem of cumulative errors in position estimation, different map matching algorithms have been studied. CompAcc [1] is based on walking paths extracted manually from Google Maps in outdoor environments such as university campuses: the trail calculated via dead reckoning from a known initial position is matched, through a similarity measure, against known walking paths in the vicinity of the estimated position. In [2] a similar approach is used: map data are expressed as a set of links corresponding to walking paths, and the estimated position and heading direction are compared to those of each link in order to find the most likely user position. FootPath [3] targets indoor applications and allows a user to select its current position and its destination inside a building, then, using sequence alignment algorithms, matches the detected steps to the path calculated from origin to destination. In [4, 5] a building floor is modeled as a set of nodes and connecting links, and map matching consists in finding the path (seen as a sequence of connected nodes) that best matches the measured user trajectory. In [6] an indoor map is defined as a set of rectangular areas connected by links; when the position estimated via dead reckoning moves from one area to another, if the destination area is not connected to the origin area the algorithm corrects the estimated position by searching for the nearest connected area.

Another technique for integrating map data in a PDR system to correct errors induced by sensor readings is based on particle filtering. A particle filter models user movement as a stochastic process, whose randomness is introduced by noise in sensor readings. User position is estimated by applying a weighted average to a number of independent estimations (represented by particles), each of which is obtained from sensor data by applying one or more random components to the formulas used to calculate the displacement. Weights are assigned to different particles based on map information.

The most frequently used type of information from indoor maps to correct position estimation via particle filtering is the location of walls or other fixed obstacles inside buildings [7, 8, 9]. Since users cannot cross these obstacles while walking, if a particle hits an obstacle, its weight is set to zero, so that its position does not contribute to the estimation of the user position.

In [10], dead reckoning position estimation is matched (through particle filtering) with map data where a floor is divided in small tiles labeled as pathway, room space, or wall. Particles entering or crossing a tile labeled as wall are given a zero weight. In addition, the weight of particles located in tiles labeled as pathway is modified in order to give a higher weight to particles in the middle of the pathway, based on the fact that people tend to walk in the middle of corridors instead of near walls.

3. PEDESTRIAN DEAD RECKONING

The majority of PDR systems represent pedestrian movement as a discrete sequence of displacements: a step detection algorithm identifies the single steps made by a walking person, while a step model calculates the amount of displacement caused by each step.

The sensor type most frequently used for step detection is the accelerometer, which measures its acceleration along the 3 spatial directions *x*, *y* and *z*. These directions are relative to the orientation of the device equipped with the sensor, whose relationship with the heading direction of the user depends on how the device is carried by the user. In order to have signal measurements independent from sensor orientation, the magnitude of the acceleration can be used instead of its single components. The localization method described in [10], which has been implemented in this study, uses the magnitude of the acceleration signal to detect user steps.

During each step, the acceleration pattern exhibits one or more peaks; the step detection algorithm in [10] tries to find the significant peaks defining the boundary between contiguous steps. Significant peaks are distinguished from non-significant ones by means of two threshold values: a magnitude and a duration threshold. The first value is compared against the difference between the acceleration value at a peak and the following values before the next peak: if this difference does not reach the threshold value, the peak is discarded. The duration threshold indicates the minimum temporal distance required between a significant peak and the next peak. The steps detected from significant peaks are then subjected to further checks in order to reduce the probability of false step detection.

Once steps are detected as described above, the displacement due to each step must be determined. The displacement can be expressed with the polar coordinates direction and length, which are calculated separately.

In order to determine the direction of user movement, an additional sensor is utilized: the magnetometer, which measures the intensity of the magnetic field along the 3 spatial directions. The orientation of the sensor device during a step is estimated combining the acceleration and magnetic field measurements at the so-called *inference point* of the step. In this implementation the inference point is determined as the first point in time during a step when the acceleration crosses the value $g \approx 9.8$ m/s^2.

In this study, a mobile phone is used as sensor device; in order to determine the user direction from the phone orientation, two assumptions are made:

1. when a user starts a localization session, the phone is oriented in the direction of the first step, as when the user operates on the phone watching its screen
2. before beginning to walk, the phone is either left at the previous position, or put at its final position (e.g. in a pocket) where it is kept for the entire duration of the localization session

Due to the first assumption, the direction of the first step can be derived directly from the initial orientation of the phone. From the orientation calculated at the inference point of the first step, a transformation matrix is derived which represents the phone orientation change from the initial position to the final position. The second assumption guarantees that from the phone orientation at a generic step *n* it is possible to calculate the orientation that the phone would have had if it was kept in its initial position, and then the user direction at step *n*.

Once the direction of user steps has been determined, the only missing piece of information for the PDR system is the length of each step. In the step model used in [10], the step length *L* is a linear function of the step frequency *f*:

$$L = a \cdot f + b \tag{1}$$

where *a* and *b* are parameters which can be generic or personalized for a specific user. In this implementation, the values $a = 0.22$ m/Hz and $b = 0.28$ m have been used as parameters of the generic step model.

4. MAP MATCHNG WITH OPENSTREETMAP

In this study, map matching is used, via particle filtering, to reduce the inaccuracy of dead reckoning. Indoor localization methods using map matching depend on the availability of digital map data. While outdoor maps are readily available because of the possibility to acquire them automatically from aerial or satellite views, the availability of maps for indoor environments is more limited. Adoption of a standard format to represent indoor environment data is desirable to facilitate creation and distribution of indoor maps.

OpenStreetMap [11] is a collaborative effort to provide free worldwide maps. The format used by OpenStreetMap to represent map data is based on three primitive types: *nodes*, *ways* and *relations*. A node represents a geographic location and is described by its latitude and longitude coordinates. A way is an ordered collection of nodes and represents a path, which can be open (i.e. the last node is different from the first node) or closed (i.e. the first and last node are the same). A relation is a set of other entities (which can be nodes, ways, or other relations), called relation members, and represents a logical entity inside a map. Every element can have different tags, used to encode additional descriptions of the map entity it represents.

IndoorOSM [12] is a proposed extension to OpenStreetMap designed to describe indoor settings. In IndoorOSM, a building is represented as an OpenStreetMap relation whose members are the building

floors; in turn, each floor is a relation whose members are ways corresponding to the different building parts inside the floor. Each building part (room, corridor, etc.) is represented by a closed way indicating the contour of the part. Doors are represented by particular nodes in the way, which are identified as being doors by the presence of a specific tag; another tag associated to these nodes indicates the door width. From this information it is possible to derive the location of the walls delimiting a building part and the passages allowing entering and exiting the part. A corridor or pathway is a building part marked with a specific tag indicating that it is a corridor.

In the localization method described in [10], the particle filtering algorithm requires information on the position of walls and corridors inside a building. As shown above, IndoorOSM supports encoding this type of information, thus in this study IndoorOSM has been used to represent map data.

The accuracy of the step model in (1) depends on how well its parameters reflect user walking characteristics. Given the initial values of *a* and *b*, each particle of the particle filter is assigned parameter values obtained by adding a random component (drawn from a uniform distribution) to *a* and *b*, so that for a step with frequency *f* the step model of a generic particle *i* calculates the step length as follows:

$$L_i = a_i \cdot f + b_i \tag{2}$$

where a_i and b_i are the parameters assigned to particle *i*. The displacement of the particle is determined by adding a random component to the calculated step length and adding another random component to the heading direction of the step; both components are drawn from a Gaussian distribution.

During user movement, if the constraints of the map cause many of the particles to have a low (or zero) weight, a process called *re-sampling* is performed, where low-weight particles are replaced with new particles. In this implementation, when re-sampling takes place the position of new particles is obtained by adding a random component, drawn from a Gaussian distribution, to the coordinates of the current estimated user position.

During re-sampling, the parameters of the step model of a given particle may or may not be changed depending on whether the user is making a turn (i.e. a change in direction) at the current step. In this implementation, if a turn is detected, for each particle with zero weight the parameters of its step model are replaced with those of the nearest particle with non-zero weight; if no turn is detected, each particle keeps the current values of its parameters. The algorithm for turn detection is based on the direction estimated at the inference point of each step, as explained in [10]; in this study, a configurable threshold is used for detection of a turn and for determination of turn initiation and termination.

5. EXPERIMENTAL RESULTS

The localization method described in [10] has been implemented and evaluated with a mobile phone application. This localization method contains several parameters; Table 1 reports the values of the main parameters used in experiments.

Table 1. *Experiment parameter values*

Step detector magnitude threshold	2 m/s^2
Step detector duration threshold	0.3 sec
Standard deviation of particle position	0.2 m
Standard deviation of step model *a* parameter	0.01 m/Hz
Standard deviation of step model *b* parameter	0.01 m
Standard deviation of step length	0.22 m
Standard deviation of step direction	22.5 °
Particle re-sampling threshold	0.1
Turn detection threshold	18°

During tests, a user conducted several tracking sessions; at each session, the user selected his initial position in the building map in the mobile phone and then walked 5 times along a closed path inside the building, keeping his phone either in hand (oriented in the user direction), or in his pants pocket. These tests have been repeated with different values of the standard deviation of particle position. Test results are summarized in Tables 2 and 3, which contain the mean value and the standard deviation (in parentheses) of the localization error measured at the end of each lap of the user in the closed path.

Table 2. *Localization error with phone in hand*

Standard deviation	1	2	3	4	5
default	1.44 (0.99)	1.08 (0.846)	1.82 (1.3)	3.33 (2.26)	5.4 (2.77)
0.05 m	1.21 (0.415)	1.57 (0.752)	1.88 (0.909)	1.75 (0.979)	2.86 (1.97)
0 m	0.638 (0.388)	1.33 (0.588)	1.87 (0.961)	2.23 (1.18)	3.13 (1.31)

Table 3. *Localization error with phone in pocket*

Standard deviation	1	2	3	4	5
default	5.43 (0.966)	10.9 (1.04)	15.9 (1.77)	21.8 (2.84)	26.6 (4.7)
0.05 m	1.93 (1.22)	3.27 (1.49)	4.54 (2.73)	7.66 (4.25)	10.9 (5.99)
0 m	1.39 (0.768)	1.15 (1.24)	1.88 (1.79)	2.67 (1.55)	2.61 (2.05)

Fig. 1 (a) is an example of a tracking session with the phone kept in hand, where measurement errors are easily corrected by the particle filter. The user walked 5 times following the closed path depicted with arrows, starting from the location identified by a rounded rectangle (the doors of the building are not represented in the figure, but are present where the path crosses the walls). The calculated path is depicted with a dotted line.

Fig. 1 (b) contains an example of calculated path when the error from sensor measurements is high. After a few laps, the calculated path shifts from the true path and goes outside the building. Once outside, the particle filter is unable to correct the estimated position, because

there are no environmental constraints, thus the calculated path is characterized by the cumulative error typical of uncorrected PDR systems. In addition, this example, which refers to a localization session where the mobile phone was kept in the pants pocket of the user, shows how the phone movement inside the pocket creates noise in the estimated user direction.

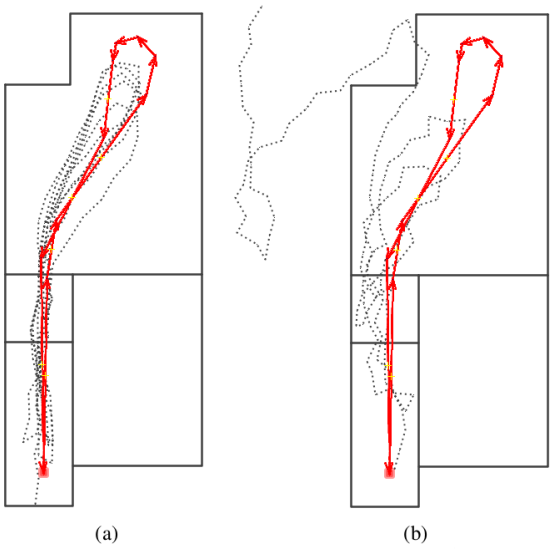

Fig. 1. Tracking session examples in a 4.8x12 m^2 area, (a) with no wall crossings and (b) with wall crossings

6. DISCUSSION

In the case of walking sessions with the phone kept in hand, the calculation of the user path is less prone to errors, and the particle filter is able to compensate most measurement inaccuracies. With the phone kept in pocket, the movement of the phone during walking is more chaotic, and as a result heading estimation errors are more likely to distort the calculated user path. This is the reason why the localization error is larger for in-pocket versus in-hand cases, as shown in Tables 2 and 3.

When measurement errors lead many particles of the particle filter to hit a wall and then to be re-sampled, the re-sampling strategy influences the position calculated at the next user step. If re-sampled particles are located at a random position centered around the current estimated position, some particles may be located at the other side of the wall compared to the current position. If measurement errors at the next user steps are similar to those of previous steps, the particles at the other side of the wall are less likely to hit the wall than the remaining particles. As a consequence, the estimated user position after a few steps may be at the other side of the wall, leading to a calculated path which crosses the wall, as shown in Fig. 1 (b). While this is undesirable in most cases, it gives a certain flexibility to the algorithm and can be useful to have a less constrained environment which allows for inaccuracies of the building map. For example, if the map does not contain a door between two rooms which is present in the actual building, with this approach the particle filter does not prevent tracking user movement through that door. The probability of wall crossings in the calculated path decreases with decreasing values of the standard deviation of particle position during re-sampling, because re-sampled particles are less scattered around the current position and are less likely to be located at the other side of a wall. If the position of re-sampled particles does not contain a random component (as when the standard deviation is set to zero), then the algorithm prevents wall crossings. Experimental results shown in Tables 2 and 3 demonstrate this behavior.

7. REFERENCES

[1] I. Constandache, R. R. Choudhury, and I. Rhee, "Towards mobile phone localization without war-driving", *Infocom, 2010 Proceedings IEEE*, pp.1-9.

[2] S. H. Shin, C. G. Park, and S. Choi, "New map-matching algorithm using virtual track for pedestrian dead reckoning", *ETRI journal* 32, No. 6 (2010), pp. 891-900.

[3] J. Agila Bitsch Link, P. Smith, N. Viol, and K. Wehrle, "FootPath: accurate map-based indoor navigation using smartphones", *Proc. of 2011 Int. Conf. on Indoor Positioning and Indoor Navigation (IPIN)*, pp. 1-8.

[4] W. Shih and K. Lan, "Using smartphone with un-scaled map for indoor localization", *Proc. of 9th Annual IEEE Communications Society Conf. on Sensor, Mesh and Ad Hoc Communications and Networks (SECON)*, 2012.

[5] P. Gilliéron, D. Buchel, I. Spassov, and B. Merminod, "Indoor navigation performance analysis", *ENC GNSS*, 2004.

[6] P. Pombinho, A. P. Afonso, and M. B. Carmo, "Indoor positioning using a mobile phone with an integrated accelerometer and digital compass", *INForum*, 2010.

[7] M. Angermann and P. Robertson, "FootSLAM: Pedestrian Simultaneous Localization and Mapping Without Exteroceptive Sensors - Hitchhiking on Human Perception and Cognition", *Proc. of the IEEE 100 (Special Centennial Issue)*, 2012, pp. 1840-1848.

[8] S. Beauregard, Widyavan, and M. Klepal, "Indoor PDR performance enhancement using minimal map information and particle filters", *Position, Location and Navigation Symposium*, 2008 IEEE/ION, pp. 141-147.

[9] H. Leppakoski, J. Collin, and J. Takala, "Pedestrian navigation based on inertial sensors, indoor map, and WLAN signals", *Journal of Signal Processing Systems* 71, No. 3 (2013), pp. 287-296.

[10] F. Li, C. Zhao, G. Ding, J. Gong, C. Liu, and F. Zhao, "A reliable and accurate indoor localization method using phone inertial sensors", *Proc. of the 2012 ACM Conf. on Ubiquitous Computing*, pp. 421-430.

[11] OpenStreetMap, http://www.openstreetmap.org [Accessed: February 25, 2015]

[12] IndoorOSM, http://wiki.openstreetmap.org/wiki/IndoorOSM [Accessed: February 25, 2015]

The 7th International Conference on Engineering and Technology
ICET-2015, Phuket, June 19-20, 2015
Prince of Songkla University, Faculty of Engineering
Hat Yai, Songkhla, Thailand 90112

FEM Modeling of the Multi-Segment Lumbar Spine for Humanoid Robots

Marko Penčić[1]*, Branislav Borovac[1], Dušan Kovačević[1]
[1]University of Novi Sad, Faculty of Technical Sciences, Novi Sad, Serbia
*mpencic@uns.ac.rs

Abstract: *The paper presents FEM modeling of lumbar structures for humanoid robots. Multi-segment structure allows lateral flexion ±30º and rotation ±45º, also combination of these two movements. FEM modeling is performed for amplitude positions. The highest strains are for lateral flexion and highest resultant displacements occur in combination "lateral flexion + rotation" (values are 10 times higher than required). The factor of safety for stresses is 1,4. Zone of maximum stresses is the pin in one of the joint links. Pin calculation gives factor of safety above 8, which is 6 time higher than factor of safety obtained from FEM modeling.*

Key Words: ***FEM modeling, multi-segment lumbar spine, humanoid robot***

1. INTRODUCTION

In humanoid robotics, most robots that are developed have rigid torso and their mobility is limited and unnatural [1]. The flexibility of the torso is essential for achieving human-like movements. Robots that have a flexible spine can absorb shocks and mechanical impacts during movement and therefore are safer when making physical contact with humans or objects [2]. Incorporating the spine in the trunk of robots increases the mobility and the range of the robot arm's reach.

In this paper FEM modeling of the lumbar spine is presented with the aim of reconstruction of existing solutions [3]. The research is conducted within the provincial project based on development of socially acceptable robot named "SARA", which presents a mobile anthropomorphic platform for research of socially acceptable behavior of the robot.

FEM model is formulated in software "Solid Works" by using 3D finite element with contour and transitional conditions that simulate the real behavior of links and joints. Numerical analysis is conducted in accordance with the assumption of a completely linear behavior of the structure, which is confirmed by the results - strain is within the limits of elasticity of the applied materials and deformation displacements and rotations have small values compared to the dimensions of the structure, that is FEM model.

2.1. Spinal column and its mobility

Spinal column or spine (*columna vertebralis*) is a fundamental part of the skeleton and it extends along the back side of the neck and torso [4]. The spinal column is built of bones that are placed on top of one another and called vertebrae. Vertebrae are not commensurate. The movements of the spinal column are enabled with intervertebral joints and intervertebral rings - discus, that are inserted between two adjacent vertebrae [5]. Due to the elastic part of these rings - discs, it is possible to perform locomotor activities of spinal column and better amortization. In the region of the spinal column following movements can be distinguished: flexion - bending forward and extension - bending backward (Fig. 1-a), lateral flexion - side bending (Fig. 1-b) and rotation - torsion (Fig. 1-c).

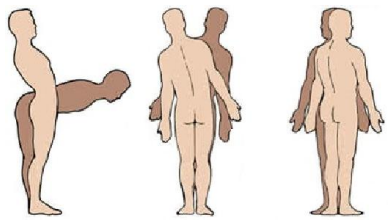

a) *b)* *c)*

Fig. 1. The human spine movement: a) flexion/extension, b) left/right lateral flexion and c) left/right rotation

The mobility of lumbar spine in the sagittal plane (laterally) for the movements of flexion is about 40º and for the movements of extension is about 30º. Total movement of lateral flexion is about 50º, that is 25º to the left and to the right side. The movements of rotation is about 20º, which is 10º for each side [6].

2. MULTI-SEGMENT LUMBAR SPINE

The prototype of the lumbar structure designed for humanoid robots is developed based on biomechanical characteristics of human spine (Fig. 2-a) [7]. It is a serial related structure with has 6 DOFs and consists of three equal segments - joints (2 DOFs per segment). Multi-segment lumbar structure provides movements of lateral flexion ±30º, which is ±10º per segment (Fig. 2-b) and the rotation of the spine ±45º, which is ±15º per segment (Fig. 2-c), as well as the combination of these two movements (Fig. 2-d).

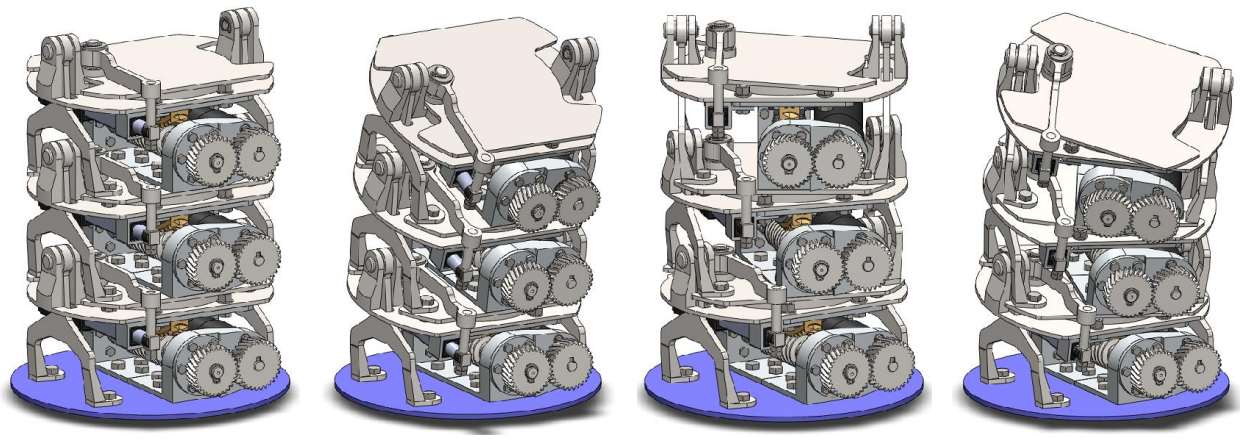

a) *b)* *c)* *d)*

Fig. 2. The lumbar structure: a) in initial upright position, b) lateral flexion 30º, c) rotation (torsion) 45º and d) lateral flexion 30º + rotation (torsion) 45º

In the development phase of lumbar structure, flexion movements were ignored, because the bending of the body forward to an angle of 45º occurs in the hip joints. Thoracic part of the spine will be immobile and it is provided for incorporating of the necessary electronics. The total height of this prototype is 201 mm, 150 mm in diameter and weight of 6 kg (which is 2 kg per segment).

The movements of lateral flexion are provided with drive which consists, per segment, from one DC motor and two toothed gearing, helical gear and worm gear. Worm gear is self-locking, so in dormant phase the lumbar structure retains any position (motor is without brake) without energy consumption. The movements of rotation are provided with drive consisting of linear actuators and axial bearings. The axial bearing consists of an inner ring - the upper plate and the outside of the ring - lower plate, and is constructed by the technology of radial bearings with a four points of contact (Fig. 3). Rotating the upper plate relative to the lower plate is performed by means of a linear actuator [8].

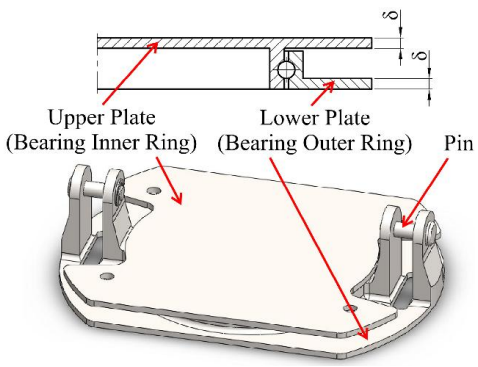

Fig. 3. Axial bearing - horizontal support

2.1. Load of the lumbar structure

Besides the kinematic-dynamic requirements, it is necessary that the lumbar structure fulfils following requirements: functionality, high carrying capacity and reliability, low backlash of the gearbox (<10 arcmin) which affects on positioning and repeatability of movement, compact design, small dimension and weight etc.

During the movement, the lumbar structure is loaded with changeable forces and moments. It connects head, neck, shoulders lifting mechanism, arms etc. (these mechanisms are under development). Hands of the robot, depending on the position can further load the segments, that is why it is necessary to examine the real model.

Assumed mass of all parts and elements that are above the lumbar structure is 25 kg. In Fig. 4 are shown lumbar structures inclined at the angle of 30º. Both structures, in vertical position, have the same height from the center of mass (MC) to the base. The first structure (Fig. 4-a) consists of three equal segments, where each segment is inclined, relative to the previous one, at an angle of 10º, for a total of 30º, while the other structure (Fig. 4-b) consists of one segment, inclined at an angle of 30º.

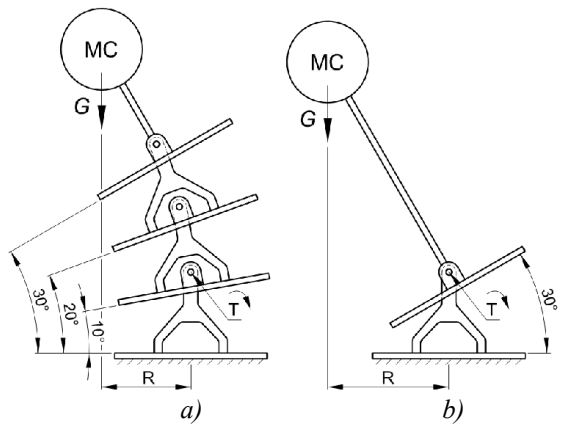

a) *b)*

Fig. 4. Lumbar structure used as reference in segment design process

From the Fig. 4 it can be concluded that the force arm R is higher in the lumbar structure consisting of one segment and significantly lower with multi-segmental structure. Multi-segment structure provides a wider range of mobility. With smaller force arm, smaller torque values are required to actuate the joints - segments. In that case it is possible to apply smaller actuators (in power and dimension) which directly reduces dimensions of the segments, that is lumbar structure.

3. FEM MODELING AND DISCUS RESULTS

FEM modeling is performed for the amplitude positions of the structures (lateral flexion ±30º and lateral flexion ±30º + rotation ±45º) depending on the thickness of the bearing plates δ (Fig. 3 and Fig. 5).

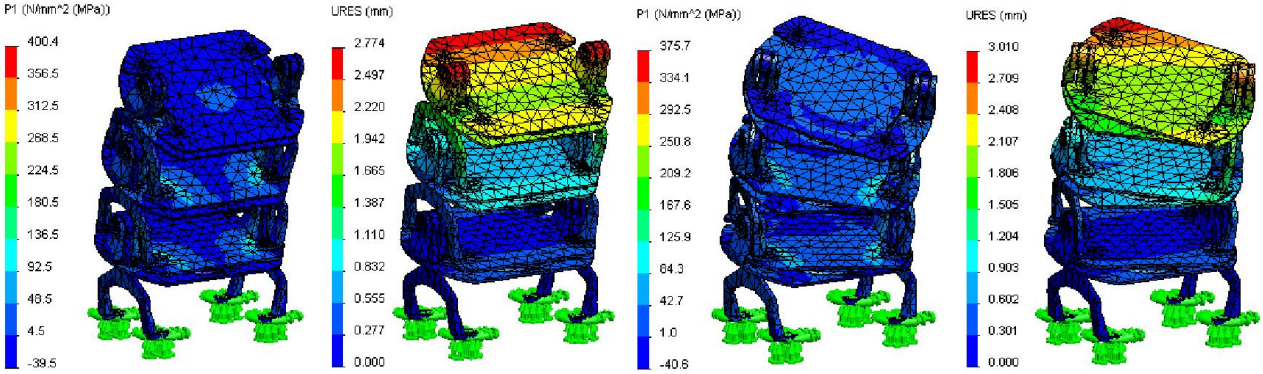

a) *b)* *c)* *d)*

Fig. 5. The lumbar structure - FEM modeling (SolidWorks): a) lateral flexion 30º - principal stresses, b) lateral flexion 30º - resultant displacement, c) lateral flexion 30º + rotation 45º - principal stresses and d) lateral flexion 30º + rotation 45º - resultant displacement

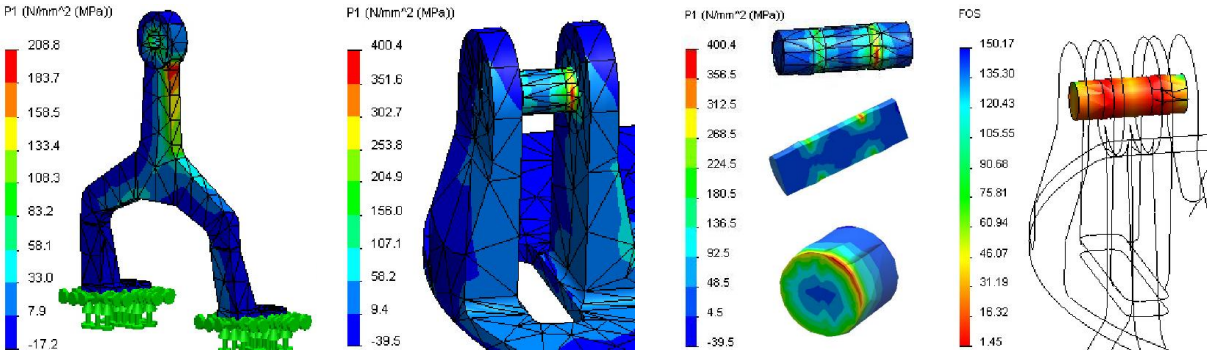

a) *b)* *c)* *d)*

Fig. 6. Elements of lumbar structure - FEM modeling (SolidWorks): a) vertical support - principal stresses, b) lower plate bearing with pin - principal stresses, c) longitudinal and cross section of pin - principal stresses and d) safety factor of most loaded part - pin

Table 1. *FEM modeling of the lumbar structure - lateral flexion ±30º*

Plate hickness δ mm	Principal Stresses $\sigma_1 \geq \sigma_2 \geq \sigma_3$			Resultant Displacement u_{res} mm	Factor of Safety $(\sigma_{Limit}/\sigma) > 1$
	σ_1 N/mm^2	σ_2 N/mm^2	σ_3 N/mm^2		
1,5	421,5	-100,7	-404,3	3,201	1,38
1,8	470,7	73,3	-405,8	3,062	1,23
2,0	412,0	70,6	-386,1	2,980	1,41
2,2	388,4	65,1	-391,8	2,888	1,48
2,5	400,4	-64,7	-373,4	2,774	1,45

Table 2. *FEM modeling of the lumbar structure - lateral flexion ±30º + rotation ±45º*

Plate thickness δ mm	Principal Stresses $\sigma_1 \geq \sigma_2 \geq \sigma_3$			Resultant Displacement u_{res} mm	Factor of Safety $(\sigma_{Limit}/\sigma) > 1$
	σ_1 N/mm^2	σ_2 N/mm^2	σ_3 N/mm^2		
1,5	409,9	-85,3	-405,6	3,476	1,42
1,8	412,2	-68,3	-385,2	3,311	1,41
2,0	375,2	61,7	-380,2	3,010	1,53
2,2	391,5	63,0	-375,1	3,126	1,48
2,5	375,7	57,4	-378,1	3,010	1,53

For the position of rotation of ±45º, strain is significantly lower so this analysis is omitted in the results. The load acting on the lumbar structure is approximated (ball weight of 25 kg at a distance of 250 mm). Material of lumbar structure is carburizing steel 16MnCr5.

The geometric model of the lumbar structure contains numerous geometric elements that have no significance for FEM modeling because it does not affect the stress-deformity image of the object. Therefore, an idealized model is formed in which insignificant details are casted off (pins and screws are approximated with rollers). The discretized model is developed based on the model zone and adjusted number of contact surface elements and consisted of 44.534 nodes and 23.089 finite elements in form of a tetrahedron.

In Tab. 1 is given an overview of the main stresses (σ) and the resultant displacement (u_{res}) for five different thickness (δ) bearing plates (horizontal support), for the

position of lateral flexion ±30º. In Tab. 2 is given an overview of the main stresses (σ) and the resultant displacement (u_{res}) for the position of lateral flexion ±30º + rotation ±45º. Tables show a relatively high value of resultant displacements that are higher in case of lateral flexion ±30º + rotation ±45º. Higher stresses and lower factor of safety are for the position of lateral flexion ±30º. From Fig. 5-a i Fig. 5-c it is impossible to determine the zone of maximum stresses, that is why parts of the lumbar structure that are assumed to be most loaded - vertical support (Fig. 6-a) and pin (Fig. 6-b,c,d) are analysed. Further FEM analysis determined a zone of maximum stresses - one of the pin joint links, whose main normal stresses and the factor of safety are given in Tab. 1 i Tab. 2.

Based on the analysis of the FEM modeling results two problems stand out: high values of stress in the pin and the large resultant displacements of bearing plates. The first problem would likely lead to self-locking joint link, because of the intensity and nature of the load, and the other to the vibration of the lumbar structure, which would adversely affect the functionality, control and repeatability of movement.

Pin calculation (according to theory of Strength of Material) gives factor of safety above 8, which is 6 time higher than the factor of safety obtained from FEM modeling.

4. CONCLUSION

In paper is presented FEM modeling of lumbar structures, designed for humanoid robots, with the aim to reconstruct the existing solutions and to expand the range of movements. Multi-segment lumbar structure, which is based on human spine, allows lateral flexion movements of ±30º and rotation of ±45º, as well as the combination of these two movements.

FEM modeling is performed for the amplitude positions of the structure and for five different thickness of the bearing plates. The highest stress values are for "lateral flexion", while the highest resultant displacement elements of structure occur in combination "lateral flexion + rotation" (values are 10 times higher than required). The factor of safety for stresses is 1,4. Zone of maximum stresses is one of the pin joint links structure.

Based on the analysis results of FEM modeling two problems stand out: high values of stress in the pin and the large resultant displacements of bearing plates. The first problem would likely lead to self-locking joint link, because of the intensity and nature of the load, and the other to the vibration of the lumbar structure, which would adversely affect the functionality, control and repeatability of movement.

Pin calculation (according to theory of Strength of Material) gives factor of safety above 8, which is 6 time higher than the factor of safety obtained from FEM modeling.

Further work on the development of lumbar structure (beside to the existing movement of lateral flexion and rotation) will include an analysis of models with movements forward - flexion and backward - extension. It will, besides widening of range of spinal positions and robots arm's reach, contribute to more natural and human-like movements.

In this development phase of lumbar structure, movements of flexion are ignored, because the bending of the spine forward to an angle of 45º is achieved by rotation in the hip joints.

In developing lumbar structure it is necessary to solve the problem of high stresses in the joint links and large displacement of the bearing plates. Incorporation of the joint in the pelvis for movements forward - backward, will further increase the load and stresses of structure, which is necessary to examine on the new FEM model.

ACKNOWLEDGEMENT

This work was funded by the Ministry of education and science of the Republic of Serbia under contract III44008 and by Provincial secretariat for science and technological development under contract 114-451-2116/2011.

5. REFERENCES

[1] I. Mizuuchi, R. Tajima, T. Yoshikai, D. Sato, K. Nagashima, M. Inaba, Y. Kuniyoshi, and H. Inoue, "The Design and Control of the Flexible Spine of a Fully Tendon-Driven Humanoid "Kenta",", *Proceedings of the IEEE/RSJ International Conference on Intelligent Robots and Systems,* 2002, Lausanne, Switzerland, pp. 2527–2532.

[2] I. Mizuuchi, M. Inaba, and H. Inoue, "A Flexible Spine Human-Form Robot – Development and Control of the Posture of the Spine", *Proceedings of the 2001 IEEE/RSJ International Conference on Intelligent Robots and Systems*, 2001, Maui, Hawaii, pp. 2099–2104.

[3] M. Penčić, S. Savić, J. Tasevski, M. Raković and B. Borovac, "A Robot Multi-Segment Lumbar Spine – Mechanical Model and Control Algorithm", *The 6th PSU-UNS International Conference on Eng. and Technology (ICET-2013)*, Novi Sad, Serbia, May 15-17, 2013, Paper No. T10-2.1, pp. 1-5.

[4] M. Mihalj, "Humans anatomy", Educa, Novi Sad, 2001. (*in Serbian*)

[5] D. Obradović, Lj. Mijatov-Ukropina and Lj. Stojišić, "Osteology for Medicine Students", Zmaj, Novi Sad, 2003. (*in Serbian*)

[6] D. Nikolić, "Kinesiology", College of Health Studies, Ćuprija, 2007. (*in Serbian*)

[7] M. Penčić, "Lumbar Spine Development for Humanoid Robots", Master thesis, Faculty of Technical Sciences, University of Novi Sad, 2012. (*in Serbian*)

[8] S. Savić, M. Raković, M. Penčić and B. Borovac, "Nonlinear Motion Control of Humanoid Robot Upper-Body for Manipulation Task", Facta Universitatis: Automatic Control and Robotics, 2014. Vol. 13, No. 1, pp. 1-14.

The 7th International Conference on Engineering and Technology
ICET-2015, Phuket, June 19-20, 2015
Prince of Songkla University, Faculty of Engineering
Hat Yai, Songkhla, Thailand 90112

Low Population Density Influence on Waste Management System in Serbia

Dusan Milovanovic[1]*, Nemanja Stanisavljevic[1], Miodrag Zivancev[1], Bojan Batinic[1], Dejan Ubavin[1], Maja Djogo[1], Marjan Ranogajec[2]
[1]University of Novi Sad, Faculty of Technical Sciences, Novi Sad, Serbia
[2]Hertie School of Governance, Berlin, Germany
*Email of corresponding author: dusanmilovanovic@uns.ac.rs

Abstract: *Waste management practice in Serbia can generally be characterized as undeveloped, since waste management only includes waste collection and disposal on landfills. This practice resulted in over 3,600 waste disposal sites distributed all over the country. In order to reduce negative impacts associated with waste disposal (mostly on unsanitary controlled and uncontrolled landfills) the waste management strategy in Serbia is oriented towards construction of regional sanitary landfills. The largest problems in organised waste collection systems in Serbia are peripheral parts, mostly long-distance settlements, rural zones and inaccessible areas. The goal of this paper is to evaluate contribution of peripheral parts of five small municipalities in Serbia, to the overall improvement of waste management practice in municipalities. Hence, the influence of low populated part of selected municipalities on the future optimization of waste management systems is presented. Research within municipalities of Aleksandrovac, Bela Crkva, Krupanj, Kursumlija, Svilajnac included data collection about waste management systems and municipal waste management generation and composition. In addition material flow analysis was used to present the status quo of waste management in selected municipalities. Assessment of collected data about generated waste and population in central settlement of selected municipalities, as well as the data for all other settlements within each municipality is performed in order to assess the importance and influence of low-density areas on future optimization of waste management systems. Due to distinctiveness of certain municipalities there is a clear need for specific and adequate waste management system.*

Key Words: ***Population density / Waste disposal / Material flow analysis***

1. INTRODUCTION

Waste management practice in Serbia can generally be characterized as undeveloped, since waste management only includes waste collection and disposal on landfills. This practice resulted in over 3,600 waste disposal sites distributed all over the country. In order to reduce negative impacts associated with waste disposal (mostly on unsanitary controlled and uncontrolled landfills) the waste management strategy in Serbia is oriented towards construction of regional sanitary landfills.

The collection of MSW in the Republic of Serbia is generally based on the collection of mixed waste. Primary source separation, followed by the collection of separately collected fractions of (mostly) PET and paper, is implemented in several developed cities. The proportion of the population falling under an organised collection system in Serbia is around 60–65%. The largest problems in organised waste collection systems in Serbia are peripheral parts, mostly long-distance settlements, rural zones and inaccessible areas.

The goal of this paper is to evaluate contribution of peripheral parts of five small municipalities in Serbia, to the overall improvement of waste management practice in municipalities. Hence, the influence of low populated part of selected municipalities on the future optimization of waste management systems is presented.

2. METHODS

Based on considered criteria's (up to 30.000 inhabitants; level of development belonging to the second, third and fourth group; lack of private operator to provide services in waste management) following municipalities were selected for research: Aleksandrovac, Bela Crkva, Krupanj, Kuršumlija and Svilajnac,.

Methodology applied for the analysis consists from: analysis of municipal waste generation and composition; collection of data about agriculture waste generation; collection of data about industrial waste generation; modeling of status quo and development of waste management scenario by MFA; evaluation and comparison of the scenarios.

This research was performed by applying the Material Flow Analysis as basis for evaluation of status quo, and for further scenarios, evaluation and simulation of different alternatives of local waste management. Data

about municipal waste generation and composition from the industry and agriculture were used as an input for material flow analysis.

The joint characteristics of all investigated municipalities are:

- single public utility company in charge of collection and disposal of waste;
- partial waste collection, mainly from the urban areas;
- organized waste disposal at unsanitary municipal landfills (one per each municipality);
- existence of numerous wild dumpsites in rural parts.

The waste collection service is charged mostly by the size of living area per household, with the exception of the municipality of Svilajnac, where the fee is equal for all households in the amount of 270 RSD (2,35 EUR) per month.

Assessment of collected data about generated waste and population in central settlement of selected municipalities, as well as the data for all other settlements within each municipality is performed in order to assess the importance and influence of low-density areas on future optimization of waste management systems.

This paper presents detailed results of material flow analysis for a case study in municipality of Bela Crkva. The same scenarios are developed for each municipality. However, evaluation of results includes all five municipalities.

3. RESULTS AND DISCUSSION

Research was conducted on five selected Municipalities based on the defined criteria. Table below gives general data on waste management within the Municipalities, with the highlight on waste amounts in central settlement and other settlements in each Municipality.

Table 1. *General waste management data*

Municipality	Amount of waste in the central settlement t/year	Amount of waste in peripheral settlements t/year	Number of settlements
Aleksandrovac	1866,97	6040,162	55
Bela Crkva	2877,666	2731,3165	14
Krupanj	1661,715	4827,739	23
Kuršumlija	3152,17	1505,525	90
Svilajnac	2593,204	4049,84	22
Municipality	**Generated amount per capita kg/cap/year average**	**Population of central settlement**	**Population of the Municipality**
Aleksandrovac	298	6265	26534
Bela Crkva	324,5	8868	17285
Krupanj	373	4455	17398
Kuršumlija	245	12866	19011
Svilajnac	284	9131	23391

The common characteristic for the Municipalities is that the all settlements (central and peripheral) are distant from each other, which makes waste collection system difficult and costly.

Municipality of Bela Crkva (Picture 2.) takes up the area of 353 km², with the population of 17.367 people. The Municipality annually generates around 5634 tons of municipal solid waste. Current situation in municipal waste management of Bela Crkva includes only partial collection of generated waste. 60% of the total population in the municipality is covered by waste collection system. Collected waste is disposed on landfill that does not meet the standards of sanitary waste disposal. Remaining waste generated in the municipality (2300 tons per year) is not in the system of municipal waste management and it is usually disposed on illegal dumps. Primary separation of recyclable materials is on a very low level. Only 3 tons of PET per year are separately collected as potential recyclables. Status quo of waste management in municipality Bela Crkva is presented in Figure 1.

Picture 2. *Bela Crka Municipality with the central settlement and other settlements*

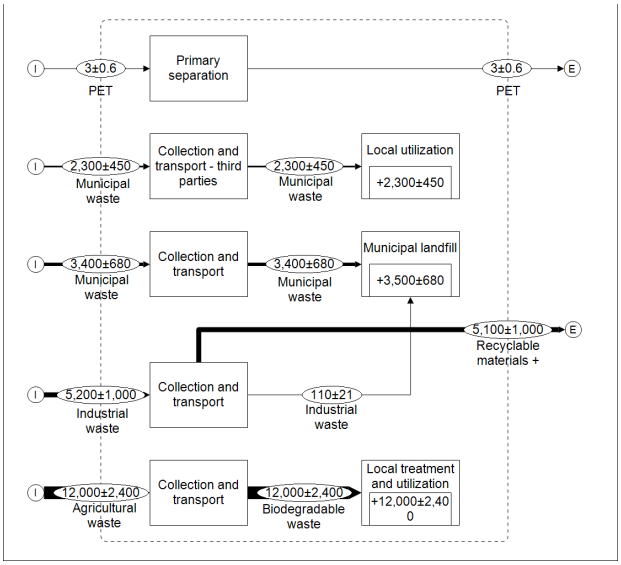

Figure 1: *Status quo, t/yr*

Scenario I

Waste management in the municipality of Bela Crkva in scenario 1 primarily involves increase of coverage of organized municipal waste collection system to up to 100 % of the population. It is expected that 25 % of recyclable fractions (paper/cardboard, PET, glass, metal) will be separated at organized collection point. "Home composting" is provided only for households with individual type of housing outside urban settlements. Around 700 tons of garden and kitchen waste will be

treated in home composting units. Generated compost will be used within the municipality (depending on produced compost quality). Mixed MSW will be collected and transported directly to the regional center for further processing together with inert industrial waste (106 tons per year). Scenario I for the municipality of Bela Crkva is presented in the Figure 2. Red export flow is transported to the waste management regional center

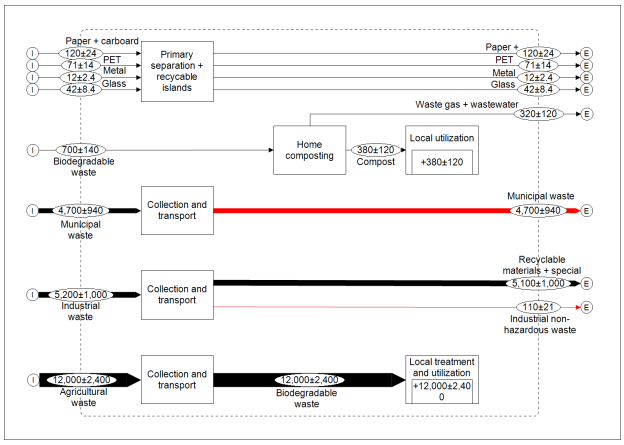

Figure 2. *Scenario I, t/yr*

Scenario II

In scenario II municipal solid waste will be collected in two bins. In a dry bin, and wet bin. 1200 tons and 3500 tons of recyclable materials will be collected respectively. Waste collected in dry bin will be transported to the waste separation plant (located in municipality) where the different categories of waste will be separated. Waste collected in a wet bin will be transported directly to the regional center, without pre-treatment, for further processing.

Scenario III

In scenario III in addition to home composting of garden and kitchen waste, the primary separation of 440 tons of green garden waste is introduced. This fraction will be composted in central composting plant and compost will be utilized within the municipality. Municipal solid waste will be collected in two bins. In dry bin recyclable materials will be collected and transported to the separation plant where the different categories of waste will be separated. In wet bin residual waste will be collected and transported to the biological pre-treatment in the municipality. After treatment, stabilized waste will be transported to a regional center for further processing.

Scenario IV

In this scenario MSW will be collected in three bins. Recyclable materials collected in the dry bin will be transported to the separation plant, where the separation of recyclables will take place. Biodegradable waste collected in bio bin will be transported to anaerobic digestion plant consisted of anaerobic unit mechanical pre-treatment and composting unit. Together with biodegradable municipal waste, suitable agriculture waste will be treated. In third bin residual waste will be collected. This fraction will be without treatment transported directly to the regional center for further management.

Cost analysis

Material flow analysis has described how potential waste management upgrades in selected Municipalities could improve and optimize current systems, and therefore reduce costs and even generate revenue in the future (Scenario IV). Figures 3 and 4 present the level of investment and operational costs for each scenario in each selected Municipality.

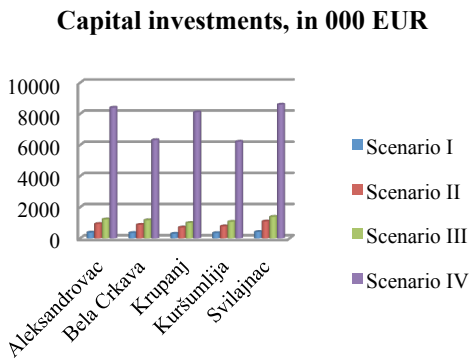

Figure 3. *Capital investments required for each Scenario*

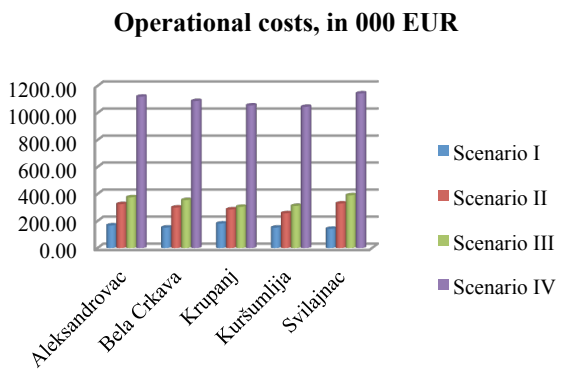

Figure 4. *Annual operational costs for each Scenario*

4. CONCLUSIONS

Developed scenarios indicate the difference between waste generation contribution among peripheral and central part of municipalities, and clearly indicate the importance of prioritization between different populated areas.

Identified problems of waste management in selected municipalities include: low GDP and therefore lower income, subsequently causing smaller amounts of waste, distributed on longer distances within municipalities. Due to distinctiveness of certain municipalities there is a clear need for specific and adequate waste management system.

Since, peripheral settlements do not generate sufficient amount of waste, and the costs of waste collection from such distant areas are high and inefficient, home composting and other domestic on-site

waste treatment options are the most adequate solutions in low population density areas.

5. ACKNOWLEDGMENT

This research is performed under financial support by GIZ, in the framework of „IMPACT“ project in Serbia.

6. REFERENCES

[1] Belevi, H. & Baccini, P. (1989): Long-term behavior of municipal solid waste landfills. Waste Management & Research, 7, 43–56.
[2] Brunner P.H., Fellner J., (2006) “Setting priorities for waste management strategies in developing countries,” Waste Management & Research 25, 234-240
[3] Brunner P.H., Recheberger H., (2004) Practical Handbook of Material Flow Analysis, Lewis Publishers, USA.
[4] IPCC 2006, 2006 IPCC Guidelines for National Greenhouse Gas Inventories, Prepared by the National Greenhouse Gas Inventories Programme, Eggleston H.S., Buendia L., Miwa K., Ngara T. and Tanabe K. (eds). Published: IGES, Japan.
[5] Obernosterer et al., “Urban Metabolism - The City of Vienna”, Institute for Water Quality and Waste Management Vienna University of Technology Austria, 1998
[6] Stanisavljevic, N., Ubavin, D., Batinic, B., Fellner, J., & Vujic, G. (2012). Methane emissions from landfills in Serbia and potential mitigation strategies: a case study. Waste management & research: The journal of the International Solid Wastes and Public Cleansing Association, ISWA, 30(10), 1095–103. doi:10.1177/0734242X12451867
[7] Vujić G., Jovičić N., Redžić N., Jovičič G, Batinić B., Stanisavljević N., Omran A., A fast method for the analysis of municipal solid waste in developing countries - case study of Serbia, Environmental Engineering and Management Journal, August 2010, Vol.9, No. 8, 1021-1029
[8] Brkić M., Janić T., Potential amounts of biomass for production of energy in Serbia, Journal of Contemporary Agricultural Engineering, November 2011, Vol.37, No. 3, 225-234
[9] Batzias, F. a., Sidiras, D. K., & Spyrou, E. K. (2005). Evaluating livestock manures for biogas production: a GIS based method. *Renewable Energy*, *30*(8), 1161–1176. doi:10.1016/j.renene.2004.10.001

The 7th International Conference on Engineering and Technology
ICET-2015, Phuket, June 19-20, 2015
Prince of Songkla University, Faculty of Engineering
Hat Yai, Songkhla, Thailand 90112

Investigation of air pressure drop through porous wheat straw bed

Đorđije Doder[1]*, Borivoj Stepanov[2]
[1] University of Novi Sad, Faculty of Technical Sciences, Novi Sad, Serbia
[2]University of Novi Sad, Faculty of Technical Sciences, Novi Sad, Serbia
*Email of corresponding author: dj.doder@uns.ac.rs

Abstract: *In this paper, the results of experimental investigation of air pressure drop while flowing through wheat straw bed are shown. According to Darcy's law, the smaller is porosity of bed, the bigger pressure drop will appear. Investigation was conducted using three different porosities (or three bed densities), and for two different air flow rates. These results may be important for future development of efficient biomass combustion facilities. The measurement methods and facility characteristics are described in more details.*

Key Words: ***Biomass combustion, air pressure drop, porosity, baled straw***

1. INTRODUCTION

Biomass represents one of the most valuable energy resources nowadays. Recently, it becomes more popular since using of this resource could provide sustainable exploitation and positive ecology effects. Biomass could be combusted in existing facilities with certain adaptation, or in new facilities especially designed for such purposes.

Serbia has great potential for using biomass as primary energy resource. Solid agricultural waste stands out as one of the most reliable resources, because of its big amounts and quality at first place. Next table shows the amount of agricultural biomass gathered in province of Vojvodina during 2003-2007 period.

Table 1. *Biomass production in Vojvodina region from 2003. to 2007. [5]:*

Biomass type	Yield [tones/year]
Wheat	1.120.074
Barley	154.964
Oats	12.14
Rye	4.506
Soy	620.358

From previous table, we can conclude that wheat straw is the most important resource, so this experiment was conducted just for wheat.

Due to all of these reasons, combustion science and industry in Serbia should be focused on designing furnaces of high efficiency.

In conventional furnaces, straw bale combust while air circulates around it, but if air flows through the bale, it would result in better combustion process, with total facility efficiency increased, and smaller emission of CO in combustion products. So, with internal air flow, we can significantly intensify process of combustion, because that is how we enhance overall contact surface of air and fuel particles.

The aim of this paper was to determine total pressure drop as well as local pressure drops along straw bed height, so we can get better insight of internal air flows through porous bed and made optimal combustion conditions, considering flow rate of theoretical air for combustion.

Hence, we should primarily provide better availability of air to individual fuel particles, instead of immediately increasing air flow rate.

2. POROUS MEDIA FLOW FUNDAMENTALS

Mathematical models that describe flow through porous bed have their role to predict mass and energy transport through the media. They are created from laws of conservation of mass, energy and momentum with application of thermodynamic relations. If we define porosity of media as:

$$\varepsilon = \frac{V_p}{V_t} = \frac{V_p}{V_p + V_s} \tag{1}$$

where ε is porosity and V_p, V_p, and V_s are volumes of pores, total volume of bed and volume of solid particles, respectively. Porosity estimation is experimental, it is non-dimensional (m^3/m^3) and has value between 0 and 1.

We can express relation between porosity and pressure gradient from different forms of Darcy's law The most relevant form is ([1] or [2]):

$$q = -\frac{1}{\mu} K(\nabla p - \rho g) \tag{2}$$

where q represents Darcy's velocity, K permeability, ∇p is pressure gradient, μ dynamic viscosity, ρ fluid density and g is gravitational acceleration.

If we use bed porosity instead of permeability, where relation between these factors is:

$$K = \frac{d^2}{32} \cdot \varepsilon \qquad (3)$$

where d is average diameter of one individual, we get the different shape of Darcy's law, where total pressure drop is involved:

$$\frac{\Delta p}{L} = \left(\frac{\mu}{K}\right)\frac{dV}{dt}\frac{1}{A} \qquad (4)$$

or

$$\Delta p = \frac{32\mu}{\varepsilon d^2} \cdot \dot{V} \cdot \frac{1}{A} \cdot L \qquad (5)$$

where A presents cross-sectional surface of bed, and L is bed height, or length.

Porosity is variable across the layer, so the average porosity was estimated by the method of "pouring" where two vessels were used – one with straw placed inside and one without it. If we pour up both vessels to the same height, volume (or mass) of filling liquid will be different and then we can calculate porosity just using ratio of this volumes. The calculated porosities are 0.91, 0.82 and 0.79, for three different densities that are chosen according to dimensions of measuring vessels in laboratory.

3. EXPERIMENTAL INVESTIGATION

Investigation was conducted on experimental facility placed in laboratory for thermal engineering, at Institute of mechanical engineering building, Faculty of technical sciences, Novi Sad University.

3.1. Measuring method and facility description

Figure 1. Working part of facility with pressure measuring ducts

Pressure was measured on three points along the bed height. For this purposes, classical method of U-tubes was used, so statical pressure inside the bed was calculated from U-tube pressure difference readings.

Facility scheme is shown in next figure, where 1 and 1' points are presenting working parts of facility - 1 was for originally designed configuration, but this configuration was upgraded by adding 1' part, which has similar characteristics as part 1, but it's smaller and more convenient because of small availability of fuel, i.e. wheat straw. Point 2 is air duct, 3 is electrical centrifugal fan, 4 is air inlet, in point 5 there is flow measuring aperture, 6 is regulating valve, 7 is inlet air pressure measuring point, and 8,9 and 10 are other pressure measuring points. After 10 air comes to outlet.

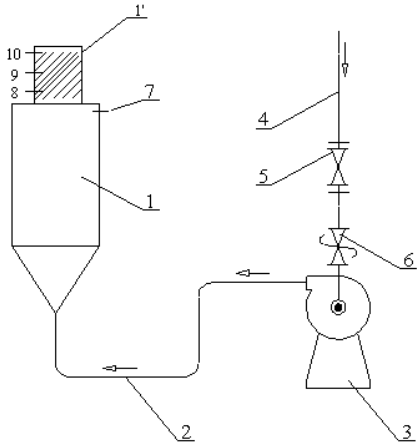

Figure 2. Facility scheme

Flow rate was measured using already mentioned aperture in point 5, by measuring pressure differences before and after aperture disturbance, and calculating flow from relevant relations. The calculation and fixing parameters are proposed in literature [3]. Flow rates measured are very close to fan's flow rates given by manufacturer, and that is confirmation that flow rate calculations are correct.

Investigation was conducted for three different porosities, and for two air flow rates for each porosity - full and approximately 50 % reduced flow rate (by 50% reduction, half'-closed valve is understood). Calculated flow rates are 370 m^3/h of air for open valve and 279 m^3/h for half-closed valve. Fan manufacturer's data shows flow rate of 400 m^3/h, which is close to 370 m^3/h if we neglect flow resistances.

4. RESULTS ANALISYS AND CONCLUSION

In next diagrams, obtained results are presented. Upper curve represents characteristic of full flow rate and lower one characteristic of reduced flow rate.

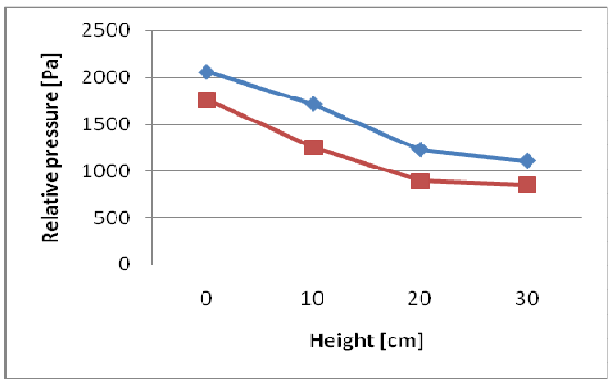

Figure 3. Pressure drop for porosity of ε=0.91

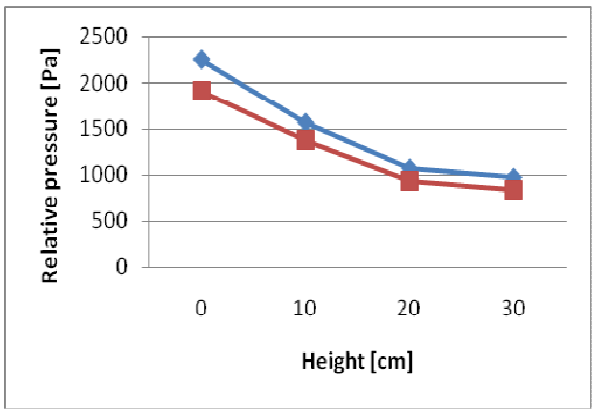

Figure 4. Pressure drop for porosity of ε=0.82

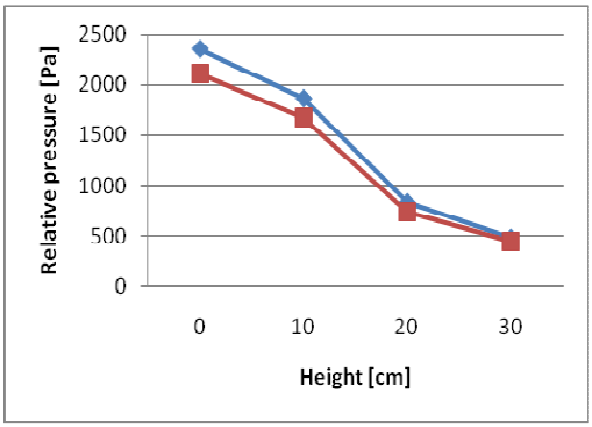

Figure 5. Pressure drop for porosity of ε=0.79

In the end, total pressure drop dependence in relation to bed porosity can be expressed with next diagram. Again, upper curve is for full flow rate:

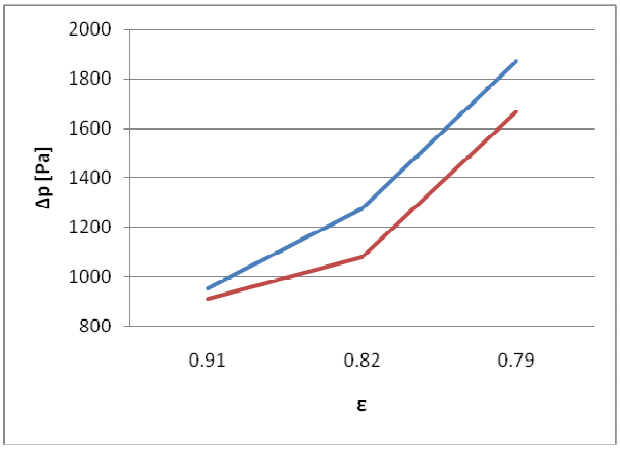

Figure 6. Pressure difference for different porosities

After drawing of all diagrams, we can see that they are corresponding to relations (2) and (5).

If we analyze them, we can make some conclusions that are important for combustion technology. For instance, we can confirm hypothesis that we first should provide better contact between air and fuel particles, and after that eventually increase the amount of air fed to combustion chamber. Mechanically, we can obtain this with so-called "shaking" of straw bale, while air should be brought from down side of bale, so it can flow through. Anyway, different combustion technologies can offer different solutions, but this results should provide certain theoretical basis for kinetics of combustion. We can notice that higher points have smaller pressure drops (or smaller pressure gradients). This fact could be explained with assumption of appearance of developed porous media flow, i.e. main stream is split in many smaller streamlines that stand friction and drag forces of less intensity.

Also, we can conclude that both characteristic curves are very similar, and practically we can predict distance between them. As height is growing, curves of both flows become very close to each other, although flow rate difference is relatively big. This means, that bigger flow rates don't have significant influence on outer pressure, what supports previously mentioned hypothesis.

This results should be compared with realistic bale porosities, since that was not possible in our laboratory conditions, in first place because of small straw reserves. Relation (5) also shows pressure drop dependence of bale cross-sectional surface, which is logical because bigger surface existence leads to a bigger friction force appearance.

There also may be some errors done during the experimental process. The errors that could appear are those from bad read-offs of pressure differences in U-tubes, or from neglecting the bale internal humidity. Anyway, this kind of errors doesn't affect curves shapes, nor their distance along the diagram.

5. REFERENCES

[1] W. G. Gray, K. O'Neill, “On the general equations for flow in porous media and their reduction to Darcy's Law,” *Water Resources Research, Volume 12, Issue 2, pages 148–154, April 1976*

[2] M. Dong, Francis A.L. Dullien: "*Multiphase flow handbook - Porous Media Flows“, 2006*

[3] M. Bukurov: "*Mehanika fluida (Fluid Mechanics)“, University of Novi Sad, Faculty of Technical Sciences, 2009*

[4] T. Janić, M. Brkić, Z. Kurunci, *"Kinetics of wheat straw bales combustion", Agricultural Faculty, University of Novi Sad, 2009*

[5] http://apv-nauka.ns.ac.rs, "*Develpoment of biomass market“,2010*

The 7th International Conference on Engineering and Technology
ICET-2015, Phuket, June 19-20, 2015
Prince of Songkla University, Faculty of Engineering
Hat Yai, Songkhla, Thailand 90112

Speech Emotion Classifier using Support Vector Machine with FFT and MFCC

Chaidiaw Thiangtham [1]*, Jakkree Srinonchat [2]
[1,2] Signal Processing Research Laboratory, Department of Electronics and Telecommunications Engineering, Faculty of Engineering, Rajamangala University of Thanyaburi, Thailand
*chaidiaw@gmail.com

Abstract: *Speech emotion recognition (SER) research area is recently interested to apply for intelligent system such as a communication by human speech to machine, robot or computer. Speech emotion feature extraction, which is a key major to achieve the speech emotion classification, is an importance step for SER. This article presents the speech emotion classifier using support vector machine (SVM) with Fast Fourier transform (FFT) and Mel Frequency Cepstral Coefficient (MFCC). These techniques use the advantage of frequency to operate the system. Berlin Database of Emotion Speech (BDES) is used as the input speech. It contains 7 emotion speeches: anger, boredom, disgust, fear, happiness, neutral and sadness. Support vector machine uses for classification emotion speech. The result shown that the support vector machine performs to classify the speech emotion in the best condition with the FFT and MFCC which it depends on the type of emotion. SVM gives the highest accuracy classification value as 93% between sadness speech emotions with the other speech. It means that the sadness speech emotion is distingue from the other speech.*

Key Words: ***Speech emotion feature/ FFT/ MFCC/ Speech emotion recognition***

1. INTRODUCTION

Speech Emotion Recognition is interesting to research in recent years because it can apply to many application such as a communication with robot or computer, E-leaning system for select suitable lesson for student and call center system for detect emotional speech from human. To achieve the speech emotion recognition system, speech emotion feature extraction is a major key it. The speech feature of each speech emotion can identify and classify speech emotion type. There are many ways for extracted feature from speech such as Linear Predictive Coefficients (LPC), Linear Spectral Frequency (LSF), Zero-Crossing (ZC), Mel-Frequency Cepstrum Coefficients (MFCC) [1-6] etc, which have an advantage and disadvantage in each technique.

There are some of research works which have been done in the speech emotion recognition. A study of zero-crossing with peak-amplitudes in speech emotion classification is introduced in [4]. The results shown that it provides the technique to extract the emotion feature in time-domain, which still got the problem in amplitude shifting. The emotion recognition from speech is descripted in [5]. It used the Gaussian Mixture Model (GMM) for extractor of feature speech. The GMM is provided the good results to reduce the back ground noise, however it still have to focus on random noise in GMM for recognition model. The speech emotion recognition using hidden markov model and support vector machine is explained in [6]. The results shown the average performance of recognition system according to the features of speech emotion still has got the error information. Thus [1-6] provides the recognition performance which still requires more focus on speech features.

This article present speech emotion feature extraction using the support vector machine with Fast Fourier Transform (FFT) and Mel-Frequency Cepstrum Coefficients (MFCC) which the FFT can provide the faster computation time than the Discrete Fourier Transform (DFT) [10]. This article uses the standard Berlin Database of Emotion Speech (BDES), which is open source can download from website, to be the input signal. It contains 7 emotion speeches: anger, boredom, disgust, fear, happiness, neutral and sadness. All sentence speech by professional actors and actresses (5 actors and 5 actresses). The FFT, MFCC and Support Vector Machine are explaining in next section. Also the experiment and result provide to be discussed.

2. FEATURE EXTRACTION

2.1. Fast Fourier Transform

The Fast Fourier transform (FFT) [7] is a discrete Fourier transform algorithm which reduces the number of computations needed for N points from 2 N2 to 2 N lg N , where lg is the base-2 logarithm as shown in (1)

$$X_k = \sum_{n=0}^{N-1} x_n e^{-i2\pi k \frac{n}{N}} \ , k = 0, \dots, N-1 \quad (1)$$

Energy Spectral Density and Power Spectral Density

Energy, or power, spectrum analysis is concerned with the distribution of the signal energy or power in frequency domain [7]. For a deterministic discrete-time signal, the energy spectral density is defined as

$$|X(f)|^2 = \left| \sum_{m=-\infty}^{\infty} x(m) e^{-j2\pi f m} \right|^2 \quad (2)$$

The energy spectrum of x(m) may be expressed as the Fourier transform of the autocorrelation function of x(m) as

$$|X(f)|^2 = X(f)X^*(f) = \sum_{m=-\infty}^{\infty} r_{xx}(m) e^{-j2\pi f m} \quad (3)$$

Where the variable rxx(m) is the autocorrelation function of x(m). The Fourier transform exists only for finite energy signals. An important theoretical class of signals consists of stationary stochastic signals which, since they are stationary, are in finitely long, have infinite energy, and therefore do not possess a Fourier transform. For stochastic signals the quantity of interest is the power spectrum density defined as the Fourier transform of the autocorrelation function [7].

Non-Parametric Power Spectrum Estimation

The classic method of estimation of the power density spectrum of an N sample record is the periodgram introduced by Sir Arthur Schuster in 1989. The periodogram is defined as

$$\hat{P}xx(f) = \frac{1}{N} \left| \sum_{m=0}^{N-1} x(m)\, e^{-j2\pi f m} \right|^2 = \frac{1}{N} |X(f)|^2 \quad (4)$$

The power spectral density function or power spectrum for short, defined in (4) is the basic of non-parametric methods of spectral estimation. Due to finite length and the random nature of most signals, the spectra obtained from different records of signal very randomly about the average spectrum. A number of methods have been developed which attempt to reduce the variance of the periodogram [7].

2.2. Mel-Frequency Cepstrum Coefficients (MFCC)

Mel Frequency Cepstral Coefficients (MFCCs) are a feature extraction widely used in speech emotion recognition. The MFCC is one of feature extraction for extract speech parameter which includes background noise and emotion. Speech generated by human which sound determines by shape vocal tract, tongue, teeth etc. The shape vocal tract also generated power spectrum and MFCC will find accurately represent of speech. Because an audio signal is constantly changing. So we have to frame the signal into short frames about 20-40 ms a frame. Then calculate the periodogram estimate of power spectrum and applied the Mel filter bank to power spectrum and then sum the energy of each filter and of each frame. The Mel scale will makes our features match more closely human hear. We are converting from frequency to Mel scale by using the following formula.

$$Mel(f) = 2595 \times log\left(1 + \frac{f}{700}\right) \quad (5)$$

And to go from Mel scale back to frequency:

$$M^{-1}(m) = 700(exp(m/1125) - 1) \quad (6)$$

The final step takes the Discrete Cosine Transform (DCT) of the log filter bank energy by using the following formula.

$$c[n] = \sum_{m=1}^{M} F[m]\, cos\left(\frac{\pi n(m-1)}{2M}\right), \quad 0 \le n \le M \quad (7)$$

2.3. Support Vector Machine (SVM)

Support vector machine is an algorithms for solve the problem of data classification and data analyze. Support Vector Machine creates the linear line for separate data set into two classes, which this line is called the hyper plane. In partially, there are many hyperplane in implementation but SVM will select the best linear line. The best linear line is has a maximum margin to the nearest data point. In Figure 1, the H2 is the best linear line because it separates data with the maximum margin and samples data on the margin. This is called the support vectors.

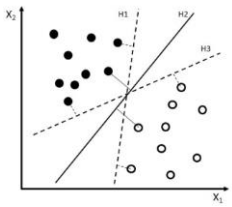

Fig. 1. Hyperplane

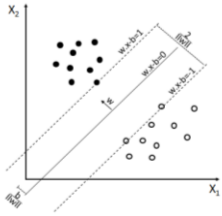

Fig. 2. SVM Structure

Support Vector Machine classifiers is basically performed very good for classification linearly data point by using the following formula.

For x of the first class.

$$\langle w.x \rangle - b_0 \ge 1, \forall y = 1 \quad (8)$$

For x of the second class.

$$\langle w.x \rangle - b_0 \le -1, \forall y = -1 \quad (9)$$

Where, (x, y) is the pair of training set. Here, $x \in R^n$ and

$$y \in \{+1, -1\} \quad (10)$$

SVM classifiers applied Kernel function for nonlinear classifier by mapping the data into a higher dimensional space which called the feature space where data can be classified using a linear classifier by using the following formula.

Polynomial Kernel:

$$k(x_i, x_j) = (1 + x_i . x_j)^d \quad (11)$$

Radial Basis Function Kernel:

$$k(x_i, x_j) = exp(-\gamma \parallel x_i - x_j \parallel^2) \quad (12)$$

Sigmoid Kernel:

$$k(x_i, x_j) = tanh(kx_i . x_j) - \delta \quad (13)$$

3. EXPERIMENT AND RESULT

Berlin Emotion Database (BDES) is used to be the speech input to test in this experiment. The BDES is record by Technical University of Berlin. There are 10 professional artists speakers (5 male and 5 female) and speaker's old between 21-36 years old. This data base has seven difference emotion speeches for speak emotion speech and record with sampling frequency of 16 kHz, 16 bit, mono audio file in wav format. Those data contains of 10 sentences in each person, five short and five long

sentences. Every emotion speech is screened by twenty professional listeners. First data base consist about 800 utterances and after screened pass about 500 utterances. Berlin Emotion Database easy for access and download from website. It is very useful for speech processing research. In this research, firstly, speech emotion is pass through pre-emphasis for improve the signal-to-noise ratio and reduce discontinuities in the end of each frame, which includes the framing, windowing and filtering. The FFT and MFCC are used to speech emotion feature extraction. Then, the speech emotion feature is classified using Hold-Out cross validation for support vector machine.

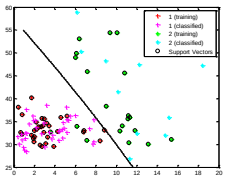

Fig.3.Anger with Boredom

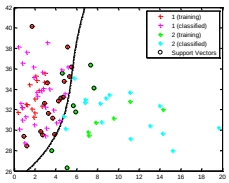

Fig. 4. Anger with Fear

3.1. Fast Fourier Transform

Table 1. *FFT female emotion speech*

Emotion	Anger	Boredom	Disgust	Fear	Happiness	Neutral	Sadness	Average
Anger		92	97	88	56	77	96	84
Boredom	93		62	63	77	56	71	70
Disgust	81	62		40	71	55	88	66
Fear	91	62	42		75	52	86	68
Happiness	66	73	69	80		63	77	71
Neutral	83	64	62	58	81		77	71
Sadness	99	74	82	77	83	79		83
Average all speech emotion = 73%								

Table 1. The average accuracy value of emotion classification is 73%. The anger emotional speech is clearly different from the other emotional speech, which it shown the average accuracy value as 84%. In contrast, the disgust provides the average accuracy value as 66% which it is a minimum distingue form the other speech.

Table 2. *FFT male emotion speech*

Emotion	Anger	Boredom	Disgust	Fear	Happiness	Neutral	Sadness	Average
Anger		90	90	74	67	86	94	84
Boredom	89		87	88	78	85	70	83
Disgust	90	90		47	80	53	100	77
Fear	73	96	83		73	92	100	86
Happiness	49	80	72	58		65	94	70
Neutral	88	72	80	88	75		82	81
Sadness	96	68	100	100	97	92		92
Average all speech emotion = 81%								

Table 2. The average accuracy value of emotion classification is 81%. The sadness emotional speech is clearly different from the other emotional speech, which it shown the average accuracy value as 92%. In contrast, the happiness provides the average accuracy value as 70% which it is a minimum distingue form the other speech.

3.2. Mel Frequency Cepstrum Coefficient

Table 3. *MFCC female emotion speech*

Emotion	Anger	Boredom	Disgust	Fear	Happiness	Neutral	Sadness	Average
Anger		57	81	64	56	58	61	63
Boredom	77		75	62	89	79	80	77
Disgust	79	80		70	80	88	85	80
Fear	72	58	65		91	94	92	79
Happiness	82	91	71	78		75	80	80
Neutral	99	80	94	89	76		52	82
Sadness	99	80	93	87	89	53		84
Average all speech emotion = 77%								

Table 3. The average accuracy value of emotion classification is 77%. The sadness emotional speech is clearly different from the other emotional speech, which it shown the average accuracy value as 84%. In contrast, the anger provides the average accuracy value as 63% which it is a minimum distingue form the other speech.

Table 4. *MFCC male emotion speech*

Emotion	Anger	Boredom	Disgust	Fear	Happiness	Neutral	Sadness	Average
Anger		70	90	69	59	59	80	71
Boredom	85		73	64	71	73	65	72
Disgust	57	47		47	44	83	75	59
Fear	67	66	77		80	75	78	74
Happiness	74	53	80	84		65	74	72
Neutral	85	63	85	78	65		70	74
Sadness	92	53	70	78	91	70		76
Average all speech emotion = 71%								

Table 4. The average accuracy value of emotion classification is 71%. The sadness emotional speech is clearly different from the other emotional speech, which it shown the average accuracy value as 76%. In contrast, the disgust provides the average accuracy value as 59% which it is a minimum distingue form the other speech.

3.3. Fast Fourier Transform + Mel Frequency Cepstrum Coefficient

Table 5. *FFT+MFCC female emotion speech*

Emotion	Anger	Boredom	Disgust	Fear	Happiness	Neutral	Sadness	Average
Anger		89	76	91	83	98	98	89
Boredom	94		82	65	88	91	93	86
Disgust	87	83		58	71	86	83	78
Fear	87	68	60		95	92	82	81
Happiness	84	92	77	92		80	89	86
Neutral	96	87	89	92	80		69	86
Sadness	98	96	90	88	91	83		91
Average all speech emotion = 85%								

Table 5. The average accuracy value of emotion classification is 85%. The sadness emotional speech is clearly different from the other emotional speech, which it shown the average accuracy value as 91%. In contrast, the disgust provides the average accuracy value as 78% which it is a minimum distingue form the other speech.

Table 5. *FFT+MFCC male emotion speech*

Emotion	Anger	Boredom	Disgust	Fear	Happiness	Neutral	Sadness	Average
Anger		91	93	91	71	98	99	91
Boredom	93		77	84	84	80	86	84
Disgust	83	88		57	68	89	70	76
Fear	95	86	83		76	92	98	88
Happiness	79	78	96	76		80	91	83
Neutral	97	75	95	92	78		90	88
Sadness	96	75	100	100	97	90		93
Average all speech emotion = 86%								

Table 5. The average accuracy value of emotion classification is 86%. The sadness emotional speech is clearly different from the other emotional speech, which it shown the average accuracy value as 93%. In contrast, the disgust provides the average accuracy value as 76% which it is a minimum distingue form the other speech.

4. SUMMARY

This article presents speech emotion classify using support vector machine with FFT and MFCC. The FFT and MFCC are specially used for features extraction. The BDES is used as speech input, which contains emotional speech more than 460 speeches. The SVM is used to classify the type of the speech emotion which exploits the frequency domain coefficients. The experiment results are show in Table 1-6. It found that the SVM gives 85% and 86% of average accuracy, with the coefficients of FFT+MFCC in the term of female and male speech respectively, which are better than FFT and MFCC only. In the term of emotion type, it found that the sadness emotion speech is clearly a difference from other emotional speech which the SVM provides 93% of average accuracy from the other speech. While the disgust emotion speech has got only 76% of average accuracy from the other emotion speech.

5. REFERENCES

[1] D. D. Joshi and M. B. Zalte, Speech Emotion Recognition: A Review, J. Electronics and Communication Engineering, 4 (2013) 36 – 41

[2] M. E. Ayadi, M. S. Kamel and F. Karray, Survey on Speech Emotion Recognition: Features, Classification Schemes, and Databases, 4 (2011), 572 - 587

[3] I. A. Chiriacescu, Automatic Emotion Analysis Based On Speech, M.Sc. THESIS Delft University of Technology, 2009

[4] S. Ying and X. Zhang, A study of zero-crossing with peak-amplitudes in speech emotion classification, International Conference on Pervasive Computing, Signal Processing and Applications, 2010, pp. 271 – 274.

[5] N. Thapliyal and G. Amoli, Speech based emotion recognition with Gaussian mixture model, J. Advanced Research in Computer Engineering & Technology, 5 (2012), 45 -52.

[6] A. B. Ingale and D.S.Chaudhari, Speech emotion recognition using hidden markov model and support vector machine, J. Advanced Engineering Research and Studies, 3 (2012), 112- 120.

[7] S. V. Vaseghi, Advanced signal processing and digital noise reduction, Wiley&sons, 2012.

[8] Thapanee Seehapoch and Sartra Wongthanavasu,Speech Emotion Recognition Using Support Vector Machines, 2013 5th International Conference on Knowledge and Smart Technology (KST)

[9] A.Milton, S.Sharmy Roy and Tamil Selvi, SVM Scheme for Speech Emotion Recognition using MFCC Feature, J. Computer Applications (0975-8887) Volume 69- No.9, May 2013

[10] G.Purna Chandra Rao, B.Ashok and B.Saritha, Design and Implantation of High Speed FFT Processor for OFDMA System Using FPGA, J. Advanced Research in Computer and Communication Engineering Vol. 2, Issue 7, July 2013

The 7th International Conference on Engineering and Technology
ICET-2015, Phuket, June 19-20, 2015
Prince of Songkla University, Faculty of Engineering
Hat Yai, Songkhla, Thailand 90112

Controller Embedded Oscilloscope Functionality for Power Converter Applications

Porobic Vlado*, Rapaic Milan, Grabic Stevan, Adzic Evgenije, Vekic Marko
University of Novi Sad, Faculty of Technical Sciences, Novi Sad, Serbia
*poroba@uns.ac.rs

Abstract: *In this paper, oscilloscope functionality embedded in digital signal processor software controlling power converter is investigated. Hardware and especially software guidelines for the realization of an efficient and minimum intrusive scope are described. Data flow bandwidth, as well as protocol details between personal computer and digital signal processor in terms of control DSP limitations are discussed. Proposed oscilloscope represents compact solution, which can be easily incorporated in wide variety of power electronics controlled DSP systems.*

Key Words: ***Embedded oscilloscope/ DSP/ power electronics***

1. INTRODUCTION

The performance of a modern controller architecture allows an intelligent approach in order to reduce the complete system costs of power electronics control applications using cheaper actuators, fewer sensors, smaller sizes of EMI filters, etc. Beside product system cost, efficient energy management as well as short time to market rate are important issues which must be fully optimized [1].

In that sense, exploitation of already installed equipment and especially research field in power electronics area beside fundamental control functionality has strong needs for supervision. Regarding control structure and huge number of variables, contemporary systems are increasingly complex. Therefore, whole system insight must be profound as much as possible. In that manner, an controller embedded oscilloscope functionality with minimum intrusive feature as possible would be very useful. Beside measurable system variables (currents, voltages, speed, etc.), it could provide all controller internal variables values also. In that way, an embedded oscilloscope may reduce or eliminate the need for external oscilloscope and/or measurement, thus reducing system complexity and at the same time increasing its observability.

In general, power converter controller can be instantiated in DSP and/or FPGA structure [2, 3]. DSP solution includes in a single chip, the control algorithms and the interface modules with the power converter, such as pulse width modulation (PWM) generators, encoder, etc. Therefore, the controller electronic is cheaper, more robust and compact. Also, the fault rate is considerably reduced and the data transfers between processors are eliminated while programming is significantly simpler. Thus, considering that FPGA is used less frequently or mostly as auxiliary controller, as well as avoiding special complex control systems [4, 5], here is targeted oscilloscope function incorporated in an typical DSP system.

In this paper, detailed analyze and realization of an DSP embedded oscilloscope functionality is shown. Hardware as well as software implementation constrains are examined. Generalized scope approach and protocol specifications details which enables displaying all variables values available in DSP are given. Flexible variables selection, which is done according user generated project file with variable names and addresses, changing their values, as well as decimation regarding PWM acquiring sample instants during device operation is explained.

2. EMBEDDED OSCILLOSCOPE - HARDWARE DETAILS

Power converter controller has to function in a real time strictly, therefore all operations regarded to signal acquiring and processing must be finished till the new sampling period. In that sense, desired scope functionality must not disturb fundamental control function of DSP. Consequently it has to be minimum intrusive considering processing time consumption, available controller memory (RAM), as well as occupied pins number used to communicate to the personal computer (host). Regarding that connection to the host is to be done via universal serial bus (USB), there are discussed several possible options. Internal USB module incorporated in power converter DSP is not standard

option, as well as it demands some knowledge of USB data transfer details and thus this is discarded as a solution. Reasonable proposition is some market ready USB to DSP converter chip. In that sense, connection type between them is discussed in the sequel.

Parallel interface (over several digital lines, e.g. dedicated external memory interface (EMIF)), together with direct memory access (DMA) offers huge dataflow rate [5]. As it occupies so many DSP pins, especially ones which are used for converter control, this approach is eliminated here.

Serial Peripheral Interface (SPI) is high speed synchronized communication with clock (SPICLK), data in and data out line, therefore it requires only 3 DSP pins [6]. The master initiates data transfer by sending the SPICLK signal. For both the slave and the master, data is shifted out of the internal shift registers on one edge of the SPICLK and latched into the shift register on the opposite clock edge. As a result, both controllers send and receive data simultaneously. The application software must determine whether the data is meaningful or dummy data. There are three possible methods for data transmission:

- master sends data; slave sends dummy data
- master sends data; slave sends data
- master sends dummy data; slave sends data

The master can initiate data transfer at any time because it controls the SPICLK signal. The software, however, determines how the master detects when the slave is ready to broadcast data. Therefore, although it is high speed and synchronous communication, SPI significantly complicates oscilloscope implementation and thus is eliminated here.

JTAG (Joint Test Action Group) interface is used as a programming and debugging tool, but is not an standard option, moreover it is not completely accessible protocol to the end-user, thus cannot be used for the embedded oscilloscope also.

In view of the fact that even low cost DSP has universal asynchronous receive transmit bus (UART) as a communication option, this is chosen as a final solution. It features independent, full duplex communication between nodes, which suits oscilloscope needs. UART low dataflow speed attribute is nowadays significantly diminished, since data are first packed in the converter placed near the DSP (i.e. short distance, which is noise resistant) and only afterwards sent differentially over USB cable to the host. In general, the chosen converter [7] is a single chip solution which can deal with JTAG, SPI, I2C and UART signals thus offering a high degree of flexibility for other applications also.

3. EMBEDDED OSCILLOSCOPE - SOFTWARE DETAILS

In this chapter, oscilloscope software details are described. According data transfer speed and memory limits of the chosen DSP, general scope strategy and protocol specification details regarding communication message format are given. At the end, DSP software structure overview with some details are described.

Here is considered case with eight DSP observable variables, each four bytes long. Since DSP for power converter operates at fixed PWM rate, there is chosen PWM frequency of *20kHz* (f_{PWM}) which is the worst case, since maximum PWM frequency for all cases ranged above several hundred *Watts* is bellow that value. In general, "ideal" scope data rate, meaning that all variables values are transferred uninterruptable to the host would be (*bps* - bits per second):

$$desired_data_rate = f_{PWM} \cdot \text{var}_num \cdot \text{var}_length = 20000 \cdot 8 \cdot (4 \cdot 8) = 5.12 Mbps \qquad (1)$$

This case comprise only pure data values without any communication overhead bytes, which means that desired data rate should be even higher. The chosen USB converter [7] and USB protocol specification [8] defines high data rates (480Mbps - High speed USB), but system bottleneck is UART maximum achievable speed which cannot reach desired. Therefore data are buffered in the DSP and then sent in packets, what is explained in the sequel.

For the maximum UART speed (921.6kbps), DSP buffered data (8kwords of internal RAM) are sent to the host, finally resulting in 8 channels with 500 points per screen, 32 bit/channel and refresh rate of 4 screens per second. When only 1 channel is selected the resolution goes to 4000 samples per screen. In general, number of screen points strongly depends on the taken buffer size (DSP RAM size). For the chosen DSP [9], size of taken scope buffer represents 25% of total available RAM memory, which leaves enough room for user code and data. Furthermore, if user code is placed in FLASH memory, scope buffer can be even larger. In this particular case, 8 channels, each with 500 samples per screen can be obtained (or fewer channels with adequate increase in a number of samples). If larger signal screen-shot is needed, an external memory should be used.

Data are acquired in a single DSP buffer and sent immediately as they placed in it. Two buffer approach is discarded in order to avoid extensive DSP memory usage. There are two possible oscilloscope modes, Fig 1. The first one is the fast mode, where data are collected with small decimation value (*d*), i.e. every PWM time instant. Data acquiring is stopped when buffer end is reached, afterwards new data collection is started only after all data are sent. Transferred data are held unchanged on the oscilloscope screen (host) for one buffer sending time. In a slow oscilloscope mode (high decimation value) data are acquired and sent continuously, as well as they are shown smoothly on the host side.

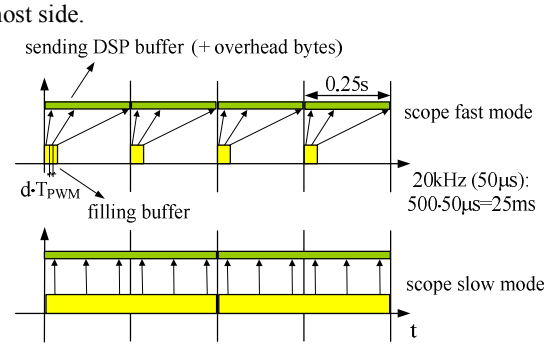

Fig. 1. Time schedule of DSP buffer filling and sending

In general, regarding standard trigger option, scope has two basic modes: AUTO and NORMAL.

AUTO mode implies that samples are acquired and transferred to the host continuously, i.e. there is no special event which will start data collection. Buffer is filled with sampled data from zero index, up to its maximum. As it is explained in the single buffer strategy, buffer data are sent immediately, as they are collected. When buffer is fully sent to host, both indexes (for acquiring and sending) are reset and process is started from the beginning.

NORMAL mode assumes that data collection will start only when chosen variable value equals desired threshold value, in variable selected rising or falling edge case. Additionally, preferred time offsetted data just before trigger instant could be saved in the buffer also. This scope mode is useful when system variable step response, e.g. motor current or speed, is examined. Its detailed explanation is given in Fig. 2. (note numbered time instants as well as acquiring and sending data phases). Samples are acquired, but not sent to the host, all the time before trigger time instant (a1-a2). In the trigger time instant (a2), DSP calculates end index value (a4) up to which it will fill buffer (which depends on the user chosen time offset before trigger instant). Immediately after the buffer is full (a4), DSP starts sending data to PC (s5). During this data send time (s5-s8), new trigger is impossible. Therefore, this situation differs from the AUTO scope mode in start indexes values for acquiring and sending data: they are zero in AUTO mode, and movable in NORMAL mode.

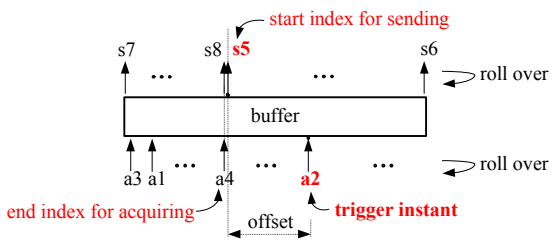

Labels: **1** ÷ **8** - time instant; **a** - acquire; **s** - send

Fig. 2. Principle of NORMAL triggering mode

Buffered data are sent to the host in packet frames. In order that host extracts variable values from the received packet, some encoding technique must be applied. In that manner, data and packet format take very important place in oscilloscope realization. There are two possible options: ASCII (American Standard Code for Information Interchange) character-encoding scheme and pure binary data format. Their comparison can be done easily on the one data byte example, in the sequel. Considering hexadecimal value of the byte, every digit must be coded as separate sign in ASCII case, meaning that one information byte needs two bytes for sending it to the host:

$$157_{dec} = 9D_{hex} = "9"+"D" = 57_{ASCII} + 68_{ASCII} \qquad (2)$$

Frame start and end fields, as well as command and error parts are easily coded in ASCII case. In a pure binary option, one information byte is sent directly without any transformation, while frame control fields must be coded specially since must not be mixed with information data. Regarding that huge amount of data has to be transferred from DSP to host in oscilloscope case, there is chosen binary format of sent data. Proposed structure regarding binary message format is shown in the Fig. 3.

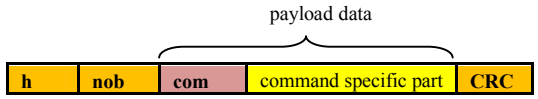

h - header
nob - number of (following) bytes
comm - command
CRC - Cyclic redundancy check field

Fig. 3. Proposed data frame structure

Every packet consists of overhead and payload data. Overhead data starts with header (*h*) needed for host synchronization and number of following bytes (*nob*) at the beginning, as well as cyclic redundancy check (*CRC*) bytes at the end. Payload data contains command (*comm*) and *command specific bytes* such as variable addresses, values, decimation, etc. There are defined several commands: *connection test*, *start/stop scope*, *write (*variable*)*, *read (*variable*)*, *flag* (read DSP internal flag register, containing some errors), *trigger* (AUTO/NORMAL, with trigger details such as trigger variable, level, time offset).

In order to have easily embeddable oscilloscope functionality in any DSP controlling power converter, an algorithm structure is proposed, Fig. 4. In the *ScopeHandlerInit()* function UART pins as well as main data and auxiliary buffers with accompanying pointers are initialized. *ScopeHandlerMain()* function checks whether there is host data to be received, parse them and do appropriate action such as start scope, variable write, etc. If scope is active, this function fills sending buffer with main buffer data. *ScopeHandlerPWM()* function is placed at the end of user PWM interrupt routine. Depending on chosen variable names, decimation and trigger mode, it fills main buffer with data. Consecutively, the scope frequency range is directly tied to the user PWM frequency. All described functions are optimized in order not to waste DSP processing time, since it must control power converter in a real time. For the considered DSP [9], occupied time by scope was less than 2μs of total PWM time, i.e. bellow 5% of total time.

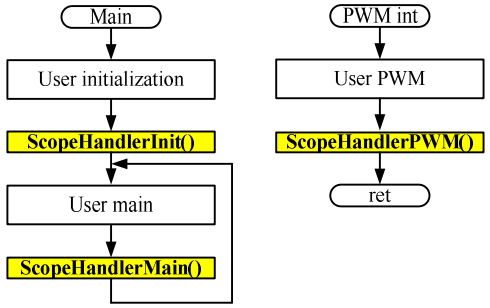

Fig. 4. Oscilloscope functions position in user algorithm

Oscilloscope decimation and variable selection is simply done via drop down list in a user application window, shown in Fig. 5 [10]. According DSP environment generated project, host application from file

with mapped variables (.map extension) parse variables names and their addresses. Consequently, addresses are sent to DSP, which then grabs data from that memory locations. In that manner, user is completely released from explicitly specifying variables names/addresses since they are dynamically changed as soon as project is generated. Trigger settings are shown in Fig. 6.

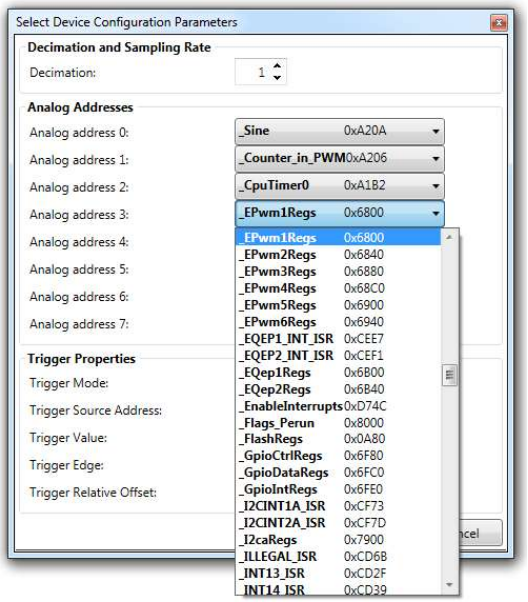

Fig. 5. Oscilloscope decimation and variable selection

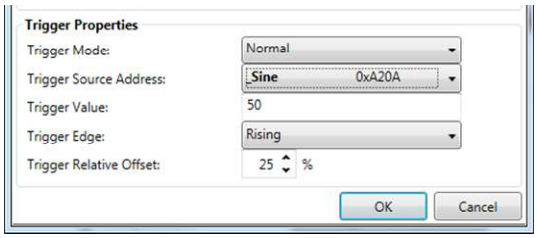

Fig. 6. Oscilloscope trigger settings

Finally, after start of the scope, signals are graphically presented on the panel, in a real time, Fig. 7. Regarding host side high computing capability, acquired signals can be dynamically filtered, as well as can be done their harmonic analyze on PC side (lower part of the figure), thus freeing DSP processing time.

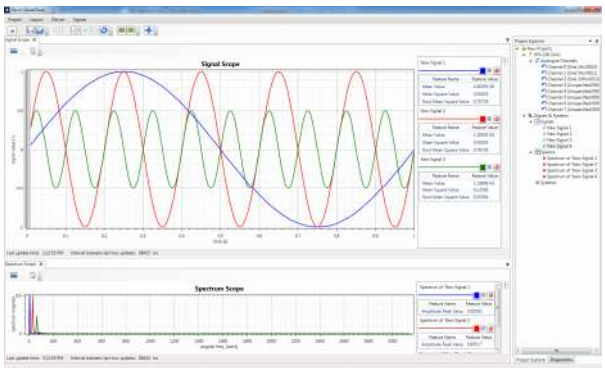

Fig. 7. Oscilloscope panel

4. CONCLUSION

In this paper, non intrusive oscilloscope, intended to be built in an digital signal controller application is analyzed. Hardware and software details of the solution are discussed in details. Proposed oscilloscope structure provides supervision of not only power converters DSP systems, but wider area of power electronics devices also. Since it is actually generic and well optimized regarding execution speed, flexibility and cost, it can help in debugging and control of a range of power electronics devices during research as well exploitation phase.

ACKNOWLEDGMENT

This research was partially co-funded by the Ministry of Education, Science and Technological Development of Republic of Serbia under contract No. III 042004.

5. REFERENCES

[1] J. Popović-Gerber, J. Oliver, N. Cordero, T. Harder, "Power Electronics Enabling Efficient Energy Usage: Energy Savings Potential and Technological Challenges", *Power Electronics, IEEE Transactions on*, 2011, Vol. 27, No. 5, pp. 2238-2353.

[2] C. Buccella, C. Cecati, H. Latafat, "Digital Control of Power Converters—A Survey," *IEEE Transactions on Industrial Informatics,* 2012., Vol. 8 No. 3, pp. 437-447.

[3] P. M. Menghal, A. Jaya, Laxmi, "Real Time Control of Electrical Machine Drives: A Review", *IEEE International Conference on Power, Control and Embedded Systems (ICPCES)*, Allahabad, India, Nov. 29-01. Dec., 2010., pp. 1-6.

[4] R. Godbole, S. Bhattacharya, "Design and Development of a Flexible Multi-Purpose Controller Hardware System for Power Electronics and Other Industrial Applications", *Industry Applications Society Annual Meeting, 2008. IAS '08. IEEE*, Edmonton, Alta., 5-9 Oct. 2008, pp.1-6.

[5] J. Bueno, A. Hernandez, F. Rodríguez, C. Giron, R. Mateos, S. Cobreces,"A DSP and FPGA-Based Industrial Control With High-Speed Communication Interfaces for Grid Converters Applied to Distributed Power Generation Systems", *IEEE Trans on Industrial Elect.*, 2009., Vol. 56 No. 3, pp. 654-669.

[6] TMS320x2833x, 2823x Serial Peripheral Interface (SPI), Reference Guide [Online]. Available: *www.ti.com*

[7] FT2232H, Dual USB to Serial UART/FIFO IC [Online]. Available: *www.ftdichip.com*

[8] Universal Serial Bus Revision 2.0 Specification. [Online]. Available: *www.usb.org/developers/docs*

[9] TMS320F28335, Floating point DSP, [Online]. Available: *www.ti.com*

[10] Online available: *www.perun-power.com*

The 7th International Conference on Engineering and Technology
ICET-2015, Phuket, June 19-20, 2015
Prince of Songkla University, Faculty of Engineering
Hat Yai, Songkhla, Thailand 90112

Energy and Economic Effects of Electricity and Heat Cogeneration with Combined Technologies of Corn Cobs Gasification and Gas Turbines

Milana Guteša[1], Branka Gvozdenac-Urošević[2], Vojin Grković[3]
[1,2,3]University of Novi Sad, Faculty of Technical Sciences, Novi Sad, Serbia
* Email of corresponding author: milanagutesa@uns.ac.rs

Abstract: *This paper presents the performance and economic analysis of the gas turbine with co-firing of the gas from the corn cob gasification and natural gas. Adiabatic and non-adiabatic expansion in the turbine is considered. The analysis is performed parametrically with the corn cob gasification gas to natural gas ratio. The volumetric energy content of gas fuels with different the gas from the corn cob gasification share, therefore with different calorific values, is compared by use of the Wobbe Index. In the energy and economic analysis are treated following configurations: single manifold, dual manifold and separate gas systems.*

Index terms: ***co-firing, corn cob gas, gas turbines, cogeneration***

1. NOMENCLATURE

AD – adiabatic expansion
BIG/GT–biomass integrated gasifier/gas turbine
BIG/CC–biomass integrated gasifier/combined cycle
CGR – corn cob gas ratio
DM – dual manifold
LCV – low calorific value
NAD – non adiabatic expansion
SM – single manifold
SGS – separate gas system
T_{IT}– turbine inlet temperature (K)
WI – Wobbe Index

2. INTRODUCTON

The most effective way of biomass utilization is transformation into fuels for power production. Gas turbines fueled by integrated biomass gasifiers are a promising option for electricity generation from renewable resources. Gasification of agriculture originated biomass and further mixing of the obtained gas with natural gas enable use of biomass as secondary energy on wide territory, as well as with simple connection to different energy consumption sectors [1]. Gas turbines due to stable flame through combustion are very flexible, and thus suitable for biomass utilization. The biomass integrated gasification/gas turbine cycle (BIG/GT) with co-firing of the gas derived from biomass and natural gas was analyzed in literature [2], where modeling results show that no significant modifications or de-rating will be necessary if the natural gas content is higher than 35–50%.

The problem of burning LCV gases in gas turbines of different design was the subject of interest of various researchers and turbine designers. However, in the published literature the term LCV gas is used for gas of LCV in the range of 13.0 to 22.84 MJ/sm^3 [3], 18 to 21 MJ/sm^3 [4], 5.96 MJ/sm^3 [5], 2.5 to 4 MJ/sm^3 [6], or generally LCV gas like in [7]. Configuration of multiple fuel system related to the calorific value of the gas fuel that is intended to be burned in a gas turbine is analyzed in [7]. In the analysis are treated following configurations: single manifold, dual manifold and separate gas systems.

The volumetric energy content of different gas fuels, caused by different calorific values, can be compared by use of the Wobbe Index. The general expression for WI is given in literature [3, 8], while in [7] is given expression that includes the temperature effect on the gas compressibility. The ratio of WI of the fuel for which the turbine is designed and WI of the LCV fuel indicates the necessary change in pressure drop if no design changes are made in fuel supply system, injection and control system.

Gases with relatively close Wobbe Indices can, in principle, ran in the same fuel control system. In contrary, gases with unlike Wobbe Indices need different configurations of fuel system including the necessary nozzle pressure drop. In [7] is quoted ±5% as possible variation in WI that can handle some of standard fuel gas control systems without adjustments; however in literature [3] that range is ±10%.

Combustion of gas fuel of the Wobbe Index more or less lower than those, for which gas fuel system and entire gas turbine are designed, represents off-design regime for the gas

turbine. In such a case in principle it is not possible to maintain designed turbine inlet temperature (T_{IT}). New operation regime of the gas turbine with new parameters of energy transformation processes including new T_{IT} can be estimated by numerical simulation. The simulation model should comprise both possible expansion processes in gas turbines: adiabatic process when no cooling of the turbine blades is applied and non-adiabatic expansion process when the cooling of the blades exists. For analysis of the gas turbine off-design regime when corn cob gas and natural gas are co-fired is developed the simulation model based on literature [9-11]. Results of the performed numerical simulations are briefly explained in the following wording.

3. RESULTS OF NUMERICAL SIMULATION

The analysis in this paper is performed for gas from corn cobs gasification based on the available experimental data published in literature [12, 13]. Gas obtained in the process has very low calorific value and thus belongs to so called LCV gases.

The developed simulation models are used for the analysis of energy effects of electricity and heat cogeneration with combined technologies of corn cobs gasification and gas turbines. The analysis is performed parametrically with the mass ratio of corn cob gasification gas and natural gas (CGR) as a parameter. In the analysis are comprised different gas turbine design features. Three configurations of multiple gas fuel systems are considered like: single manifold referred as SM, dual manifold referred as DM and separate gas systems, referred as SGS. Two types of energy transformation processes in the gas turbines are also considered: adiabatic, referred as AD and non-adiabatic, referred as NAD.

Regarding energy generation are considered pure electricity generation and cogeneration of electricity and heat for district heating system and/or for the industrial consumers. For all these variants basic Joule (Bryton) cycle was assumed.

In Fig. 1 is presented the variation of Wobbe Index as function of CGR, for three considered configurations of fuel gas systems. The field of possible operation for each configuration is also indicated.

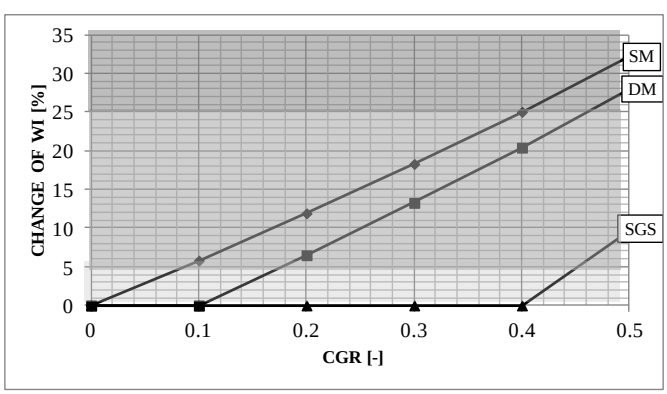

Figure 1. Variation of Wobbe Index as function of CGR, for the considered configurations of fuel gas system

In Fig. 2 is presented the variation of calculated value of turbine inlet temperature as function of CGR, for the considered configurations of fuel gas systems. The design value of T_{IT} equal to 1400 K is arbitrary selected for the purpose of the off-design process analysis. In the case of single manifold gas fuel system, with increasing content of gas from corn cobs gasification in the fuel gas mixture T_{IT} falls significantly. Dual manifold gas fuel system enable maintaining the designed value of T_{IT} in the CGR range of 0 to 10%, while separate fuel gas systems enable maintaining the designed value of T_{IT} in the CGR range of 0 to 40%.

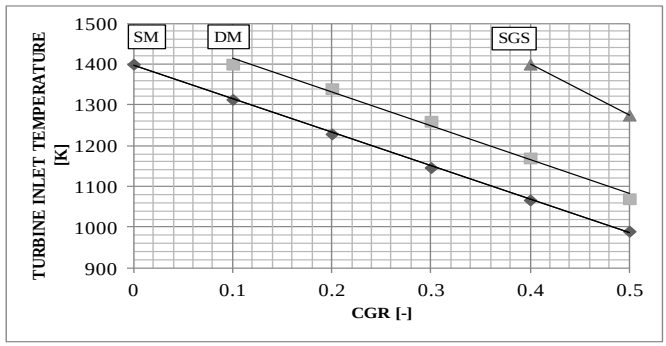

Figure 2. Variation of calculated value of T_{IT} as function of CGR, for the considered configurations of fuel gas systems

Increased portion of gas from corn cob gasification in fuel gas mixture causes reduction of turbine inlet temperature as well as the reduction of turbine exhaust temperature and therefore appropriate reduction in efficiency, as can be seen from Fig. 3. Data in Fig. 3 correspond to the adiabatic expansion. The reduction of efficiency is greatest in the case of single manifold gas fuel system and the smallest in the case of separate gas fuel systems (Fig. 3). For example when the gas from corn cob gasification participates with 50% in fuel gas mixture, in the case of separate gas fuel systems the reduction of efficiency amounts about 1.3 percent points, while in the case of single manifold system the reduction of efficiency amounts about 5.8 percent points. On the other hand technical solution with separate gas fuel systems is the most costly from all three considered gas fuel systems.

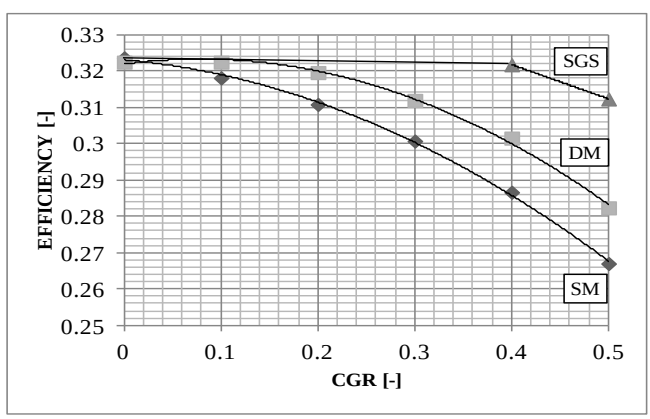

Figure 3. Efficiency versus CGR in the case of adiabatic expansion for the considered configurations of fuel gas systems

Cooling of gas turbine blades provide lower metal temperatures and thus enable operation with higher values of T_{IT} with the same blades alloy. For the cooling purpose is used air taken from compressor discharge and, if found as appropriate, from one or more bleeding points at the compressors casing.

Necessary quantity of cooling air depends to the heat amount that must be removed from the blades. As a consequence of the blades cooling non-adiabatic expansion process occurs. Developed model for numerical simulation of the gas turbine process in non-adiabatic conditions, similarly to the previous one, enables calculation of all process parameters with different type of fuel and different fuel gas systems configurations.

In the case of air cooling, the higher values of turbine inlet temperatures can be applied, depending to the amount of heat that can be removed away, or in other words depending to the designed cooling air mass flow, and thus enable better overall efficiency.

In the case of cogeneration of steam the heat recovery steam generator (HRSG) is used, while in the case of cogeneration of hot water the appropriate boiler is used. In the analysis is assumed that in each design variant, the gas temperature at the outlet of the HRSG or at the outlet of water boiler amounts 378 K, while the turbine inlet temperature amounts 1400K.

Although the plants efficiency is significantly affected by the ratio of gas from corn cobs gasification and natural gas, the cogeneration process enable significant increase of the gas turbine plant's efficiency as can be seen in Fig. 4. This efficiency increase is the basis for economic gain for the overall plant comprising both corn cobs gasification plant and gas turbine cogeneration plant. The curves in Fig. 4 correspond to the single manifold gas fuel system.

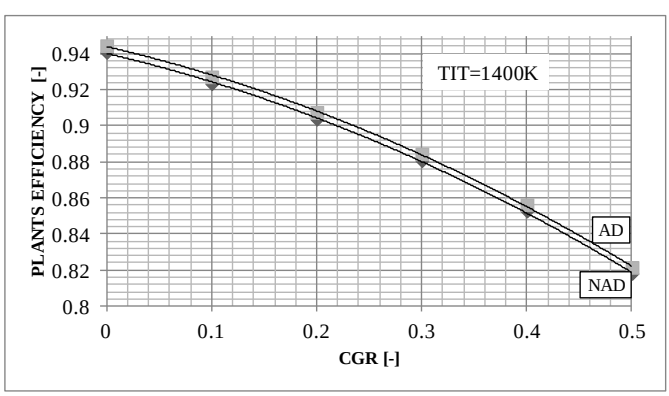

Figure 4. Cogeneration plants efficiency as functions of CGR for adiabatic and non-adiabatic expansion processes

4. ECONOMIC ANALYSIS

Designed unit for gasification corn cob is described in [14]. The type and technical features of the gas generators were described in literature [12, 13]. Nominal power of the selected gas turbine, at the generator terminals is 6 MW. For calculation of annual average energy generation it is estimated 3000 h/a of gas turbine operation in winter season and 3000 h/a in summer season. Amount of average annual power generation is presented in Fig 5.

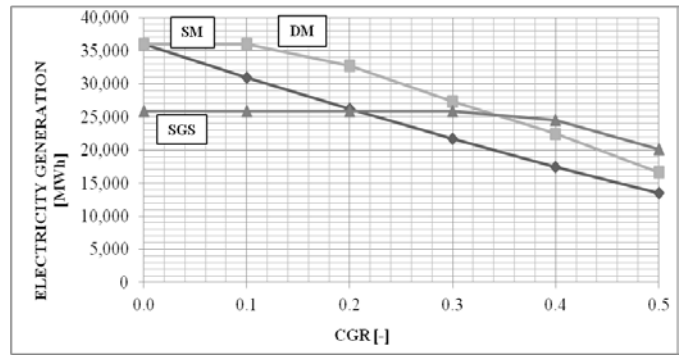

Figure 5. Electricity generation versus CGR for the considered configurations of fuel gas systems

Economic analysis is performed for already presented three different technical solutions of the gas turbine regarding gas fuel system and for three types of energy generation. It is assumed that all produced heat is delivered to the end user. For the investment estimation literature data are used [15], the costs of consultant's services, licensing, commissioning and miscellaneous are included. Total investment cost for Single manifold is 5.1051, Dual manifold is 5.1817 and Separate gas system is 5.2838 Mil €.

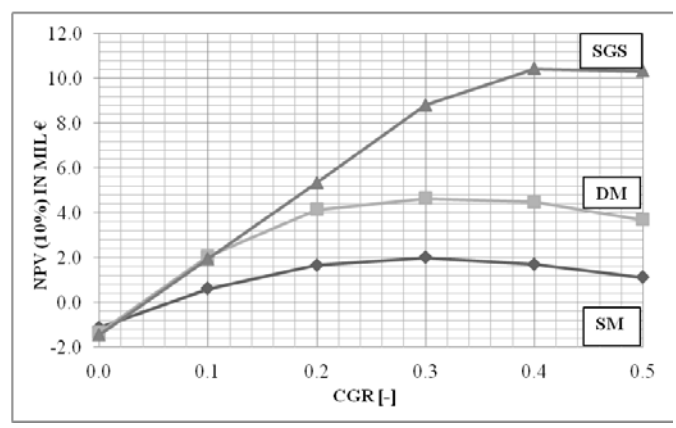

Figure 6. Net present value (10%) in 20 year period as functions of CGR for three analyzed fuel gas systems

It is assumed that investment maintenance cost is 11% of investment after every 6 years of operation. In addition annual maintenance cost of 0.5 c€/kWh for produced electricity is taken in calculation as well as annual administrative and other cost as 6% of produced value [15]. Serbian average natural gas price is used, and price for producer gas is 0.021 €/m^3 with 4900 kJ/m^3 low calorific value [14]. In calculation of the expected income current Serbian feed in tariffs are used (natural gas cogeneration 8.89 c€/kWh, power plant on different kind of biogas 12.31

c€/kWh and current market price of delivered heat for district heating systems. Based on presented estimations, assumptions and expectations following graphs are made.

In all analyzed cases NPV value of the project is negative only when natural gas is used without mixing. All analyzed financial indicators in those cases are the lowest.

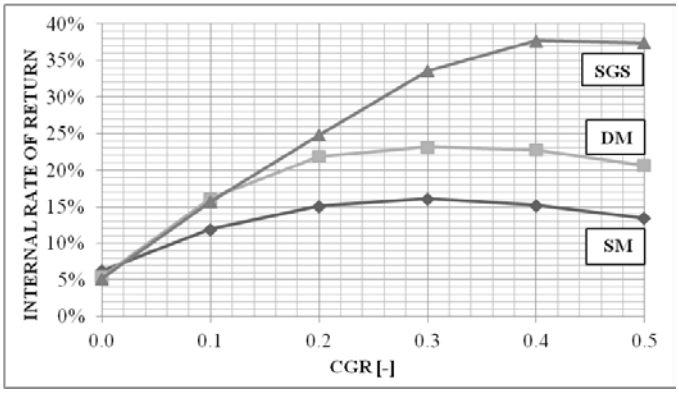

Figure 7. IRR as functions of CGR for three analyzed fuel gas systems

When analyzing only presented economical parameters installation with separate gas systems with 0.4 and 0.5 CGR it can be seen as most economically justified option even thought this system has highest investment cost. Accumulated case flows for SGS option when burning only natural gas will enter the positive zone in 13th year; CGR is 0.1 in 6th year; CGR 0.2 in 4th year and when CGR are 0.3, 0.4 or 0.5 in 3rd year.

5. CO_2 EMISSION REDUCTION

Implementation of this project except of financial justification is going to have social and environmental benefits. The annual potential reduction of CO_2 is going to be achieved through reduction of natural gas using gas from gasification.

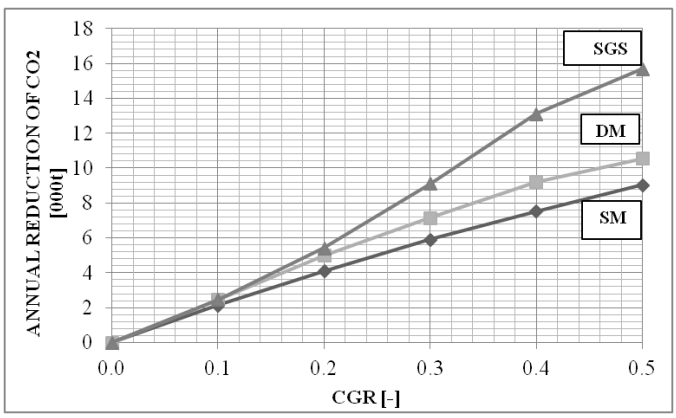

Figure 8. Reduction of CO_2 as functions of GCR for three analyzed fuel gas systems

6. CONCLUSION

Cogeneration energy plants based on corn cobs gasification integrated with gas turbine and HRSG can obtain good performance, provided that the multiple fuel system is selected consentient with the fuel gas mixture.

Economic analysis has pointed out certain benefits of such a plant that justifies the hypotheses. However, further work is necessary in order to define optimal mixture of corn cob gas and natural gas, as well as plants design features and other plants parameters.

7. ACKNOWLEDGMENT

This work is done within the project titled „Development of CHP demonstration plant with gasification of biomass“ (Project No. 33049), partially financed by the Ministry of Education, Science and Technological Development of the Republic of Serbia.

8. REFERENCES

[1] A.V. Bridgwater, A.J. Toft, J.G. Brammer, “A techno-economic comparison of power production by biomass fast pyrolysis with gasification and combustion”, Renewable Sustainable Energy , 2002, Vol. 6, pp 181–248

[2] M. Rodrigues, A. Walter, A. Faaij, “Co-firing of natural gas and biomass gas in biomass integrated gasification/combined cycle systems”, Energy, 2003, Vol. 28, pp 1115–1131

[3] G.J. Meier, W.S.Y. Hung and V.M. Soon, “Development and Application of Industrial Gas Turbines for Medium-Btu Gaseous Fuels”, Transaction of the ASME, Vol. 108, 1986, pp 182-190.

[4] M. Koyama, H. Fujiwara, “Development of a Dual-Fuel Gas Turbine Engine of Liquid and Low Calorific Gas”, JSME International Journal, Series B, 2002, Vol. 49, pp 224-229.

[5] C.E. Neilson, “LM2500 Gas Turbine Modifications for Biomass fuel Operation”, Biomass and Bioenergy, Pergamon, Vol. 15, 2010, pp 269-273.

[6] B. Adouane, P. Hoppesteyn, W. de Jong, M. van der Wel, K.R.G. Hein, H. Spielthoff, “Gas turbine combustor for biomass derived LCV gas, a first approach towards fuel-NOx modelling and experimental validation”, Vol. 22, 2002, pp 959-970.

[7] W.I. Rowen, “Design considerations for Gas Turbine Fuel Systems”, GE Company, 1991, Vol. 28, pp 1-17.

[8] K. Liu and V. Sanderson, “The influence of changes in fuel calorific value to combustion performance for Siemens SGT-300 dry low emission combustion system”, Fuel, 2013, Vol. 103, pp 239-246.

[9] K.J. Müller, “Grundzüge der Thermischen Turbomaschinen”, Vorlesung, Institut für Thermische Turbomaschinen und Energieanlagen, Universität Wien, 1991.

[10] V. Grković, “Thermal turbomachines – theoretical fundaments”, Faculty of Technical Sciences, Text Book edition, Novi Sad, 2008.

[11] G. Y. Van Wylen and R. E. Sontang, “Fundamentals of Classical Thermodynamics”, Wiley, New York, 1976.

[12] G. Jankes and M. Milovanović, “Biomass gasification in small-scale units for the use in agriculture and forestry in FR Yugoslavia”, Thermal Science, 2001, Vol. 5(2).

[13] T.B. Reed and A. Das, “Handbook of Biomass Downdraft Gasifier Engine Systems 1988: Biomass Energy Foundation”, 140.

[14] G. Jankes, T. Simonović, M. Trninić, N. Tanasić, M. Stamenić, M. Stanojević, “Advantages of the System for the Gasification of Biomass for Combine Heat and Power Production in Serbia”, Proceedings from 28th International Process Engineering Congress- PROCESING 2014, Belgrade, Serbia, September, 2014, ISBN 978-86-81505-75-5

[15] B. Gvozdenac Urošević, Model of distributed cogeneration planning and its integration into regional energy system (PhD thesis), University of Novi Sad, Faculty of technical sciences, 134 pages, Author’s reprint, COBISS SR-ID 267666183, 2011, (in Serbian)

The 7th International Conference on Engineering and Technology
ICET-2015, Phuket, June 19-20, 2015
Prince of Songkla University, Faculty of Engineering
Hat Yai, Songkhla, Thailand 90112

Advanced Wind Energy System with Sensorless Controlled Six-phase Generator

Boris Dumnic[1]*, Dragan Milicevic[1], Bane Popadic[1], Vladimir Katic[1], Zoltan Corba[1],
[1]University of Novi Sad, Faculty of Technical Sciences, Novi Sad, Serbia
*Email of corresponding author: dumnic@uns.ac.rs

Abstract: *Renewable energy sources, especially wind energy conversion systems (WECS), exhibit constant growth. Increase in power and installed capacity led to advances in WECS topologies. Multi-phase approach presents a new development direction, with several key advantages over three-phase systems. Paired with a sensorless control strategy, multi-phase machines look to take primacy over standard solutions. This paper presents speed sensorless vector control of an asymmetrical six-phase induction generator based on a model reference adaptive system (MRAS). Suggested topology and developed control algorithm show that sensorless control can yield appropriate dynamic characteristics for the use in WECS with increase in reliability and robustness.*

Key Words: ***Wind energy/Multi-phase machine/Vector control/Speed estimation***

1. INTRODUCTION

In the recent years of the last decade wind energy conversion systems (WECS) exhibited very positive trend of rapid development, increasing the share of WECS in global energy generation accordingly. Recently, it has been reported that cumulative power of installed WECS worldwide was over 318 GW at the end of the 2013 [1], with just over 35 GW installed during the same year. Future of wind energy market looks bright, with forecast showing the trend of stabilization after the 2014 and expected annual market growth at 6-10 % before 2018, potentially ending the 2018 at global cumulative installed capacity just about 600 GW [1].

High penetration of the renewable energy sources, especially WECS, led to the introduction of different new technologies and solutions in order to deal with known deficiencies of classical systems [2, 3]. Currently deployed WECS topologies have achieved their limit, especially with respect to their power rating. Mostly bound by the advances in power electronic converters, there are several approaches in overcoming these constraints. As proposed in [3], two major directions in the further development of WECS are: multi-winding (multi-phase) generators with distributed converters and multiple generators with distributed gearbox. Clear disadvantage of the latter topology lies in the complex gearbox system, which can significantly increase the price, and maintenance cost of the system. Furthermore, complex gearbox system can lead to severe decrease in WECS reliability.

On the other hand, using multi-phase generators in WECS offer several advantages in addition to increasing the power rating of the system. In the midst of multiphase machine types one concept claimed its place as one of the most interesting and most investigated. Those are asymmetrical six-phase (dual three-phase) induction machines that have two three phase winding sets with spatial shift of 30 electrical degrees [4, 5]. Multi-phase drives, with six-phase induction machines, are featured in the highly reliable applications, making them a perfect fit for the use in wind energy applications. With the standard benefits that induction machine offers, introduction of multiple phases allows the drive to become prominently immune to failure. Unlike their three-phase counterparts, six-phase machines in WECS can operate under faulty conditions by a simple reduction to a system with lower phase number. As a result, the robustness and reliability of the drive is greatly increased. Additionally, six-phase machine offers a variety of control options, regarding operating regimes with wind power lower than nominal, with the possibility of maintenance cost reduction by applying the suitable optimization and selecting appropriate number of phases for power transfer. Moreover, using six-phase machine in WECS will lessen the mechanical stress of the system components since they have significantly lower torque ripple [4]. With the increase in efficiency, by proper control of the machine side converter, the WECS based on a six-phase induction machine makes for a robust, relatively inexpensive and highly reliable solution.

Considering main advantages of such a drive, the extension of the field oriented control (FOC) principle from three-phase to six-phase machines offers well-known, robust and computationally non-demanding algorithm [6]. However, proper implementation of the vector control algorithm requires accurate rotor speed signal, in order to provide the decoupling between machine torque and flux. More often than not, acquiring such signals can have negative impact on the system robustness and reliability. This is particularly

emphasized by the harsh environmental and WECS operating conditions. Reliability of the WECS can, therefore, be improved by eliminating the speed sensor, whilst reducing maintenance cost.

Elimination of the speed sensor is possible with the use of six-phase induction generator states and outputs estimation algorithms. Model Reference Adaptive System (MRAS) speed estimation algorithm provides simple and reliable technique, with dynamic performances similar to those of standard drives that include speed measurement [7]. The introduction of speed estimation technique based on MRAS algorithm to the six-phase induction machine drive will greatly complements positive features of the overall system. Furthermore, known MRAS insufficiencies can be surpassed by the same improvements established for standard three-phase induction machine drives [8, 9].

This paper will present the speed sensorless vector control of an asymmetrical six-phase induction machine. Speed estimation technique is based on a MRAS algorithm adjusted for the use in asymmetrical six-phase induction machine. Simulation results will show that the speed estimation method is capable of tracking the rotational speed of the machine under realistic conditions. Proposed technique is computationally very efficient and easy to implement, which, in addition to its robustness, makes it suitable for implementation in WECS.

2. MATHEMATICAL MODEL OF THE SIX-PHASE INDUCTION MACHINE

Mathematical model for the six-phase induction machine, used in this paper is developed using the Voltage Space Decomposition (VSD) theory [10]. As provided by the theory applying the amplitude invariant VSD transformation matrix, to the stator and rotor voltage equations in the original domain (a,b,c,x,y,z), will yield three two-dimensional orthogonal (decoupled) subspaces ($\alpha,\beta,\mu_1,\mu_2,z_1,z_2$). The fundamental components and harmonics of the order $k=12\bullet n\pm1$ (n=1,2,3...) are contained in α-β subspace as shown in equation (1). Other subspace, designated by μ_1-μ_2, and shown in equation (2) contains the loss producing components paired with harmonics of the order $k=6\bullet n\pm1$ ($n=1,3,5...$). The final, z_1-z_2 subspace contains zero-sequence components. In regard to the topology and mutual interconnection of the two three-phase windings the z_1-z_2 subspace components are equal to zero, and are not presented in this paper.

The machine electromagnetic torque in stationary (α,β) reference frame can be expressed as:

$$T_e = 3\cdot\frac{P}{2}\cdot\frac{M}{L_r}\left(\psi_{\alpha r}\cdot i_{\beta s}-\psi_{\beta r}\cdot i_{\alpha s}\right) \tag{3}$$

Mathematical model after transformation to the synchronous rotating reference frame is identical to the three-phase machine as it is presented in [5].

3. SPEED SENSORLESS VECTOR CONTROL SCHEME

A wide range of operation for the IFOC controlled drive makes this strategy viable for motor drives and power generating applications [11]. Using the proper decomposition transformations, and by aligning the reference frame with the rotor flux orientation (as it is described in [3, 7]), decoupled control of the machine flux and torque can be obtained as:

$$\psi_{rd} = \frac{L_m}{(1+sT_r)}i_{ds} \qquad i_{qs}^* = \frac{2L_r}{3pL_m\psi_{rd}}m_c \tag{4}$$

where rotor time constant is defined as $T_r = L_r / R_r$, L_r is rotor self-inductance and L_m is magnetizing inductance. If we assume constant flux, i.e. that the *d*-axis controller sets the flux of the machine to the desired (nominal) value, the generator torque becomes directly proportional to machine *q*-axis current. Maximum Power Point Tracking (MPPT) algorithm uses speed signal to calculate torque reference consequently leading to *q*-axis current reference according to equations (4).

Six-phase machine rotor speed signal, necessary for MPPT algorithm, is estimated based on MRAS observer. Figure 1. presents three main components of the MRAS observer: reference model, adaptive model and adaptation mechanism [7]. Reference model is a mathematical representation of the machine, having to faithfully reflect the current state of the machine. This mathematical representation does not feature value estimated by MRAS observer, i.e. rotor speed. Adaptive model provides the insight in estimated value validity, since the mathematical representation include the estimated value of MRAS observer. Adaptation mechanism will, according to a predefined function, reach the estimated speed value using the difference between relevant values in reference and adaptive models.

$$\begin{bmatrix} v_{\alpha s} \\ v_{\beta s} \\ 0 \\ 0 \end{bmatrix} = \begin{bmatrix} R_s+\left(L_{ls}+M\right)\cdot p & 0 & M\cdot p & 0 \\ 0 & R_s+\left(L_{ls}+M\right)\cdot p & 0 & M\cdot p \\ M\cdot p & \omega_r\cdot M & R_r^{'}+\left(L_{lr}^{'}+M\right)\cdot p & \omega_r\cdot\left(L_{lr}^{'}+M\right) \\ -\omega_r\cdot M & M\cdot p & -\omega_r\cdot\left(L_{lr}^{'}+M\right) & R_r^{'}+\left(L_{lr}^{'}+M\right)\cdot p \end{bmatrix}\cdot\begin{bmatrix} i_{\alpha s} \\ i_{\beta s} \\ i_{\alpha r} \\ i_{\beta r} \end{bmatrix} \tag{1}$$

$$\begin{bmatrix} v_{\mu_1 s} \\ v_{\mu_2 s} \\ 0 \\ 0 \end{bmatrix} = \begin{bmatrix} R_s+L_{ls}\cdot p & 0 & 0 & 0 \\ 0 & R_s+L_{ls}\cdot p & 0 & 0 \\ 0 & 0 & R_r+L_{lr}\cdot p & 0 \\ 0 & 0 & 0 & R_r+L_{lr}\cdot p \end{bmatrix}\cdot\begin{bmatrix} i_{\mu_1 s} \\ i_{\mu_2 s} \\ i_{\mu_1 r} \\ i_{\mu_2 r} \end{bmatrix} \tag{2}$$

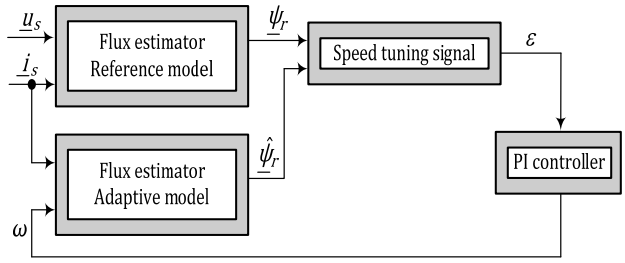

Fig. 1. MRAS based rotor speed observer.

Rotor speed estimation is achieved by comparing rotor flux linkages, gained using machine voltage equations for stator and rotor windings. Mathematical representation of reference and adaptive model estimator are given in the equations (5) and (6) respectively.

$$\psi_{rd}^{s} = L_r \Big/ L_m \left[\int \left(u_{sd}^{s} - R_s i_{sd}^{s} \right) dt - L_s' \, i_{sd}^{s} \right]$$

$$\psi_{rq}^{s} = L_r \Big/ L_m \left[\int \left(u_{sq}^{s} - R_s i_{sq}^{s} \right) dt - L_s' \, i_{sq}^{s} \right] \tag{5}$$

$$\hat{\psi}_{rd}^{s} = 1 \Big/ T_r \int \left(L_m i_{sd}^{s} - \hat{\psi}_{rd}^{s} - \hat{\omega} T_r \hat{\psi}_{rq}^{s} \right) dt$$

$$\hat{\psi}_{rq}^{s} = 1 \Big/ T_r \int \left(L_m i_{sq}^{s} - \hat{\psi}_{rq}^{s} + \hat{\omega} T_r \hat{\psi}_{rd}^{s} \right) dt \tag{6}$$

where parameter L_s' is the stator transient inductance, superscript s indicates stationary reference frame and symbol ^ denote estimated quantities.

Adaptation mechanism is based on PI-type controller and is represented by $\hat{\omega} = (K_p + \frac{K_i}{s}) \cdot \varepsilon$, where $\varepsilon = \hat{\psi}_{rd}^{s} \psi_{rq}^{s} - \psi_{rd}^{s} \hat{\psi}_{rq}^{s}$.

4. SIMULATION RESULTS

In order to verify proposed theoretical consideration of applying sensorless vector control to six-phase induction generator in WECS with MPPT, Matlab/Simulink model of the system was developed. The basic implemented of proposed control scheme is shown in Fig. 2. The control of the system has separate stages for current and speed control loops, which operate under different sampling time.

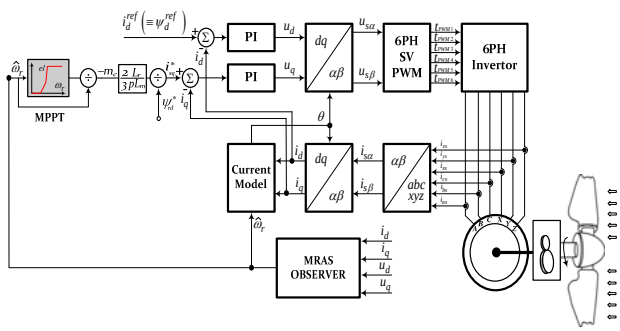

Fig. 2. Sensorless vector control of a six-phase induction generator with MPPT algorithm.

During the simulations, d-axis current is kept constant, consequently keeping the machine operating with nominal flux value. In order to generate the q-axis current reference, MPPT algorithm is employed. Speed signal necessary for the implementation of MPPT algorithm and IFOC control strategy is acquired by speed estimation using MRAS observer. Torque reference is acquired using wind data and wind turbine model defined in Wind Turbine Blockset for Matlab/Simulink [12].

Figures 3-7 show simulation results for WECS with six-phase induction generator operating under variable average wind speed ranging from 10-13 m/s. IFOC strategy, with MRAS estimated rotor speed signal and MPPT algorithm, is tested. In Fig. 3, wind turbine shaft and six-phase generator electromagnetic torque is presented. It can be observed that IFOC with MPPT algorithm is successfully implemented since the maximum available wind power is converted to electrical. Obvious difference between these torques is a consequence of rotating mass inertia – generator, turbine and gearbox. Fig. 4 presents machine flux and torque producing currents, clearly showing that decoupled control with constant machine flux is achieved. Successful implementation of sensorless control and high precision of rotor speed estimation is shown in Fig. 5. Estimated speed signal perfectly matches actual machine rotor speed.

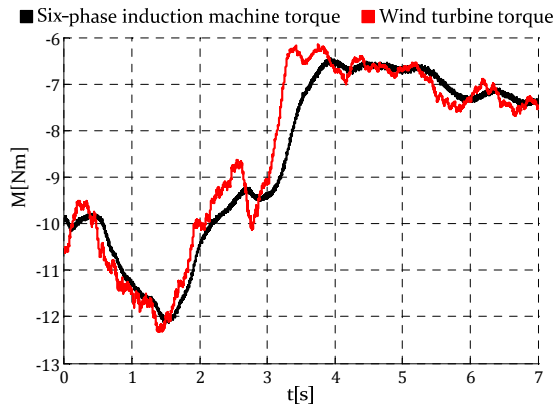

Fig. 3. Wind turbine and machine torque.

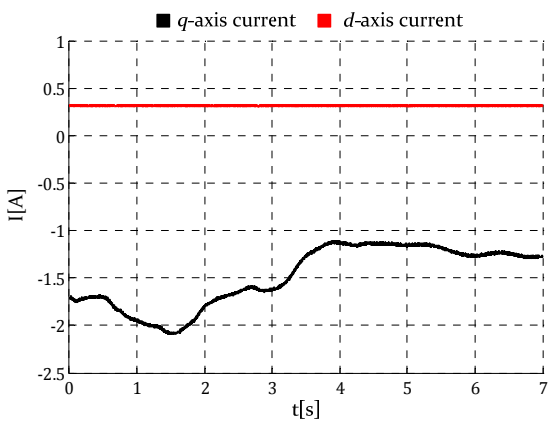

Fig. 4. Machine flux and torque producing currents.

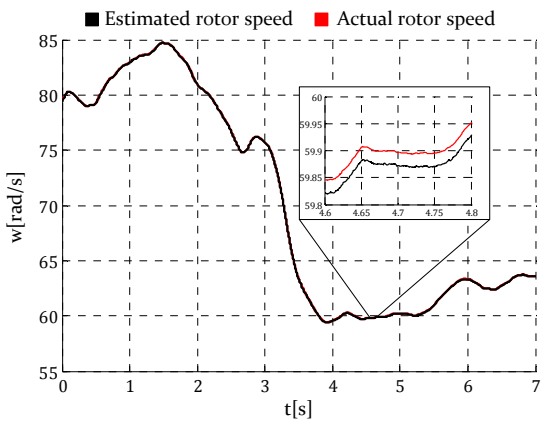

Fig. 5. Machine MRAS estimated and actual rotor speed.

During WECS operation under proposed condition six stator phase currents are sinusoidal, which can be confirmed in Fig. 6. According to VSD theory and applied novel modulation strategy [5], high efficiency of control is achieved. This is verified by Fig. 7, showing negligible level of loss producing current components (μ_1-μ_2), and α-β components make an ideal circular shape.

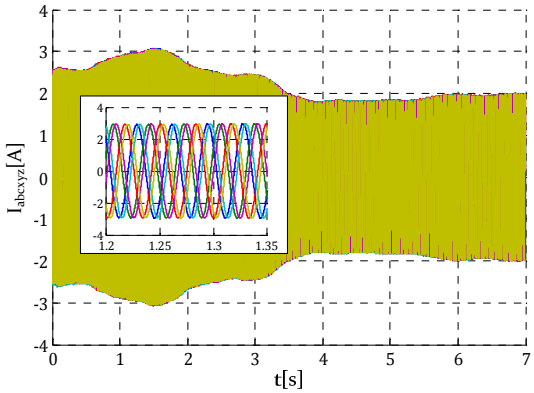

Fig. 6. Stator currents in time domain.

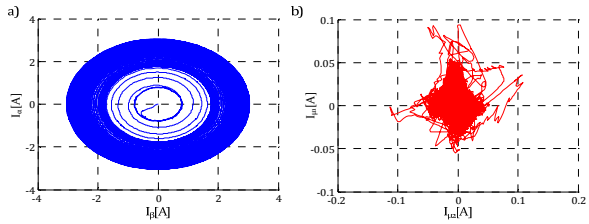

Fig. 7. Current components in α-β and μ_1-μ_2 subspaces.

5. CONCLUSION

Advanced system for conversion of wind energy, equipped with six phase induction generator is presented in this paper. IFOC with rotor speed estimation using MRAS is proposed and verified through simulation results. Furthermore, a novel modulation technique allowed for the improvement of control efficiency. Simulation results show that high dynamic performances of WECS with six-phase induction generator under sensorless vector control were achieved. Proposed topology significantly improves system reliability and robustness, while allowing WECSs to overcome key insufficiencies of standard solutions. In the future research proposed topology and control strategy will be practically implemented and verified.

6. REFERENCES

[1] GWEC Report, Global Wind Report – Annual market update 2013, *Global Wind Energy Council*, 2013.

[2] N. S. Patil, Y. N. Bhosle, "A Review On Wind Turbine Generator Topologies", *International Conference on Power, Energy and Control (ICPEC)*, pp. 625-629, 6-8 Feb. 2013.

[3] B. Wu, Y. Lang, N. Zagari, S. Kouro, Power Conversion and Control of Wind Energy Systems, *John Wiley and Sons, IEEE Press*, USA, 2011.

[4] E. Levi, R. Bojoi, F. Profumo, H.A. Toliyat, S. Williamson, "Multiphase induction motor drives - a technology status review", *The Institution of Engineering Technology, IET, Electric Power Applications, EPA*, Vol. 1, Issue. 4, pp. 489-516, 2007.

[5] D. Milicevic, V. Katic, Z. Corba, M. Greconici, "New Space Vector Selection Scheme for VSI Supplied Dual Three-Phase Induction Machine," *Advances in Electrical and Computer Engineering*, vol. 13, no. 1, pp. 59–64, 2013.

[6] R. Bojoi, F. Farina, F. Profumo, A. Tenconi, "Dual-Three Phase Induction Machine Drives Control-A Survey" *IEEJ Transection IA*, Vol.126, No.4, pp. 420–429, 2006.

[7] P. Vas, Sensorless Vector and Direct Torque Control, *Oxford Univ. Press, NY*, 1998, ch. 4.

[8] P. Vas, Artificial-Intelligence-based Electrical Machines and Drives: Application of Fuzzy, Neural, Fuzzy-neural, and Genetic-algorithm-based Techniques, *Oxford University Press*, 1999, ch. 5.

[9] B. Dumnic, V. Katic, V. Vasic, D. Milicevic, M. Delimar, "An Improved MRAS Based Sensorless Vector Control Method for Wind Power Generator" *Journal of Applied Research and Technology – JART*, Vol. 10. no. 5, pp. 687-697, October 2012.

[10] Y. Zhao, T.A. Lipo "Space vector PWM control of dual three-phase induction machine using vector space decomposition", *IEEE Transactions on Industry Application*, Vol. 31, pp. 1100–1108, 1995.

[11] F. Blaabjerg F. Iov, T. Kerekes, R. Teodorescu, "Trends in Power Electronics and Control of Renewable Energy Systems", *14th International Conference of Power Electronics and Motion Control*, K1-K19, EPE-PEMC 2010.

[12] F. Iov, A. D. Hansen, P. Sorensen, F. Blaabjerg "Wind Turbine Blockset in Matlab/Simulink," *UNI. PRINT Aalborg University*, March 2004.

The 7th International Conference on Engineering and Technology
ICET-2015, Phuket, June 19-20, 2015
Prince of Songkla University, Faculty of Engineering
Hat Yai, Songkhla, Thailand 90112

Solar PV System Grid Integration Issues - Harmonics

Vladimir A. Katic, Zoltan Corba, Boris Dumnic, Dragan Milicevic, Stevan Grabic, Nenad Katic
University of Novi Sad, Faculty of Technical Sciences
*Email of corresponding author: katav@uns.ac.rs

Abstract: *Solar PV systems show high current distortion in low radiation intervals. The paper investigates this problem, using computer simulation and harmonics measurements in the field. It is shown that single plant possesses no threat to the system. However, in case of multiple PV systems some negative effect (resonance or voltage distortion) may be expected.*

Key Words: ***PV systems, Power Quality, Harmonics***

1. INTRODUCTION

Application of renewable energy sources for electricity generation has been accepted worldwide as the most efficient method in fighting the effects of green houses gasses emission on clime changes. EU power mix at the end of 2014 shows that great changes have been made in recent years towards higher implementation of renewable energy sources [1,2]. The share of renewable energy sources (RES) in electricity generation has been risen up to 41.4% (379.2 GW), out of which there are 15.15% (140.7 GW) of hydro power, 14.1% (128.7 GW) of Wind power, 9.7% (88 GW) of Solar power and 2.43% (21.8 GW) of rest of the RES.

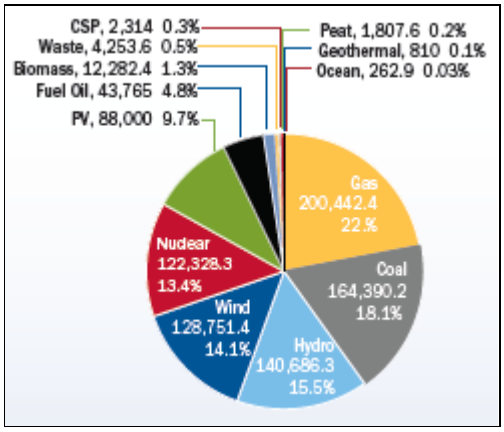

Fig. 1. EU power mix 2014 (MW) [1].

Fig. 2 shows annual share of installed electrical power capacities per energy source. It can be observed that from 2008 more than 50% was in area of renewable energy. In 2014 it reaches almost 80% of all new installed capacities. It shows high commitment of EU to reach the 2020 goal of 20% of energy coming from the RES and 20% reduction of green-house gases emission.

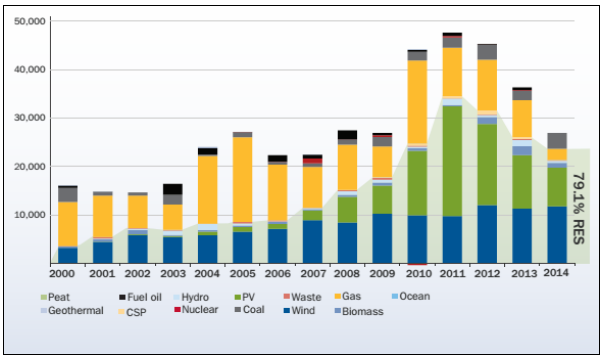

Fig. 2. New installed electrical power in EU [1].

Serbia, as candidate country for EU membership, is investing great efforts to install new RES capacities. There is a good potential, but the main problem is lack of funds for building large power plants [3]. Therefore, the main efforts are focus on smaller capacities, which is resulting in slow progress. Nevertheless, in the last 5 years 47.7 MW of new electrical generating units are put into operation, while 96.7 are under construction [4]:

Table 1. *Serbian RES capacity: operating and in-build [4]*

RES in Serbia (March 2015)	Operating [MW]	In build [MW]	Total [MW]
Solar PV systems (Sum)	7.2457	2.7041	9.9498
On the ground	4.665	1.335	6.0
Roof-top (0.03 – 0.5 MW)	1.0855	0.9145	2.0
Roof-top (≤0.03 MW)	1.4952	0.4546	1.9498
Wind Power plants	0.5	93.95	94.45
Small Hydro plants	34.8617	0	34.8617
Biogas	4.862	0	4.862
TOTAL:	47.4694	96.6541	144.1235

Most of the PV systems in Serbia are directly connected to the public grid (in-grid systems) supplying the "green" energy. In such a case the electric power quality is of great importance. The paper presents some

experiences with a small roof-top PV plant operation regarding power quality and more precisely harmonics issues.

2. HARMONICS OF IN-GRID PV SYSTEMS

Power quality (PQ) of generated power (output voltage and current) of the in-grid solar PV systems is regulated and controlled by the grid operator [5,6]. The PV system is not allowed to integrate into the system if it generates PQ problems to the grid. Special attention is paid to the harmonics. In Serbian regulation, small power plants are treated in the document TP 16, where among other conditions, detailed recommendation for voltage and current harmonics limits are given [7]. It should be mentioned that general PQ conditions and harmonics limits for European countries are given in EN50160 standard or in IEC 61000 series of standards (in USA IEEE Standard 519-1992 is applied, also) [8].

Large solar PV systems are normally built on the ground and connected to medium voltage (MV) network through power transformer. It is well known that the output current is distorted, while large power is generating into the distribution network, as transformer is operating with voltage higher than rated [9]. On the other hand, roof-top solar PV systems are usually of low power and connected directly (without transformer) to the low voltage (LV) grid. In that case, PQ issues are directly related to grid inverter operation and characteristics.

One of the first roof-top solar PV plants in Serbia was constructed in Novi Sad, on the roof of the Faculty of Technical Sciences – solar PV plant "FTN Novi Sad" [2,3]. It has been operating successfully, without significant problems since 2011. According to the national regulation, presented in the TP 16, voltage and current harmonics are defined as maximum permitted values in Amperes and Volts (in respective tables), taking into account the level of short-circuit power at the PV system connection point. In that way, operation at rated power is considered, only.

However, during regular control of output terminals PQ parameters, high values of current distortion (total harmonic distortion of output current – THDI) during low solar irradiation (low output power) intervals have been noticed. The THDI is defined according to EN50160 standard as:

$$THDI = \sqrt{\frac{\sum_{n=2}^{\infty} I_n^2}{I_1^2}} \cdot 100\,\% \qquad (1)$$

where n is harmonic order and fundamental frequency is f=50Hz. Such a definition is different than the one in the TP16. That may present a problem as by the TP16 everything may be well, but according to EN50160 harmonics values may be way above the limits. This issue is discussed further in the paper.

3. PV SYSTEM SIMULATION MODEL

To address the above mentioned problem, a solar PV system simulation model has been developed using Matlab-Simulink tools [10]. Due to lack of space, the model will be presented with a schematic diagram, only (Fig.3). PV panel, DC/DC Boost converter, Three-phase Inverter, RL connection circuit and the public grid symbol may be recognized and distinguished.

Simulation results show the PWM structure of the output voltage (Fig.4), which is filtered by the RL connection circuit to sinusoidal wave-shape according to requirements of the grid. The output current is of similar shape and the harmonics distortion should be les then 2% at output powers above the 0.5 of the rated.

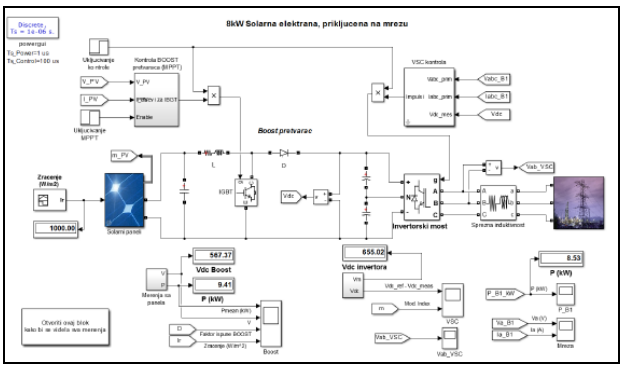

Fig. 3. Solar PV System simulation model schematics.

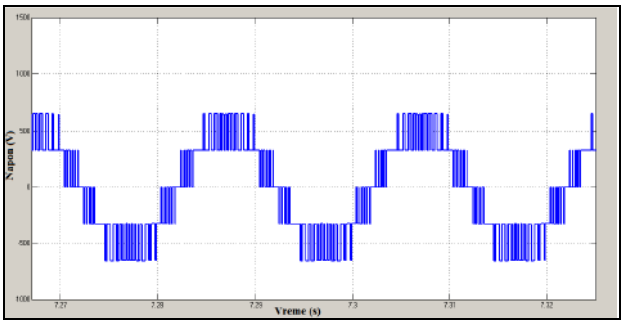

Fig. 4. Inverter output voltage (phase A)

4. MEASUREMENT RESULTS

The PQ parameters of the roof-top solar PV plant "FTN-Novi Sad" are regularly measured and controlled. The measurements are conducted at the PV system inverter output, at the point of common coupling (connection) to the grid. Fig. 5 shows the measurement instrumentation set-up and connections at the SMA inverter output (blue-black box in the left-hand figure). The latest measurement session was in December 2014, which lasted 4 days. Figs. 6-8 present some of the recorded results: output power and current, voltage and current THD and statistical presentation of THD results (cumulative probability of THDU and THDI). From Fig.6 it is obvious that there were three days with god (sunny) weather (24-25.12.2014. & 27.12.2014.), one day with some clouds (23.12.2014.) and one day with lots of clouds (26.12.2014.). Power and current pattern are very similar as output voltage is stiff grid voltage (230V ±5%). Fig.7 shows that the output voltage harmonic level (THDU) is low, between 1.7% and 3.1% and that 95% probability is $THDU_{95\%}$=2.7%. This value is actually not result of the PV system operation, but more likely the effect of all non-linear loads connected to the same grid. Moreover, the level of voltage harmonic is much lower than stipulated limits in mentioned EN and

IEC standards (THDU≤8%) or in the IEEE standard (THDU≤5%) [8].

Fig. 5. Measurement set-up at the PV output.

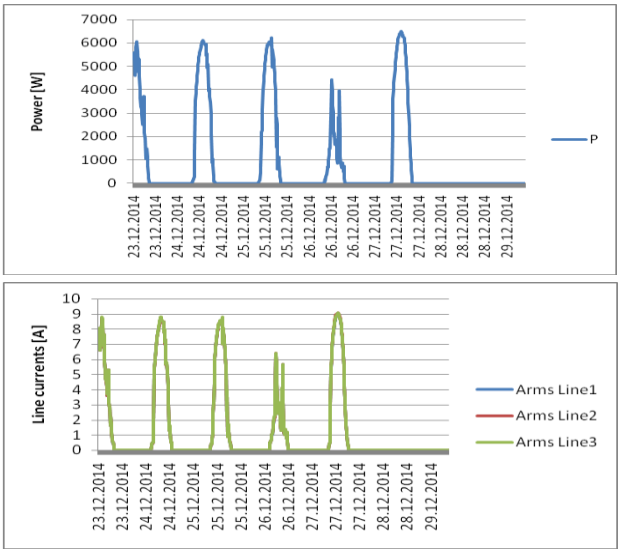

Fig. 6. Output power (above) and current (below) – Dec.2014.

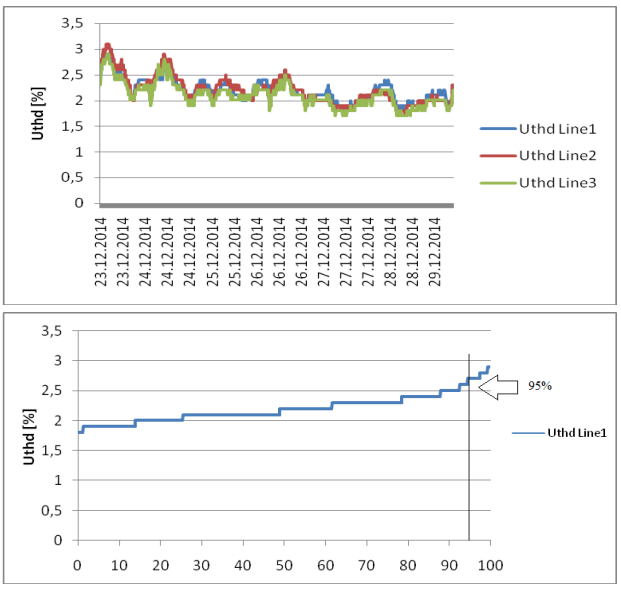

Fig. 7. Voltage harmonics (THDU): Daily values (above) and cumulative probability (below) – Dec.2014.

However, current harmonics, presented in Fig.8, show very high levels. Some peacks are over 250%! It is obvious that the highest values were recorded in morning and evening hours, when solar radiation is low. Some increased THDI values can be observed during cloudy day (26.12.2014.), also in periods with lower radiation. Cumulative probability curve shws that 95% probability value is as high as $THDI_{95\%}$=52%. This is much higher than permited by IEEE Standard 519-1992, which limits total current distrotion at 20% for low power loads [8].

Similar results have been obtained in other (previous) measurement sessions, so they need to be further discussed. Fig.9 shows a recording from January 2014 mesurement session. Again, high current harmonics values have been noticed in low solar radiation intervals.

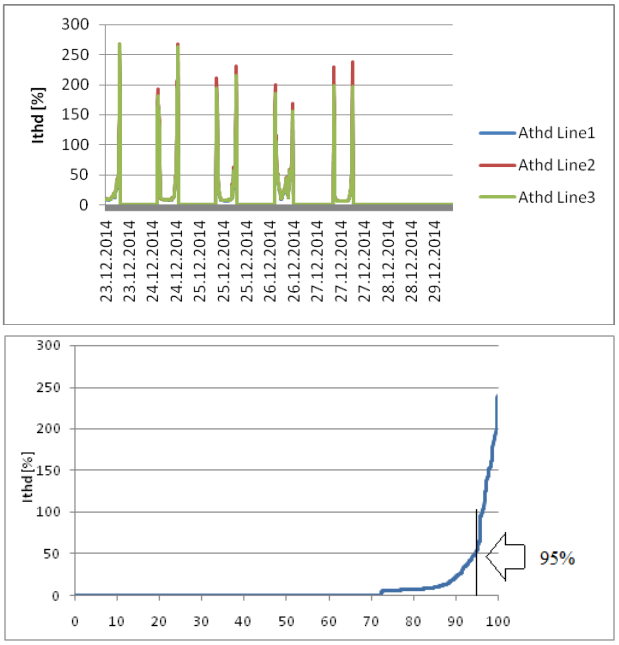

Fig. 8. Current harmonics (THDI): Daily values (above) and cumulative probability (below) – Dec.2014.

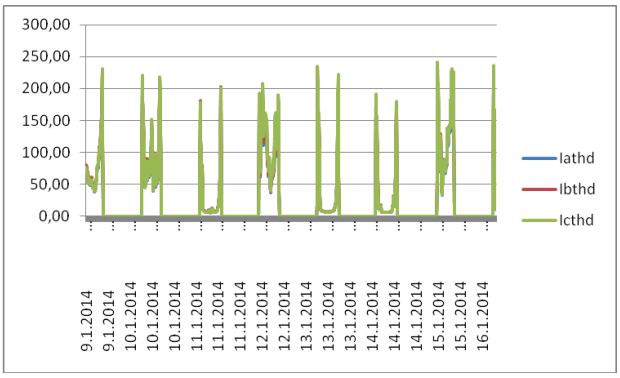

Fig. 9. Current harmonics (THDI) – Jan.2014.

5. DISCUSSION

High current harmonics are recorded during low radiation intervals, i.e. when inverter output power is significantly bellow rated. As voltage is dictated by the grid, the main problem is high current distortion. Fig.10 shows a sample of voltage and current waveform of line 3, while Fig.11 current waveforms of all three lines together with spectrum and harmonics values of line 1 current. High current distortion can be notices – the current is way out of sinusoidal wave shape.

Although such a case might be regarded as intolerable, the fact that the PV system in these intervals

is generating very low power means that such a distortion does not possess no threat to the public grid power quality. Still, it may provoke resonance or some other negative effects, especially if there is a large number of such PV systems connected to the same grid. Also, their cumulative effect may distort grid voltage, also. Such a case has not been recorded yet, but need to be investigated using developed simulation model as further work on this topic.

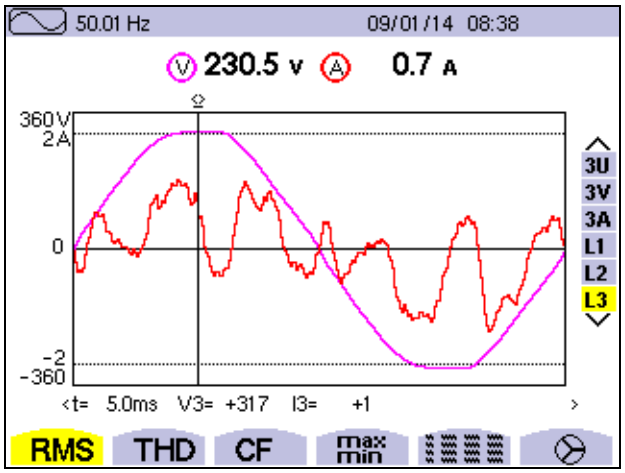

Fig. 10. Line 3 voltage and current waveform.

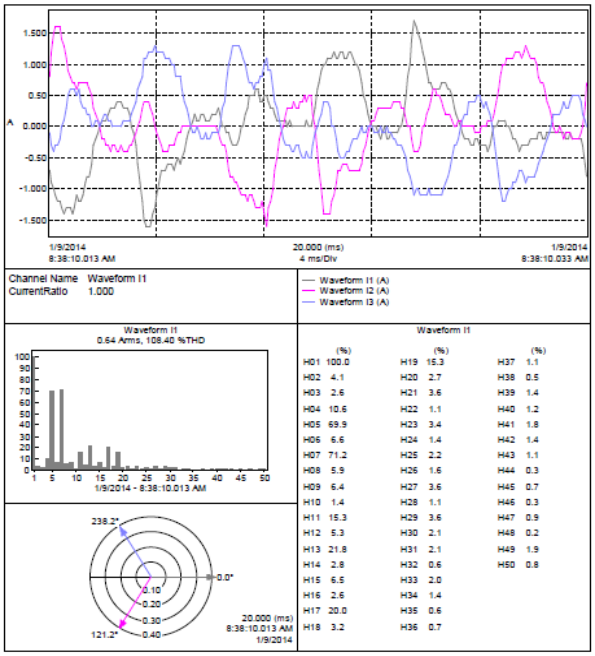

Fig. 11. Waveforms of all three lines and spectrum and harmonics values of line 1 current.

6. CONCLUSIONS

During regular control of the solar PV system power quality parameters, high values of current distortion have been noticed during low solar irradiation intervals. In these cases total harmonic distortion is much higher than allowed by international standards. It is concluded that this should not be a problem, as PV system generates low power, much smaller in comparison to the short-circuit power of the grid. However, if there is a large number of such installation (for example in a village) connected to the same (radial) power line, this may have some negative effects.

ACKNOWLEDGMENT

This paper is a result of the scientific project No. III 042004 entitled "Smart Electricity Distribution Grids Based on Distribution Management System and Distributed Generation", funded by Republic of Serbia, Ministry of Education, Science and Technological Development.

7. REFERENCES

[1] Ivan Pineda, Justin Wilkes, "Wind in Power – 2014 European Statistics", European Wind Energy Association, 2015, Available On-line: http://www.ewea.org/

[2] Vladimir Katic, Zoltan Corba, Dragan Milicevic, Boris Dumnic, Bane Popadic, Evgenije Adzic, "Overview of Solar PV Energy Market in Serbia", *Proc. of the PSU-UNS 6th International Conference on Engineering and Technology – ICET 2013*, Novi Sad, Serbia, 15-17 May 2013, Key-Note Lecture (Invited Paper), Paper No. IP-3.1, pp.27-32.

[3] Tomislav Pavlovic, Dragana Milosavljevic, Ivana Radonjic, Lana Pantic, Aleksandar Radivojevic, Mila Pavlovic, "Possibility of electricity generation using PV solar plants in Serbia", *Renewable and Sustainable Energy Reviews*, Vol. 20, April 2013, pp.201–218

[4] http://www.mre.gov.rs/doc/registar150302.html

[5] Raymond Hudsona, Gerd Heilschera, "PV Grid Integration – System Management Issues and Utility Concerns", *Energy Procedia*, Vol.25 (2012), pp.82–92. doi:10.1016/j.egypro.2012.07.012

[6] Vladimir Katic, "Grid Integration of Renewable Energy Conversion Systems", *Proc. of the PSU-UNS 4th International Conference on Engineering Technologies – ICET 2009*, Keynote Lecture, April 28-30, 2009, Novi Sad, Serbia, pp.27-39.

[7] ***, "Technical recommendations No. 16: Basic technical requirements for connection of small power plants to the power distribution system", Electric Power Industry of Serbia, May 2003. (In Serbian)

[8] R.Dugan, M.McGranaghan, S.Santoso, H.Wayne Beaty, "Electrical Power System Quality", 2nd Edition, McGraw-Hill, New York, 2003.

[9] Jinbin Zhao, Yawei Wang, Keqing Qu, Fen Li, "Analysis and evaluation of current distortion for photovoltaic system with isolation transformer", *IET Renewable Power Generation*, Vol. 8, Issue 7, 2014, pp. 757–764, doi:10.1049/iet-rpg.2013.0393

[10] G.Cibula, M.Fejsa, I.Halkic, M.Kokotovic, "Mathematical and Computer Modeling of a Solar PV plant", Seminar paper, Course: *Renewable Electrical Energy Sources*, Supervisor: Prof. V.Katic, Master Studies, Faculty of Technical Sciences, Novi Sad, 2015 (In Serbian).

The 7th International Conference on Engineering and Technology
ICET-2015, Phuket, June 19-20, 2015
Prince of Songkla University, Faculty of Engineering
Hat Yai, Songkhla, Thailand 90112

Basic Properties of Structural LWAC Based on Waste Materials

Vlastimir Radonjanin[1]*, Mirjana Malešev[1], Miroslava Radeka[1], Ivan Lukić[1], Vesna Bulatović[1]
[1]University of Novi Sad, Faculty of Technical Sciences, Novi Sad, Serbia
*Email of corresponding author: radonv@uns.ac.rs

Abstract: *The paper presents the research of structural lightweight concrete (LWAC) with lightweight recycled aggregate and high volume of fly ash. The basic idea of the research was to develop concrete composite with satisfactory mechanical properties and improved thermal properties and simultaneously to solve problems with landfill of industrial waste materials, such as silica stone sludge, paper sludge and fly ash.*

Key Words: ***Lightweight Concrete, Waste, Recycled Aggregate, Mechanical Properties***

1. INTRODUCTION

Structural lightweight aggregate concretes (LWAC) are special group of lightweight concretes. These concretes have a number of advantages in relation to ordinary concrete (eg. reducing weight of structure, reducing overall loads on foundations and soil, better thermo-technical performance, better fire resistant, better resistant to freezing, etc.), but have also its disadvantages, among which considerably larger amount of cement (about 450kg/m^3) is emphasized [1]. This disadvantage has particularly been underlined in the last years, due to the increasing environment pollution and greenhouse effect, in which the cement industry has a significant role.

The manuals for the selection of type and quantity of component materials for structural LWAC often recommend that it is the best to use high amount of Portland cement with high-class strength (i.e. CEM I 42.5) [2]. Nevertheless, production of this type of cement has the largest influence on the environment.

The justification for using large quantities of high strength class cement lies in the explanation of the way how load is transmitted in LWAC. Unlike regular weight concrete, where both macro structural components (cement matrix and coarse aggregate) participate in load transmission, in LWAC the load is transmitted by cement matrix only. Therefore, cement matrix of LWAC has to have high mechanical properties and has to coat lightweight aggregate grains well [2]. One m^3 of LWAC approximately consists of 0.1m^3 cement, 0.2m^3 effective water and pores in cement paste and 0.7m^3 aggregate.

In order to check the justification of applying large quantities of high strength class cement (CEM I 42.5), as well as to determine the possibility of decreasing cement quantity in LWAC, changing CEM I with Portland composite cement and substituting part of CEM I with other cementitious materials, experimental testing was performed.

Besides decreasing of cement quantity, the possibility of use of LWA based on industrial waste materials in structural LWAC, was investigated.

The basic idea of this experiment was to decrease the impact of LWAC on the environment, and also to lower the unit price of LWAC while at the same time preserving the structural performance of the concrete.

2. EXPERIMENTAL INVESTIGATION

Experimental investigation encompassed four types of lightweight aggregate concrete and one normal weight concrete NWC (with natural river aggregate) as referent concrete.

The type and quantity of the cement were varied in first three LWAC mixtures. Two types of cement were used, which differ not only in composition, but also in class (42.5 and 32.5). Two different quantities of cement (400 and 450kg/m^3) were varied, also.

In fourth LWAC mixture 50% of cement was substituted with fly ash and metakaolin.

The following properties of hardened concrete were examined: compressive strength; modulus of elasticity; dynamic modulus of elasticity; drying shrinkage; water absorption; capillary water absorption; water penetration under pressure; splitting tensile strength and flexural strength. Due to limited space, compressive strength and modulus of elasticity which are relevant for structural concrete are presented in this paper.

2.1. Methods

Compressive strength was tested after 2, 7 and 28 days on the 15cm cubes, according to the ISO 4012. All samples were cured in water. Additional set of three samples was cured in the air to obtain information about influence of curing method on compressive strength.

Static modulus of elasticity (E) was determined according to the ISO 6784.

Dynamic modulus of elasticity (Ed) was determined by measuring the ultrasonic pulse velocity through the concrete. Both moduli were tested on cylinders Ø150, H=300mm at age of 28 days.

Total number of tested samples was 75.

2.2 Component materials and mix design

The following component materials were used [5]:

- Portland cement CEM I 42.5R, (Lafarge-BFC Serbia, γ_s=3100kg/m^3),
- Portland composite cement CEM II/B-M (S-V-L) 32.5 R (Lafarge-BFC Serbia, γ_s=3020kg/m^3)
- Normal weight aggregate (natural river aggregate, fractions 0/4mm, 4/8mm i 8/16mm),
- Lightweight aggregate (expanded clay, Leca – Laterlite, fraction 2-3mm, water absorption 12,1%, Italy,
- Lightweight recycled aggregate – "ZAG"; made of 40% silica stone sludge, 40% paper sludge and 20% fly ash with appropriate thermal treatment; water absorption 33,2% (Ljubljana, Slovenia),
- Fly ash (siliceous fly ash – class "F" according to ASTM C 618; power plant "Nikola Tesla B" Obrenovac – Serbia, γ_s=2100kg/m^3), additionaly pulverised and activated by grinding,
- Metakaolin HR (Metamax – USA, γ_s=2500kg/m^3),
- Superplasticizer (HWRA) (Sika ViscoCrete 4000BP, "Sika", γ_s =1080kg/m^3),
- Water.

Cement *Fly ash* *Metakaolin*

Fig. 1. *Component materials - cementitious materials*

River aggregate 0-4mm *LWA "LECA" 2-3mm* *LWA - recycled "ZAG", 4-8mm*

Fig. 2. *Component materials – used types of aggregate*

The mix design was based on the following conditions [5] [6]:

- the same consistency (slump = 12 ± 2cm),
- absolute volume of binder and water of approximately 0,3m^3, and absolute volume of aggregate approximately 0,7m^3,
- grain size distribution of aggregate mixture in the form of continuous curve,
- additional amount of water was determined based on lightweight aggregate water absorption after 30 minutes (12,1 for LECA and 33,2% for ZAG),
- the amount of superplasticizer depending on the need for achieving the required consistency (0,5-0,6%m_{binder}),
- effective water cement ratio 0,4 – 0,5, depending on the amount of cement.

The compositions of the investigated concrete mixtures are given in Table 1.

Table 1. *Concrete mix composition (kg/m^3)*

Concrete type	LSLL1	LSLL2	LSLL4	LSLL5	NWC
CEM I	450	-	400	244	450
CEM II	-	450	-	-	-
Water	180	180	180	183	180
Additional water	119.5	119.5	121.2	119.5	-
NWA: 0/4mm	749	749	771	760	851
NWA: 4/16mm	-	-	-	-	885
LWA:Leca 2-3mm	90	90	91	90	-
LWA:ZAG 4-8mm	327	327	332	327	-
Fly ash	-	-	-	97.6	-
Metakaolin	-	-	-	24.4	-
Superplasticizer	2.25	2.7	2.00	3.3	3.15

3. RESULTS AND DISCUSSION

3.1 Compressive strength

Results of testing of concrete compressive strength (f_c) for different ages and concrete density (γ_c) are given in Table 2. In the same table, 28-day compressive strengths ($f_{c,28}^+$) obtained on samples cured in the air, are presented also. Testing of compressive strength and typical fracture of the LWAC cube are shown in Fig. 3 and 4.

Table 2. *Concrete compressive strength*

Concrete type	LSLL1	LSLL2	LSLL4	LSLL5	NWC
Binder type	CEM I	CEM II	CEM I	CEM I + FA +MK	CEM I
m_c (kg/m^3)	450	450	400	244	450
γ_c (kg/m^3)	1812	1760	1751	1714	2348
$f_{c,2}$ (MPa)	24.3	13.6	21.0	13.8	41.4
$f_{c,7}$ (MPa)	29.5	22.0	26.1	20.5	53.3
$f_{c,28}$ (MPa)	**33.3**	**31.6**	**29.4**	**25.9**	**60.4**
$f_{c,28}^+$ (MPa)	34.3	30.5	30.1	28.5	-

Fig. 3. *Testing of compressive strength*

Fig. 4 *Typical fracture of the LWAC cube*

Development of LWAC compressive strength is presented in Fig. 5.

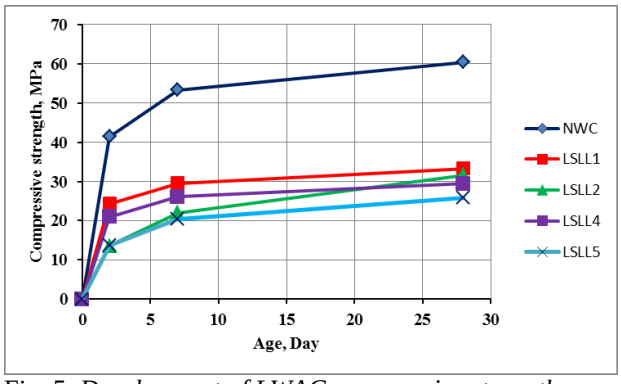

Fig. 5. *Development of LWAC compressive strength*

Analysing the results presented in Table 2 and Fig. 5, the following can be concluded:

- The type of the used coarse aggregate has a significant influence on the compressive strength regardless of concrete age. This conclusion was derived after comparing the compressive strength of the types of concrete that contain the same quantity of cement CEM I (LSLL1 and NWC). The difference in compressive strengths was additionally influenced by the cement matrix quality. The quality of cement matrix of LSLL concretes was lower due to substitution of a part of river fine aggregate with lightweight fine aggregate "LECA".
- By increasing the concrete age, the difference in compressive strength between NWC and LWAC also increases, which is explained by gradual incorporation of coarse river aggregate grains in the load transfer, as opposed to LWA, whose contribution to the concrete strength decreases over time.
- By increasing the concrete age, the influence of the cement type/class on the compressive strength of LWAC is also significantly decreased. This conclusion is confirmed by comparing the LSLL1 and LSLL2 concrete. The difference in strength is significant for the early age concrete (10.7MPa) and gradually decreasing with age, so that at 28 days is 1.7MPa. This statement is supported by different hydration speed between CEM I and CEM II.
- The influence of mineral admixtures in concrete can be explained in a similar way. By comparing the strength of LSLL1 and LSLL5, it can be concluded that the difference in strength is gradually decreased by increasing the age. It should be taken into account that the difference in the cement quantities between these two concrete types is 206 kg.
- By increasing the quantity of cement, the compressive strength of LWAC is also increased. This correlation is almost linear (LSLL1 and LSLL4). Nevertheless, it can be noticed that the difference between compressive strengths of LSLL1 and LSLL4 is 3MPa only.

The influence of curing method on 28-day compressive strength is shown in Fig. 6.

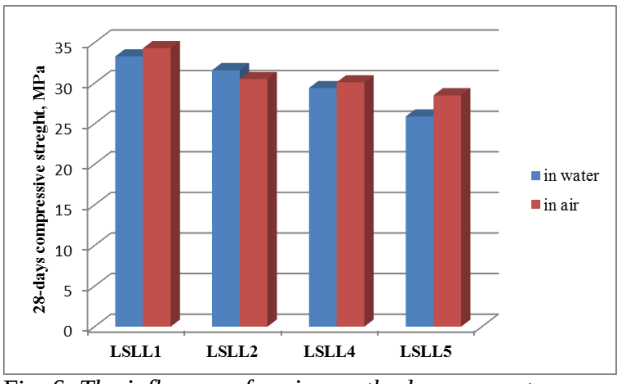

Fig. 6. *The influence of curing method on concrete compressive strength*

Small difference between compressive strengths of LWAC cured in water and in the air (0.7 - 2.6 MPa) is result of open porosity of lightweight aggregate "ZAG" and specific procedure of LWAC preparation. By prewetting, lightweight aggregate accumulate enough water which enables hydration of cement without wet curing. This phenomenon is known as "self-curing of concrete".

Slightly higher compressive strengths of LWAC cured in air are consequence of condition of samples prior to testing. It is well known that wet concrete samples always have smaller compressive strength than dry concrete samples.

3.2 Static and dynamic modulus of elasticity

Testing of static modulus of elasticity (E) is shown in Fig. 7. The modulus of elasticity was calculated as the difference of the measured stresses and strains on an upper level (i.e. 1/3 of the value of compressive strength) and a lower level (stress for ε=0.01mm).

Fig. 7. *Testing of static modulus of elasticity*

Dynamic modulus of elasticity (E_d) was determined by measuring the ultrasonic pulse velocity through the concrete and calculated by the equation [7]:

$$E_d = v^2 \cdot \gamma \qquad (1)$$

Obtained results are shown in Table 3.

Table 3. *Moduli of elasticity of LWAC and NWC*

Concrete type	LSLL1	LSLL2	LSLL4	LSLL5	NWC
m_c (kg/m^3)	450	450	400	244	450
E (GPa)	18.02	17.28	15.27	13.43	35.22
E_D (GPa)	26.92	24.28	22.84	-	49,24
E/E_d [%]	0.669	0.711	0.669	-	0.715

Comparing concrete LWAC and NWC it can be seen that light aggregate "ZAG" significantly reduces the modulus of elasticity. The difference between E of NWC and LSLL1 is ~ 50%, and is a consequence of the lower mechanical properties of coarse lightweight aggregate and higher deformations of cement matrix of LSLL concretes due to substitution of a part of river fine aggregate with lightweight fine aggregate "LECA".

The influence of type / class of cement on the value of the modulus of elasticity is small (the difference is 0,74GPa, or 4%).

The influence of cement quantity on modulus of elasticity is visable when concrete LSLL1 and LSLL4 are compared: higher amount of cement – higher modulus of elasticity. The lowest value of modulus of elasticity has concrete LSLL4 with cement content of 244kg/m^3 and mineral admixtures.

Analysing ratio between E and E_D it can be concluded that strong linear relation could be established:

$$E = 0.7 \cdot E_d \tag{2}$$

4. CONCLUSION

Based on comparative analysis of the results of investigated properties of lightweight aggregate concrete and normal weight concrete, it was concluded:

- Structural lightweight aggregate concrete, as a special type of lightweight concrete, due to their good performance, have a number advantages when compared to ordinary concrete. Nevertheless, the future application of structural lightweight aggregate concrete will depend largely on the possibility of decreasing the cement quantity, i.e. the quantity of the cement clinker.
- In this study, due to the poor quality of the lightweight aggregate that was obtained from industrial waste material, as well as due to the larger specific surface area of the lightweight aggregate grains, the minimum amount of cement is about 400kg/m^3. With this amount of cement were obtained 28-compressive strength approximately 30MP.
- It is obligatory to apply chemical admixtures of HRWRA type, because of their positive influence on the concrete strength.
- By combining larger quantities of fly ash and smaller quantities of metakaolin, the total amount of cement is reduced to 244kg/m^3, with satisfactory LWAC 28-day compressive strength of approximately 26MPa.
- 28-day compressive strength of investigated LWAC concretes ranged between 26 and 33MPa, depending on the type and quantity of cement/binder. These values can be accepted as satisfactory, considering the fact that the bulk density of tested LWAC is lower for more than 500kg/m^3 compared to ordinary concrete (NWC).
- "Self-curing" is significant advantage of concrete made with aggregate that have open porosity. Namely, if the porous aggregate is pre-saturated with water, then in the process of hardening, cement will spend the accumulated water in the pore space of aggregate for hydration.
- Values of static modulus of elasticity of LWAC with lightweight recycled aggregate “ZAG” are in the range of 15 and 18GPa and are significantly lower then the values of referent concrete with natural river aggregate.
- There is good correlation between static and dynamic modulus of elasticity for investigated LWAC.

Acknowledgment

The work reported in this paper is a part of the investigation within the research project TR 36017 "Utilization of by-products and recycled waste materials in concrete composites in the scope of sustainable construction development in Serbia: investigation and environmental assessment of possible applications", supported by the Ministry of Science and Technology, Republic of Serbia. This support is gratefully acknowledged.

5. REFERENCES

[1] Chandra, S., Berntsson, L.: "Lightweight Aggregate Concrete - Science, Technology and Applications", Noyes Publications, William Andrew Publishing, New York, U.S.A., 2002.

[2] FIP manual of lightweight aggregate concrete, Surry University Press, Glasgow and London, 1983.

[3] LWAC – Material Properties, Economic Design and Construction with LWAC State of the Art, Document BE96-3942/R2, 1998, 1-111.

[4] ACI Committee: "ACI 213-03: Guide for Structural Lightweight-Aggregate Concrete", 2003.

[5] Malešev, M., Radonjanin, V., Radeka, M., Milovanović, V, Lukić, I.: "Basic Properties of Structural Lightweight Aggregate Concrete in Relation to Type and Quantity af Cementitious Materials - Part 1", DIMK Serbia, International Symposium, Proceedings, 2011,159-168.

[6] Radonjanin, V., Malešev, M., Radeka, M., Lukić, I., Milovanović, V.: "Basic Properties of Structural Lightweight Aggregate Concrete in Relation to Type and Quantity of Cementitious Materials - Part 2", DIMK Serbia, International Symposium, Proceedings, 2011, 169-178.

[7] Bungey, J., Millard, S. G., Grantham, M. G.: Testing of concrete in structures, 2006, Taylor & Francis.

[8] How-Ji Chen, Tsong Yen, Kuan-Hung Chen: "Evaluating Elastic Modulus of Lightweight Aggregate", Materials Journal, Vol. 100, Issue 2, 2003, pp. 108-113.

The 7th International Conference on Engineering and Technology
ICET-2015, Phuket, June 19-20, 2015
Prince of Songkla University, Faculty of Engineering
Hat Yai, Songkhla, Thailand 90112

LWAC Based on Waste Materials and Application in Thermally Improved Masonry

Mirjana Malešev[1], Vlastimir Radonjanin[1]*, Vesna Bulatović[1], Ivan Lukić[1], Gordana Broćeta[2]
[1]University of Novi Sad, Faculty of Technical Sciences, Novi Sad, Serbia
[2]University of Banja Luka, Faculty of Architecture and Civil Engineering, Banja Luka, Bosnia and Herzegovina
*Email of corresponding author: miram@uns.ac.rs

Abstract: *The paper presents the research of possibility of structural lightweight concrete (LWAC) with lightweight recycled aggregate and high volume of fly ash for production of hollow masonry block with satisfactory mechanical and thermal properties. The basic idea of the research was to develop masonry concrete block with improved thermal properties. Production of such masonry LWAC blocks follows the idea of energy efficiency and sustainable development in sense of preserving and protecting the environment by reduction of emission of CO_2 and decreasing depletion of resources of natural row materials. The basic thermal and technical properties of developed blocks are given in the paper, also.*

Key Words: ***Masonry Block, Lightweight Concrete, Waste, Recycled Aggregate, Energy Efficiency***

1. INTRODUCTION

Due to the rapid reduction of reserves of non-renewable sources of energy and building raw materials, global warming and greenhouse gas emissions, energy efficiency and sustainable development become a priority of modern society, especially in the field of construction and energetics.

Energy efficiency in buildings is crucial for saving primary energy. Any reduction of energy consumption for heating and cooling of residential, public and industrial buildings is an important contribution to the energy balance of a country. A large part of the total thermal energy that is lost through the envelope of buildings belongs to the facade walls. The masonry bricks and blocks are often used for construction of the walls of the building envelope. In contemporary civil engineering priority is given to hollow ceramic and concrete masonry blocks.

This paper presents the research and development of a special hollow masonry block, made of lightweight aggregate concrete. Lightweight aggregate was produced from industrial wastes - silica stone sludge, paper sludge and fly ash. Due to the selection of the optimal composition of lightweight aggregate concrete, properties of several different concretes were tested and analyzed [5, 6]. Additional data about this part of the research could be found in paper "Basic Properties of Structural LWAC Based on Waste Materials" by Radonjanin, Malesev et al. (ICET 2015).

2. PILOT PRODUCTION OF LWAC MASONRY BLOCK

For making of hollow blocks lightweight aggregate concrete in which 50% of cement was replaced with fly ash and a small amount of metakaolin, was selected. In this LWAC lightweight recycled aggregate was chosen as coarse aggregate. Mix design was done according to procedure proposed by [3, 4].

Basic data about component materials and mix proportion of this LWAC are given below.

2.1 Component materials and mix proportion

- Portland cement CEM I 42.5R, (Lafarge-BFC Serbia),
- Normal weight fine aggregate – NWA, (natural river aggregate),
- Lightweight aggregate (expanded clay, Leca – Laterlite, fraction 2-3mm, Italy),
- Lightweight recycled aggregate – "ZAG"; made of 40% silica stone sludge, 40% paper sludge and 20% fly ash with appropriate thermal treatment; water absorption 33,2% (Ljubljana, Slovenia),
- Fly ash – FA, (siliceous fly ash – class "F" according to ASTM C 618; power plant "Nikola Tesla B" Obrenovac – Serbia),
- Metakaolin HR – MK (Metamax – USA),
- Superplasticizer (HWRA) (Sika ViscoCrete 4000BP, "Sika"),
- Water.

Table 1. *Mix composition of concrete LSLL5 (kg/m^3)*

CEM I	Water	Add. Water	NWA	LWA Leca	LWA ZAG	FA	MK	Sika HRWR
244	183	119,5	760	90	327	97,6	24,4	3,3

2.2 Masonry block design

The nominal dimensions of the block, the size and arrangement of the holes are selected on the basis of analysis of the dimensions of modern concrete blocks and are presented in Fig. 1.

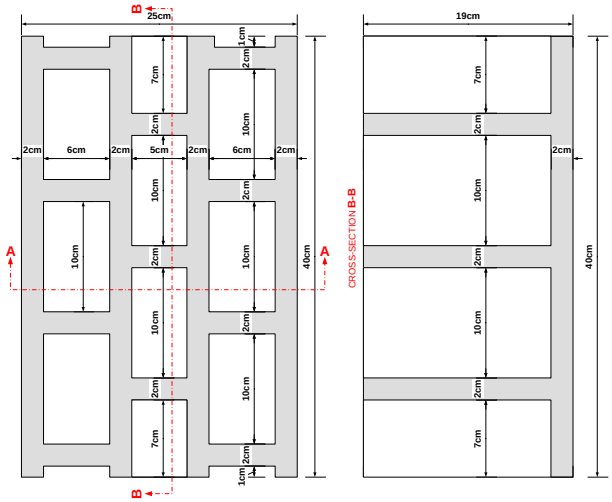

Fig. 1. *Basic dimensions of the hollow LWAC block*

In the aim of providing good placing of the concrete, 2cm wall thickness of the block is selected.

2.3 Production of the LWAC masonry block

The blocks are produced in the laboratory. For their formation wooden molds were used. In order to further improve the thermal properties of the blocks, internal hollows were filled with expanded polystyrene (Fig. 2). A total of five hollow block masonry.

Fig. 2. *Placing of LWAC in the prepared mold*

The blocks are demolded after 24 hours and cured in water. After 28 days blocks were prepared for testing of compressive strength (Fig. 3).

Fig. 3. *LWAC masonry block prepared for testing*

3. RESULTS AND DISCUSSION

3.1 Compressive strength of blocks

Figure 4 shows the procedure for determining the compressive strength of hollow masonry blocks.

Fig. 4. *Testing of compressive strength of LWAC block*

Basic geometrical, physical and mechanical properties of holow masonry block are presented in Table 2. All data in the table are average values of 5 results.

Table 2. *Basic data of the masonry LWAC block*

Nominal dimensions	25x40x19cm
Net volume of the block	9534cm^3
Total volume of the block	18544cm^3
Gross bearing surface of the block	976cm^2
Average weight of the block	19.75kg
Volumetric mass density of the block	1056kg/m^3
Weight of 1m^2 wall (d=0.25m), with both sides plastered with compo mortar	3.5kN/m^2
Average compressive strength	9.0MPa
The lowest compressive strength	8.45MPa

Based on the obtained mechanical properties it can be concluded that this block can be used as masonry block for bearing walls.

3.2 Determination of the thermal conductivity of LWAC masonry block

Calculation procedure of the thermal conductivity of LWAC masonry block was performed according to ISO 6946 [2].

Characteristic section of the block for determination of the thermal conductivity is shown in the Fig. 5.

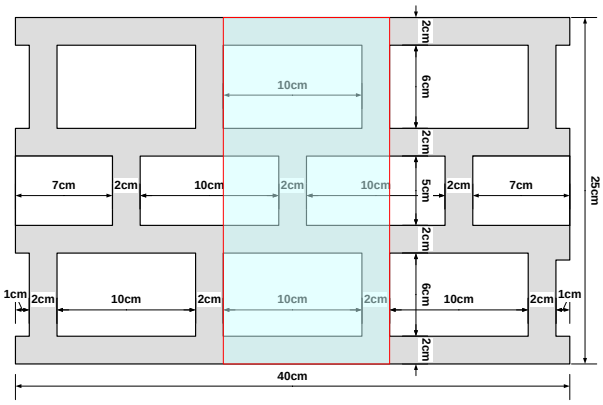

Fig. 5. *Characteristic section of the block*

Dimensions and marks of the layers in the characteristic section of the block are presented in Fig. 6.

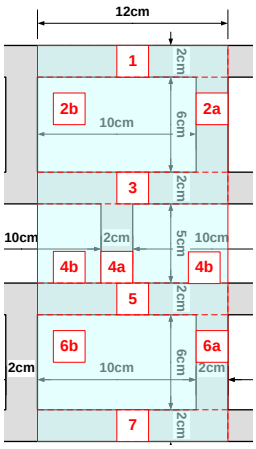

Fig. 6. *Dimensions and marks of the layers*

Basic data for the calculation of thermal conductivity of LWAC are:

$M_{block,\ ave}$= 18376g
V_{block}= 18544cm^3
V_{LWAC}= 9534cm^3
V_{EPS}= 9010cm^3
γ_{EPS}= 20kg/m^3=0.02g/cm^3
M_{EPS}= 0.02·9010=180g
M_{LWAC}= 18376-180=18196g
γ_{LWAC}= 1900kg/m^3=1.9g/cm^3

According to EN 1745 [1], Annex A, Table A.9 (Elements of LWAC), for γ_{LWAC}=1900kg/m^3, thermal conductivity of LWAC is:

$$\lambda_{LWAC}=1.205 W/(m^2K)$$

Table 3. *Physical characteristics and thermal resistance of layers*

	Layer	d m	λ w/(m·K)	R m^2/(w·K)
i				0.13
1	LWAC	0.02	1.205	0.0166
2a	LWAC	0.06	1.205	0.0498
2b	Expanded polystyrene	0.06	0.036	1.6667
3	LWAC	0.02	1.205	0.0166
4a	LWAC	0.05	1.205	0.0415
4b	Expanded polystyrene	0.05	0.036	1.3889
5	LWAC	0.02	1.205	0.0166
6a	LWAC	0.06	1.205	0.0498
6b	Expanded polystyrene	0.06	0.036	1.6667
7	LWAC	0.02	1.205	0.0166
e				0.04

LWAC masonry block consist of thermal homogenous and nonhomogeneous layers which are perpendicular to the heat transfer. Total thermal resistance of this type of building element is calculated according to:

$$R_T = \left(R_T' + R_T''\right)/2 \qquad (1)$$

where:
R_T' - the upper limit value of thermal resistance
R_T'' - the lower limit value of thermal resistance

The formula for calculation of upper limit value of thermal resistance R_T' is:

$$R_T' = \frac{1}{\frac{f_1}{R_{T1}} + \frac{f_2}{R_{T2}} + \frac{f_3}{R_{T3}}} \qquad (2)$$

Schematic view of characteristic cross-sections for calculation of upper limit value of thermal resistance R_T' is given in Fig. 7.

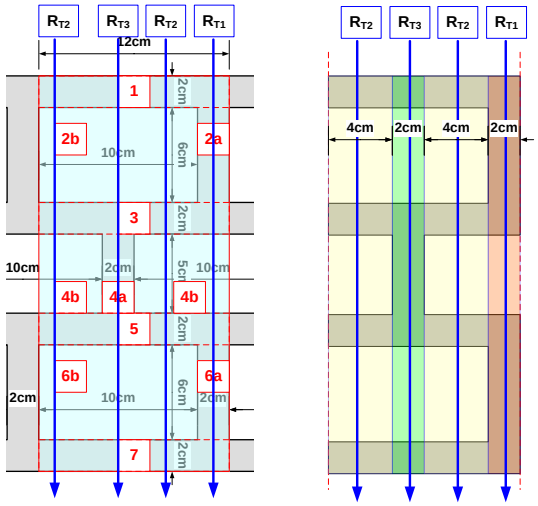

Fig. 7. *Schematic view of total thermal resistances of characteristic cross-sections*

The arrangement of layers in characteristic cross-sections for calculation of total thermal resistances (R_{T1}, R_{T2} and R_{T3}) is given in Fig. 8.

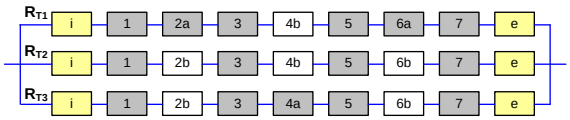

Fig. 8. *The arrangements of layers in characteristic cross-sections for calculation of R_{T1}, R_{T2} and R_{T3}*

Calculated values of total thermal resistances are:

$$R_{T1} = R_{si} + R_1 + R_{2a} + R_3 + R_{4b} + R_5 + R_{6a} + R_7 + R_{se}$$
$$R_{T2} = R_{si} + R_1 + R_{2b} + R_3 + R_{4b} + R_5 + R_{6b} + R_7 + R_{se}$$
$$R_{T3} = R_{si} + R_1 + R_{2b} + R_3 + R_{4a} + R_5 + R_{6b} + R_7 + R_{se}$$
$$R_{T1} = 1.7249\ {}^{m^2K}/_{W}$$
$$R_{T2} = 5.2364\ {}^{m^2K}/_{W}$$
$$R_{T3} = 3.6112\ {}^{m^2K}/_{W}$$

Participations of surface area 1, 2 and 3 are:

$$f_1 = {}^{2}/_{12} = 0.1667$$
$$f_2 = {}^{8}/_{12} = 0.6666$$
$$f_1 = {}^{2}/_{12} = 0.1667$$

The upper limit value of thermal resistance R_T' is:

$$R_T' = \frac{1}{\frac{0.1667}{1.7249} + \frac{0.6666}{5.2364} + \frac{0.1667}{3.6112}} = 3.702 m^2K/W$$

The formula for calculation of the lower limit value of thermal resistance R_T'' is:

$$R_T'' = R_{si} + R_1 + \boldsymbol{R_2} + R_3 + \boldsymbol{R_4} + R_5 + \boldsymbol{R_6} + R_7 + R_{se} \quad (3)$$

Schematic view of characteristic cross-sections for calculation of lower limit value of thermal resistance R_T'' is given in Fig. 9.

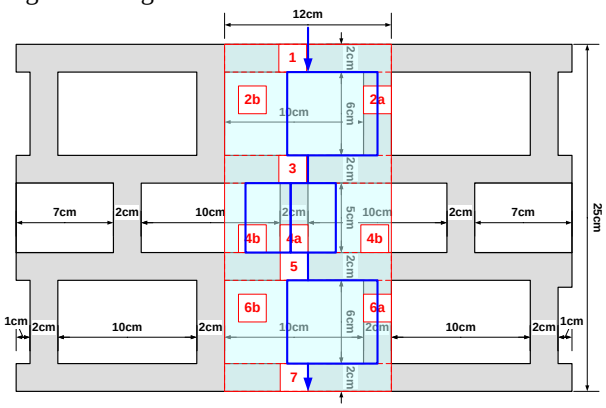

Fig. 9. *Schematic view of equivalent thermal resistances of characteristic cross-section*

The arrangement of homogenous (R1, R3 and R5) and nonhomogeneous layers (R2, R4 and R6) in characteristic cross-section is given in Fig. 10.

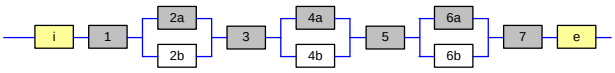

Fig. 10. *The arrangements of homogenous and nonhomogeneous layers in characteristic cross-section*

Equivalent thermal resistances of nonhomogeneous layers are:

$$R_2 = \frac{1}{\frac{f_{2a}}{R_{2a}} + \frac{f_{2b}}{R_{2b}}}$$

$$R_4 = \frac{1}{\frac{f_{4a}}{R_{4a}} + \frac{f_{4b}}{R_{4b}}}$$

$$R_6 = \frac{1}{\frac{f_{6a}}{R_{6a}} + \frac{f_{6b}}{R_{6b}}}$$

$$f_{2a} = {}^{2}/_{12} = 0.1667$$

$$f_{2b} = {}^{10}/_{12} = 0.8333$$

$$f_{2a} = f_{4a} = f_{6a}$$

$$f_{2b} = f_{4b} = f_{6b}$$

$$R_2 = 0.2599\ {}^{m^2K}/_{W}$$

$$R_4 = 0.2166\ {}^{m^2K}/_{W}$$

$$R_6 = 0.2599\ {}^{m^2K}/_{W}$$

The lower limit value of thermal resistance R_T'' is:

$$R_T'' = 0.9728 m^2K/W$$

Total thermal resistance of LWAC masonry block, R_T is:

$$R_T = \frac{R_T' + R_T''}{2} = 2.3374 m^2K/W$$

$$R_T = R_{si} + R + R_{se}$$

$$R = R_T - R_{si} - R_{se} = 2.1674 m^2K/W$$

$$R = \frac{d_{block}}{\lambda_{block}}$$

$$\lambda_{block} = 0.25/2.1674 = 0.115 W/(mK)$$

4. CONCLUSION

Based on the analysis of the results of laboratory testing of mechanical properties and analytical determination of thermal properties of LWAC hollow masonry block, it was concluded:

- LWAC hollow masonry block has satisfactory compressive strength, so it can be used for bearing masonry walls or for facade walls in skeletal structures.
- The low value of thermal conductivity of LWAC hollow masonry block enables its application in energy efficient buildings.
- LWAC hollow masonry block is obtained from concrete with a significant share of industrial waste materials, and can be classified into the category of environmentally friendly products.

Acknowledgment

The work reported in this paper is a part of the investigation within the research project III 42012 "Energy efficiency enhancement of buildings in Serbia and improvement of national regulative capacity for their certification", supported by the Ministry of Science and Technology, Republic of Serbia. This support is gratefully acknowledged.

5. REFERENCES

[1] EN 1745: Masonry and masonry products – Methods for determining design thermal values

[2] ISO 6946: Building components and building elements – Thermal resistance and thermal transmittance Calculation method

[3] FIP manual of lightweight aggregate concrete, Surry University Press, Glasgow and London, 1983.

[4] LWAC – Material Properties, Economic Design and Construction with LWAC State of the Art, Document BE96-3942/R2, 1998, 1-111.

[5] ACI Committee: "ACI 213-03: Guide for Structural Lightweight-Aggregate Concrete", 2003.

[6] Malešev, M., Radonjanin, V., Radeka, M., Milovanović, V, Lukić, I.: "Basic Properties of Structural Lightweight Aggregate Concrete in Relation to Type and Quantity af Cementitious Materials - Part 1", DIMK Serbia, International Symposium, Proceedings, 2011,159-168.

[7] Radonjanin, V., Malešev, M., Radeka, M., Lukić, I., Milovanović, V.: "Basic Properties of Structural Lightweight Aggregate Concrete in Relation to Type and Quantity of Cementitious Materials - Part 2", DIMK Serbia, International Symposium, Proceedings, 2011, 169-178.

The 7th International Conference on Engineering and Technology
ICET-2015, Phuket, June19-20, 2015
Prince of Songkla University, Faculty of Engineering
Hat Yai, Songkhla, Thailand 90112

Dielectric Properties of Palm Oil and Coconut Oil under Thermal Ageing

N. A. Mohamad[1], N. Azis[1]*, J. Jasni[1], M.Z.A. Ab Kadir[1], R. Yunus[2], M. T. Ishak[3], Z. Yaakub[4]

[1]Center for Electromagnetic and Lightning Protection Research (CELP), Faculty of Engineering, Universiti Putra Malaysia, Serdang, Selangor, Malaysia
[2]Institute of Advanced Technology (ITMA), Faculty of Engineering, Universiti Putra Malaysia, Serdang, Selangor, Malaysia
[3]Department of Electrical and Electronic Engineering, Faculty of Engineering, Universiti Pertahanan Nasional Malaysia, Sungai Besi, Kuala Lumpur, Malaysia
[4]Hyrax Oil Sdn. Bhd, Klang, Selangor, Malaysia

*Email of corresponding author: norhafiz@upm.edu.my

Abstract:*This paper presents an experimental study on the dielectric properties of palm oil and coconut oil under thermal ageing with presence of insulation paper. The type of palm oil used in this study is refined, bleached and deodorized olein. The ageing experiment was carried out at 130 °C for 7, 14 and 28 days and the dielectric properties of the oils such as AC breakdown voltage, dielectric dissipation factor, relative permittivity and resistivity are measured. It was found that there is no significant effect of ageing on most of the dielectric properties of palm oilandcoconut oil.*

Key Words:*Palm Oil/ Coconut Oil/ Dielectric Properties/ Thermal Ageing/ AC Breakdown Voltage/ Transformers*

1. INTRODUCTION

Among the alternative oil proposed as dielectric insulating fluid in transformers is vegetable oil. It is biodegradable, non-toxic and has high fire/flash points. It consists of triglycerides which is derived from one molecule of glycerol and three fatty acids [1]. The fatty acids of triglycerides can be classified into saturated, poly-unsaturated and mono-unsaturated [2, 3]. The physical and chemical properties such as oxidation stability, viscosity and ageing characteristics of vegetable oil are mainly determine by the fatty acids in triglycerides [4].

Palm Oil (PO) and Coconut Oil (CO) are among the common types of vegetable oils that are currently been investigated for application in transformers. There are different types of PO that can be extracted from the palm nut and the most common type of PO proposed for application in transformers is Refined, Bleached, Deodorized Palm Oil (RBDPO) [5, 6]. On the other hand, Virgin Coconut Oil (VCO) is proposed as dielectric insulating fluid due to its antioxidant properties [7].

Previous studies on RBDPO and CO mainly covers on the AC breakdown voltage, dielectric properties such as dielectric dissipation factor, relative permittivity, resistivity, partial discharge, physical and chemical properties including viscosity, acidity and moisture under new condition [8-12]. There are still less studies been carried out to examine the performance of RBDPO and CO under accelerated thermal ageing.

This paper examines the dielectric properties of RBDPO and CO under accelerated thermal ageing with presence of insulation paper. TheAC breakdown voltage, dielectric dissipation factor, relative permittivity and resistivity of all samples are measured and analysis is carried out to assess its performance after subjected to thermal ageing.

2. EXPERIMENTAL SET-UP

2.1. Test Samples

The samples used in this study were 2 samples of RBDPO Olein and 1 sample of CO. Both RBDPO and CO were obtained from readily available cooking oil products in the market. Table 1 shows the composition of fats and vitamin E/A of these oil.

Table 1. *Fat, vitamin E/A contents of all samples*

Samples (in 100ml)	S. fat (g)	P-U.S. fat (g)	M-U.S. fat (g)	V. E (mg)	V. A (µg)
RBDPOA	45.4	11.6	43.0	4.4	264
RBDPOB	43.0	14.0	43.0	75.0	-
CO	92.8	3.6	3.6	-	-

* S. fat= Saturated fat, P-U.S. fat= Polyunsaturated fat, M-U.S. fat= Monounsaturated fat, V. E= Vitamin E, V. A= Vitamin A

CO has the highest content of saturated fat and does not contain any vitamin E and Vitamin A. On the other hand, RBDPOA and RBDPOB have almost the same composition of saturated/unsaturated fats. RBDPOA has vitamin E and vitamin A while RBDPOB has only vitamin E.

2.2. Pre-processing and Thermal Ageing Procedure

All oil samples were first filtered 3 times through a membrane filter with pore size of 0.2µm. Next, they were dried in vacuum oven for 2 days at 85 °C. On the other hand, the insulation papers were first dried in a vacuum oven at 105 °C for 2 days and later impregnated with oil samples. The ratio of oil and paper used in this study was 20:1 (450 g oil and 22.5 g insulation paper). All samples were filled with nitrogen gas in order to reduce the contact with oxygen. Finally all samples were sealed with the bottle cap enforced with PTFE tape to minimize the contact with the environment. The ageing temperature was set at 130 °C and all samples were aged for 7, 14, and 28 days.

2.3. AC breakdown voltage

The AC breakdown voltage test was carried out according to ASTM D1816 by an automatic oil breakdown test set BAUR DPA 75C at ambient temperature [13]. The test was carried out using VDE electrode with a diameter of 36 mm facing each other at a gap distance of 1 mm. The voltage ramping rate was set at 0.5 kV/s. The volume of the oil tested is 400 ml and the time interval between each breakdown was set at 5 minutes. In total, 50 AC breakdown voltages were obtained and the average value was taken for the study.

2.4. Dielectric dissipation factor, relative permittivity and resistivity

The dielectric dissipation factor, relative permittivity and resistivity were measured according to IEC60247 by a BAUR DTL C oil tester [14]. All samples were tested at 90 °C. The volume of the oil in the test container is around 70 ml.

3. RESULT AND ANALYSIS OF DATA

3.1. AC breakdown voltage

RBDPOA and RBDPOB show a slight reduction trend of AC breakdown voltages after 7 days of ageing as shown in Fig. 1. After 14 days of ageing, the AC breakdown voltages of RBDPOA continue to slightly decrease while for RBDPOB, it increase and the value after 28 days of ageing is 35.4 kV. On the other hand, CO shows a slight increment trend of AC breakdown voltages from start until 14 days of ageing. The highest percentage of differences on the AC breakdown voltages between RBDPO and CO after 7, 14 and 28 days of ageing are 10%, 25% and 15% respectively.

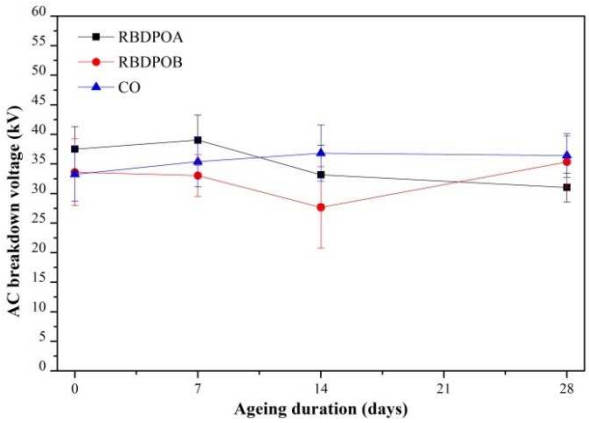

Fig. 1. AC breakdown voltages of all samples

3.2. Dielectric properties

3.2.1 Dielectric dissipation factor

The dielectric dissipation factors for CO is high initially, however it reduce significantly after start of ageing where the percentage of reduction is 92% as shown in Fig. 2. The dielectric dissipation factors of CO remain highest throughout the ageing duration. It is observed that there is no significant effect of ageing on the dielectric dissipation factors of RBDPO. The dielectric dissipation factors for RBDPOAfluctuate at values between 0.037 and 0.049 throughout the ageing duration. On the other hand, the dielectric dissipation factors for RBDPOB decrease initially and start to increase linearly after 7 days of ageing.

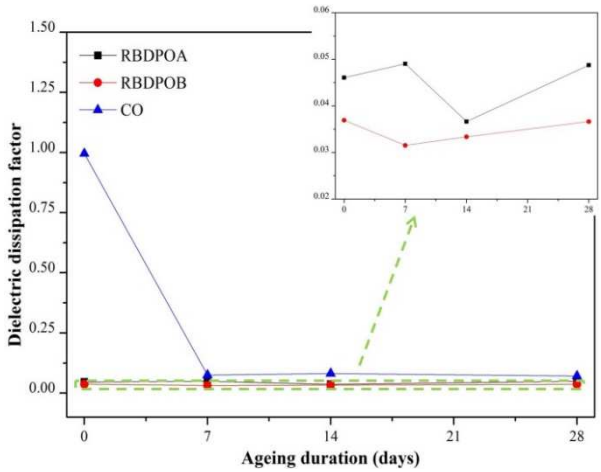

Fig. 2. Dielectric dissipation factors of all samples

3.2.2 Relative permittivity

There is no significant effect of ageing on the relative permittivities of the all samples as shown in Fig. 3. The highest relative permittivities for RBDPO and CO are 2.86 and 3.03 respectively throughout the ageing duration. All samples show a slight reduction of relative permittivities from the start of the ageing. After 7 days of ageing, the relative permittivities of RBDPOA, RBDPOB and CO remain almost unchanged until 28 days of ageing. The relative permitivities of CO remains highest throughout ageing duration.

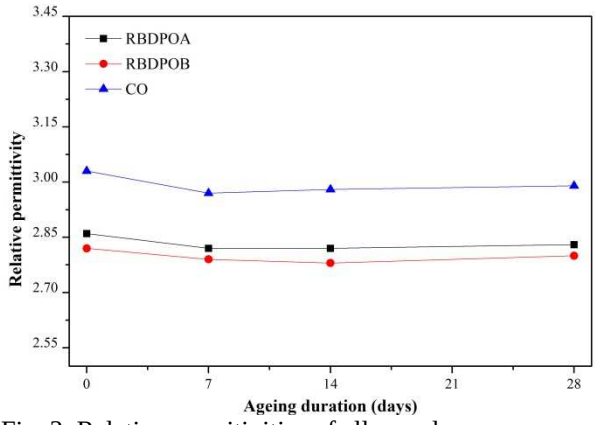

Fig. 3. Relative permitivities of all samples

3.2.3 Resistivity

All samples show an increment trend of resisitivities from start of ageing as shown in Fig. 4. After 7 days of ageing, the resisitivities of RBDPOA and CO start to reduce almost linearly and the values at 28 days of ageing are 3.35 GΩm and 2.56 GΩm respectively. The resisitivities for RBDPOB start to reduce after 14 days of ageing and the final value at 28 days of ageing is 2.63 GΩm.

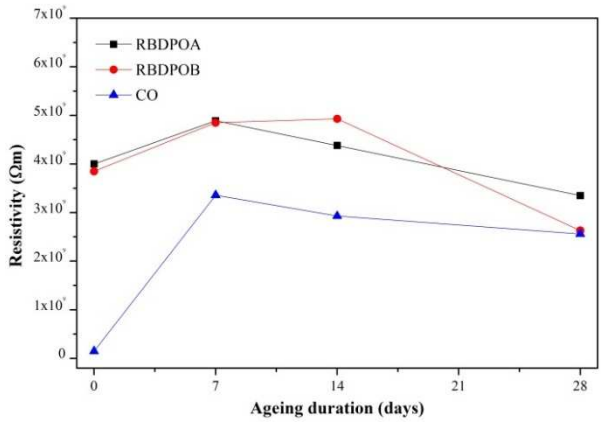

Fig. 4. Resistivities of all samples

4. CONCLUSION

Based on this study, it was found that there is no siginificant effect of ageing on the breakdown voltages of RBDPO and CO.The dielectric dissipation factors and relative permittivities for RBDPO remain almost unchanged throughout the ageing duration. The resistivities of RBDPO and CO increase initially and reduce at the later stage of ageing. There is no significant effect of vitamin E and A on the dielectricpropertiesof both RBDPOA and RBDPOB under thermal ageing.

5. ACKNOWLEDGEMENT

The authors would like to thank Ministry of Education and Universiti Putra Malaysia for the funding under FRGS scheme (03-02-13-1280FR), (03-02-13-1279FR), PUTRA IPM and IPB schemes (GP-IPM/2013/9401500), (GP-IPB/2014/9440801). Special thanks to Hyrax Oil Sdn. Bhdand Malaysia Transformer Manufacturing Sdn. Bhd.for the technical support.

6. REFERENCES

[1] C. P. McShane, "Vegetable-oil-based dielectric coolants," *IEEE Industry Apllication Magazine,* vol. 8, pp. 34-41, 2002.

[2] M. Augusta and G. Martins, "Vegetable oils, an alternative to Mineral Oil for Power Transformer – Experimental Study of Paper Aging in Vegetable versus Mineral Oil," *IEEE Electrical Insulation Magazine,* pp. 7-13, 2010.

[3] C. P. McShane, "Natural and Synthetic Ester Dielectric Fluids: Their Relative Environmental, Fire Safety, and Electrical Performance," *Commercial Power Systems Technical Conference,* pp. 1-8, 1999.

[4] J. Viertel, K. Ohlsson, and S. Singha, "Thermal Aging and Degradation of Thin Films of Natural Ester Dielectric Liquids," *IEEE International Conference on Dielectric Liquids,* 2011.

[5] A. A. Abdelmalik, "Chemically Modified Palm Kernel Oil Ester: A possible Sustainable Alternative Insulating Fluid," *Journal of Sustainable Materials and Technologies,* 2014.

[6] N. Azis, J. Jasni, M. Z. A. A. Kadir, and M. N. Mohtar, "Suitability of Palm Based Oil as Dielectric Insulating Fluid in Transformers," *Journal of Electrical Engineering & Technology,* vol. 9, pp. 662-669, 2014.

[7] H. M. Ghazali, A. Tan, S. M. Abdulkarim, and M. H. Dzulkifly, "Oxidative Stability of Virgin Coconut Oil Compared with RBD Palm Olein in Deep-fat Frying of Fish Crackers," *Journal of Food, Agriculturer & Environment,* vol. 7 (3&4), pp. 23-27, 2009.

[8] U. Khayam, A. Rajab, and Suwarno, "Dielectric Properties, Partial Discharge Properties, and Dissolved Gas Analysis of Ricinnus Oils as Biodegradable Liquid Insulating Materials "*International Conference on Condition Monitoring and Diagnosis (CMD),* 2012.

[9] K. Kiasatina, M. Kamarol, M. Zulhilmey, and Y. A. Arief, "Breakdown Characteristics of RBDPO and Soybean Oil Mixture for Transformer Application," *International Conference on Electrical, Control and Computer Engineering (INECCE),* pp. 219-222, 21-22 June 2011.

[10] S. S. Sinan, S. N. Shawaludin, J. Jasni, N. Azis, M. Z. A. Kadir, and M. N. Mohtar, "Investigation on the AC breakdown Voltage of RBDPO Olein," *IEEE Innovative Smart Grid Technologies - Asia (ISGT Asia),*pp. 760-763, 20-23 May 2014.

[11] N. A. Mohamad, N. Azis, J. Jasni, M. Z. A. Ab Kadir, R. Yunus, M. T. Ishak, Z. Yaakub, "A Study on the Dielectric Properties of Palm Oil and Coconut Oil," *IEEE International Conference on Power and Energy (PeCON)* -, pp. 109-112, 1-3 December 2014.

[12] S. Tenbohlen, "Aging Performance and Moisture Solubility of Vegetable Oils for Power Transformer," *IEEE Transactions on Power Delivery,* vol. 25, no. 2, pp. 825-830, 2010.

[13] ASTM D1816, "Standard Test Method for Dielectric Breakdown Voltage of Insulating Liquids using VDE Electrodes."

[14] IEC60274, "Measurement of Relative Permitivity, Dielectric Dissipation Factor and D.C. Resistivity of Insulating Liquids."

The 7th International Conference on Engineering and Technology
ICET-2015, Phuket, June 19-20, 2015
Prince of Songkla University, Faculty of Engineering
Hat Yai, Songkhla, Thailand 90112

Hydrogen Gas Sensor Using Double SAW Resonator System

Zainab Yunusa [1,2], Mohd Nizar Hamidon [1,4*], Alyani Ismail [3], Maryam Mohd Isa [4], Mohd Hanif Yaacob [3], Saeed Rahmanian [5], Siti Azlida Ibrahim [3,6] and Arafat A.A Shabaneh [3]

1 Institute of Advanced Technology, Universiti Putra Malaysia, 43400 Serdang, Selangor, Malaysia;
2 Department of Electrical Engineering, Bayero University Kano, P.M.B 3011 Kano, Nigeria;
3 Department of Computer and Communications, Universiti Putra Malaysia, 43400 Serdang, Selangor, Malaysia;
4 Department of Electrical and Electronics Engineering, Faculty of Engineering, Universiti Putra Malaysia 43400 Serdang, Selangor, Malaysia;
5 Department of Mechanical and Manufacturing Engineering, Faculty of Engineering Universiti Putra Malaysia, 43400 Serdang, Selangor, Malaysia;
6 Faculty of Engineering, Multimedia University, 63100 Cyberjaya, Selangor, Malaysia

*Email of corresponding author: mnh@upm.edu.my

Abstract *This paper presents a hydrogen gas sensor based on Double Surface Acoustic Wave Resonator (DSAWR) system configuration. Two commercial SAW resonators were employed to develop the DSAWR system. The sensing layer was prepared using functionalized Carbon Nanotubes (CNT) with polyaniline nanofibers. The sensing layer was integrated into the DSAWR system and measurements were carried out with different hydrogen gas concentrations at 40 °C. Results obtained showed response of the sensor to hydrogen gas with good response and recovery time with good sensitivity which be as a sensor node.*

Key Words: *Double SAW resonator, Hydrogen gas, Polyaniline nanofibres*

1. INTRODUCTION

This paper presents a new technique for the development of hydrogen gas sensor system using the DSAWR system. Hydrogen gas sensing is very crucial because it is colourless, odourless and flammable with an explosive limit of 4% in air [1]. Surface Acoustic Wave Technology (SAW) technology have been widely used for hydrogen sensing and have shown to be promising. The different configurations of SAW including SAW delay lines and single SAW resonators have also been reported [2]–[5] and have proved to be reliable. However, the DSAWR sensor system which was first proposed for hydrogen sensing at room temperature as shown in [6] .In this paper, the same system was proposed but at a slightly higher temperature of 40 ^{0}C employs two commercial resonators with different resonance frequencies. The sensor response is obtained based on the difference between these two frequencies. With this system, the slightest drifts in temperature will be compensated and it has potentialities for wireless applications. The sensing layer will be composed of funcionalized MWCNT and polyaniline nanofibres.

Hydrogen gas sensing using polyaniline and its composite as sensing material with measurements at room temperature have been reported but in the SAW delay line configuration [7]–[10]. In this paper, polyaniline will be used in DSAWR configuration system.

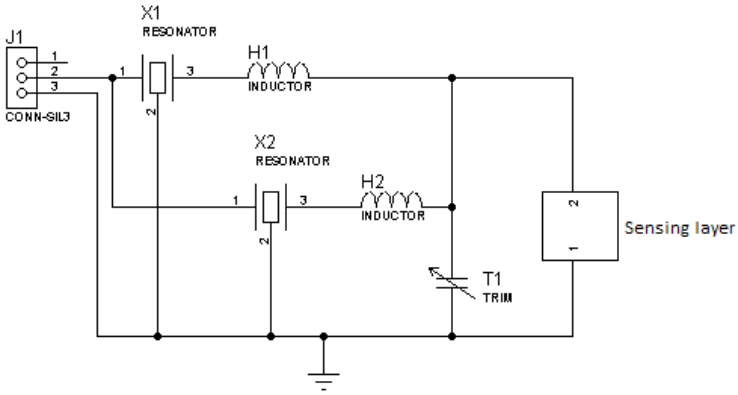

Figure 1 Proposed circuit schematic for the DSAWR sensor system

2. METHODOLOGY

2.1 Design of DSAWR with the sensing layer

The complete proposed circuitry schematic layout of Figure 1 was fabricated on a PCB. It consists of two commercial SAW resonators with different resonance frequencies. Each of the resonators is matched to an L-matching circuit as shown in Figure 1.
A sensing layer will be connected in parallel with the capacitor. Therefore the sensing layer acts like a resistor because the resistance of the sensing material changes upon interaction with gas molecules while the function of the variable capacitor is for tuning. The detailed fabrication of the sensing layer has been published in [6].

2.2 Preparation of sensing layer

The sensing layer was made up of double layer with functionalized multi walled carbon nanotubes (MWCNT) and polyaniline nanofibres. Functionalization of MWCNT was done by introduction of acids into commercial MWCNT supplied from Hanghzou company from China. and polyaniline nanofibres. The polyaniline nanofibres were synthesized from chemical polymerization using aniline, acid and potassium peroxide The sensing materials were coated onto the sensing platform using a spray brush technique. The sensing layer was then integrated into the matching circuit and measurements were taken using Anritsu Vector Network Analyzer (VNA).

2.3. Gas sensing measurements

The gas sensing measurement set-up schematic is illustrated in Figure 2 and it consists of a computerized Aalborg mass flow controllers which controls synthetic air and hydrogen gas at a flow rate of 0.2 ml/min. The mass flow controllers were connected to both hydrogen and air respectively. A command module was connected to a computer and controlled by an automated Labview program that controls the gas sensing process. Measurements were carried out with a VNA connected to the SMA connector of the DSAWR system. Measurements were carried out at 40 ^{0}C. Air was purged in for 30 minutes so as to stabilize the system while hydrogen gas was introduced for 10 minutes and this was repeated for all concentrations. The gas chamber was heated by a heater and then a thermocouple was inserted into the chamber so as to monitor the temperature throughout the measurement process.

3. RESULTS

The sensing layer was characterized using Hitachi FESEM and the result is as shown in Figure 3 and it shows densely forests of MWCNT which are 20 to 40 nm in diameter. The polyaniline nanofibres is noticed to form clusters at different spots which is as a results of spraying with an air brush. However, this is just a surface morphology to reveal the presence of the polyaniline nanofibres.

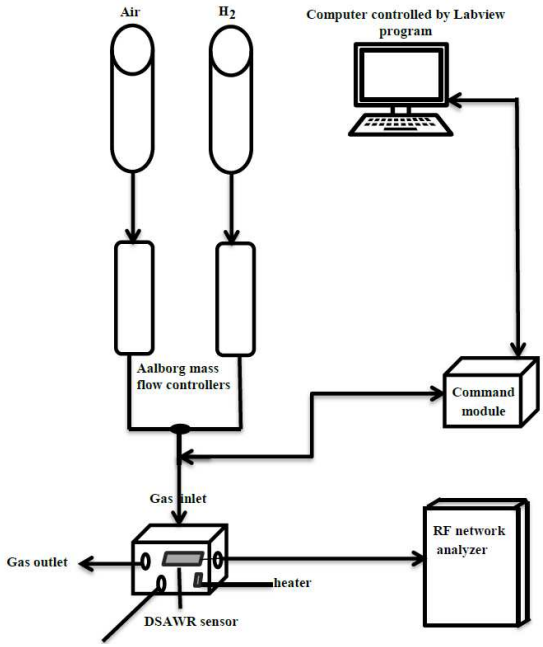

Figure 2 Gas sensing measurement set-up

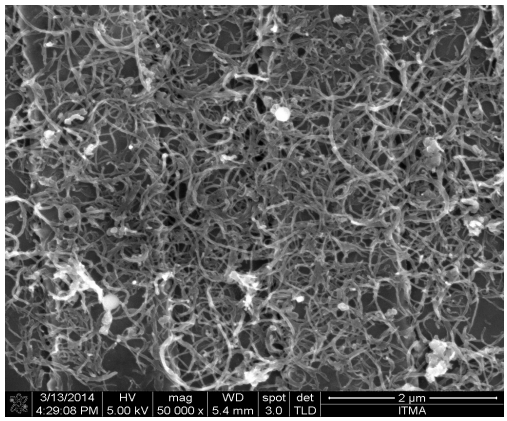

Figure 3 FESEM of MWCNT and polyaniline nanofibres

The sensor was exposed to different hydrogen gas concentrations after attaining a temperature of 40 ^{0}C. The response of the sensor when exposed to hydrogen concentration at 40 ^{0}C is plotted in Figure 4. The response was obtained based on the frequency difference between the two resonant frequencies of the resonators. Hydrogen sensing using polyaniline nanofibres as sensing material have been shown in literature at room temperature. In this paper, the sensing was carried out at a slightly higher temperature so as to compare with the past work. As compared to room temperature measurement as shown in [6] the response times and recovery times were observed to be faster due to the effect of temperature, the molecules gain more kinetic energy and more momentum as such they can react with the target gas much faster as compared with the room temperature.

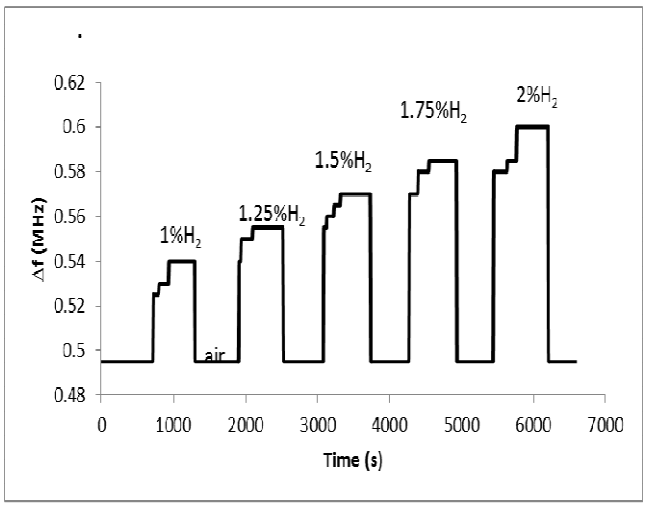

Figure 4 Response of sensor to different hydrogen concentrations at 40 ^{0}C

It could also be observed that the effect of temperature is also noticeable on the Δf as compared with room temperature measurements in the past work. It increases from 0.525 in case of 1 % at room temperature as reported to about 0.54 in this paper. This increase is manifested in all other hydrogen gas concentrations. Response time was recorded to be 3.2 minutes for 1 % hydrogen concentration while it reduces steadily as the gas concentration increases with the fastest of 40 seconds for 2 % hydrogen gas concentration. Similarly recovery times were much faster than the room temperature with an average recovery time of 3.5 minutes.

Figure 5 shows a plot of frequency shift versus hydrogen concentration. The frequency shift is expressed based on the difference between Δf_{gas}-Δf_{air}. The slope of the graph of Figure 5 gives the sensitivity of sensor to be 6 Hz/ppm. It could be noticed that the sensitivity of our sensor has doubled from 3 Hz/ppm at room temperature to 6 Hz/ppm at 40 ^{0}C.

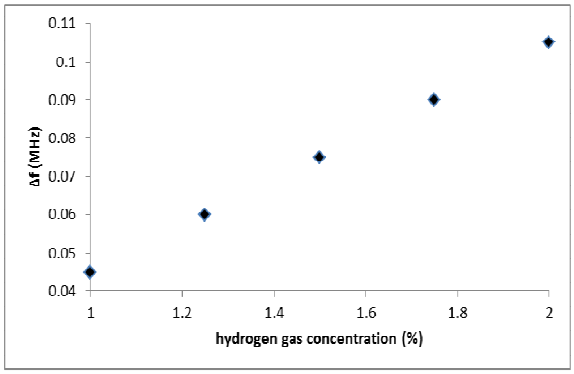

Figure 5 Frequency shift versus hydrogen concentration

4. CONCLUSION

In this paper, a DSAWR sensor system was proposed and developed. The sensing layer was made up of functionalized MWCNT and polyaniline nanofibres. Gas sensing results were conducted at 40 ^{0}C with different hydrogen concentrations of between 1-2 %. Results obtained showed good response and recovery times of 40 seconds for 2 % hydrogen gas concentration and 3.5 minutes recovery time. The sensor showed good sensitivity of 6 Hz/ppm which makes it a potential material for hydrogen gas sensing.

REFERENCES

[1] T. Hübert, L. Boon-Brett, G. Black, and U. Banach, "Hydrogen sensors – A review," *Sensors Actuators B Chem.*, vol. 157, no. 2, pp. 329–352, Oct. 2011.

[2] A. Z. Sadek, W. Wlodarski, Y. Li, W. Yu, X. Li, X. Yu, and K. Kalantar-Zadeh, "A ZnO nanorod based layered ZnO/64 degrees YX LiNbO(3)SAW hydrogen gas sensor," *Thin Solid Films*, vol. 515, pp. 8705–8708, 2007.

[3] A. Z. Sadek, W. Wlodarski, Y. X. Li, W. Yu, X. Li, X. Yu, and K. Kalantar-zadeh, "A ZnO nanorod based layered ZnO / 64 ° YX LiNbO 3 SAW hydrogen gas sensor," vol. 515, pp. 8705–8708, 2007.

[4] W. Jakubik, M. Urbańczyk, and E. Maciak, "SAW hydrogen gas sensor based on WO3 and Pd nanostructures," in *Procedia Chemistry*, 2009, vol. 1, pp. 200–203.

[5] M. David, M. Arab, C. Martino, L. Delmas, F. Guinneton, and J. Gavarri, "Carbon nanotubes / ceria composite layers deposited on surface acoustic wave devices for gas detection at room temperature," *Thin Solid Films*, vol. 520, no. 14, pp. 4786–4791, 2012.

[6] Z. Yunusa, M. N. Hamidon, A. Ismail, M. M. Isa, M. H. Yaacob, S. Rahmanian, S. A. Ibrahim, and A. A. A. Shabaneh, "Development of a Hydrogen Gas Sensor Using a Double Saw Resonator System at Room Temperature," *Sensors*, vol. 15, pp. 4749–4765, 2015.

[7] R. Arsat, X. F. Yu, Y. X. Li, W. Wlodarski, and K. Kalantar-zadeh, "Hydrogen gas sensor based on highly ordered polyaniline nanofibers ϵ," vol. 137, pp. 529–532, 2009.

[8] A. Z. Sadek, W. Wlodarski, K. Shin, R. B. Kaner, and K. Kalantar-zadeh, "A Room Temperature Polyaniline / SnO 2 Nanofiber Composite Based Layered ZnO / 64 ° YX LiNbO 3 SAW Hydrogen Gas Sensor," pp. 208–211, 2006.

[9] A. Z. Sadek, W. Wlodarski, K. Shin, R. B. Kaner, and K. Kalantar-zadeh, "A polyaniline / WO 3 nanofiber composite-based ZnO / 64 ◦ YX LiNbO 3 SAW hydrogen gas sensor," *Synth. Met.*, vol. 158, pp. 29–32, 2008.

[10] P. Lobotka, P. Kunzo, E. Kovacova, I. Vavra, Z. Krizanova, V. Smatko, J. Stejskal, E. N. Konyushenko, M. Omastova, Z. Spitalsky, M. Micusik, and I. Krupa, "Thin polyaniline and polyaniline/carbon nanocomposite films for gas sensing," *Thin Solid Films*, vol. 519, pp. 4123–4127, 2011.

The 7th International Conference on Engineering and Technology
ICET-2015, Phuket, June19-20, 2015
Prince of Songkla University, Faculty of Engineering
Hat Yai, Songkhla, Thailand 90112

Investigation on Touch Area of Under Foot Pressure Based-on Weight Measurements

O. Hussein, W.Z. Wan Hasan, A. Che Soh. H. Jafaar

Department of Electrical and Electronic Engineering, Faculty of Engineering,

*Email of corresponding author: wanzuha@upm.edu.my

Abstract: *This paper present a precise and detailed study for the touch area on the foot based on amplifier gain settings of individual sensors that are distributed over the plantar insole area, the idea is to fill the insole area with sensor size areas that satisfy covering almost the foot touch area. The procedure includes steps have to be implemented to achieve accurate reference values with respect to body weight. The values of individual sensor points have been evaluated for the both (Foot-Sensor-Insole-Ground) and (Foot- Sensor- Ground). It is found that, there is a wide range difference between the test points in each case and the existence of the insole reduced the pressure weight. A percentage value according to total body weight has been assigned to be utilized as reference points in future studies.*

KeyWords: ***Foot Plantar Pressure, Force Sensor, Weight Measurement, Sensor Distribution, Operation Amplifier.***

1. INTRODUCTION

Pressure sensors have been incorporated into footwear for gait and motion analysis, and for other applications, over thelast few years. Several studies of shoe insole pressure sensorshave been suggested different positions for placing insolepressure sensors and sensor units.so that we took a Flexi Force Sensor to be our under study sensor. Generally a linear relation with the applied load would simplify the process of calibration and measurements but, there is a non-linear region governs some ranges in our application, a look-up table storied in the computer to relatively overcome these parts of operation. To drive the signal of the force sensor with adequate and suitable value to achieve high resolution as well as low cost and power consumption, an inverting op-amp with standard biasing voltage is attempted to get the measurements as shown in Figure1, while the sensors would be as the input resistor of the adaptor circuit which is behave as an amplifier or attenuator depending on the range of pressure.

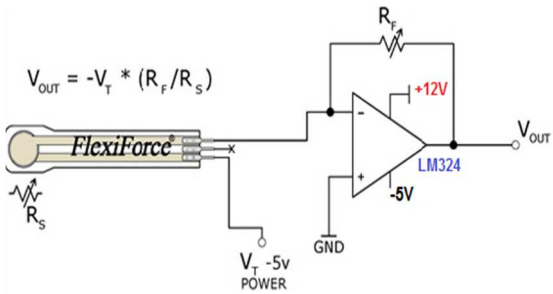

Fig.1 Sensor driving circuit

Many applications have been used to detect the pressure under the foot. The price of the commercial insole is very high so these applications used just for the athletes and it's difficult to the common people to have these applications. The distribution of the sensors vary regarding to the different applications and also the position is different from application to other. With the application of the Centre of Pressure Measuring and gait phase identification the work will be done in such a way that the gait phase and center of pressure are identified using an algorithm without consideration of the physical weight in real-time algorithm is independent from the Order of signals fl – f5 and FS, the identification can be achieved with100% precision1 . For the application of in-shoe plantar pressure monitoring system they will realize real time parameter measurement based on regression equation of level walking with 5 signals came from 5 pressure sensor the result estimated with good and reasonable accuracy 2 The application of designing Cost Effective Plantar Pressure Distribution Analysis System for the Dynamically Moving Feet they measured the Plantar pressure between the foot and shoe during dynamic movement in real-time and the requirement to get a linear relationship between the applied force and the output voltage, the sensitivity was changed each time to obtain this linearity and the above approach was repeated for each sensitivity value, or the feedback resistor value (Rs), until a close approximation of linearity was

obtained 3 With the application of In-Shoe Plantar Pressure Measurement and Analysis System they designed in-shoe plantar pressure based on fabric sensor array and A knitted fabric coated with carbon-black-filled silicon Was used as the strain sensing element and the result accuracy is 5 % with drift less than 5 % 4 . The application of an insole embedded foot pressure sensor calculated real-time detection of the foot pressure sensor with feedback controlled functional electrical stimulation (FES) system for the correction of foot drop in hemiplegics based on the discrete pressure sensors in the insole thy get the localized information5 .the application of Diabetic Foot Ulcer Monitoring they showed the criticality of sensor architectural trade-off (the number and location of sensors and the sensor size) to design an individualized Pressure-sensing insole based on conducting on 87 patients, with 103 existing foot ulcers, ulcers were located mostly beneath the metatarsal heads (56.3%), under the toes (32.1%), and at the heel (1.9%)6 .The application of Pressure Sensor Positions on Insole used for Walking Analysis they used the commercial pressure measurement system (Pedar-x, Novel, Germany) to collect the foot pressure they hypothesized that the correlation between 11 subjects and 99 pressure sensor positions will help us to decide the positions in which the insole pressure sensors should be placed, reduce the number of sensors7.

2. Experimental Set-up

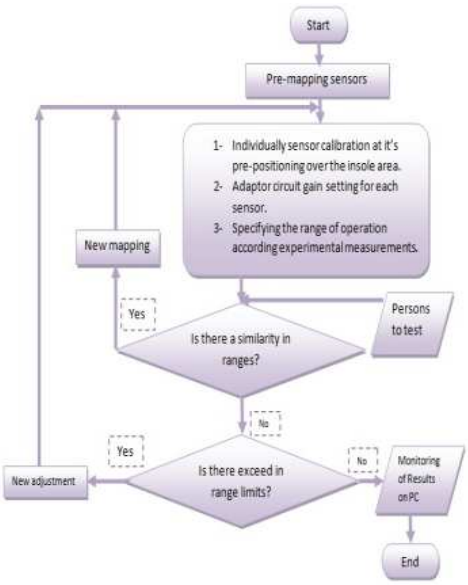

Fig. 2 Flow Chart of Evaluation Procedure

Refer to the above flow chart and the circuit in Fig. 2, the outputs of all the adaptor circuits are connected to the inputs of the data acquisition card which has a limit range of 5V as a maximum value to its input which is the value that we based on to adjust the feedback resistors of the individual adaptor circuits to approach the optimum cover of range variation.

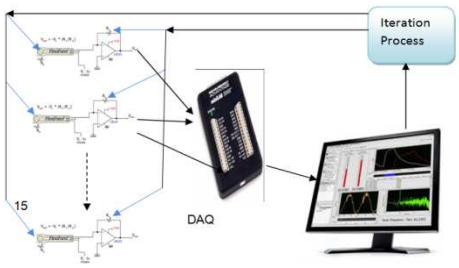

Fig.3 Diagram of Evaluation System

2. 1 Evaluation Procedure

1- Individually gain setting and sensor calibration is done so as to get high measuring resolution.
2- Data acquisition system is selected which reads the measurements of the number of selected pressure sensors to process the data under analysis algorithm.
3- Setting the maximum range of each individual sensor amplifier or attenuator gain based on the sensor location and the applied physical force.
4- Design a primary mapping for 15 sensors in a specific potential distribution on the foot planter as show in Fig. 4

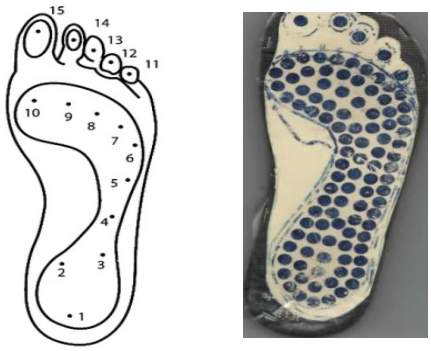

(A) (B)

Fig. 4 The Sensors Distribution on Insole

3. RESULT AND ANALYSIS OF DATA

3.1 Individual Touch Area

Experimental results of the feedback resistors values at dedicated sensor position with specific weight of 100kg. According to the sensors distribution on the insole as shown in Fig. 4(A), there are 15 area have been investigated in order to find the maximum touch output based on 100kg weight. For example at position 15, the range of mass has contributed the touch range from 02-4.2V. The individual results are described as in Table 1. The relation between touch output and maximum touch can be found in Fig 5, which showed the linearity of the position points against maximum point. Throughout these results, the maximum touch will be used as the

break point when detecting a pressure for under foot of diabetic patient.

Table 1. *Sensor Setting Values*

Feed Back Resistance	Position	Range of Mass of individual point	Touch Output (V)	Maximum touch Output (v)
670k ohm	15	1.5kg	0.2	4.2
850 k ohm	14	1 kg	0.2	4.9
850 k ohm	13	1 kg	0.6	4
2 M ohm	12	0.5 kg	0.17	4.3
5 M ohm	11	200 g	0.35	4.8
285 k ohm	10	3kg	0.36	4.7
2 M ohm	9	0.5 kg	0.5	4.1
850k ohm	8	1 kg	1.05	4.1
850 k ohm	7	1 k g	0.85	4.6
850k ohm	6	1 kg	1.1	4.1
620 k ohm	5	700 g	1	4.9
620 k ohm	4	700 g	1.6	4.4
850 k ohm	3	1 kg	1.6	4.1
435 k ohm	2	2 kg	1.7	4
285 k ohm	1	3 kg	1.7	4

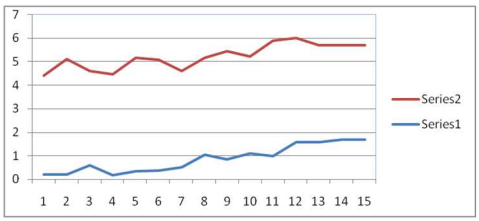

Fig. 5, Individual Sensor Outputs Variation Values

3.2 Full Touch Area

As described in Fig 4(B), the filled the insole area with sensor size areas that satisfy covering almost the foot touch area. By applying the above procedures for 100kg weight, the voltage of each sensor are measured for both Foot-Sensor-Insole-Ground (FSIG) and Foot- Sensor-Ground (FSG) as described in the Fig.6. The results showed that with 100kg of weight, both results were not same, for example at position 15 the touch voltage for FSG is more than 2V and for FSIG is 0.5V. It is found that, there is a wide range difference between the test points in each case and the existence of the insole reduced the pressure weight. A percentage value of the total body weight need to be considered reference points in future studies. A part from that, the base layer of distribution sensor also need to considered.

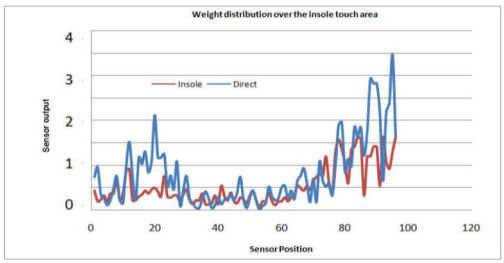

Fig.6 Weight distribution over the insole

4. CONCLUSION

An investigation of relation between pressure distribution and total body weight has successfully carried out. The results of study has showed significant finding between mass individual point and maximum touch which is indicated that the most touch area need to be considered as a break point for detecting under foot pressure especially for insole application. The other consideration that needs to be take account was base layer of pressure distribution which need clearly defined in order to validate the pressure values.

5. ACKNOWLEDGEMENT

The authors would like to thank Ministry of Education and Universiti Putra Malaysia for the funding under FRGS scheme (03-02-13-1280FR), (03-02-13-1279FR), PUTRA IPM and IPB schemes (GP-IPM/2013/9401500), (GP-IPB/2014/9440801).

6. REFERENCES

[1] Dragoljub Surdilovic, Zhang Jinyii and Rolf Bemhardt 'Gait Phase and Centre of PressureMeasuring System' Fraunhofer Institut for Produktionsanlagen und KonstruktionstechnikPascalstrasse 8-9, 10587-Berlin Germany. 02004 IEEE.

[2] Ren Lvping , Li Deyu,Liu Chengrui, Yang Yang,Qian Yajun , Yang Songyan, Pu Fang,Niu Haijun' Design of in-shoe plantar pressure monitoring system for daily activity exercise stress assessment'(2011) 4th International Conference on Biomedical Engineering and Informatics (BMEI).

[3] R. Karkokli, Member, IEEE, K.M.Valter McConville, Ph.D., Member, IEEE. Ryerson University, Toronto, ON' Design and Development of a Cost Effective Plantar PressureDistribution Analysis System for the Dynamically Moving Feet' Proceedings of the 28th IEEE EMBS Annual International Conference New York City, USA, (Aug 30-Sept 3), (2006)

[4] Lin Shu, Tao Hua, Yangyong Wang, Qiao Li, David Dagan Feng, Fellow, IEEE, and Xiaoming Tao, Member, IEEE' In-Shoe Plantar Pressure Measurement and Analysis System Based on Fabric Pressure Sensing Array' IEEE transactions on information technology in biomedicine, VOL. 14, NO. 3, (MAY 2010).

[5] Sukanta Kumar Sabut, Ratnesh Kumar, Manjunatha Mahadevappa' Design of an insole embedded foot pressure sensor controlled FES system for foot drop in stroke patients' Proceedings of 2010 International Conference on Systems in Medicine and Biology.December (2010), liT Kharagpur, India

[6] Sarah Ostadabbas, Adnan Saeed, Mehrdad Nourani Matthew Pompeo, M.D. Sensor Architectural Tradeoff for Diabetic Foot Ulcer Monitoring' 34th Annual International Conference of the IEEE EMBS San Diego, California USA, (28 August - 1 September), (2012).

[7] Kanitthika K., and Soo Chan K. Pressure Sensor Positions on Insole used for Walking Analysis IEEE ISCE 2014 1569949045

The 7th International Conference on Engineering and Technology
ICET-2015, Phuket, June 19-20, 2015
Prince of Songkla University, Faculty of Engineering
Hat Yai, Songkhla, Thailand 90112

Software for Market Validation of the Recycling Equipment

Pavlović Milan[*1], Arsovski Slavko[2], Tadić Danijela[3], Pavlović Aleksandar[4], Tomović Aleksandar[5]
[1]University of Novi Sad, Faculty of Technical Sciences, Novi Sad, Serbia
[2]University of Kragujevac, Faculty of Engineering, Kragujevac, Serbia
[3] University of Kragujevac, Faculty of Engineering, Kragujevac, Serbia
[4]PFB Design, Belgrade, Serbia
[5]University of Belgrade, Faculty of Mechanical Engineering, Belgrade Serbia
[*]Email of corresponding author: milanpavlovic50@gmail.com

Abstract: *The market validation of any recycling equipment presents the last phase of developing process of a new product. The considered problem is defined into ISO 9000:2008.The developed software can be realized into seven steps and it is based on the proposed mathematical model. A new model for market validation of device for recycling is proposed which includes both quantitative and qualitative factors. The uncertainties into the relative importance and values of factors are described by pre-defined linguistic expressions. These linguistic variables are modelled by triangular fuzzy numbers.Factor weights is given by fuzzy AHP. The obtained results represent an input for future research which should include a good benchmark base for tested different devices which use in reverse logistic chains and their continuous improvement.*

Key Words: ***software/market validation/uncertainties/ fuzzy AHP***

1. INTRODUCTION

Increasing global competition forces companies to increase the profit constantly and to improve competitive positioning. Manufacturing enterprises are expanding simulation models to obtain both quality of products, and to enable the validation of the products. The validation is vital to reduce process faults and to facilitate efficient and effective engineering changes [1]. On the other hand, the validation of new physical products is of primary importance for customer perception. In the literature, there are many definitions of the validation term. According to [2] and [3] validation is method that is used for confirming that a product meets its respective specifications and fulfils its intended purpose. The definition given by ISO 9000 validation is focused on fulfilling an intended use or application.

There are many methods used for the market validation of products projects which can be based on the market analyses, benchmarking tool, mathematical statistics, etc. In this paper, author's attention is focused on the recycling equipment. The uncertainties in: (1) the relative importance of factors (2) the some sub-factor values and (3) the customer satisfaction levels are described by management team. They use linguistic expressions is close to the human way of thinking. Modeling of linguistic terms is based on the fuzzy sets theory [4]. Fuzzy set theory resembles human reasoning in its use of approximate information and uncertainty to generate decisions. In this paper, all uncertainties are modeled by triangular fuzzy sets.

The relative importance of each pair of factors is stated as fuzzy group decision making problem [5]. By using fuzzy agreeing method, the consensus of decision maker's opinions can be achieved. Handling of FAHP is performed by an approach which is introduced by [1]). This approach does not involve cumbersome mathematical operation, and it has the ability to capture the vagueness of human thinking style. In the literature, this approach is most widely used [6,7].

The software is based on the proposed a new fuzzy model.

The paper is organized in the following way. The section 2 describes the evaluation framework. A new software for determining the market validation of recycling equipment is proposed in Section 3. Conclusions are presented in Section 4.

2. EVALUATION FRAMEWORK

Results of good practice show that market validation of every piece of recycling equipment should be performed and have the strong influence on the economies of countries and environmental protection. Assessment of market validation for every piece of recycling equipment has to be observed as a separate and unique problem.

Step 1. In this step, management which leads to increasing costs, decreasing product quality team which assesses market validation of considered equipment is established. Generally, management team can be presented by index set $E=\{1...e...E\}$, where e is the index for decision maker while E is the total number of decision makers of management team.

Step 2. The software is defined into seven steps: (1) defining the business the strategy, competencies, business model and product concept, (2) defining of product context to entry the market, (3) identification of the leader in the area and positioning with respect to him, (4) defining key values for buyers, (5) testing of key values for buyer with respect to the competition, (6) defining the market strategy, (7) marketing strategy correction for product positioning.

Step 3. In this paper, the factors which influence to market validation of device for recycling oils are identified by management team. The identified factors are based on considered device performances. Each factor should be decomposed into many sub-factors. Formally, factors and their sub-factors are presented by set indices $I=\{1...i...I\}$, and, $J_i = \{1, \dots, j., , , J_i\}$, respectively. The index for identified factor and their sub-factor are denoted as *i* and *j*, respectively. The total number of identified factors and their sub-factors are presented by I and $J_i, i = 1, \dots, I$, respectively.

Step 4. All the identified factors which can lead to reduction of safety of equipment are usually not of the same relative importance. The assessment of the relative importance of identified factors is stated as fuzzy group decision making problem. The fuzzy pair-wise comparison matrix of the relative importance of factors is constructed. It is assumed that decision makers of management team have equal importance, so that the values of the elements of this matrix are obtained by fuzzy averaging method. By using the extent analysis method in [1], the weights vector of each identified factors is given. The relative importance of sub-factors under each identified factor are equal.

Step 5. All sub-factors are both quantitative and qualitative. The values of quantitative factors are measurable and presents by crisp numbers. The crisp values are given by measurement and using evidence data. The qualitative factor values are assessment by management team. It is assumed that management team makes decision by consensus in assessment values of device for recycling oils problem.

3. STEPS OF DEVELOPED SOFTWARE

In this Section, steps of the developed software are presented. The all steps are presented by GUI Screens (in further text only screens).

Step 1. Defining the business strategy, competences, business model and product concept. The information of this steps are: size of enterprise, annual profit, the share in total income from the new product income, number of employees on new product implementation, product's life cycle and investments in new product. The pieces of information of the second screen are: production capacity of full product, outsourcing potentials, development quality and product quality. The third screen contains the following pieces of information: knowledge and skills of product development employees, knowledge and skills of ICT sector, knowledge and skills in marketing, team work knowledge and skills, production knowledge and skills

Step 2. Cover the defining of the product context form market entry. The first screen of this step shows next pieces of information: product's name, price, capacity, reliability, competitiveness and selling rate. The second screen contains questions: Who, Why and Where buys.

Step 3. Cover the identification of leader in this area and making the position with respect to him.

Step 4. Cover the recognition of key values for a buyer. Key values for buyers are shown in Table 1.

Step 5. Cover the testing the key values with respect to competition from buyer's view.

The Algorithm of proposed fuzzy model is presented in the following.

Step 1. Calculation of aggregated values of the relative importance factor i, over factor i' by using the fuzzy averaging method:

$$\tilde{W}_{ii'} = \frac{1}{E} \cdot \tilde{W}^{e}_{ii'},\ i, i' = 1,..,I; i \neq i'; \quad (1)$$
$$e = 1,..,E$$

In this paper, the fuzzy rating of each pair of considered factors is described by all decision makers. Their assessment are represented as a TFNs $\tilde{W}^{e}_{ii'} = \left(x; l^{e}_{ii'}, m^{e}_{ii'}, u^{e}_{ii'}\right), i, i' = 1,...,I; i \neq i'$; $e = 1,..,E$ with the lower and upper bounds $l^{e}_{ii'}$, $u^{e}_{ii'}$ and modal value $m^{e}_{ii'}$, respectively.

Table 1. *Factors and their sub-factors*

Marketing factor (i=1)	**Factor of occupational safety and servicing (i=3)**
Lead time to customer (j=1)	Occupational safety level (j=1)
Rating market and production costs (j=2)	Maintainability (j=2)
Market entry velocity (j=3)	The possibility of using for different fluids (j=3)
Customer satisfaction level (j=4)	
Factor of environmental protection (i=2)	
Level of satisfaction of demands of environmental protection (j=1)	
The percent of materials which can be not recycled from recyclable materials (j=2)	
Reusability level of developed device (j=3)	

Step 2. Construct the fuzzy pair-wise comparison matrix of the relative importance of the factors:

$$\tilde{WF} = \left\lfloor \tilde{W}_{ii'} \right\rfloor_{IxI},\ i, i' = 1,..,I; i \neq i' \quad (2)$$

Step 3. Weights vector of the considered factors is calculated by applying the concept of extent analysis which is developed in [1]:

$$W = \left(w_1,..,w_i,...,w_I\right) \quad (3)$$

Step 4. Calculate the normalized crisp sub-factor values by applying the simple normalization procedure:

(a) for a benefit type sub-factors

$$r_{ij} = \frac{v_{ij}}{t^{*}_{ij}},\ j = 1,..,J_i; i = 1,..,I \quad (4)$$

(b) for a cost type sub-factors

$$r_{ij} = 1 - \frac{v_{ij} - v^{\min}_{ij}}{t^{\max}_{ij}},\ j = 1,..,J_i; i = 1,..,I \quad (5)$$

where $t^{\max}_{ij}, t^{\min}_{ij}$ is the target and the lowest value of crisp sub-factor j under factor i.

Step 5. Calculate the normalized uncertain sub-factor values by applying the modified linear normalization procedure [8]:

(c) for a benefit type sub-factors

$$\tilde{r}_{ij} = \left(\frac{L_{ij}}{U^{*}}, \frac{M_{ij}}{U^{*}}, \frac{U_{ij}}{U^{*}}\right),\ j = 1,..,J_i; i = 1,..,I \quad (6)$$

(b) for a cost type sub-factors:

$$\tilde{r}_{ij} = \left(\frac{L^{-}}{U_{ij}}, \frac{L^{-}}{M_{ij}}, \frac{L^{-}}{L_{ij}}\right),\ j = 1,...,J_i; i = 1,..,I \quad (7)$$

Where:

$U^{*} = U^{\max}_{ij}$, $j = 1,...,J_i$; $i = 1,..,I$

$L^{-} = L^{\min}_{ij}$, $j = 1,...,J_i$; $i = 1,..,I$

and L is the total number of linguistic expression which are defined for describing uncertain sub-factor values.

Step 6. Calculate the weighted normalized values of identified factors, $\tilde{C}_i$:

$$\tilde{C}_i = w_i \cdot \frac{1}{J_i} \cdot \sum_{j=1}^{J_i}\left(r_{ij} + \tilde{r}_{ij}\right) = \left(z; Li, M_i, U_i\right. \quad (8)$$

Step 7. Defining the market strategy

The first screen requires next information: buyer's profile, market trends and design. The second screen contains information about macro trends, the third about industrial trends and the fourth screen contains information about potentials about product placement.

Step 8. Strategy of marketing correction and product placement. This step is based on the results from the previous step.

4. CONCLUSION

In this paper, the software for market evaluation problem of equipment is treated. The proposed market validation factors are presented as well as constraints and the steps for assessment. The assessment uncertainties in the relative importannce factors and values some their sub-factors is based on fuzzy sets theory. The fuzzy approach is easy to understand and flexible as well as tolerant to imprecise data.

In the literature, there are almost no papers in which assessment market validation is performed in exact way. It can be said that the main contribution of this paper is the development of a mathematical model and software for evaluation recycling equipment with respect to market. Finally, marketing strategy lead to learn and improve of identified factors. The proposed model clearly identifies the weakest identified factors which should be the input for creating an enhanced business strategy in reverse logistic chain.

The general limitations of the model are the need for well structured factors.

Acknowledgment

This research is supported by the Ministry of Science and Technological Development, Republic of Serbia, Grant No 35033"Sustainable development technology and equipment for the recycling of motor vehicles".

REFERENCES

[1] Chang, D., Y., (1996). Applications of the extent analysis method on fuzzy AHP.*European J. of OperationalResearch*, 95 649-655.

[2] Babuska, I, Oden, J.T. (2004). Verification and Validation in Computational Engineering and Science: Basic Concepts. *Computer Methods in Applied Mechanics and Engineering* 193 (36-38), 4057-4066.

[3] Plant, R., Gamble, R. (2003). Methodologies for the Development of Knowledge-based Systems. *Knowledge Engineering Review* 18 (1), 47-81.

[4] Zimmermann, H.J., *Fuzzy set Theory and its applications*. Kluwer NijhoffPublising: Boston, 2001.

[5] Sadi-Nezhad, S., Damghani, K., 2010. Application of a fuzzy TOPSIS method based on modified preference ratio and fuzzy distance measurement in assessment of traffic police centers performance. *Applied Soft Computing*, Vol. 10, N0.4, 1028-1040.

[6] Seçme, Y.N., Bayrakdaroğu, Kahraman, C. (2009). Fuzzy performance evaluation in Turkish Banking Sector using Analytic Hierarchy 11709.Process and TOPSIS, *Expert Systems with Applications*, 36 11699-11709.

[7] Tadić, D., Gumus, T.A., Arsovski, S., Aleksić, A., Stefanović, M. (2013). An evaluation of quality goals by using fuzzy AHP and fuzzy TOPSIS methodology. *Journal of Intelligent & Fuzzy Systems*, 25, 547-556.

[8] Shih, H., S., Shyur, H., J., Lee, E.S. 2007. An extension of TOPSIS for group decision making. *Mathematical and Computer Modelling* 45 (7/8), 801-813.

Author Index

Evgenije Adžić 123, 127, 194
Aco Antić 115
Slavko Arsovski 227
N. Azis 218
Valentina Basarić 56
Bojan Batinic 147, 183
Levent Bayındır 175
Robert Bicker 163, 171
Bojan Bircanin 151
Vuk Bogdanović 52, 56
Apidet Booranawong 72
Branislav Borovac 80, 179
Gordana Broćeta 214
Vesna Bulatović 210, 214
Maja Čavić 44
Sakchai Chantasri 60, 68
Somyot Chirasatitsin 24, 28
Juntima Chungsiriporn 155
Zoltan Corba 202, 206
Andrew Davison 5
Maja Djogo 147, 183
Nikola Djukic 167
Đorđije Doder 187
Boris Dumnic 202, 206
Marin Gostimirovic 104, 151
Stevan Grabić 119, 127, 194, 206
Vojin Grković 198
Leposava Grubić-Nešić 115
Milana Guteša 198
Dušan Gvozdenac 17
Branka Gvozdenac-Urošević 198
Mohd Nizar Hamidon 221
W.Z. Wan Hasan 224
O. Hussein 224
Siti Azlida Ibrahim 221
Maryam Mohd Isa 221
M. T. Ishak 218
Alyani Ismail 221
Zoran Ivanović 119, 123, 127
A. Che Soh. H. Jafaar 224
J. Jasni 218
Nattha Jindapetch 72
M.Z.A. Ab Kadir 218
Kong Kamollertvara 40
Isoon Kanjanasurat 159
Siwarin Kanthik 21
Nenad Katic 206
Vladimir Katić 119, 123, 202, 206
Metawat Kavilkrue 135
Sommart Khamkleang 32
Witchakon Khuankaew 135
Tossapon Kijpitak 139
Kittipong Kimapong 64, 68
Jeerasuda Koseeyaporn 36
Milan Kostić 44
Pavel Kovac 104, 151
Srdjan Kovacevic 147
Dušan Kovačević 115, 179
Milovan Lazarevic 88
Warush Leekasem 48
Chaiwat Lersviriyanantakul 72
Chusak Limsakul 92
Zagorka Lozanov-Crvenković 100
Ivan Lukić 210, 214
Mirjana Malešev 131, 210, 214
Ildiko Mankova 104
Nikola Maodus 147
Manoon Masniyom 1, 21
Bojan Matić 100, 131
Milovan Medojevic 96
Dragan Milicevic 202, 206
Dusan Milovanovic 183

Author Index

Patchareerat Mitchorb 112
Slavica Mitrović 115
N. A. Mohamad 218
Igor Mujan 96
Paramin Neranon 163, 171
Jelena Nikolić 115
Milutin Nikolić 80
Emilija Nikolić-Đorić 100
Biljana Ratkovic Njegovan 76
Wasinee Noonpakdee 112
Gordana Ostojic 88, 167
Winai Ouypornprasert 40
Zoran Papić 52, 56
Parinya Pattanadech 1
Aleksandar Pavlović 227
Milan Pavlovic 84, 227
Marko Penčić 179
Milana Peric 96
Jovan Petrovic 96
Vladan Petrovic 151
Aumnad Phdungsilp 9
Pornchai Phukpattaranont 72, 92
Angkoon Phinyomark 92
Wanchai Pijitrojana 139
Monsak Pimsarn 143
Paitoon Poolsukho 60
Pramote Poonnayom 64
Bane Popadic 202
Vlado Porobić 119, 123, 127, 194
Denduang Pradubsuwun 48
Chaiya Praneetpongrung 60
Kawalin Prathomravee 155
Vladimir Pucovski 151
Franck Quaine 92
Miroslava Radeka 210
Vlastimir Radonjanin 131, 210, 214
Nebojša Radović 131
Saeed Rahmanian 221
Mirko Raković 80
Marjan Ranogajec 183
Milan Rapaic 194
Cheewarak Rodniam 24
Krzysztof Rokosz 151
Chonmaphat Roonnapak 5
Nenad Ruškić 56
Hassan Awadat Salem 100
Mahdee Samae 28
Nenad Saulić 52
Srđan Savić 80
Borislav Savkovic 104, 151
Milenko Sekulic 104
Arafat A.A Shabaneh 221
Milan Simeunović 52
Sakkarin Sinchai 36
Trirat Soemsap 108
Siniša Sremac 131
Jakkree Srinonchat 190
Srecko Stamenkovic 76
Nemanja Stanisavljevic 183
Stevan Stankovski 88, 167
Borivoj Stepanov 187
Danijela Tadić 227
Srdjan Tegeltija 88, 167
Branislav Tejic 167
Chaidiaw Thiangtham 190
Kanokpong Thongkorn 143
Sirinee Thongpanja 92
Aleksandar Tomović 84, 227
Danupon Tonnayopas 13
Suradej Tretriluxana 159
Dejan Ubavin 147, 183
Marko Vekić 119, 123, 127, 194

Author Index

Kasin Vichienchom 139
Bogdana Vujic 84
Paramote Wardkein 36
Wisitsree Wiyaratn 155
Mohd Hanif Yaacob 221
Z. Yaakub 218
Paiboon Yaemphuarn 64
Rapipat Yongmanee 13
R. Yunus 218
Zainab Yunusa 221
Miodrag Zivancev 183
Miodrag Zlokolica 44

Main sponsor